University of Cyprus

DEPARTMENT OF CIVIL AND ENVIRONMENTAL ENGINEERING

CHARACTERIZATION OF THE STRUCTURAL PERFORMANCE OF STRAIN-HARDENING FIBER REINFORCED CEMENTITIOUS COMPOSITES

ANTROULA GEORGIOU

A Dissertation Submitted to the University of Cyprus in Partial Fulfillment of the Requirements for the Degree of Doctor of Philosophy

May 2017

VALIDATION PAGE

Doctoral Candidate: Antroula Georgiou

Doctoral Thesis Title: Characterization of the Structural Performance of Strain-Hardening Fiber Reinforced Cementitious Composites

The present Doctoral Dissertation was submitted in partial fulfillment of the requirements for the Degree of Doctor of Philosophy at the ***Department of*** *Civil and Environmental Engineering and was approved on the 4th of May 2017 by the members of the* ***Examination Committee****.*

Examination Committee:

Research Supervisor:_____

(Name, position and signature)

Research Co-Supervisor:_____

(Name, position and signature)

Committee Member:_____

(Name, position and signature)

Committee Member: _____

(Name, position and signature)

Committee Member: _____

(Name, position and signature)

Committee Member: _____

(Name, position and signature)

DECLARATION OF DOCTORAL CANDIDATE

The present doctoral dissertation was submitted in partial fulfillment of the requirements for the degree of Doctor of Philosophy of the University of Cyprus. It is a product of original work of my own, unless otherwise mentioned through references, notes, or any other statements.

……..

Antroula Georgiou

ΠΕΡΙΛΗΨΗ

Η συνεχόμενη επέκταση του δομημένου περιβάλλοντος και η υιοθέτηση δυτικών προτύπων στον "αναπτυσσόμενο" κόσμο δημιουργούν νέα ζητήματα και ανάγκες σχετικά με την βιωσιμότητα του σκυροδέματος. Οι πρόσφατες εξελίξεις στο βιώσιμο και οικολογικά φιλικό δομικό σχεδιασμό έχουν οδηγήσει στην ανάγκη μείωσης των υλικών λατόμευσης (αδρανή), της περιεκτικότητας σε νερό του σκυροδέματος και του τσιμέντου στο οποίο οφείλονται οι εκπομπές CO2, και την αντικατάστασή τους με ανακυκλωμένα υλικά ή βιομηχανικά παραπροϊόντα. Μια από τις πιο ελπιδοφόρες προσπάθειες για την αειφόρο ανάπτυξη του σκυροδέματος είναι η χρήση της ιπτάμενης τέφρας (ΙΤ), ένα παραπροϊόν της βιομηχανίας ενέργειας που διαφορετικά καταλήγει σε χώρους απορριμμάτων δημιουργώντας πολλά περιβαλλοντικά προβλήματα. Όταν χρησιμοποιείται ως μερική αντικατάσταση του τσιμέντου (συνήθως 10-20%), η ΙΤ λειτουργεί ως ποζολάνη ενισχύοντας την ανθεκτικότητα και την αντοχή του σκυροδέματος σε βάθος χρόνου.

Στην παρούσα μελέτη η χρήση της ΙΤ πραγματοποιείται σε ασυνήθιστα υψηλά επίπεδα αντικατάστασης του τσιμέντου της τάξης του 60%. Τα χονδρόκοκκα αδρανή εξαλείφονται και το τσιμεντοειδές υλικό που προκύπτει είναι ενισχυμένο με συνθετικές ίνες που ενισχύουν την αντοχή σε συρρίκνωση και εφελκυσμό, όπως επίσης και την ικανότητα παραμόρφωσης. Το αποτέλεσμα είναι ένα πραγματικά καινοτόμο τσιμεντοειδές υλικό με εντυπωσιακή ολκιμότητα σε εφελκυσμό, που διατηρεί την εφελκυστική του αντοχή σε τιμές παραμορφώσεων μέχρι και 200 φορές μεγαλύτερες από την ικανότητα παραμόρφωσης του κανονικού σκυροδέματος. Με σχετική επικάλυψη των ινών ελέγχεται η συνεργασία των ινών με την τσιμεντούχα μήτρα, βελτιώνοντας έτσι αποτελεσματικά και την ικανότητα παραμόρφωσης του υλικού και τον τρόπο αστοχίας του σκυροδέματος.

Η διαθεσιμότητα αυτών των νέων τσιμεντοειδών υλικών με ολκιμότητα σε εφελκυσμό είναι μια ευκαιρία για την ανάπτυξη εναλλακτικού σχεδιασμού των κατασκευών σκυροδέματος που θα εκμεταλλεύεται την αυτογενή περίσφιξη που παρέχεται από τις ίνες επιτρέποντας σημαντική οικονομία στην χρήση των εγκάρσιων οπλισμών χάλυβα, για πιο ανθεκτικές και βιώσιμες κατασκευές. Ωστόσο, προκειμένου να ενσωματωθούν στους σύγχρονους κανονισμούς υπάρχει μεγάλη ανάγκη για τον προσδιορισμό των ιδιοτήτων αυτών των νέων τύπων σύνθετων υλικών. Στην παρούσα διατριβή, η οποία περιλαμβάνει αναλυτική και πειραματική διερεύνηση, η έμφαση δίνεται στο χαρακτηρισμό της συμπεριφοράς αυτών των τύπων σύνθετων υλικών υπό εφελκυσμό, θλίψη, κάμψη, διάτμηση, συνάφεια ράβδων χάλυβα αγκυρωμένων σε μήτρες όλκιμων τσιμεντοειδών υλικών καθώς επίσης και δομικών μελών που υπόκεινται σε ανακυκλιζόμενη ένταση. Προτείνονται βαθμονομημένες πειραματικές μέθοδοι χαρακτηρισμού αντοχής / ικανότητας παραμόρφωσης και κατάλληλα συσχετισμένα προσομοιώματα της μηχανικής συμπεριφοράς του υλικού προκειμένου να υποστηρίξουν συστάσεις σχεδιασμού για δομικά μέλη που υποβάλλονται σε πολύπλοκες εντατικές καταστάσεις. Τα πειραματικά αποτελέσματα χρησιμοποιούνται επίσης για τη βαθμονόμηση των παραμέτρων που χρειάζονται για μη γραμμική

προσομοίωση με χρήση πεπερασμένων στοιχείων δομικών μελών που κατασκευάζονται από όλκιμα τσιμεντοειδή σύνθετα μείγματα. Από τις δοκιμές φαίνεται ότι σε περιπτώσεις όπου η ρηγμάτωση πραγματοποιείται με σχηματισμό ενός μεγάλου δικτύου λεπτών ρωγμών (δηλ. κατανεμημένης μη-γραμμικότητας), το υλικό επιδεικνύει γενικά ανώτερη συμπεριφορά. Αυτά τα ευρήματα υποδηλώνουν ότι είναι εφικτή η κατασκευή μιας νέας γενιάς τσιμεντοειδών υλικών, όπου η αντοχή εφελκυσμού και η ικανότητα παραμόρφωσης είναι τόσο υψηλές ώστε να παρέχουν ένα εντελώς διαφορετικό πλαίσιο για τη διαμόρφωση της μηχανικής συμπεριφοράς του σκυροδέματος και επακολούθως των λεπτομερειών όπλισης. Επιπρόσθετα η βελτιωμένη απόδοση μπορεί να οδηγήσει σε μικρότερες διαστάσεις δομικών μελών, μείωση της ποσότητας χάλυβα οπλισμού ιδιαίτερα για την περίπτωση της διάτμησης και περίσφιξης, διευκολύνοντας έτσι τις κατασκευαστικές και ενεργειακές απαιτήσεις.

ABSTRACT

With the increasing development of the built environment and the trend in the developing world towards a consumer-driven lifestyle, the question of concrete's sustainability gains a new perspective. The recent developments in sustainable and ecologically friendly design of structures has led to the need for reducing materials extracted from the earth (aggregates), water content of concrete and cement that produces CO_2, and replacing them with recycled materials or industrial byproducts. One of the most promising attempts for the sustainable development of concrete is the use of fly ash (FA), a byproduct of the energy industry that otherwise ends up in wastelands creating lots of environmental problems; when used as partial cement replacement (usually 10-20%), FA functions as a pozzolan enhancing the durability and long term strength of the end product.

In the present study the use of FA is taken to unusual levels of cement replacement in the range of 60%. Coarse aggregate is eliminated and the resulting cementitious material is reinforced with synthetic fine-diameter fibers to enhance shrinkage and tensile strength and deformation capacity. The result is a truly innovative cementitious material with impressive ductility in tension, which sustains its tensile strength up to strains that are 200 times greater than the cracking strain of normal concrete; through pertinent coating of the fibers the compliance of their bond-slip behavior in the cementitious matrix is controlled thereby effectively controlling the deformation capacity and mode of failure.

The availability of novel cementitious materials with ductility in tension is an opportunity for the development of alternative designs of concrete structures that take advantage of the autogenous confinement provided by the fibers enabling significant economy in the use of transverse steel reinforcement, for more durable and sustainable structures. However, in order to incorporate these materials in modern codes there is an outstanding need to determine the properties of these new types of composites. In the present thesis, which includes both analytical and experimental components, the focus is placed on the characterization of the behavior of these types of composites under tension, compression, flexure, shear, as well as of the bond mechanism of steel bars embedded in strain hardening structural members and their response under reversed cyclic loading. A number of test procedures and strength / deformation capacity models are proposed through calibration with experimental results in order to support design recommendations for structural members subjected to complex states of stress. The experimental results are also used to calibrate the parameters for advanced nonlinear finite element modeling of structural components made of strain-hardening cementitious composites. From the tests it was seen that in cases where cracking behavior was marked by the formation of a large network of fine cracks (i.e., distributed nonlinearity), a superior overall material toughness was obtained. These findings suggest that a whole new generation of cement based materials is possible, where tensile strength and strain capacities are so high that they provide a totally different context for the formulation of concrete

mechanics and consequent reinforcement detailing. Additionally this improved performance can lead to more slender member dimensions, reduced amounts of steel reinforcement particularly for shear and confinement, easing construction effort and energy requirements.

Acknowledgements

The research reported in this thesis was undertaken in the Department of Civil and Environmental Engineering, University of Cyprus, under the overall guidance of Professor S. J. Pantazopoulou.

I wish to sincerely thank Prof. S. Pantazopoulou, the supervisor of this project, for her invaluable help and constant encouragement. Professor Pantazopoulou was not only present and helpful at every step and difficulty of this Thesis, but also she was an inspiration. Other than her help in providing the necessary funding, her assistance in performing the experimental program, the experiences she assured I was provided with by participating in multiple conferences and the knowledge I was transferred by being her assistant in various lectures at the Department of CEE are a valuable asset that I will carry with me through the rest of my life. The helpful advice given by the co-supervisor Prof. M. Petrou, and the assistance given by Prof. I. Ioannou are also gratefully acknowledged.

Thanks are extended to the technical staff of the Department of Civil and Environmental Engineering, for their assistance in the experimental program. Additionally, thanks are due to Special Scientist Dr. Nikos Archontas, PhD Candidate Periklis Savva, PhD Candidate Anthos Ioannou, MSc student Vasilis Loizou for their assistance for mixing and casting of the specimens.

The financial assistance provided by the University of Cyprus through a six-month scholarship under the program “New Researchers” is greatly appreciated. Additionally I would like to thank Emily Tsirides and the Company Tsircon for their assistance in providing the various coating materials used for this research and Kuraray Europe for providing part of the PVA fibers used in the experimental program.

Finally, I wish to express my sincere gratitude to my family for their constant encouragement and understanding.

to my mother and father

Table of Contents

List of Figures

List of Tables

Chapter 1: Introduction

1.1 Objective

A disadvantage of conventional concrete is its low flexural strength and ductility in tension. Cementitious materials are very brittle in tension demonstrating abrupt loss of resistance in the cracked direction upon formation of a crack. Brittleness is considered an inherent trait of cement hydrates owing to the amorphous nature of the material microstructure, where hydrates are held together through weak van-der-Waals bonds. Crack is thought to initiate internally (in the gel structure) during hydration, even prior to the application of any external load; cracking concentrates particularly at the point of contact between gel and aggregates due to the unilateral growth of binding, but it is also owing to the stress concentrations created in the gel around the aggregates due to different material stiffness. Apart from disrupting the path of stress transfer, cracks cause numerous durability problems behaving as effective capillary pores. The effects on durability are compounded by the free ingress (through the cracks) of agents that are needed to initiate chemical processes such as carbonation and chloride-induced loss of alkalinity in concrete promoting corrosion of concrete and reinforcement. When many microcracks align to form a larger crack then the tensile strength is lost normal to the crack path and no load may be transferred beyond that point across the crack.

The addition of fibers to enhance the tensile and flexural capacity of structural materials through crack control is an ancient idea that is now spearheading novel developments in the area of high-performance cementitious materials. In ancient times it was customary to use organic fibers (from straw or wool) in mud bricks and lime-mortars thereby enhancing their resilience and strength. Fibers, if bonded properly, can bridge cracks and enable load transfer, thereby delaying brittle failure; in hybrid mixes which contain different sizes of fibers these phenomena may occur at several different scales of the material structure where each fiber length type is effective so long as the crack length is less or within the same order as the fiber length; a fiber type is rendered inactive when the crack length and width of the process zone bypass and exceed the fiber size. In the context of reinforced cementitious materials containing only a single fiber type, structural performance in the ultimate limit state requires steel reinforcement to control run-away cracks that have propaged to lengths that bypass the length of the individual fibers. Damage of concrete is a phenomenon marked by uncontrolled expansion in the directions of tensile stress, i.e., orthogonal to compression, whereas failure ocassionally is quantified by effective Poisson's ratios that exceed the limit of incompressibility. However, with the addition of fibers the dilative behavior of concrete enduring damage is improved dramatically; the reduced rate of expansion effected by the fibers is equivalent to the action of confining lateral pressure in common concrete – splitting failures are suppressed also, and generally this phenomenon is known as a "confining effect" induced by fibers.

At the same time, through proper mix design, stress concentrations may be minimized by eliminating any form of coarse aggregate from the cementitious mix design. Lack of coarse aggregates is deprecating to familiar secondary strength mechanisms known collectively as "aggregate interlock" – but the compensation is that denser packing is achieved in the material microstructure which promotes reduced capillary pores and pore connectivity for the benefit of corrosion resistance and durability. Nevertheless, the behavior effected by fine aggregate may be enhanced even further when combined with pertinent admixtures or cement-replacing additives that moderate the heat of hydration and ensuing shrinkage.

Figure 1.1: Various types and geometries of fibers.

Currently, the state of the art is focused on the use of synthetic fibers in self-consolidating, fine-aggregate cementitious mixes that demonstrate strain hardening properties in tension, outstanding crack control and improved durability performance. Fibers used are of different shapes, material and/or composition. Most popular till now are metal fibers, polyvinyl-alcohol (PVA) fibers, polypropylene (PP), UHMW polyethylene (PE) and carbon-fibers (shown in Fig. 1.1). Fiber dimensions vary ranging from a few millimeters to very small sizes in the order of micrometers. Recognizing that mass reinforcement is used to effect an increase in tensile strength and deformation capacity, today fiber reinforced cement composites (FRCC) are classified according to their mechanical performance in tension. Thus, they are distinguished in strain softening and strain hardening materials as depicted in Figure 1.2. Strain softening fiber reinforced cement composites (SHFRCC) are classified further according to their response in bending to deflection-hardening or deflection-softening [1].

The term "Strain softening" means that deformation is localized at a single crack and in the process zone surrounding it. In the case of "Strain hardening", deformation occurs within multiple parallel fine cracks with elastic stretching of the material between them, as shown in Fig. 1.3. The Engineered Cementitious Composites (ECC) is a special category of strain hardening FRCC that has a typical axial tensile strength of 4 to 6 MPa and an axial tensile strain capacity of 3-5% ([2], [3]).

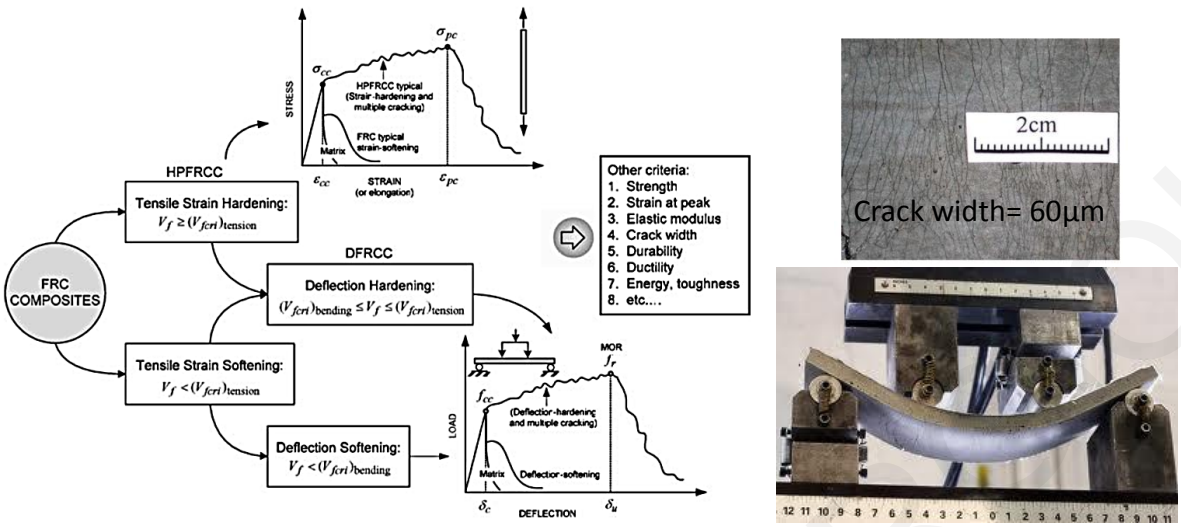

Figure 1.2: Classification of FRC composites based on their tensile stress-strain response [1].

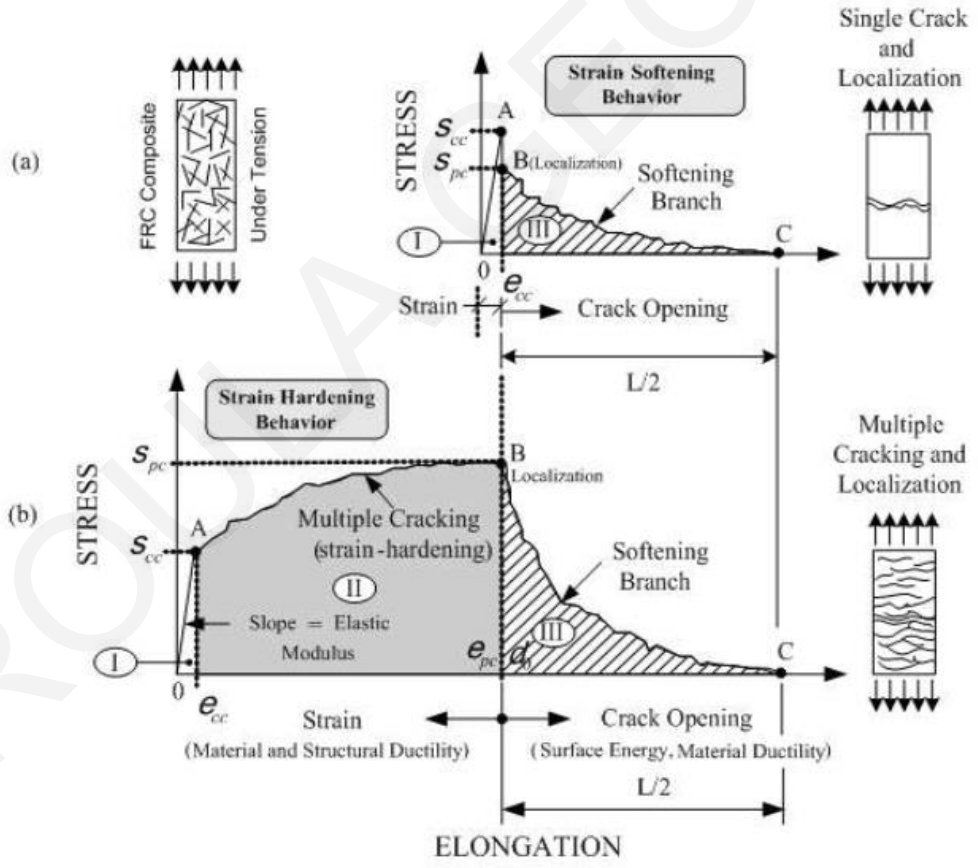

Figure 1.3: Typical stress-elongation curves in tension of fiber reinforced cement composites [4]

A critical feature of the material for securing very large strain capacity is the requirement that the process of cracking stabilization be delayed or even be entirely avoided, so that multiple rather than localized cracking may develop for a large range of the plastic domain of the response (note that the

term crack localization refers to the point when new cracks cease to form with increasing load, but rather, the existing cracks begin to widen). Currently, the state of the art in research revolves around the use of short discontinuous fibers in self-consolidating, fine-aggregate cementitious mixes. The objective is to enhance the composites' flexural strength, ductility and toughness and furthermore to limit the width of cracks thereby eliminating further deterioration due to environmental effects. Each type of fiber develops a different type and intensity of binding with the surrounding matrix and the final product´s characteristics are greatly affected by this property, referred to hereon as *specific bond*. In the present investigation, preliminary tests on two types of fibers have been used, namely, PP and PVA fibers. All PP fibers have a hydrophobic surface while the PVA fibers are characterized by a hydrophilic surface.

When mixed in concrete the two types of fibers demonstrate completely different behaviors. The PP fibers develop no chemical bonding with the surrounding concrete and a very low contact friction due to their hydrophobic surface, contrary to the PVA fibers which are hydrophilic and display high chemical bonding to the cement hydrates (due to a very large number of free hydroxyls on their surface). This is the reason why if used in the same matrix design in equal fractions, the effect and contribution of the two fiber/specific bond types will be different.

Preliminary experimental data from sample Modulus of rupture tests were conducted to establish the achieved material toughness. It was found that PVA fibers alone increase greatly the tensile strength of the matrix but produce solids with a limited strain capacity. Strong bonds created between the free hydroxyl groups on the fiber's surface and the matrix, lead to brittle rupture of the fibers and interfacial strength that is increasing with time. This guided the research into an attempt to alter the mode of failure from fiber rupture to partial pull-out failure, achieved by controlling the specific bond through surfactants, i.e., by coating the surface of the fibers with different kinds of agents at different mass ratios. From the tests it was seen that in cases where cracking behavior was marked by formation of a large network of fine cracks, a superior overall material toughness was obtained. These preliminary findings suggest that a whole new generation of Cement based materials is possible, where tensile strength and strain capacities are so high that they provide a totally different context for formulation of concrete mechanics and consequent reinforcement detailing.

The aim of the present research was to develop Strain Hardening Fiber Reinforced Cementitious Composites (SHFRCC) with high fracture toughness that could be exploited in the precast Industry in the future in Cyprus using local materials and to characterize the material's performance in direct tension, compression and shear with reference to both the primary and the secondary mechanisms of resistance, as well their interaction with steel reinforcement with regards to the bond-slip properties effected in the presence of fiber confining effect. As many of these effects and in particular the large deformation capacity, ductility and toughness are of particular interest in seismic performance, it was

also deemed relevant to examine the behavior of these materials when used as matrix in larger scale structural elements under static or cyclic behavior (the scale of the experiments being to a great extent determined by the size of the available testing frame). The development of such composite materials will give multiple advantages in the field of construction, widening the area of capabilities for innovative cement-based products and will enable the development of effective rehabilitation solutions to durability problems encountered in existing structures due to the adverse environmental conditions on the island.

Looking at the problem from the angle of sustainability it is relevant to note here that the construction industry is one of the biggest polluters of the planet. From the extraction and use of raw materials, the construction of structures, the operation and maintenance up to their demolition, the construction industry is responsible for high energy consumption, pollution, creation of 5% of the global CO_2 emissions and a general ecological waste generation and land and resource depletion. After the 1987 UN summit, "sustainable development" was defined as a new target goal engaging countries in "meeting the present needs without compromising the ability of future generations to meet their needs". Sustainability in construction should incorporate elements of economic efficiency, environmental performance and social responsibility by following two distinct paths: use of novel and waste materials and long-term structural performance and durability. Towards this path, the mechanical properties of SHFRCC for construction are examined for fulfilling the above requirements. This type of material made with hybrid Polyvinyl Alcohol Fibers if used with high amounts of fly ash (>60% of cement replacement), exhibits advantageous mechanical properties in terms of very large tensile strain capacity and ductility and could be considered the future of sustainable cement based construction. The challenge that remains is to establish design rules and analysis procedures or expanding those available for conventional structures, so as to promote the use of sustainable materials in the upgrading and recycling of the existing building environment but also for new constructions.

The availability of cementitious materials with ductility in tension is an opportunity for the development of alternative designs that enable significant economy in steel reinforcement, for more durable and sustainable structures. However, to incorporate these materials in modern codes there is an outstanding need to determine the mechanical properties of these new types of composites. In the present research, which includes both analytical and experimental components, the focus is placed on the interpretation of the behavior of these types of composites under various loads such as tension, compression, flexure and direct shear (push-off tests); this is a first step into drawing design recommendations for structural members subjected to complex, real-life states of stress.

1.2 Structure of the thesis

Other than a small introduction to the use of fibers in cementitious composites made within this chapter, the 2nd Chapter of this thesis includes a more thorough review of Strain Hardening Fiber Reinforced Cementitious Composites (SHFRCC) with PVA fibers and/or high volume fly ash as cement replacement, based on bibliographic research. The formation of multiple cracking due to the pull-out failure of the fibers and the influence of the interfacial bond between the fibers and the matrix is approached as a parameter influencing the ductility of the composite in tension.

In the 3rd Chapter a preliminary experimental investigation on the influence of the interfacial bond properties on the compressive and flexural performance of fiber reinforced cementitious composites is examined. Towards this research four different types of coating agents with various percentages per weight of fibers were applied on PVA fibers that were later used to produce small scale prismatic specimens which were tested under flexure and compression at various ages. This procedure was used to decide on the final mix that would later be used for structural components under various mechanical loads.

In Chapter 4 the experimental research program is described in detail. The various mix designs that were used for each casting along with the specimens that were produced are presented in detail. Study variables of the mix designs are the length of the PVA fibers (8 and 12 mm) and the surface conditions of the fibers, by using plain or coated fibers. Test specimens dimensions and procedures are described in detail. The tests that were adopted were direct tension, compression, splitting, three point bending, four point bending on small scale beams with various shear span aspect ratios, push off tests, small scale beams under four point bending with steel reinforcement (longitudinal and/or transverse), pullout tests and large scale steel reinforced members under reversed cyclic loading. The testing setup, displacement control rate and measuring equipment are also described.

Various methods are proposed from Standards and researchers such as the uniaxial tensile test, the splitting test, the three and four point bending tests for determining through reverse engineering the uniaxial tensile stress-strain curves of FRC. Due to the difficulty in conducting uniaxial tensile tests most Code provisions use indirect methods in determining the tensile σ-ε curves of cementitious materials. In Chapter 5 the results obtained from four different methods (direct tension, splitting, three point bending and four point bending) are compared to each other. Additionally an inverse analysis procedure is proposed for determining indirectly the tensile σ-ε curve from bending tests, taking into consideration the shear span length of the prisms used for the test.

The compressive capacity of concrete is related to its lateral expansion. The cracks that form parallel to the compressive stresses are responsible for failure. The use of fibers in the cementitious matrix shows improvement in the compressive response, since fibers crossing the cracks resist lateral expansion. In Chapter 6 the results from SHFRCC samples under compression are compared with

specimens of the same matrix without fibers confined with well known methods such as stirrups or FRP sheets.

In Chapter 7 the flexural response of small scale beams made of SHFRCC with deformed steel bars is investigated. The use of the SHCC increases the Moment capacity of beam members due to the contribution of fibers bridging the cracks in the region of the beam under tension. Analysis of the beam's cross section with layers gives the Moment-curvature diagrams specifying the characteristic points of the behavior. The analysis is then used to extract closed-form equations that can be used to establish the flexural strength of R/SHFRCC members for design purposes.

The shear strength of R/SHFRCC beams containing no steel reinforcement, and then with longitudinal and longitudinal/shear reinforcement is investigated in Chapter 8. Experimental results of beams with different shear span ratios are used indicating the increased shear resistance due to the action of the fibers bridging the cracks. The known strut and tie model method is used to determine the failure load of the beams by taking into consideration the tensile contribution of the fibers giving a good approximation of the experimental results. Also a new approach for the determination of the shear strength of members with flexural reinforcement is established by connecting the bond capacity of the longitudinal bars to the shear strength of beams. Additionally push-off tests are described in the chapter as means to determine the shear strength without the influence of bending moments occurring in the cross section.

The interfacial bond-slip law between deformed steel bars and SHFRCC is investigated in Chapter 9. The experimental results of steel bars of two different diameters and multiple embedment lengths and covers are used to determine the beneficial influence of a strain hardening composite to the bond-slip law due to the confining effect of the fibers. The results are then compared to Code provisions for determining the bond-slip design values.

In Chapter 10 the behavior of SHFRCC large scale members under reversed cyclic loading with the minimum shear reinforcement is compared to that of properly designed members based on the provisions of Eurocode 8 Part 1 [5] for Medium Ductility Class (DCM). The beneficial action of the confining effect of the fibers is investigated based on the resilience and toughness demonstrated by the specimens, the ductility of the members as well as the energy absorption in the full cycle reversals.

Finally in Chapter 11 Nonlinear Finite Element Modeling (FEM) of various specimens from the experimental program was performed in an advanced Finite Element Simulation platform [6]. Due to the strain hardening properties of the composites in tension the Concrete Damage Plasticity model was used for the SHFRCC material. Calibration of the Plasticity parameters was first performed by using the uniaxial tension and compression experimental results and afterwards those models were used to simulate the small scale beam members, with or without steel reinforcement.

Chapter 2: Review on fiber reinforced composites, use of fly ash as cement replacement and structural performance of SHFRCC

Fiber reinforced cementitious composites with strain hardening behavior in tension is a new type of cementitious material that overcomes the inherent brittleness of cementitious materials in tension exhibiting postcracking resilience and impressive tensile deformation capacity. The first efforts to develop materials with these types of characteristics begun in the 1990s, however the scaling-up of this technology is still not fully matured. Nevertheless, strain-resilient cementitious materials are considered as the future of concrete construction in that they open up the prospects for several innovative solutions and opportunities that may enhance ductility at ultimate limit states and durability and service life performance of structures. Normal concrete behaves in a brittle manner and the development of design procedures for reinforced concrete structures has been driven by the need to supplement reinforcement so as to make up for the deficiency in tensile strength of concrete beyond cracking. However, for this new type of material to be used in construction, a lot remains to be done in the direction of certification, proof testing and establishment of essential supporting evidence in the form of experimental and analytical results regarding repeatability and dependability of its mechanical behavior. In this Chapter a summary of the state of the art on Strain-Hardening Cementitious Composites (SHFRCC) is presented, including a critical overview of the design practices proposed in the bibliography.

2.1 Strain Hardening Fiber Reinforced Cementitious Composites

Crack formation in cementitious materials begins internally during hydration, even prior to the application of any external load due to internal mechanisms such as convection of pore water, bleeding, plastic settlement, thermal and shrinkage strains and stress concentrations imposed by external restraints. It proliferates particularly at the contact between gel and aggregates as this is a region of weakness due to the unilateral growth of binding, and is owing to stress concentrations due to different stiffness of the materials in contact. Under applied load the distributed micro cracks progress and align preferably in directions orthogonal to principal tension, producing macro cracks. Upon further loading cracks reach a critical width that results in unstable and catastrophic propagation of failure.

The result is a brittle response in tension marked by macroscopic cracking at tensile strains as low as 0.1-0.2‰. Owing to this, the established design procedures neglect the contribution of concrete to strength mechanisms that rely on the tensile resistance of the material. However, mass embedded reinforcement provided in the form of fibers, can bridge the cracks and sustain tensile load transfer up to high levels of deformation, thereby delaying or mitigating brittle failure. A variety of fibers have been used comprising different shapes, materials and/or composition. Thus, apart from steel and

natural fibers, several alternative synthetic fibers have been shown to produce favorable characteristics (e.g. polyvinyl-alcohol – PVA, polypropylene - PP, polyethylene – PE, and carbon –CF fibers). The fibers' diameter range from millimeters down to few micrometers whereas their aspect ratios range from less than 10 to values in the several hundreds. Cocktails of fibers of different lengths and consistency have also become popular in the context of functionalized materials, each fiber type being effective in a different range of material deformation. So, finer shorter length fibers operate in a small geometric scale, and when flaws overcome their range of applicability, they still serve to confine the anchorage of the next fiber size in the material geometric scale.

An exciting prospect in the advent of fiber-reinforced cementitious composites (FRCC) is the development of strain-resilient materials that may sustain adequate tensile strength up to high levels of deformation through the addition of a pertinent type and amount of mass reinforcement in properly designed cementitious mixes. Based on the macroscopic mechanical behavior of FRCs in direct tension they are classified as strain softening (SSCC) and strain hardening materials (SHFRCC) [1], [7]. Strain softening means that deformation is concentrated at a single crack and in the area around it. In the case of strain hardening, deformation occurs within multiple parallel fine cracks with elastic tensile deformation of the material in between.

Resilience of the material in tension depends to a great extent on the type and intensity of binding between the fibers and the surrounding matrix. This property is referred to as *specific bond*. For example, PP and PE fibers develop no chemical bonding with the surrounding concrete and a very low contact friction due to their hydrophobic surface whereas steel fibers need mechanically induced anchorage in order to transfer stresses. In the present Thesis, research is concentrated on PVA fibers, whose special characteristic is the fiber's hydrophilic surface (due to a very large number of free hydroxyls on their surface) which displays high chemical bonding to the cement hydrates. This aspect offers a vehicle for moderation and control, through proper surfactants, of the specific bond values.

By adding short, randomly distributed fibers the process of fracture can be modified. Fibers suppress the formation of cracks and their propagation and growth. After casting, the mix water evaporation and autogenous process of concrete hydration causes shrinkage strains which if restrained can result in excessive endogenous stress and cracking. This is a serious concern especially on large-area surface placements. Fibers in this occasion can engage water in the mix and reduce bleeding and segregation [8]. In the hardened state if fibers are properly bonded they interact with the matrix, at the level of micro cracks, and bridge the cracks providing stress transfer and delaying the crack growth. After the peak tensile capacity is reached fibers continue to restrain macro-crack opening.

The most important capability of fiber reinforced concretes (FRCs) is their "toughness" or energy absorption. The fiber pull-out mechanism is one of the parameters determining the final toughness index of the material, and as such, it is therefore of great importance. Interfacial debonding between

fiber and the matrix interface commence at the fiber entry and propagates towards the free end of the fiber thereby absorbing mechanical energy. Today it is common practice to enhance fiber bonding with the surrounding matrix usually by means of proper surface deformation (relief) of the fibers, although if excessively anchored, fibers may develop stresses that exceed their strength and fracture in the process. In that case energy absorption is limited by the anchorage failure of the fiber mechanism. Therefore the most effective exploitation of the fiber system would be to aim for a pull-out failure of the fibers occurring at a fiber stress close to - but lower than its tensile strength.

The description of a fracture model in the case of a strain hardening material is more complex than the classic brittle materials where fracture can be completely defined by a single parameter, the tensile strength at fracture. Fiber bridging occurs behind the tip of a propagating crack where fibers that intersect the crack-path undergo bond-slip processes and provide additional closing pressures. Attempts have been made to model fracture in FRC using the J-Integral method as proposed by Marshall and Cox [9]. However this is only a crack initiation criterion that fails to define conditions of continued crack growth.

In Strain Hardening Fiber Reinforced Cementitious Composites (SHFRCC) various types of fibers may be used. The fiber's type can vary thereby affecting the minimum volume fraction required for strain hardening behavior. It was shown that in the case of PVA fiber composites, ductility may be enhanced with a surface treatment reducing the bond properties [10] due to their hydrophilic surface properties (details of the PVA fibers chemical structure is provided in detail in Par. 3.2.4). Quite to the contrary, the PP, or PE fibers require increase of the frictional bond (roughening of the lateral surface by exposing the fibers to strong corrosive chemicals [11]) along with fiber strength for the same results. SHFRCCs experience plastic deformation with increasing stress transfer at which multiple cracks develop. These crack widths increase from 0 to 60 μm for an average strain up to 1% and then – according to the available experimental reports - the crack width remains constant through the whole plastic phase, until the peak load is reached. Localization of deformation in a single crack ensues, with the composite experiencing strain softening behavior beyond that point.

Numerous attempts have been made using the PVA fibers as provided by the manufacturers but the results have shown significantly low tensile strain capacities in the order of 0.5-1% even with amounts of fibers higher than 2% [10]. The PVA fibers tend to develop very strong chemical bonding with cement due to the presence of hydroxyl group in its molecular chains. This high bonding leads to fiber rupture and therefore eventually impacts negatively the resulting tensile deformation capacity of the composite [12]. A strong slip-hardening response during fiber pullout was observed to cause shear delamination failure of the PVA fiber [13].

The bond characteristics of the contact surface between fibers and matrix depends both on frictional resistance and chemical bond. The latter represents the requirement for a certain nonzero force to act

on the fiber-matrix interface before the interfacial chemical bond may be broken. Thus, some extent of debonding is needed to allow for deformation of the debonded fiber segment to produce a crack opening δ [10]. Figure 2.1 shows the progressive damage of the fiber as it is pulled out of the matrix when no surface coating is applied [10].

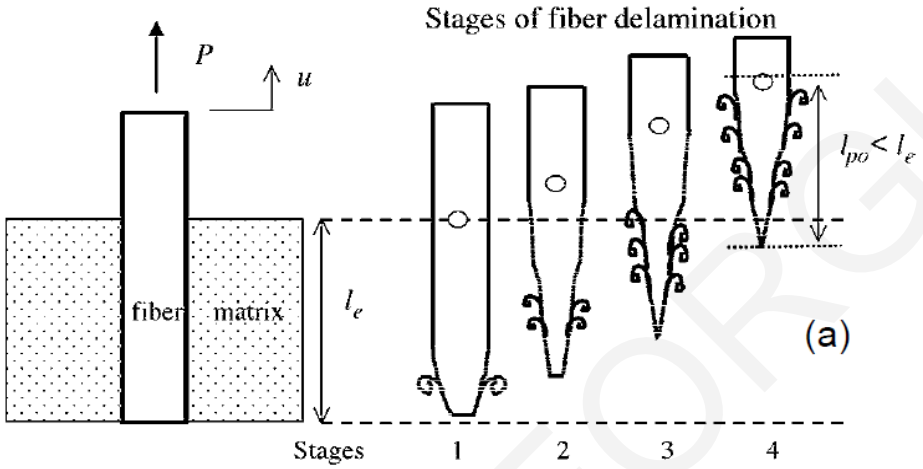

Figure 2.1: Fiber delamination during slip hardening [10]

In experimental research conducted by Li et al. [14] it was found that the interface resistance was gradually reduced by increasing the amount of oiling agent on the fibers, while the type of oiling is not provided. Figure 2.2 shows the decreasing values of frictional bond τ_o and chemical bond G_d as a function of oiling agent content, measured in single fiber pull-out tests, as well as the target values determined theoretically. The plot suggests that oiling agent contents in excess of 0.6-0.8% would be needed to achieve strain-hardening.

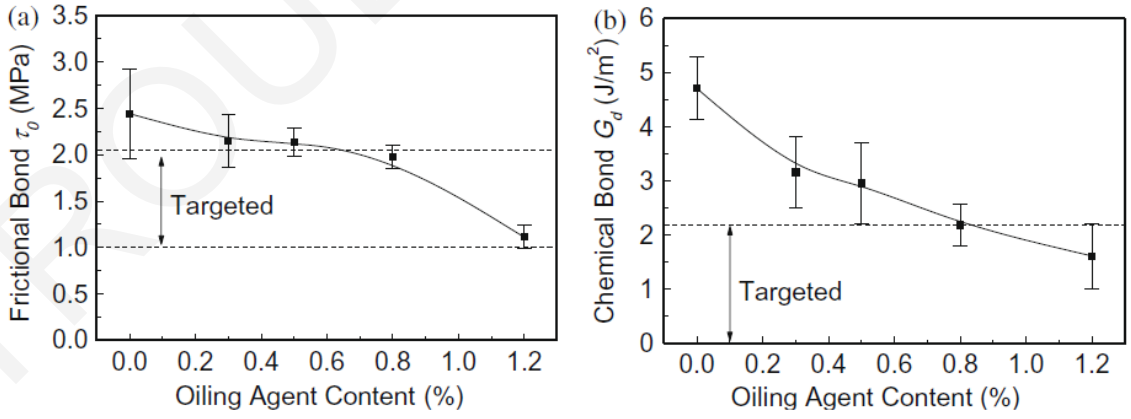

Figure 2.2: Effect of coating content on interface: (a) frictional bond and (b) chemical bond [14]

Composite dog-bone tensile tests using the same fiber and the same five levels of oiling content (same with those in Fig. 2.2) reveal that the tension strain capacity was enhanced from less than 1% to more than about 5% (Figure 2.3) when increasing the coating of the fibers from zero to 1.2% per weight of fibers.

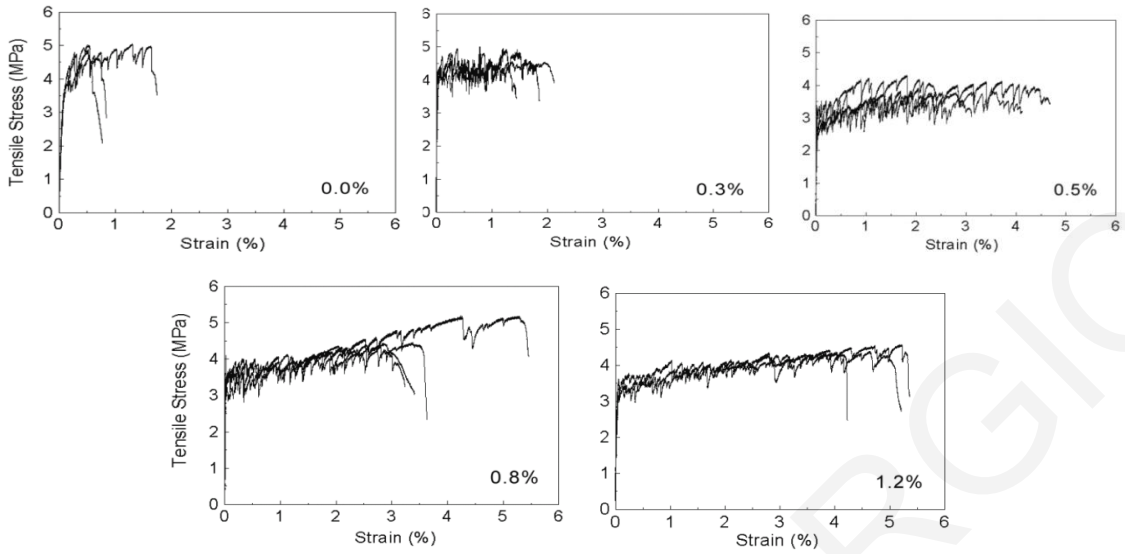

Figure 2.3: Deformability of the composites as a function of "oiling agent" content [14]

The tensile strain capacity and multiple crack spacing as a function of "oiling-agent" content are shown in Fig. 2.4. It is clear that the composite reaches multiple crack saturation when the oiling content reaches about 0.6-0.8% as expected. The concepts for strain-hardening condition have been validated by at least two studies involving SHFRCC (also referred to in the literature by the generic term Engineered Cementitious Composites or ECC) mass reinforced with PE and PVA fibers. Li et al. [15] studied the transition from quasi-brittle to ductile behavior for a set of composites reinforced with PE fibers. They varied the sand content in the matrix, which directly influenced the matrix toughness and the interface properties.

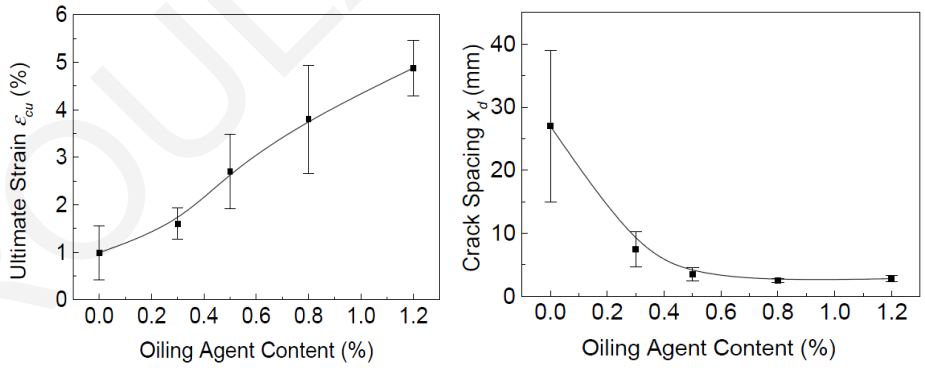

Figure 2.4: Tensile strain capacity and multiple crack spacing as a function of oiling content [10]

The above discussions reveal that the design strategies for PE-ECC and PVA-ECC are very different. For the PE fiber with very high tensile strength and low bond properties, enhancing the interface bond strength leads to strain-hardening. An attempt to increase bond strength of PE fibers using plasma treatment process was pursued by Li et al. [16], resulting in composites with tensile strain capacity of up to 7%. In contrast, for the PVA fiber with high chemical bond and moderate fiber strength, the design strategy calls for a reduction in interfacial chemical and frictional bond. In both

cases, the matrix composition must be controlled to limit the toughness. These design strategies in micromechanics provide guidelines for tailoring of material constituents for targeted composite performance.

Crack control plays an important role in limiting chloride or other deleterious gas penetration in the matrix and the accumulation of critical concentration of these substances on the surface of steel reinforcement. The denser microstructure due to the use of fly ash, as well as crack width restriction that is provided by the fibers, increase the resistance of these types of SHFRCC and evidently their durability [17]. Şahmaran and Li [18] studied chloride penetration by immersion tests of cracked beams under four point bending and found that the SHFRCC matrix reduced chloride penetration as compared to common mortar in uncracked specimens. In the case of cracked beams under four point bending, the crack width was found to be insensitive to the deformation level and therefore the chloride diffusivity was almost constant in the case of SHFRCC, contrary to what occurred in the case of plain mortar where it increased exponentially with increased deformation.

In comparing reinforced beams made of mortar and SHFRCC, Miyazato and Hiraishi [19] exposed beams made of the two materials under accelerated chloride while maintaining the beams under constant load. The same load produced a single crack in the mortar beam with 0.3 mm width while it generated several cracks of 0.1 mm in the case of the SHFRCC matrix. The conclusion was that the SHFRCC beam showed reduced corrosion rate. Also in the SHFRCC beams spalling was unlikely to occur not only due to the reduced rate of corrosion but also due to the fibers that bridge the cracks surrounding the reinforcement, providing passive lateral confinement to expansion. As shown by Li and Stang [20] crack widths were independent of member size reflecting the intrinsic material properties, and by this the SHFRCC was shown to have high material resistance against the widening of the cracks, a parameter that additionally restrains drying shrinkage and cracking thereby improving serviceability performance.

2.2 Fly ash as cement replacement and Sustainability

Construction in human history dates back to the prehistoric years, with the use of perishable materials such as leaves, branches, and animal hides and later with more durable natural materials such as clay, stone, and timber. Those materials were used to create from small scale houses to large scale bridges and pyramids, but they always had the advantage, being natural, that they could be either reintegrated in the environment through disintegration, or they could be re-used; in no case, however, were they waste, and ecologically harmful at that. Figure 2.5 shows a time history of the evolution of the use of concrete. The first use of hydraulic materials such as concrete appeared in the Roman era in the form of a hydraulic lime mortar enhanced by the addition of volcanic ash (a pozzolan that had the ability to harden under water). But until the nineteenth century and the industrial revolution, synthetic

materials such as roman-type concrete were only used for special and important structures and not at a broad scale. After the industrial revolution the use of reinforced concrete was popularized, and was used since in a great range of projects, not only in special constructions but also in small private residences. The use of steel and concrete (Reinforced Concrete) was massively produced from that point onwards, but in no case could the proponents of RC foresee the problems created by its wide range use for the future generations and the planet.

Figure 2.5: Evolution of concrete through the ages

As it was promoted by the aggressive post-industrial model the flow of production would follow a linear approach from the harvesting of the essential natural resources, the creation and use of composite products and their disposal in landfills. This approach has also been used in the construction industry. Materials are first extracted from natural resources: lime and clay for the production of cement, crushed rocks to be used as coarse/fine aggregates (natural river sand), and manufactured alloys of iron and carbon for reinforcing steel. Cement and aggregates are then mixed with water and the result of the chemical reaction is a formidable solid material (concrete) which is used extensively throughout construction. Due to the environmental effects (carbonation), natural phenomena (earthquakes), and climate conditions (rain, snow, wind, sea coast chlorides) structures, especially those having no great importance [21], are designed and built for a service life in the range of 50 years. In the end of the service life period, those structures are in most cases turned into construction waste, that may contain lead, asbestos or other hazardous substances and heavy metals. After crushing those are disposed of in wastelands. The first environmental movements in the 70s, that followed the energy crisis, triggered the concept of developing “closed-loop” approaches to the production process, mimicking and integrating the symbiotic biological ecosystems they exploited [22], [23], [24]. In the years after, the theory of “The Treadmill of Production (ToP)” as developed by Schnaiberg [25] offers an explanation of the expansion of environmental problems in the modern era by relating advances in technology and the drive for production and consumption synergistically, leading to a cycle of production that necessitates more production and argues that environmental problems cannot be solved in such a system, since growth puts ever-increasing demands on the environment by extracting natural

resources and generating pollution. Thus, achieving environmental sustainability requires radical restructuring of the political economy and a move away from growth dependence.

Other than the waste materials produced at the end of the life time of structures, the construction industry is also responsible for CO_2 emissions. This year's COP21 United Nations Conference on climate change has issued a resolution to limit the rate of global warming through a global reduction of the responsible emissions. The production of Portland cement is accountable for 5% of global CO_2 emissions, owing to the extreme heat required for its production: producing a ton of cement requires 4.7 million BTUs of energy, equivalent to about 180 kg of coal, and generates nearly a ton of CO_2. Cement's production is growing by 2.5% annually, and is expected to rise from 2.55 billion tons in 2006 to 3.7-4.4 billion tons by 2050 with the equivalent amount of CO_2 emitted to the environment [26]. In addition to the emissions, cement and concrete production is responsible for the excessive consumption of lime, clay and burning energy required in the process; also for the use of water and graded crushed aggregate materials.

According with the 1987 UN definition, "sustainable development" is "meeting the present needs without compromising the ability of future generations to meet their needs". With the increasing development of the built environment throughout the globe and the trends among people in the "developing" world to adopt a consumer-driven lifestyle, the question of concrete's sustainability gains new perspective. Recycling in general (i.e. of aggregates) is pursued as one alternative at the cost of yet more energy and resources in order to process materials to a re-usable state.

The recent developments in sustainable and ecologically friendly design of structures has led to the need of reducing materials extracted from the earth (aggregates) and water content of concrete and cement that produces carbon dioxide; the goal is to replace them with recycled materials or byproducts. One of the most promising attempts for sustainable development for concrete is the use of fly ash (FA), a byproduct of the energy industry that otherwise ends up in wastelands creating lots of environmental problems. Depending on its classification fly ash may be used in concrete as a cement replacement at a maximum amount of 40% as per ACI [27]. Fly ash acts in the cementitious composites as a pozzolan, reacting chemically with calcium hydroxide and forming compounds possessing cementitious properties. Shrinkage and tensile strength and deformation capacity are enhanced by means of synthetic fine-diameter fibers leading to truly innovative cementitious materials with impressive ductility in tension, sustaining their tensile strength up to strains that are 200 times greater than the cracking strain of normal concrete.

A holistic approach by world governments should include taking into consideration that we are not the last human generation on the earth nor the only inhabitants of this planet. The ever increasing number of aged structures that are in the end of their service life, or have accumulated extensive damage, or no longer meet the Modern Codes' provisions for earthquake resistance or durability, may

be up to 70% of the built environment in the developed countries. This enormous percentage of existing old structures requires great expenditure for rehabilitation and maintenance. Roughly fifty percent of the total expenditure for construction is needed for maintenance and repair in many industrial countries [28].

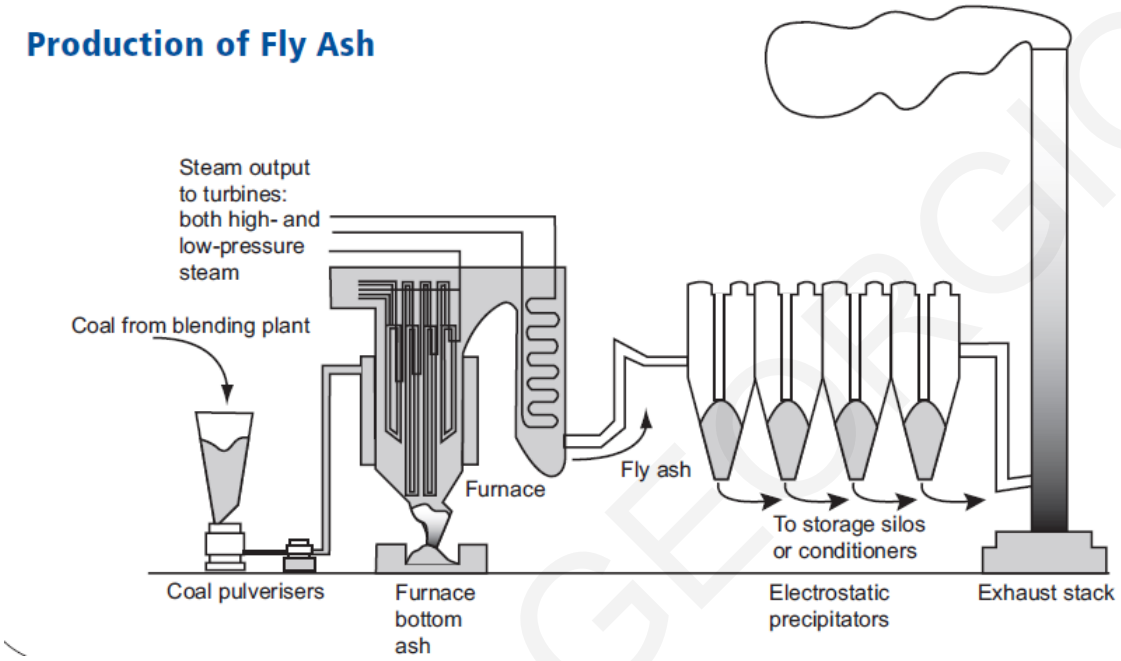

Figure 2.6: Production of Fly Ash [29]

The first research concerning the use of fly ash as a supplementary material for concrete was published in the beginning of the 19th Century [30]. Fly ash is a by-product of burning pulverized coal in electricity-generating stations (Fig. 2.6). It is the residue that is carried away by the flue gases and it is collected by separators. The composition of the raw materials that are burned (anthracite, bituminous, sub-bituminous and lignite) and the burning conditions within the generating stations may give different mineralogical and chemical composition to the produced fly ash at different stations. Independent of the differences all fly ashes include substantial amounts of silicon dioxide (SiO_2) (both amorphous and crystalline), aluminum oxide (Al_2O_3) and calcium oxide (CaO), the main mineral compounds in coal-bearing rock strata. They also may include one or more of the following elements or substances found in trace concentrations (up to hundreds ppm): arsenic, beryllium, boron, cadmium, chromium, hexavalent chromium, cobalt, lead, manganese, mercury, molybdenum, selenium, strontium, thallium, and vanadium, along with very small concentrations of dioxins and PAH compounds [31], [32]. Until the beginning of the last century fly ash was released into the atmosphere but later air pollution control standards required that it be captured prior to release, since that procedure created environmental and health concerns. New legislation has led to a reduction in the amount of fly ash emissions to less than 1% of ash produced. In the United States fly ash that is captured from emitting is generally stored at the power plants or placed in landfills. This procedure was questioned in

Dec. 22, 2008, when a containment dike ruptured (Fig. 2.7) at Kingston Fossil Plant near Kingston, Tenn., and sent 4.2 billion L of coal fly ash slurry over 122 hectares of surrounding land, damaging homes and flowing into nearby rivers. This spill was the largest fly ash release in U.S. history. Cleanup costs were estimated to run anywhere between $525 million and $825 million, not including potential long-term cleanup [33]. Therefore, there is a major need in recycling of the total amount of fly ash produced for a series of reasons such as contamination of the air, use and contamination of landfills, dangers of spilling and contamination of water basins, risks not only for human but also for the environment.

Figure 2.7: Dec. 22, 2008 a containment dike ruptured at Kingston Fossil Plant near Kingston, Tenn [33]

The most prevalent use of fly ash reported until now, and the one that holds promise to absorb most of the produced fly ash, is its use in concrete as a cement replacement. Due to its chemical composition fly ash may be used in concrete contributing to its mechanical properties either by hydraulic or pozzolanic activity, or both. A pozzolan is a siliceous or siliceous and aluminous material which, in itself, possesses little or no cementitious value but which will, in finely divided form and in the presence of water, react chemically with calcium hydroxide at ordinary temperature to form compounds possessing cementitious properties [34]. Fly ashes with high calcium content also exhibit hydraulic properties. Wide range utilization of fly ash in concrete started in the middle of the previous century after the pioneer work done at the University of California, Berkeley [35]. Nowadays Standards have been accepting the use of percentages of up to 30% of fly ash as cement replacement, while this level may change according to the special features of each construction's specifications. For example, levels of up to 50% of cement replacement with fly ash have been reported in massive structures such as dams or foundations for temperature control.

Standard specifications for the classification of fly ash depend upon different characteristics if the North American Standards or the Canadian standards are taken into consideration. In North America [36] fly ash is divided based on its type of origin and composition (See Table 2.1) while the Canadian Standard (CSA) [37] separates fly ash in three classes based on their calcium content (See Table 2.2). The amount of CaO used in CSA indicates whether the fly ash will only have pozzolanic properties

(<8%) or it will also have hydraulic properties. Fly Ashes with high amounts of CaO may produce concrete with moderate strength even without any use of cement.

Table 2.1: Chemical Requirements as per ASTM [36]

Class	$SiO_2+Al_2O_3+Fe_2O_3$ %	SO_3 max, %	Moisture content %	Loss of ignition %
N—Raw or calcined natural pozzolans that comply with the applicable requirements for the class as given herein, such as some diatomaceous earths; opaline cherts and shales; tuffs and volcanic ashes or pumicites, calcined or uncalcined; and various materials requiring calcination to induce satisfactory properties, such as some clays and shales.	70.0	4.0	3	10.0
F—Fly ash that meets the applicable requirements for this class as given herein. This class of fly ash has pozzolanic properties.	70.0	5.0	3	6.0
C—Fly ash that meets the applicable requirements for this class as given herein. This class of fly ash, in addition to having pozzolanic properties, also has some cementitious properties.	50.0	5.0	3	6.0

Table 2.2: CSA specification for FA

Type F	<8% CaO
Type Cl	8-20% CaO
Type CH	>20% CaO

In Figure 2.8 the calcium content (as per CSA) is compared to the sum of the oxides (SiO2 + Al2O3 + Fe2O3) (as per ASTM) for the same fly ashes. All fly ashes that meet CSA Type F or Type CH would be classified as Class F and Class C by the ASTM C618 [36]. However, most fly ashes that meet CSA Type CI could be classified by ASTM as either Class C based on the coal source or as Class F based on the sum of the oxides [29].

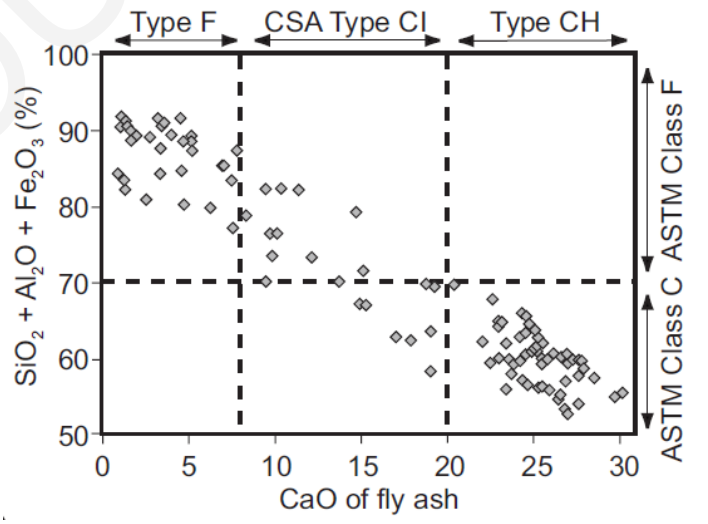

Figure 2.8: Relationship between calcium oxide content and the sum of the oxides ($SiO_2+Al_2O_3+Fe_2O_3$) for 110 North American fly ashes [29].

Fly ash has been used up till now as a cement replacement for almost one century and its advantages and disadvantages have been thoroughly examined throughout the globe. Although fly ash may in some occasions be used in great percentage as cement replacement, the North American Standards [38] have placed an upper bound to its use from the wider market. Class C fly ash is recommended to be used as a cement replacement in the order of 20-35%, while class F fly ash only between the limits of 15-25%, even though research in the last years has expanded to the use of High Volume Fly Ash (HVFA) composites, consisting of more than 70% of fly ash as cement replacement [39]. Benefits from the use of fly ash in concrete may be categorized in those which refer to the fresh mix state and those related to the hardened mix properties.

Fly Ash consists of glass spheres from 0.01-100 μm in size, with a typical particle diameter in the order of 50 μm. For the fresh state of concrete, if fly ash has high fineness, due to the spherical shape of its particles it reduces friction amongst all particles and therefore increases workability. Consequently the water content of the composite may be decreased with a gross approximation reported by Thomas [29] to be a reduction of water of 3% for every 10% cement replacement by fly ash. This water reduction also increases the composite's strength. The spherical shape of the particles also increases workability and consolidation and reduces segregation. In the case of HVFA concrete the improved rheological properties make it perfect for use in self compacting concrete [40]. Bleeding of concrete is a form of segregation, where the lighter water rises above all other materials in the mix, while the solid components of concrete do not have the ability to withhold it. Due to the decreased water content the bleeding of composites with fly ash decreases.

One of the most important reasons for the use of fly ash in concrete is the low setting rate and the reduction of the internal heat produced thereof, that in mass concrete constructions would initiate autogenous shrinkage and internal microcracking. Examples of mass replacement of hydraulic cement with fly ash in order to reduce generation of heat during hydration in construction are that of the Thames Barrage in the United Kingdom and the Upper Stillwater Dam in the United States [27]. This may also count as a disadvantage if there is the necessity of having higher strengths achieved in early ages. Even more in cold weather the setting time increases, delaying significantly the initial and final setting time. The higher the calcium content in fly ashes the more of an increase of the setting time is observed, as compared with the low calcium content fly ashes, due to their increased hydraulic properties.

Clearly, there is delay in setting time which affects the properties of hardened concrete. There might be a lower compressive strength if concrete is tested at early ages, but at later stages fly ash continues to react, with the hydration products resulting in higher strengths and a denser microstructure, if the curing is sufficient. This denser microstructure also positively affects the permeability of concrete containing fly ash to water and gas convection and therefore increases its

durability. Additionally low calcium content fly ashes can control alkali-silica reaction, due to the reduction of alkali hydroxides in the presence of fly ash.

2.3 Combination of fly ash with PVA fiber reinforced composites

The interaction of fly ash with PVA fibers was examined by various research groups (Song and Zijl [41], Wang and Li [42], Peled and Shah [43]). Peled and Shah [43] studied the behavior of 6 mm long PVA fibers in a matrix without fly ash and the same matrix with 70% replacement of cement to fly ash. They reported that the fly ash addition decreased the flexural strength by 50% but he also examined the influence of the fly ash on the surface properties of the PVA fibers. The fiber surface of the composites without fly ash with long fibrils and roughness was indicative of the high friction between the fiber and the matrix suggesting stronger bond and a tendency for a rupture failure mode. Additionally AFM (Atomic Force Microscopy) analysis that was conducted showed rougher surfaces of the matrix with fly ash around the fibers indicating greater porosity in the case when fly ash is used, leading to reduction in bond strength.

Song and Zijl [41] studied the addition of fly ash in fiber reinforced composites primarily to decrease the cost of these composites but also to investigate the beneficial effect of fly ash on their direct tensile properties. They used the fly ash replacement as opposed to coating of the fibers with oiling agents as a measure to decrease the interfacial bond between the fibers and the matrix. The spherical geometry of the fly ash particles was assumed to modify the interface and enable pull-out. Their mix designs consisted of 12 mm PVA fibers in a 2.5% by volume of the composite and a varying fly ash percentage. The research results showed that a percentage of fly ash over 30-40% does not participate in the hydration process but it works only as a filler material and does not influence strength values. However, an increase in deformability was witnessed with increased volume fraction content of fly ash. The researchers suggest that the unhydrated FA particles contribute to the crack pattern, giving rise to areas of weakness and limiting the intensity of interface bond from the fibers to the matrix, leading to small crack spacing of fly ash PVA composites. Finally they concluded that there is an issue of scatter in the experimental results that has to be further improved whereas age was found to affect the results due to the continued hydration of fly ash.

Wang and Li [42] adopted two approaches in order to tailor the performance of the composite and increase its ductility. The first one was to use coating on the fibers and the second one was to introduce fly ash in the matrix. Both of these technics were meant to decrease the interfacial bond between the fibers and the matrix leading to pull out behavior rather than rupture of the fibers. They proposed a fly ash/cement ratio of 1.2 which is well beyond the limits ever considered before as possible and they added 12 mm PVA fibers. They reported a peak of strain capacity at 10 days, that decreases with increased age of the composite. The tests they performed on freeze-thaw cycles exhibited excellent

durability of the fly ash composite and cracking behavior under restrained shrinkage that was much better than concrete due to strain hardening.

2.4 Durability of SHFRCC

Durability of strain hardening cementitious composites was investigated by many researchers. A report by RILEM TC208-HFC [44] was issued as well as an article outlining the main results [45] of the former committee. The research focused particularly on SHFRCC composites with the ability to develop multiple finely spaced cracks with small widths. This characteristic of cracking was researched in terms of durability as a material potential to be used for maintenance and rehabilitation of structures that suffer from moisture, gas and salt ingress. Resistance to moisture, gas and salt penetration was measured as an important durability mechanism. It was reported that matrix densification was significantly reduced in Ultra High Performance FRC (UHPFRC) [46] and in SHFRCC. In particular diffusivity was reduced by the inherent crack control of these materials [17]. Permeability tests indicated that the flow rate was lower in FRC than in plain concrete, even though this flow rate difference was negligible when crack widths were less than 100 μm. Immersion tests proved that chloride penetration depth was reduced in uncracked SHFRCC specimens compared to uncracked mortar. Comparing SHFRCC and concrete beams loaded in flexure to the same deflection, Miyazato and Hiraishi [19] observed a reduced penetration depth in SHFRCC, indicating that SHFRCC was effective in reducing the diffusion of chloride ions under combined mechanical and environmental conditions, due to the increase of the number of cracks in the SHFRCC beam and their lower widths for the same level of deformation as compared to the normal concrete beams. The same research also showed significantly reduced corrosion rate of R/SHFRCC members while spalling would be unlikely to occur at the latter stages of the corrosion process for these composites due to their ductility. In freeze-thaw testing of SHFRCC, even though normal concrete survived only up to 110 cycles and at that point it had deteriorated severely, the SHFRCC specimens survived 300 cycles without degradation of the dynamic modulus.

2.5 Self-compacting SHFRCC

All the advantages attributed to SHFRCC could be retracted in practice in cases of insufficient vibration or consolidation of concrete, as these usually lead to poor material quality that eventually deteriorates the durability of concrete structures. Therefore, the need for high workability or self-consolidation of concrete has been recognized as a means to improve the quality and reliability of constructed facilities, especially in Japan. Self-compacting concrete requiring no mechanical energy to consolidate in construction sites has been successfully developed and commercialized [47].

SHFRCC without self-compacting properties requires high-frequency vibration to place the fresh mix into molds. The incorporation of fibers in SHFRCC has made the placing of SHFRCC a more challenging task than concrete. The efficiency of fibers can be significantly reduced if fibers are not uniformly distributed due to the low workability of fresh SHFRCC mix. Thus, development of a self-compacting SHFRCC that can flow into molds of complex shape under gravity without any consolidation is highly desirable. This self-compaction capability of SHFRCC can be even more important especially when heavy reinforcing details are encountered. To achieve self-compaction, the fresh SHFRCC mixes should be easily deformable and should have sufficient segregation resistance. This objective may be prescribed on the rheological characteristics of fresh mix, which are affected by the inter-particle microstructure, the fiber properties, and the interfacial properties between the matrix and fibers.

Specific requirements include:

• The fresh matrix should have optimal viscosity and low yield stress to provide good deformability, while preventing phase separation.

• During the casting process, the suspension should maintain its initial flowability.

• The flow properties of fiber-free mix should be minimally disturbed upon fiber addition to prevent poor fiber dispersion due to high fiber aspect ratio and/or high fiber volume fraction.

• The fiber surface should have optimal wettability with the fresh cementitious mix so that the fresh mix can flow homogeneously through reinforcements or complex formwork shapes without any phase separation or clogging.

To satisfy material performance in both the fresh state and the hardened states, the processing parameters which affect flow properties of fresh SHFRCC are carefully controlled in order to minimize disturbance of the micromechanical optimization for strain hardening performance of the hardened cementitious composite. According to [47] the aim of producing self-compacting SHFRCC is fulfilled by optimizing the amount of coarse aggregate in order to minimize the friction between aggregates that increases the resistance to concrete flow.

2.6 Use of SHFRCC for structural elements

2.6.1 Code Provisions for fiber reinforced composites

Application of Fiber Reinforced Composites (FRC) in building structures was limited up till now due to lack of extensive experimental documentation of the material's performance in structural components and the absence of detailed design provisions regarding their use. Relatively recently, FRC was recognized by design codes as a structural material (Section 11.4.6 in the ACI Committee 318 [48] and New Model Code (2010) [49]. A significant part of current research on the use of FRC in structural elements has been focused on the use of steel fiber reinforced concretes (SFRC). Relevant

ACI and Model Code provisions have been mostly supported by tests on various SFRC structural components, where the material often exhibits strain softening behavior.

Fiber reinforced concrete (FRC) was included in the New Model Code 2010 [49] for the first time. The base line of the rules listed in Chapter 5.6 are based on experience with steel fiber reinforced concrete. A basic differentiation is made between strain hardening and strain softening FRC. The code states in the beginning of Clause 5.6.2.2 that uniaxial tensile testing is not advised for standard testing due to the difficulty in performing the test and proposes the use of bending tests on notched prisms and the use of inverse analysis to determine the stress-crack width relation. In the same paragraph the code refers to strain hardening materials which can be obtained for high fiber contents and in order to guarantee the hardening in tension, the code suggests that the tensile behavior must be identified by means of uniaxial tension tests, carried out on unnotched specimens (e.g. dogbone). For the compressive behavior of FRC the New Model Code [49] states that "the compressive relations valid for plain concrete apply to FRC as well" and acknowledges the beneficial effect of the fibers that can reduce brittleness of concrete in compression. The design of structural members with FRC, is reviewed in Section 7.7. For beams without shear reinforcement Section 7.7.3.2.2 gives the shear resistance as:

$$V_{Rd,F} = \left\{ \frac{0.18}{\gamma_c} \cdot k \left[100 \cdot \rho_l \left(1 + 7.5 \cdot \frac{f_{Ftuk}}{f_{ctk}} \right) \cdot f_{ck} \right]^{1/3} + 0.15\sigma_{cp} \right\} \cdot b_w \cdot d \tag{2.1}$$

where f_{Ftuk} is the tensile strength of the FRC obtained from an axial-tensile test (without specifying the procedure, specimen dimensions or testing setup). Equation 2.1 as stated is based on steel fiber concrete research and should be checked for other types of materials. In beams with shear and longitudinal reinforcement Section 7.7.3.2.3 states that the total shear resistance is the sum of the concrete contribution, the shear reinforcement and the contribution of the fibers intersecting the design shear crack. In Section 7.7.3.2.4 it is stated that the minimum shear reinforcement may be omitted if the following condition is fulfilled:

$$f_{Ftuk} \geq \frac{\sqrt{f_{ck}}}{20} \tag{2.2}$$

Again Eq. 2.2 is based on steel fiber concrete research and should be checked for other types of materials. Also when a large amount of longitudinal reinforcement in the compressive zone is present, sufficient volumetric ratio of transverse reinforcement (stirrups) should be used in order to prevent buckling of the rebars.

Design recommendations specific to strain hardening cementitious composites (SHFRCC) have been published till now only by the Japan Society of Civil Engineers (JSCE) [50], addressing structural analysis and design of SHFRCC members. These build on the established specifications for ordinary concrete structures [51] whereas no material-specific expressions and analysis procedures have been

given, that would specifically pertain to the strain hardening properties of the matrix in steel-reinforced SHFRCC (R-SHFRCC) members; exception to this are the limit states of axial compression in R-SHFRCC, and the use of SHFRCC as a strengthening material (externally bonded tension layer) which is frequently used in order to increase the flexural strength of conventionally reinforced concrete members [50].

Section 6.3.3 of the JSCE Recommendations deals with the issue of shear design of linear members. The shear strength of a member of SHFRCC and steel may be obtained by Eq. 2.3. As seen in this Equation the shear capacity of a HPFRCC member is the sum of the contributions of the matrix V_{cd}, the fibers V_{fd} and the shear steel reinforcement. The contribution of the matrix is derived from the specification for normal concrete. The term quantifying the beneficial actions of the fibers is prescribed by the Recommendations for Design and Construction of Ultra High-Strength Fiber Reinforced Concrete Structures [52]. The beam strength, V_{yd} as stated by the code is assumed to be reduced by a factor of 0.7 due to the multiple cracking that occurs in the serviceability limit states for these types of composites:

$$V_{yd} = V_{cd} + V_{sd} + V_{fd} + V_{ped} \tag{2.3}$$

The design shear capacity of the fibers is given by the following Equation:

$$V_{fd} = \left(f_{vd} / \tan\beta_{\mathrm{u}}\right) \cdot b_w \cdot \mathrm{z} / \gamma_{\mathrm{b}} \tag{2.4}$$

In the case where the member is partly reinforced by HPFRCC, then shear strength should be determined by appropriate methods, such as tests, as stated by the Recommendations. The Recommendations gives a series of tests that may be performed to obtain the shear strength of beam members with and without the use of stirrups and a comparison of the experimental results to the strength estimates obtained from the shear equation (Eq. 2.3), but it is also stated that the test data available are too limited and in general proper testing should be used for verification for different height or reinforcement ratios. The case of reversed cyclic loading and its impact on the degradation of shear capacities of members is not mentioned at all within these Recommendations.

The JSCE proposes Test Method 2: Testing method of uniaxial tensile strength in order to obtain the stress-strain curve of SHFRCC in tension. The testing apparatus recommended has a fixed support on one end of the specimen and a pin support on the other end. The recommended load application is a constant specimen deformation rate of 0.5 mm per minute, while the minimum number of specimens is five. In regards to the specimens dimensions the recommendations suggest that the minimum size of the specimen is at least equal to the fiber length and twice the maximum aggregate size.

The Japan Concrete Institute (JCI) issued a Standard in 2007 describing an indirect method that could be used to determine the tensile stress-strain properties of SHFRCCs (JCI-S-003-2007 [53]). The standard uses a square cross section beam (100 mm) under four point loading with a total span length

of 300 mm. The test requires a curvature measuring equipment whereas the load is applied with a machine head speed of 0.3 mm/min. The Standard recommends that the results should be discarded if fracture occurs outside the pure bending span. Then appropriate equations are proposed that use an inverse analysis method to extract σ-ε properties of the material in tension from the M-φ curves obtained from the four point bending test. The prisms used have a shear span ratio of 1. Due to the fibers acting as a flexural reinforcement, the interaction of moment and shear capacity in short beams could result in variation of the load obtained and plays an important role on the curve obtained from inverse analysis.

2.6.2 Applications of SHFRCC

The Recommendations for the use of SHFRCC issued by the JSCE helped broaden their application and many examples of their use are found nowadays in Japan. Most applications are in retrofit purposes but also in new construction (precast coupling beams, sprayable SHFRCC) where special members made completely from SHFRCC are used. Rokugo et al. [54] report a series of application examples made in Japan. For retrofitting purposes HPFRCC has been applied as a surface protection layer increasing the life time of structures such as concrete dams, waterway structures or retaining walls. Figure 2.9 (a) and (b) shows the spray application of a 15 mm thickness SHFRCC on an aged dam in order to prevent water penetration by limiting the crack widths. The same procedure is adopted for the waterway structure of Fig. 2.9 (c) and (d). The retaining walls in Fig. 2.9 (e) and (f) were damaged by alkali-silica reaction (ASR) and were covered also by SHFRCC to limit water penetration and reduce the progression of the ASR reaction. For this specific case close observation showed that after 4 years of exposure, multiple fine cracking was maintained.

Figure 2.9 (a) Dam retrofitting application overview, (b) Direct spray construction, (c) and (d) Waterway structure, (e) and (f) Retaining wall retrofitting application [54]

Figure 2.10 (a) shows the retrofitting of a viaduct's girders and beams with SHFRCC. The composites are placed over the existing members which are already cracked with various crack widths and is expected to resist flexural fatigue loading. In Fig. 2.10 (b) the anti-seismic application of R/SHFRCC as coupling beams connecting two structural walls on a 27 story high rise building is shown. The coupling beams were precast (500x900x1650 mm) and designed for a target drift of 3.3% with a crack width at that drift of 0.2mm, that would not require repair.

Figure 2.10 (a) Viaduct retrofitting, existing structure and direct spray construction and (b) Application of R/SHFRCC coupling beam [54]

Rokugo [55] notes the use of SHFRCC in expansion joints of bridges in order to reduce noise and deterioration. As shown in Fig. 2.11 (a) this was applied on an existing expressway in Japan, where the SHFRCC plates with wire mesh was fixed with anchor bolds on the slabs. All movement was absorbed by the deformation of the SHFRCC with multiple fine cracking. In Fig. 2.11 (b) the application of a multilevel FRC in a tunnel lining in Hide Tunnel is depicted. The top layer was sprayable SHFRCC over fiber carbon grids and was chosen in order to prevent carbonation and spalling through water tightness of the layer. Additionally the construction time and cost was reduced.

Figure 2.11 (a) ECC joints in expressway and (b) Tunnel lining with SHFRCC [55]

2.7 Conclusions

Strain Hardening Cementitious Composites are a novel material with excellent performance. In order to widen their use in construction the primary need is to experimentally study the behavior and performance of the material under various loading conditions both in the micro-level but also in large

scale structural members. Standardized and proofing tests will be the basis for the establishment of methods for a reliable evaluation of the structural performance of members comprising SHFRCC. Before they are widely accepted in construction, the SHFRCC materials would need to be incorporated in existing codes and standards, with specific directions regarding pertinent design procedures for static, seismic and durability purposes. A future target would also be a comparative evaluation in comparison to normal concrete when used in reinforced concrete structures, with particular reference to the reduction of costs as would be effected by reducing the member dimensions and detailing requirements. Application in existing structures for repair or new structures should be broadened by collaboration of research and industry, in order to inform the public for their improved capabilities.

Chapter 3: Preliminary Investigation of Fiber Reinforced Composites

3.1 Introduction

As a prerequisite for scaling-up of the technology developed in the field of novel cementitious materials it is essential to secure sustainable access to resources for continued production. This is why before embarking on further developments in the area of SHFRCC it was essential to ensure that it is possible to fabricate the basic mix for the developed composites using materials that may be found in Cyprus and find a coating agent for the fibers that would create a strain hardening composite. Two different types of fibers were used in the study, with appropriate mix designs. This chapter summarizes the materials, mix designs and test results and a preliminary analysis of the experimental findings.

3.2 Experimental investigation

3.2.1 Mix designs selection

Extensive research has been carried out on optimizing the mix design for the basic cementitious matrix in light of the requirements for the target self-consolidation and the fiber´s properties (volumetric content, surface area, and surface binding). Selection was made from among a variety of proposed mix designs by various researchers as shown in Table 3.1. Thus, for the PVA fibers the mix design was ECC-M45 designed by Lepech and Li [56]. This mix design was developed for large scale casting. The materials of the original mix design consist of ordinary Portland cement (OPC, one part by weight of the total), fly ash (1.2 parts by weight-p.b.w. of cement), silica sand (0.8 p.b.w. of cement), water (0.56 p.b.w. of cement), high range water reducer (0.012 p.b.w. of cement) and 2% by volume of fibers as shown in Table 3.2.

Table 3.1: Various mix designs for PVA fibers through literature

Research Ref.	V_f (%)	cement	water	sand	fly ash	HRWR	max strain %	max tensile strength	Max comp. strength
[57]	2	1	0.53	0.8	1.2	0.03	4	600 psi	8.7 psi
[57] M45+	2	1	0.58	0.8	1.2	0.03			6.7 psi
[58]	2	1	0.58	0.8	1.2	0.013	3	700 psi	
[59]	2	1	0.53	0.8	1.2	0.03	3.7	6 MPa	80 MPa
[60]	2	0.7	0.39	0.5	0.3	3 Ml/kgcm	4	4.5 MPa	45 MPa
[61]	2 2 2	1 1 1	0.27/cm 0.26/cm 0.26/cm	0.8 1.1 1.4	1.2 2 2.8	0.13 0.014 0.016	2.1 3.5 3.7	5.3 4.6 4.9	54 MPa 46 MPa 37 MPa
[17] kg/m^3	26	578	319	462	694	7.51	>3	4.5 MPa	
[62]	2 2 2	1 1 1	0.58 0.53 0.53	0.8 0.8 0.8	1.2 1.2 1.2	0.03 0.03 0.014	2.5 2.5 2.2		46 MPa 60 MPa 62.4 MPa

Adjustments have been made on the materials and quantities according to the availability of products in Cyprus. Thus, the cement used was Portland Composite Cement EN 197-1 CEM II / A-M

(L-S) 42.5 R. Silica sand used in the ECC-M45 had a maximum grain size of 300 μm. This material is only imported in Cyprus from Germany and therefore additionally to that, tests on available materials in the local market were used for comparison reasons upon their influence on the properties of the final product. The local sand that was not pure silica sand was sieved to remove all particles greater than 300 μm and washed with the 63 μm sieve to remove all smaller particles since they mostly comprised of high quantities of clay that would induce instability in the final product. The fly ash was of type F as used in the original design and was also imported since the fly ash produced by the Power-plant in Cyprus has not yet been classified.

Table 3.2: Engineered Cementitious Composite mix design proportions by weight for ECC-M45.

Mix Designation	Cement	Fly Ash (Type F)	Sand (fine silica sand)	Water	HRWR	Fiber (V/V)
M45	1.0	1.2	0.8	0.56	0.012	0.02

Various mix designs for polypropylene fibers and or polyethylene fibers through the literature are summarized in Table 3.3. In the case of the PP-fiber reinforced mix, proportioning was adjusted to the one proposed for High Tenacity Polypropylene Fibers (HTPP) by Yang [63] due to the same surface binding property (i.e. hydrophobia) of the two fibers. The mix was used as in the reference and also modified with the use of a small amount of sand, whereas none had been used in the reference mix. Additional adjustments were made to the quantity of the high range water reducer (HRWR) used and two types of superplastisizer (SP) were tested as it was shown by experiments that the first type had to be used in approximately twice the amount required to achieve the required self-consolidating performance of the original mix and also doubled the setting time of the mix.

Table 3.3: Various mix designs for PP or PE fibers through literature

Research Ref.	cement	fly ash	sand	silica fume	HRWR	water	fibers	W/C
[64]	755	-	1130	113	27	232	6.5%PP	0.27
[65]	1	0.15	1	-	No ref.	0.5	1.5%PE	0.43
[66]	1	0.15	1	-	No ref.	0.4	1.5-2%PE	0.35
[11]	412	1154	-	-	6.6	363	18 kg	0.23
[47]	1	-	0.5	-	0.04+HPMC0.013	0.3	1%PE	0.3
[67]	1	-	0.5	0.1	0.01	0.35	2%PE	

The density of FRC varies from that of concrete due to the lack of coarse aggregates. It is estimated approximately at 2000 kg/m^3. The mixture consists of fine silica sand to maintain adequate stiffness and volume stability. The silica sand has a maximum grade of 250 μm and a mean size of 110 μm. According to Fisher and Wang [2] the particle size of all matrix components should be properly graded to achieve self-consolidating fresh properties. The dense microstructure must be achieved through optimization of the particle size distribution of the composite. Due to the small size particles within the composite the ones governing the ideal particle distribution are cement, mineral admixture (fly ash)

and sand [2]. The ideal gradation of particles to produce dense packing and good workability was determined by Fuller and Thomson [68] and are expressed by Eq. 3.1 where f_d is the fraction of particles smaller than d, d is the particle size smaller than D (mm) and d_{max} is the maximum particle size (mm).

$$f_d = 100 \cdot \left(\frac{d}{d_{\max}} \right)^{0.5} \tag{3.1}$$

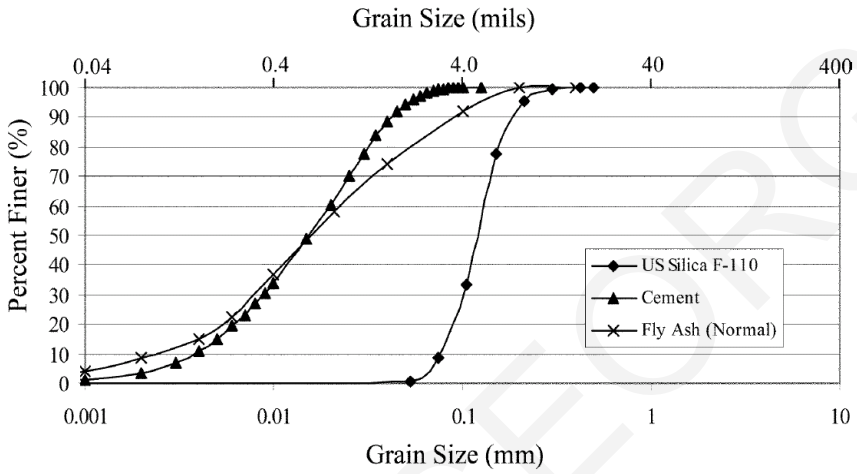

Figure 3.1: Grain size distribution for ECC component materials [56]

Figure 3.1 shows the grain size distributions of the materials used in a typical SHFRCC composite, i.e. the cement, the fly ash and the silica sand. Four mixes obtained by varying the sand content were tested by Lepech and Li [56] to establish the mix with the closest grain distribution to the optimum as shown in Fig. 3.2. The composition of the solid particle system is determined by fitting the composite particle size distribution to the ideal curve and reducing the deviation. Using this procedure the mass proportions between the solid ingredients is determined.

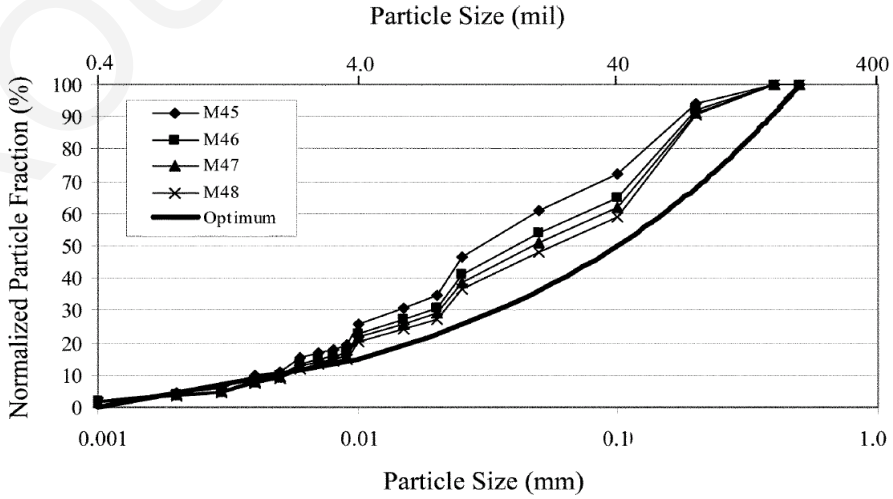

Figure 3.2: Aggregate grain size distributions for various mixes of ECC and optimal aggregate grain size distribution curve [56]

In pristine conditions PVA fibers have strong interfacial chemical and frictional bonds, which demands high amount of fibers in order to achieve strain-hardening response. Lowering chemical and frictional bonds are effective approaches to reduce the critical amount of fibers. For PVA fibers a percentage of 2% is enough to generate strain hardening properties of the final product. Also a high range water reducing admixture is necessary to maintain the desired fresh property during mixing and placing. The properly mixed SHFRCC material should have a creamy texture. To ensure self-consolidating properties the characteristic deformability factor should be measured.

The use of silica sand also helps to control the toughness of the composite and enhance bond friction at the matrix–fiber interface by filling up the pores. Fly ash and super-plasticizer (SP) are used to lower the W/C ratio and to improve workability during concrete casting. In addition, Methyl Cellulose (MC) is used to enhance the workability of the mixed materials, to avoid material segregation, and to improve the fiber distribution during mixing. MC has generally been used as a viscosity agent to prevent segregation of superplasticized cementitious suspension of high W/C ratio ranging from 0.5 to 0.619. In this type of composites, MC is incorporated into the matrix to preserve initial flowability of the mix at low w/c ratio. At the optimal concentration, MC can prevent flocculation among particles without increasing the overall viscosity due to the excluded volume effect. Besides, it can also prevent segregation caused by particle collision. From the viscosity data described above, it can be concluded that the cementitious suspension without MC or with high MC concentration induces the strongly flocculated structure resistant to shear deformation, while the suspension with optimal MC concentration prevents it. Studies [47] suggest that the MC dosage of 0.013% results in an optimal deformability in the cement paste. When fine aggregates are added to the cement paste, the deformability is expected to be optimal as well with this MC concentration.

3.2.2 Mixing Procedure

Fluid consistency of the cementitious mortar through the mixing process is very essential. Usually in normal concrete grinding force and blending effects are developed due to coarse aggregate dropping from the top of the drum. This does not exist in ECC mixing. This is why the feeding rate of the raw materials must be carefully tuned. Successful mixing procedure must take the following steps, [2]:

- Weight all materials, add HRWR to 20% of the water.
- Mix the sand, fly ash and 1/3 of the cement and dry mix for 1 to 2 sec
- Add about 80% of the water (fluid consistency and flowable mixture is obtained)
- Add the rest of cement and water with HRWR alternately at a rate not to cause accumulation of large lumps of cement and mix for 3 to 4 sec until the material is homogenous and sufficiently fluid
- Add the fibers and mix for an additional 5 to 6 min until the fibers are well dispersed.

On other research conducted by Shin et al. [69] FRCC was mixed with the following steps: First, powder cement, fly ash, and fine aggregates were mixed uniformly in dry condition using a rotary mixer for two or three minutes, followed by gradual addition of water. The liquefied MC and SP were sequentially added to the mix. The mixture with additives was maintained in a very diluted and uniform condition for about three minutes. After 3 min, the short fibers were evenly added into the mix and stirred for three minutes.

Rheological characterization through the slump test:

A standard concrete slump cone is filled and emptied on to a plate. The two orthogonal diameters are measured and the factor is then calculated:

$$\Gamma = \frac{(D_1 - D_0)}{D_0} \tag{3.2}$$

where D_o is the cone diameter and D_1 is the average of the two orthogonal diameters of the composite after spreading. The minimum value of Γ should be 2.75 as per Lepech and Li [58]. When the mix will be under mixing and transport for a long time, the use of a hydration stabilizer has been found effective to maintain good deformability without affecting the hardened properties. Also good mortar viscosity (established through a Marsh flow cone test) can ensure good fiber dispersion.

3.2.3 Materials

The target of the research was to examine the mechanical properties of a self-consolidating cementitious mix that would form the basis of the development of a SHFRCC, with high percentage of cement replacement with fly ash and the study of its performance with the addition of fibers. The mix design selected was ECC-M45 [56] suitable also for large scale casting. The materials and quantities were adjusted to the local available options.

Cement

The cement used was Portland Composite Cement EN 197-1 CEM II / A-M (L-S) 42.5 R. This type of Blended Cement is produced using pure calcite limestone and is more impermeable and dense as compared to OPC, with a higher degree of workability and reduced plastic shrinkage. The compressive strength of this particular cement at 28 days is equivalent to that of 42.5 R OPC and superior at 2 and 7 days.

Sand

Two types of sand were used in the experimental program. Silica sand used in the ECC-M45 had a maximum grain size of 300 μm. This material is not available in Cyprus and therefore a local sand was used as one of the sands. The local sand used was sieved to remove all particles greater than 300 μm and washed with the 63 μm sieve to remove all smaller particles since they mostly comprised of high quantities of clay that would induce instability in the final product as shown in Fig. 3.3. This type of sand is called hereafter as Sieved.

The second part of sand used was silica sand, which was imported from Germany. The characteristic of this product is spherical crystal quartz particles showing a very narrow grain size distribution, a low content of side minerals and a high SiO_2 content as well as a very special light color. The sand particles vary from 0.06 to 0.3 mm. The percentage of silica oxide is in the order of 98.6%, while some small quantities of Al_2O_3, Fe_2O_3 and TiO_2 are contained. The grain size distribution is shown in Table 3.4. The Mohs Hardness of this product is 7, while raw density is 2.65 gr/cm^3 and bulk density is 1.35 gr/cm^3.

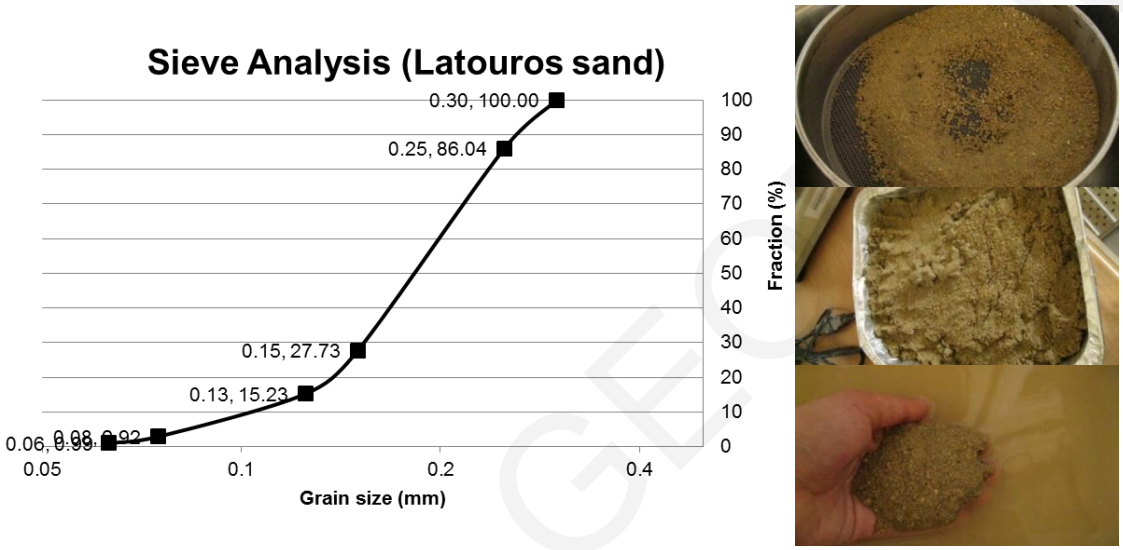

Figure 3.3: Sieve analysis of local sand and sieve procedure

Table 3.4: Grain size distribution of silica sand

Sieve (mm)	Percent retained %
<0.063mm	1
0.063-0.1mm	7.5
0.1-0.2mm	86
0.2-0.315mm	5.5

Fly Ash

The Fly Ash used was Eurocrete Fly Ash. This fly ash has both pozzolanic and physical properties that enhance the performance of concrete and it complies fully with ASTM C618 and EN 206, Type F ash. This fly ash contains extremely fine (0.45 μm) latently reactive silicon dioxide. The presence of this substance gives greatly improved internal cohesion and water retensivity. The concrete becomes extremely cohesive and the pumping properties are substantially improved. In the set concrete the latently reactive silicon dioxide forms a chemical bond with free lime. When used in combination with a recommended superplasticizer, the resulting cementitious product will show the following properties:

- Excellent workability
- Reduced water demand
- Reduced heat generation

• Increased durability
• Increased ultimate strength
• Increased resistance to abrasion
• Greatly increased impermeability
• Greatly increased resistance to gas permeability
• Highly reduced chloride diffusion

Eurocrete Fly Ash contains no chlorides or other potentially corrosive substances. The dry bulk density is 1000 kg/m^3. The company providing the product proposes 20-40% replacement of cement content by weight. Mixing should be performed by adding the fly ash to the cement before gauging water with an optimum mixing time of 90 seconds.

Type F fly ash has pozzolanic properties. A pozzolan is a siliceous or siliceous and aluminous material which, in itself, possesses little or no cementitious value but which will, in finely divided form and in the presence of water, react chemically with calcium hydroxide at ordinary temperature to form compounds possessing cementitious properties [36]. Class F FA is typically a byproduct of combustion of anthracite or bituminous coal for the production of electricity, but may also be obtained from burning sub-bituminous coal and lignite. Class F FA has been used in other studies as cement replacement at fractions ranging from 20-30% of the mass of cementitious material but in this research the amount of FA used was 120% by weight of the amount of cement for the cases with the PVA fibers (that is, one part of hydraulic material in the final mixture comprised 45% cement and 55% fly-ash). The use of local fly ash for the experimental program was not possible since the fly ash produced in Cyprus derives from the burning of mazut and has not yet been classified for its use in concrete as cement replacement (this work is in progress).

Polyvinyl alcohol fibers (PVA)

In the present investigation 8mm and 12 mm long, 39 μm diameter PVA fibers were used. The nominal tensile strength was 1600 MPa, Young's Modulus was 40 GPa, the fibers' strain capacity was 6.5% and the density was 1300 kg/m^3. The fibers used were specially coated with the coating agent and percentage determined from the preliminary study (see Par. 3.2.4). The fibers were provided from a Japanese company named KURARAY, which made this synthetic fiber called Kuralon K-II that is based on polyvinyl alcohol (PVOH) resin.

Polypropylene fibers (PP)

The PP fibers have a density of 0.91 gr/cm^3, Young's modulus of 7 to 9 GPa and a tensile strength of 400-500 MPa. Products in this category are commercially known as: a. MERAFLEX, b. FIBRIN 623 with surface: non coated, c. BELGIAN with various diameters and lengths (a. d=20 μm/l_f=8 mm, b. d=50 μm/l_f=6 mm, c. d=34 μm/l_f=12 mm). All PP fibers have a hydrophobic surface.

3.2.4 Coating of PVA fibers

PVA fibers have free hydroxyl groups in their molecular chain as seen in Fig. 3.4 (a) (information provided by the producer). These free hydroxyl groups create chemical bonding with the surrounding cementitious matrix. The high chemical bonding leads to fiber rupture rather than fiber pull-out when under tension, resulting in higher strength but lower ductility fiber reinforced cementitious composites. Tests on fibers being pulled-out of the matrix showed fiber shear-delamination rather than pull-out. Additionally due to the fibers' hydrophilic nature poor fiber dispersion and uneven distribution in the matrix may appear. Hydroxyls have a strong tendency to form intra-fiber bonds and clump together the fibers as seen in Fig. 3.4 (c) which represents the original state provided by the manufacturer. Several attempts have been made by various researchers in order to increase ductility of PVA cementitious composites by coating the fibers' surface and decreasing chemical bonding. The type of the coating surfactant and the amount of coating are both parameters that need to be tested simultaneously in order to find the optimum composite behavior. If the amount of coating of the fibers is too high then the interfacial bond will be too low and fiber slippage occurs.

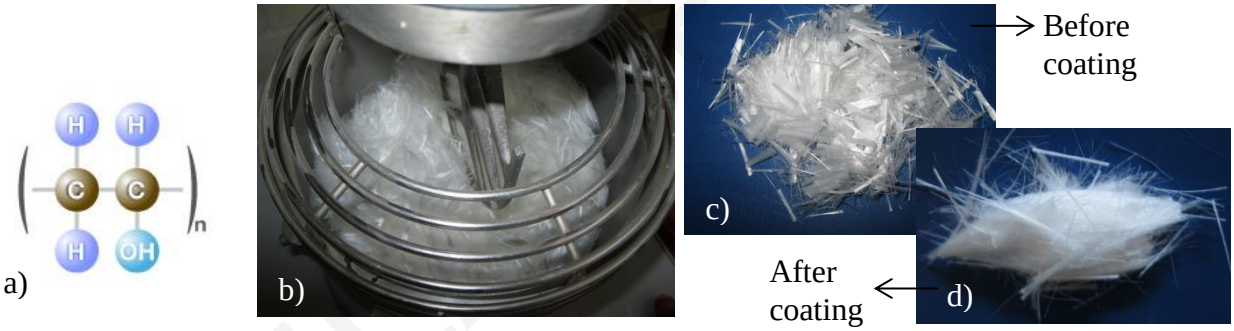

Figure 3.4: a) Chemical formula of PVA fibers, b) mixer for coating the fibers, c) PVA fibers in their original state and d) PVA fibers after coating.

The fibers that are chemically treated will no longer create bonds either between fibers or between fibers and the cementitious matrix. The used coating can bind the hydroxyl functional groups on the fibers' surface either by physically blocking their surface or by chemically bonding to them and preventing them to create other chemical bonds. Various chemicals may be used in this process such as: polyamine compounds; cationic quaternaryamine compounds; cationic, anionic and non-ionic surfactants; alkylalkoxylsilane, alcoxylsilane and halide organosilane. Additionally surfactants and debonders may also be applied. These chemicals may be used alone or in combinations [70].

3.2.4.1 Procedure of coating

Fiber treatment can be carried out by various methods. Some of them apply treatment in aqueous or organic solutions and in these cases de-watering is required. Fiber treatment may also be conducted by

dry methods such as spraying. Fibers in this study were coated several hours prior to the composite mixing. The fibers were added to a small mixer with the coating and a small percentage of water and were mixed for 30 min. For example for a fiber reinforced cementitious matrix of 0.038 m^3 (76.7 kg) with a percentage of fibers of 2% by volume, a quantity of 1000 gr of PVA fibers were used. The 1000 gr of fibers were mixed with 66 gr of coating and 100 ml of water. After mixing of the fibers with the coating the fibers were no longer connected in bundles (Fig. 3.4 (d)).

3.2.4.2 Types of coating used

In order to achieve a strain hardening composite with a notable ductility, an optimal combination of materials should be made. The chemical bond between the PVA fibers and the surrounding concrete should be reduced, so as to enable partial, controlled slipping of the fibers. To enable control of the surface properties of the hydrophilic fibers, four types of coating were tested. The four different types of coatings were used in different amounts of coating of the fibers. Those coatings were two types of oils (O1 and O2) and two types of soaps (S28 and S38) as shown in Fig. 3.5. Oil 1 was a natural oil, while Oil type 2 was a lubricant for molds. Multiple percentages of the coating agents were also used. By changing the amount of coating it was possible to achieve different coating ratios of the fiber's surface.

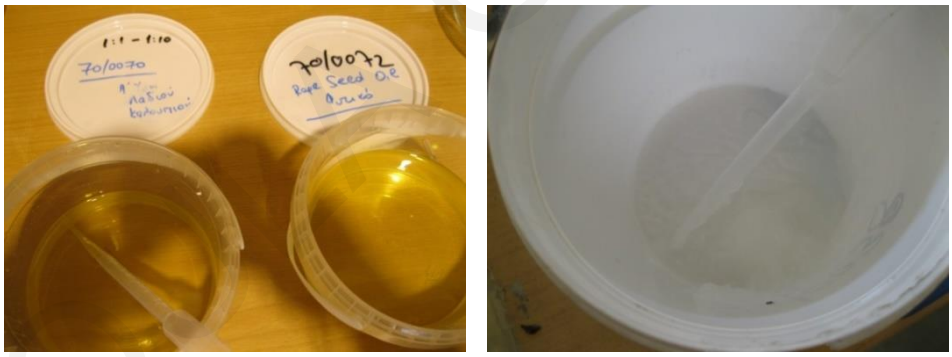

Figure 3.5: Oil and soap coating agents

Table 3.5: Characteristics of coating agent S38

Description: Linear alcohol ether sulfate (~2 moles of E.O.) in aqueous solution		
Characteristics	Value Ranges	Units
Appearance at 25°C	Flowable paste	-
Anionic active matter (MW 384)	68.0-70.0	% mass
Unsolphated matter (HPLC)	≤ 4.0	% mass
pH (5%)	7.0-9.0	-
Colour (5% active matter)	≤ 20	Klett
Dioxane	≤ 50	ppm
Sodium Sulfate	≤ 2.0	% mass

The coating material that best fitted the aims of the research as concluded from the preliminary study was coating S38 which was an Alcohol Ether Sulfate with the properties shown in Table 3.5 used

with at a percentage of 6.6% per weight of fibers. Alcohol Ether Sulfate is an anionic surfactant with foaming profile making the product suitable for use as air-entraining admixture in concrete and mortar mixtures, as a foaming agent in the production of gypsum boards, or as a foaming agent in fire-fighting foam concentrates. Therefore the coating that was used is a material that is already used in specific types of concrete and is not harmful in any case.

3.2.5 Mix designs

The mix designs for all the types of fibers adopted in the present investigation are listed in Table 3.6. The types of fibers, percentage of fibers, type of coating and percentage of coating per weight of fibers, as well as the materials proportioning are listed in detail.

Table 3.6: Mix designs for all preliminary tests

No	FIBER TYPE	COATING	coating %weight of fiber	SAND TYPE	DEFOAMER	FIBERS (kg)	C	FA	S	W	SP
B1	PP1	-	-	SIEVED		0.4	1.00	2.51	0.99	0.79	0.014493
B2	PP1	-	-	SIEVED		0.27	1.00	1.19	0.80	0.57	0.02255
B3	PVA8mm	-	-	SIEVED		0.27	1.00	1.20	0.80	0.56	0.023936
B4	PVA8mm	O1	1.2	SIEVED		0.05	1.00	1.20	0.80	0.58	0.014331
B5	PVA8mm	O2	1.2	SIEVED			1.00	1.20	0.80	0.58	0.023955
B6	PVA8mm	O2	3.3	SIEVED		0.00666	1.00	1.20	0.80	0.58	0.024056
B7	PVA8mm	O2	6.6	SIEVED		0.00666	1.00	1.20	0.80	0.58	0.024056
B8	PVA8mm	O2	13.2	SIEVED		0.00666	1.00	1.20	0.80	0.58	0.024056
B9	PVA8mm	S28	3.3	SIEVED		0.00666	1.00	1.20	0.80	0.63	0.024056
B10	PVA8mm	S28	2.42	SIEVED		0.00666	1.00	1.20	0.80	0.58	0.024056
B11	PVA8mm	S28	1.67	SIEVED		0.00666	1.00	1.20	0.80	0.63	0.024056
B12	PVA8mm	S28	6.6	SIEVED		0.00666	1.00	1.20	0.80	0.63	0.024056
B13	PVA8mm	S38	1.67	SIEVED		0.00666	1.00	1.20	0.80	0.63	0.024056
B14	PVA8mm	S38	2.42	SIEVED		0.00666	1.00	1.20	0.80	0.63	0.024056
B15	PVA8mm	S38	3.3	SIEVED		0.00666	1.00	1.20	0.80	0.63	0.024056
B16	-			SIEVED		-	1.00	1.20	0.80	0.58	0.011978
B17	PVA8mm	-	-	SIEVED		0.03333	1.00	1.20	0.80	0.58	0.023955
B18	FIBRIN 623			SILICA		0.00683	1.00	2.80	1.12	1.37	0.01973
B19	BELGIAN12mm			SILICA		0.00683	1.00	2.80	1.12	1.37	0.01973
B20	FIBRIN 623			SILICA		0.00683	1.00	2.81	0.00	0.89	0.02067
B21	BELGIAN12mm			SILICA		0.00683	1.00	2.81	0.00	0.89	0.02067
B22	PVA8mm			SILICA		0.114	1.00	1.20	0.80	0.58	0.01522
B23	PVA8mm	S28	13.2	SILICA		0.0722	1.00	1.20	0.80	0.64	0.02489
B24	PVA8mm	S38	6.6	SILICA		0.0722	1.00	1.20	0.80	0.64	0.01929
B25	PVA8mm	S38	6.6	SILICA	0.001268		1.00	1.20	0.80	0.62	0.02398
B26	PVA12mm	S38	6.6	SILICA	0.0182	0.09464	1.00	1.20	0.80	0.61	0.02453
B27	PVA8mm	S38	6.6	SILICA	0.04		1.00	1.20	0.80	0.64	0.01197

3.2.6 Fabrication of the specimens

To prepare mix B1, sand was mixed with two thirds of the water for 1 min and subsequently, cement, fly ash and HRWR while the remaining one third of the water was added mixing continuously for 3 min; lastly, the fibers were added slowly and mixed for another 6 min. This sequence presented some difficulties in that the volume of the final composite was much less than the capability of the available mixing drum and from the start it was noticed that the material added (only sand and water) could not be thoroughly mixed. The procedure had to be stopped several times so that the contents of the drum would be manually mixed.

Prior to the addition of fibers the mix was clearly very flowable. After the fibers were introduced the mix became evidently viscous with clumping of the fibers. Additional water was added in the mix. The additional water made the mix more flowable, and reduced the stiffness that was introduced by the fibers. It was attempted to compact the material when placed in the molds but it was obvious that the mix did not behave well to that. Some compaction was obtained by tapping on the walls of the mold from the outside. Due to the poor flowability, cavities of air were trapped on the side surfaces of the molds for the PP1 mix design, as became obvious after demolding. The specimens were demolded more than 24 hours later, (but the mix took several more days to fully harden), and were placed in water for 28 days.

In the second mix design B2 and all further mixes a different mixing sequence was tested for comparison and was found to be effective enough. The amount of composite was too low for the specific drum dimensions so all the dry materials were firstly added together. After mixing for 2-3 min the full amount of water and half the superplasticizer were added and mixed thoroughly until no clumps were visible. At this phase the mixing was stopped and the cementitious fresh mix showed signs of very good flowability. Then the fibers were slowly added with the rest of the superplasticizer and mixing was continued till they were evenly distributed.

Prior to the addition of fibers the mix was self consolidating (Fig. 3.6(a)). As soon as the fibers were added, even though in the relatively small percentage of 2% by volume, the mix became instantly less flowable and the addition of extra water reducer (super-plasticizer) was necessary this time.

Figure 3.6: Mix flowability prior (left) and after the addition of fibers (middle) and measurement of the slump test diameters (right)

3.3 Tests on hardened concrete and results

Usually when specimen size is very small from the stage of casting a marked bias emanates from the tendency of the fibers to be preferentially layered in a two-dimensional plane rather that acting as actual mass reinforcement. This was observed in the specimens of the first mix, and therefore in subsequent tests specimens were cut off from bigger blocks to secure the three-dimensionality of dispersion. Only early samples of the B3 mix which were cast directly in small molds (approximately 8 mm equal to the length of the fiber) may be assumed to suffer from a 2-D dispersion of fibers – these are considered in this study in a qualitative light only. Also some specific tests such as direct tension dog-bone coupons have a thickness of 25 mm and since they can not be cut from thicker elements, their behavior in stresses and strain tends closer to a 2D dispersed model. Therefore a further need of determining an index between the 2D and 3D distribution between the two models must be put under investigation.

3.3.1 Compression

All tests under uniaxial compression are listed in the following table:

Table 3.7: Specimen size and age of testing (for compression)

MIX No	MIX DESIGNATION	TEST	AGE	on charts	Loading rate
B1	PP1	compression cube	58	B1-58d-1	80 (N/s)
B1	PP1	compression cube	58	B1-58d-2	80 (N/s)
B4	O1	uniaxial LC compression	7	B4-7d-1	80 (N/s)
B4	O1	uniaxial LC compression	7	B4-7d-2	80 (N/s)
B4	O1	uniaxial LC compression	15	B4-15d-1	80 (N/s)
B4	O1	uniaxial LC compression	15	B4-15d-2	80 (N/s)
B5	O2	uniaxial LC compression	8	B5-8d-1	80 (N/s)
B5	O2	uniaxial LC compression	8	B5-8d-2	80 (N/s)
B5	O2	uniaxial LC compression	14	B5-14d-1	80 (N/s)
B5	O2	uniaxial LC compression	14	B5-14d-2	80 (N/s)
B4	O1	uniaxial LC compression	29	B4-29d-1	80 (N/s)
B4	O1	uniaxial LC compression	29	B4-29d-2	80 (N/s)
B5	O2	uniaxial LC compression	29	B5-29d-1	80 (N/s)
B5	O2	uniaxial LC compression	29	B5-29d-1	80 (N/s)
B16	NCC	uniaxial DC compression	28	B16-28d-1	60 με/s
B16	NCC	uniaxial DC compression	28	B16-28d-2	30 με/s
B17	FCC	uniaxial DC compression	28	B17-28d-1	30 με/s
B17	FCC	uniaxial DC compression	28	B17-28d-2	30 με/s

3.3.1.1 Cubic specimens

Uniaxial compression tests were conducted on small concrete cubes (≈50 mm) from the PP1 mix that were saw-cut from the bigger prism specimens. The compressive strength is calculated as the maximum load at failure divided by the loaded area of the specimen. The load was applied with force control at a constant rate of 80 N/s.

Figure 3.7: PP1B compression tests-failure cracks

Under pure uniaxial compression the failure cracks generated were approximately parallel to the direction of the applied load with some cracks forming at an angle as shown in Fig. 3.7. Friction at the end platens due to restrained lateral expansion of concrete combined with the small aspect ratio of the specimen led to the development of a three dimensional state of stress as evidenced by the inclined cracks near the ends. Note however that in no case was there any spalling and deterioration of the test block, a result that is in sharp contrast with the reported behavior of concrete cubes after crushing in the case of conventional concrete. Collapse in those cases would be marked by the excessive lateral expansion beyond attainment of strength; this type of failure is avoided herein owing to the confining action of the fibers.

In general, the compressive properties of SHFRCC are compared to those of normal concrete, reportedly ranging from 20 to 95 MPa, while the elastic modulus is lower (15-35 GPa) due to the lack of coarse aggregate in the mix. The results for PP1 at 58 days are given in Table 3.8.

3.3.1.2 Prismatic specimens

Additional preliminary tests were carried out on small prism specimens with an aspect ratio of two, in order to eliminate the local end effects under load control with a loading rate of 80 N/s. These tests demonstrated an increase of ductility in compression. The prism dimensions were 40×40×80 mm. Due to the small size of the aggregates in FRCC this class of material is generally more compliant than normal concrete, attaining its strength at a higher axial compression strain ($\varepsilon_{co} \approx 0.0035$). Tests were performed also under displacement control using a rate of 30-60 με/s. Strain gauges were placed on three sides of the specimens. Strain gauges on two opposite sides measuring vertical strain -parallel to the load, and on the 3rd orthogonal side, a strain gauge was installed to measure lateral strain. The Poisson's ratio obtained by all these tests and for all specimens seems to be very low and maybe

unrealistic, therefore additional tests should be made with more accurate instrumentation-such as circumferential extensometers (as described in Chapter 4) on cylinders in order to fully determine the behavior of the composite in uniaxial compression.

Figure 3.8: Compressive prism specimens failure cracks (O11, O12, O13, O16, O22A, O22B, O24, O26, NCC1, NCC2, FCC1, FCC2)

Figure 3.8 shows the test results from the compressive tests on the prism specimens of Table 3.7. The beneficial action of the fibers is evident on the failure crack formation of all the specimens. Specimens without fibers (NCC1 and NCC2) show multiple cracks, lateral expansion and a brittle mode of failure. In none of the cases with the fiber mixes the specimens showed spalling. Rather,

multiple cracking was observed with small crack widths around the specimens. Near the failure load one of the cracks in each specimen localized (i.e. it widened in comparison to the rest of the cracks whose width remained constant). Through the wider crack it is evident that the fibers either pulled-out (for the mixes with the coated PVA fibers) or ruptured (for the mixes with the plain PVA fibers).

The maximum load, compressive strength and strain at maximum load are listed in Table 3.8. The compressive strength of the specimens with the Polypropylene fibers (B1) gave the lowest compressive capacity from all mixes, even though these specimens have an aspect ratio of 1, that due to the confining action of the platens should have resulted in higher strength values than specimens with an aspect ratio of 2 or higher. The highest compressive strength was obtained from the specimens without any fibers in the mix design (NCC), while simultaneously they presented the smallest axial strain at maximum load from all specimens, in the range of 3.5‰.

Table 3.8: Test results all specimens under compression

Mix	**Specimen**	**Fibers**	**Type**	**Age**	**P_{max} (kN)**	**σ_{max}**	**ε (at σ_{max})**
B1	PP1C	PP	cube	58	81.08	34.42	-
B1	PP1D	PP	cube	58	84.36	36.02	-
B4	O11A	PVA/O1	prism	7	21.943	13.71	0.0045
B4	O11B	PVA/O1	prism	7	18.597	11.62	0.0023
B4	O13A	PVA/O1	prism	15	47.453	29.66	0.0048
B4	O13B	PVA/O1	prism	15	48.693	30.43	0.0043
B4	O16A	PVA/O1	prism	29	68.232	42.65	0.0043
B4	O16A	PVA/O1	prism	29	72.761	45.48	0.0052
B5	O22A	PVA/O2	prism	8	65.195	40.75	0.0044
B5	O22B	PVA/O2	prism	8	74.517	46.57	0.0051
B5	O24A	PVA/O2	prism	15	64.172	40.11	0.0033
B5	O24B	PVA/O2	prism	15	73.406	45.88	0.0045
B5	O26A	PVA/O2	prism	29	88.276	55.17	0.0048
B5	O26B	PVA/O2	prism	29	86.625	54.14	0.0039
B16	NCC1	-	prism	28	105.211	65.76	0.0035
B16	NCC2	-	prism	28	92.165	57.60	0.0023
B17	FCC1	PVA	prism	28	105.079	65.67	0.0039
B17	FCC2	PVA	prism	28	96.106	60.07	0.0040

Comparing the compressive strength between the mixes with different coatings, O1, O2 and the case of no coating, we obtain the values of 44 MPa, 54 MPa and 63 MPa respectively as shown in Fig. 3.9. A very important conclusion is derived from these results. It is evident from the stress strain curves that the ultimate compressive stress of the composite decreases when the fibers are coated and this relates with the effect of the coating on the fiber-matrix interface bond. Coating O1 has effected a

reduction by almost 30% (from 65 to 40 MPa) on the compressive capacity as compared to O2 which showed a 15% decrease (55 MPa).

Compressive strength is a material parameter that is directly related to its tensile behavior. During compressive loading, Poisson's effect causes lateral expansion to the specimen, and when its tensile strength is surpassed, multiple tensile cracks, parallel to the loading direction initiate and connect. If no confinement is present then the specimen deteriorates and fails. When fibers exist in the mix, they bridge the cracks and provide lateral confinement.

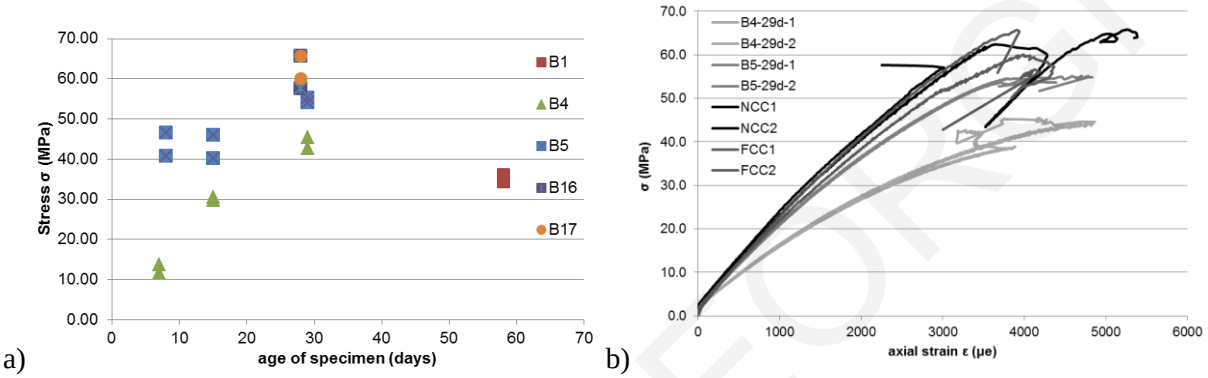

a) b)

Figure 3.9: (a) Variation of maximum compressive stress with age and (b) Stress-strain curves of different mixes at 28 days

Fibers bridge the cracks passing stresses from one side of the crack to the other through the bond mechanism. In the case of PVA fibers without any coating strong chemical bonds exist between the fibers' surface and the surrounding matrix. When coating is applied then these strong bonds are reduced and failure is no longer due to rupture of the fibers but owing to partial pull-out. Different coating materials lead to higher or lower reduction of these chemical bonds and this is responsible for the great difference between mixes with the exact same matrix composition and fiber content but with different types of coating on the fibers.

Figure 3.10 (a) and (b) shows the stress-strain curves of the mixes with PVA fibers and two different coatings at various ages. Both curves show an increase in the compressive strength with age, but with a different rate between the two different coatings. For the specimens with coating type O1, strength increases almost linearly with age, while for coating O2 strength at 8 and 14 days is almost the same while it increases by about 10 MPa for the specimens of 28 days. Additionally the modulus of Elasticity increases with increasing age. Strain at maximum compressive strength is higher than that of normal concrete with values between 4.5 to 5‰.

Lateral expansion measured from strain gauges depicted in Figure 3.10 (c) and (d) as Poisson's ratio vs axial strain, shows very peculiar values in the range of very small axial strains not reported in previous research and a probable cause could be the insufficient sensitivity of the instruments. Additional measurements must be obtained also from other methods in order to verify if the above measurements are dependable.

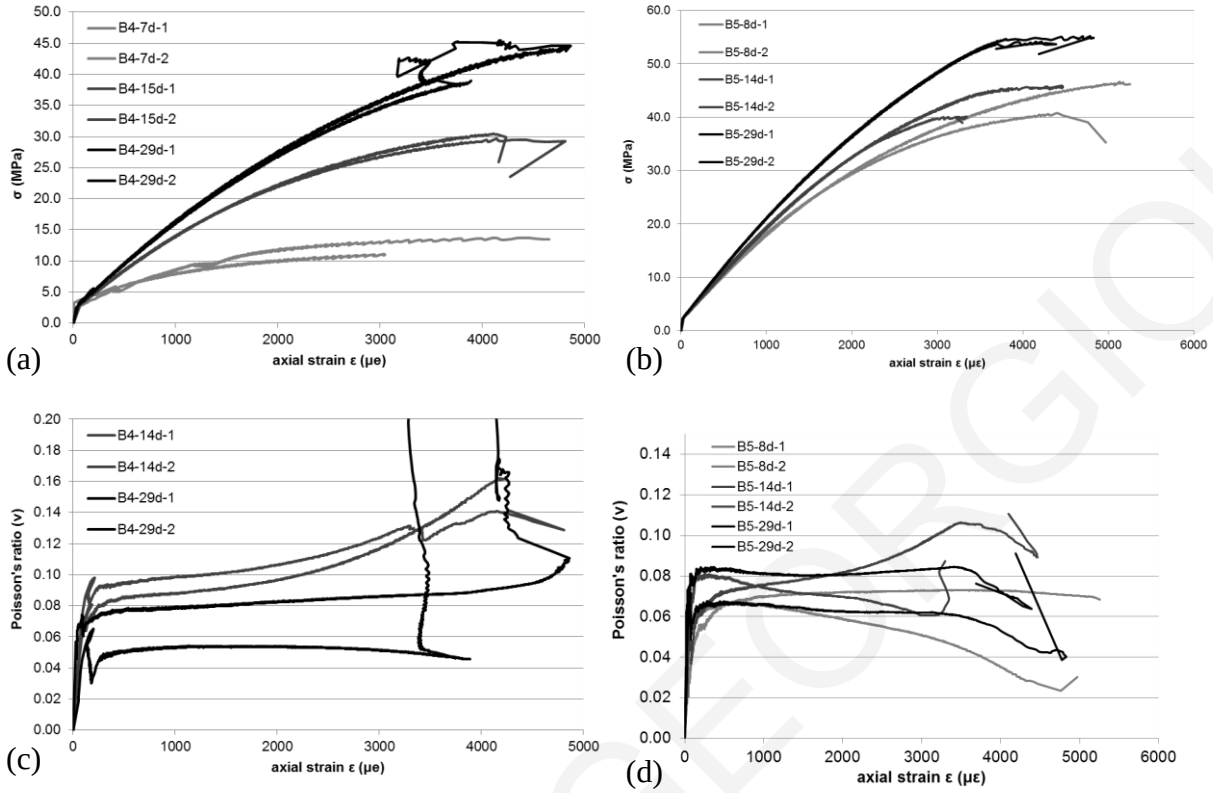

Figure 3.10: (a), (b) Stress-strain curves of B4 and B5 mix design on various ages and (c) and (d) Poisson's ratio vs axial strain

3.3.1.3 Cylinders under uniaxial compression

Uniaxial compression tests were performed well into the post-peak range under displacement control using a closed-loop, servo hydraulic controlled testing machine at a loading rate of 1.50 μm/s. Specimens were cylinders, 100 mm in diameter and 200 mm in height. Axial deformations were measured using two linear variable differential transducers (LVDTs) mounted on opposite sides of two rings that were attached on the specimen over a gauge length of 140 mm. An additional LVDT measured the deformation over the entire length of the specimen, through the displacement of the platens. The displacement control of the machine was based on this LVDT. Circumferential elongation was measured using a circumferential extensometer (chain), placed at the middle of the height of the specimen. The testing setup and equipment are shown in Fig. 3.11 (a).

Compressive stress-axial strain-lateral strain curves extracted from the experimental measurements are reported in the diagrams of Figure 3.11 (b), (c), (d). Stress is computed by dividing the recorded load by the area of the cross section while axial deformation is obtained as the average of the two opposite LVDTs oriented parallel to the load, divided by the 140 mm distance between the gripping equipment. Lateral strain is extracted by the deformation of the extensometer divided by the perimeter of the cylinder. Lateral deformation was a very important parameter that was required for the analysis

of the composites' behavior under compression since softening of the compressive strength is directly related to cracking parallel to the direction of loading and lateral expansion.

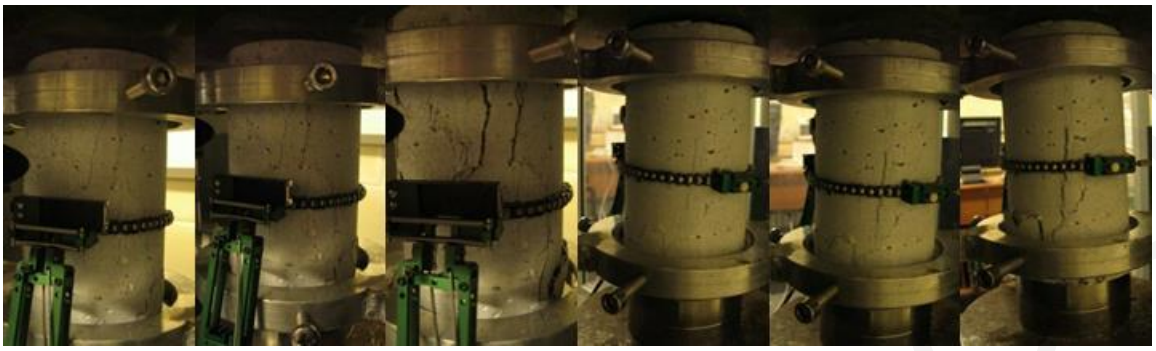

(a)

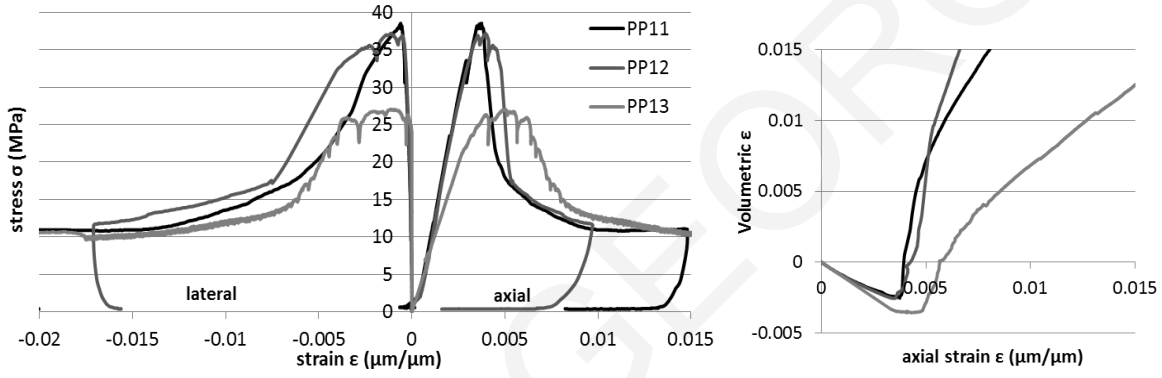

(b)

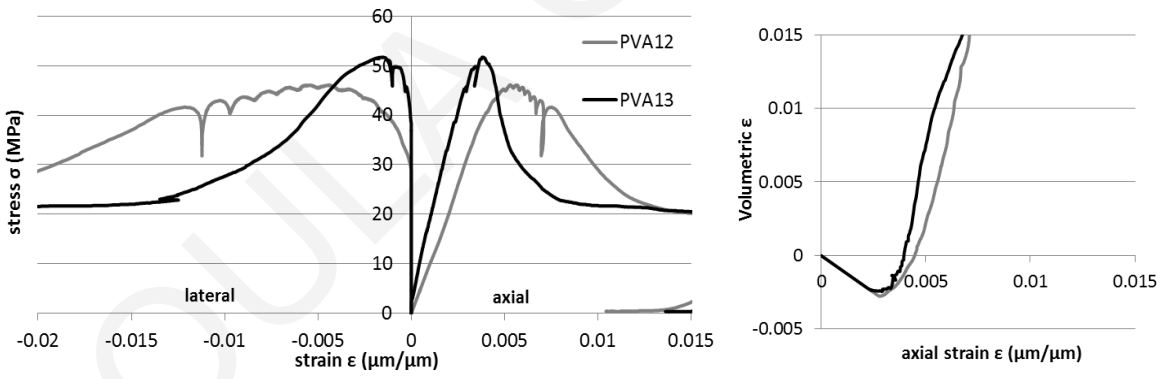

(c)

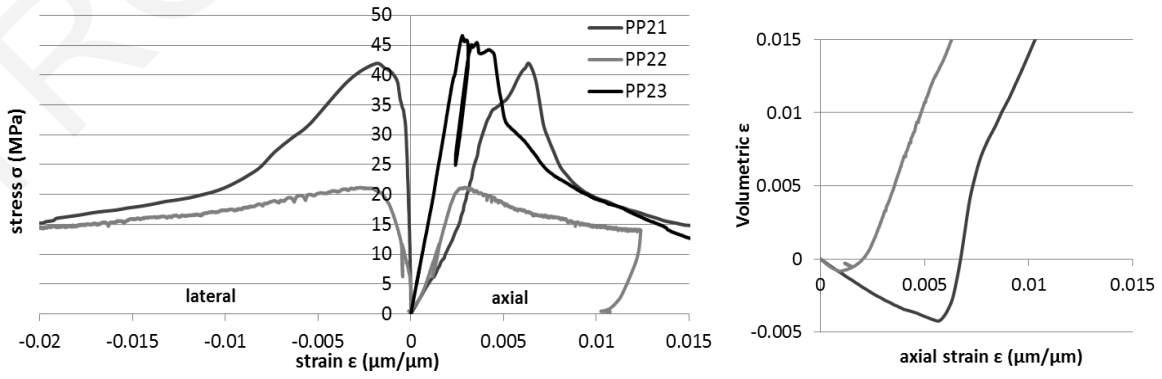

(d)

Figure 3.11: (a) Test setup for uniaxial compression and measuring equipment, Crack evolution for PP-fiber reinforced cementitious composite (PP-2) and (b), (c), (d) stress-axial strain-lateral strain curves extracted from the experimental measurements and volumetric-axial strain curves

Based on the uniaxial compression experimental results of fiber reinforced cementitious composites as shown in Figure 3.11 multiple cracking is displayed all around the specimen. No evidence of deterioration or collapse is exhibited even after a 60% drop of the postpeak capacity under compression. The estimation of the Poisson's ratio for these tests was not possible since in the early range of strain values the chain is slow to engage owing to the low amount of dilation, therefore in the following tests three strain gauges were used for this purpose.

3.3.2 Splitting tests

The split-cylinder tensile test is a commonly used testing method, also prescribed in modern codes and standards, for obtaining the concrete's tensile strength. The split tensile test estimates the direct tensile strength of concrete from the value of the load applied along a diametric plane of the cylinder, generating a parallel diametric splitting crack. Strains are not of any interest in this kind of tests for the normal concrete mixes, but in the case of a strain hardening composite the behavior under this loading is proven to give multiple cracking parallel to the direction of loading spreading over an area that is more than 20% of the cylinders' diameter wide.

Tests have been performed on cylinders of 100 mm diameter and 200 mm height. Tests were carried out under displacement control with a deformation rate of 8.33 μm/s as measured by one of the two LVDTs placed perpendicular to the loading axis, thereby measuring the lateral deformation along a diameter. Loading setup is as shown on Figure 3.12. Tests carried out are shown in Table 3.9.

Table 3.9: Split Tensile tests performed

MIX No	MIX DESIGNATION	AGE
B1	PP1	408
B2	PP2	401
B3	PVA1	363

The failure cracks from the three specimens are shown in Figure 3.12. The fiber reinforced composites show a different behavior than normal concrete. In normal concrete usually one crack is formed and then the specimen is split in two parts not able to sustain any additional load. As seen in the pictures with the FRCs multiple cracking is observed parallel to the main crack. Two hinges are clearly formed on the top and bottom sides of the main crack at the places where the specimen is in contact to the loading platens. Only the B2 mix specimen cracked and separated into two parts while the other two specimens were still together in one assembly after the test was terminated. Fibers in mixes B1 and B2, (which were polypropylene fibers), were pulled out from the matrix, as seen clearly at the crack locations. On the other hand in the case of the PVA fiber mix (B3) it was evident with naked eye that fibers were ruptured at the crack location.

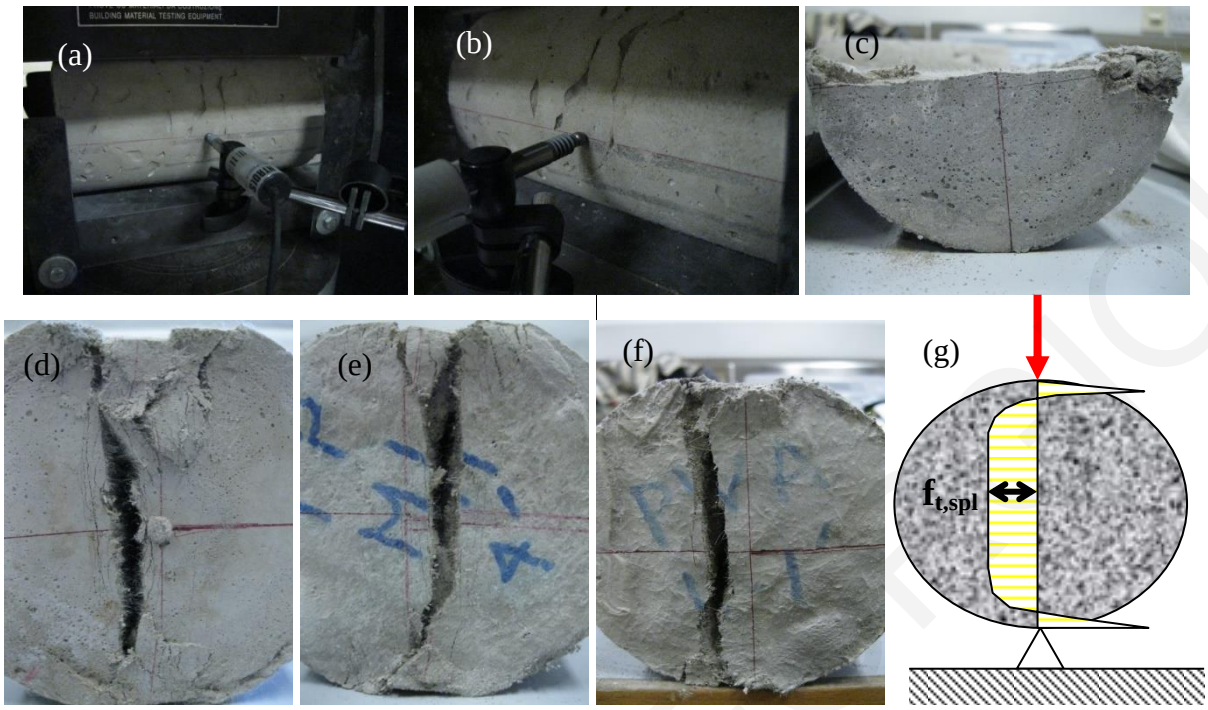

Figure 3.12: (a) and (b) Displacement controlled split tensile tests testing setup, (c)-(f) failure cracks of specimens B1, B2 and B3 and (g) stress distribution

The machine load-horizontal expansion curves obtained from split cylinder tests are depicted in Figure 3.13 and show an unexpected behavior. Peaks are followed by lower bounds. This is attributed to the change of stress field after the main crack was formed. It was evident that load after localization of the main crack passes through the hinges and gets distributed to the two separated parts of the specimens on each side of the main crack (Fig. 3.12 (f)). From the above tests we will only use the first peak stress and strain points as shown in the second graph of Fig. 3.13 to extract the tensile stress capacity of the mixes.

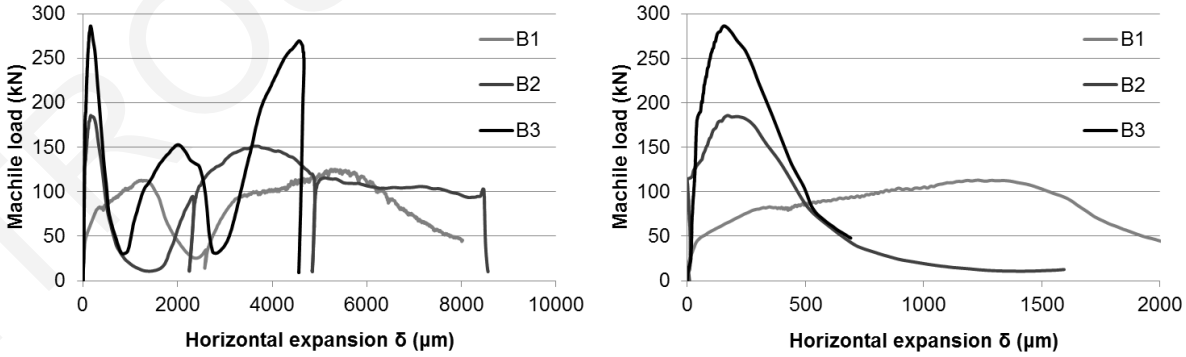

Figure 3.13: Machine load-horizontal expansion curves from cylinder splitting tests

The split tensile strength of the materials is calculated from the experimental results of a splitting test as given in ASTM C496 standard [71] by Equation (3.3), taking into consideration the length of the specimen *l*, and its diameter *d*. From the test results a strain hardening behavior is observed, with a

first yielding load value and a peak load value after the crack localization and softening branch. Load, stress and deformation values for yield and maximum are listed in Table 3.10 with the corresponding splitting strength values.

$$f_{sp} = \frac{2P}{\pi \cdot l \cdot d} \tag{3.3}$$

Table 3.10: Splitting test results (load, deformation, stress)

mix	P_{yield} (kN)	P_{max} (kN)	δ_{yield} (μm)	δ_{max} (μm)	$f_{sp,yield}$ (MPa)	$f_{sp,max}$ (MPa)
B1	39.2	112	18.2	1358	1.25	3.57
B2	115.4	184	31.5	217.4	3.67	5.86
B3	185.846	286.209	46.8	159.5	5.92	9.11

3.3.3 Three point bending

Flexural strength of the concrete specimens was determined by the use of three-point loading on simple prisms (having various thickness values, ranging from 8 to 20 mm, and a span length ranging from 80-130 mm). This testing procedure produces flexural strength values that tend to be higher than those obtained through four-point bending – in the latter specimen form failure usually localizes in the constant moment region, whereas in the former, the apparent strength increase is owning to the shear-flexure interaction effects.. The load was at first applied using force-control up to the first peak value where the first crack formed and then the procedure was continued under displacement control sustaining an approximately constant rate. The specimens' characteristics are listed in Table 3.11.

Table 3.11: Specimen size and age of specimen at testing

MIX No	MIX DESIGNATION	on charts	AGE	dimensions (mm)
B1	PP1	B1-50d	50	50×18×130
B1	PP1	B1-58d	58	50×18×130
B3	PVA1	B3-4d	4	71×8×103
B3	PVA1	B3-28d-1	28	55×8×80
B3	PVA1	B3-28d-1	28	53×8×80
B4	O1	B4-7d-1	7	39×8×136
B4	O1	B4-7d-2	7	39×16×136
B4	O1	B4-15d-1	15	38×18×135
B4	O1	B4-15d-2	15	38×18×135
B4	O1	B4-29d-1	29	38×17×135
B4	O1	B4-29d-2	29	38×19×135
B5	O2	B5-8d-1	8	41×19×135
B5	O2	B5-8d-2	8	41×19×135
B5	O2	B5-14d-1	14	39×19×135
B5	O2	B5-14d-2	14	39×17×135
B5	O2	B5-29d-1	29	40×17×135

B5	O2	B5-30d-1	30	40×18×135
B6	O2	B6-14d	14	37×16×135
B6	O2	B6-28d	28	37×19×135
B7	O3	B7-14d	14	39×18×135
B7	O3	B7-28d	28	39×17×135
B8	O4	B8-14d	14	40×19×135
B8	O4	B8-28d	28	40×16×135
B9	S28-22	B9-15d	15	36×18×135
B9	S28-22	B9-28d	28	36×17×136
B10	S28-16	B10-13d	13	40×20×135
B10	S28-16	B10-27d	13	40×20×135
B11	S28-11	B11-15d	15	40×16×135
B11	S28-11	B11-28d	28	40×19×136
B12	S28-44	B12-14d	14	40×19×135
B12	S28-44	B12-28d	28	40×16×136
B13	S38-11	B13-15d	15	40×17×135
B13	S38-11	B13-28d	28	40×19×136
B14	S38-16	B14-15d	15	40×17×135
B14	S38-16	B14-28d	28	40×19×136
B15	S38-22	B15-15d	15	39×17×135
B15	S38-22	B15-28d	28	38×18×136
B16	NCC	B16-15d-1	14	39×18×136
B16	NCC	B16-15d-2	14	40×18×136
B16	NCC	B16-29d-1	29	38×17×135
B16	NCC	B16-29d-2	29	39×18×135
B17	FCC	B17-15d-1	14	40×18×136
B17	FCC	B17-15d-2	14	40×18×136
B17	FCC	B17-29d-1	29	40×18×135
B17	FCC	B17-29d-2	29	40×17×135
B18	PP3	B18-28d	28	40×17×137
B19	PP4	B19-28d	28	41×16×137
B20	PP5	B20-28d	28	41×17×137
B21	PP6	B21-28d	28	40×16×137
B22	FCC2	B22-15d	15	39×18×148
B24	S38-44	B24-15d	15	41×17×137
B24	S38-44	B24-30d	30	
B24	S38-44	B24-37d	37	
B25	S38-44-DF	B25-14d	14	
B26	S38-44-12-DF	B26-14d	14	
B26	S38-44-12-DF	B26-28d	28	

Specimens of approximately 17 mm in height were cut from larger ones to eliminate the fiber-orientation effect.

3.3.3.1 Tests without coating of the fibers

Load was applied using force-control up to the first peak value which coincided with the first crack formation, and then the procedure was continued under displacement control sustaining an approximately constant rate. When compared with the results from testing plain matrix specimens (with no fibers), marked by sudden collapse after the peak and separation of the test beam in pieces, the fiber-reinforced specimens showed remarkable ductility and strain hardening prior to a slow strain softening decay of strength near the end of test. First, the testing of the mix design for the two types of fibers with their original surface properties gave the expected results. The PP fibers with the hydrophobic surface cracked attaining the composite material's peak tensile load and then deformation was concentrated at one single crack. In the case of the PP fibers type 1 (mix B1), more than one cracks opened at small deformation levels (Fig. 3.14 (a)), but very quickly all the deformation was localized at the crack under the point load. The attained stress level never increased more than the first peak the intensity of which is related with the mix design and most importantly depends on the cementitious matrix composition. The tensile stress resultant attained after that first peak stress is the sum of the forces in fibers bridging across the crack. The stress resultant carried by the fibers is only the force that develops by friction at the interface between the fiber and the matrix. As there is only one crack in this case, deformation of the beam is also related to the slip of the fibers. So the bond-slip law of the interface controls the behavior of the member.

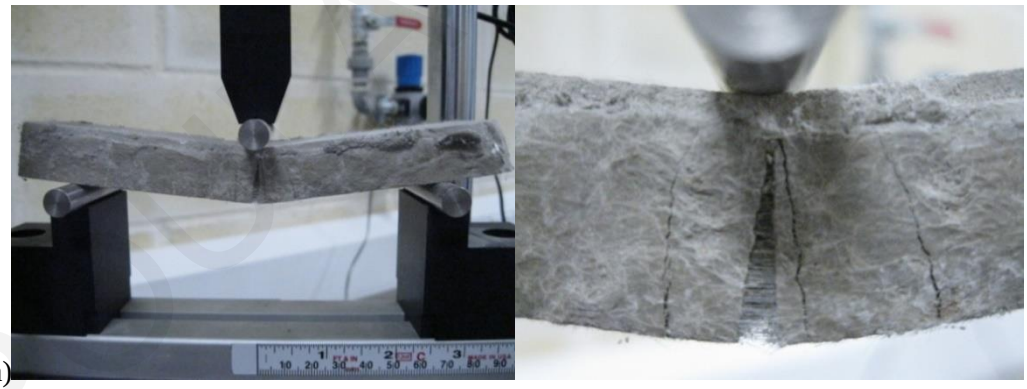

(a)

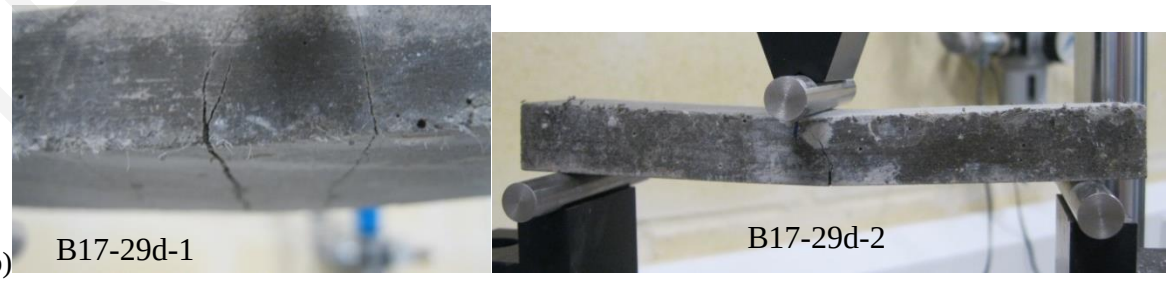

(b)

Figure 3.14: (a) PP1A (mix B1) large deflection and fibers bridging crack action and (b) Tests with PVA fibers without coating

The polypropylene specimens cracked upon attainment of peak strength but continued to be able to withstand high values of load carrying capacity, very close to the peak, whereas additional cracking occurred at higher deflection levels. The fibers were visible, bridging the crack opening without complete pullout and from their stretched appearance it was evident that transfer of stress occurred throughout the crack height. The crack progressively widened from the crack tip to the top face of the specimen. At higher deflections the top side of the specimen exhibited compression cracks but the material was still capable of sustaining high values of stress. During displacement control tests displacement was increased in steps; for each increment, the specimen reached a local peak force which immediately decreased by a margin of about 20%, possibly owing to redistribution of internal stresses along the fibers and/or creep of the fiber material in tension.

PVA fibers without coating were tested (mix B17 – see Fig. 3.14 (b)) examining the difference in behavior for chemical interface bonding; a significant reduction of ductility with localization of deformation in a single crack was noted, followed by an extreme rise of strength (almost doubling of strength). The adhesion was strong enough to render the fiber itself the most compliant component of the mix whereby crack opening now occurred due to fiber elongation rather than pullout, leading to brittle fracture of the fibers and severe localization of all deformation in a single crack. Even in this case, however, the strain capacity attained by the composite was about 100 times more than the value expected for conventional normal strength concrete whereas the tensile strength became much higher.

In order to compare the capacity and ductility of the different types of mixes, nominal stress-deflection diagrams were reduced from the three-point bending tests. Here stress was obtained following the modulus of rupture expressions used by the ASTM Standard C293 [72]:

$$\sigma = \frac{3P \cdot L}{2 \cdot b \cdot d^2} \tag{3.4}$$

In Eq. 3.4 σ is the Modulus of rupture (stress, in MPa), P is the maximum measured applied load (in N), L is the span length (distance between the support and load application point, in mm), and b/d is the average cross section aspect ratio (width/depth) of the specimen (in mm). The stress obtained from the above calculation is not the actual strength. It is valid only for the linear part of behavior where neutral axis is at specimen's mid-height and the stress distribution may be assumed linear to the maximum (yield) strength at the top and bottom surfaces; thus calculation is exact up to yielding. After yielding, fibers bridge the full depth of the tension region of the cross section up till the maximum stress, so the full cross section is participating in the transfer of load. In this context, Eq. 3.4 is no longer exact, but is used to normalize the load of various specimens for comparison purposes. Beyond that limit fibers begin to rupture or pull out and the deflection thereafter is produced in its entirety by localizing of deformation at one specific crack.

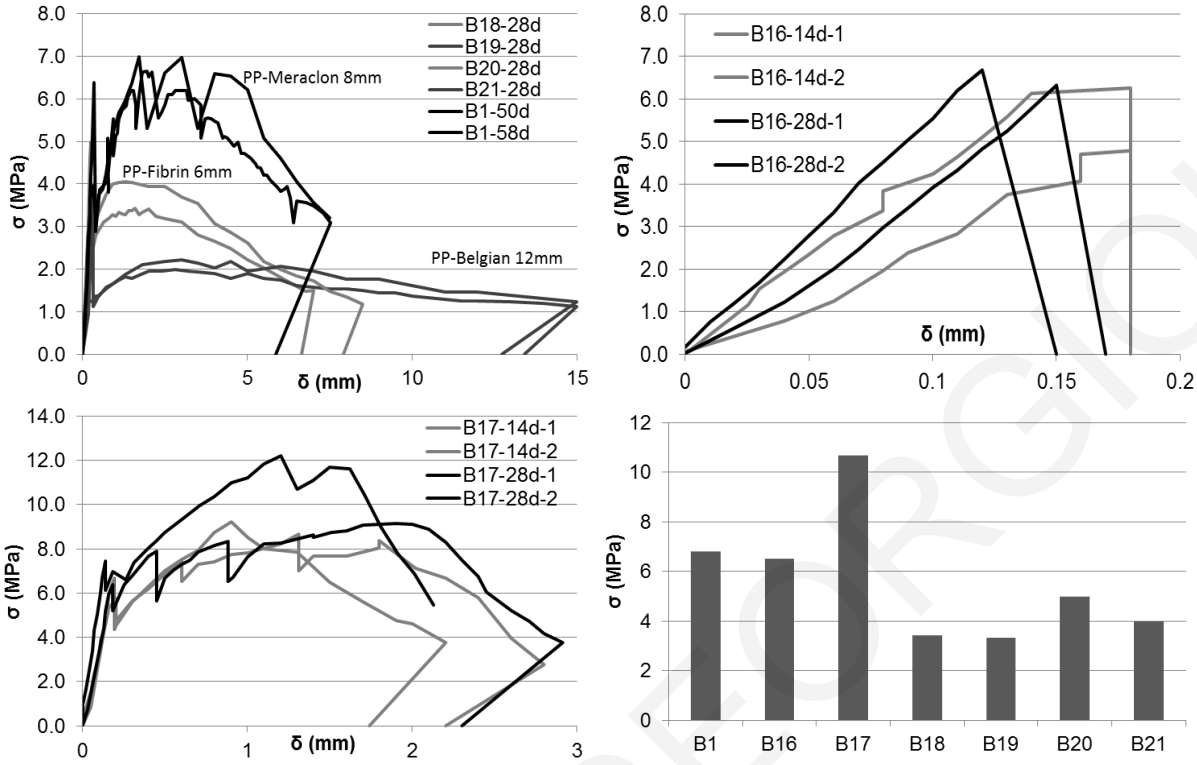

Figure 3.15: Collective plot of all three point bending tests of prisms without fibers without coating

From Figure 3.15 it is evident that Polypropylene fibers with a hydrophobic surface give longer deflections in the three point bending tests, but all this deformation is concentrated at a single crack under point load. It can also be seen that there is a first peak strength which is never attained again after that, since the load carrying mechanism is the friction between the fiber's surface and the surrounding matrix. The deflection is related to the length of the fiber as it can be seen that for longer fibers there is a larger maximum deflection. In the case of the PVA hydrophilic surface, strength continues to increase with increasing deflection. But in this case, due to chemical bonding, deflection is only related to the elongation of the fiber in the open crack width, which is related to the high modulus of elasticity of these fibers.

Comparing fibers with different types of surface properties shows that each type of fiber develops a different type and intensity of bond with the surrounding matrix and the final product´s behavior are greatly affected by this property. According to previous research [73] on the two types of fibers, namely, PP and PVA fibers, completely different behaviors were recorded. The PP fibers developed no chemical bond with the surrounding matrix and a very low contact friction due to their hydrophobic surface, contrary to the PVA fibers which are hydrophilic and display high chemical bonding to the cement hydrates owing to a very large number of free hydroxyls on their surface. This is why if the same amounts of the two fiber types are used in the same basic matrix design, their effect and contribution will be different.

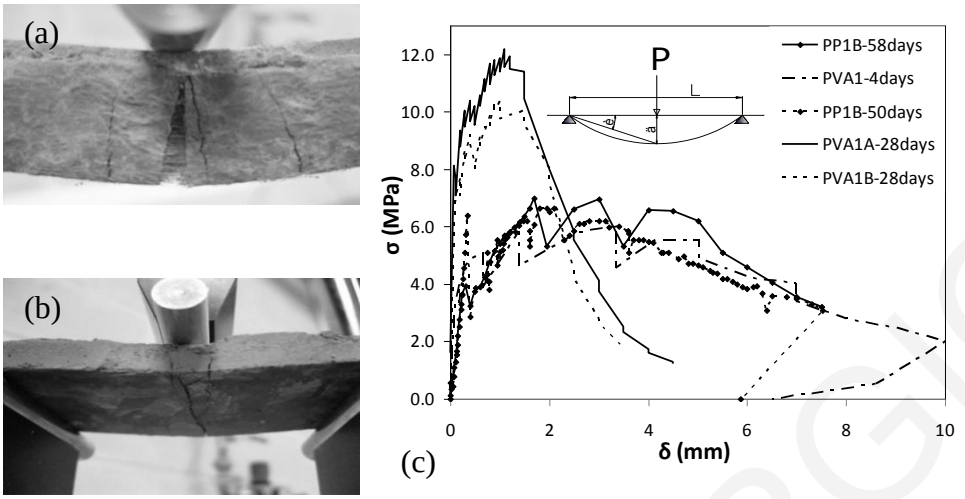

Figure 3.16: (a) PP1A and (b) PVA1a 3 point bending specimen and (c) Stress-Deflection of PP (hydrophobic) and PVA (hydrophilic) cementitious composite mixes

This difference is highlighted in Figure 3.16. The PVA fibers develop a strong chemical bond with the matrix with no slip, and therefore the full amount of measured displacement is owing to the elongation of the fibers crossing the cracks, thereby developing the full amount of load with their tensile capacity. The deformation is developed in a limited number of cracks. The apparent stiffness is very high; therefore the elongation in the free crack width is limited and the material displays a quick (in deformation capacity) development of strength and a reduced rotation capacity of θ_u=2.5%.

In contrast, due to their hydrophobic nature the PP fibers slip from the surrounding matrix displaying large deformations within the crack width (θ_u=7.6%). But they exhibit only limited number of cracks because of early crack-stabilization (beyond this point no new cracks form, whereas deformation localizes in the existing cracks) followed by local failure due to fiber pullout. The strength developed is based on the limited friction of the fibers with the surrounding cement, depending also on the frictional contact area. It was the objective of the present study to enable controlled tensile response of the cementitious product in terms of ductility and multiple crack formation through direct intervention on the surface binding characteristics of fibers.

3.3.3.2 Tests with coating of the fibers

By using different quality and quantity coatings on the PVA fibers an increase in the number of cracks was observed, occurring mostly prior to strength deterioration due to localization of cracking of the specimen, with a commensurate increase in apparent ductility. Specimens of all mix designs showed high values of deflection in the range of 3 mm (corresponding to an ultimate chord rotation prior to crack localization of θ_u=4.6%). The tests showed the formation of multiple cracking with very small crack widths extending over a wide process zone rather than being concentrated under the load.

The fluctuation of the load at the stations after a brief displacement increment was much smaller as the percentage of coating increased (accompanied by an increase in the number of cracks).

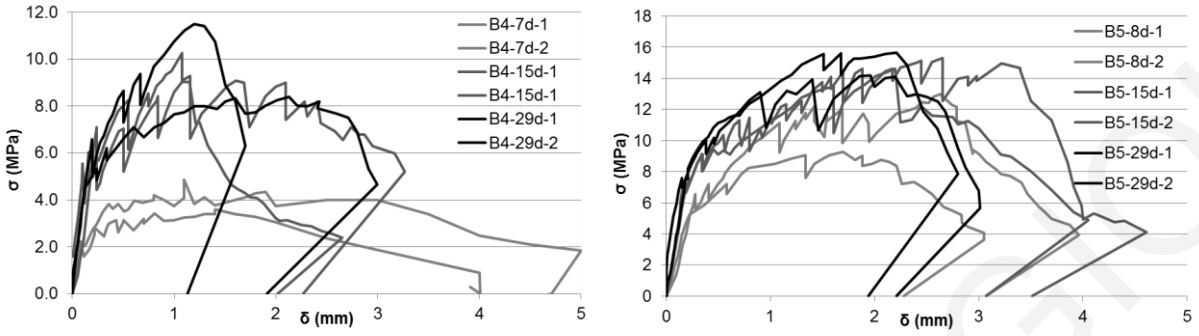

Figure 3.17: Variation of flexural tensile stress-deflection curves on various ages

Figure 3.17 shows the variation between the stress-deflection curves of mixes B4 and B5 on three different ages. The two different types of coating affect differently the stress-deflection diagrams of the mixes. The value of maximum strength is greater in the order of 30% in the B5 mix (with coating O2) as compared with mix B4 (coating O1). Also the hardening, deflection and area under the stress-deflection diagram is greater in the mix B5 (Fig. 3.18), leading to enhanced energy dissipation. Age shows to increase strength, whereas in the deflection for both mixes, maximum deflection is obtained for the test of 15 days of age and it decreases from there on with age.

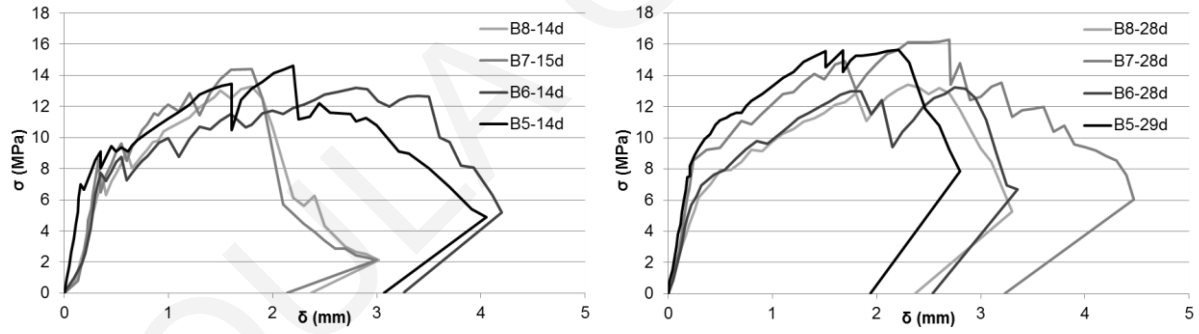

Figure 3.18: Variation of flexural tensile stress-deflection curves on various ages and coating percentages with O2 coating (B5=1.2%, B6=3.3%, B7=6.6%, B8=13.2%)

Analysis of the multiple cracking phenomenon must be studied with reference to the bond-slip law of the interface between the fibers and the matrix. The bond-slip law is affected by the coating of the fibers and age. The strain hardening behavior can be interpreted on the basis of the tension stiffening effect which appears in concrete under tension due to the longitudinal steel reinforcement. Towards this direction the fraction of fibers working effectively in the direction of loading must be calculated. Additionally the characterization of the three types of bond slip laws must be made, considering a) elastic stiff τ-s law associated with chemical bonding on the interface between concrete and uncoated PVA fibers, b) elasto-plastic relationship with partially coated PVA fibers, and c) elastic τ-s law with very low stiffness from PP fibers.

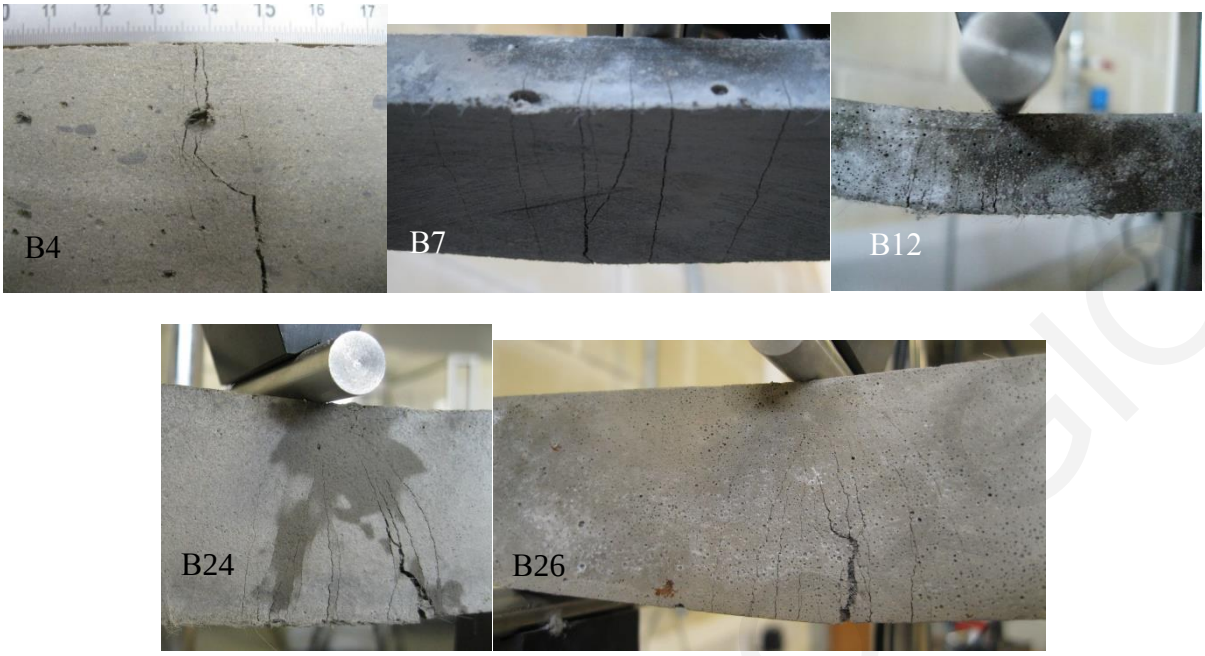

Figure 3.19: Crack behavior of various fractions and types of coating at 28 days

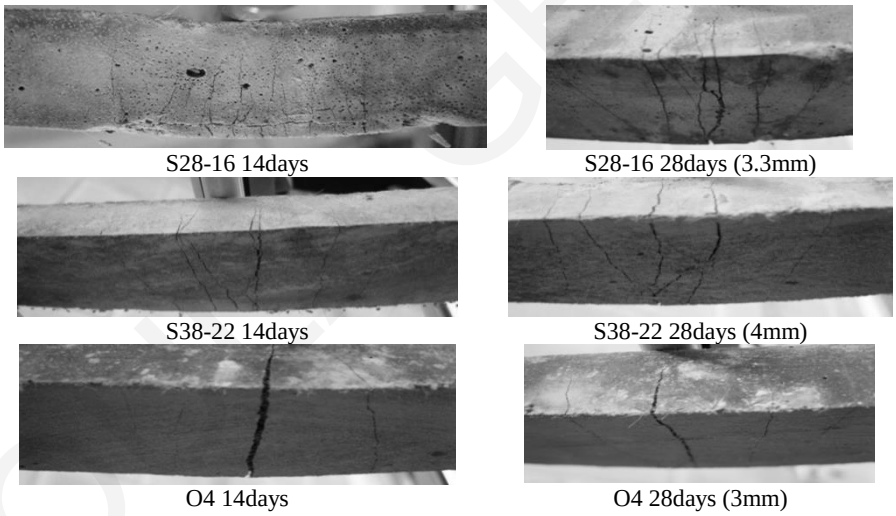

Figure 3.20: Three point bending of various types/percentage of coating and age (deflection at photo capture moment is listed where available)

The crack behavior of various types and fractions of coating at 28 days is depicted in Fig. 3.19. The younger mix specimens at 14 days exhibited a very ductile behavior with approximately the same or higher tensile strength (Figure 3.20). This was the rule on all types and ratios of coating. The fiber's bonding in the matrix increased with age altering the deformation pattern of the individual fibers: from controlled pullout which led to distributed cracking in the early stage, bond increased with age. At 28 days the adhesion was strong enough to render the fiber itself the most compliant component of the mix whereby crack opening now occurred partially due to fiber elongation rather than pullout, leading to less ductile deformation capacity. Even in this case, however, the strain capacity attained by the

composite was about 50 times the value expected for conventional normal strength concrete whereas the tensile strength became much higher.

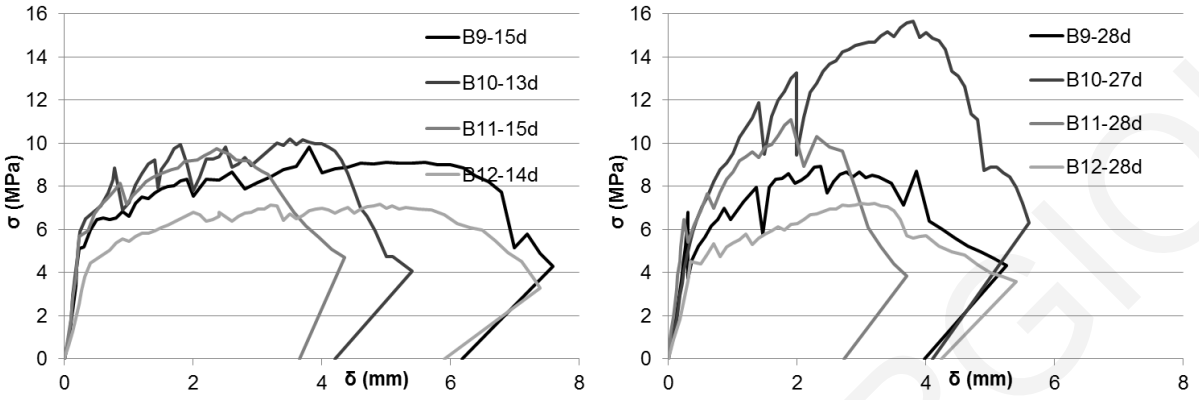

Figure 3.21: Variation of flexural tensile stress-deflection curves on various ages and coating percentages with S28 coating (B9=3.3%, B10=2.42%, B11=1.67%, B12=6.6%)

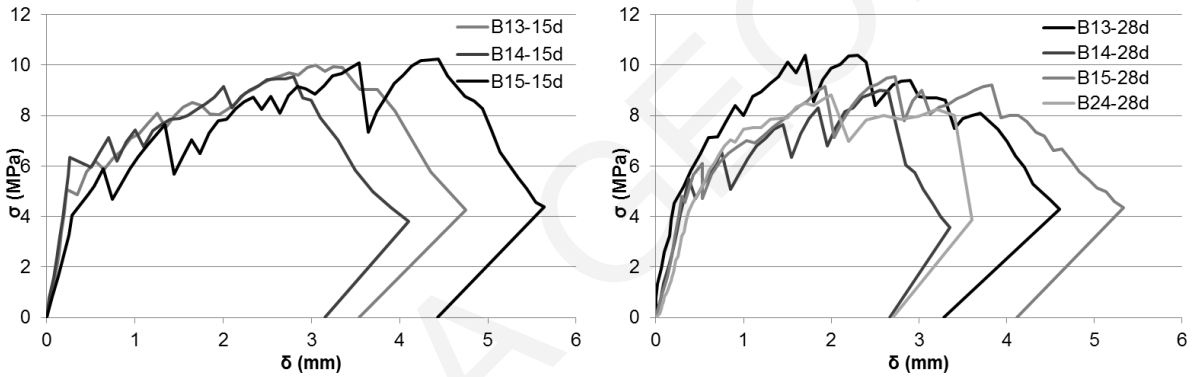

Figure 3.22: Variation of flexural tensile stress-deflection curves on various ages and coating percentages with S38 coating (B13=1.67%, B14=2.42%, B15=3.3%, B24=6.6%)

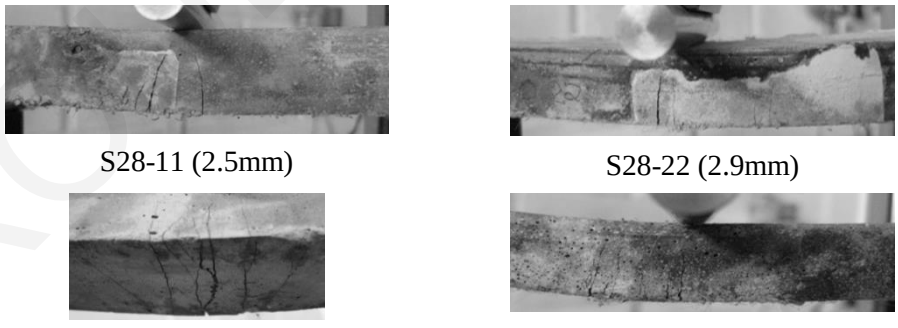

S28-11 (2.5mm) S28-22 (2.9mm)

S28-16 (3.3mm) S28-44 (5.4mm)

Figure 3.23: Three point bending of various percentage of coating at 28 days (peak recorded deflection is listed in the photo capture)

Specimens of all mix designs showed high values of deflection in the range of 4 mm (corresponding to an ultimate chord rotation prior to crack localization θ_u=6%) as shown in Fig. 3.21 and 3.22. The tests showed the formation of multiple cracking (Fig. 3.23) with very small crack width extending over a wide process zone rather than being concentrated under the load. The fluctuation of the load at the

stations after a brief displacement increment was much smaller as the percentage of coating increased (increase of cracks number).

3.3.4 Four point bending tests

3.3.4.1 Four point bending test with a notch

Four point bending tests on notched beams were carried out in order to examine the effect of the fibers over existing cracks in the region of a constant moment load without shear forces and the fracture energy. The propagation of the crack is measured from the center point deflection. The testing setup is as shown in Figure 3.24. The specimen is placed on the machine horizontally with respect to the casting direction. The test is carried out under displacement control with a displacement rate of 0.83 μm/s up till a deflection of 300 μm and then 3.33 μm/s as per ASTM C1609 [74]. The notch had a depth of 30 mm. All the tests that were carried out with this type of loading are shown in Table 3.12.

Table 3.12: Mix designations of specimens tested under 4 point bending with a crack

MIX	MIX DESIGNATION	AGE	on charts	dimensions (mm)
B1	PP1	356	B1-356d-1	100×100×300
B1	PP1	356	B1-356d-2	100×100×300
B1	PP1	357	B1-357-3	100×100×300
B2	PP2	398	B2-398d-2	100×100×300
B3	PVA1	341	B3-341d	100×100×300

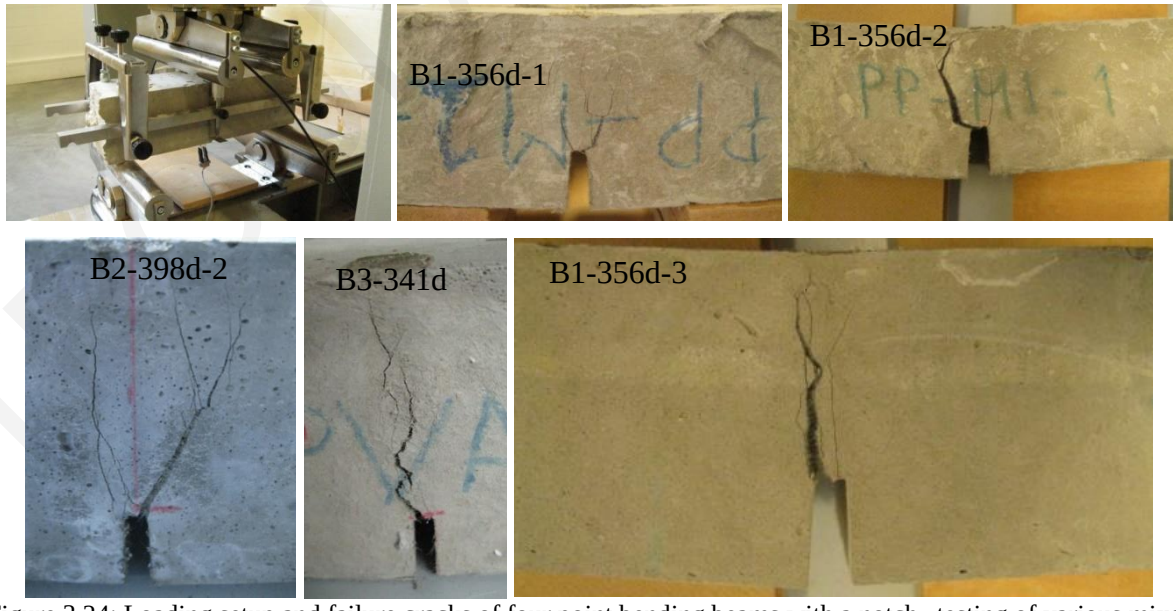

Figure 3.24: Loading setup and failure cracks of four point bending beams with a notch--testing of various mixes

The crack patterns from the above tests for all specimens are shown in Figure 3.24. Multiple cracks were developed on the specimens initiating from the notch and propagating towards the compressive

zone of the beams for all mixes. After the peak load the deflection was the result of one main crack at which all the deformation was concentrated. At this major crack the fibers showed to pull out from the matrix in the cases with the PP fibers, or rupture in the case of the mix with PVA fibers.

Figure 3.25 shows the Load-deflection/crack opening curves for all specimens. The three materials seem to have the same initial stiffness. In the case of specimen B1-356d-1 the test was stopped at a point due to instrument malfunction and then it was started again from the beginning with the results of Curve B1-356d-2. This is why the initial stiffness of the second curve is compliant with the unloading branch of the first curve. Of great interest is the resultant Load-Crack opening displacement curve used to determine the fracture energy released on the crack penetration front. The load capacity of the matrix with the PVA fibers was double the capacity of the PP mixes. This is attributed to the higher stiffness of the PVA fibers and their ability to create chemical bonding with the surrounding matrix leading to fiber rupture than pullout. On the other hand the PP fibers, due to their tendency to pull-out from the matrix show higher deflection capacity in comparison to the PVA mix.

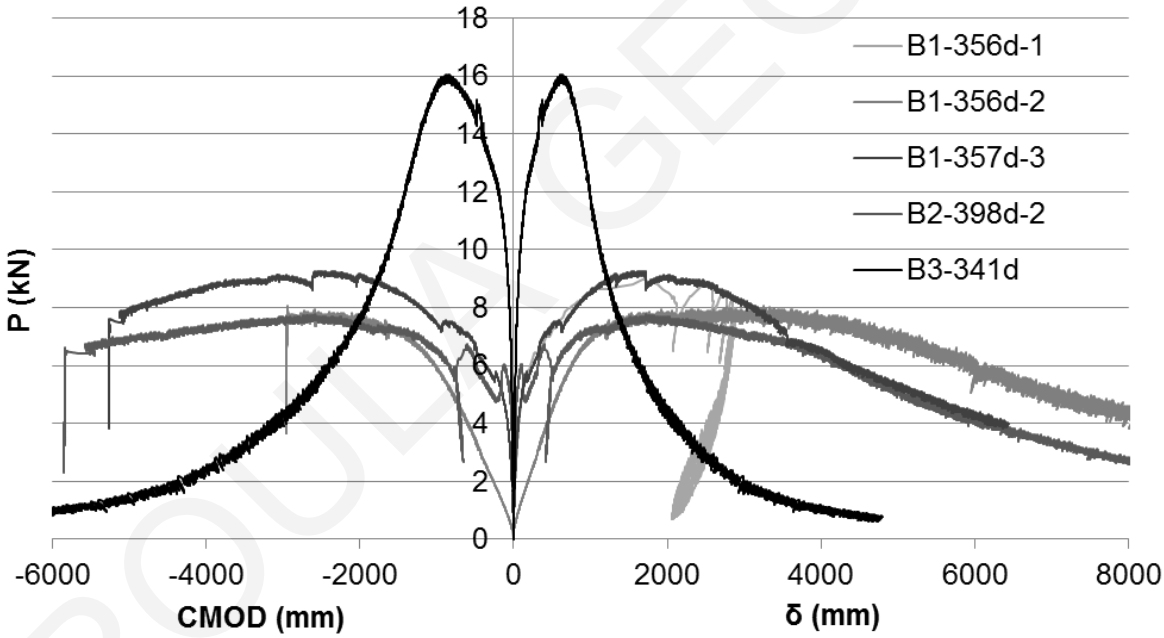

Figure 3.25: LOAD-deflection/CMOD curves for various cement composites

3.3.4.2 Four point bending test without a notch

Four point bending tests without notch were also performed on various mix designs. The setup and loading rate were the same as in paragraph 3.3.4.1. Tests with the various mix designations are shown in Table 3.13. The test is carried out under displacement control with a displacement rate of 0.83 μm/s up till a deflection of 300 μm and then 3.33 μm/s as per ASTM C1609 [74]. Also the same test was performed on a sample with a span to depth ratio of 1 and a depth to span ratio of two by varying the height of the specimen in the specimen series. The age of the specimens was over 360 days in order to

quantify the ductility beyond the time varying processes of strength development that altered the response within the first 28 days.

Table 3.13: Four Point Bending Displacement control tests

MIX No	MIX DESIGNATION	AGE	on charts	dimensions (mm)
B2	PP2	365	B2-365d	100×100×300
B3	PVA1	360	B3-360d-2	100×100×300
B2	PP2	401	B2-401d-4	50×100×300

Load-deflection curves of the above samples are shown in Figure 3.26 and cracking patterns in Figure 3.27. Multiple cracking is observed in all specimens. Higher load capacity is observed again in the case of the PVA mix design. After maximum load deformation was concentrated in one single crack that was either in the constant moment region or under the load application points.

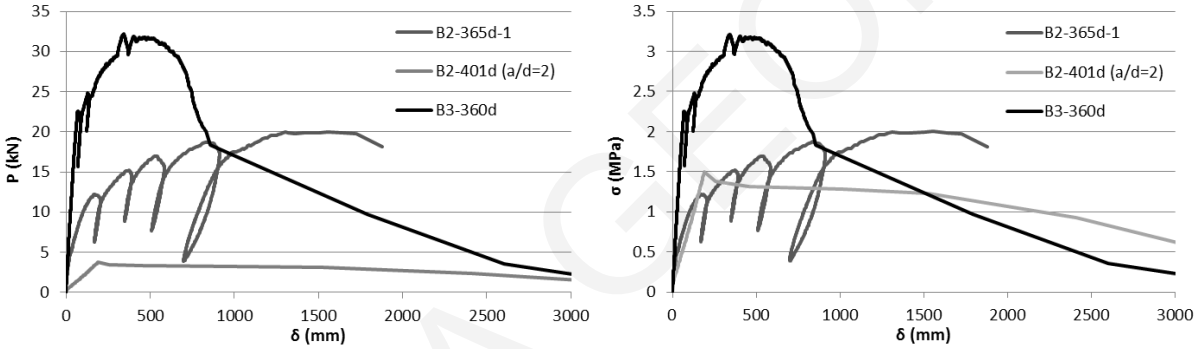

Figure 3.26: Load-deflection and stress-deflection diagrams of four point bending tests

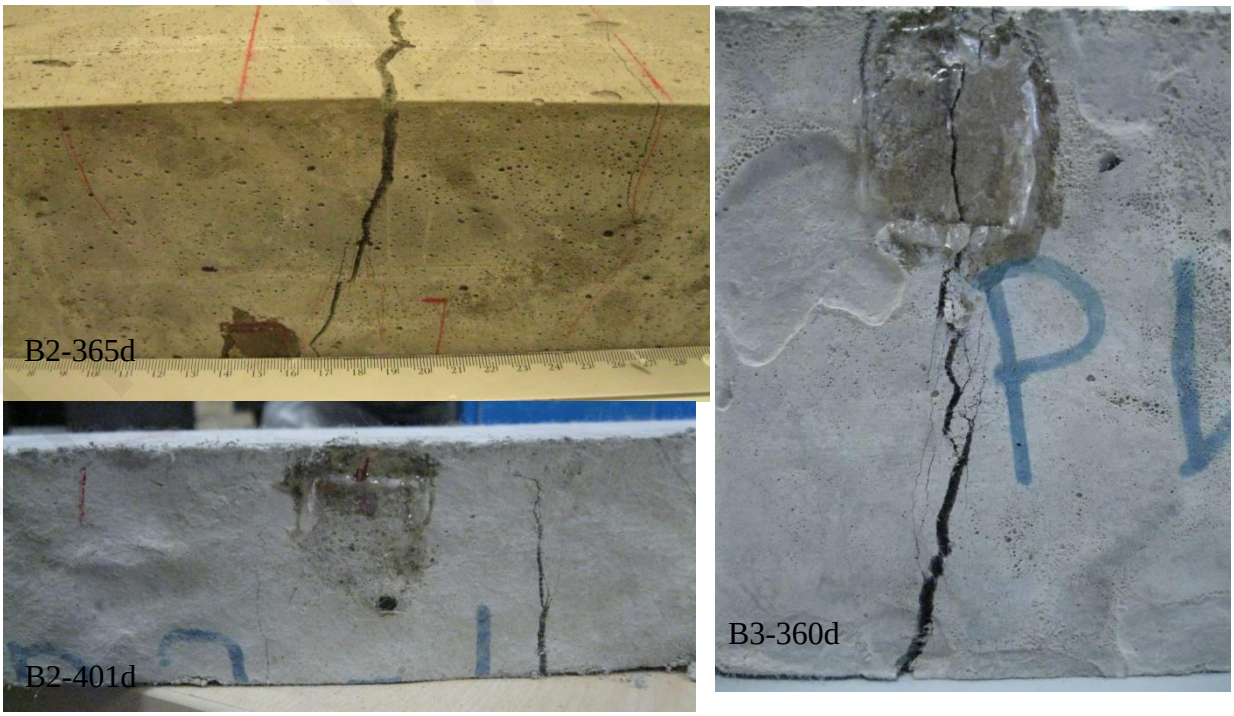

Figure 3.27: Failure modes of four point bending tests on beams without a notch

3.3.5 Uniaxial tensile tests

3.3.5.1 Review of the direct tensile testing methods

In the case of normal concrete the determination of its tensile strength and strain is performed by indirect methods due to its brittle nature and the subsequent inability to perform uniaxial tensile tests. Therefore codes and standards refer only to the indirect methods used to determine the tensile strength of concrete that is used for analysis and design purposes. Lately fiber reinforced composites have been introduced in the Model Code [49], usually with steel and polypropylene fibers that exhibit strain softening behavior in direct tension. The MC-Chapter 5.6 advises against the performance of uniaxial tensile tests due to the difficulty in performing and interpreting them and proposes three point bending tests with a preformed notch and the corresponding inverse analysis to be performed to extract the tensile stress-strain relation. Other researchers have proposed methods for conducting uniaxial tensile tests. These tests require special gripping devices and some examples proposed are shown in Fig. 3.28. Important parameters are the load transfer paths with regards to the stress concentration and the possible moment introduction in the cross section. If the specimens have a uniform cross section, failure at the end of the grips is observed and the gauge length is difficult to be established. When the cross section gets wider at the ends for the gripping mechanism, if not designed correctly, failure might occur at the points where the cross section changes geometry due to stress concentrations. This phenomenon is also observed when anchors are placed at the specimen ends.

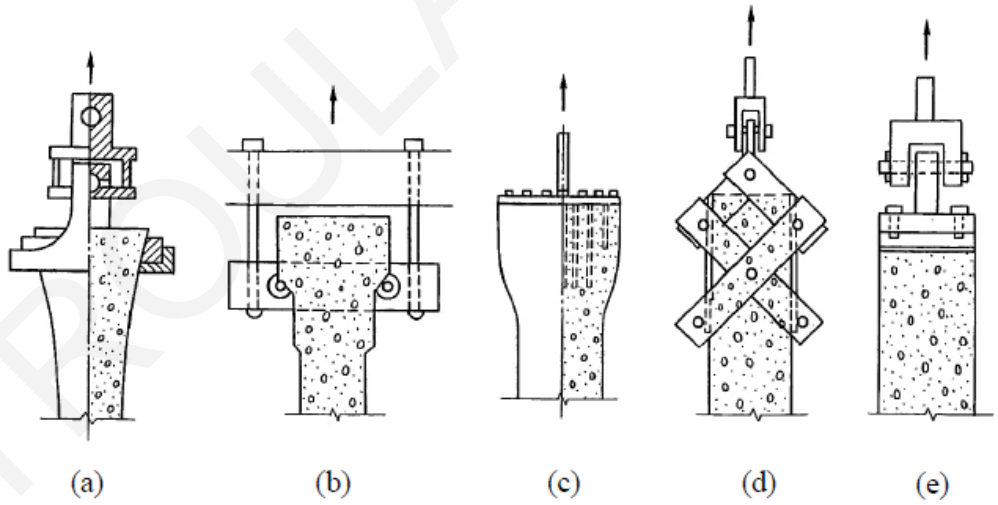

Figure 3.28: Examples of end shapes for direct tensile test [75]

The boundary conditions that are possible to be used are either unrestrained rotation or restrained rotation or a combination of these in the two ends. Whatever the end connections, the non-uniformity of the material matrix, the precision of the specimen's shape, the stiffness of the loading machine and the setup conditions all contribute to the occurrence of bending moments at the cross sections [76]. The

best condition to reduce these moments is with freely rotating pivots however if cracking occurs at one side of the specimen a secondary moment is unavoidable to occur causing errors in stress and strain evaluation.

Also scale effects are very important to be considered. It is a well-known fact that smaller specimens show higher strengths due to the size of defects such as air voids, drying shrinkage or material segregation. Additionally the ratio of the fiber's length to the specimens' dimensions may change the 3D distribution of the fibers over the cross section to 2D if not designed correctly.

In terms of geometry, Chandrangsu [77] showed that the size of specimens affects the strain value at the peak stress and the difference between small and large specimens could be as high as three times with small specimens being more ductile than large specimens. In term of alignment, Toutanji et al [78] applied a small confining pressure to the side of a specimen to ensure that the loading direction is always parallel to the specimen. Since FRCCs are not homogeneous, secondary flexural moment can be developed when fixed loading platens are used. This will cause redistribution of stress within a specimen and lead to higher fracture toughness than can be achieved with freely rotating boundaries (pins, [79].)

A series of materials were tested by Kanakubo [80] under uniaxial tension using different specimen dimensions and geometry as well as testing setups (shown in Fig. 3.29). The first setup (T1) has a small cross-section of 30x13 mm and was designed by Kanda and Li [81], where due to the dimensions of the specimen fiber orientation is 2-dimentional. The other three types of specimens have larger sectional dimensions ensuring better 3-dimentional orientation of the fibers. T2 has a cross-section of 100x60 mm (designed by Shimizu et al. [82]), T3 has a circular cross-section of 70 mm (by Furuta et al. [83]) and for T4 ordinary cylinder specimens were used (by Sato et al. [84]). In order to limit secondary moments pin-fix end conditions were selected for specimens T1, T2 and T3. Kanakubo [80] reports that out of the three specimens tested for each mix design, one of them failed outside the LVDT's measuring range, while in some specimens loading could not be completed due to delamination of the steel plates. In the case of the T4 specimen due to the fix-fix condition, a large bending moment was created and first cracking point could not be determined. The tensile tests for the various setups were conducted for the same mix designs and as a result various tensile strengths were observed with a tendency of the T1 testing setup to give the maximum values and the T4 setup to give the lowest. Also strains at maximum stress were greater for the T1 and T2 setups. This tendency for the case of the T1 setups to give greater values of stress is attributed to the 2-dimensional distribution of the fibers. The tensile strength shows a coefficient of variation (COV) in the order of 5-15%, while the COV for the strain values shows greater scattering.

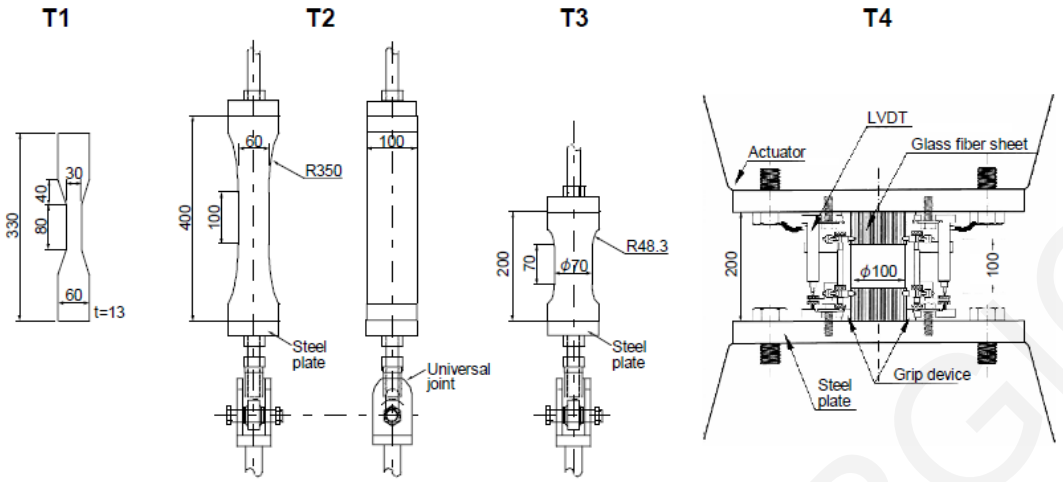

Figure 3.29: Testing setup performed for comparison reasons of uniaxial tension tests [80]

Other researchers used dog-bone specimens as the one shown in Fig. 3.30 that either use gripping mechanisms to load the specimens in uniaxial tension or use holes on the two sides of the specimen from which the specimen is pulled.

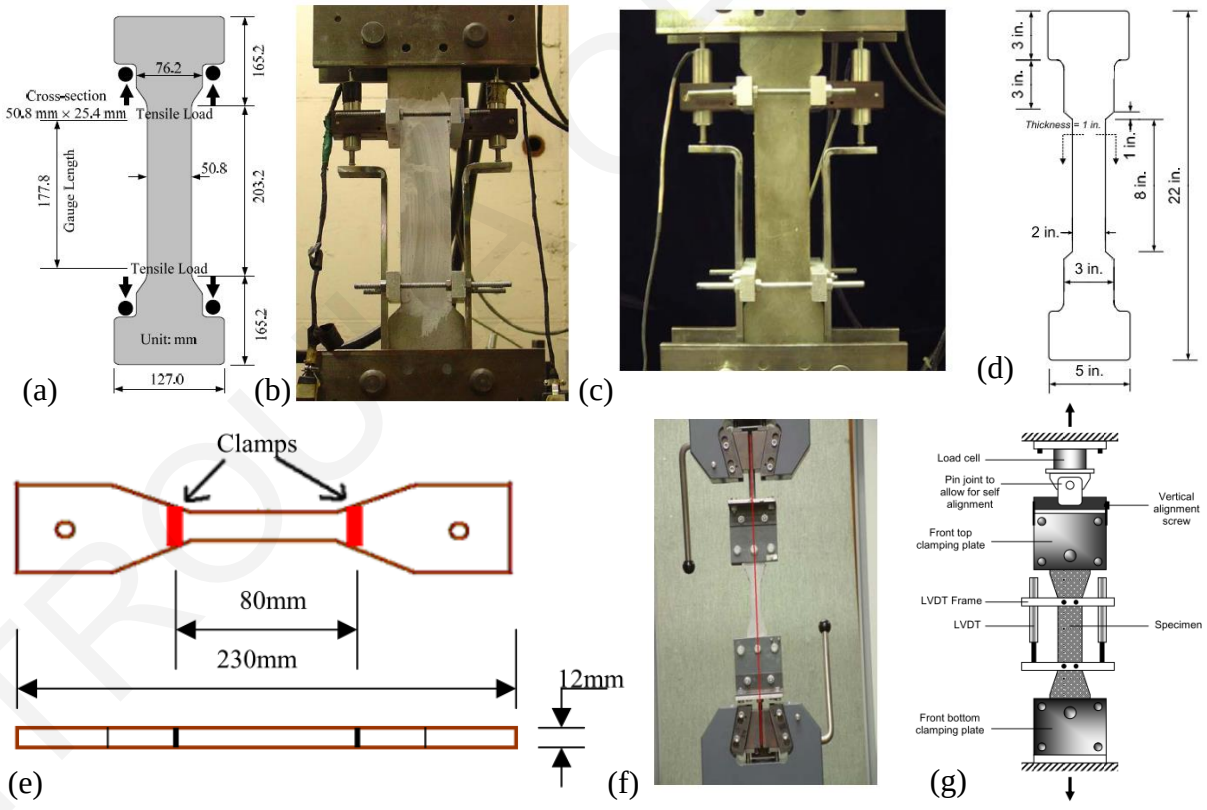

Figure 3.30: Dog bone specimens (a) dimensions and (b) test setup (Likhitruangsilp [85]) by Sirijaroonchai [86], (c) test setup and (d) dimensions by Song [87] (e) and (f) by Molapo [88], (g) by Chao [89]

3.3.5.2 Design of uniaxial tensile test setup and coupon

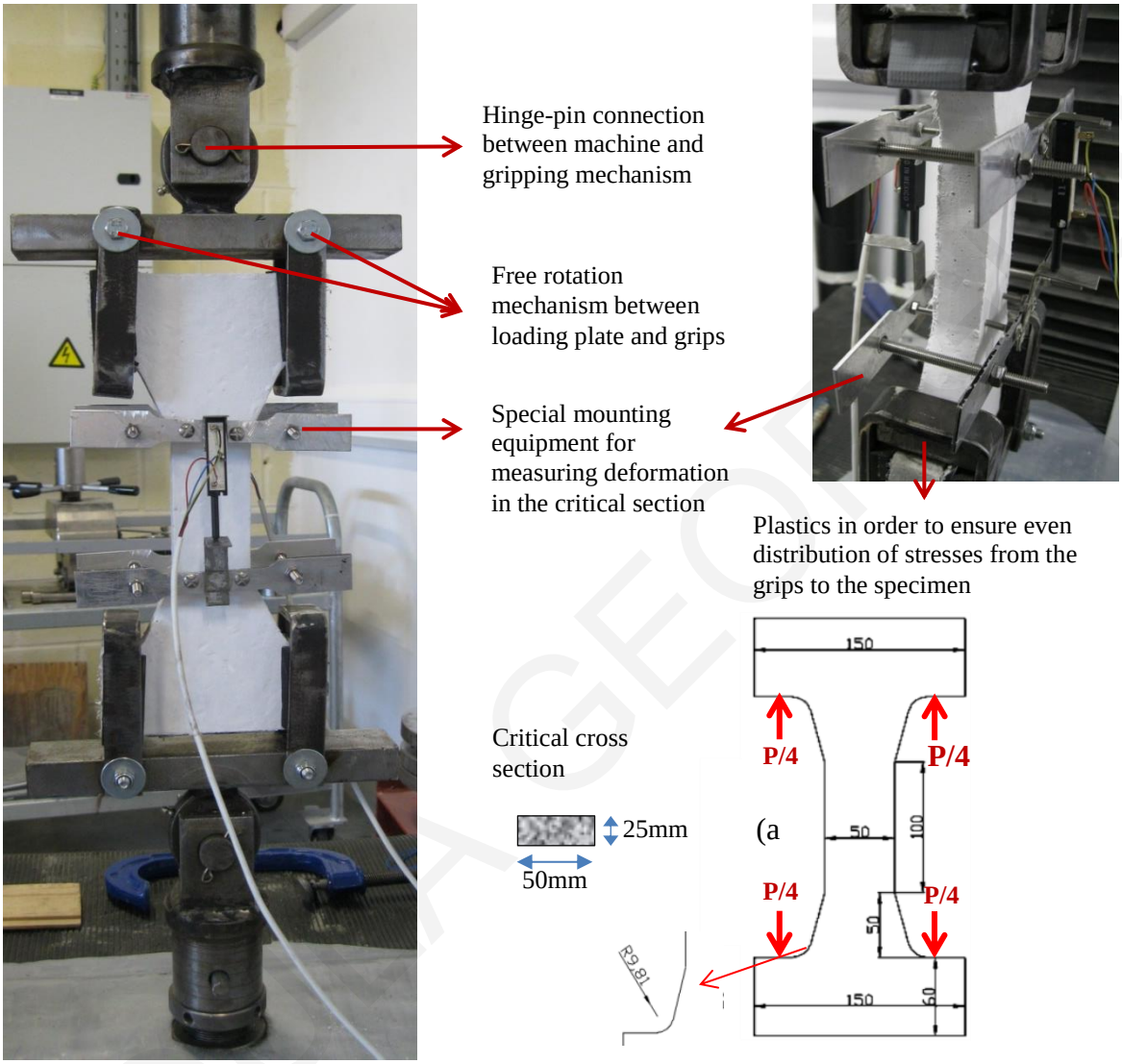

Figure 3.31: Direct tensile test setup

Taking into consideration research that was conducted up till now for the uniaxial tensile tests of ductile fiber reinforced composites a special dog-bone coupon and mounting equipment was designed for the purposes of this research. The characteristics that the test should comply to were the following: a) gripping should ensure spherical pin end conditions in order to limit secondary moments, b) specimens' cross-section should ensure 3-dimensional distribution of the fibers, c) the specimen should not be glued to the specimen or have holes on the loaded ends that would lead to uneven stress distribution or failure paths at the loading points, d) the specimen should have a gradually changing cross-section with dimensions that become bigger at the ends in order to ensure that cracks concentrate in the central, narrower area so that they can be recorded and monitored, e) easy mounting of the specimens on the gripping mechanism should be ensured. Taking into consideration the above

conditions the gripping equipment that was specially designed for the prototype dog-bone specimen used in the present study for testing the tensile strength of concrete is shown in Fig. 3.31.

Nonlinear Finite element modeling and analysis was carried out on various specimen dimensions and geometries, with the software ABAQUS [6], in order to ensure that the desired failure mechanism would occur; that is, multiple cracking within the central region of the specimen having the smallest cross-section dimensions. The final dimensions that were used in the experimental program are also shown in Fig. 3.31 while the steel molds that were used to cast the specimens are shown in Fig. 3.32 while the uniaxial tensile specimen simulation by Finite Element Modeling (FEM) is described in detail in Chapter 11.

The tests were carried out with displacement control of the longitudinal translation of the machine. The test were carried out on a floor standing self-reacting servo—controlled testing frame with a load cell capacity up too 300 kN (Lloyd). Displacement rate was 0.0025 mm/s. Deformations were measured using LVDTs mounted on the two wider opposite sides of the coupons over a 100 mm gauge length in the narrowest region of the specimen where the cross section was 25x50 mm. Plastic pillows were placed between the gripping mechanism and the coupon to distribute stresses and avoid localization. The testing setup had spherical hinges on both sides (Fig. 3.31) to assure self-correction of possible miss-alignment and that no spurious stresses other than axial loading would be developed within the measuring range.

Figure 3.32: Direct tensile test coupon dimensions and molds for casting

Table 3.14: Tests under uniaxial tension

DATE	MIX No	MIX DESIGNATION	AGE	on charts
06-02-14	B22	FCC2	15	B22-15d
18-02-14	B22	FCC2	27	B22-27d
07-04-14	B24	S38-44	15	B24-15d
23-04-14	B24	S38-44	30	B24-30d
30-04-14	B25	S38-44-DF	14	B25-14d
29-05-14	B26	S38-44-12-DF	14	B26-14d
12-06-14	B26	S38-44-12-DF	28	B26-28d

Uniaxial tensile stress-strain curves were extracted through this test for all the fiber reinforced cementitious composites that were used (Fig. 3.33). Stress was calculated as the Machine Load divided by the critical cross section area of 25x50 mm. Strains were the averaged deformation of the two opposite LVDTs divided by the measuring length of 100 mm. All tests carried out under this setup are shown in Table 3.14.

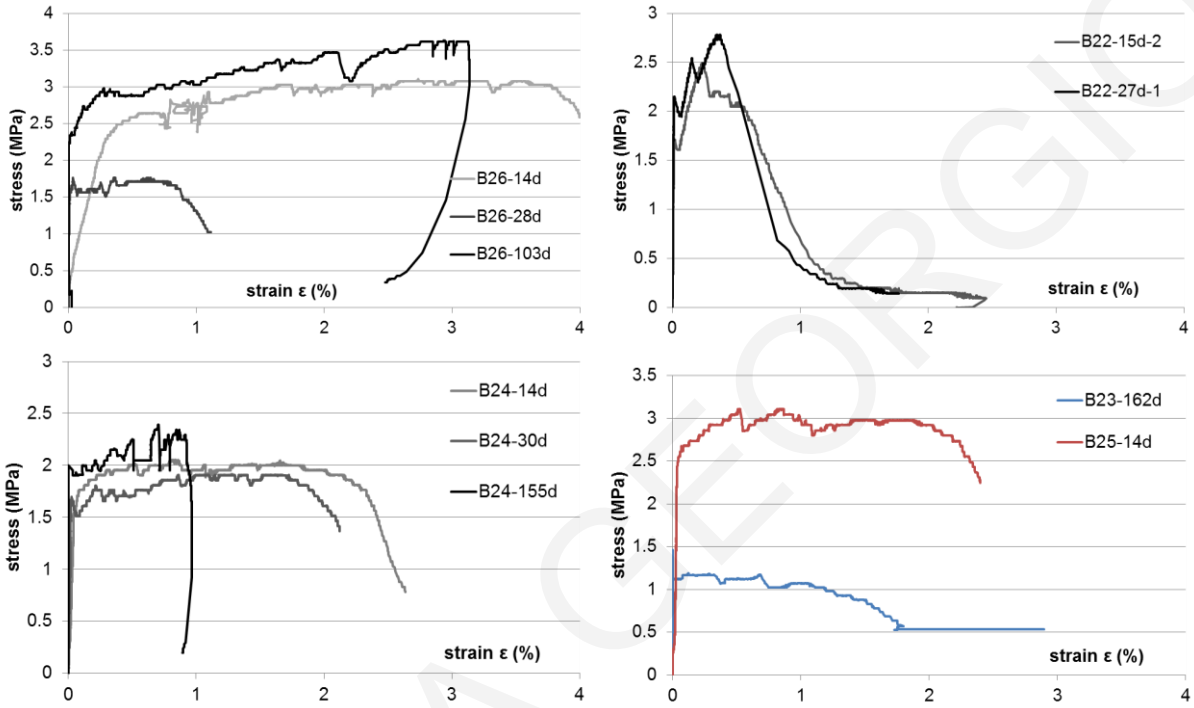

Figure 3.33: Direct Tensile Stress-Strain Curves

The specimens were sometimes witnessed to start cracking from one side only, and upon further widening of the cracks, the crack spread throughout the whole width of the coupon. The specimens also were very susceptible to internal defects such as voids, which in this situation could cause failure by sudden rupture of the specimen. This is not characteristic of the material if specimens are of larger size, since the ineffective area would be a rather small fraction, i.e., not leading to sudden crack localization.

Chapter 4: Experimental Program

4.1 Introduction

A critical feature of cementitious composites for securing very large strain capacity is the requirement that cracking stabilization be delayed or even entirely avoided, so that multiple - rather than localized - cracking may develop so as to achieve a large range of the plastic domain in the response curve. Preliminary experimental data from sample uniaxial compression, tension, three and four point bending tests, as described in Chapter 3 were conducted on mixes containing various types of fibers and fiber coating ratios. It was found that PVA fibers of 8 and 12 mm length increase greatly the tensile strength of the matrix but produce cementitious solids with a limited tensile strain capacity that does not exceed a value of 1%. Strong bonds created between the free hydroxyl groups on the fiber's surface and the matrix, lead to brittle rupture of the fibers as the interfacial strength increases with time. This motivated research into an attempt to alter the mode of failure from fiber rupture to partial pull-out failure, to be achieved by coating the surface of the fibers. In the present chapter the series of tests conducted in order to investigate the effect on the mechanical properties of the composite induced by surface treatment of the fibers is described; length of fiber is another important parameter considered, as it affects the mode of failure and the resulting strain capacity of the composite. The age of the composite may also be a significant factor, as it affects both the bond properties between the fibers and the matrix and the stiffness properties of the matrix, since fly ash shows delayed reactivity due to its pozzolanic nature, but this parameter was kept constant by performing the tests at the age of 100days.

Little documented test evidence is available regarding the performance of strain hardening fiber reinforced cementitious materials (SHFRCC) when used as matrix in reinforced concrete structural members. Without this background, there is no quantitative basis for safely implementing this material in structural design. Some adhoc guidelines have been issued by professional organizations [1, 50, 90–92], however, SHFRCC has not yet been incorporated in Modern Codes. This is consistent with the fact that this application is rather recent and therefore not fully supported with the critical mass of data and observation regarding the structural performance of the resulting members. Previous investigations underscore the need for improved design expressions so as to quantify dependably the strength of SHFRCC members in shear and flexure, as this is the most prevalent state of stress in practical RC member detailing (Kabele and Kanakubo [93]).

After the preliminary research the best combination of a coating material and content ratio as described in Chapter 3, was used to create the SHFRCC mixes for a series of experimental texts. The specimens created were especially designed in order to examine the mechanical behavior of strain hardening composites under various loading conditions. Tests that were used were: direct tension, uniaxial compression, split cylinder test, three point bending, four point bending, four point bending

with various shear span ratios, small scale beams with various shear span ratios and reinforcement percentages, push-off tests with and without rebars, pull-out tests and reverse cyclic displacement testing of a larger beam specimen (half scale) containing a low shear reinforcement ratio. In this chapter the experimental program is described in detail regarding the materials used for the mixes, the specimen details and the experimental setup for all tests. Specimens comprising control mixes having the same matrix design but without the addition of fibers were also tested for comparison for many of the test setups. Due to the large volume of composite needed for the whole experimental program and the lack of any ready mix procedure, the specimens were cast in groups, on different dates but always keeping the same mix designs.

The materials used for the mix designs are described in detail in Chapter 3. Table 4.1 shows the mix designs used for the final experimental program.

Table 4.1: Mixture proportions

	FIBER TYPE	CEMENT (kg)	FLY ASH (kg)	SAND (kg)	WATER (kg)	SP (L)	DF (ml)	coating (gr) (S38)	FIBERS (kg)	Total weight (kg)	Total Volume (m^3)	C	FA	S	W	SP	ρ_f (%V)	ρ_c (%M)
F1	PVA8	39.53	47.44	31.63	22.93	0.47	-	-	1.85	142.00	0.07	1.00	1.20	0.80	0.58	0.012	2.0	-
F2	PVA12	21.35	25.62	17.08	12.38	0.26	-	-	1.00	76.70	0.04	1.00	1.20	0.80	0.58	0.012	2.0	-
F3	PVA8	21.23	25.48	16.99	13.14	0.25	46.02	66.70	1.00	77.10	0.04	1.00	1.20	0.80	0.62	0.012	2.0	6.7
F4	PVA12	21.23	25.48	16.99	13.14	0.25	46.02	66.70	1.00	77.10	0.04	1.00	1.20	0.80	0.62	0.012	2.0	6.7
F5	-	71.54	85.84	57.23	39.49	0.86	-	-	-	254.96	0.13	1.00	1.20	0.80	0.55	0.012	-	-
F5B	-	7.53	9.04	6.02	4.37	0.09	-	-	-	27.05	0.01	1.00	1.20	0.80	0.58	0.012	-	-
F5C	-	7.53	9.04	6.02	4.37	0.09	-	-	-	27.05	0.01	1.00	1.20	0.80	0.58	0.012	-	-
F6	PVA12	73.74	88.49	58.99	44.24	1.28	160.00	231.33	3.47	266.74	0.13	1.00	1.20	0.80	0.60	0.017	2.0	6.7
F7	PVA12	113.77	136.52	91.01	68.26	1.97	247.00	357.00	5.35	411.53	0.21	1.00	1.20	0.80	0.60	0.017	2.0	6.7
F8	PVA12	68.89	82.67	55.11	41.34	1.19	149.00	215.40	3.24	249.20	0.12	1.00	1.20	0.80	0.60	0.017	2.0	6.6
F9	PVA12	51.08	61.29	40.86	30.65	0.61	-	-	2.40	184.49	0.09	1	1.2	0.80	0.60	0.012	2.0	-
F10	-	120.42	144.51	96.34	69.84	1.45	-	-	-	432.55	0.22	1	1.2	0.80	0.58	0.012	-	-
F11	-	34.98	41.98	27.99	17.98	0.42	-	-	-	123.36	0.06	1	1.2	0.80	0.51	0.012	-	-
F12	-	34.98	41.98	27.99	17.98	0.42	-	-	-	123.36	0.06	1	1.2	0.80	0.51	0.012	-	-
F13	-	20.1	24.12	16.08	11.66	0.241	-	-	-	72.20	0.04	1	1.2	0.80	0.58	0.012	-	-
F14	PVA12	20.9	25.1	16.7	12.5	0.25	-	-	0.976	75.45	0.04	1	1.2	0.80	0.60	0.012	2.0	-

DF: Defoamer

SP: Superplasticizer

ρ_f: percentage of volume of fibers to the total mix volume

ρ_c: percentage of weight of coating to the total weight of fibers

PVA8: PVA fibers with a length of 8mm

PVA12: PVA fibers with a length of 12mm

*The specimens extracted for each mix and the type of testing conducted are described in Appendix 4A.

4.2 Specimen Preparation-Mixing and Casting Procedure

The mixing sequence that was used took into consideration the special character of the materials and their impact on the rheological properties of the mix. The first step was mixing of all the dry materials –cement, fly ash and sand; this was performed within the mixer for at least 30 minutes. The water was mixed separately with the super-plasticizer prior to adding it to the cement in order to ensure full development of the chemical reaction between the super-plasticizer and the cement. For the case of the mixes without fibers the liquid part was then slowly added to the drum and mixed together until the mixture had the proper rheological properties by performing a slump flow test. For the case of the fiber reinforced composites 90% of the liquid part was added in the dry material mix. Once the dry components were adequately mixed with the liquid part, fibers were slowly added in small amounts and the rest of the liquid part was added in the end. Care was taken in order to ensure that fibers would not lump. Mixing sequence is depicted in Fig. 4.1. Once the mixing procedure was completed the specimens were cast into molds.

Figure 4.1: Mixing sequence of cementitious composites

Specimens were cast without any vibration on account of the self-compacting properties of the mixtures and were kept in molds for 24 hours while being covered with plastic sheet. After that, the specimens were moist-cured for 100 days. The specimens without reinforcement were kept under water whereas reinforced specimens were wrapped in burlap and kept wet on a daily basis. The age of the specimens was shown to compromise the ductility of the material, as interfacial bond

properties between the matrix and the fiber change with age becoming stronger, thereby eliminating pullout of fibers in favor of strain localization, fracturing of fibers and subsequent widening of cracks as hydration matures. Also the use of high volume of fly ash in the mix resulted in a lower rate of strength increase. For this reason, all tests were performed at the age of 100 days.

4.3 Specimen Design

Tests were carried out on a series of specimens to characterize the mechanical properties of the mixes with and without the use of fibers under various loading conditions. Additional tests were also carried out to test the structural behavior of the proposed material in the presence of steel reinforcement, so as to support the derivation of design equations – these will be presented in the following chapters. In each case, three identical specimens were tested for each type of test and mix design. Specimens were tested at the age of 100 days, in order to acquire the long term mechanical properties of the composites, since the presence of fly ash along with the coating of the fibers change the interfacial bond properties between the fibers and the matrix and therefore impact the multiple cracking phenomenon, thereby altering the material's strain capacity [94].

4.3.1 Uniaxial tension tests

The tests were carried out on a floor standing testing machine with a load cell capacity of 300 kN (Lloyd LR300K), using displacement control of the longitudinal translation of the machine. The displacement rate was 0.0025 mm/s. Deformations were measured using LVDTs mounted on the two wider opposite sides of the coupons over a 100 mm gauge length in the narrowest region of the specimen where the cross section was 25x50 mm. Plastic pillows were placed between the gripping mechanism and the coupon to distribute stresses and avoid localization. The testing setup had spherical hinges on both sides to ensure self-correction of possible miss-alignment and that no spurious stresses other than axial loading would be developed within the measuring range. The gripping equipment that was specially designed is shown in Fig. 4.2. The final dimensions that were used in the experimental program as well as the steel molds that were used to cast the specimens are shown in Fig. 4.2. Direct tensile tests that were carried out for all the mixes are listed in Appendix 4A.1.

Uniaxial tensile stress-strain curves were extracted through this test for all the fiber reinforced cementitious composites that were studied. Stress was calculated as the Machine Load divided by the critical cross section area of 25x50 mm. Strains were obtained as the averaged deformation of the two opposite LVDTs divided by the measuring length of 100 mm. All mixes' tensile stress-strain curves from the experimental tests are depicted in Appendix 4B.1. The uniaxial σ_t-ε curves were later used for analysis purposes and for Finite Element Modeling (FEM). In order to investigate the influence of the fiber's length and coating on the tensile behavior of the composites four mixes were specially designed for this purpose. F1 mix had 8mm PVA fibers without coating, F2 mix had 12mm PVA fibers without coating, F3 mix had 8mm PVA fibers with coating and F4

mix had 12mm PVA fibers with coating. Analysis of the results is given in Chapter 5. For each mix design three identical specimens were tested at the age of 100 days. Uniaxial tensile tests were also carried out for all mixes in order to establish their uniaxial tensile capacity for design purposes.

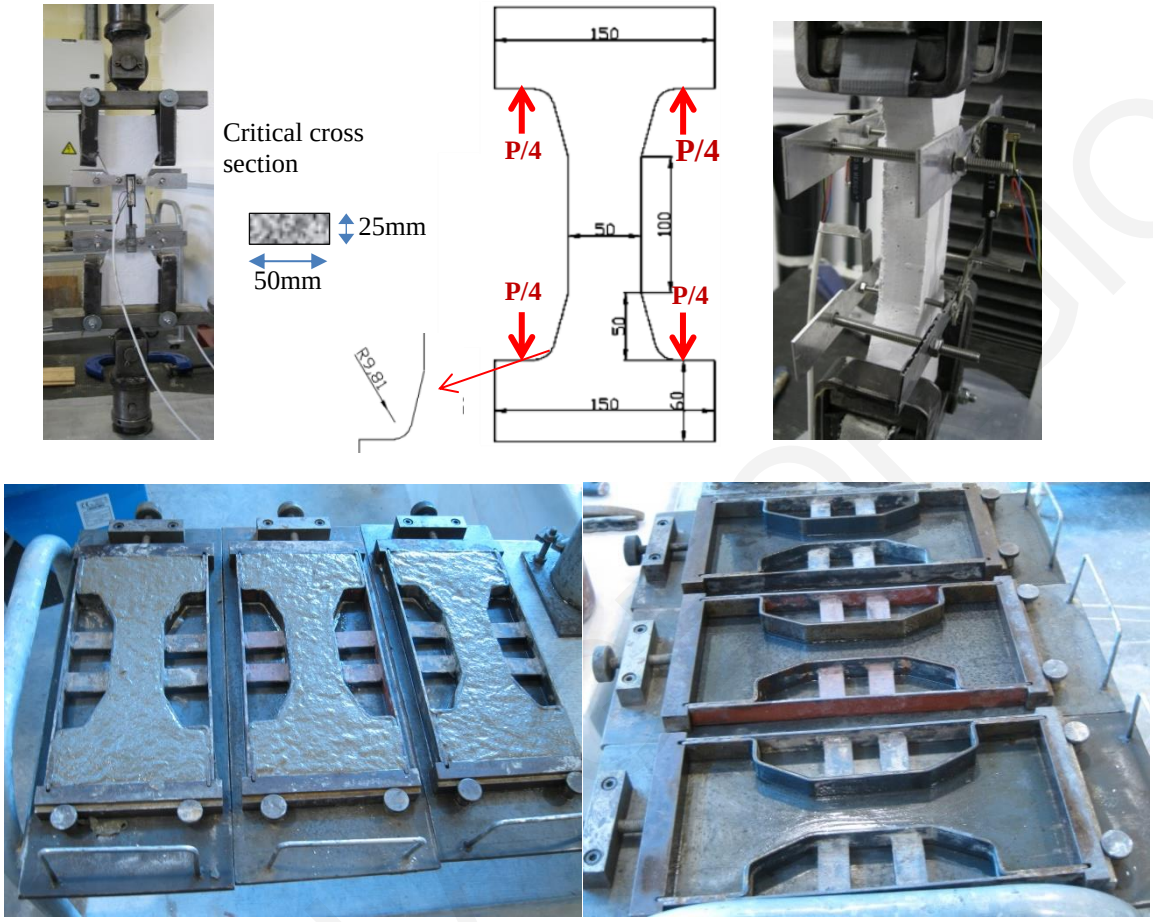

Figure 4.2: Direct tensile test setup and Direct-tension coupon dimensions and molds for casting

4.3.2 Uniaxial compression tests

Uniaxial compression tests were performed well into the post-peak range under displacement control using a closed-loop, servo hydraulic controlled testing machine at a loading rate of 1.50 μm/s. The specimens were cylinders, 100 mm in diameter and 200 mm in height. Axial deformations were measured using two linear variable differential transducers (LVDTs) mounted on opposite sides of two rings that were attached on the specimen over a gauge length of 140 mm. An additional LVDT measured the deformation over the entire length of the specimen, through the displacement of the platens. The displacement control of the machine was based on this LVDT. Circumferential elongation was measured using a circumferential extensometer (chain), placed at the middle of the height of the coupon. Additionally 3 stain gauges were fixed (2 parallel to the loading direction and 1 perpendicular to the load) for the estimation of the Poisson's ratio (note that in the early range of strain values the chain is slow to engage owing to the low amount of dilation). Testing setup and equipment are shown in Fig. 4.3. A list of specimens with their dimensions and characteristics are reported in the Appendix's Table 4A.2.

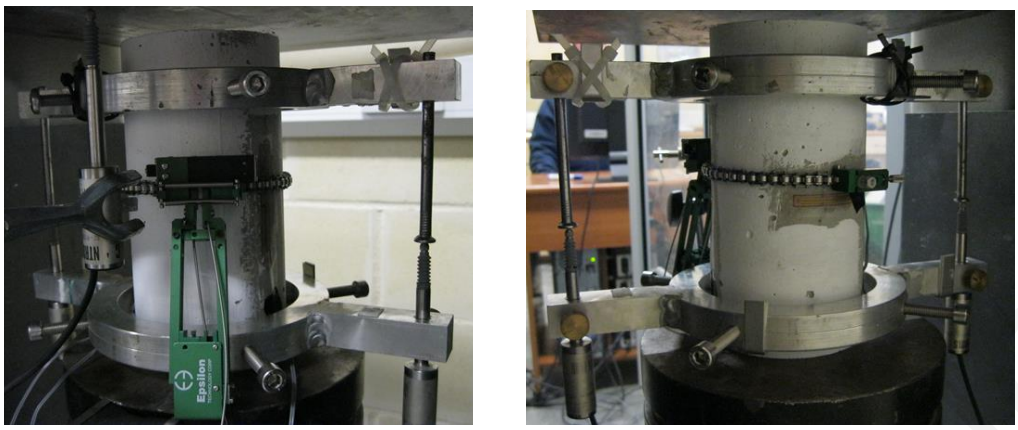

Figure 4.3: Test setup for uniaxial compression and measuring equipment

Compressive axial stress - axial strain - lateral strain curves extracted from the experimental measurements are reported in the diagrams of Appendix 4B.2. Stress is computed by dividing the Load by the area of the cross section while axial deformations are obtained as the average of the two opposite LVDTs divided by the 140 mm distance between the gripping equipment. Lateral strain is extracted by the deformation of the extensometer divided by the perimeter of the cylinder.

Compression tests were performed on all mix designs with and without fibers (F5, F13) to be used as control mixes in order to correlate the improvement of the behavior when fibers are used. In this regard, lateral deformation was considered a very important behavioral parameter. Past work has shown that the extent of damage in concrete may be quantified by the lateral expansion of the cross section supporting the axial load; indeed, softening of the compressive strength is directly related to cracking parallel to the direction of loading and lateral expansion. As a corollary to that, the effect of confinement is reflected in the degree of restraint provided against lateral expansion. In fact, confinement of plain concrete has been studied extensively over the years to the extent that strength and strain models that relate the confined material properties with the confining pressure are calibrated and are considered to be rather accurate.

In order to quantify the passive confining influence provided by the internal fiber reinforcement, it was decided to compare its response with that of plain concrete subjected to well controlled confining pressure. Several levels of confining pressure were enacted in the experiment. To this objective both cases with steel stirrups and with FRP wrapping (Glass and Carbon) were considered. Tests were performed on mix designs without fibers; the influence of the fiber length and coating on confinement effectiveness is also investigated as previously with the mixes F1, F2, F3 and F4.

The properties of the FRP sheets are shown in Table 4.2. The sheets were supplied in 600 mm width rolls. The elongation at break of the carbon wrap was 1.8%. A special resin was used for the dry application of the wraps (provided by the producer - commercial name Sikadur-330) which is a two-part epoxy-based impregnating resin. This has a tensile strength of 30 MPa and Modulus of Elasticity of 4.5 GPa. According to the manufacturers' instructions, in order to apply the wrap on the cementitious cylinder the surface was adequately prepared and dried to a maximum moisture

content of 4%. Prior to mixing both parts of the adhesive were thoroughly stirred separately. The tins of the two parts come in 4 kg and 1 kg for Part A and Part B respectively; thus a 4:1 mix ratio by weight is used. For the application of the wraps the surface was first cleaned thoroughly and then the resin was applied with a roller on the surface. Then the Sica-Wrap was placed carefully in the required direction, while applying resin over the wrap.

Table 4.2: FRP sheet material characteristics

SikaWrap	Type	Tensile strength (MPa)	Modulus of Elasticity (GPa)	Weight (gr/m^2)	Depth (mm)	Type of wrap	Type of application
SikaWrap230 C/45	Carbon	4300	238	230	0.131	Knotted single direction	Dry
SikaWrap 430 G/25	Glass, Type E	2300/3400	76	445	0.172	Knotted single direction	Dry

In the case of the cylinders wrapped with FRP sheets an adequate anchorage length of the sheets should be provided in order to ensure that failure mode is rupture of the FRP confinement. The critical anchorage length l_c was calculated based on Eq. 4.1 as reported by Pantazopoulou et al. [95] for the two types of wraps. The crack width w_{cr} at the debonding limit was taken equal to 0.5 mm and the tensile strength of the material was extracted from four point bending tests performed on the cementitious matrix as proposed by the Model Code [49].

Active anchorage strength: $$l_b = \sqrt{\frac{w_{cr} \cdot E_f \cdot n \cdot t_f}{f_{fb,d}}} \quad (4.1)$$

where w_{cr}=0.5 mm is the assumed crack width, E_f is the Modulus of Elasticity of the FRP material, n is the number of layers, t_f is the thickness of each layer and $f_{fb,d}$=f_{ctm}=2.0 MPa is the bond strength of the FRP wrap assumed to be equal to the tensile strength of the composite. For each type of wrap and number of layers the minimum anchorage length is provided in Table 4.3.

Table 4.3: Active anchorage length used for each specimen

Wrap	Number of Layers	Specimens	E (MPa)	t_f (mm)	l_b (mm)
SikaWrap230 C/45	1	F13-C1, F13-C2, F13-C3	238	0.131	88.29
SikaWrap230 C/45	2	1F5F2, 2F5F2, 3F5BF2	238	0.131	124.86
SikaWrap230 C/45	3	1F5BF3, 2F5CF3, 3F5CF3	238	0.131	152.92
SikaWrap 430 G/25	1	F13-G1, F13-G2, F13-G3	76	0.172	57.17
SikaWrap 430 G/25	2	F13-2G1, F13-2G2, F13-2G3	76	0.172	80.85

Uniaxial compression tests for the confined specimens were carried out at a displacement controlled rate of 3 μm/s. The rate at which the FRP-wrapped coupons were tested was greater than that of the unconfined concrete in order to keep the testing time within a logical frame. In deciding the displacement rate the objective is that it be slow enough so that the test is quasistatic and therefore no rate effects may be traced in the material performance. The value of the greater strain rate was then compared with a graph depicted in Fig. 4.4 (from M. Pajak [96]) that shows the strain

rate effect on compressive strength of concrete, leading to the conclusion that the strain rates used, for the order of magnitude of their values, have almost no effect on the compressive strength of concrete (DIF or Dynamic Influence Factor ≈1).

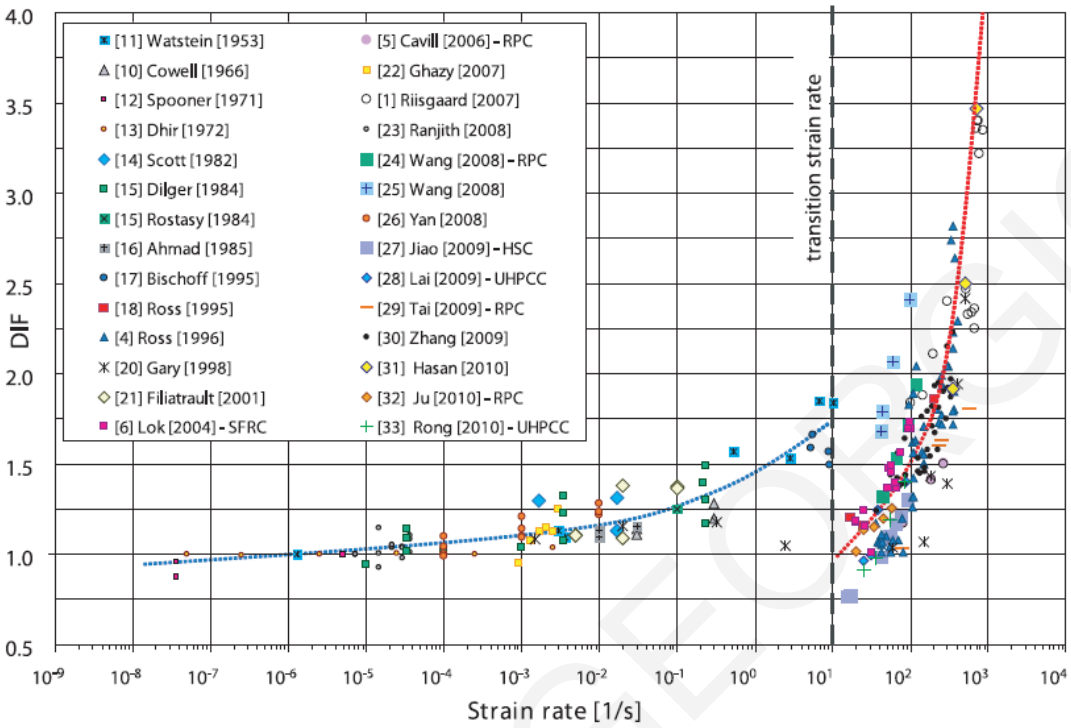

Figure 4.4: Strain rate effect on the compressive strength of cementitious composites [96]

Uniaxial compression tests were carried out also on the matrix consisting of high amounts of Fly Ash (FA) as cement replacement with the use of various volumetric ratios of transverse steel; stirrups had a bar diameter of 8 mm with a yield tensile strength of 500 MPa and 15 mm clear cover as shown in Fig. 4.5. Loading was displacement controlled at a rate of 1.5 μm/s.

Table 4.4: Confinement by stirrups used for each specimen

Name	stirrup spacing s (mm)	Specimens	A_{sw}	b_c	ρ_w	b_o	α_s	α_n	α	ω_w (%)
S8	80	F5S8-1, F5S8-2, F5S8-3	50.3	70	0.050	62	0.355	1	0.355	0.359
S5	50	F5S5-1, F5S5-2, F5S5-3	50.3	70	0.080	62	0.597	1	0.597	0.574
S3	30	F5S3-1, F5S3-2, F5S3-3	50.3	70	0.134	62	0.758	1	0.758	0.957

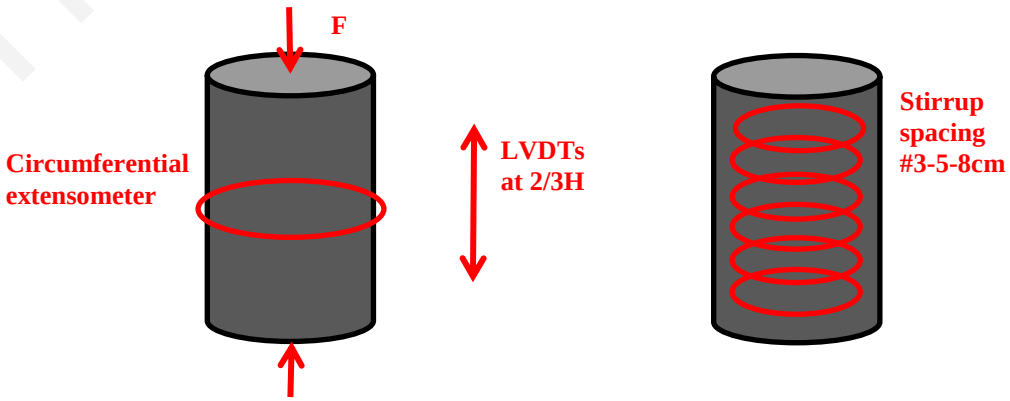

Figure 4.5: Test setup for compression of cylinders with steel stirrups

The volumetric ratio of transverse steel (ρ_w is a geometric value referring to circular stirrups volume divided by the volume of the confined core) and the mechanical ratio ω_w which is the product of the geometric ratio times the ratio of material strengths is listed for all specimens in Table 4.4; the relevant mathematical definitions are given by Eq. 4.2:

$$\rho_w = \frac{4A_{sw}}{b_c \cdot s},\ f_{cc} = f_c + 2\omega_w, \text{where } \omega_w = \frac{4A_{sw}}{b_c \cdot s} \cdot \frac{f_y}{f_c} = \rho_w \cdot \frac{f_y}{f_c};\ a = a_s \cdot a_n, \tag{4.2}$$

In Eq. (4.2), A_{sw} is the area of one bar, b_c is the diameter of the core (to the outside of the stirrups), α is the confinement effectiveness coefficient, $\alpha_s=(1-s/2b_o)\cdot(1-s/2h_o)$ for hoops and $\alpha_s=(1-s/2b_o)$ for spirals, a_n=1 for circular hoops.

4.3.3 Split cylinder tests

The tensile strength of normal concrete is within 8 and 15 percent of the compressive strength. The actual value is strongly affected by the type of test that is performed to determine the tensile strength, the type of aggregate, the compressive strength and the presence of a compressive stress transverse to the tensile stress field. Due to the difficulty of conducting direct tensile tests for normal concrete, various codes propose indirect determination of the tensile strength of concrete. ASTM C496 [71] proposes cylinder splitting as a more straightforward method to determine the tensile strength of normal-strength concrete; in this arrangement a compression cylinder is placed on its side and loaded in compression along its length. The vertical diametric plane of the specimen is stressed in biaxial tension and compression as shown in Fig. 4.6 ((a), (b), (c) and (d) by MacGregor [97]). Normal stresses range from high transverse compression at the top and bottom to almost uniform tension in the central region of the specimen (Fig. 4.6 (d)). Tensile failure occurs rather than compressive failure due to the triaxial state of stress around the load application point that prevents compressive failure. As per ASTM C496 [71] the maximum load sustained by the specimen is divided with the appropriate geometrical factors to obtain the tensile splitting strength. The same standard indicates that the splitting tensile strength is greater than the direct tensile strength and lower than the flexural strength and is used to evaluate the shear resistance provided by concrete and to determine the development length.

The cementitious mixes that did not contain any fibers were expected to fail in a brittle manner similar to that of normal concrete by forming a single diametric crack parallel to the load. In the case of strain hardening composites multiple cracks were expected to open parallel to the load as shown in the preliminary tests of Chapter 3, with the fibers bridging the cracks and transferring load over a wider area. In the final experimental program, splitting tests were conducted under displacement control based on the displacement of one of the LVDTs measuring lateral expansion at a constant stroke rate of 0.50 mm/min on 100 mm diameter cylinders having a length of 100mm.

Deformation of the specimens in the direction of tensile stresses was measured by two LVDTs placed orthogonally to the loading plane as shown in Figure 4.6 (f) and (e). Split cylinder tests for all mixes are reported in Appendix 4A.3. The results from all tests are depicted in the figures of

Appendix 4B.3 as well as the photographic evidence of crack formations. The Figures of Appendix 4B.3 report the Load versus the diametric elongation (dx) parallel to the axial stresses and the Load versus diametric elongation (dy) parallel to the loading axis in millimeters. Diametric elongation is the sum of deformations measured by the two horizontal LVDTs.

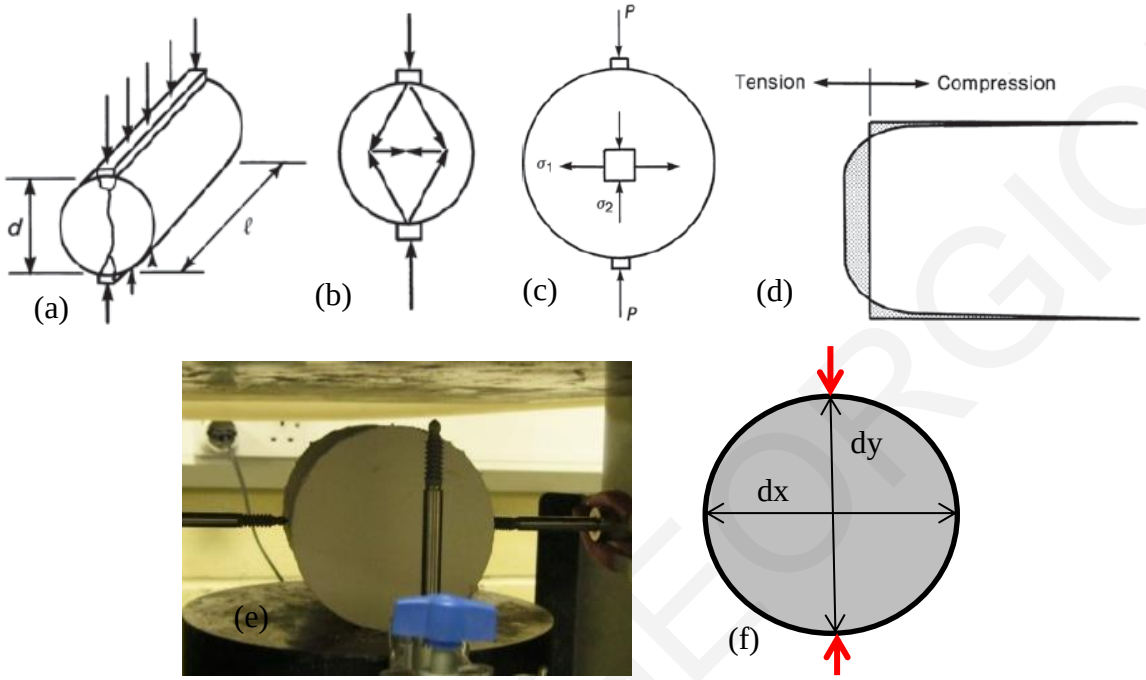

Figure 4.6: Split cylinder test by MacGregor [97] (a) Test procedure, (b) Simplified force system, (c) Stresses on element, (d) Distribution of σ1 on vertical diameter and (e) Split tensile test setup and (f) LVDTs for measuring deformation

4.3.4 Three point bending tests

Small size beams having a 100 mm square cross section and 500 mm length were tested under 3-point load (Fig. 4.7) at a displacement rate of 3 μm/s using a closed-loop servo-hydraulic testing machine. Tests were conducted according with standards, using displacement control of the loading point; the intent was to observe the evolution of the multiple cracking phenomenon with strain hardening up to crack localization and strain softening. Geometric details of the test setup and specimens are given in Figure 4.7. Three LVDTs were used to record the vertical deflection at the supports and at the load point (midspan of the beam specimens as shown in Fig. 4.7); very large deflections were recorded in the SHFRCC specimens, owing to multiple cracking developed over the plastic hinge region.

Flexural tests of the type considered are routinely used to obtain tensile strength indirectly from the flexural strength [49]. Three-point bending generally overestimates the strength as compared to four-point bending [72], but in this setup the static relationship between moment and shear is the same as that of a cantilever under point load, developing a “plastic hinge” region next to the loading point. The shear span for these tests is a=200 mm, giving a shear span ration of a/h=2. The specimens extend 50 mm over the supports in order to ensure proper support conditions.

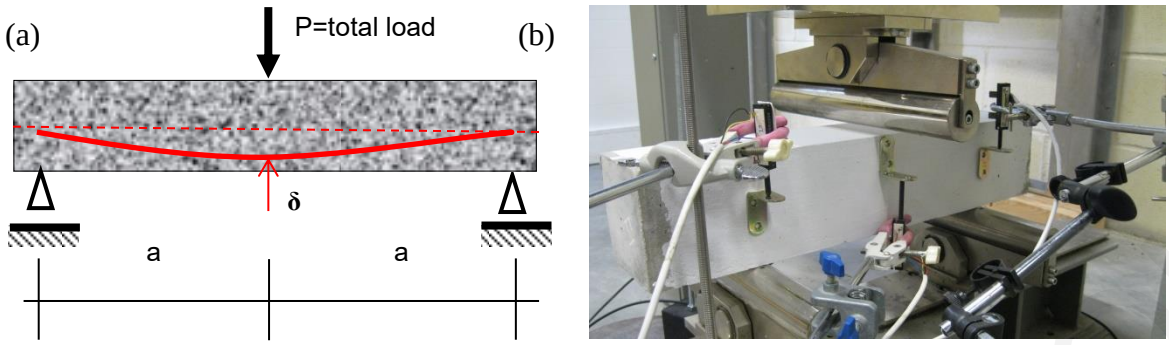

Figure 4.7: Three point bending test setup and LVDTs

The specimens from all mix designs that were subjected to three-point bending tests are listed in Appendix 4A.4. The load history and midpoint deflection for all tests are depicted in the Figures of Appendix 4B.4 as well as the crack patterns that were observed. Load-point deflection is computed by extracting the averaged deformation over the supports as measured by two LVDTs, from the midpoint LVDT deformation.

4.2.5 Four point bending tests

Flexural tests with a constant moment region in the center of the span such as those considered in the present section are routinely used to obtain tensile strength indirectly from the flexural strength [49]. ASTM C78 [98] uses a plain concrete beam that is loaded at the third points to calculate the modulus of rupture, assuming linear distribution of stress and strain. The advantage of a four-point bending setup is that the middle third of the beam develops pure flexure with no simultaneous action of shear. This enables an easy analysis of the state of stress in the middle region and thus, dependable estimates of the tensile stresses. To address the needs and objectives of the present thesis, a series of scaled beam tests were undertaken, investigating the structural performance of members under combined shear and flexure.

The first parameter of the experimental study was the shear span to depth ratio, (aspect ratio), and its effect on the contribution of the SHFRCC material in the mechanics of shear of structural elements. The experimental program of the four point bending tests was divided in two parts. The first part consisted of beams of SHFRCC matrix with various aspect ratios ranging from 0.4 up to 3.5 tested under four point bending (4PB) as well as beams with the same mix but without any fibers at a shear span ratio of 1. This first part was intended to quantify the influence of the fiber contribution to the web shear strength capacity as well as the influence of the shear span ratio to the failure mechanism of the beams. The second part of the experimental program investigated the interaction of steel reinforcement (longitudinal and transverse) with the use of fibers in the composite. Reference beams with the same mix design without any fibers but with the use of steel reinforcement were used to quantify the contribution of reinforcement to shear strength. In this second part the shear span ratio, as well as the percentage of the flexural reinforcement were used to change the mode of failure between shear and flexure.

A series of four-point bending tests were carried out on the small scale beams reported in the Table of Appendix 4A.5; specimens comprised a SHFRCC matrix, however for the sake of comparison a series of reference specimens were also made of the same matrix but without the fibers. On account of the brittle failure of the HVFA composite and in the absence of longitudinal reinforcement, failure was expected to occur in the constant moment region between the load application points, resulting from the attainment of peak tensile strength in the extreme layer under tension; this failure mode was not influenced by the shear span ratio. The parameter of study for the SHFRCC-specimens without steel reinforcement was the shear span aspect ratio which was assigned the following values: a*/h* = 0.4, 0.6, 1, 1.5, 2, 3 and 3.5. In the case of the fiber reinforced composite, due to the strain hardening properties of the material in tension, multiple cracking and increase of the load bearing capacity was observed. In this case the influence of the shear span ratio on the failure mode of the beams was investigated.

The combined action between the fiber composite and the simultaneous use of flexural and shear reinforcement was investigated for the shear span ratios of a/h=1, 2 and 3.5 by the introduction of tension reinforcement at different area ratios and/or stirrups. Thus, the magnitude of shear force demand is determined by controlling the flexural strength of the beam cross section; this was achieved by varying the area ratio of the flexural reinforcement and the shear span ratio. Three identical specimens were tested for each parameter combination.

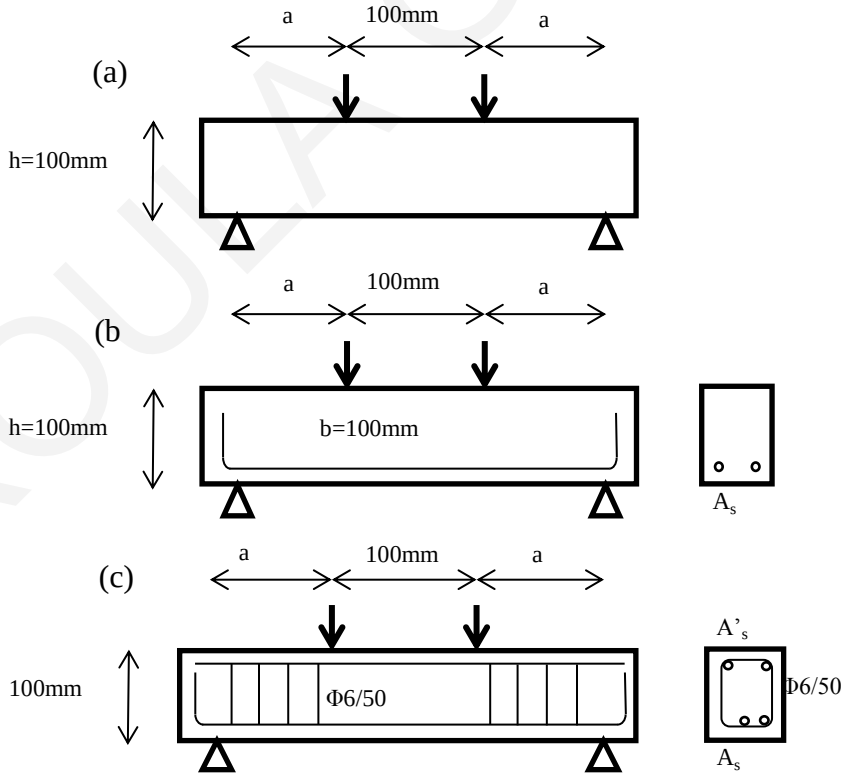

Figure 4.8: Test configuration for four point bending and reinforcement details for (a) specimens without reinforcement – beam strength controlled by the resistance of the cementitious composite; (b) beams with flexural reinforcement placed so as to increase the magnitude of shear demand in the beam shear spans; (c) beams reinforced with longitudinal bars and stirrups for shear strength.

Tests on beams under four point loading were carried out using a constant distance between the intermediate load points equal to 100 mm whereas the constant square cross section of the prisms was 100x100 mm as shown in Fig. 4.8. The beams were supported on end rollers at a variable distance "a" ranging from 40 mm to 350 mm (i.e., a/h ratios ranging from 0.4 to 3.5). Beams extended 25-50 mm over the supports in order to ensure proper anchorage of the longitudinal reinforcement. They were tested under displacement control at a displacement rate of 1.5 μm/s and 3 μm/sec for the plain and reinforced beams respectively with the load applied at the intermediate loading points. Five LVDTs were used to record the vertical deflection at the supports, at the load points and in the midspan of the beams as shown in Figure 4.9. The specimen identification code and specimen dimensions are given in Appendix 4A.5 for the beams without steel reinforcement and Appendix 4A.6 for the steel reinforced beams. Flexural failure in this type of test was concentrated in the constant moment region (i.e. the central length of 100 mm - thus, the maximum flexural strength was attained in that region, accompanied by flexural cracks) whereas shear failure (expressed by shear cracks) would be expected to occur over the adjacent shear spans. Three samples were tested for each shear span ratio (a/h). Figures in Appendix 4B.5 and 4B.6 depict the Load-load point deflection diagrams as well as the crack formation for all beams tested under four point bending.

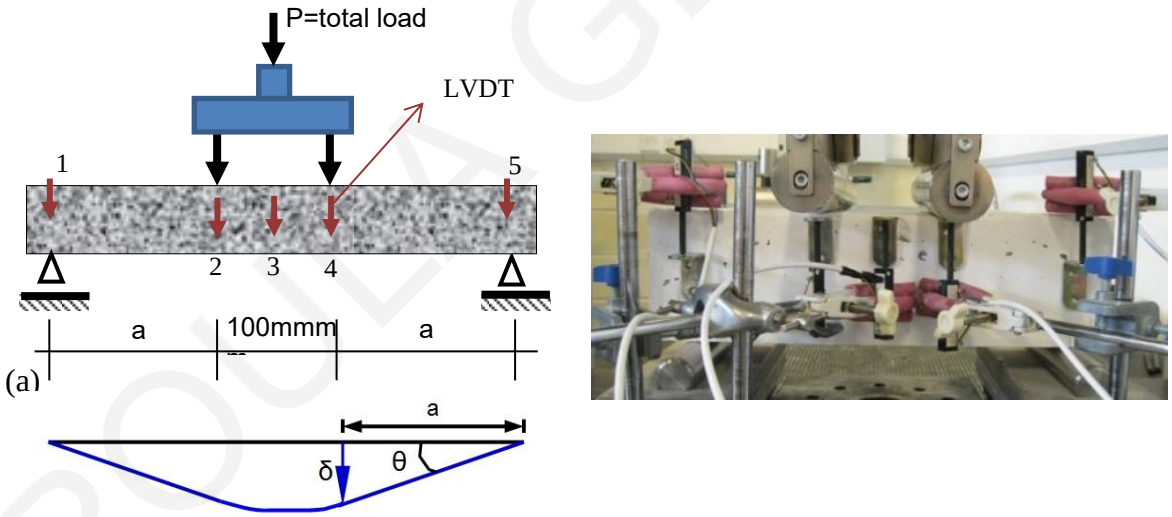

Figure 4.9: Test setup and LVDTs for four-point bending test setup. Definition of specimen rotation θ in the shear span (reference to rotation capacity).

4.3.6 Push-off tests

Some of the most important parameters contributing to shear resistance of normal concrete are a) the dowel action intersecting the cracks, b) the friction between crack faces and aggregate interlock, c) the residual diagonal strength of cracked concrete. On the other hand, the SHFRCC matrix lacks any coarse aggregates, consisting only of sand usually with particle diameters less than 300μm. Additionally for improving the sustainability of these composites the matrix has great amounts of cement replacement by fly ash, even in the order of 60%. The lack of coarse aggregate eliminates aggregate interlock in the shear resistance mechanism whereas the use of the short fibers

affects the overall shear behavior and their interaction with the steel stirrups when these exist. Clearly, the mechanics of shear transfer in this type of composite studied are very different from what is currently known for normal concrete. Nevertheless, studying the behavior in shear is considered a priority and prerequisite for improving the implementation of the composites in structural applications.

Apart from beam testing shear behavior was also studied using the so-called direct shear tests; in fact this test type may elucidate the basic shear transfer mechanics, whereas beams are more relevant to member behavior in flexure-shear. Past studies of FRC in shear indicate that fibers generally improve shear strength and ductility of concrete and that they may partially be used to reduce the amounts of stirrups [65]. The push-off tests conducted in this thesis were intended to experimentally quantify the shear strength to the tensile properties of the material in light of the fact that the sliding plane of the direct shear specimen experiences pure shear which is equivalent to simple diagonal tension.

The push-off specimen form is depicted in Fig. 4.10. The specimens had dimensions of 250x500x100 mm as shown in Figure 4.10, with a shear plane area of 100x200=20000 mm^2 as proposed from previous research [99], [100]. Two were the parameters of the investigation: a) the mix design – the use or not of fibers and b) the presence of steel stirrups crossing the shear plane. The specimens with stirrups had the configuration of Figure 4.10 (c). Three identical specimens were tested for each type of test and mix design.

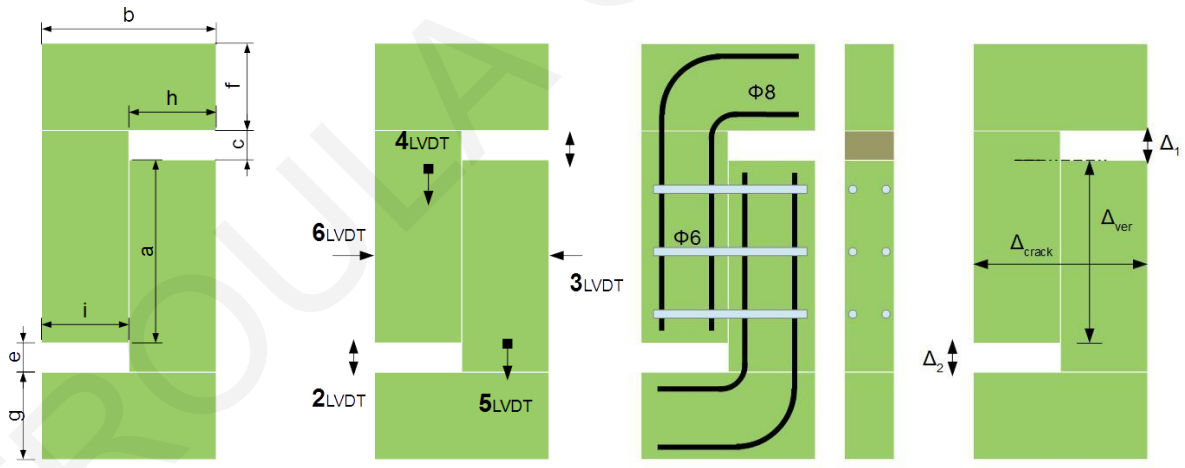

Figure 4.10: (a) Push-off specimen and dimensions, (b) LVDTs positions and measuring lengths, c) steel reinforcement, d) definition of deformation for graphic presentation

The specimen's classifications and name are outlined in Appendix 4A.7. The mix with a high volume fly ash as cement replacement and the same mix with the addition of PVA fibers were both examined. Manufacturing of the specimens took the following steps: a) The steel configuration was prepared for the specimens (no reinforcement was necessary for the configuration of the specimens with SHFRCC and no stirrups). Vertical reinforcement was found to be necessary for the configuration of specimens without fibers and without stirrups because when tested without, failure occurred in modes other than sliding along the shear plane. Vertical reinforcement was tied using

closed stirrups of 6mm diameter, b) Reinforcement was placed in the molds with the appropriate spacing. In order to create the recesses needed to form the shear plane, polyurethane prisms were placed in the molds and firmly secured in order not to move during casting, c) Casting of the specimens was performed without the use of any vibration since both of the mixes were self-compacting, d) After the specimens were casted they were left in molds for 24 hours, covered with plastic sheets, e) Specimens were demolded and placed in water if not containing any reinforcement, while the ones that had reinforcement were wrapped in wet burlap and covered by plastic sheet until the testing date. Specimens were tested at the age of 100 days, in order to acquire the long term mechanical properties of the composites, since the presence of fly ash, as well as the coating of the fibers, change the interfacial bond properties between the fibers and the matrix and therefore the multiple cracking phenomenon, thereby impacting the strain capacity of the material [94].

For the push-off specimens 6 LVDTs were used, as shown in Figure 4.10 (b) to measure displacements at various positions. LVDTs #3 and #6 were used to measure horizontal displacement of the specimen, which is actually the vertical crack width defined normal to the shear plane. The specimens were tested at a rate of 15 μm/sec. Failure modes and Load-deformation curves for all mixes are given in Appendix 4B.7.

4.3.7 Pull-out tests

Tests proposed by various standards usually do not simulate exactly the conditions of the pull out mechanism. The surrounding concrete is under compression in contrast to the real situations where in reinforced members the concrete surrounding the tensile reinforcement is in tension. Chapman and Shah [101] proposed a modified version of the Danish Standard [102] test that takes this aspect into consideration. In order to investigate the bond-slip law of steel reinforcement in fiber reinforced composites with strain hardening a new testing setup was designed from a modification of the above tests, taking into consideration the ductility of the materials used. This testing setup is as shown in Figure 4.11.

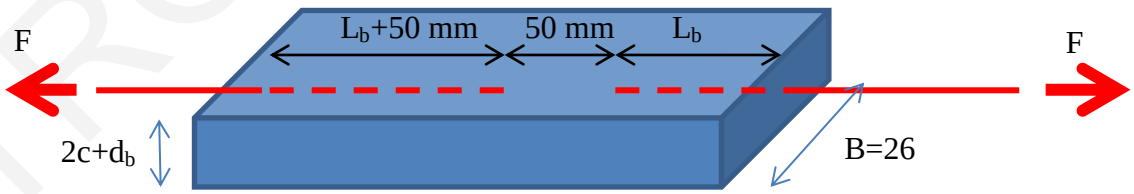

Figure 4.11: Test setup for pull out tests

Two bars of the same diameter were placed on the opposite sides of a rectangular block of SHFRCC along the same axis (back to back, with a spacing of 50 mm between the two bar ends). For each setup the bar on one end side (support bar) had 50 mm longer bond length than the test bar so as to ensure that failure will occur always on the side of the test bar. The width of the cementitious composite specimen (B=26 mm) was selected such as to ensure that the middle unreinforced length will not fail from tension even in the extreme cases when the bars will develop

yielding and hardening. Slip was measured only at the end of the shorter bar with LVDTs (as shown in Fig. 4.12(a)).

All tests were performed using displacement control with an actuator stroke rate of 0.025 mm/sec. Displacement, i.e., slip, is defined herein as the differential movement between the reinforcing bar and the surface of the concrete. The net slip is equal to the average displacement recorded by the LVDTs minus the elastic elongation of the free segment of the bar. From the data, the average equivalent bond stress, τ, was calculated in terms of the load P applied to the reinforcing bar for each specimen: $\tau = P/(\pi dL)$. The bond stress was computed assuming a uniform bond stress distribution along the embedded length of the bar. However, in reality bond stress distribution is not uniform.

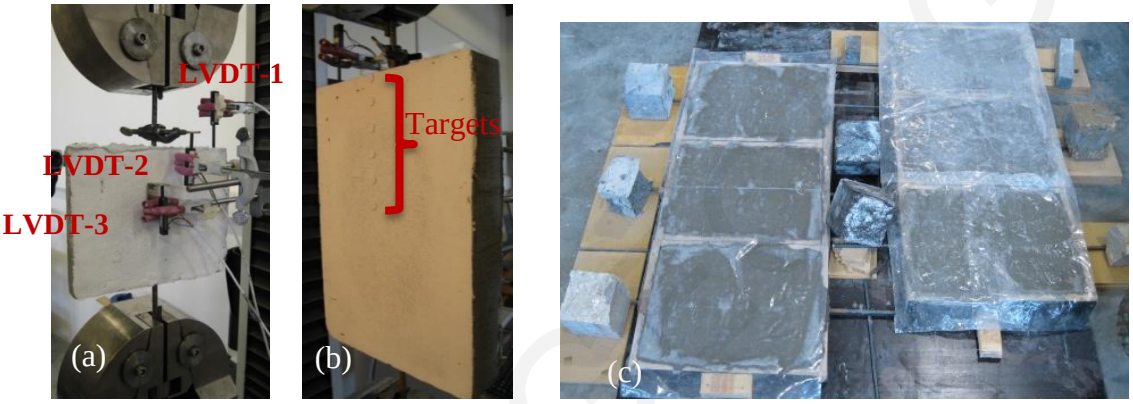

Figure 4.12: (a) Test setup for pull out tests with LVDTs measuring equipment, (b) targets and (c) casting of the specimens

The pullout specimens were cast in molds made of wood and were placed horizontally with a casting height of $2c+d_b$ as shown in Fig. 4.12 (c). Two holes were made on the top and bottom sides of the molds and the reinforcement passed through them, while outside the molds the steel bars were secured at the proper height in order to ensure that no dislocation would take place during casting and that the bars would be axially placed travelling over the same direction. The casting did not include any vibration of the FRC and after casting plastic sheets were placed over the free surface of the specimens and were left for 24hours. After that period the specimens were removed from the molds and were wrapped in wet burlap and plastic sheet and were moist cured for a period of 100 days, at which age they were tested.

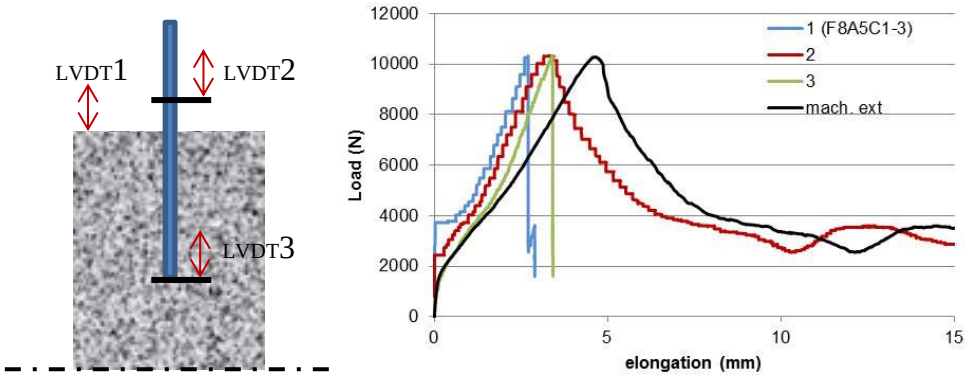

Figure 4.13: Measuring equipment for pull-out test and Load-Displacement curves for F8-A5-C1-3

Appendix 4A.8 lists the pull-out specimens that were tested for the experimental investigation of the bond mechanism of steel bars in SHFRCC matrices and Appendix 4B.8 plots the Load-displacement curves for all specimens as well as the crack failure patterns. The Load – Displacement curves include data for all three LVDTs used in the experiments as shown in Figure 4.13 as well as the machine head displacement.

4.3.8 Cyclic loading of large scale beams

The experimental research program included the reversed cyclic loading of two large scale specimens with the geometry shown in Fig. 4.14. Macroscopically, each specimen was a simply supported beam with a loading stub in the midspan; however, by means of the reinforcing arrangement in the stub each specimen actually consisted of two cantilever flexural members cast back to back, with a shear span ratio of 3.5 and connected with a stiff node used for loading by the actuator in both directions. The beams were supported on rollers both on their bottom and top faces. Each beam behaved as a cantilever with a constant shear load equal to half of the machine load and moments were linearly increasing from zero at the supports to $M=(P/2)\cdot L_s$ at the connection with the rigid node, where L_s is the shear span length. One of the two connecting flexural members of each specimen is designed as per the research target, while the other connecting beam is heavily reinforced (both in the longitudinal and transverse direction) in order to preclude any failure.

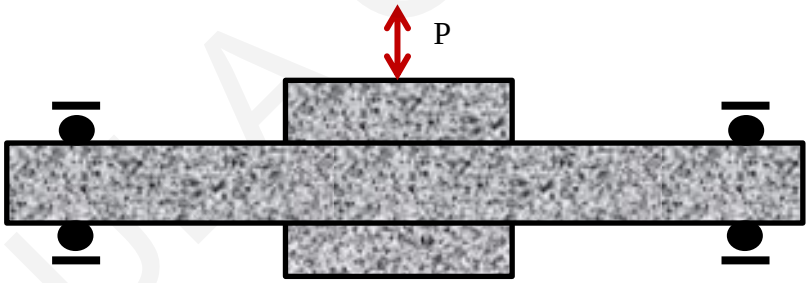

Figure 4.14: Test setup for reversed cyclic loading

One of the members was constructed with SHFRCC mix containing 2% by volume PVA fibers, while in the other the cementitious matrix was the same as that of the SHFRCC but without the fibers. The cementitious matrix was reinforced as per the Eurocode provisions for a DCM, while in the case of the SHFRCC member, the longitudinal reinforcement remained the same while the transverse reinforcement used was the minimum required to prevent buckling of the longitudinal bars as shown in Fig. 4.15. The purpose of these tests was to investigate the beneficial action of the fibers on the shear capacities of members under reversed cyclic loading.

The two large scale double beams were tested at the Concrete Technology and Structures Laboratory of the University of Cyprus. The test was conducted on a 250 kN MTS hydraulic actuator, digitally controlled and attached on a self–reacting steel frame. The double beam was supported on rollers at the edges in order to allow rotation at the supports; the central rigid node was connected to the load actuator with two plates connected to each other with high strength rods

while clamping the central stub in between. This setup does not allow horizontal translation of the central stub, while it allows the beams to expand away from the node without creating any axial loads. The supports were specifically designed for this purpose. Rollers had to be placed both on the top and bottom sides of the beams and supported on the loading frame in order to prevent upward movement during the reversed loading. The height of the supports was determined with reference to the travel capacity of the machine (reference point would be the center height of its full travel distance, in order to use the full travel for the reversed cyclic displacement history). For the central stub, the concrete specimen was placed on the bottom plate and then the MTS pushed the top plate on the concrete node up to a Load of 5 kN. Then, after the bars connecting the two plates were placed and tightened, the specimen was lifted from the central node setup and placed on the supports. Detailed description of the design of the members, testing setup and loading is given in Chapter 10.

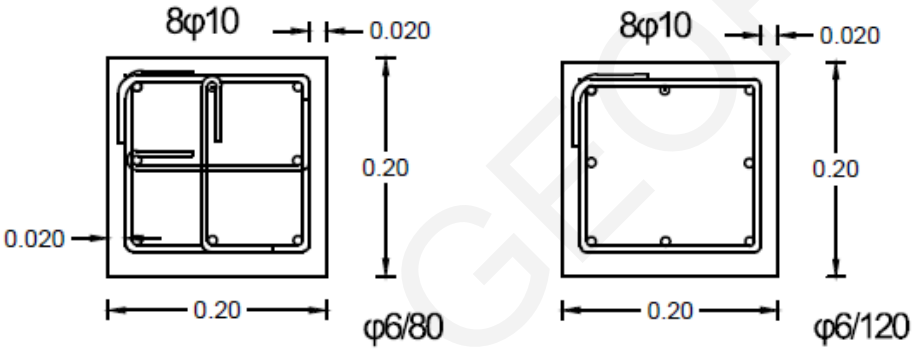

Figure 4.15: Stirrup detailing for (a) Member A: Control and (b) Member B: SHFRCC

4.4 Reinforcement stress strain curves

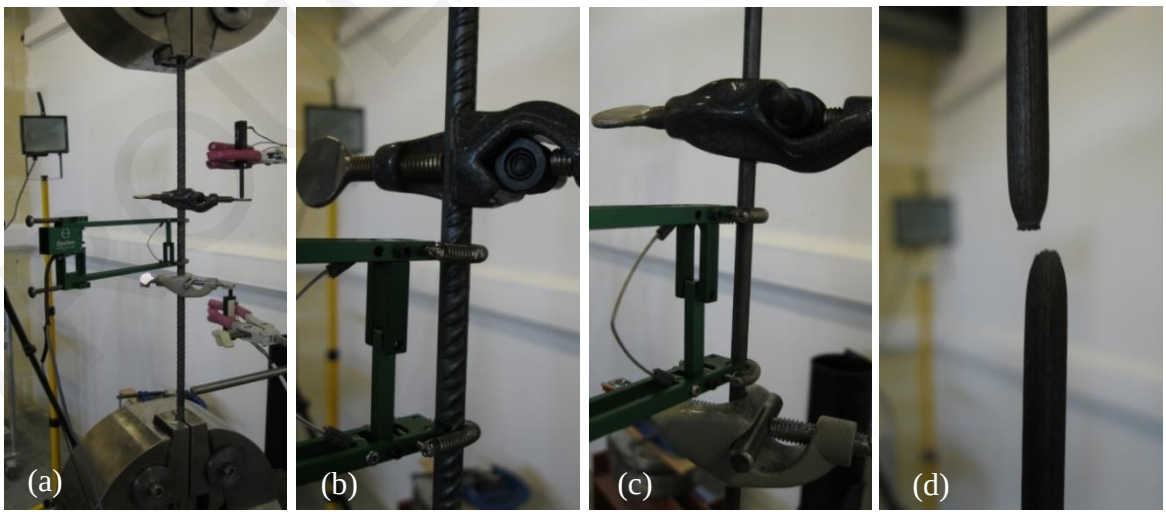

Figure 4.16: Steel bars tested under uniaxial tension (a) setup, (b) extensometer and LVDT, (c) bar of 6mm without ribs, (d) failure of bar

The steel reinforcement used in the specimens of the experimental program was tested under tension in order to extract the axial stress-strain curves. Bar coupons of 10, 8 and 6 mm diameter were tested under uniaxial tension. The loading rate was 1 mm/min and displacement was measured with two LVDTs mounted on the specimen with a gauge length of 100 mm. Additionally

an extensometer was used to verify the recordings of strain. Three sample bars were tested for each diameter.

The total load-strain curves as obtained from the uniaxial tests for the three types of bar diameters used are shown in Fig. 4.17 (a). The bars with 10 and 8 mm diameter had ribs, with a tensile yield value of 500 MPa, while the bars with 6mm diameter had no ribs and their tensile yield strength was 300 MPa. Nominal stress was calculated based on the load and the diameter of the bars as $\sigma=F/(\pi d^2/4)$.

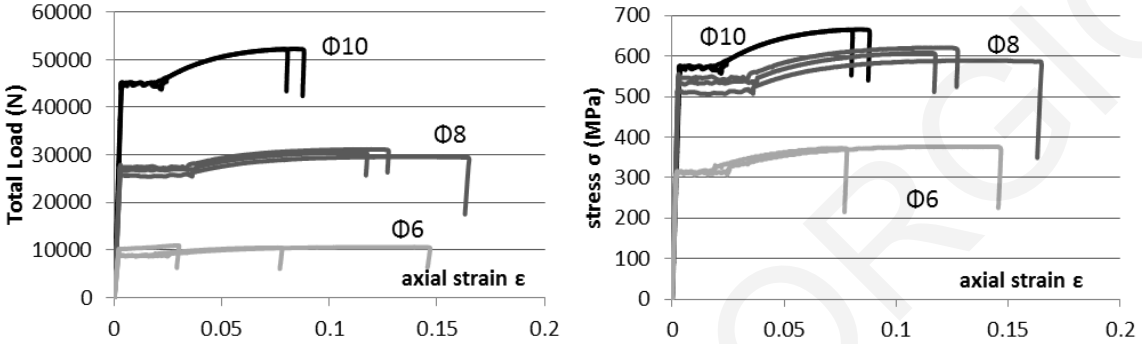

Figure 4.17: (a) Total Load-strain curves and (b) tensile stress-strain for steel bars of 6, 8 and 10mm diameter under tension

The steel reinforcement material parameters that will be used for design purposes or be imported in FE modeling are listed in Table 4.5. Detailed description of the procedure for the derivation of true stresses and strains is described in Chapter 11.

Table 4.5: Steel Reinforcement

ε_{nom}	F_{nom}	σ_{nom}	σ_{true}	ε_{tru}	ε_{pl}	E
0	0	0	0	0	0	204271.4
0.00264	27000	537.1479	538.566	0.002637	0	
0.038	27100	539.1374	559.6246	0.037296	0.034659	
0.04	27800	553.0634	575.186	0.039221	0.036584	
0.05	28500	566.9895	595.339	0.04879	0.046154	
0.075	30000	596.831	641.5934	0.072321	0.069684	
0.1	30500	606.7782	667.456	0.09531	0.092674	
0.15	30600	608.7677	700.0828	0.139762	0.137125	
0.2	30500	606.7782	728.1339	0.182322	0.179685	

4.5 Material Properties of fresh concrete

Self-compacting concrete (SCC) was originally developed to offset the growing shortage of skilled labor but has proven to be beneficial due to faster construction, better surface finishes, easier placement, improved durability and thinner concrete sections amongst others. The development of self-compacting concrete was made possible with the development of superplasticizers and its practical application, accompanied by research was combined in creating guidelines such as the EFNARC specifications [103]. SCC has the ability to flow and completely fill all spaces within the formwork under its own weight without the need of vibration, whilst maintaining homogeneity and has adequate passing ability to flow through tight openings between

steel reinforcing bars without segregation or blockage. Aggregates are usually limited to less than 20 mm. Due to its high content of fibers SCC may show increased plastic shrinkage or creep that may be reduced by the use of fibers. The workability of SCC is higher than the highest class of consistence described in EN 206 [104] and can be characterized by the following properties: Filling ability, Passing Ability, Segregation resistance

A mix can be classified as SCC if the requirements for all three characteristics are fulfilled. Based on the EFNARC specifications [103] and the available testing equipment in the University of Cyprus laboratory the test methods that were used and the characteristic property they represent are listed in Table 4.6. Typical acceptance criteria are also recorded.

Table 4.6: List of test methods for workability properties of SCC and acceptance criteria

	Method	**Property**	**Unit**	**Minimum**	**Maximum**
1	Slump-flow	Filling ability	mm	650	800
2	T_{50cm} slump flow	Filling ability	sec	2	5
3	V-funnel	Filling ability	sec	6	12
4	V-funnel at 5min.	Segregation resistance	sec	0	+3
5	L-box	Passing ability	(h_2/h_1)	0.8	1.0
6	U-box	Passing ability	(h_2-h_1) mm	0	30

4.5.1 Description of testing procedures for measuring workability

4.5.1.1 The slump flow test

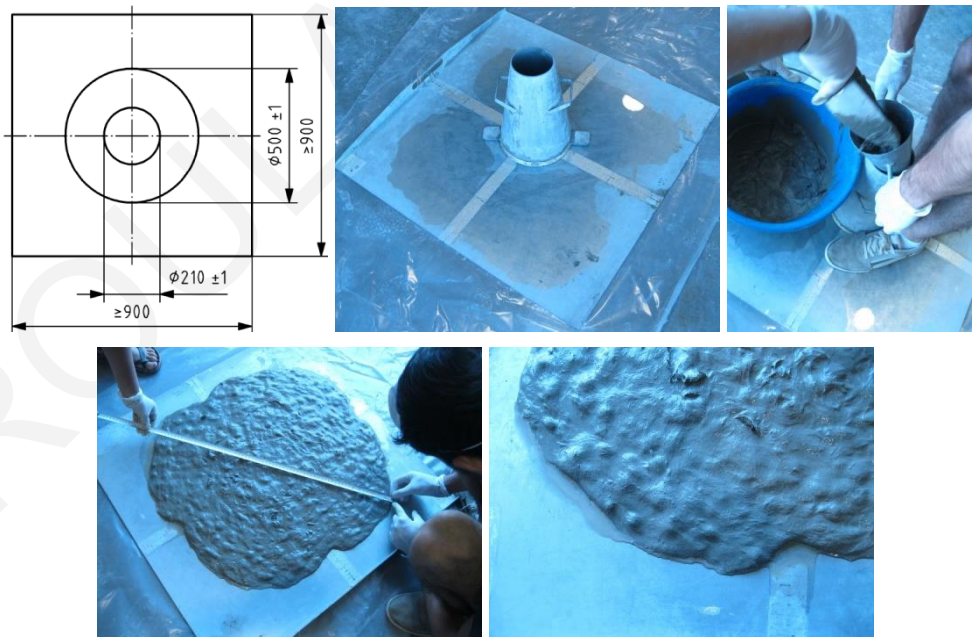

Figure 4.18: Slump flow testing apparatus

EN 12350-8:2010 [105] describes the testing procedure used to assess the flowability and flow rate of SCC by the slump flow and the T_{50cm} time. The fresh concrete is poured into a cone and when the cone is withdrawn upwards the time from commencing upward movement of the cone to when the concrete has flowed to a diameter of 500 mm is measured; this is the T_{50cm} time. The

largest diameter of the flow spread of the concrete and the diameter of the spread at right angles to it are then measured and the mean is the slump flow. The slump-flow SF is the mean of d_1 and d_2. Figure 4.18 shows the slump flow test of one of the SHFRCC mix designs.

4.5.1.2 V-funnel test

Testing procedure is performed as per EN 12350-9:2010 [106]. The funnel is cleaned and dampened inside. The gate is closed and concrete is poured in the funnel without agitation or compaction. After a delay of 10s from filling, the gate is quickly opened and the time from opening the gate to when is possible to see vertically through the funnel the container below for the first time is measured as shown in Fig. 4.19. After this the funnel can be refilled with concrete and left for 5 minutes to settle. If the concrete shows segregation then the flow time will increase significantly. The test measures the ease of flow of the concrete; shorter flow times indicate greater flowability.

Figure 4.19: V-funnel test equipment (dimensions in mm)

4.5.1.3 L-box method

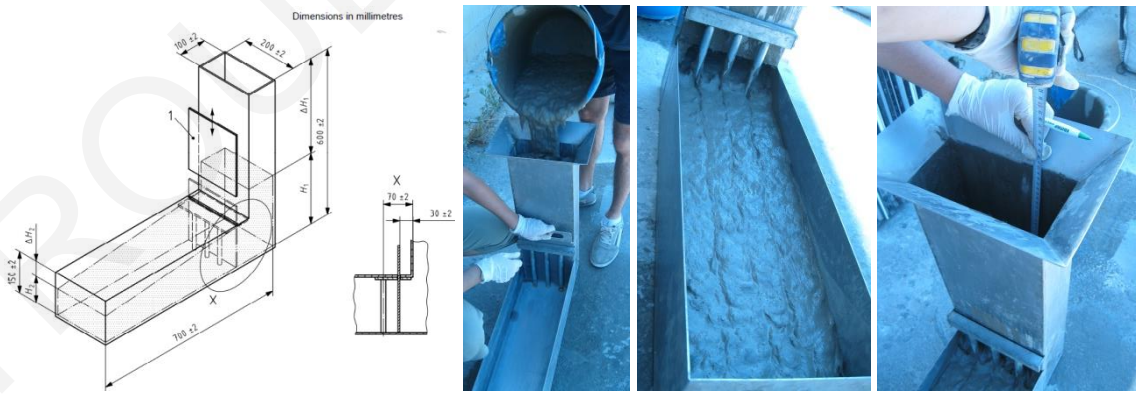

Figure 4.20: Typical general assembly of L-box showing required dimensions

Figure 4.20 shows the assembly for the L-box test as defined in the European Standards [107]. The L-box is used to assess the passing ability of self-compacting concrete to flow through tight openings, through reinforcing bars and other obstructions without segregation or blocking. The three bars simulate more congested reinforcement. The volume of concrete is allowed to flow horizontally through the gaps between the vertical, smooth reinforcing bars. The heights of the

concrete in the vertical section (H_1) and at the end of the horizontal section (H_2) are measured and the ratio H_2/H_1 is determined. The ratio is a measure of the passing or blocking behavior of SCC.

4.5.1.4 U-box test method

This test (Fig. 4.21) is used to determine the filling ability of SCC. It is reported in the specifications of EFNARC [103]. The left hand section is filled and then the gate is lifted and concrete flows upwards into the other section passing through the reinforcing bars. The height of concrete in the two sections is measured. The filling height is calculated as H_1-H_2, where H_1 is the height in the section that has been filled and H_2 is the height in the other section.

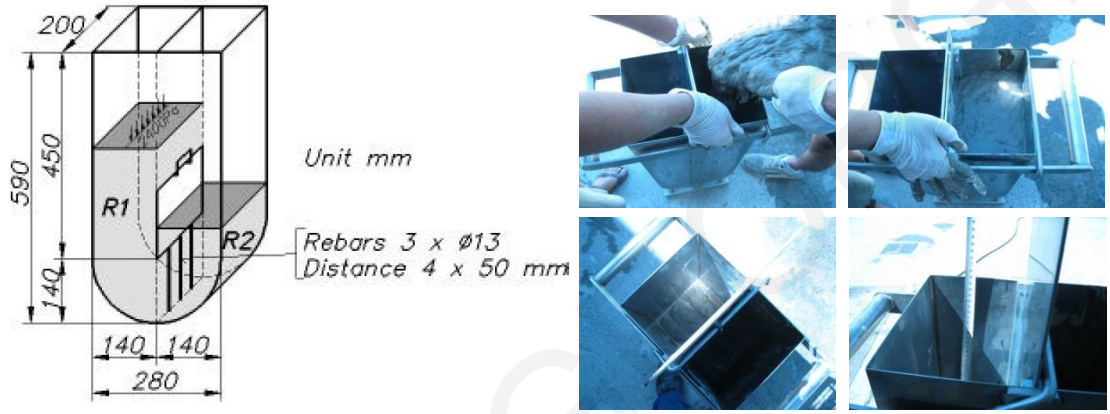

Figure 4.21: Testing setup for the U-box test

4.5.2 Results

The tests on fresh mix were conducted for two of the mixes: F13 without the use of fibers and F14 with PVA fibers of 12mm length without coating. The results on the fresh properties of the mixes are summarized in Table 4.7. Different tests for the same property, i.e. passing ability, show variation in the results indicating the mixes to be both self-compacting or outside the limits. The mix with the fibers can be considered to be self-compacting, while the mix without the fibers seems to be superfluous.

Table 4.7: List of test methods for workability properties of SCC and acceptance criteria

	Method	**Property**	**F13**	**F14**	**Minimum**	**Maximum**
1	Slump-flow	Filling ability	(900+950)/2=925	705	650	800
2	T_{50cm} slump flow	Filling ability	2	2.31	2	5
3	V-funnel	Filling ability	2.5	4.97	6	12
4	L-box	Passing ability	90/90=1	75/100=7.5	0.8	1.0
5	U-box	Passing ability	28.8-28.8=0	38-35=3	0	30

Chapter 5: Tension

5.1 Introduction

In order to establish design rules for SHFRCC structural members, conservative values of the material parameters should be used. This refers to all the essential characteristics of the material properties, including mean, average, and scatter of the experimental results. Material parameters such as stress-strain curves for tension and compression of the fiber reinforced composite need to be extracted through pertinent testing procedures. On account of the difficulty to conduct uniaxial tensile tests of brittle specimens, Codes and Standards intended for normal concrete describe indirect testing procedures for establishing the tensile strength of cementitious materials such as the splitting test or flexural tests. They then relate the tensile strength determined through reverse engineering with the uniaxial tensile strength using appropriately calibrated factors. In general, for normal concrete, various tensile testing arrangements give different strengths and this is related to the volume of the composite that is stressed under tension. It is reported by MacGregor [97] that concrete's strength decreases as the volumetric fraction of concrete that is highly stressed under tension is increased.

The experimental research for the use of fibers in concrete that was developed in the previous decades enabled the inclusion of specifications in some of the Codes, relatively recently, when FRC was explicitly recognized by design codes as a structural material (see for example, the ACI Building Code [48] - only for steel fibers, and Section 5.6 in Model Code [49]). Despite the enhanced toughness imparted by fibers, usual fiber reinforced concretes (FRCs) exhibit a drop in tensile resistance after first cracking and are referred to as strain softening materials. For this particular type of behavior the codes again describe indirect methods for determining the uniaxial tensile strength such as bending tests with a notch. They then specify an inverse analysis procedure for estimating the uniaxial tensile strength.

However, with the advent of new types of cement-based composites mostly comprising of self-consolidating mortar reinforced with PVA or other synthetic or steel fibers the problem of defining a standardized procedure for assessing the tension strength has re-emerged as a pressing research need. Some novel cementitious materials exhibit strain hardening behavior in tension (SHFRCC), marked by increase of tensile resistance after the first cracking and attainment of very large strains through the formation of multiple cracking [4, 108]. In this case uniaxial tensile tests are relatively easier to be conducted (in terms of stability of the experiment) and can yield both strength and strain properties of the cementitious composites; however the inverse engineering procedure needs to be recalibrated and modified to meet the special characteristics of the strain-hardening specimens, and the absence of aggregate interlock (due to the very small size of aggregate used in fabricating SHFRCC). Under this light, the experimental procedure used to conduct uniaxial tension tests was revisited in the present Chapter. Special hardware was designed and constructed for this purpose in the laboratories of the University of Cyprus.

Complementary tests using alternative standardized procedures were conducted as different means of assessing indirectly the uniaxial tensile strength: these included splitting tests, three point bending and four point bending tests. The use of the split cylinder test is described in most of the building codes on account of its easy execution without the need of special equipment or specimen molds.

The three point bending test was mainly considered because it is included -as a legitimate testing procedure for indirect assessment of tensile strength- in some Standards [49, 72]. Even though it is easy to perform, this type of test has the drawback that shear stresses develop in the cross section, which are usually not taken into consideration in transforming failure loads to tensile stresses and thereby strength estimates. On the other hand, the four point bending test is employed in this series of tests for comparison, since failure occurs in the constant moment region in the central part of the span, where the beam web is free of shear stress. In general, many researchers have used four point bending tests to establish the tensile strength of FRCs through inverse analysis, but in its standardized form, the shear span ratio of the typical specimen has a constant value of one. In this Chapter the effect of the shear span ratio on the developed capacity of a beam under four point bending is investigated particularly with regards to its influence on the tensile stress and strain capacity obtained from the inverse analysis of four point bending tests.

5.2 State of the Art on the use of FRCs and material properties characterization

A stable and repeatable experimental tensile stress-strain law which is needed in simulation and practical design to tension, shear, flexure and bond [7] goes beyond the need for the mere estimation of strength. Tensile properties are either characterized through direct tension tests on properly sized coupons, or indirectly through flexural tests on prisms under three or four point loading. The former are better suited for research into innovative cementitious mixes, however, there are several practical difficulties in conducting direct tension tests that include: (a) Concerns in sizing and casting of the specimens to avoid two-dimensional orientation of the fibers including minimum specimen size to fiber length ratio [109], (b) Boundary conditions during testing (pinned or fixed support), and post crack stability and alignment of the specimen [76], [80], (c) Loading rate and (d) Presence of defects that could encourage stress concentrations at the gripping points [110]. For the above reasons direct tension tests could be particularly unreliable for on-site quality control and for product characterization because of the meticulous details needed in fabrication of the specimens. According to Bazant [111], occurrence of spurious sideway flexure is common, owing to incomplete propagation of the cracks through the breadth of cross section, and deformation in such cases is non-uniform. The stress and strain fields are strongly sensitive to specimen geometry in the very small direct tension specimen; therefore development of alternative procedures, for the determination of SHFRCC's tensile properties through the familiar prism tests, and correlation thereof with the results of direct tension tests is still a practical research need.

5.2.1 Model Code

Fiber reinforced concrete (FRC) was included in the New Model Code 2010 [49] for the first time. The base line of the rules listed in Chapter 5.6 of the Model Code is as stated based on experience with steel fiber reinforced concrete, where basic failure mechanism is fiber slip. A basic differentiation is made between strain hardening and strain softening FRC. The Code states in the beginning of Clause 5.6.2.2 that uniaxial tensile testing is not advisable for standard testing due to the difficulty in performing the test and proposes the use of bending tests with crack and an inverse analysis, as shown in Fig. 5.1, to determine the stress-crack width relation. At the end of the same paragraph the Code states that for high fiber contents, strain hardening materials can be obtained and in order to guarantee the hardening in tension, the Code suggests that the tensile behavior must be identified by means of uniaxial tension tests carried out on un-notched specimens.

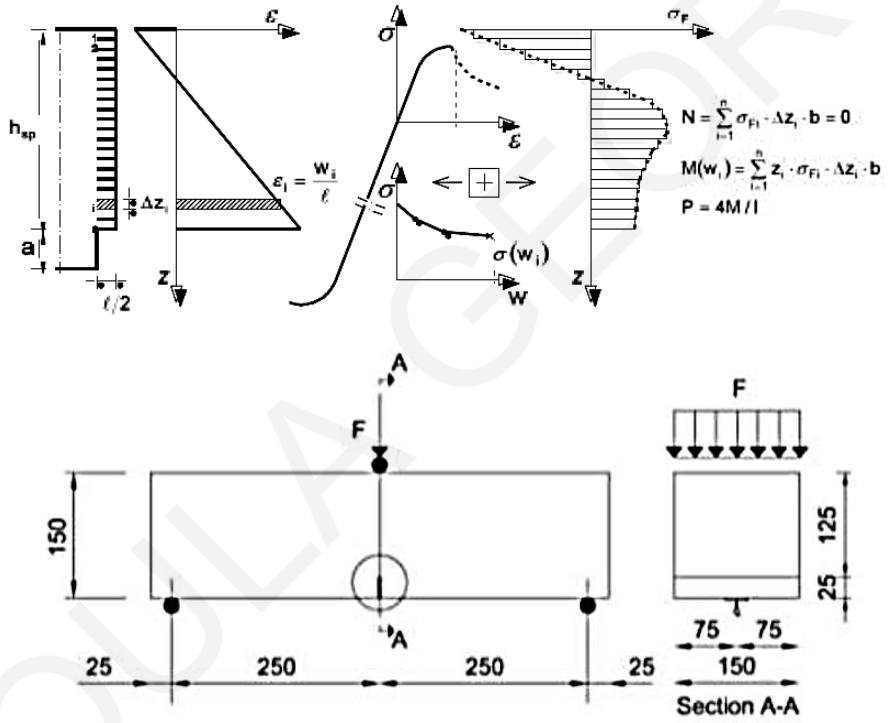

Figure 5.1: (a) Inverse analysis of beam in bending and (b) three point bending on a notched beam [49]

5.2.2 Japan Society of Civil Engineers (JSCE)

The JSCE issued in 2008 the "Recommendations for design and construction of high performance fiber reinforced cement composites with multiple fine cracks (HPFRCC)" [50]. The Recommendations propose "Test Method 2: Testing method of uniaxial tensile strength" for the determination of the tensile stress-strain curve of a SHFRCC. The testing apparatus recommends a fixed support on one end of the specimen and a pin support on the other end. The recommended load application is a constant specimen deformation rate of 0.5 mm per minute, while the minimum number of specimens used to deduct reliable results is five. In regards to the specimen's dimensions the Recommendations suggest that the minimum size of the specimen is at least the

fiber length and twice the maximum aggregate size, with proposed dimensions as shown in Fig. 5.2.

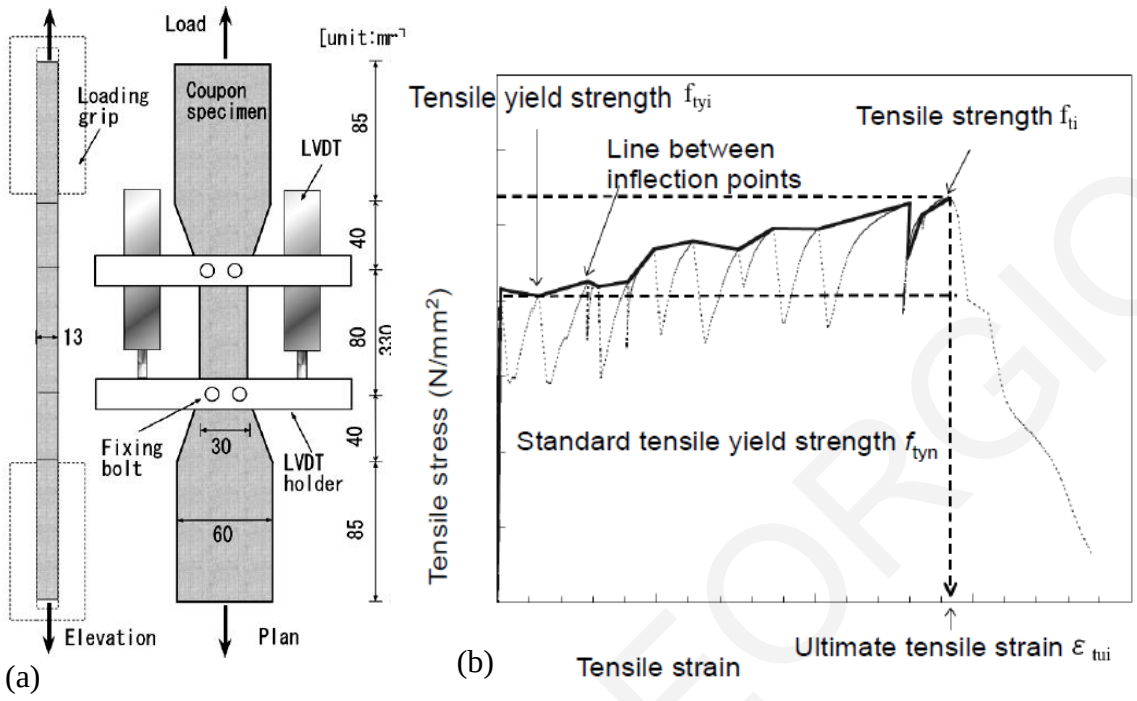

Figure 5.2: (a) Outline of uniaxial tension test and (b) Yielding point, ultimate point and tensile strength

5.2.3 Japan Concrete Institute (JCI) Standard [53]

The Japan Concrete Institute issued a Standard in 2007 called "Method of test for bending moment-curvature curve of fiber-reinforced cementitious composites" describing an indirect method determining the tensile stress-strain properties of SHFRCCs (JCI-S-003-2007 [53]). The standard uses a square cross section beam (100 mm) under four point bending with a span length of 300 mm. The test requires a curvature measuring equipment, as shown in Fig. 5.3 and the load is applied with a machine head speed of 0.3 mm/min. The Standard recommends that the results should be discarded if fracture occurs outside the pure bending span.

In the Appendix of the Standard, an "Evaluation method for tensile strength and ultimate tensile strain of fiber-reinforced cementitious composites" is given as "non-mandatory information". Equations are proposed in that section, with the results of the four point bending test. This is an inverse analysis procedure to extract the tensile strength and ultimate tensile strain properties (Eq. 5.1 and 5.2) of the material from the M-φ curves obtained from the four point bending test. The special LVTDs system that measures the strains of the top and bottom layers of the central constant moment regions are used to deduct curvature values.

$$\varepsilon_{tu,b} = \phi_u \cdot D \cdot (1 - x_{nl}) \tag{5.1}$$

$$f_{t,b} = \frac{E \cdot \phi_u \cdot D \cdot x_{nl}^{\,2}}{2 \cdot (1 - x_{nl})} \tag{5.2}$$

$$x_{nl} = -1 + 2\cos\frac{\theta}{3},\ \theta = \arccos\left(-1 + 6m^*\right),\ m^* = \frac{M_{\max}}{E \cdot \phi_u \cdot B \cdot D^3},\ x_{nl} = x_n / D \qquad (5.3)$$

where x_n is the depth of the compression zone, D is the depth of the test specimen, $M_{max}= (P_{max}/2)\cdot (l/3)$ is the maximum moment, P_{max} is the maximum applied load, l is the total span length, E is the modulus of elasticity of concrete, φ_u is the curvature at maximum load equal to $(\varepsilon_{2u}-\varepsilon_{1u})/d_o$, ε_{2u} *and* ε_{1u} are the strains at maximum load calculated by dividing the upper and lower LVDTs deformations to the contact length, d_o is the distance between the LVDTs and B is the width of the specimen.It is important to note that the equations cover composites that form multiple cracking in bending. The Standard also notes that the specimens that are prepared for testing should not be placed in molds in layers, or use tamping rod or vibration since they affect the fiber orientation.

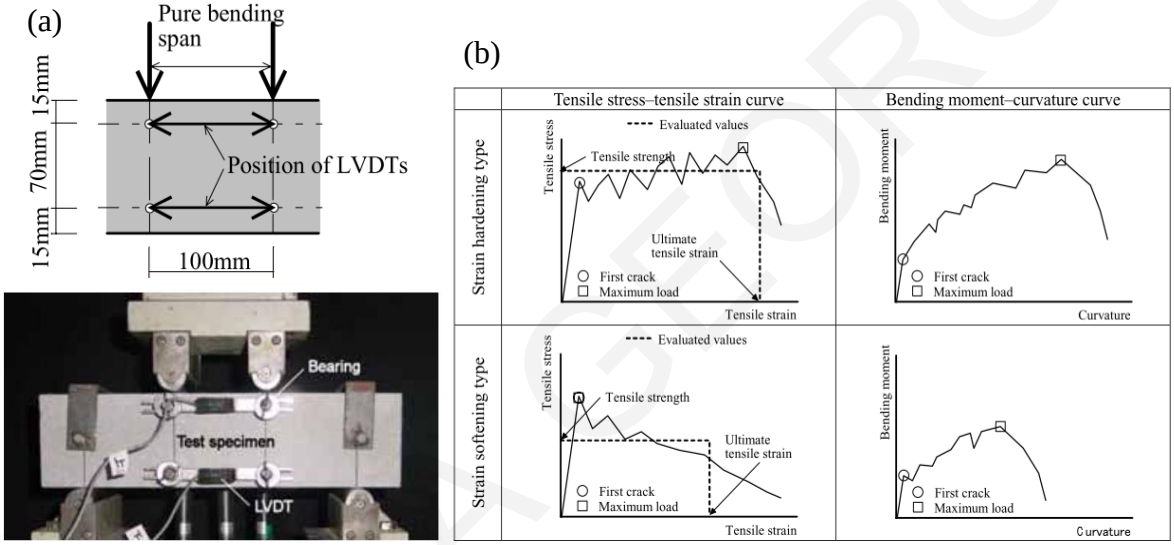

Figure 5.3 (a) Example of LVDTs setup and (b) relation between M-φ curves and σ-ε in tension

5.2.4 Comparative testing of crack formation in SHFRCC by RILEM Technical Committee 208 [112]

A comparative (round robin) study was conducted by the RILEM Technical Committee 208-HFC Subcommittee 2 [112], aiming to investigate the mechanical performance of SHFRCC on tests performed in five different laboratories of the participating institutions. The research aimed to make recommendations for a suitable test setup for characterizing cracking of SHFRCCs [112] by the use of uniaxial tensile tests. The test ages of the coupons varied between 14 and 28 days. In Figure 5.4 the coupons' dimensions and testing setups used in the five laboratories are depicted. The cross-sectional area varied between coupons from different laboratories ranging between 30x13 mm to 60x30 mm, while different boundary conditions were tested to study the variation of the results between rotational and non-rotational end conditions. Crack saturation appeared at 3% strain for almost all the specimens with fine aggregates, while it was decreased for coarser sand. A large variability was observed in the crack widths with the smaller gauge sections leading the researchers to propose a minimum width of the cross section at 30 mm if the specimens are to be used for durability tests. The smaller specimens in the study used rotationally semi-free ends while

the larger specimens used fixed boundaries at both ends and therefore it was not possible to distinguish if the specimen size or the boundary conditions were the source of variability in the test crack data.

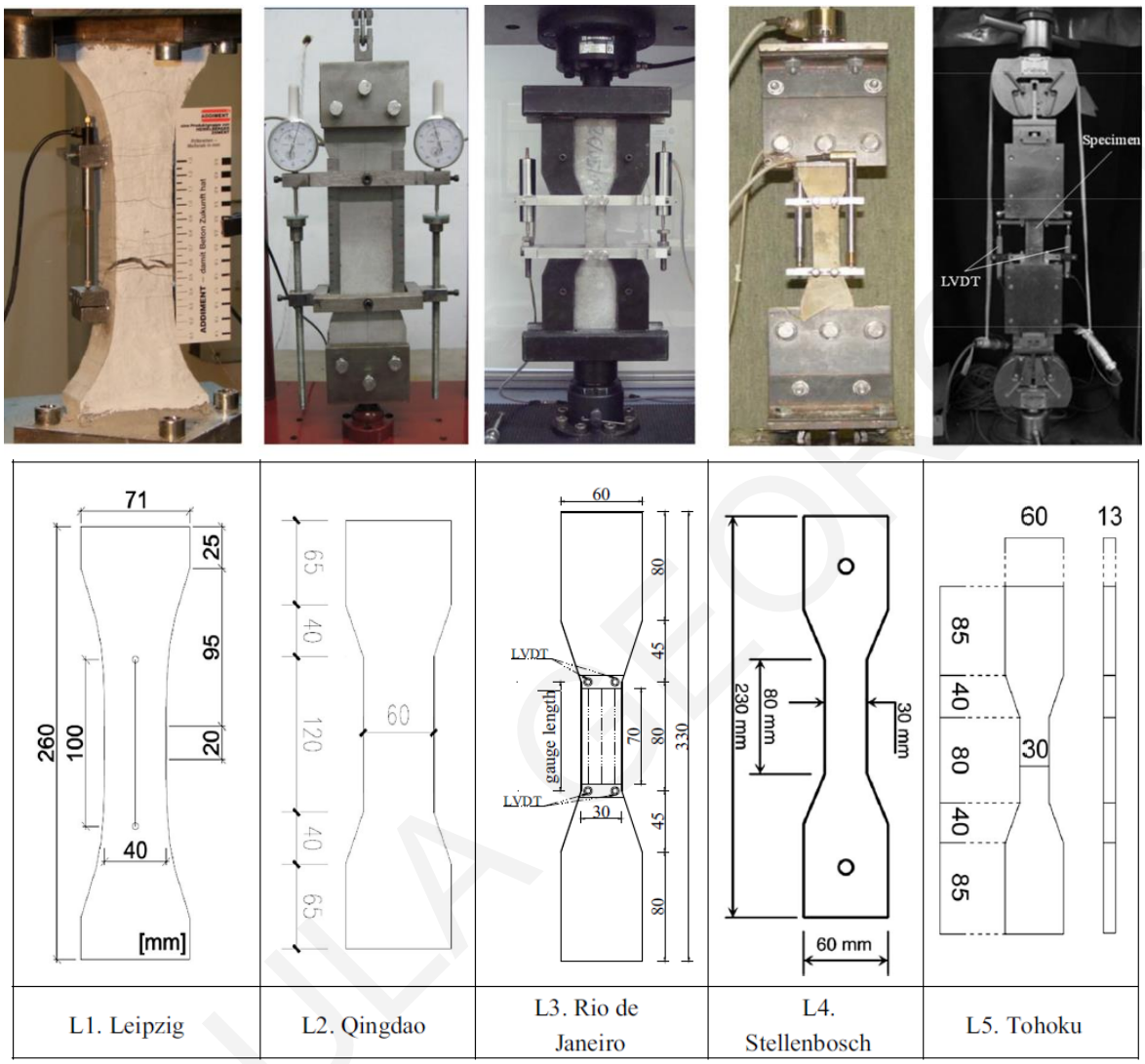

Figure 5.4: Uniaxial tension test setups and coupons conducted in different laboratories

5.3 Experimental results from direct and indirect tensile test

It was seen in the previous section that various methods and procedures are proposed for determining the σ-ε properties of SHFRCC in tension. A general testing procedure for the uniaxial test has not yet been established. Standards and researchers use many different testing methods with variations in the specimen's dimensions, the loading end conditions, and in the displacement application rate. Other standards propose the use of alternative indirect tests that are easier to be conducted and do not need special equipment, such as the three or four point bending test and give inverse analysis procedures in order to extract σ-ε curves in tension. In this Chapter a comparison is made between the experimental results of four different testing methods that are generally used to determine the tensile strength of cementitious composites. Those methods are: uniaxial tensile test, splitting test, three point bending test and four point bending test. There were no notches used in

any of the testing methods since they would impart concentration of deformation at one single location and the hardening of the composite would not be visible.

Additionally the influence of the fiber's length and interfacial bond properties between the PVA fiber and the cementitious matrix on the composite's tensile strength and strain is examined, also with regards to the various testing methods. Fiber lengths considered are 8 and 12 mm; in all cases the matrix materials and volumetric ratios remain the same including the fibers' diameter and content ratio per volume of the composite. By altering the surface properties, stress and strain capacity of the composites in direct tension are modified in a predictable manner. Considering mixes with two different lengths of PVA fibers (8 and 12 mm) was intended to illustrate the effect of fiber length on the strain hardening behavior of the SHFRCC. Two different volumetric ratios of coating on the fibers in the mix (0%, 6.6%) were considered so as to demonstrate the effect of surface specific bond properties on the final tensile characteristics of the composite (details about coating's chemical composition and coating procedure are given in Chapter 3). The percentage of the fibers was constant in all cases at 2% per total volume. In the preliminary study (Chapter 3) mix design B26 with a coating of the fibers of 6.6% by weight showed increased hardening reaching a strain at maximum load in the order of 3% at 103 days. This mix design was then used for the investigation of the experimental research. Tests were chosen to be conducted for all specimens at the age of 100 days in order to eliminate the influence of hardening of the cementitious matrix on the interfacial properties between the fiber and the matrix. Additionally the variability of the σ-ε curves in uniaxial tension is investigated between different batches of the same mix design with different volumes.

5.3.1 Uniaxial tension test

The most important behavioral parameter of FRC is the tensile strength and strain capacity. Multiple cracking is affected by the elastic properties of the fibers and of the matrix, but a decisive parameter is the bond-slip law of the fiber-matrix interface. In the tests, strain was calculated as the elongation measured by the equipment mounted on the specimens' two opposite sides and divided by the gauge length (100 mm).

During the formation of multiple cracks, the composite matrix-fiber system appears to strain-harden. Due to stress, fibers bridging the cracks elongate but they also pull-out partially from the matrix at the crack locations. In the dog-bone specimens the formation of cracks saturated the full measuring length (narrow part of the specimen) and extended beyond that towards the wider ends of the specimen when coated fibers were used (see for example Fig. 5.5 mixes F3 and F4). Beyond a limiting strain, the value of which appears to depend on the competition of interfacial bond and tensile strength and stiffness of the fibers, new cracks cease to form and crack localization occurs. In no case strain exceeded the value of 1.5% contrary to the preliminary tests. This is attributed to the change in the interfacial bond properties between the fiber and the matrix due to age. Stress (σ) is calculated as the load divided by the cross section area, whereas strain is defined as the

elongation occurring within the measuring range, divided by the length of the measuring range. Plain mix specimens (F5) were fractured incipiently during their extraction from the molds (they were very brittle) and therefore it was not possible to test them in direct tension. Figure 5.6 shows the tensile stress-strain curves for the four mixes F1 (8 mm, no coating), F2 (12 mm, no coating), F3 (8 mm, with coating) and F4 (12 mm, with coating). The stress-strain curves shows the great improvement in strength and strain values of the mixes when the longer PVA fibers are used, while the use of coating reduces stress values and increases strain capacity.

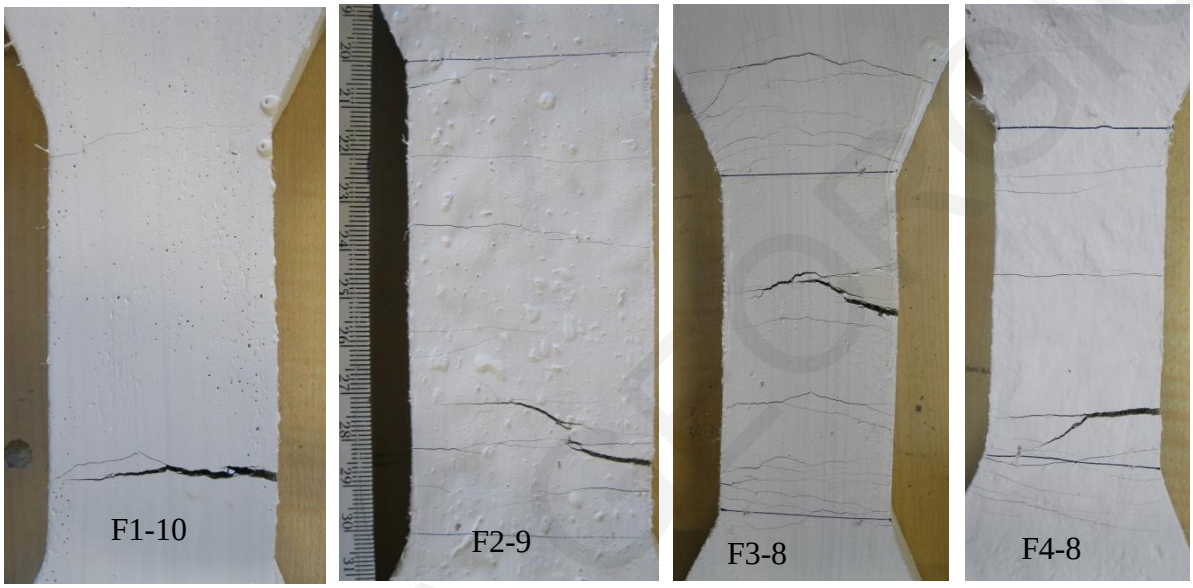

Figure 5.5: Uniaxial tension crack patterns from different mixes

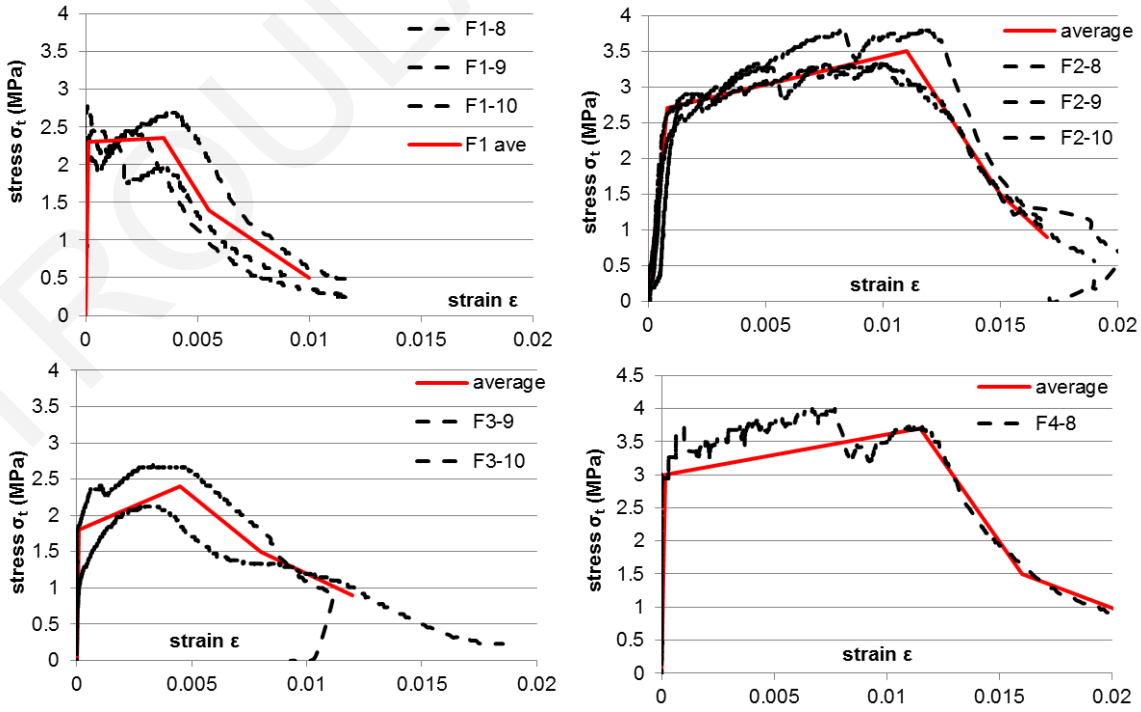

Figure 5.6: Uniaxial tension stress-strain diagrams for various mix designs

The "yield" and ultimate stress characteristic points obtained from each specimen group (according with the fiber length and coating) are collected in Table 5.1, obtained as the average of three specimens for each mix. "Yielding" corresponds to the point where a sharp change in slope is observed on the tension stress-strain curve.

Table 5.1 Characteristic points of uniaxial tension tests

Direct tension	**F1**	**F2**	**F3**	**F4**
f_{ty} (MPa)	2.36	2.62	1.43	3.08
f_{tu} (MPa)	2.38	3.45	2.39	3.67
ε_{ty} (mm/mm)	0.000132	0.001277	0.0000825	0.0003
ε_{tu} (mm/mm)	0.003403	0.01082	0.0042	0.01175

The number of fibers crossing a unit area n_f is estimated as:

$$n_f = 4 \cdot \rho_f \cdot \alpha_2 / \left(\pi \cdot d_f^2\right) \quad (5.4)$$

where, ρ_f is the volumetric ratio of fibers (here =2% for all FRC mixes), α_2 is the fiber orientation factor (taken =0.5) to account for the random orientation of fibers in space [113], and d_f the fiber diameter (39 μm). According to Eq. 5.4, the estimated number of fibers crossing a unit area in all tested samples is the same, i.e.: $n_f=4 \cdot 2\% \cdot 0.5/(\pi \cdot 0.039^2)=8.37$ fibers per mm^2. Therefore this variable depends on the volume ratio and not on the aspect ratio and diameter of the fiber used. Considering that the cross section under uniaxial tension of the specimens is equal to *25x50 mm*, it is estimated that the total number of fibers bridging the cracks and transferring stresses during the uniaxial test are, $N_f=8.37 \cdot 25 \cdot 50=10463$. This number is reduced by 50% to account for the angle of inclination, θ, of the fibers crossing the cracks ($\lambda_{eff}=0.5$ according to Archontas and Pantazopoulou [114]), since normal stress acting on the crack is obtained from the corresponding component of fiber axial stress, ($f_f \cdot sin\theta$): $N_f^{eff}=\lambda_{eff} \cdot N_f=0.5 \cdot 10463=5231.5$.

With all other parameters among the SHFRCC specimens being the same, any difference in response will necessarily be linked to the bond properties of the fiber's contact surface, which here were modified as part of the investigation. The specific bond between the fiber's surface and the surrounding cementitious matrix depends on the chemical and/or frictional stresses and the fiber contact length. The effect of fibers develops after the occurrence of first cracking in tension; thus fibers do not affect the cracking strength of the composite but the post-cracking response branch up to the attainment of the ultimate strain capacity. Tensile strength of each composite appears to be mainly dependent on the length of the fiber according to Table 5.1, estimated at 3.5 MPa (1 MPa greater) in the case where the 12 mm length fibers are used whereas it is only 2.3 MPa in the case where 8mm length fibers are used.

In their original state PVA fibers have a hydrophilic surface with free hydroxyls creating chemical bonds with the surrounding cement products. These chemical bonds are so strong that are very difficult to break leading fibers to rupture rather than pull-out [94]. The rupture strength of a single PVA fiber may be calculated based on material characteristics as $F_{f1}=f_{yf} \cdot A_f=1600 \cdot \pi \cdot 0.039^2/4=1.91$ *N*. Assuming half the fiber length as the maximum embedment

length to develop the fiber tensile strength, it is estimated that the required (theoretical) bond stress needed at the surface of a PVA fiber is 3.9 MPa for the 8 mm long fibers and 2.6 MPa for the 12 mm long fibers. These values are close to the tensile strength of the matrix. Pullout rather than rupture of the fiber would occur if the available bond strength would be less than the above estimated limit. A corollary to this is the observation that if all the fibers could reach their ultimate strength by rupture (e.g. in the case of the uncoated fibers), then the ultimate stress of the composite would be in the range of $=1.91 \cdot 5231.9/(25 \cdot 50)=8$ *MPa*. Note that based on the test results presented in Table 5.1 none of the materials has attained this ideal tensile strength value, since fibers at an angle with the loading direction may rupture prematurely due to combined cleavage at the crack surface.

In the case of rupture the local strain of the fiber at the critical cross section is, $\varepsilon_f=\sigma_f/E_f=1600/40000=0.04$; the distribution of strains decays exponentially with distance from the critical section towards the unloaded end of the fiber. If uniform bond is assumed (at half the length), the average (actual) bond strength f_{b1} that developed along the fiber matrix interface may be estimated from the experimentally measured ultimate strength of the composite (Table 5.1). The nominal number of fibers per unit area defined above, and the length of the fiber is as per Eq. 5.5.

$$\mathrm{f}_{bl} = \left(\frac{f_{tu} \cdot A_c}{N_f \cdot \pi \cdot d_f \cdot L_f} \right) \tag{5.5}$$

5.3.2 Split Cylinder test

The split cylinder test is an indirect method used to determine the tensile strength of concrete. It was first introduced in the Fifth conference of the Brazilian Association for Standardization in 1943 and since then it was proposed by most international standards such as ASTM C-496 [71], BS1881-117 [115] and was simultaneously developed in the Japanese Standards. The specimen, which is a cylinder of concrete, is placed horizontally between two loading plates. In that way the cylinder is compressed on the two diametrically opposed generators and an almost uniform tensile stress is induced in the loading plane. The rupture mechanism is governed by the maximum tensile stress that is developed along the loading diameter. Theory of elasticity relates the splitting tensile strength $f_{sp,t}$ with the tensile strength of concrete (Fig. 5.7). For perfectly brittle materials splitting tensile strength would coincide with the uniaxial tensile strength but in the case of concrete which is a quasi-brittle material splitting test overestimates the true uniaxial strength. If the material is not sufficiently brittle splitting process is completed only after a failure of compressive crushing /sliding is developed. Even though specimen's geometry, size and loading strips used play an important role in the final strength, formulas from Standards do not usually take this under consideration [116].

In the case of cementitious materials analysis of the splitting test by previews research by Rocco et al. [117] shows that the classical theory of elasticity is not able to approach correctly the actual stress distribution, with a tensile strength variation of up to 40%. Olesen et al. [118] performed a

parametric analysis of the splitting test showing that the linear elastic interpretation of the ultimate splitting force, related to the uniaxial tensile strength of the material is only valid for specific situations, for example very large cylinders, and that the splitting test is not well suited for determining the tensile strength of fiber reinforced concrete.

The use of bearing strips proposed by the Standards is required for normal concrete in order to prevent multiple cracking and crushing at the loading points. Rocco et al. [119] have shown that the growth of the principal crack is not affected by the width of the bearing strip. Two types of fracture mechanisms are recorded for normal concrete in the same research [119], one associated with central cracks and one with a secondary crack system on both sides of the bearing strips, each mechanism initiating different peak loads on the load-displacement curve. After the first crack and maximum load is reached, the specimen is unloaded by the crack extending on the edges and then the specimen is separated in two parts and load is transferred by the two parts until they evidently rupture. Rocco et al. [119] report that in the cases of small specimen sizes the peak load of the secondary crack system can become the dominant peak load.

The cylinders tested using the standard splitting procedure develop a biaxial compressive state of stress immediately under the loading line which quickly reverses to tensile (positive) stress in the central region [120]. From the theory of elasticity [121] the stress distribution perpendicular to the plane of loading is uniform tension and its magnitude is described by the following equation:

$$f_{sp,t} = 2P/(\pi \cdot l \cdot d) \tag{5.6}$$

where P is the total applied load, d is the diameter of the cylinder and l is the length of the specimen. In the case of a perfectly brittle material and without the risk of compressive failure near the loading points, the uniaxial tensile strength determines failure resulting if $\sigma = f_{ct}$.

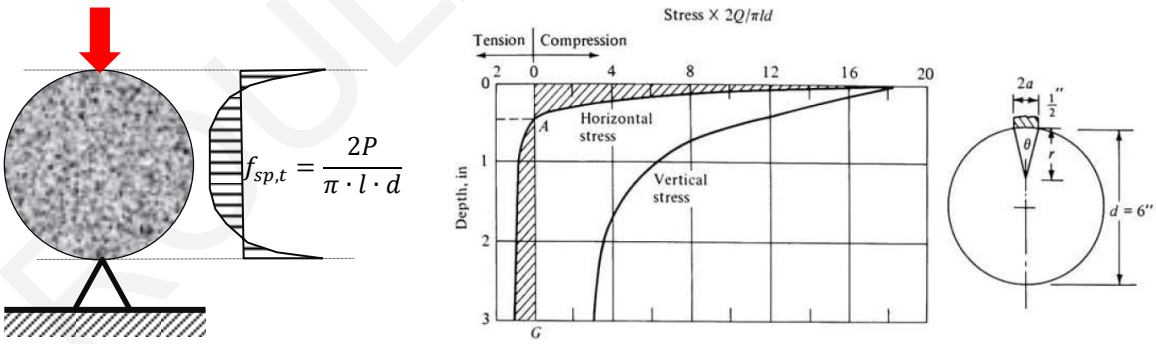

Figure 5.7 (a) Split Cylinder loading and stress distribution and (b) elastic stress distribution on the vertical diameter and dimensions of cylinder specimen [122]

It has been demonstrated that the expression used for the calculation of the maximum elastic tensile stress [Eq. (5.6)] is still valid for various plastic models [122]. In particular, the stress distribution computed using finite elements assuming a three-parameter, elasto-plastic material model (isotropic hardening) does not substantially vary from the above distribution with increasing loads up to the specimen failure. This is noted with reference to the usual practice of dismissing the splitting test because the stress distribution is considered unknown after first cracking. However

this disclaimer is not relevant in the case of FRC as the fibers confer pseudo- elastoplastic response to the matrix by controlling the crack propagation. In addition, the pattern of stress distribution shape is not affected by material softening, contrary to what occurs in flexure.

Chen [122] compared the solution to the split cylinder test by elasticity (Eq. 5.6) with the case of a perfectly plastic material by using limit analysis. The failure mechanism in that case is the cylinder being separated in four parts as seen in Fig. 5.8; the wedges in contact to the loading plates being translated towards each other and the two parts separated by the main tensile crack translating apart from each other. Two solutions are proposed based on the upper and lower-bound limits where for the calculation of the load bearing capacity it is seen that the compressive capacity, the angle of friction and the cohesion between the plates and the specimen play an important role. It was also found [122] that the indirect tensile test gives tensile strengths within ±14% of the value *2P/(πld)* and the average value from upper and lower bound solutions is identical to that of the elastic theory.

Various modes of failures are reported for the split cylinder test by previous researchers. Concrete and mortar specimens of different sizes may develop diagonal cracks in the zone near the applied load and failure of the specimen is formed with a wedge and plastic slip mechanism [119]. In the case of rocks, cement paste and ceramic materials rupture is characterized by a more complex system with multiple cracking both in the center of the specimen and secondary cracks formed on both sides of the vertical crack as shown in Fig. 5.8 (c) [119].

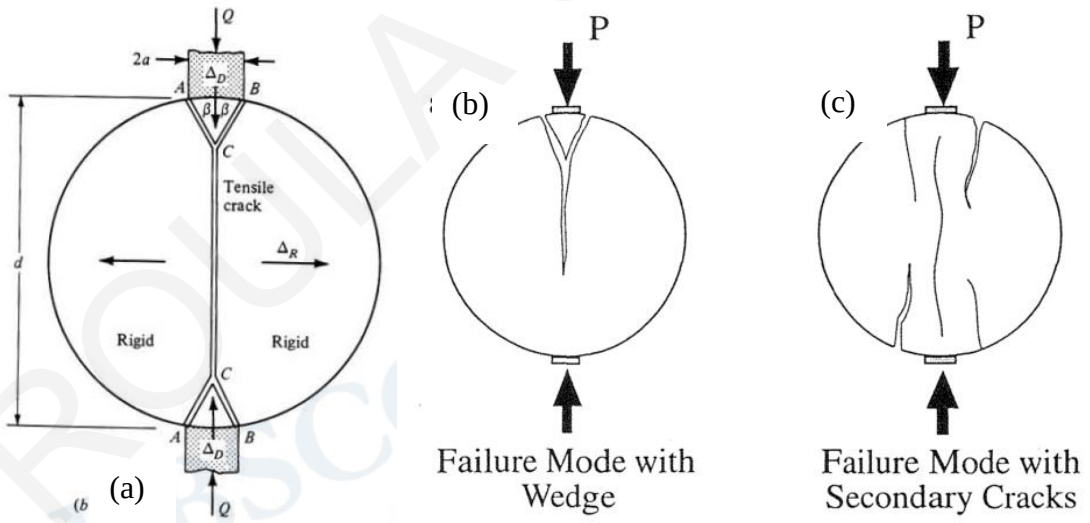

Figure 5.8: (a) Bearing capacity of a split cylinder test: failure mechanism by Chen [122] and (b) and (c) Different rupture modes by Rocco et al. [119]

In the case of strain hardening composites multiple cracks are expected to open parallel to the loading axis, with the fibers bridging the cracks and transferring load over a wider area. In the case of SHFRCC it was found that the fibers confer pseudo-elastoplastic response to the matrix by controlling the crack propagation. In addition, the pattern of stress distribution shape is not affected by material softening, contrary to what occurs in flexure. Figure 5.9 shows the sequence in the failure mode of a splitting test of the mix design F1. The composite contains 8 mm PVA fibers

without coating and as seen from Par. 5.3.1 the uniaxial tensile strength of this material under tension is in the order of 2.3 MPa. As seen in Fig. 5.9 in the beginning a crack is initiated in the middle of the specimen, parallel to the loading direction. Then as this crack continues to grow multiple cracking initiates parallel to the first crack on both sides. As the specimen decreases in height and increases in width due to cracking, the loading surface that is in touch with the plates increases and two wedges are formed. After a specific horizontal deformation, localization of deformation is concentrated in the main crack and the specimen is separated in two parts. The fibers bridging the main crack at that point have been ruptured or pulled-out and load is transferred through the hinges on the two parts separately. The test is transformed after that into a compression test. The same mode of failure is observed for all SHFRCC mix designs tested within this experimental program.

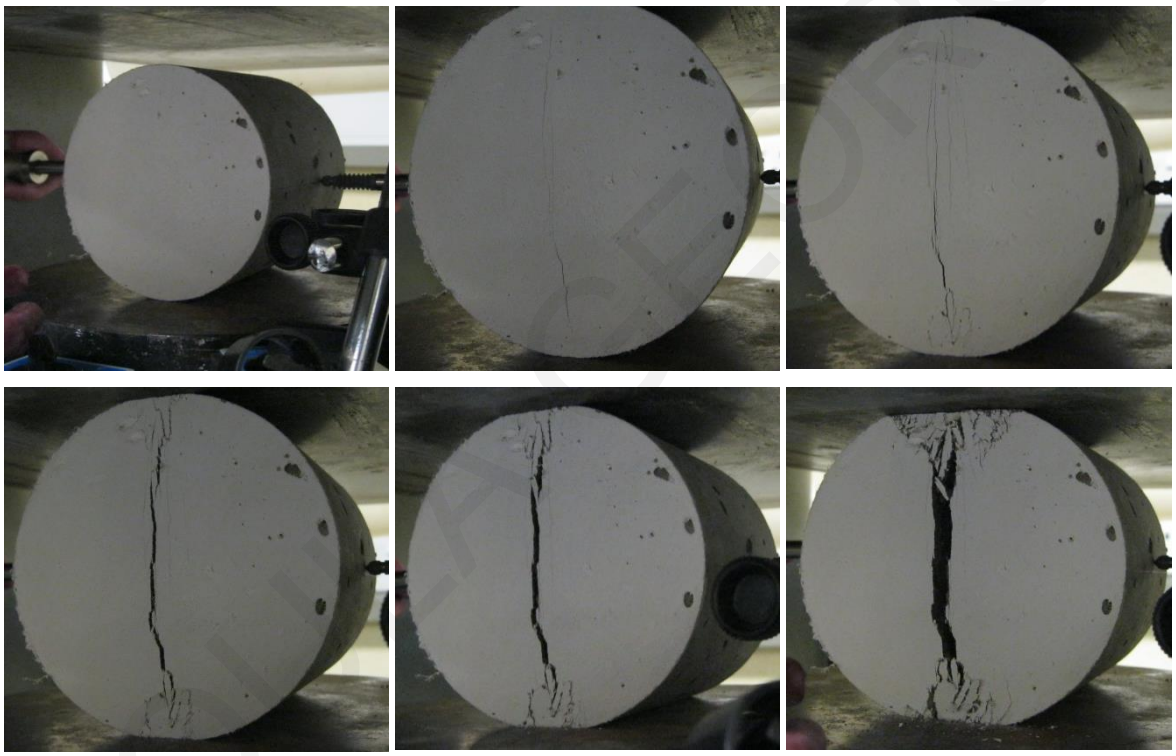

Figure 5.9: Failure sequence of split cylinder testing of F1 (specimen F1-6)

Figure 5.10 shows the failure cracks for the specimen without fibers (F5) as well as for the four SHFRCC mixes with different fiber length and coating. The crack patterns shows an improved performance of the mixes with coating on the fibers (F3, F4) where multiple cracking is most intense.

The test results depicted in Fig. 5.10 reveal the beneficial results of the addition of fibers in the cementitious matrix. Regarding the mode of failure, even though the maximum load is concentrated at one plane of the specimen, in the case of the SHFRCC mix, multiple cracks appear in a wider range on the horizontal diameter of the cylinder of approximately 20 mm (the diameter of the specimen is 100 mm). This allows the specimen to develop some strain hardening characteristics in comparison to the mix without any fibers that underwent sudden failure past the first cracking strength.

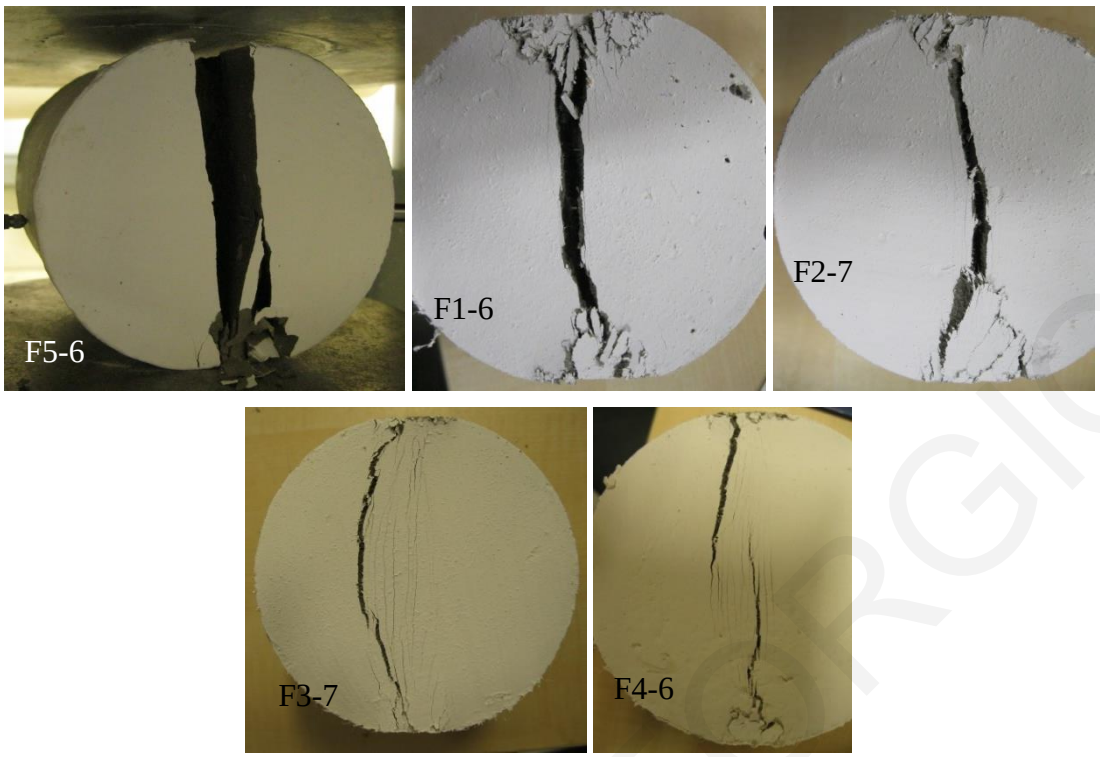

Figure 5.10: Failure cracks for mixes F1, F2, F3, F4, F5

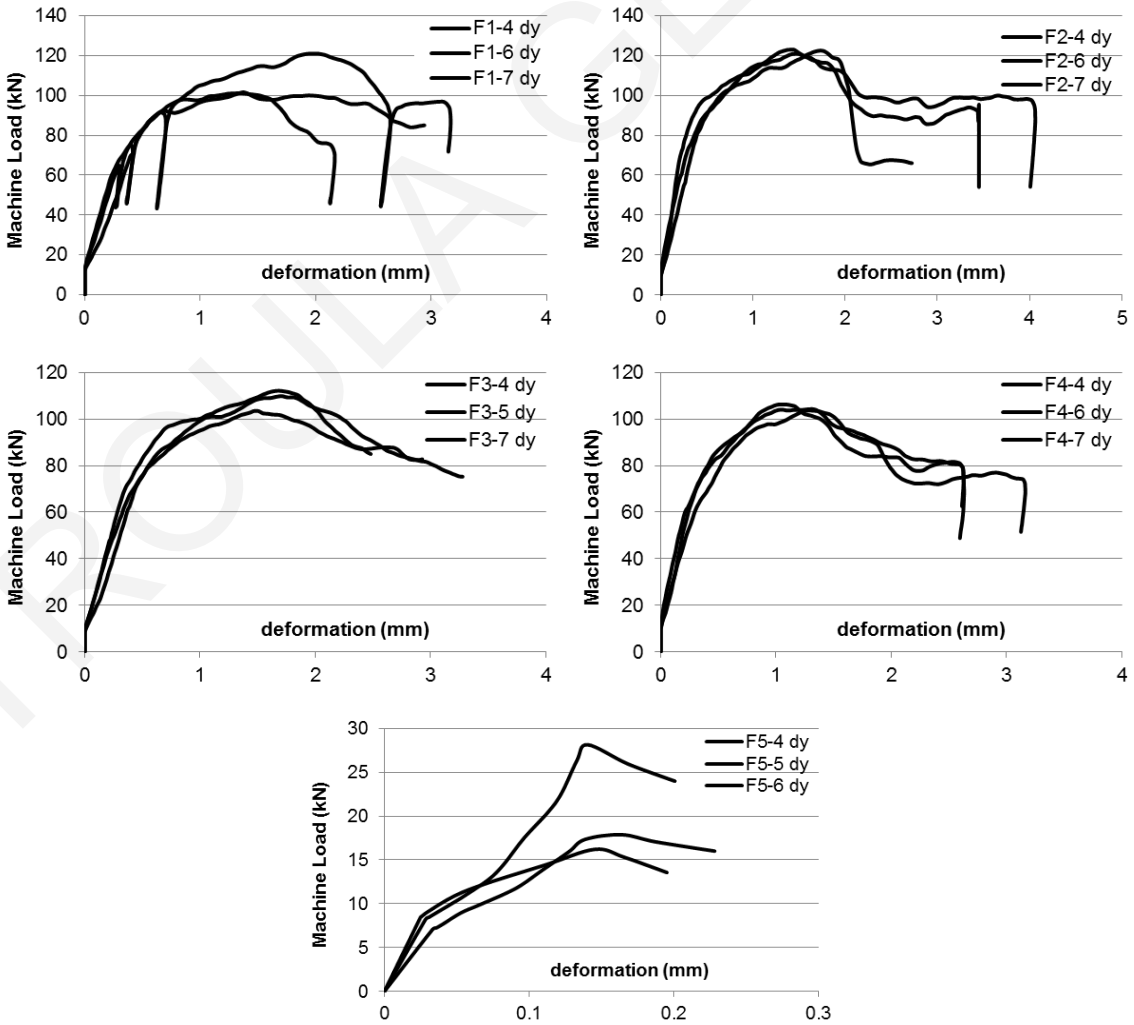

Figure 5.11: Load-vertical deformation of the splitting tests from various mixes

If the failure mode of the split cylinder test would be the tensile stress capacity of the mix design then by using the tensile strength from the uniaxial tension test failure load would be in the order of: $P=f_{ct}\cdot\pi\cdot d\cdot l/2$=36.1 kN. As seen in Figure 5.11 the Load capacity of mix design F1 reaches values between 100 to 120 kN, three to four time greater than the failure expected if the tensile strength from the uniaxial tensile test is used.

The direct tensile strength may be estimated from the spit cylinder test results after properly reducing by the multiplier A_{sp} as per the Model Code [49]. Usual values for A_{sp} vary from 0.67 to 0.95. However, as the Code states "based on more recent findings the true factor ought to exceed the value of 1.0". Here a compromise solution of A_{sp} = 1.0 has been selected. This suggests that the split cylinder tensile test estimates adequately the average mean value for the actual tensile strength of the material despite the fact that the reported values are much higher than the test results from direct tension tests (see Table 5.2).

Table 5.2: Characteristic points (yield and maximum) from split cylinder tests

split	**M8**	**M12**	**M8C**	**M12C**	**PM**
f_{ty} (MPa)	4.27	5.15	4.93	3.92	1.5
f_{tmax} (MPa)	6.87	7.77	6.91	6.67	
δ_{ty} (mm)	0.00016	0.00024	0.00105	0.00018	0.00024
δ_{tmax} (mm)	0.00606	0.00477	0.00778	0.00442	

The fibers seem to increase the first cracking stress in this case as the cracking strength of the mix without fibers (F5) is 1.5 MPa while the cracking stress of the SHFRCC is in the order of 4-5 MPa. Based on the preceding arguments it is estimated that the number of fibers working effectively on the diametric plane of each cylinder are $n_f^{eff}=\lambda_{eff}\cdot n_f=0.5\cdot 8.37\cdot 100\cdot 100=41850$. Again, if all the fibers could reach their ultimate strength followed by rupture, the ultimate force normal to the direction of loading would be $F=2P/(\pi\cdot d\cdot l)\cdot A_{sp}\cdot A_c=f_{ctm}\cdot A_c=41850*1.91$, and therefore, the ultimate tensile strength of the composite ought to be $f_{ctm}=8$ *MPa* as in the case of direct tension. This value is never attained; but in the splitting tests, it is closest to the tensile strength of the FRC containing 12 mm long fibers without coating (M12).

Through comparison with the direct tension test results it is concluded that indirect tension strength values obtained from cylinder splitting are an upper bound estimate, whereas the uniaxial tensile test yields the lower bound values. This is mainly related to the nature of each experiment since in the case of direct uniaxial tension the specimen is under plane stress, whereas the case of cylinder splitting is a state of plane strain with the longitudinal contraction owing to Poisson's ratio affecting the final capacities. Also in the split cylinder test the ultimate stress is concentrated at one single cross section (cross section directly under loading) whereas in the case of direct tensile test stress is uniform, occurring over a wider range of the specimen. This leads to unavoidable concentration of deformations in one cross section and does not permit the full strain hardening properties of the material to be developed.

5.3.3 Three Point Bending Test

The failure mode of the composite without fibers (F5) under three point bending test follows the same pattern as normal concrete. The beam behaves elastically up to the point where the ultimate layer under tension under the point load reaches the tensile strength of concrete. After the tensile strength is exerted the crack propagates towards the compressive zone of the beam rapidly and the beam fails in a brittle manner, being separated in two parts. In the case of the SHFRCC the beam behaves in a ductile manner. After the first crack is formed, it does not propagate towards the compressive zone, rather the fibers begin to work at the crack location, transferring stresses and through bond increases load capacity. After that multiple cracking is observed in the tensile region of the beam expanding on both sides under the applied load. After a maximum load is reached, no more cracks open and deformation concentrates at one single location expanding towards the compression zone of the beam with a slow descending branch. The zone where tensile cracks open is greater in the case of the longer PVA fibers (F2 and F4), having a width almost equal to the depth of the beam as shown in Fig. 5.12. Multiple cracking is also observed at the location of the neutral axis depth at the end of the tests.

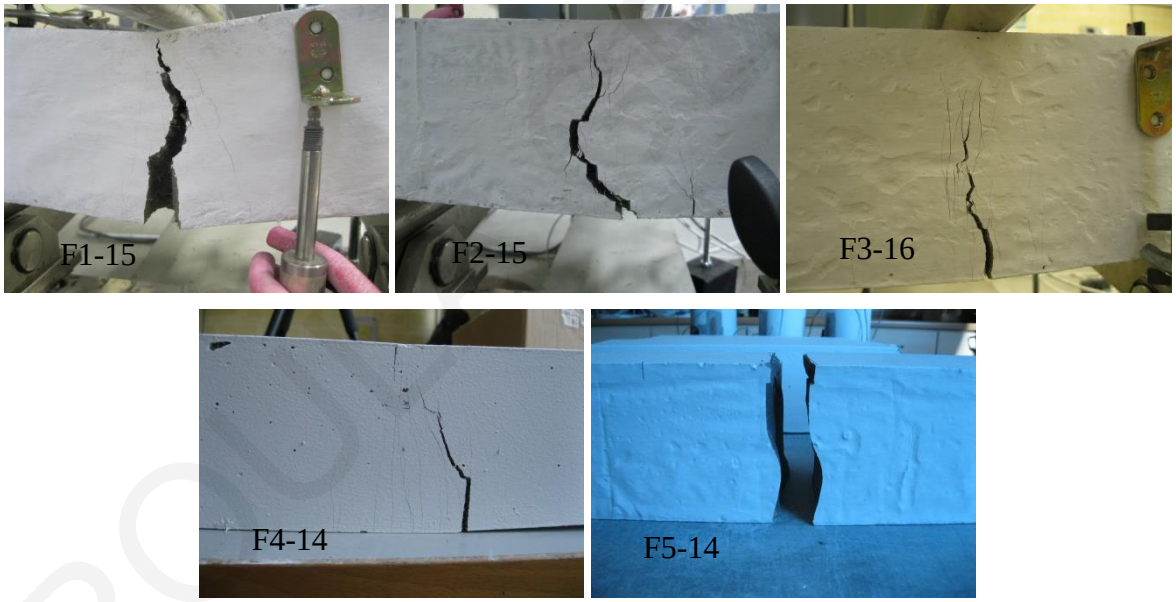

Figure 5.12: Failure cracks from three point bending tests from various mixes

The Load-Deflection diagram of the mix without fibers gives a maximum load in the order of 8 kN, while values of load and strain after the peak load were not able to be recorded by the LVDTs due to the rapid failure. The SHFRCC's Load-Deflection diagrams obtained from three point bending tests (Fig. 5.13) show a different type of behavior between different mixes. In the case of three point bending the mixes without coating (F1 and F2) have similar behavior, while mixes with coating (F3 and F4) are variating with F3 giving the lowest and F4 the highest load capacity from all mixes. Additionally the mixes with coated fibers have a steeper descending branch. Strength is greater in the case where the longer fibers have been used (F2 and F4, 12 mm). Characteristics of the composite are reflected on each test and the prevailing failure mode. In some cases a horizontal

branch appears after the peak load associated with the ability of the fibers to sustain load capacity while deformation is concentrated at the central crack, which propagates towards the compressive zone, while in the extreme layer under tension the beam has completely separated either due to rupture or complete pull-out of the fibers.

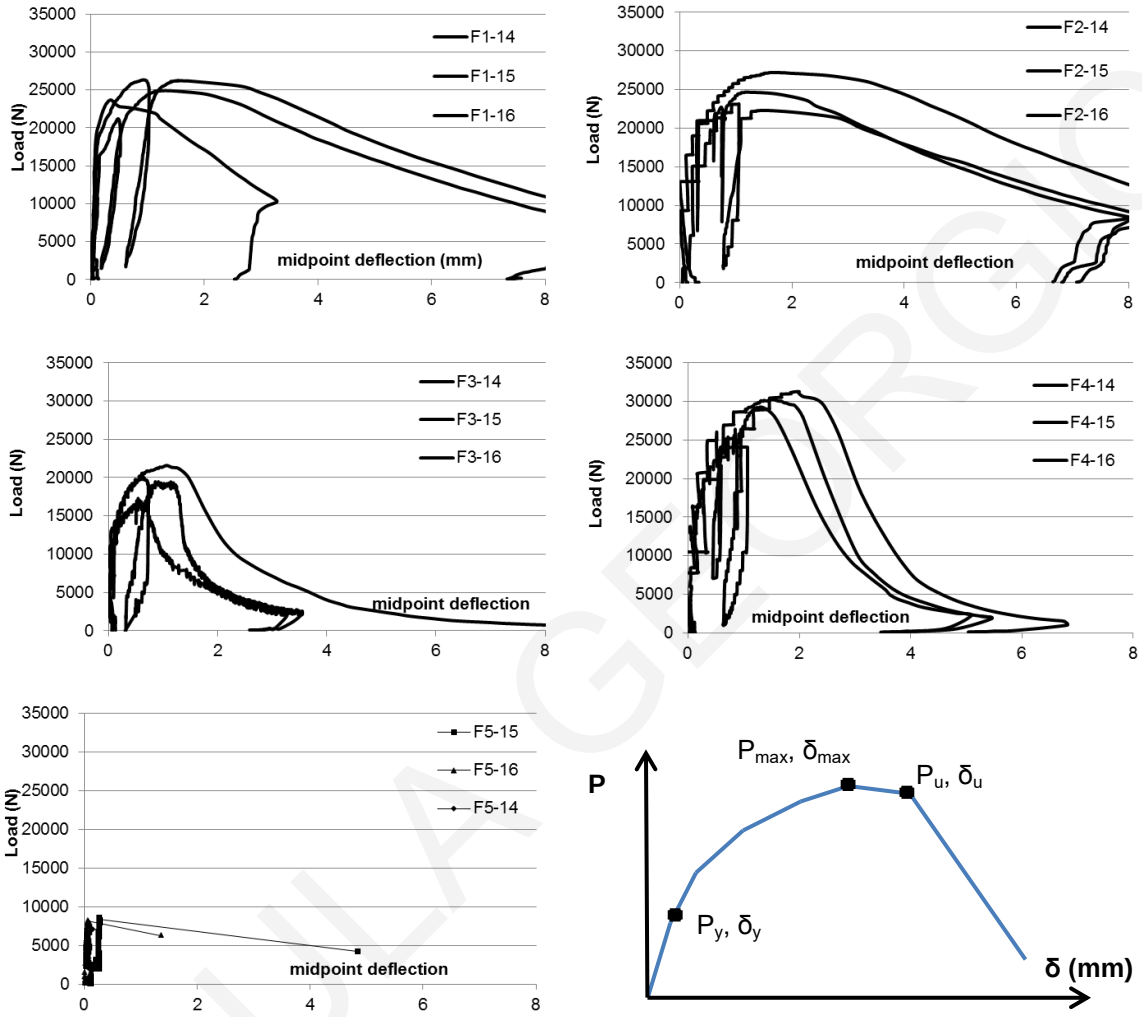

Figure 5.13: Total Load-Midspan deflection of 3PB tests and determination of characteristic points

Table 5.3: Characteristic points (yield, maximum and ultimate) from three point bending tests

	F1-3PB	**F2-3PB**	**F3-3PB**	**F4-3PB**	**F5-3PB**
M_y (Nmm)	1.0E+06	9.3E+05	7.4E+05	1.2E+06	0.81 E+06
M_{max} (Nmm)	2.5E+06	2.5E+06	2.0E+06	3.0E+06	
M_u (Nmm)	2.4E+06	2.3E+06	1.8E+06	3.0E+06	
δ_y (mm)	0.069	0.155	0.099	0.078	0.139
δ_{max} (mm)	0.88	1.35	0.75	1.44	
δ_u (mm)	1.88	2.96	1.07	1.89	

Values of peak flexural moments are calculated from the applied total loads (P) according to: $M_{3pb}=P \cdot a_i/2$, where $a_i=200$ *mm*. Midspan moments at the point of yielding (M_y), at peak load (M_{max}), and ultimate moments (M_u) associated with the initiation of softening in the load-displacement curve are listed in Table 5.3 for all the cases considered. Values of Moments and

deflections (δ) in Table 5.3 are the average values of three specimens tested each time from each mix design. Deflection values are those of the load application points.

The "yield" moment M_y which corresponds to first cracking is used to determine the flexural cracking strength of the composites as it marks the end of the ascending elastic branch. Flexural stress at the extreme tension fiber at this loading point is estimated from $f_{t,fl}=M_y/(bh^2/6)$. The direct tensile strength of the material, $f_{t,cr}$, may be estimated from this measured flexural tensile strength value again using a properly calibrated multiplier as per the Model Code [49]:

$$f_{t,cr} = A_{fl} \cdot f_{t,fl}, \quad \text{where, } A_{fl} = \frac{a_{fl} \cdot h_b^{0.7}}{1 + a_{fl} \cdot h_b^{0.7}} = 0.6, \qquad a_{fl} = 0.06 \tag{5.7}$$

In Eq. 5.7 h_b is the cross sectional depth of the flexural specimen. The associated cracking strain ($\varepsilon_{t,y}$) is obtained from the ratio of cracking stress $f_{t,cr}$ divided by the elastic modulus (E). Values of Moments and deflections (δ) in Table 5.3 are used to calculate stresses and strains (Table 5.4).

Table 5.4: Stress and strain values of various mixes as per the MC [49] from three point bending tests

	F1-3PB	**F2-3PB**	**F3-3PB**	**F4-3PB**	**F5-3PB**
f_{tfly} **(MPa) (MC)**	6.06	5.61	4.47	6.98	4.84
f_{ct} **(MPa) (MC)**	3.64	3.37	2.68	4.19	2.91
ε_{ty} **(mm) (MC)**	3.0E-04	2.8E-04	2.2E-04	3.5E-04	2.42 E-04

5.3.4 Four Point Bending Test

The failure mode of the composite without fibers (F5) under four point bending test is as brittle as that of normal concrete with an elastic behavior up to the point where the ultimate layer under tension reaches the tensile strength of concrete. In this case of four point bending a constant moment region exists between the load application points free of any shear loads. Due to this fact a wider area of the beam is under the same tensile stresses and failure may occur at any location. For the case of brittle materials this type of test results in lower tensile strength estimation in comparison to the three point bending, at which maximum stresses develop under the location of the load point and does not take into consideration other locations that could have lower strengths. In the case of the SHFRCC the beam behaves in a ductile manner. After the first crack is formed, it does not propagate towards the compressive zone, rather the fibers bridge the crack increasing the load capacity. The zone under constant moment is saturated from multiple cracking in the tensile region, with cracks having the same depth, while other cracks initiate at the beam expanding on both ends of the load point application. After a maximum load is reached, no more cracks open and deformation concentrates at one single location expanding towards the compression zone of the beam with a slow descending branch. The distance between tensile cracks is greater in the cases of the coated PVA fibers (F3 and F4) as seen in Fig. 5.14. Multiple cracking is also observed at the location of the neutral axis depth at the main crack location at the termination of the tests. After ultimate load a rapid drop of strength is observed and failure of the specimen occurs.

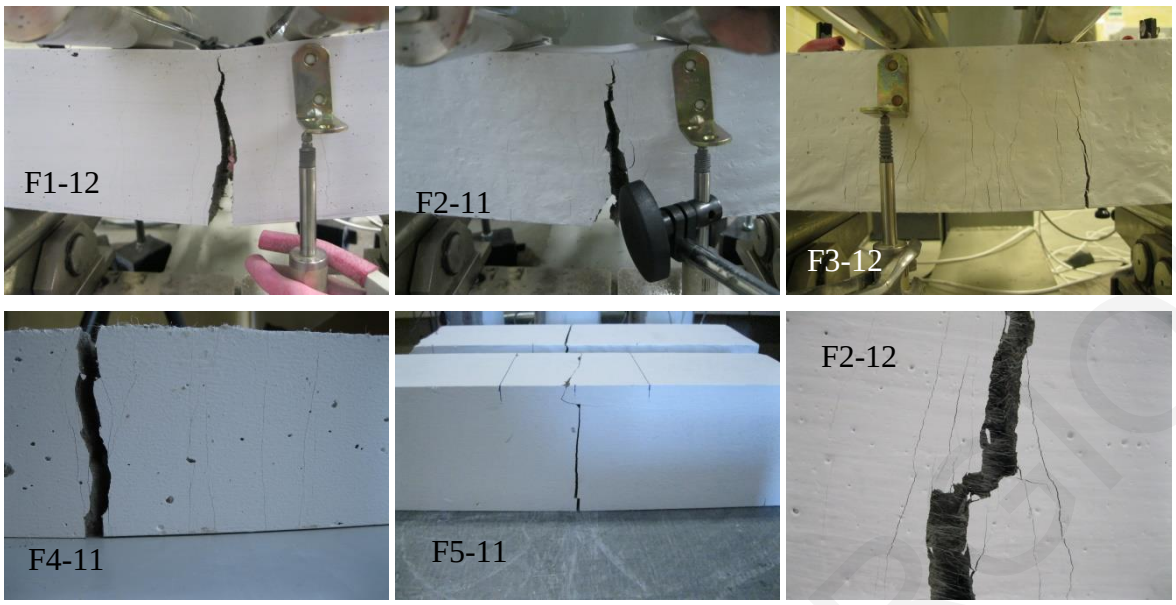

Figure 5.14: Failure cracks from four point bending tests of various mixes

The Load-Deflection diagrams obtained from the four point bending tests (Fig. 5.15) show a different type of behavior between different mixes and in comparison to the three point bending tests. In the case of four point bending the mixes with the longer fibers (F2 and F4) have greater load capacities. Values of peak flexural moments are calculated from the applied total loads (P) according with $M_{4pb}=P \cdot a_{ii}/2$, where $a_{ii}=100$ *mm*. Midspan moments at the point of yielding (M_y), at peak load (M_{max}), and ultimate moments (M_u) associated with the initiation of softening in the load-displacement curve are listed in Table 5.5 for all the cases considered as well as stress and strain values as per Eq. 5.7 of the Model Code [49].

Table 5.5: Characteristic points and stress and strain values of various mixes from four point bending tests

	F1-4PB	**F2-4PB**	**F3-4PB**	**F4-4PB**	**F5-4PB**
M_y *(Nmm)*	5.2E+05	7.8E+05	6.4E+05	7.5E+05	5.6 E+05
M_{max} *(Nmm)*	1.5E+06	1.9E+06	1.6E+06	1.9E+06	
M_u *(Nmm)*	1.5E+06	1.8E+06	1.4E+06	1.8E+06	
δ_y *(mm)*	0.025	0.140	0.115	0.108	0.171
δ_{max} *(mm)*	0.51	1.10	1.04	1.16	
δ_u *(mm)*	1.42	2.69	1.65	1.32	
f_{tfly} *(MPa) (MC)*	3.10	4.67	3.82	4.50	3.35
f_{ct} *(MPa) (MC)*	1.86	2.80	2.29	2.70	2.01
ε_{ty} *(mm) (MC)*	1.6E-04	2.3E-04	1.9E-04	2.3E-04	1.7 E-04

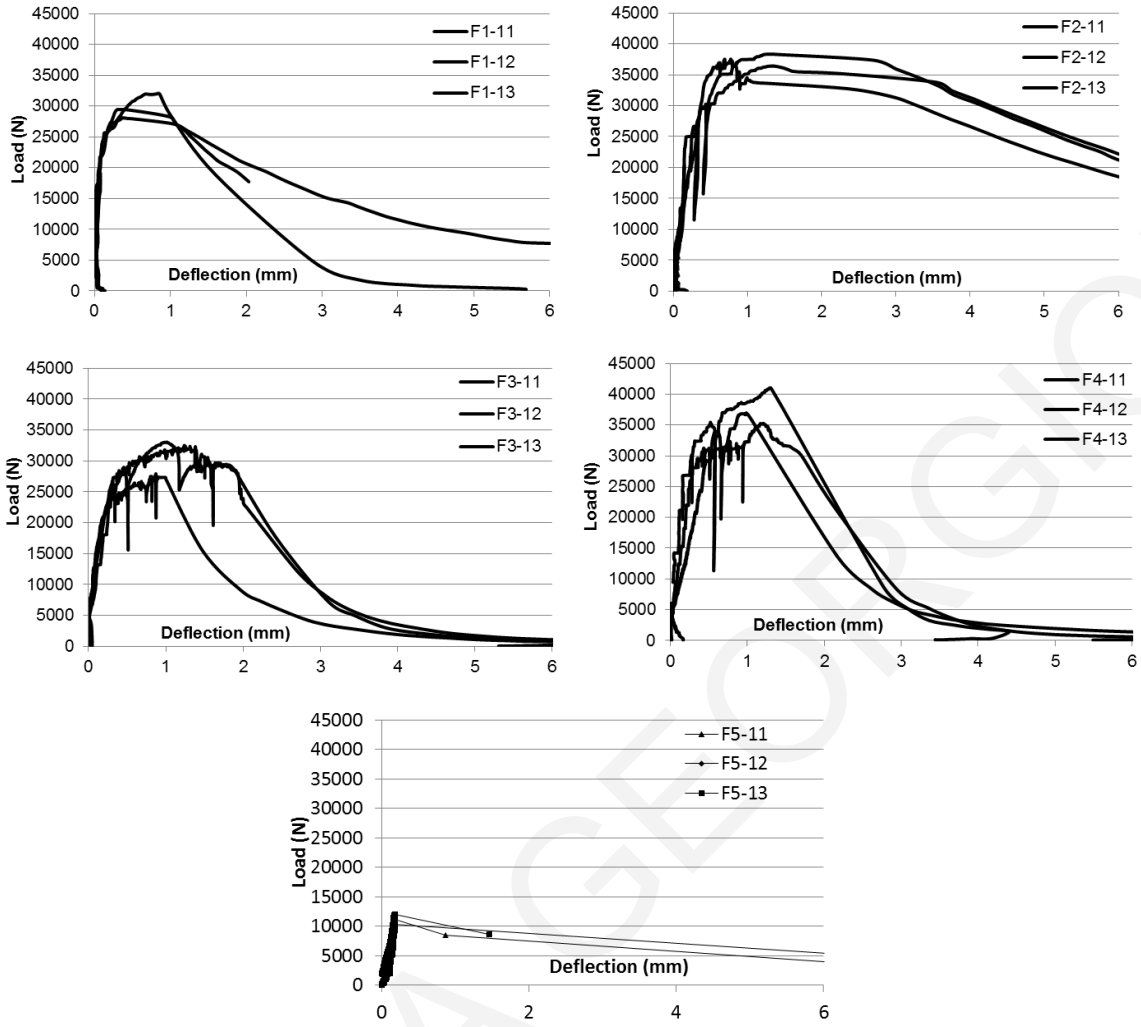

Figure 5.15: 4PB tests Total Load-load point deflection diagrams

5.4 Influence of the shear span ration on the M-φ curves used for inverse analysis

Another parameter of the experimental study was the shear span to depth ratio, known as aspect ratio, and its effect on the load capacity of the SHFRCC beams tested under four point bending. A series of beams of SHFRCC with various shear ratios ranging from 0.4 up to 3.5 were tested under four-point bending (4PB). These experiments were intended to quantify the influence of the fiber contribution to the web shear strength capacity as well as the influence of the shear span ratio on the failure mechanism of the beams. Finally mechanistic models are established, obtained from first principles, in order to interpret the structural response of the specimens (strength and mode of failure), and are used to derive simple expressions by which to estimate the failure load of the beams. Parameter of study for the SHFRCC beams was the shear span aspect ratio which was assigned the following values: a/*h* = 0.4, 0.6, 1, 1.5, 2, 3 and 3.5. In the case of the fiber reinforced composite, due to the strain hardening properties of the material in tension, multiple cracking and increase of the load bearing capacity was observed. In this case the influence of the shear span ratio on the failure mode of the beams was investigated. Three identical specimens were tested for each parameter combination.

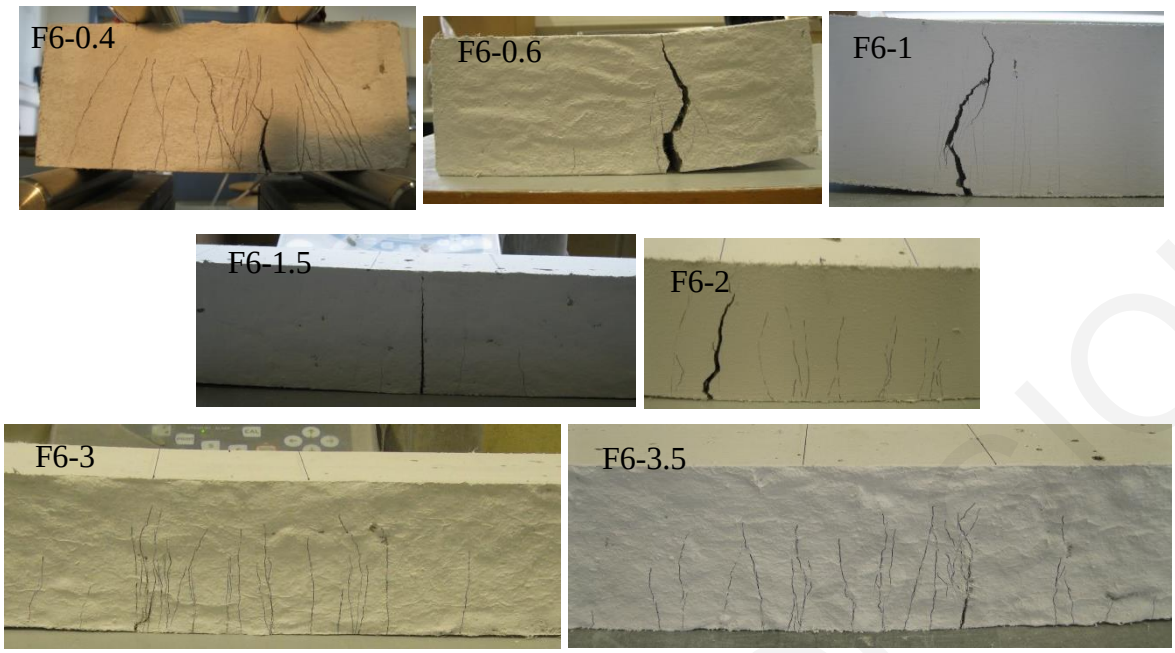

Figure 5.16: Crack pattern on beams of various a/h ratios under four-point bending

Figure 5.16 presents the crack patterns (multiple cracking and failure cracks) for the beams of various span ratios made from mix F6. In all cases with SHFRCC multiple cracking was first developed not only in the constant moment region but also within the shear span lengths propagating towards the supports with increasing load. After the initiation of multiple cracking, stiffness of the beams was reduced while the beams' capacity was increasing (strain hardening). Cracks spread to a range beyond the constant moment region up until the apparent "tension stiffening" phenomenon [94] was checked by the onset of crack stabilization. According to MacGregor [97], the occurrence of crack stabilization marks the end of new crack formation followed by localization of cracking (i.e. widening of existing cracks) and tension softening. In the following discussion, the failure modes of all tested beams are depicted and categorized according with their shear span ratio. A discrete difference between the modes of failure of the shorter span beams was evident in the pattern of crack formation. The mode of failure was mixed shear-flexure for specimens having a span ratio of equal to or less than 1 becoming more predominantly shear dependent as the aspect ratio became smaller. All tested beams with shear spans greater than 1 did not develop diagonal cracking; rather all cracks that were formed, even if they occurred outside the constant moment region, were flexural cracks. The final failure of the beams with shear spans greater than 1 was marked by concentration of deformation at a single crack location which formed within the constant moment region. It is evident that the failure mechanism of the deeper beams with a/h$\leq$*1*, is marked by the formation of struts and ties that enhance shear resistance. Struts that formed between the diagonal cracks supported the compressive forces, while the tension zone developed the tensile resistance of the cementitious material up to very large strains. Flexure-shear cracks were seen in the cases with a/h$\leq$*1*, those being the locations of eventual failure of the beams, whereas in the case of the lowest a/h=*0.4*, the diagonal cracks were very steep and this type of failure was not possible.

In the specific case of a/h=*1* failure mostly occurred exactly under one of the two points of load application and it was marked by shear cracks outside the constant moment region which, at advanced stages, became connected with the flexural cracks. The flexural cracks in the tensile zone of the beam penetrated to greater depths forcing the diagonal strut to follow a curved path at higher a/h ratios. In all other cases with a/h>*1* the cracks were mostly flexural and failure occurred within the constant moment region. The Load – LPD (load-point deflection) diagrams for each shear span ratio are shown in Figure 5.17.

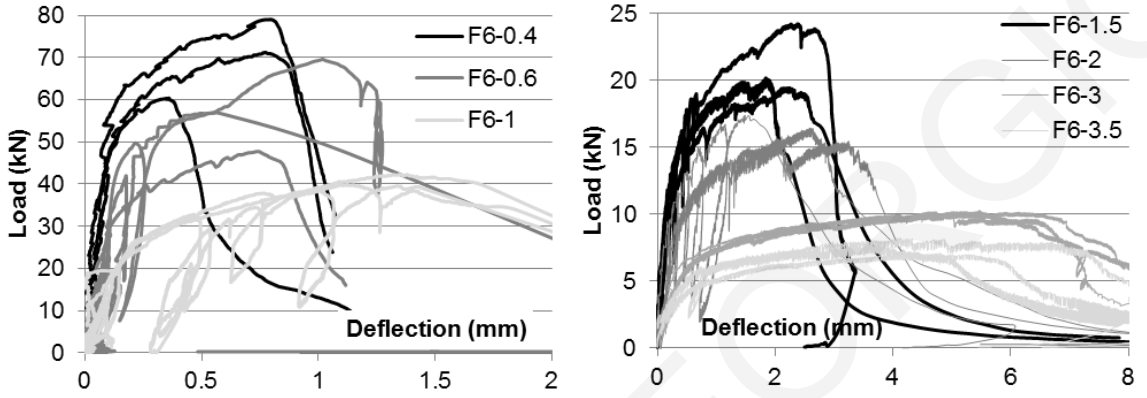

Figure 5.17: Load-Deflection diagrams of beams for the aspect ratios tested (a/h=0.4, 0.6, 1, 1.5, 2, 3, 3.5)

Important milestones from these diagrams are, the strength attained (in terms of moment/shear) and the associated chord rotation at the points of apparent yielding and crack stabilization, marked by subscripts $_y$ and $_{max}$ respectively, in Table 5.6, for all shear span ratios. Note that chord rotation θ is estimated from the average deflection at the intermediate load-points divided by the shear span (Fig. 5.18).

Table 5.6: Yield and crack stabilization points (max) in relation to shear span ratio a/d.

	a/d	δ_y	θ_y	P_y (N)	V_y (N)	M_y (kNm)	δ_{max}	θ_{max}	P_{max} (N)	V_{max}	M_{max} (kNm)
F6-0.4	**0.4**	0.06	0.0015	27500	13750	0.55	0.78	0.0196	75145	37572	1.50
F6-0.6	**0.6**	0.09	0.0015	24000	12000	0.72	0.87	0.0145	58433	29216	1.75
F6-1	**1**	0.068	0.0007	13500	6750	0.68	1.28	0.0128	40582	20290	2.03
F6-1.5	**1.5**	0.09	0.0006	7253	3626.5	0.54	2.16	0.0144	21262	10631	1.59
F6-2	**2**	0.176	0.0009	4750	2375	0.48	2.44	0.0122	16426	8213	1.64
F6-3	**3**	0.162	0.0005	3500	1750	0.53	5.20	0.0173	10153	5076	1.52
F6-3.5	**3.5**	0.17	0.0005	2471	1235.5	0.43	4.12	0.0118	7663	3831	1.34

In Table 5.6 P is the total applied load, V is the shear force within each shear span equal to $P/2$ and M is the maximum moment in the constant moment region calculated by the product $V \cdot$a. Based on the values of Moment Capacity obtained from the beams without any steel reinforcement, as summarized in Table 5.6, an interaction between the Shear and Moment strengths is evident. Even though the critical cross section of all tested beams is the same in all cases, both yield Moment and maximum Moment values seem to increase with decreasing a*/h* ratio and with increasing Shear demand. This is a first indication that the inverse analysis which is proposed by

many researchers and the JCI Standard [53] for the extraction of the tensile properties of SHFRCC, cannot result in objective values. Rather, stress-strain values thus calculated should be considered to depend upon the a/*h* ratio of the four-point bending test. This is worth noting, when considering that the starting point of the inverse analysis is the load-displacement response curve of the four-point beam test.

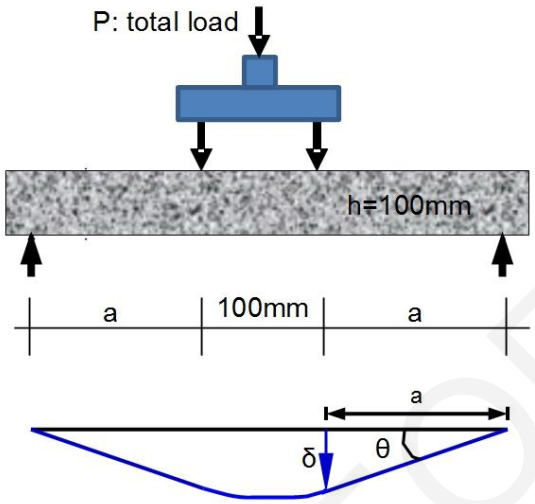

Figure 5.18: Four-point bending test setup and definition of specimen rotation θ in the shear span (reference to rotation capacity).

Figure 5.19 (a) plots the Load – LPD (load-point deflection) diagrams for each shear span ratio. The beams attain higher strength with a reduction in the shear span ratio, and commensurate reduction of midspan deflection. The plastic deflections increase with an increase in the shear span aspect ratio. In the cases where beams fail by flexural yielding, the Moment attained in the constant moment region is obtained from the product of the sustained shear (*V*) by the span length (a). In Figure 5.19 (b) this moment is plotted against the shear span length. The flexural capacity of the beams in the constant moment region appears to be nearly constant for the beams with a/h>*1*, in the order of 1.5kNm. But beams with a/h≤*1* reached higher flexural strengths than the slender beams' theoretical value based on cross sectional properties. If these results are correlated with the crack patterns recorded, it is concluded that the beams with a/h≤*1* failed in a combined flexure/shear manner. The increase in sustained flexural moment in the specimens with a/h≤*1* as compared with the more slender specimens may be attributed to the fact that the disturbed regions (i.e. the regions where steep shear stress gradients occur) influenced profoundly the shorter beams whereby the load was carried directly to the supports through the arching mechanisms without much flexural action.

The values corresponding to the yield and maximum shear load for beams of shear spans 1, 2 and 3.5 are plotted against the corresponding chord rotation ($\theta=\delta/a$) in Figure 5.20 (a). Deflection records were obtained during the tests at the support and loading points. Reported values of deflection represent the average of the displacements of the two loading points after correcting for any support displacement. The yield rotation is associated with first cracking of the constant moment region which occurred due to exceedance of the tensile strength of the material in the

tensile zone. Deformation was quantified by the amount of rotation at the supports and this was estimated by the displacement under the loading point divided by the shear span length, referred to as a drift ratio or chord rotation θ (Fig. 5.18). Thus, it was seen that beyond a drift ratio of 1.3% (corresponding to a significant rotational ductility) for the shortest beams with shear span ratio = 1 and 1.8% for the longest beams with shear span ratio = 3 (recorded in Table 5.6), deformation localized at a single crack (the crack was located within the constant moment region or under the load points) and a plateau was observed where the load capacity was kept constant while the critical crack extended through the height of the tension zone of the beam towards the compression zone [123]. Once the compression zone exceeded the crushing strain limit, post-peak softening of the beam begun, with overall strength deterioration and reduction of sustained load. Values for the chord rotation at peak load in the order of 1.3% corresponded to a rotational ductility μ_θ of nearly 18 (rotation at apparent yielding was 0.07%).

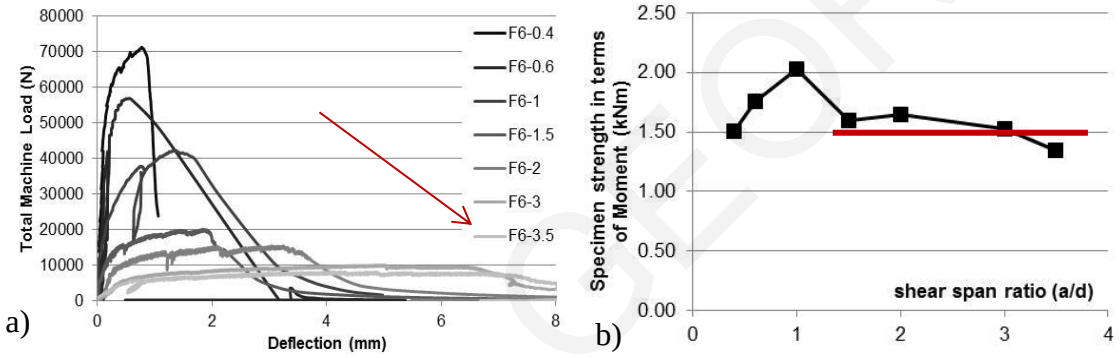

Figure 5.19: (a) Total machine load to LPD diagrams for all a/d ratios, (b) specimen strength in terms of Moment to shear span ratios

In Figure 5.20 (b) the peak values of the average shear stress normalized with respect to the mean value of tensile strength of the material are plotted against the aspect ratio (a/*h*) of the respective specimen. The tensile strength of the material, f_{tmax} was defined at 3MPa from direct tension tests of dog-bone specimens (F6-Chapter 4), as the maximum stress prior to crack localization. In the plot, the average shear stress, τ, of the beams was obtained by dividing the shear force (either yield or maximum) with the cross sectional area of the beam web and was plotted here after being normalized with respect to the material's tensile strength, f_{tmax}. Note that the average ultimate shear strength of concrete is about 50% the measured tensile stress, whereas at apparent yielding this value is 30% of f_{tmax}.

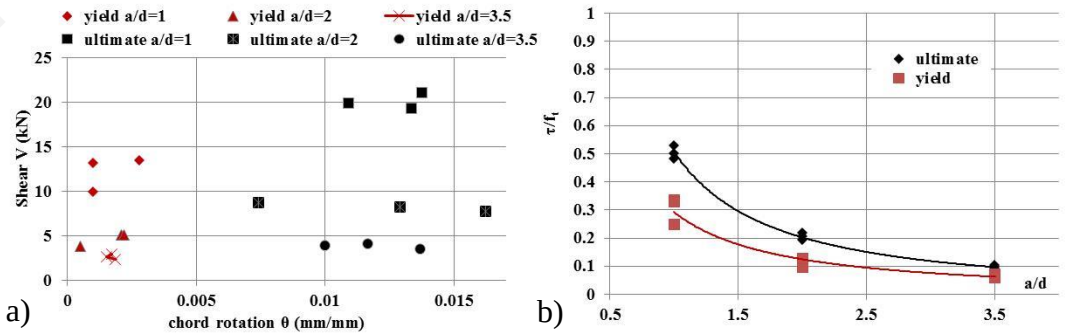

Figure 5.20: (a) Shear- Chord rotation points for yield and ultimate load for various span-lengths; (b) shear stress to tensile strength ratio plotted against aspect ratio of the shear span (a/h)

5.5 Proposal for an inverse analysis

Dog-bone tests specimens often fail outside the measuring range and/or fail due to imperfections and misalignments in unexpected ways. They require special equipment to be performed and even the connection of the mounting equipment to the machine (pin-pin, pin-fixed etc) may result in different stress-strain curves for the same material. If these strain hardening materials are to be incorporated in modern codes it is essential that an easy and reliable method should be provided in order to obtain their stress-strain behavior under uniaxial tension. The tests conducted should be easier to perform, so that they would not require special equipment and specialized personnel. For this reason a large part of the FRC-related literature has been dedicated to developing tests and methods by which to measure the tensile stress-strain properties indirectly and then to use reverse engineering to obtain the actual material properties. In this paragraph the use of an inverse analysis of a simple three or four point bending test is investigated, since most laboratories have the capability of performing such experiments. The tensile stress-strain curve may be then derived from the flexural test results using closed form expressions as those presented here. The results from the inverse analysis of beams under three point bending with a shear span ratio of 2 and four point bending of beams of various shear span ratios are deducted and are then compared to the stress-strain curves obtained from the uniaxial tensile tests.

Stress-strain curve of a fiber reinforced composite in direct tension may be estimated through inverse analysis of a three or four point bending test. A procedure that takes into consideration a crack penetration depth which corresponds to the formation of a plateau in the Load-Deflection diagram is developed here; it is postulated that the onset of a plateau marks the end of strength increase of the composite and it is associated with the attainment of the ultimate tensile strain capacity of the composite in the extreme tensile layer (as shown in Fig. 5.21). The end of the plateau corresponds to the onset of postpeak softening, initiated by failure of the extreme layer under compression or rupture of the fibers in the extreme layer under tension.

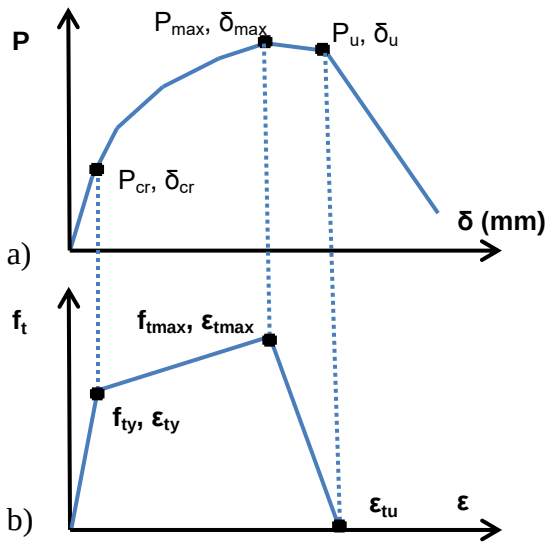

Figure 5.21: (a) Load-Deflection curves of bending test and critical points and (b) relation of the critical points to the tensile stress strain law points

To simplify calculations caused by the material's nonlinearity in the compression zone *x*, the rectangular stress block approach is used (Eqns. 5.8 and 5.9) in establishing equilibrium of sectional forces [70]. (Note that the expressions are used referring to the maximum compression strain at the extreme compression layer, ε_c^{max}, in lieu of parameter ε_c developed thoroughly in Chapter 6).

$$\text{for } \varepsilon_c^{max} < \varepsilon_{co} \qquad \alpha = \bar{\varepsilon}_c^{max}\left(1-(\bar{\varepsilon}_c^{max}/3)\right), \quad a = x\cdot\left(2-0.75\bar{\varepsilon}_c^{\max}\right)/\left(3-\bar{\varepsilon}_c^{\max}\right) \tag{5.8}$$

$$\varepsilon_{co} < \varepsilon_c^{max} < \varepsilon_{cu} \qquad \alpha = 1-\frac{1}{3}\left(\bar{\varepsilon}_c^{\max}\right)^{-1} + j\cdot\left(1-0.5\left(\bar{\varepsilon}_c^{\max}\right)^{-1}-0.5\bar{\varepsilon}_c^{\max}\right)\cdot\left(\bar{\varepsilon}_{cu}-1\right)^{-1} \tag{5.9a}$$

$$\mathrm{a} = x\cdot\frac{1-\frac{1}{6}\left(\bar{\varepsilon}_c^{max}\right)^{-2}+j\cdot\left(1-\frac{1}{3}\left(\bar{\varepsilon}_c^{max}\right)^{-2}-\frac{2}{3}\bar{\varepsilon}_c^{max}\right)\left(\bar{\varepsilon}_{cu}-1\right)^{-1}}{2-\frac{2}{3}\left(\bar{\varepsilon}_c^{max}\right)^{-1}+j\cdot\left(2-\left(\bar{\varepsilon}_c^{max}\right)^{-1}-\bar{\varepsilon}_c^{max}\right)\left(\bar{\varepsilon}_{cu}-1\right)^{-1}} \tag{5.9b}$$

The two characteristic points referred to as P_{max} and P_u identify the peak of the load-displacement envelope and the point after which deformation localizes in a single crack. Based on experimental observation, it is noted that after the peak point, localized cracks begin to widen and extend pushing upwards the neutral axis, penetrating through the depth of the tension zone, while fibers in the extreme tension layers begin to rupture. Note that where fibers have already begun to rupture, discontinuity in the tension zone penetrates inwards through part of the tension-zone's depth; let λ denote the depth of penetration of the discontinuity created through fiber rupture, measured from the tension face of the specimen (Fig. 5.22).

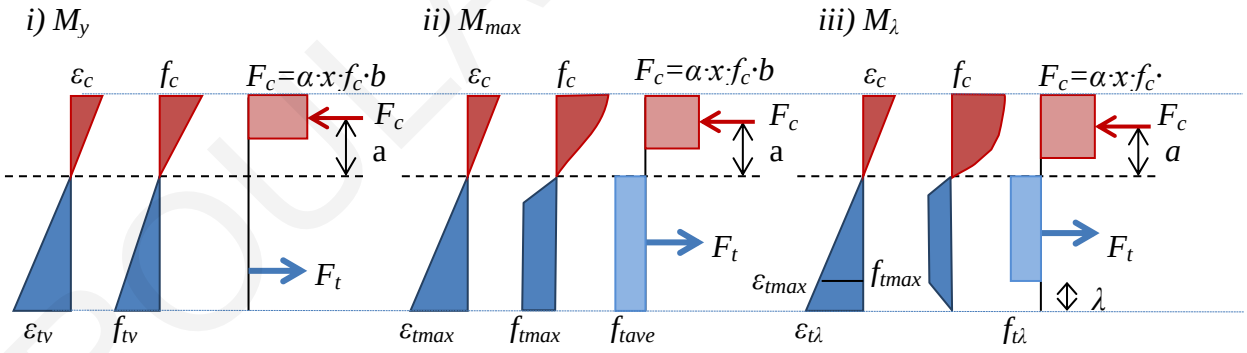

Figure 5.22: Cross sectional strain profiles, stress blocks and internal forces i) at first cracking load P_y, ii) at maximum load P_{max}, iii) at ultimate load prior to softening behaviour P_u (note the depth of rupture penetration on the extreme tension side, λ)

Beyond the ultimate point (P_u) the depth of penetration compromises the flexural strength of the element and the residual strength is gradually reduced. P_y, P_{max} and P_u are values of externally applied, vertical Loads. The M_y, M_{max} and M_λ noted in Fig. 5.22 are the midspan Flexural Moments associated with these applied loads. The Moments M_y, M_{max} and M_λ used for the strain profiles of the critical cross-section at those characteristic points of the behavior correlate to the load-deflection curves characteristic points, that are taken from the experiments.

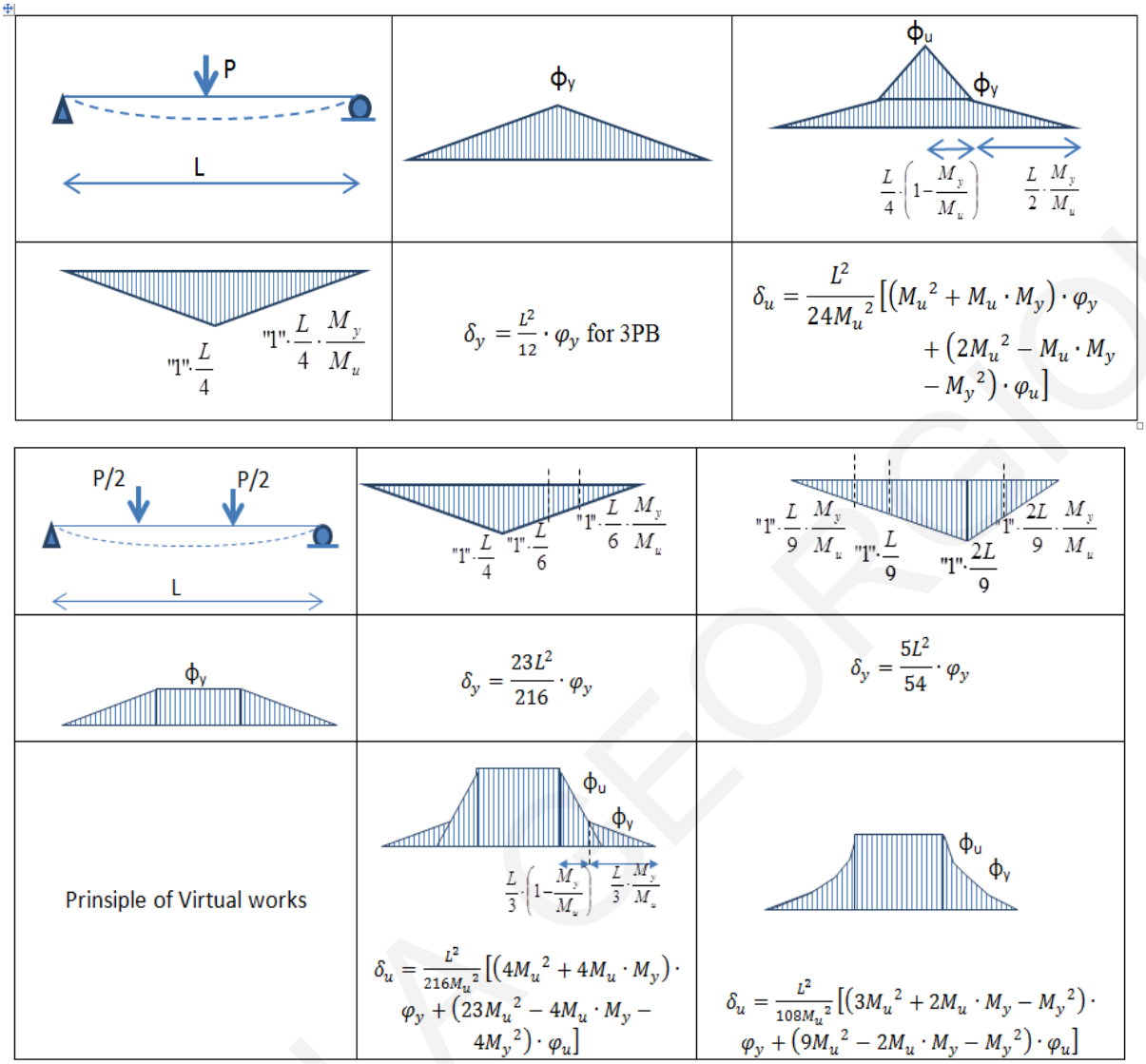

Figure 5.23: Use of principle of virtual works for the derivation of curvatures

The milestone values of the corresponding sectional curvature (φ_y, φ_{max} and φ_u) which are needed for the inverse analysis are obtained from the displacement-curvature relationship for 3-point and 4-point bending tests, which may be established through the principle of virtual work (see Fig. 5.23). Additional equations are established from equilibrium requirements of the central cross-section where the flexural moment is known given the externally applied load.

Figure 5.22 gives the stress and strain diagrams and the resulting internal forces and moments for the three characteristic points considered in the inverse analysis, namely yielding (at the point where a sharp stiffness change occurs in the trilinear envelope of the load-displacement curve), the point at maximum load, and the point at the beginning of the softening branch of the load displacement diagram; the envelope curve may be obtained from either three or four point loading. To simplify calculations the stress block in the tensile zone is substituted by a rectangular block having intensity equal to the average tensile strength (f_t^{ave}). The equations of equilibrium for each case are as follows:

Case (i) at first cracking load P_y

$$M_y = f_{ty} \cdot \frac{(h-x)}{2} \cdot b \cdot \left(\mathrm{a} + (h-x) \cdot \frac{2}{3} \right),\ \Sigma N = 0 \Rightarrow \alpha \cdot f_c \cdot x \cdot b = f_{ty} \cdot \frac{(h-x)}{2} \cdot b \qquad (5.10)$$

Case (ii) at maximum load P_{max}

$$M_{max} = f_t^{ave} \cdot (h-x) \cdot b \cdot \left(\mathrm{a} + \frac{h-x}{2} \right),\ \Sigma \mathrm{N} = 0 \Rightarrow \alpha \cdot f_c \cdot x \cdot b = f_t^{ave} \cdot (h-x) \cdot b \qquad (5.11)$$

Case (iii) at ultimate load prior to softening behavior P_u

$$M_\lambda = f_{t\lambda} \cdot (h-x-\lambda) \cdot b \cdot \left(\mathrm{a} + \frac{h-x-\lambda}{2} \right),\ \Sigma \mathrm{N} = 0 \Rightarrow \alpha \cdot f_c \cdot x \cdot b = f_{t\lambda} \cdot (h-x-\lambda) \cdot b \qquad (5.12)$$

The values of coefficient α and the lever arm, a, are determined from Eq. 5.8 or 5.9 depending on the magnitude of the peak compression strain, ε_c^{max}. Upon substitution in Equations 5.10, 5.11 or 5.12, parametric expressions for moment, curvature φ, and neutral axis depth *x*, (note that $\varepsilon_c^{max} = \varphi \cdot x$) may be derived (Eq. 5.13 to 5.17), so that for given *M* and *φ*, the neutral axis depth, *x*, may be determined. Given *x*, the maximum tension strain capacity, *ε*, and the corresponding average peak tensile strength, *f*, may be estimated from the solution. Additional equations used are: $\varepsilon_{tu} = \varphi \cdot (h-x)$; $h-x-\lambda = \varepsilon_{tu}/\varphi$, $\varepsilon_{tmax} = \varphi_{max} \cdot (h-x)$, $f_t^{max} = \alpha \cdot f_c \cdot x/(h-x-y)$. In Eqns. 5.13 to 5.17 term $\bar{\varepsilon}_c^{max}$ represents the ratio: $\bar{\varepsilon}_c^{max} = \varphi \cdot x / \varepsilon_{co}$.

Case (i) and $\varepsilon_c^{max} < \varepsilon_{co}$ $\rightarrow \mathrm{a} = x \cdot \dfrac{2 - 0.75 \cdot \phi \cdot x / \varepsilon_{co}}{(3 - \phi \cdot x / \varepsilon_{co})} + (h-x) \cdot \dfrac{2}{3}$

$$\rightarrow M_y = \left(\frac{\phi \cdot x}{\varepsilon_{co}} \right) \cdot \left(1 - \frac{\phi \cdot x}{3\varepsilon_{co}} \right) \cdot f_c \cdot x \cdot b \cdot \mathrm{a} \qquad (5.13)$$

Case (ii) and $\varepsilon_c^{max} < \varepsilon_{co}$ $\rightarrow \mathrm{a} = x \cdot \dfrac{2 - 0.75 \cdot \phi \cdot x / \varepsilon_{co}}{(3 - \phi \cdot x / \varepsilon_{co})} + \dfrac{h-x}{2}$

$$\rightarrow M_{max} = \left(\frac{\phi \cdot x}{\varepsilon_{co}} \right) \cdot \left(1 - \frac{\phi \cdot x}{3\varepsilon_{co}} \right) \cdot f_c \cdot x \cdot b \cdot \mathrm{a} \qquad (5.14)$$

Case (ii) and $\varepsilon_{co} < \varepsilon_c^{max} < \varepsilon_{cu}$ $\rightarrow \mathrm{a} = \dfrac{h-x}{2} + x \cdot \dfrac{1 - \frac{1}{6}\left(\frac{\varepsilon_{co}}{\phi \cdot x}\right)^2 + j \cdot \left(1 - \frac{1}{3}\left(\frac{\varepsilon_{co}}{\phi \cdot x}\right)^2 - \frac{2}{3}\frac{\phi \cdot x}{\varepsilon_{co}} \right) \left(\frac{\varepsilon_{cu}}{\varepsilon_{co}} - 1 \right)^{-1}}{2 - \frac{2}{3}\frac{\varepsilon_{co}}{\phi \cdot x} + j \cdot \left(2 - \frac{\varepsilon_{co}}{\phi \cdot x} - \frac{\phi \cdot x}{\varepsilon_{co}} \right) \cdot \left(\frac{\varepsilon_{cu}}{\varepsilon_{co}} - 1 \right)^{-1}}$

$$\rightarrow M_{\max} = f_c \cdot x \cdot b \cdot \mathrm{a} \cdot \left(1 - \frac{\varepsilon_{co}}{3\phi \cdot x} + j \cdot (1 - \frac{\varepsilon_{co}}{2\phi \cdot x} - \frac{\phi \cdot x}{2\varepsilon_{co}}) \left(\frac{\varepsilon_{cu}}{\varepsilon_{co}} - 1 \right)^{-1} \right) \qquad (5.15)$$

Case (iii) for $\varepsilon_c^{max} < \varepsilon_{co}$ $\rightarrow \mathrm{a} = x \cdot \dfrac{2 - 0.75 \cdot \dfrac{\varphi \cdot x}{\varepsilon_{co}}}{\left(3 - \dfrac{\varphi \cdot x}{\varepsilon_{co}} \right)} + \dfrac{\varepsilon_{t\,max}}{2\varphi}$

$$\rightarrow \mathrm{M}_{\lambda} = \frac{\varphi \cdot x}{\varepsilon_{co}} \cdot (1 - \frac{\varphi \cdot x}{3\varepsilon_{co}}) \cdot f_c \cdot x \cdot b \cdot \mathrm{a} \tag{5.16}$$

Case (iii) for $\varepsilon_{co} < \varepsilon_c^{max} < \varepsilon_{cu} \rightarrow$

$$\mathrm{a} = \frac{\varepsilon_{t\max}}{2\phi} + x \cdot \frac{1 - \frac{1}{6}\left(\frac{\varepsilon_{co}}{\phi \cdot x}\right)^2 + j \cdot \left(1 - \frac{1}{3}\left(\frac{\varepsilon_{co}}{\phi \cdot x}\right)^2 - \frac{2}{3}\frac{\phi \cdot x}{\varepsilon_{co}}\right)\left(\frac{\varepsilon_{cu}}{\varepsilon_{co}} - 1\right)^{-1}}{2 - \frac{2}{3}\frac{\varepsilon_{co}}{\phi \cdot x} + j \cdot \left(2 - \frac{\varepsilon_{co}}{\phi \cdot x} - \frac{\phi \cdot x}{\varepsilon_{co}}\right) \cdot \left(\frac{\varepsilon_{cu}}{\varepsilon_{co}} - 1\right)^{-1}}$$

$$\rightarrow M_{\lambda} = f_c \cdot x \cdot b \cdot \mathrm{a} \cdot \left(1 - \frac{\varepsilon_{co}}{3\phi \cdot x} + j \cdot \left(1 - \frac{\varepsilon_{co}}{2\phi \cdot x} - \frac{\phi \cdot x}{2\varepsilon_{co}}\right) \cdot \left(\frac{\varepsilon_{cu}}{\varepsilon_{co}} - 1\right)^{-1}\right) \tag{5.17}$$

The results obtained when applying the Inverse Analysis as described above to the experimental values, are quoted in Tables 5.7 and 5.8 for all mix designs and both for three and four point bending tests. It is noteworthy that the ultimate tensile stress resulting from the three point bending tests is always greater than the value obtained from the four point bending tests. This is a known characteristic difference between the two types of tests. Similarly, the ultimate tensile strain obtained from inverse analysis is higher in the case of the three-point as compared to the four-point bending tests.

Table 5.7: Results from inverse analysis of three point bending tests

	F8-3PB	F12-3PB	F8C-3PB	F12C-3PB
φ_y	5.2E-06	1.2E-05	7.4E-06	5.8E-06
x	48.88	33.15	34.75	48.02
ε_{ty}	0.00026	0.00078	0.00048	0.00030
f_{ty} (MPa)	5.93	4.20	3.43	6.73
φ_{max} (1/mm)	8.7E-05	1.3E-04	6.9E-05	1.4E-04
φ_u (1/mm)	2.0E-04	3.0E-04	1.0E-04	1.9E-04
x_{max} (mm)	22.36	20.08	21.89	20.28
ε_{tmax} (mm)	0.0068	0.0100	0.0054	0.0113
$f_{tavemax}$ (MPa)	5.98	5.91	4.72	7.20
f_{tu} (MPa)	6.01	6.76	5.37	7.43
x_{λ}	21.40	20.14	20.80	18.38
$\varepsilon_{tu\lambda}$	0.0156	0.0238	0.0083	0.0155
λ	44.48	46.21	27.72	22.01

Table 5.8: Results from inverse analysis of four point bending tests

	F8-4PB	F12-4PB	F8C-4PB	F12C-4PB
φ_y	3.0E-06	1.7E-05	1.4E-05	1.3E-05
x	45.72	25.25	23.56	25.88
ε_{ty}	0.00016	0.00125	0.00105	0.00096
f_{ty} (MPa)	2.86	3.13	2.50	3.04
φ_{max} (1/mm)	7.4E-05	1.6E-04	1.5E-04	1.7E-04
φ_u (1/mm)	2.1E-04	4.0E-04	2.4E-04	1.9E-04
x_{max} (mm)	18.43	15.53	13.80	14.42
ε_{tmax} (mm)	0.0060	0.0134	0.0129	0.0144
$f_{tavemax}$ (MPa)	3.46	4.24	3.47	4.24

f_{tu} *(MPa)*	3.76	4.79	3.96	4.84
x_λ	17.34	16.35	13.40	14.28
$\varepsilon_{tu\lambda}$	0.0171	0.0334	0.0212	0.0165
λ	53.47	50.22	33.84	10.97

For the case of the various shear span ratios the material's parameters are shown in Fig. 5.24. The compressive strength and strain values are used to perform the inverse analysis for the beams with shear span ratios of a/*h* = 0.4, 0.6, 1, 1.5, 2, 3 and 3.5.

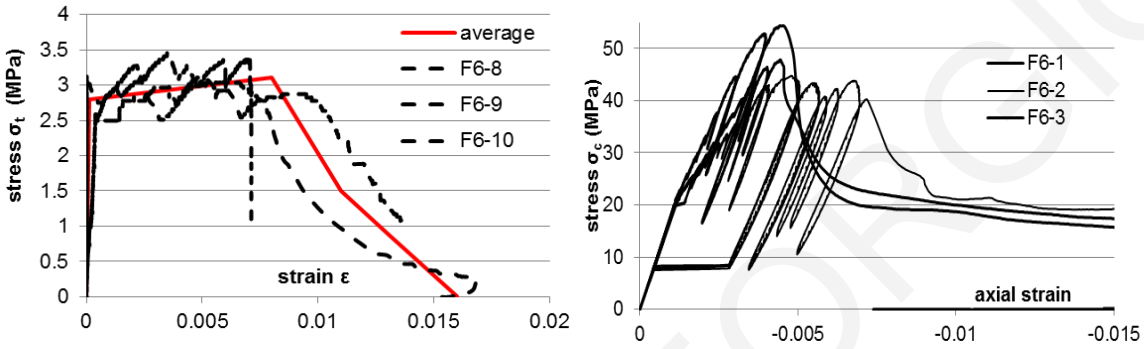

Figure 5.24: Stress-strain curve of mix F6 in tension and compression

The values of stress and strain resulting from the inverse analysis of the beams with varying shear span ratios are shown in Figure 5.25. The figure shows clearly that the estimated values of tensile strength vary with shear span ratio, following the same pattern seen in the flexural strength vs. shear span ratio as shown in Fig. 5.19 (b). The longer beams with shear span ratios ≥ 1 yield approximately equal values of tensile strength in the order of 3.5 MPa, which is close to the values obtained from the direct uniaxial tension tests as shown in Fig. 5.24. The shorter shear span beams give tensile strength values from the inverse analysis of up to 5 MPa that are 60% greater than the uniaxial tensile strength obtain from uniaxial tension tests. For the values of strain capacity obtained from the inverse analysis (shown in Fig. 5.25), the estimated values increase with decreasing shear span ratio, with values of strain in the span ratios ≥ 2 in the order of 1%, which is close to the strain values recorded at maximum load obtained from the uniaxial tensile tests.

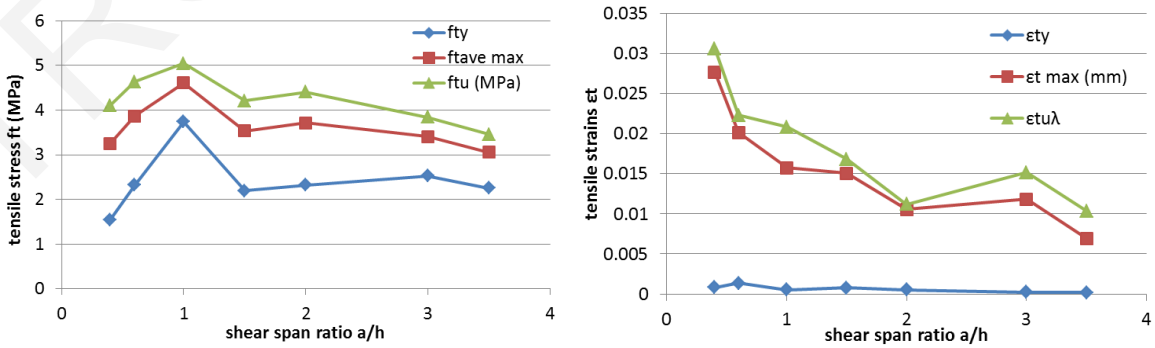

Figure 5.25: Stress and strain values obtained by the inverse analysis of beams with various shear span ratios

5.6 Relation between results obtained from different testing methods for σ-ε curves

Average values of tensile cracking strength, ultimate tensile strength and associated tensile strain capacity (i.e. values prior to crack localization) are given in the form of bar charts in Fig. 5.26. In particular, cracking stresses were obtained from the different testing methods using code-prescribed conversion factors [49]. Generally, first cracking stress values as attained from splitting test and three point bending test are higher for all types of mixes as compared to those obtained from direct tension or four point bending. This is related to the nature of the test since for in the former, ultimate stress occurs at a single cross section, whereas in the latter tests a constant stress state occurs over a finite length, thereby being more susceptible to possible internal flaws that may be found in that length.

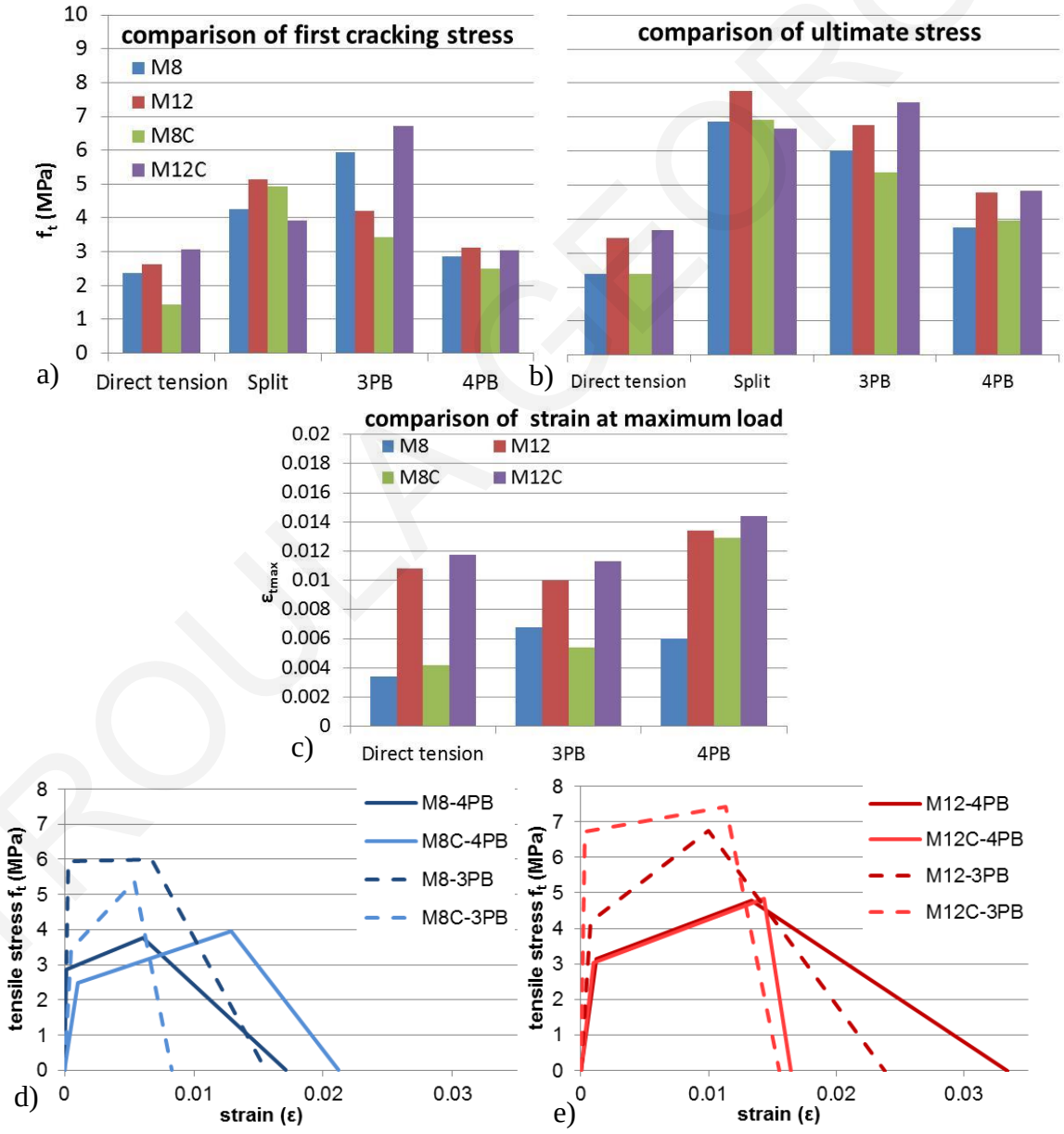

Figure 5.26: (a) first cracking strength obtained from all testing methods, (b) ultimate stress, (c) ultimate strain, (d) and (e) tensile stress-stain diagrams from inverse analysis of 3PB and 4PB tests for all mix designs

The hierarchy of cracking strengths extracted from different test methods also applies in the case of the ultimate values. For example, the strength values obtained (for all mixes) from the direct tensile test are 20% lower than those obtained from inverse analysis of the split tests and as such, they could be considered a lower bound to tensile strength. Strains obtained from the inverse analysis of the four and three point bending tests as shown in Fig. 25 (d) and (e) are similar to the strains obtained from the uniaxial tension tests in the case of the longer 12 mm fibers. For the mixes containing 8 mm long fibers a great scatter is observed between the results of the inverse analysis and the strain measured from the dogbone tests; this was particularly evident in the case of mixes containing coated PVA fibers. The values of the four point bending of beams with shear span ratio in the order of 1 give as shown in the previous section higher strength capacities than same cross-section beams with greater shear span ratios due to the stress load paths developed from the strut and tie action of deeper beams.

Chapter 6: Compression

Strain Hardening fiber reinforced cementitious composites comprise of a mix design that differs from normal concrete mixes in that no coarse aggregates are included. Containing only fine sand, and a large amount of cement replacement with fly ash it is possible to obtain a very flowable self-consolidating mix having a dense microstructure. The addition of synthetic fibers that act as mass reinforcement lead to large deformation capacities; the fibers are mobilized after the occurrence of first cracking, bridging the cracks and transferring stresses through cracked regions, thereby imparting a very resilient behavior for the material in tension. In this Chapter a parametric investigation is conducted: fibers with different physical and mechanical properties (length and surface) are examined. PVA fibers of two different lengths were used, 8 mm and 12 mm, with and without coating. Uniaxial compression displacement control tests were used to measure stress, axial and transversal deformation, modulus of elasticity and Poisson's ratio. The effective reinforcing action of fibers in confinement is quantified by modeling the non-linearity in the lateral expansion (nonlinear dilation phenomena) through calibration of the results with those obtained from an identical fiberless mix design alone or confined with known lateral pressures (stirrups or FRP), so as to estimate an equivalent confining pressure that is owing to the embedded fiber network.

6.1 Effect of fibers on compressive properties

Being heterogeneous, cementitious materials have a propensity for failure due to localization of cracking followed by loss of load carrying capacity in directions orthogonal to the orientation of the cracks. Concrete under uniaxial compression is characterized by axial splitting and fast decay of strength for axial strains that exceed the range of 0.002-0.003; failure is heralded by a significant increase in transverse strains which grow rapidly producing apparent values of the Poisson's ratio that exceed the limit of incompressibility beyond the peak (v=0.5, see [124]). Recently developed self-consolidating SHFRCC with short randomly oriented plastic fibers present the opportunity for innovative resilient materials where the brittleness and localization upon cracking is mitigated by the fibers bridging the cracks.

Results from a series of uniaxial compression tests conducted on cylinders of cementitious composites, with variables of study being the fibers (fiber length and coating) and the matrix confinement (with steel stirrups and FRPs) are presented in this Chapter. The main purpose is to document and quantify the confining effect presented by the fibers through comparisons with the response of plain concrete under measurable lateral confinement, whereby an effective passive confining stress imparted by the embedded fibers may be identified and documented. Thus a triaxial state of stress is found to develop in fiber reinforced concrete, where the internal stresses supported by

the fibers may be related to classical constitutive models for plain concrete with FRP jackets or steel stirrups.

6.2 State of the art on compressive properties of FRC

Fibers contribute to the behavior of the cementitious matrix by restraining the crack propagation as shown in previous studies [125], thereby increasing ductility of concrete. Shah and Rangan [126] have studied the variation between using fibers in comparison with the more conventional methods like using stirrups. The specimens were reinforced with 0.5% volume of steel, comprising either randomly distributed fibers or closed stirrups, with different spacing. The percentage of the stirrups was maintained constant by altering the number of the stirrups at each spacing. The stress-strain curves for these specimens are shown in Fig. 6.1. The Figure indicates that in the elastic branch of the behavior no effect may be identified in the stress-axial strain curve, but steel fibers increased the ductility by shifting the strain at maximum stress to the right of the axis and decreased the slope of the descending branch. Increase in ductility is attributed to the resistance against crack growth in the lateral direction by the fibers. When maximum stress is reached, concrete is known to dilate and finally fail due to internal microcracking. In Fig. 6.1 the strain at maximum stress of the specimens with fibers or stirrups is greater than that of plain concrete. Shifting of the strain at maximum stress shows that dilation is resisted by fibers. Fibers' resistance to lateral dilation is greater than that of the lower spacing of stirrup confinement of 2 and 4 inches.

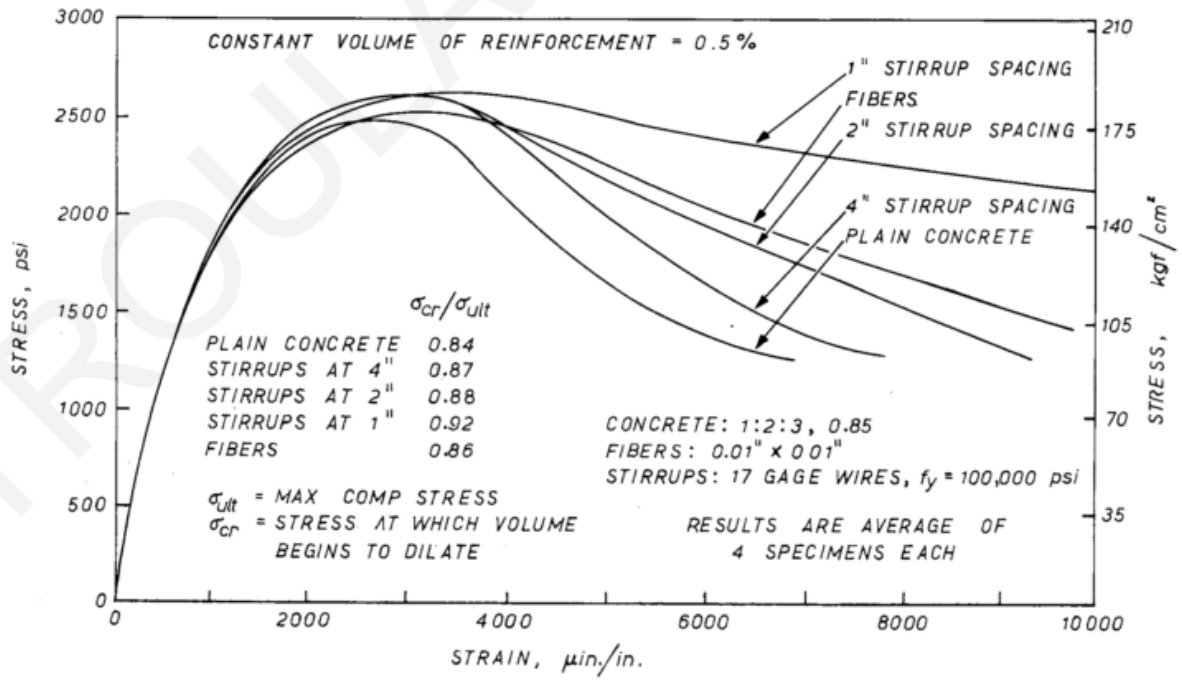

Figure 6.1: Stress-strain curves for concrete reinforced with stirrups and fibers subject to uniaxial compression [125]

6.2.1 Recommendations of JSCE

The Japan Society of Civil Engineers has issued Recommendations [50] for the design of SHFRCC in 2008. One of the most important parameters needed for design is the stress-strain law of the material under compression. The Recommendations propose the curve shown in Fig. 6.2 (a) to be employed for design purposes, followed by a constant residual value. For the initial curved zone the following equation may be applied:

$$\sigma'_c = \frac{0.85 f'_{ck}}{\gamma_c} \cdot \frac{\varepsilon'_c}{\varepsilon'_m} \cdot \left(2 - \frac{\varepsilon'_c}{\varepsilon'_m}\right) \quad (6.1)$$

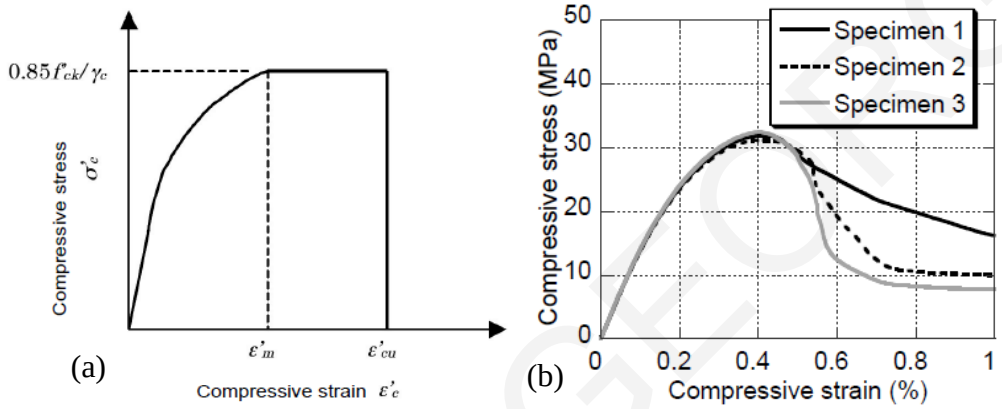

Figure 6.2: (a) Compressive stress-strain relationship and (b) example of SHFRCC σ-ε curves [50]

An example of stress-strain curve under compression of SHFRCC is shown in Fig. 6.2 (b). Strain at maximum load is in the order of 0.4%, much greater than that of normal concrete (0.2%), showing the effect of fiber confinement in compression. The JSCE Recommendations [50] suggest that Young's Modulus may be obtained by the same testing methods used for normal concrete, yielding to values in the order of 1/2 to 2/3 of that of normal concrete. Example of the relation between E and compressive strength is given in Fig. 6.3 (a). Additionally in Fig. 6.3 (b) values of the proposed Poisson's ratio are depicted.

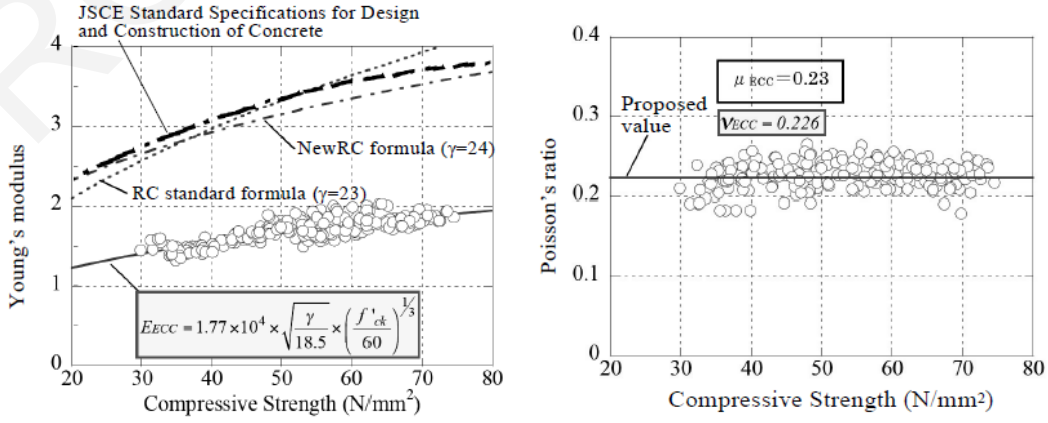

Figure 6.3: (a) Example of determination of Young's Modulus and (b) Example of determination of Poisson's ratio [50]

6.2.2 Recommendations of Model Code

The New Model Code [49] states that "the compressive relations valid for plain concrete apply to FRC as well" and acknowledges the beneficial effect of the fibers that can reduce brittleness of concrete in compression.

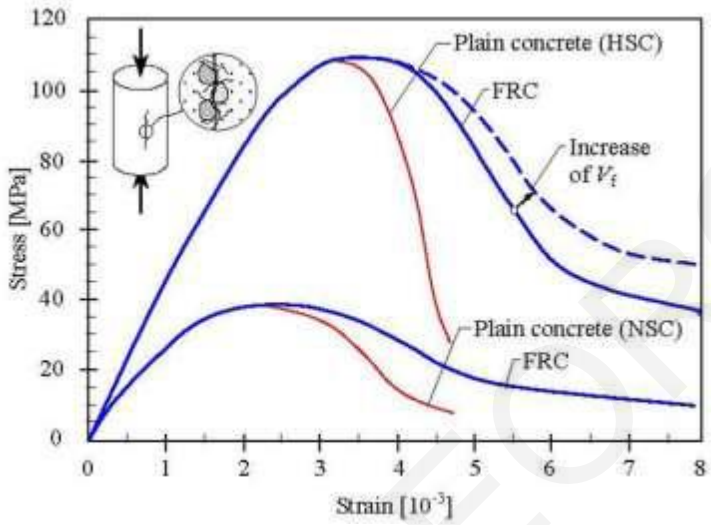

Figure 6.4: Main difference between softening and hardening behavior, from material to structural level [49]

6.3 Mixes with fibers

6.3.1 Testing procedure

Uniaxial compression tests were performed well into the post-peak range under displacement control using a closed-loop, servo hydraulic controlled testing machine at a loading rate of 1.50 μm/s. Specimens were cylinders, 100 mm in diameter by 200 mm in height. Axial deformations were measured using two linear variable differential transducers (LVDTs) mounted on opposite sides of two rings that were attached on the specimen over a gauge length of 140 mm. An additional LVDT measured the deformation over the entire length of the specimen, through the displacement of the platens. Circumferential elongation was measured using a circumferential extensometer (chain), placed at the middle of the height of the coupon. Additionally 3 stain gauges were fixed (2 parallel to the loading direction and 1 perpendicular to the load) for the estimation of the Poisson's ratio as shown in Fig. 6.5.

Two types of measuring devices were used to obtain values for the lateral deformations. One option was a circumferential extensometer and the other was strain gauges. The reason for this is the accuracy of the extensometer that cannot be used for very small values of extension and the other one is the inability of the strain gauges to measure extension after cracking of the specimen. Therefore a combination of the two measuring devices was necessary. Axial deformation was also measured primarily by two strain gauges placed on opposite sides with a length of 60 mm apart from the ring-

LVDT system mentioned above. The LVDT readings were transformed to strain and the tangent modulus of elasticity was determined at a 45% of the peak stress. Finally the stress-strain diagram of each specimen for the full behavior containing the post-peak region was established by the LVDT readings over the full length of the specimens between the platens mentioned earlier. The initial slope of this curve was replaced by a straight line with a slope according to the modulus of elasticity previously calculated. This procedure was necessary since the elongation between the platens is affected by the boundary conditions between the specimen and the platens.

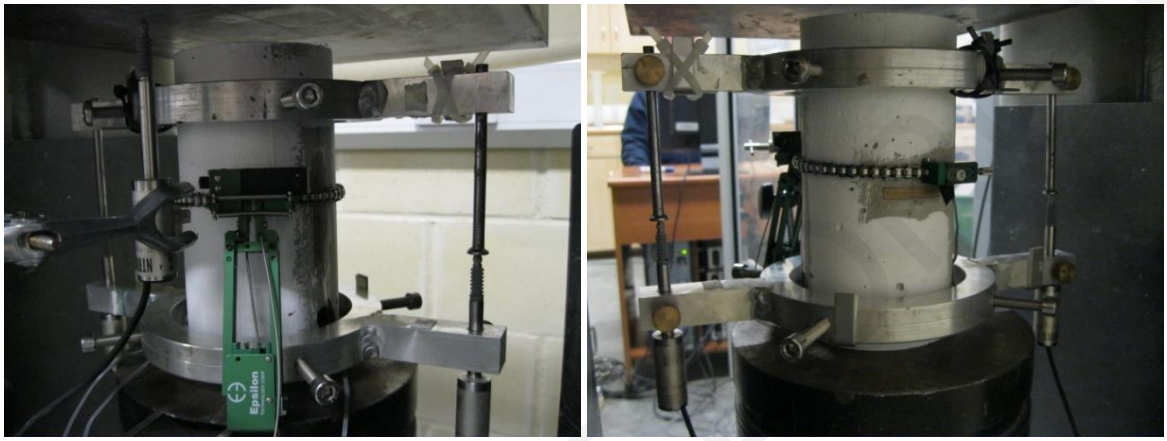

Figure 6.5: Experimental test setup for uniaxial compression and measuring devices

Five mix designs were used for the investigation of the effect of fibers in the compressive behavior of cementitious composites. The first mix was the matrix without any fibers referred to as plain mix PM (F5). The matrix had a special mix design therefore it was necessary to be tested separately. The mix design's special characteristics are the high amount of fly ash as cement replacement, the lack of any coarse aggregates (maximum aggregate is sand <300 μm) and self-consolidation. This matrix is then used for the fiber reinforced composite mix. Four different mixes were prepared with the same amount of fibers (2% by volume) but with different fiber characteristics; F1 had 8 mm PVA fibers without coating, F2 had 12 mm PVA fibers without coating, F3 had 8 mm PVA fibers with coating and F4 had 12 mm PVA fibers with coating.

6.3.2 Experimental results

The crack formations after the uniaxial compression tests of the various mixes are shown in Figure 6.6. A great discrepancy is observed between the results of the unreinforced and the fiber reinforced specimens. Specimens without any fibers cracked and suddenly collapsed. In the absence of fibers deterioration of the specimens and fragmentation into small pieces occurred. Cracks were vertical, parallel to the load and extended far inside the core of the specimen. After sudden collapse the specimens seemed unable to carry any remaining loads. In the case of the fiber reinforced composites multiple cracking is displayed all around the specimens. Cracking was visible close to 70% of the

maximum load, with formation of multiple parallel cracks that increased in number up to the attainment of the peak load. Up till the end of the test no spalling of the specimen was observed. After peak load depletion was slower than in the case of the PM (F5) and the specimens after the test seemed solid enough and able to withhold a remaining load. A major crack was formed in all cases of SHFRCCs at the end of the test that had a steeper slope in the cases of the fibers with coating (in Fig 6.6 specimens F1 and F2 the crack extended from the bottom of the specimen to the side surface while in specimens F3, F4 the crack extended from the bottom face to the upper face of the specimen). Through these major cracks, the fibers seemed stretched, pulled or ruptured.

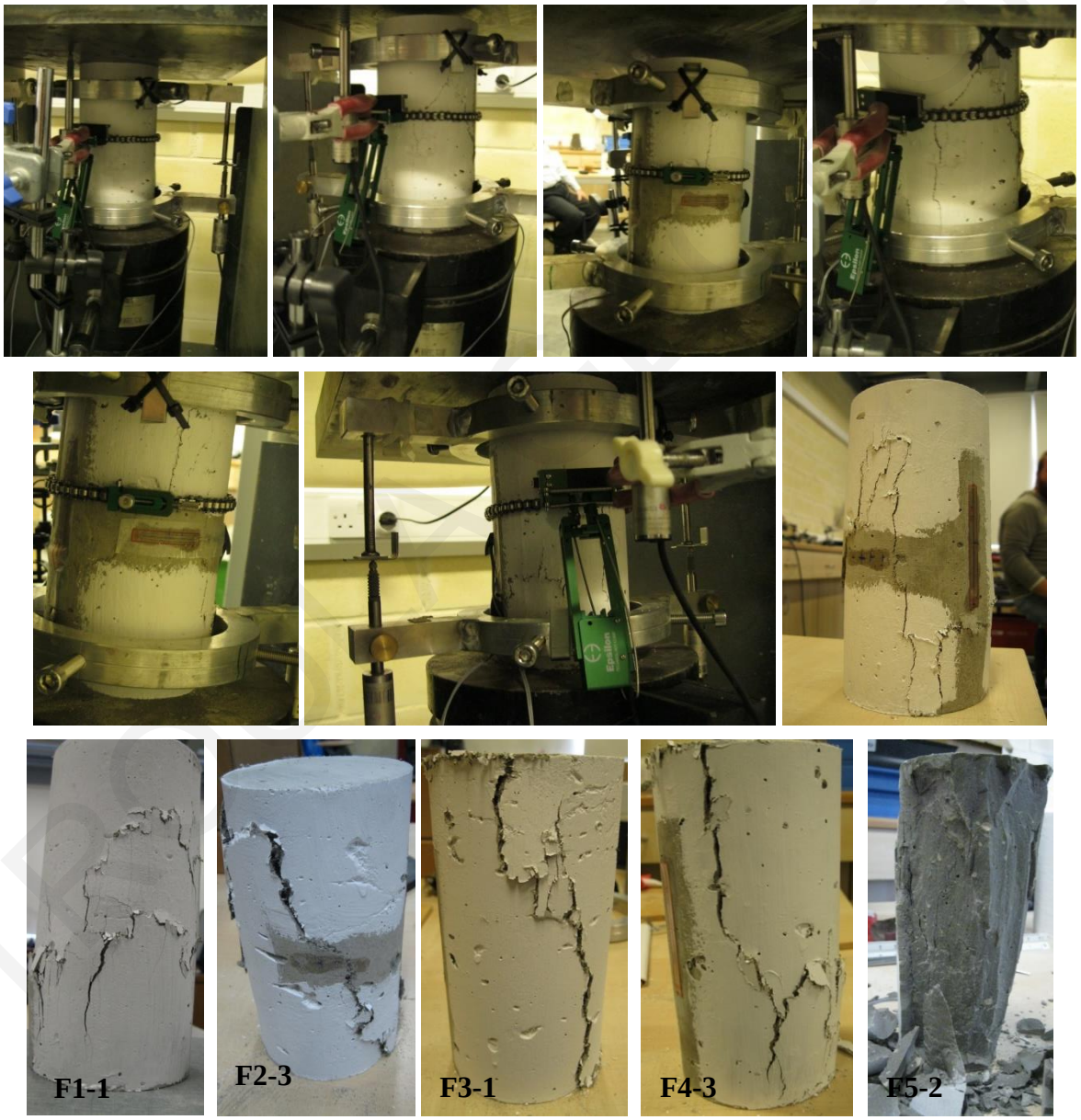

Figure 6.6: Sequence of crack development for specimen F4-1 and Compression test crack formation on various mix designs

Figure 6.7 plots the axial stress-axial strain (right) and axial stress-lateral strain (left) obtained from the compression tests of the SHFRCC materials and the results for the same matrix without fibers (mix F5). The compressive stress of the material without the use of fibers reached an ultimate stress value of 50 MPa (average of three tested specimens), but with the use of fibers, this stress value was decreased. Both strength levels attained were deemed sufficiently high for the construction needs envisioned, which would be focused on the benefits that may be attained through strain-resilience in the tensile response. Certainly, higher compressive strength could be achieved by moderating the content of fly-ash, at the detriment of tensile strain capacity and resilience, which however is the attribute sought here. So, for our purpose, the addition of high amounts of fly-ash was helpful and beneficial for the needed compliance of the fiber-matrix bond mechanism, which is essential in securing the fine, distributed crack formation as opposed to the familiar single plane of fracture seen in conventional FRC and common concretes.

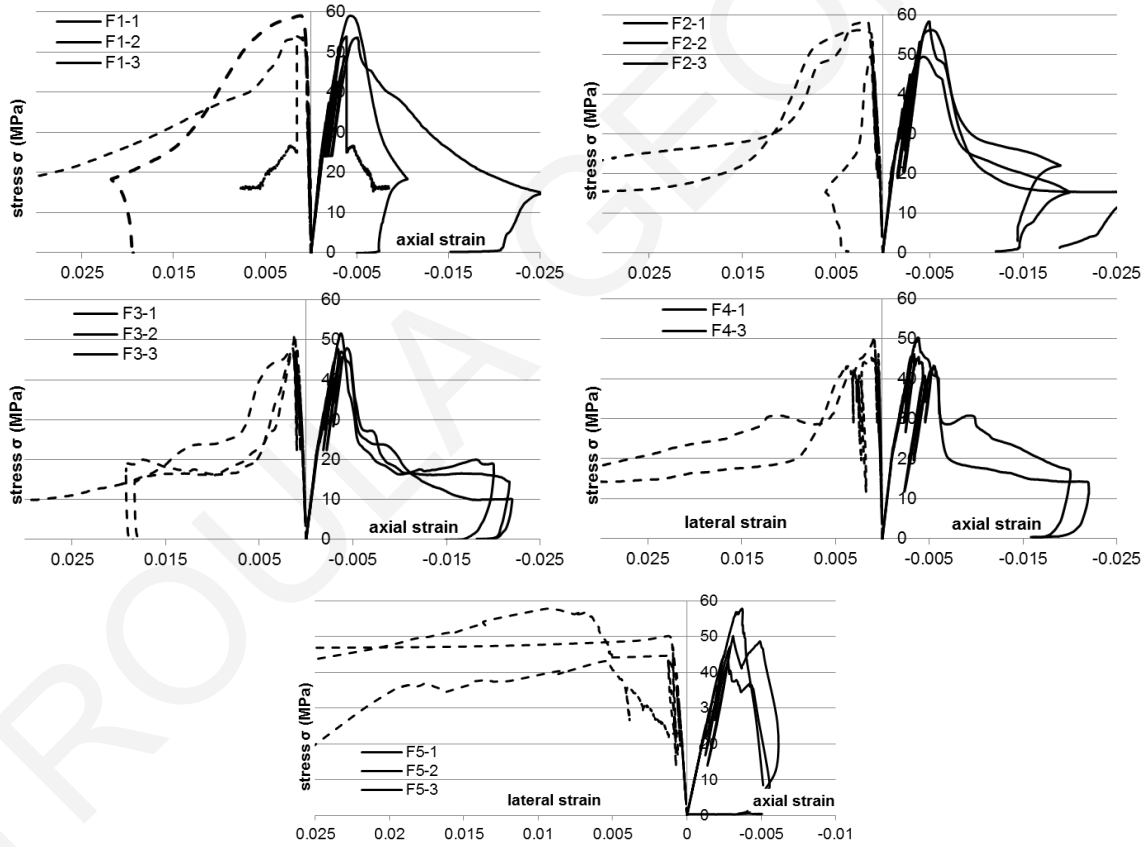

Figure 6.7: Stress-axial/lateral strain of various mix designs with and without fibers

An increase by 0.5% in the axial deformation of SHFRCC at peak load was reported, a value that is comparable to those obtained for the plain mixes; however, a stable descending branch marked the improved performance of the SHFRCC mixes. Note that lateral expansion is responsible for the steepness in the post peak branch in the compressive stress-strain response of concrete (Zanganeh and Pantazopoulou [127]). However, in the presence of fibers the behavior was improved and the post-peak

decay was much milder as fibers were mobilized in the lateral direction bridging the cracks, transferring load and limiting lateral expansion of the cylinder under compression, as evidenced by the restricted growth of post-peak lateral strain as compared to the plain concrete specimens which undergo excessive, uncontrolled lateral expansion (Fig. 6.7). The stress-strain curves suggest that past the peak load, concrete with fibers behaves as if passively confined. The intensity of the effective confinement owing to the role of fibers is directly related to the materials' characteristic stress-strain behavior under tension.

The modulus of elasticity of the composites and the average Poisson's ratios are listed in Table 6.1 along with compressive strength and corresponding strain at peak response. The plain matrix (F5 - no fibers) reached a uniaxial compressive strength of 50 MPa. Addition of uncoated PVA fibers increased the strength to 55 MPa, whereas coated fibers caused a minor strength loss to 48.5 MPa. An increase of the axial deformation corresponding to peak load (ε_{cmax}=4.2‰) was observed in the case of SHFRCCs as compared to the plain matrix (ε_{cmax}=3.2‰); FRC response was also marked by a prolonged descending branch. Lateral deformation owing to concrete dilation was significant in the post peak branch as cracks propagate diminishing the load bearing capacity. In the case of FRC mixes the fibers were mobilized in the lateral direction bridging the cracks and transferring load, thereby producing a confinement effect. This partially restrained the process of lateral expansion of the cylinder under compression, as evidenced by the reduced growth rate of lateral strain as compared to the PM specimens; note that past the peak the PM specimens disintegrated into brittle fragments whereas the SHFRCC specimens remained in one piece continuing to carry about a third of the peak load up to very large deformation. The stress-strain curves suggest that beyond the peak load, concrete with fibers behaves as if partially confined, with the confining stress being directly related to the material's stress-strain response under tension.

Table 6.1: Material parameters and characteristic points of stress-strain diagrams under compression

	ν	E (MPa)	$\sigma_{c,o}$	$\varepsilon_{c,o}$	$\varepsilon_{c,50}$ (50% f_c)	Z (MPa)	$\varepsilon_{cu,20}$
M8	0.22	20716	55.51	0.00444	0.00858	6704.11	0.011064
M12	0.22	19160	54.64	0.00484	0.00930	6125.56	0.011976
M8C	0.23	19157	49.11	0.00383	0.00675	8409.25	0.008502
M12C	0.23	20149	48.22	0.00360	0.00907	4407.68	0.012352
PM	0.33	19653	50.37	0.00319	0.00497	14148.88	0.006038

The Modulus of Elasticity for these composites (determined from the compression stress-strain diagram at 45% of peak load) was low, in the range of 20 GPa due to the elimination of aggregates in the mix design (Table 6.1). Table 6.1 gives the average of three samples in each of the tested mixes. Poisson's ratio, ν, differed between the FRCs (≈0.22) and the plain matrix (≈0.33). In the absence of coarse aggregates the class of materials examined is generally more compliant than normal concrete, attaining their strength, f_c, at higher axial compression strain values (ε_{co} ≈ 0.0032 for PM). Note that for

concrete class C50 the code-prescribed values of strain at peak stress is 2.5‰; the ultimate strain in the post-peak region is taken as 3.4‰ (based on Table 5.1-8 of the Model Code [49]) while strain at peak stress increases with compressive strength [128], [21]. At failure, dislocations at discrete fracture zones occur, that are related to the specimen size and the capacity of the material for stress redistribution. In fiber composites the inclined shear band develops over the full height of the specimen and not over a limited length, whereas the specimen maintains integrity (i.e. fragments are not disconnected) presenting a non-negligible post-peak capacity up to large axial strains; this residual resistance is attributed to the confining effect of the fibers engaged in the lateral direction (restraining the dilation).

6.3.3 Model for SHFRCC in compression

The design stress-strain curve for concrete in compression [129] is a conservative approximation to the response of SHFRCC where the postpeak descending branch extends to axial strains of *1%* at a residual strength equal to 50% of the peak (Table 6.1). Transverse reinforcement increases the residual strength to values above $75\% \cdot f_c$ at *1%* strain. Ultimate strain for confined concrete $\varepsilon_{cu,85}$ is defined as the strain on the post-peak softening branch associated with a residual strength of $0.85 f_c$ [129]. This value is approximated in terms of the confining pressure σ_{lat}, following the relationship: $\varepsilon_{cu,85}=0.0035+0.2\sigma_{lat}/f_c$ [21]. Fibers therefore act as lateral confinement thereby restraining the lateral expansion by bridging the cracks, passively exerting an effective lateral pressure, σ_{lat} on the material.

Based on the original Kent and Park [130] confined model, the confined concrete reaches its maximum strength f_c', while it maintains its residual strength of $0.2 f_c'$ at large strains. This was also observed in the uniaxial compression tests of the fiber reinforced cementitious composites; therefore this confinement model was found to also fit the results where confinement is intrinsic, owing to the role of the fibers. The stress-strain relationship assumed for concrete under uniaxial compression is shown in Figure 6.8. The ascending branch is approximated using a Hognestad type parabola (Eq. 6.1) extending from zero stress to the compressive strength (f_c), with ε_{co} the strain corresponding to the peak compressive stress. Beyond that strain value the strength degrades with increasing compressive strain with a linear descending branch that extends down to a residual strength of $\sigma_{res} = 0.2 f_c$, according with Eq. (6.2) below, as shown in Fig. 6.8. This behavior is modelled using the confinement model by Park et al. 1982 [131], whereby the slope of the descending branch, Z is calculated from the postpeak strain ($\varepsilon_{cu,50}$) associated with a 50% reduction of strength ($Z=0.5 f_c/(\varepsilon_{cu,50}-\varepsilon_{co})$), (Fig. 6.8, Table 6.1).

for $\varepsilon_c<\varepsilon_{co}$ $$\sigma_c = f_c\left[2\frac{\varepsilon_c}{\varepsilon_{co}}-\left(\frac{\varepsilon_c}{\varepsilon_{co}}\right)^2\right] \quad (6.1)$$

for $\varepsilon_{co}<\varepsilon_c<\varepsilon_{cu}$ $$\sigma_c = f_c-(\varepsilon_c-\varepsilon_{co})\cdot Z \geq (1-j)\cdot f_c \quad (6.2)$$

Values of maximum stress, strain at maximum stress and slope of the descending branch are obtained after calibration of this model with the results of the experimental uniaxial compression tests

conducted on composite samples and are listed in Table 6.1. Parameter (j) in Equation 6.2 marks the fraction of compression resistance lost at the ultimate strain of the composite, i.e., $j=1-(f_u/f_c)$.

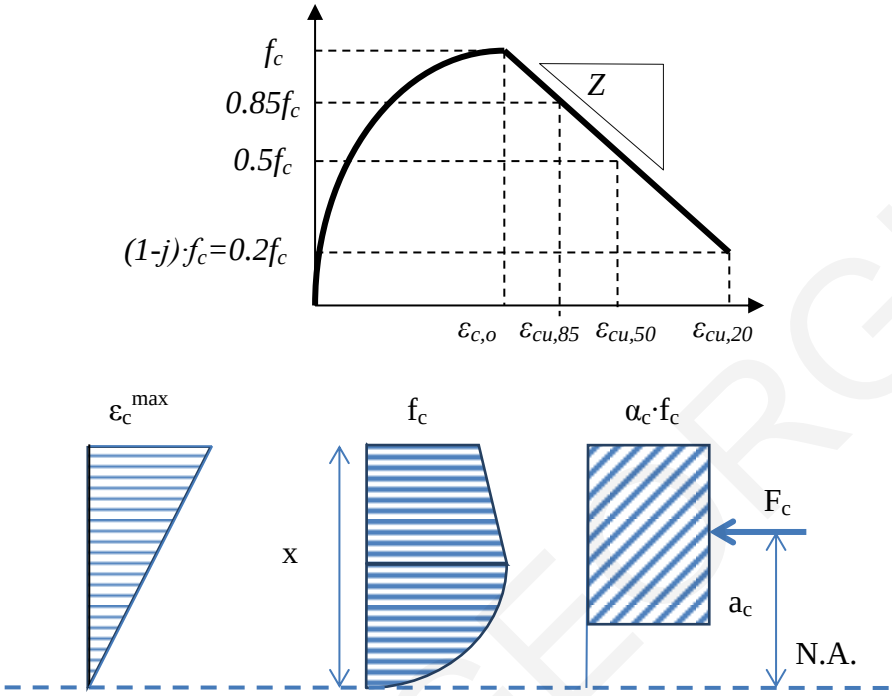

Figure 6.8: Stress-strain law under compression and equivalent stress block

For PM (mix F5), Z is more than double the corresponding values reported for SHFRCCs, underscoring the precipitous decay of the post-peak branch in the stress strain response of unreinforced material and by contrast, the mitigating effect of the fibers in SHFRCCs. Parameter ε_{cu} is used to define the slope of the post-peak descending branch in the stress-strain curve under compression. For uniformity ε_{cu} is usually associated with a predetermined fraction of post-peak strength loss in the axial stress – axial strain compression curve. Residual strain $\varepsilon_{cu,20}$ associated with σ_{res} is referred to hereon as the nominal ultimate strain capacity of the material (Table 6.1, Fig. 6.8) that corresponds to 80% loss of strength.

In flexural analysis the material stress-strain law in compression (Eq. 6.1 and 6.2) is used in order to relate normal strain with the corresponding stress over the height of the compression zone, x (Figure 6.8). As was done in conventional flexural analysis of normal concrete, the complexity caused by the nonlinearity of the stress-strain law over a varying strain profile is simplified using an equivalent rectangular stress block to calculate a uniform stress intensity ($\alpha_c \cdot f_c$) and the point of application of the stress-resultant, along the height of the compression zone; the expressions below are obtained assuming the stress-strain laws given by Eq. 6.1 and 6.2, and refer to the maximum compression strain at the extreme compressed fiber of the cross-section, ε_c^{max}, and its relative magnitude with respect to ε_{co}. Normalized strain is: $\bar{\varepsilon} = \varepsilon / \varepsilon_{co}$.

for $\varepsilon_c^{max} < \varepsilon_{co}$

$$\alpha_c = \bar{\varepsilon}_c^{\max} \cdot \left(1 - \frac{\bar{\varepsilon}_c^{\max}}{3}\right) \tag{6.3a}$$

$$a_c = \frac{2 - 0.75 \cdot \bar{\varepsilon}_c^{\max}}{3 - \bar{\varepsilon}_c^{\max}} \cdot x \tag{6.3b}$$

for $\varepsilon_{co} < \varepsilon_c^{max} < \varepsilon_{cu}$

$$\alpha_c = 1 - \frac{1}{3}\left(\bar{\varepsilon}_c^{\max}\right)^{-1} + j \cdot \left(1 - 0.5\left(\bar{\varepsilon}_c^{\max}\right)^{-1} - 0.5\bar{\varepsilon}_c^{\max}\right) \cdot \left(\bar{\varepsilon}_{cu} - 1\right)^{-1} \tag{6.4a}$$

$$a_c = x \cdot \frac{1 - \frac{1}{6}\left(\bar{\varepsilon}_c^{\max}\right)^{-2} + j \cdot \left(1 - \frac{1}{3}\left(\bar{\varepsilon}_c^{\max}\right)^{-2} - \frac{2}{3}\bar{\varepsilon}_c^{\max}\right)\left(\bar{\varepsilon}_{cu} - 1\right)^{-1}}{2 - \frac{2}{3}\left(\bar{\varepsilon}_c^{\max}\right)^{-1} + j \cdot \left(2 - \left(\bar{\varepsilon}_c^{\max}\right)^{-1} - \bar{\varepsilon}_c^{\max}\right)\left(\bar{\varepsilon}_{cu} - 1\right)^{-1}} \tag{6.4b}$$

6.4 Mixes with stirrups

Uniaxial compression tests were also carried out on the matrix consisting of high amounts of fly ash as cement replacement with the use of stirrups, by varying their spacing and therefore the volumetric ratio of confinement reinforcement. The stirrups were steel bars of a diameter of 8 mm with a yield tensile strength of 500 MPa and 15 mm clear cover. Cylinder dimensions were 100 mm in diameter and 200 mm in height. Loading was displacement controlled at a rate of 1.5 μm/s.

Table 6.2: Confinement by stirrups used for each specimen

Name	**stirrup spacing s (mm)**	**Specimens**	**ρ_w**	**b_o**	**α_s**	**α_n**	**α**	**ω_w (%)**
S8	80	F5S8-1, F5S8-2, F5S8-3	0.050	62	0.355	1	0.355	0.359
S5	50	F5S5-1, F5S5-2, F5S5-3	0.080	62	0.597	1	0.597	0.574
S3	30	F5S3-1, F5S3-2, F5S3-3	0.134	62	0.758	1	0.758	0.957

The stirrup spacing varied between 3, 5 and 8 mm. Three specimens for each different spacing were tested. The steel reinforcement ratio for shear (ρ_w, comprising cylindrical stirrups) and the volumetric percentage (ω_w) listed for all specimens in Table 6.2 is defined according with Eq. 6.5.

$$\rho_w = \frac{4A_{sw}}{b_c \cdot s},\ \omega_w = \frac{8A_{sw}}{b_c \cdot s} \cdot \frac{f_y}{f_c},\ a = a_s \cdot a_n, \tag{6.5}$$

where A_{sw} is the area of one bar, b_c is the diameter of the core (out-to-out of the stirrups), ω_w is the ratio of the volume of confining hoops to that of the confined core to the centerline of the perimeter

hoop times f_y/f_c, α is the confinement effectiveness factor, $\alpha_s=(1-s/2b_o)\cdot(1-s/2h_o)$ for hoops, a_n=1 for circular hoops.

Specimens were cast without any vibration due to the self-compacting properties of the mixture. The specimens were moist-cured in the molds for 24 hours. After that the cylinders with steel stirrup reinforcement were wrapped in burlap and were moist-cured daily for 100 days. The age of the specimens has shown to have an effect on the ductility of the material, as high amounts of cement replacement with fly ash leads to slower attainment of the full strength. In greater ages of the specimens this phenomenon is limited. The use of confinement changes the type of failure. Spalling of the concrete cover was observed in all cases but strength deterioration decreased with denser stirrup spacing.

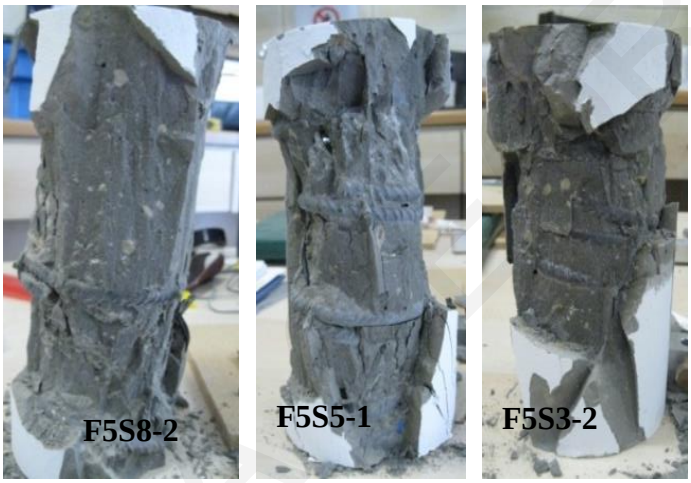

Figure 6.9: Crack evolution for plain cementitious composite with stirrups

Results of the uniaxial compression tests on the 200×100 mm cylinders are plotted in Fig. 6.10. Each curve represents a single specimen and is marked by the respective batch code name. On the horizontal axis strains parallel and orthogonal to the direction of load are presented (right and left side of the figure respectively). The vertical axis represents the applied stress. The additional confinement changes the load carrying capacity, the axial deformation at maximum load, as well as the lateral expansion of the specimens. In the case of confinement by circular stirrups (F5S3, F5S5, F5S8), there is a decrease of the maximum load bearing capacity by a decrease of the distance between the stirrups. This is attributed to the weakening of the cover and its easier deterioration, as it is attached to less matrix and more stirrups. Evidently there is little effect by the use of stirrups every 80 mm By decreasing the distance to 50 mm the post-peak behavior changes to a more ductile one, while the smallest stirrups spacing decreases significantly the slope of the descending branch almost to a plateau.

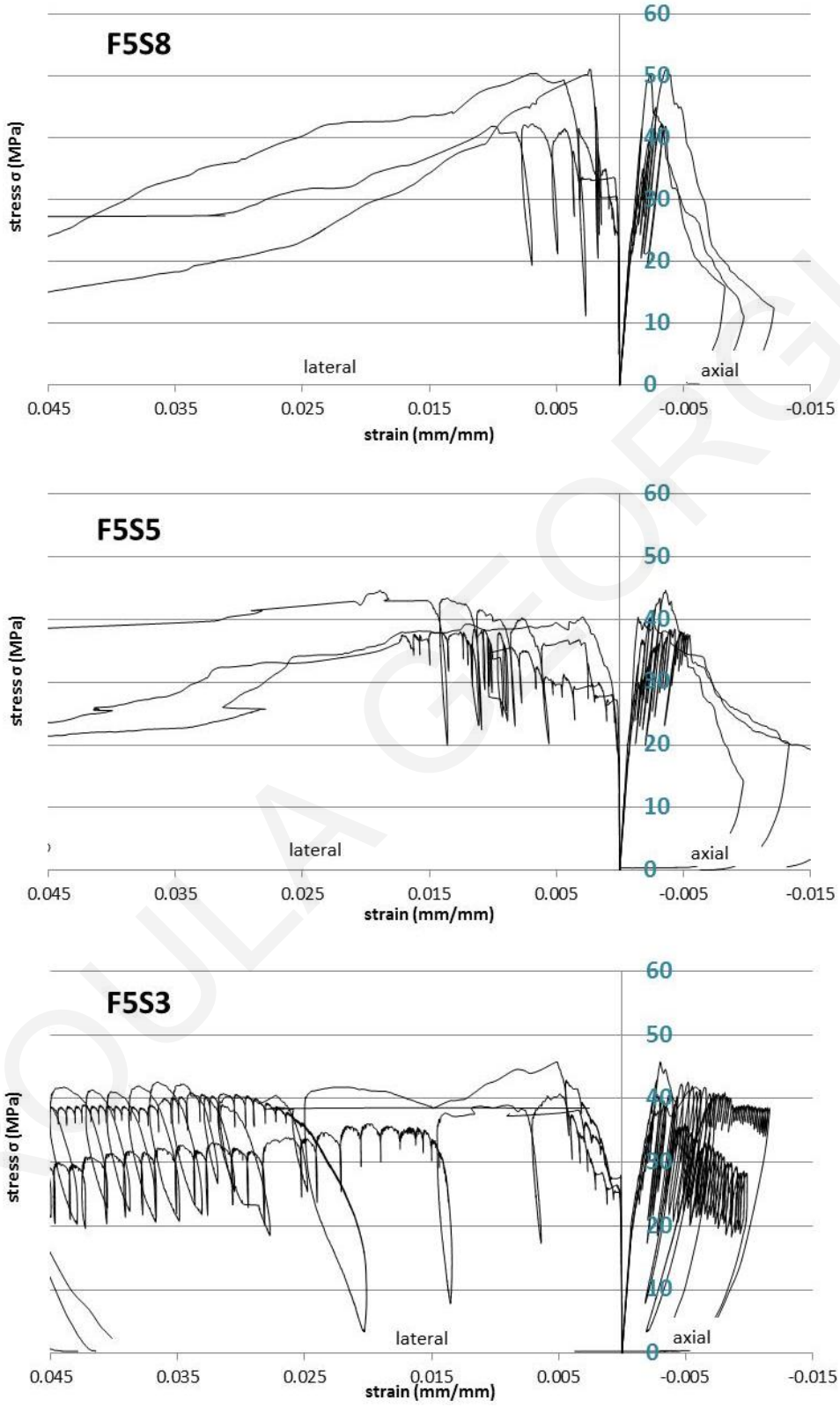

Figure 6.10: Stress-axial/lateral strain for cylinders with steel stirrups

6.5 Mixes with FRP layers

Other than confinement by steel stirrups the method of confinement with FRP sheets is examined. The FRP sheets were provided by SIKA and their properties are shown in Table 6.3. Detailed description of the application of the FRP wraps on the cylinder specimens are given in Chapter 4. Also for each type of wrap and number of layers the minimum anchorage length is provided in Chapter 4. Table 6.3 gives the specimen designation, mix design, confinement method and test speed when FRP sheets are used for confinement. The test speed of the FRP confined cylinders was doubled due to the great increase of bearing capacities and the time required to complete the tests. A different designation of the specimens is recorded in the last column of the Table in order to ease comprehension of the results in diagrammatic form. PM refers to the mixes without any confinement. For the confined specimens denomination takes the form of i.e. **3C-2**. The first number indicates the number of layers of FRP used (for this case 3 layers) and the letter after indicates the type of FRP (G for Glass FRP and C for Carbon FRP). The last digit indicates which of the three specimens tested for each combination is depicted.

Table 6.3: Confinement by FRP sheets used for each specimen

Specimens	MIX	Confinement	DATE	SPEED	
F5-1/2/3	F5	None	16/3/2015	1.5μm/sec	PM-1/2/3
F14-1/2/3	F14	None	15/5/2016	1.5μm/sec	PM-1/2/3
F14G-1/2/3	F14	1 layer glass FRP	15/5/2016	3μm/sec	1G-1/2/3
F14-2G-1/2/3	F14	2 layers glass FRP	16/5/2016	3μm/sec	2G-1/2/3
F14C-1/2/3	F14	1 layer carbon FRP	16/5/2016	3μm/sec	1C-1/2/3
1/2/3-F5F2	F5	2 layers carbon FRP	18/3/2016	3μm/sec	2C-1/2/3
1/2/3-F5F3	F5	3 layers carbon FRP	23/3/2015	3μm/sec	3C-1/2/3

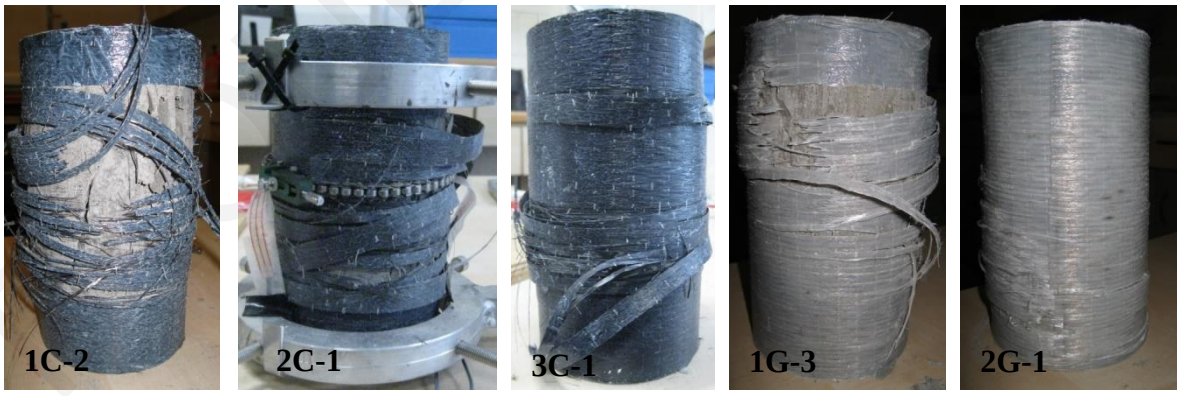

Figure 6.11: Failure of cylinders with FRP wraps

When FRP sheets were used for confinement, the behavior changed from softening to hardening, with a sudden collapse when the FRP sheets ruptured, upon attainment of their ultimate strain (Figure 6.10).

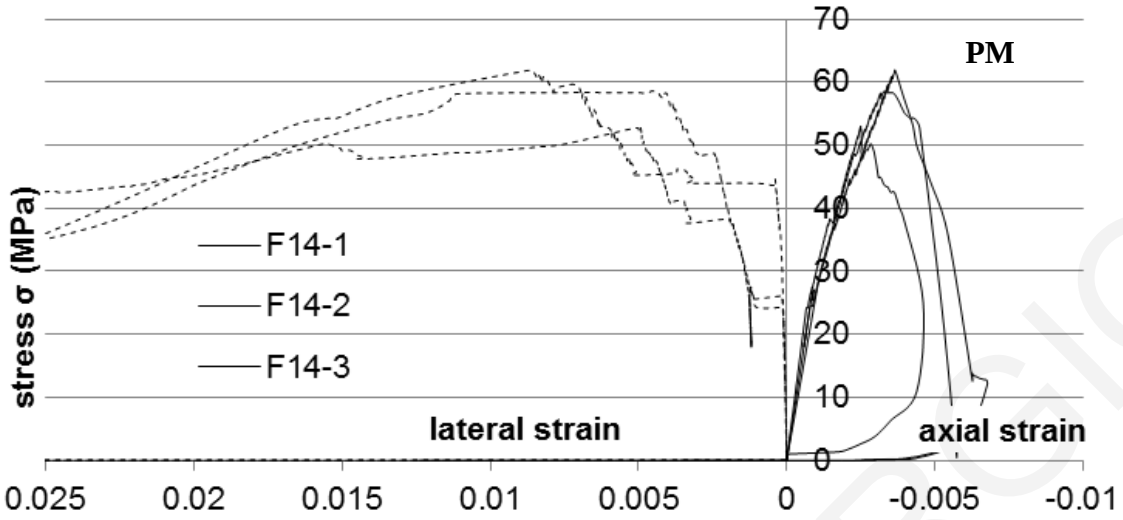

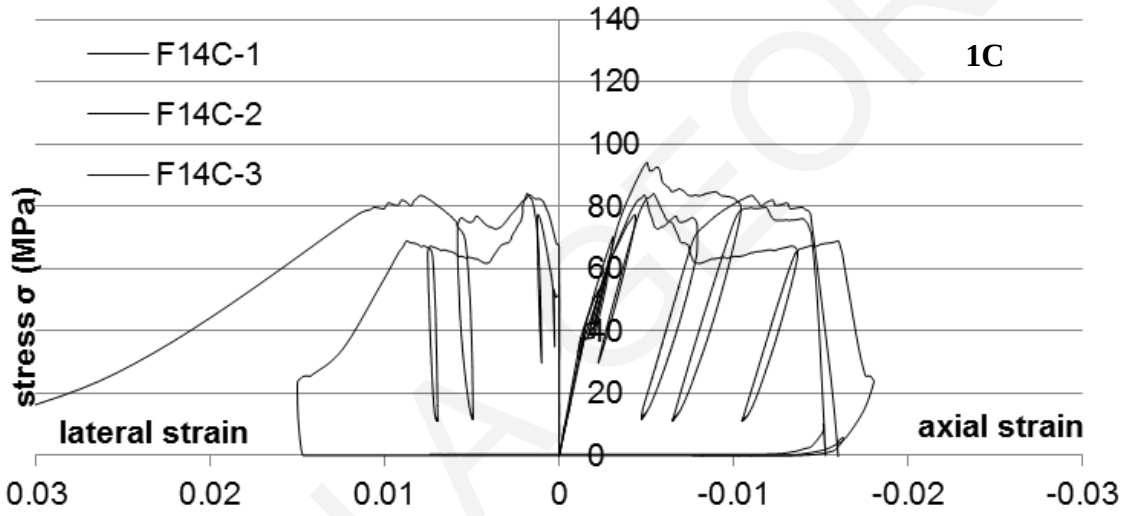

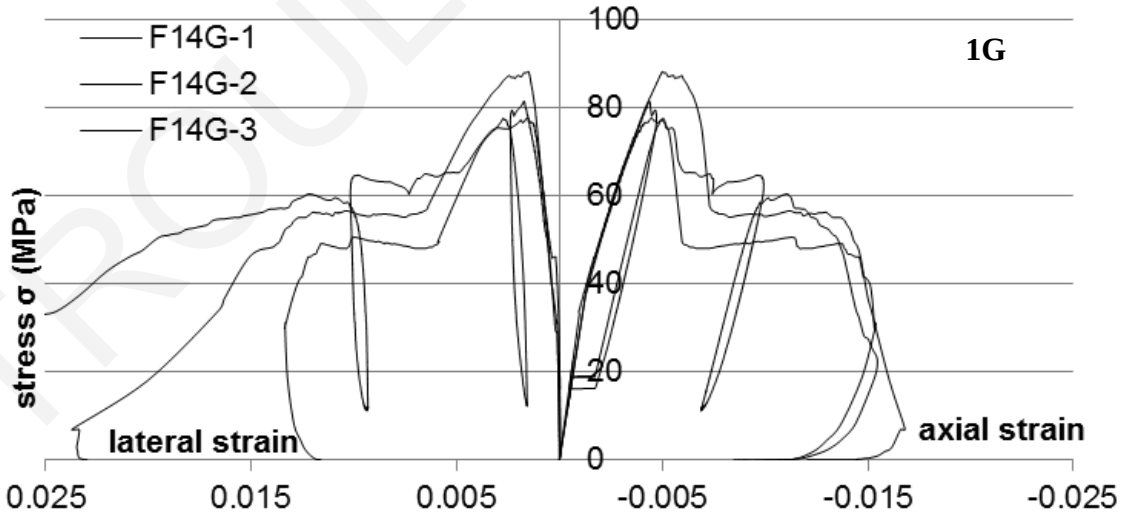

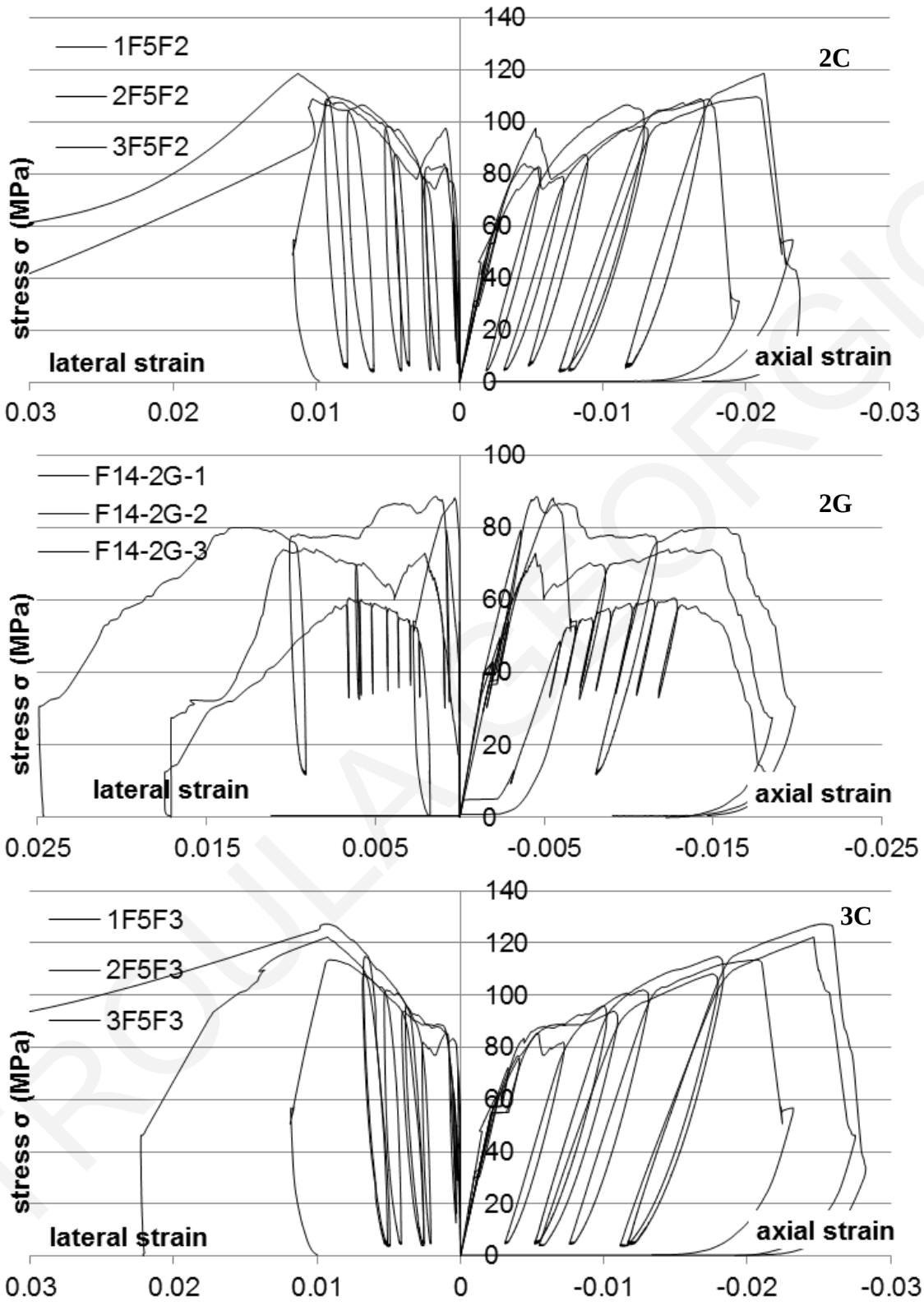

Figure 6.12: Stress-axial/lateral strain diagrams for all specimens with FRP sheets

The results of the uniaxial compression tests on the 200×100 mm cylinders are plotted in Fig. 6.12. The additional confinement changes the load carrying capacity, the axial deformation at maximum load

as well as the lateral expansion of the specimens. In the case of carbon FRP, even for only 2 layers wrapped around the specimen (2C), the compressive capacity is doubled, and even after apparent yielding associated with cracking of the matrix inside the FRP, there is an increase in the stress capacity and a plateau up to a ductility of 2.5. In this area of the plateau, lateral strain is steeply increasing but it always remains lower in magnitude than the axial strain (i.e. apparent dilation ratio < 0.5), mainly owing to the increasing magnitude of lateral confining pressure exerted by the linearly elastic FRP material. At a lateral strain of 1% the FRP ruptures and the bearing capacity suddenly collapses.

Both types of FRP sheets increase the occurrence of first cracking strain of the matrix from 55 MPa to approximately 80 MPa. The glass FRP of one and two layers, as well as the one layer of carbon FRP, do not show an increase in strength after first cracking, contrary to the two and three layers of carbon FRP that present hardening up to values of 120 MPa strength. While the transition from one to two layers of each FRP type plays a significant role in the overall response, no important difference appears between the two and three layers of carbon FRP, indicating that important role in the strength capacity plays the restraint to lateral expansion of the cylinders related to the strain capacity of the FRP and not the stress that is provided by the number of sheets.

6.6 Comparison of axial-lateral strains between different confinement methods

6.6.1 Overall response

The results of all uniaxial compression tests on cylinders are plotted in Fig. 6.13. Each curve represents a single specimen (one of three tested) and is marked by the respective batch code name (curves are not averaged). On the horizontal axis strains parallel and vertical to the direction of load are presented. The vertical axis represents the applied stress. The addition of confinement changes the load carrying capacity, the axial deformation at maximum load as well as the lateral expansion of the specimens. By adding fibers in the mix (F1, F2, F3, F4) the behavior is similar to that obtained from stirrup confinement (F5-S8/S5/S3) but with an increase of compressive capacity and a shift of strain at peak load at 5‰ strain, in comparison to the plain cementitious matrix (PM) at 3‰.

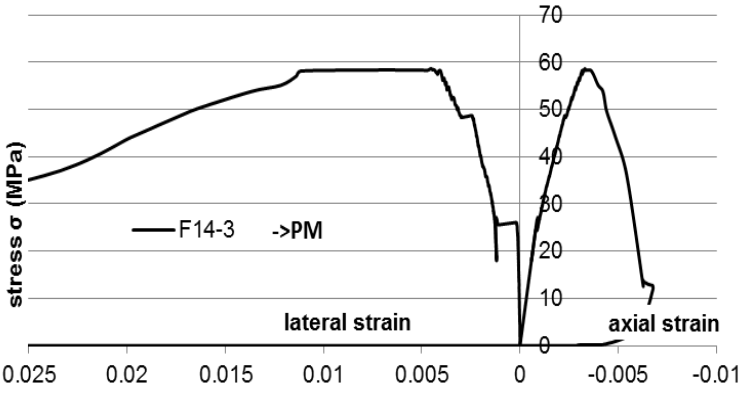

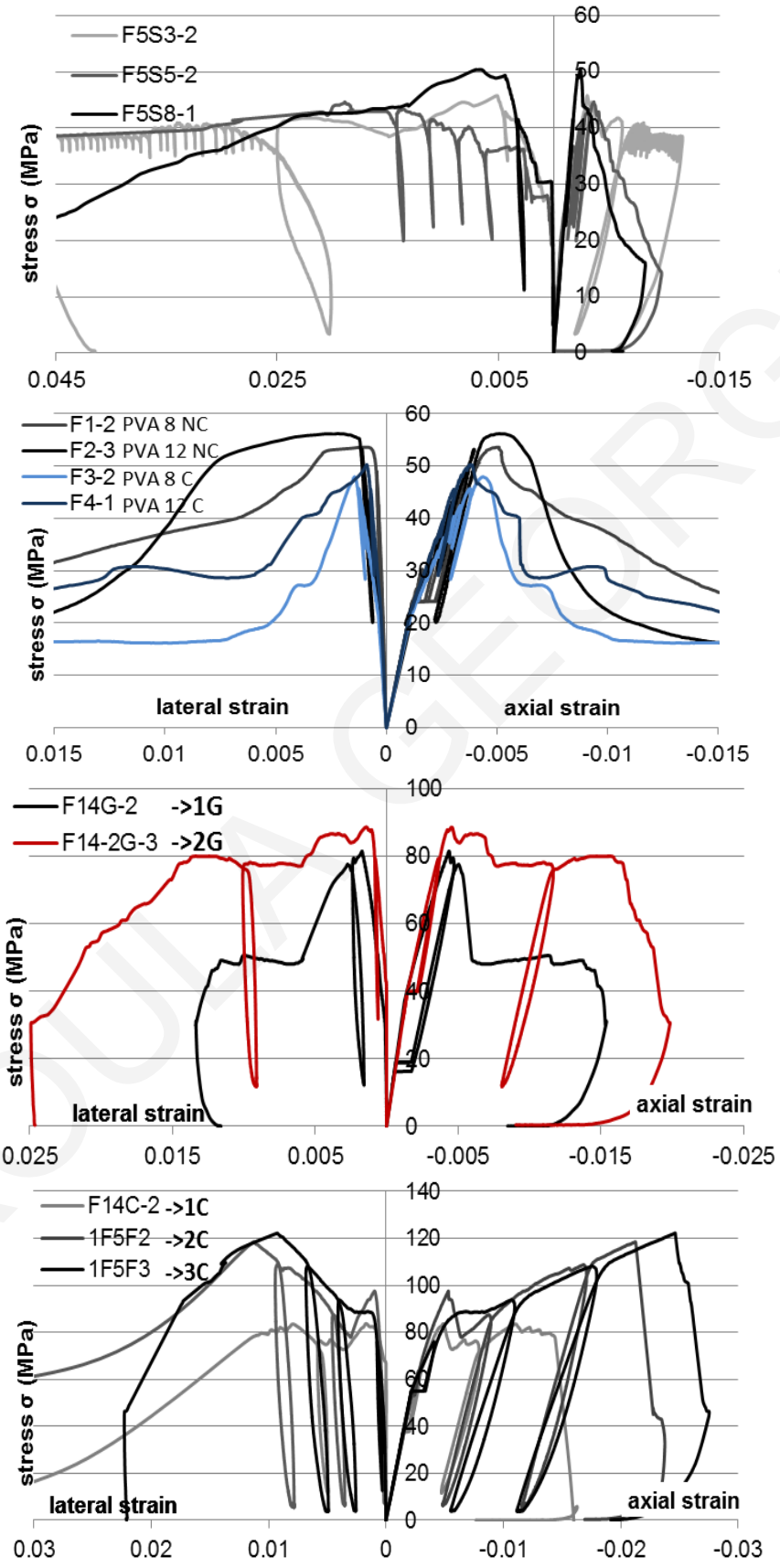

Figure 6.13: Stress-axial/lateral strain diagrams for all specimens

Note that the fibers are more effective in restraining lateral expansion than stirrups; the effective confined strength being closer to that obtained with specimens having densely spaced stirrups, as the stress-strain curve in both occasions holds a plateau after the yielding. It is therefore evident that the plateau of the fiber reinforced composite can be attributed to their strain softening/hardening capacities in tension. The circumferential extension caused by the Poisson's ratio is captured by the fibers crossing cracks.

In the initiation of cracking the plain composite behaves the same with the composite reinforced by stirrups. But the rate of volumetric expansion changes after lateral strain has reached 1.5% and stirrups are passively working confining the cylinder under compression. The results of FRP, indicating a plateau in the post cracking region, resembles the confinement of concrete by stirrups rather than by FRPs. In the case of FRPs circumferential extension is defined by the modulus of elasticity of the FRP polymers and as the material within them is compressed and deteriorated accumulating energy. The stress-strain curve shows only increase in load up to sudden rupture of the FRP and complete loss of strength. Table 6.4 shows the peak strength, modulus of elasticity and strain at peak stress for the specimens confined with FRP sheets. For the case of the stirrups and the FRP, the effective Modulus of Elasticity increased to 27 GPa, as shown on the summary of Table 6.4. In the case of the FRP confinement the stress-strain curve presents a bilinear behavior for a large range of deformation, reaching significantly higher stresses than the stirrup confined and the FRC mixes. The first peak is identified by a sharp change in slope. Strength and the corresponding strain at first peak did not change with regards to the addition of layers. The addition of layers increased the maximum load and delayed volumetric expansion. Failure of the specimens happened in all cases by rupture of the FRP at a lateral strain of 5.5%.

Table 6.4: Characteristics of specimens confined with FRP sheets

	Specimens	σ_{max} ***(MPa)***	***E (MPa)***	ε ***(at max stress)***
PM	F5-1/2/3	50.37	19652.71	-0.0032
PM	F14-1/2/3	57.86	19500.00	-0.0032
G1	F14G-1/2/3	82.38	31138.77	-0.0046
G2	F142G-1/2/3	83.68	24957.51	-0.0078
C1	F14C-1/2/3	87.34	28168.54	-0.0051
C2	1/2/3-F5F2	112.26	27192.66	-0.0198
C3	1/2/3-F5F3	121.06	27406.24	-0.0236

6.6.2 Lateral confinement

The abscissa in all diagrams of Figure 6.14 is the axial strain in the direction of loading. The respective coordinates from the top diagram to bottom are the lateral strain, the volumetric strain ε_v

(=ε_{axial}+2 ε_{lat}) and the applied axial stress. The diagrams refer to the fiber reinforced mixes with variating PVA length and coating properties (mixes F1, F2, F3 and F4). It is evident that the addition of fibers influences the postpeak response of the matrix by improving its deformation capacity and reduces the strength loss from the peak value. The addition of fibers did not affect the Modulus of Elasticity as it was approximately the same as that of the plain matrix (20 GPa).

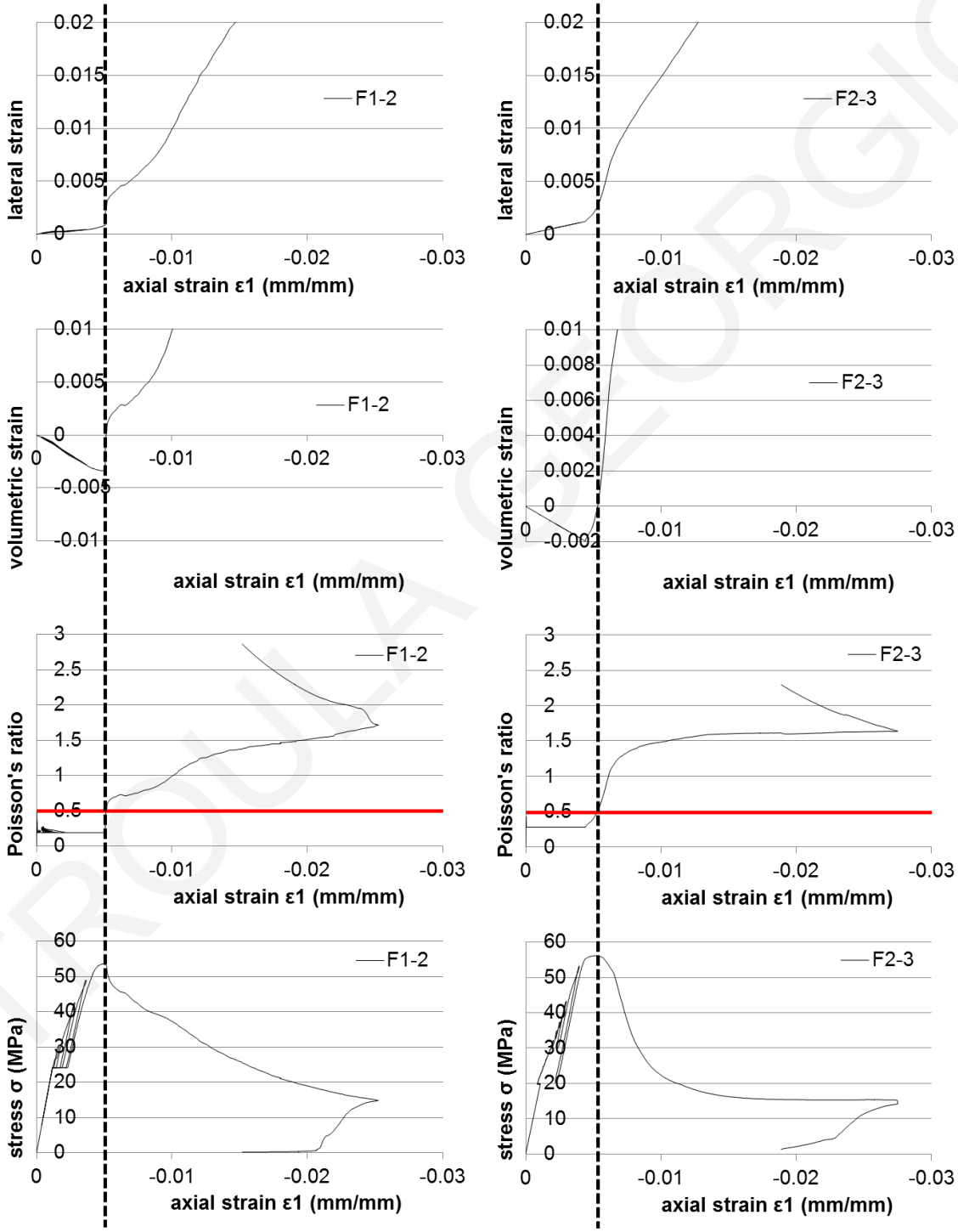

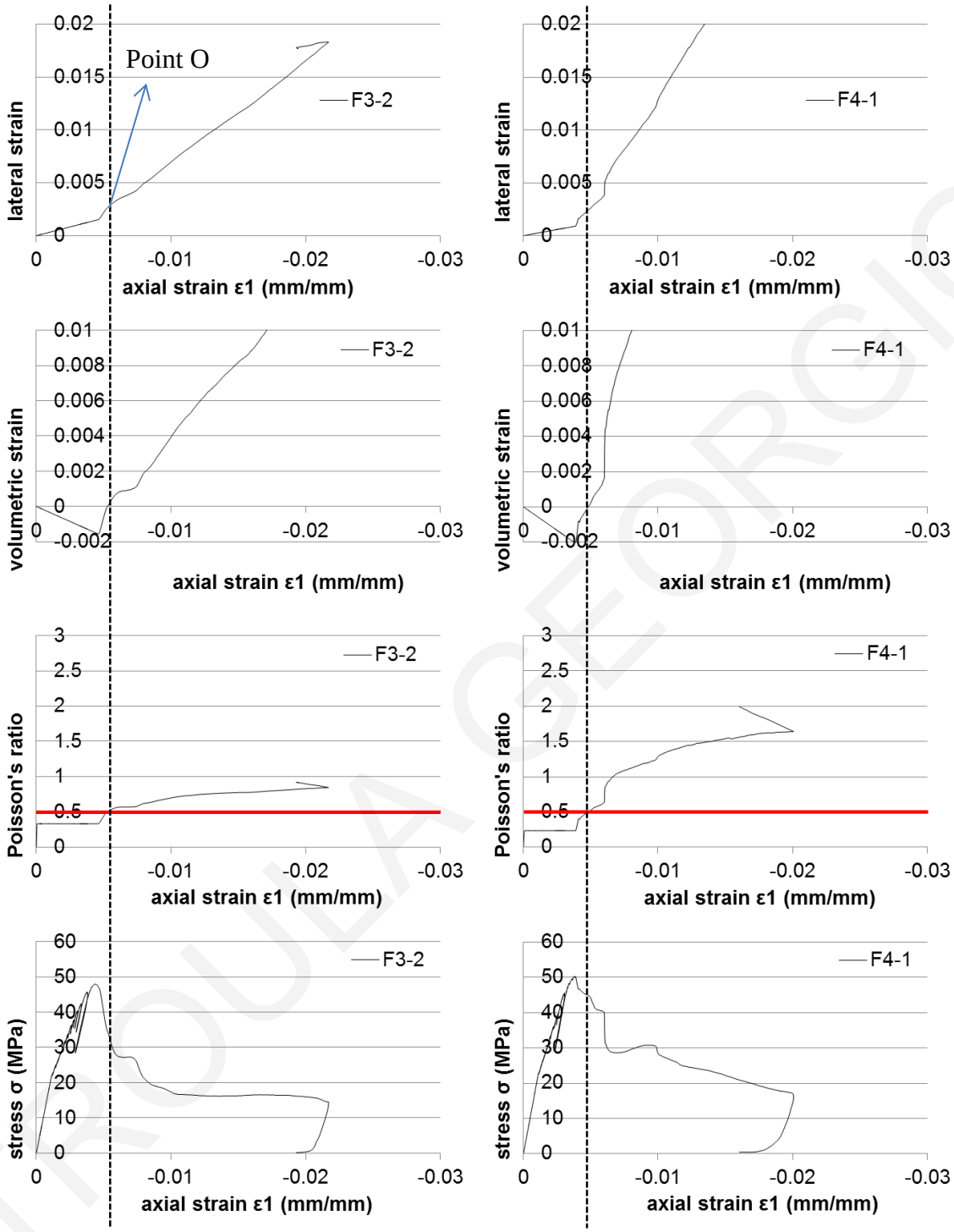

Figure 6.14: From top to bottom a) Lateral strain-axial strain, b) Volumetric strain-axial strain, c) Apparent Poisson's ratio-axial strain and d) Stress-axial strain for all fiber reinforced mixes

The failure of concrete is usually affiliated with the reversal of volumetric strain from net contraction to dilation as cracking progresses [124, 132]. Also the rate of volumetric strain reversal has been shown to characterize deformation capacity and the rate of strength degradation. A low rate of expansion is evident in the case of fibers, as they bridge the cracks, transferring stresses through them

and therefore applying passive confinement to the cylinder in the full extension of its cross section. The onset of strength loss is delayed from 3.1‰ for the plain matrix to 4.4‰ for the PVA-fiber reinforced composites.

6.7 Analysis of the uniaxial compression strength based on lateral expansion

6.7.1 Decay of strength based on lateral expansion

As axial strain increases after the peak load (Fig. 6.14) a rapid increase in lateral strain takes place. Up till the maximum load the composites with the higher strengths have a greater increase in lateral strain manifesting faster accumulation of damage. At this point it is evident that fibers have not yet been engaged in lateral deformation. The rate of lateral to axial strain is reversed having the less steep slope for the coated-PVA composite after an axial strain of 0.5% and a lateral strain of 0.8% (Point O-Inflection Point in Figure 6.14 (a) lateral to axial strain of F3-2). In the volumetric expansion to axial strain diagram (Fig 6.14) there is a linear elastic volumetric response that contracts at a rate of (*1-2v*) up to the onset of cracking. The composites stop to decrease in volume at the point where the curves reach the horizontal axis and thereafter volumetric expansion appears. The composites without coating reach zero volumetric expansion at a higher axial strain suggesting a lower rate of lateral expansion. In normal concrete volumetric stain reaches a zero value at a level of uniaxial strain ε_1^* of about 80-100% of the strain at peak stress, whereas in the case of fiber reinforced composites ε_1^* is at the starting point of strength decrease suggesting fiber confinement working prior to that level. Also the rate of increase between the curves changes at Point O, with the composites of coated-PVA fibers having the smallest slope and therefore the lower lateral expansion to axial contraction ratio. Comparing coated and not-coated fiber mixes maximum strength coincides with zero volumetric expansion at an effective Poisson's ratio of 0.5 for the not-coated fibers while for coated fibers it happens at lower Poisson ratios. After Point O Poisson's ratio ceases to increase rapidly turning almost to a stable value of approximately 1.5 for the non-coated fibers while it maintains lower values for the coated ones. Reflecting the previous information in Figure 6.14, a Poisson's ratio of 0.5 seems to be reached at the end of the axial stress plateau for the composites without coating on the fibers, marking the onset of the degrading segment of the curve and Point O marks the initiation of the remaining stress plateau.

Based on previous experimental data by Imran [133] there is a critical level of volumetric strain in the range of 0.75- 1.25% corresponding to the well known "transition" point in the stress coordinates. Beyond that level of contraction alterations in the microstructure are associated with gel failure. In the case of fiber composites, this point is no longer a failure point but a change of the mechanism transferring the stresses, mainly focusing on the properties of the fibers bridging the cracks and their interfacial bond relation to the matrix. This transition point marked before as Point O is a margin after which the magnitude of the area strain decreases with increasing axial strain due to the increasing

lateral pressure related to the fibers. The problem of multiaxial stress state (compression due to loading and lateral confinement due to fibers) is not considered a pressure-dependent problem, but as restraint-dependent one according with Pantazopoulou [134].

The ε_v-ε_{axial} plot is an indicator of internal damage and the area between that curve and a 45 degree ($\varepsilon_v=\varepsilon_1$ in that case) line represents the area increase per unit area of cross section supporting the load [132] as shown in Fig. 6.15. In this case volumetric strains of up to -3% (minus symbol indicates contraction) are reached for the 8mm PVA un-coated fibers mix and up to -2% for PVA mix designs where usual values for unconfined concrete are in the order of -0.5%.

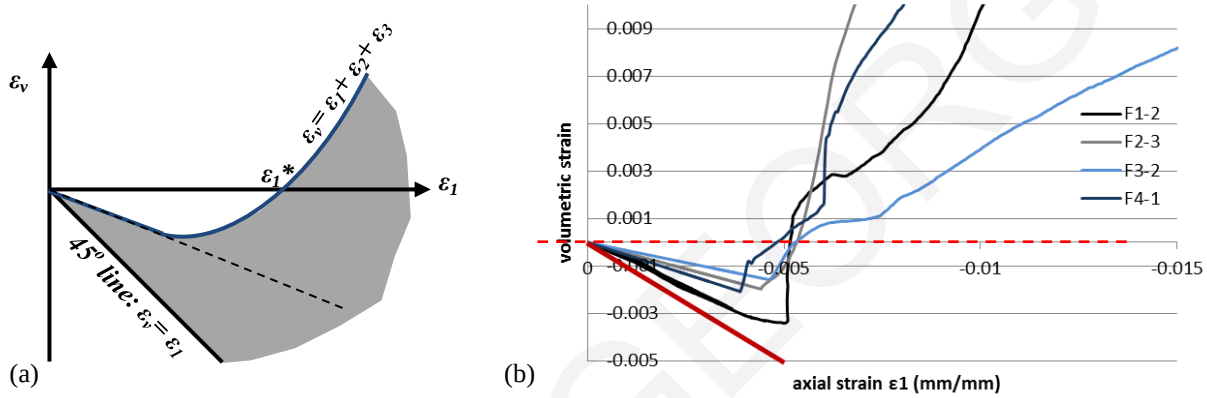

Figure 6.15: Physical significance of area strain a) definition of volumetric strain plot [132] b) area strain of FRC mixes

6.7.2 Confining role of fibers (restraint to transverse expansion)

Archontas and Pantazopoulou [135] interpreted the internal confining effect generated by fibers as shown in Fig. 6.16. Normal compression stress generates transverse tensile strains ε_{lat}; due to these strains, the fibers crossing an arbitrary plane B-B' parallel to the compression develop tensile stresses and forces $f_{f,i}$: A passive confining pressure σ_{lat} is required in order to counteract the stress resultant of the fiber forces normal to the B-B' section. The equivalent transverse confinement in this case is,

$$\sigma_{lat} = -\lambda_{eff} \cdot n_f \cdot A_f \cdot f_{f,i} \quad where, \quad f_{f,i} = E_f \cdot \varepsilon_{lat} \le f_{b,f} \cdot 0.5\ell_f \cdot \pi d_f \tag{6.6}$$

where n_f is the number of fibers crossing an arbitrary unit area of the bulk material (given in Chapter 5, Eq. 5.4), A_f is the fiber cross sectional area, $f_{f,i}$ is the stress of the arbitrary fiber, $f_{b,f}$ the bond strength of the fibers, ℓ_f the fiber length and d_f is the fiber diameter.

Lateral restraint in compression is reflected in the material stiffness by delaying or mitigating damage due to transverse expansion normal to the direction of principal compression, leading to a commensurate increase in compressive strain capacity at peak stress, ε_c. Although other effects (entrapped air and disruption of the gel structure) prevent an evident increase of compressive strength where cohesion is of paramount importance), yet the effect of the confining pressure is seen in the sustained axial strain with no loss of load carrying capacity for a prolonged range exactly because the

lateral pressures, σ_{lat}, prevent the uncontrolled lateral growth of the material under compression. Figure 6.17 gives the comparison of all the stress-axial/lateral strain curves for different confinement methods that were tested under compression.

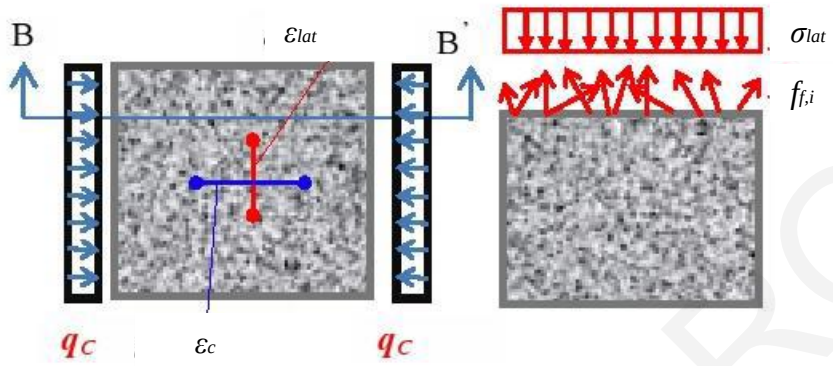

Figure 6.16: Passive confinement function in directions orthogonal to the compression stress field q_C, under a transverse tension strain field ε_{lat} owing to Poisson- effect. and estimation of equivalent lateral confining pressure, σ_{lat} (Archontas and Pantazopoulou [135])

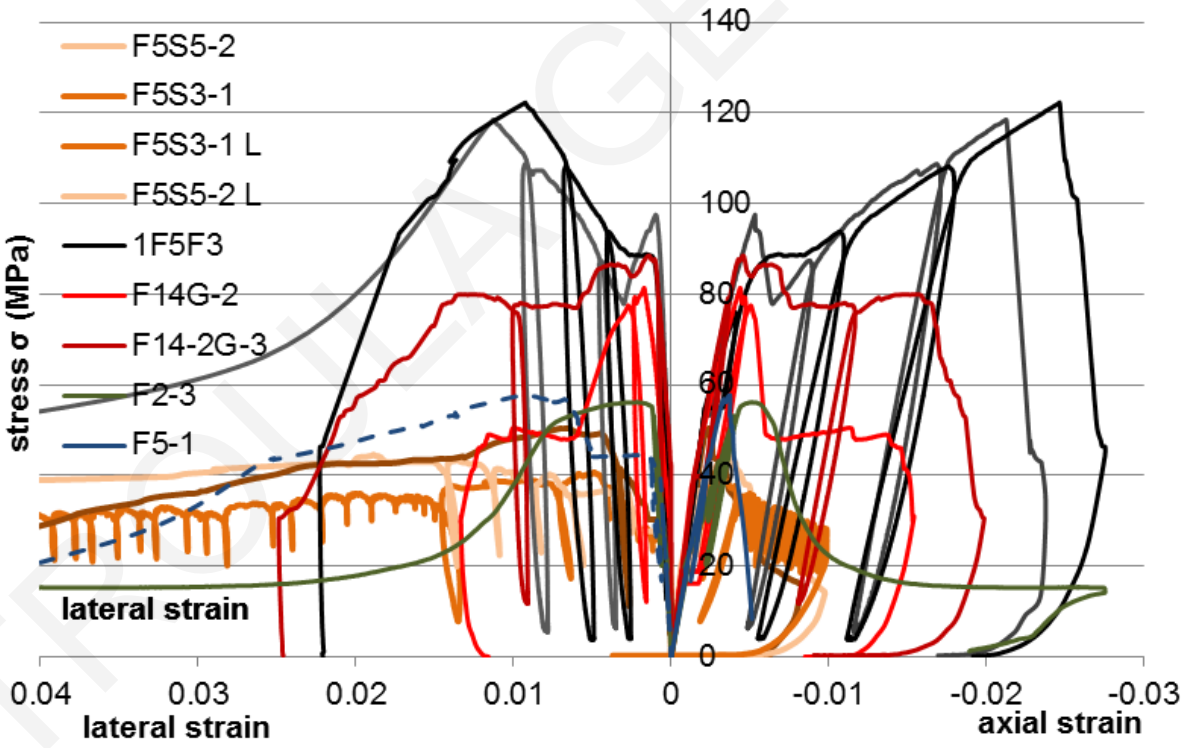

Figure 6.17: Stress-axial/lateral strain of compression test for all specimens with various confining methods

Figure 6.17 shows that the SHFRCC resembles the performance of the specimens confined with stirrups at a spacing of 50 mm. The stress values of the F5S5 cylinders are corrected by dividing the total load to the confined area and the adjusted diagrams are compared in Fig. 6.18 with those of one of SHFRCC with 12 mm PVA fibers. Values of lateral strain of the F5S5 specimens are not considered

since the extensometer that was placed on the perimeter of the specimen measures the total lateral deformation that occurred both in the confined core and the cover of the specimen.

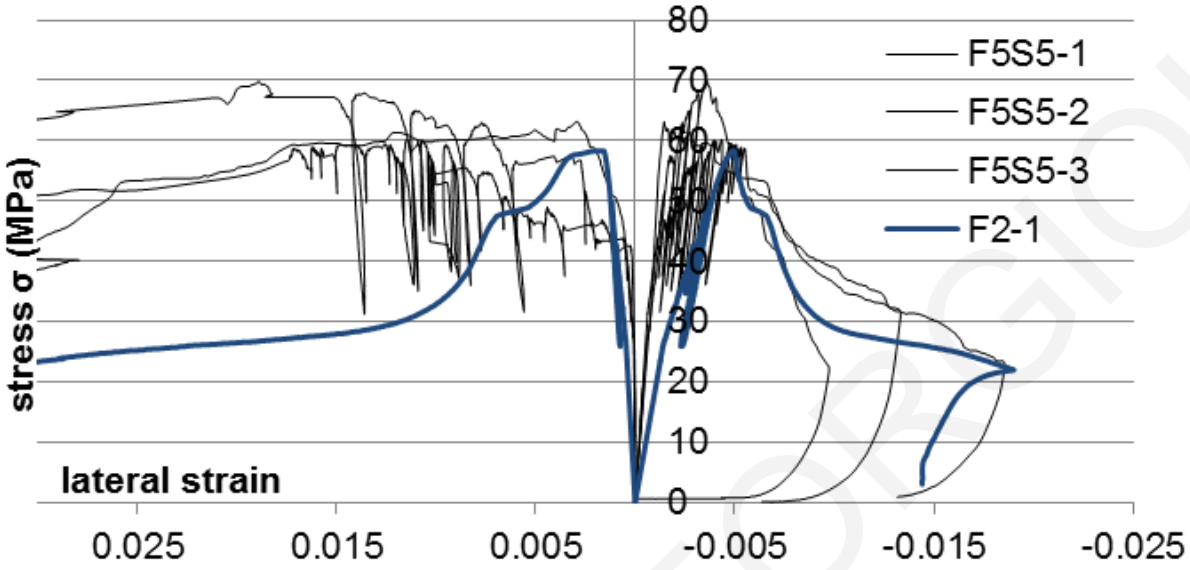

Figure 6.18: Stress-axial/lateral strain of compression test for stirrup confined specimens (F5S5) and SHFRCC (mix F2-12mm PVA fibers)

The equivalent confining pressure provided by the stirrups in the F5S5 specimens is calculated based on Eq. 6.7.

$$\sigma_{lat} = \alpha_s \cdot \rho_v \cdot f_{y,st} / 2 \qquad (6.7)$$

where $\alpha_s=(1-s/(2d'))^2=(1-(42/2/62))^2$ = 0.43, $\rho_v=4\cdot50\cdot3.14\cdot62/(3.14\cdot62^2\cdot50)$ = 6.4% and $f_{y,st}$=500 MPa. Therefore the lateral confinement provided by the 8mm stirrups at a spacing of 50 mm is equal to $\sigma_{lat}=0.43\cdot6.4\%\cdot500/2=7.2$ MPa. This is the equivalent confining stress that is also provided by the fibers to the SHFRCC specimens (F2-1). Revisiting Table 5.2 that gives the characteristic points of the split cylinder tests on the specimens with the F2 mix design one can find that the average splitting strength of the F2 mix specimens was calculated as 7.7 MPa. In conclusion it is found that the confining pressure provided by the fibers equals to its splitting strength by considering that its lateral confinement matches the confinement provided by the stirrups with a spacing of 50 mm.

6.8 Summary and Closure

Within this Chapter the behavior of fiber reinforced strain hardening composites under uniaxial compression was studied, and a quantitative comparison of the confining effect of the fibers was obtained through parallel tests on the plain matrix and the plain matrix confined by stirrups or FRP sheets. A model was proposed for the simulation of the uniaxial stress-strain curve as well as equations determining the equivalent stress block parameters of SHFRCC for analysis purposes. The lateral and volumetric behavior of the composites was investigated with the results obtained from a

circumferential extensometer used in the experimental study. Lateral strain is a modified amount of the internal cracking that is influenced past the inflection point by the effective fiber confinement. By using the lateral confinement provided by one of the methods (stirrups with 50 mm spacing) that had similar stress-strain curves to those obtained by one of the SHFRCC mixes (F2), the lateral confinement provided by the fibers was calculated and it was compared to the split cylinder strength provided by specimens of the same mix design concluding that lateral confinement provided by the fibers in the lateral dimension of a cylinder specimen under compression is the same as the splitting strength of that material.

Chapter 7: Flexural Behavior of Reinforced SHFRCC (R/SHFRCC) members

7.1 Introduction

In this Chapter the results of the Steel Reinforced beams comprising fiber-reinforced strain hardening cementitious composites (R-SHFRCC) are presented in order to discuss the mechanical response of structural members constructed with SHFRCC. In previous chapters it was shown that when PVA fibers are used to reinforce a cementitious mix they may contribute substantially to the flexural resistance and tension strain capacity of the composite. This Chapter summarizes a detailed experimental program that comprises a total of 18 specimens, which were tested under four point bending with shear span ratios of 2 and 3.5 in order to ensure flexural failure. Variables of the specimens were the amount of tension and compression steel reinforcement, the availability of confinement (stirrups) and the shear span aspect ratio. Test results illustrated the beneficial action of the fibers in the tensile zone of the beams through bridging of cracks and transferring loads, while in the compressive zone of the beams, fibers restrained lateral expansion and led to ductile compressive failure at very large compression strain levels.

SHFRCC materials are the future of cement based construction as they provide the opportunity for innovative technologies that exploit the great resilience of these new products. Towards this objective the present chapter focusses on flexural actions of SHFRCC components. With reference to the estimation of design parameters of reinforced flexural members comprising SHFRCC cementitious matrix, a number of reinforced beams with SHFRC matrix are examined experimentally in order to establish the parametric sensitivity of strength and deformation capacities at the onset of yielding and at the ultimate limit state. Design expressions necessary for practical dimensioning of steel reinforcement for strength and ductility are derived and corroborated through the experimental results.

Recently guidelines have been introduced for FRC as a structural material in design codes (Section 11.4.6 in ACI Building Code [48] and Model Code [49]). Despite the enhanced toughness imparted by fibers, usual fiber reinforced concretes (FRCs) included in these two Codes exhibit a drop in tensile resistance after first cracking and are referred to as strain softening materials. However, the new types of cement-based composites of the type examined in the present work (self-consolidating mortar reinforced with synthetic or steel fibers and exhibiting strain hardening behavior [4, 108]) have not yet been included in Codes.

A significant part of current research on the use of fiber composites in structural elements has been focused on the use of steel fiber reinforced concretes (SFRC). Relevant ACI provisions have been mostly supported by tests on various SFRC structural components, where the material often exhibits strain softening behavior. Recommendations specific to strain hardening cementitious composites (SHFRCC) have been published up till now only by the JSCE [50], addressing structural analysis and design of SHFRCC members. These build on the established specifications for ordinary concrete

structures [51] whereas no material-specific expressions and analysis procedures that would pertain to the strain hardening properties of the matrix in steel-reinforced SHFRCC (R-SHFRCC) members are given. Exception to this are the limit states of axial compression capacity of R-SHFRCC, and the use of SHFRCC as a strengthening material (externally bonded tension layer) to increase the flexural strength of conventionally reinforced concrete members [50].

It was illustrated in earlier chapters of this thesis that PVA fibers mixed in cementitious mortars can lead to composites with strain hardening behavior under tension [4]. To control the strength the fiber-matrix interface pertinent surfactants were introduced in the mix design to moderate the development of strong covalent bonds with the free hydroxyl ions on the PVA fibers – this procedure was described in Chapter 3 of the thesis. Note that surface-coated fibers enhance the resistance to flexure acting as pseudo-ductile reinforcement: after initial crack formation (notional yielding), the apparent ductility is achieved through controlled debonding and pulling out of the fibers that bridge the cracks, thereby increasing the members' overall toughness and resistance [136]. Thus, compared to the strain softening matrices already addressed by Codes, the SHFRCC composites sustain the tensile zone strength (thereby affect sectional equilibrium) even for tensile strains as high as 1% or more: this sustained resistance is expected to contribute to the flexural strength of a reinforced member. Furthermore, in the context of flexural behavior, the SHFRCC matrix also enhances the ductility of the compression zone due to the confining effect imparted by the fibers on the cementitious matrix [137]. The combined contribution of fibers both in the tensile and also in the compressive zones of structural R-SHFRCC members are considered here for the establishment of design expressions for flexural strength and rotation capacity of such members.

Open issues concern lower and upper limits for longitudinal flexural reinforcement so that post-cracking strength is at least equal to the cracking moment, whereas occurrence of compression failure prior to yielding of the tensile reinforcement may be precluded. These measures ensure adequate ductility in the concrete member and the structure as a whole. Although normal concrete and high strength concrete have been investigated thoroughly in this respect [97], upper limits have not been established as of yet regarding the combined use of tension steel reinforcement with tension-resilient cementitious materials to likewise ensure ductile structural behavior. The interaction of the two sources of tensile strength in the cross sectional equilibrium of a structural component is evaluated through calibration of the experimental results obtained from the tests described in Chapter 4, on reinforced-beams with SHFRCC matrix. Flexural sectional analysis is used to provide insights with regards to the strain and stress distribution over the cross section at characteristic points of response. A model for designing cross-sections of SHFRCC structural elements is subsequently developed based on the experimentally calibrated stress-strain laws of the material in tension and compression which was described in Chapters 5 and 6.

7.2 Current Bibliography-Research on R/SHFRCC flexural members

To establish a context for the present investigation the international experimental literature on SHFRCC-steel reinforced beams is reviewed in the present section. It is noted that the number of tests is still considered very sparse because of two factors: (a) The great variability in the mix design and fiber types used, and (b) the difficulty in producing large batches of the novel mixes as this type of production at a large scale requires expensive mixing facilities. So the available specimens for the most part are intensely variant. Of the various published works two are of greater relevance to the objective of the present chapter, as follows:

Han et al. [138] performed a series of tests on reinforced concrete members under flexure by replacing concrete with SHFRCC. The reinforcing steel was a specially developed steel with a yield strength in the order of 800 MPa with control specimens having steel of normal yield value of 400 MPa. For the case of the normal yield reinforcement the specimen with the SHFRCC matrix (NTB-EXPE 70) exhibited superior behavior to the normal concrete specimen (NTB-CON 70), with the creation of multiple cracking both in the constant moment region but also in the shear spans, increasing flexural ductility (see Fig. 7.1). The beam with the steel of higher yield strength and normal concrete (HTB-CON 70) showed 20% greater load capacity in regards to the normal steel reinforced beam, but excessive shear cracks were formed leading the beam to shear failure, something that was avoided when the concrete was replaced with SHFRCC (HTB-EXPE 70) and the multiple cracking behavior appeared with 90% increase in the load bearing capacity.

Figure 7.1: Failure behavior of beams (130×170×1460 mm) [138]

Alyousif et al. [139] studied the behavior of ECC beams with various steel reinforcement ratios and shear span ratios (1, 2 and 3) and a constant cross-section of 125×250 mm, with the details as shown in Fig. 7.2. Due to the high amounts of steel reinforcement all beams consisting of normal concrete failed in shear contrary to the beams with the same shear span ratios and percentage of reinforcement but with

SHFRCC that experienced yielding of the flexural reinforcement. Beams with the lowest shear span ratio of 1 failed in shear, one of the beams of shear span ratio of 2 had a combined shear/flexural failure while the other had a clear flexural failure with crushing of the concrete in the compression zone of the beam. The beams with the longest span ratio of 3 failed in a flexural manner with crushing of the compression zone.

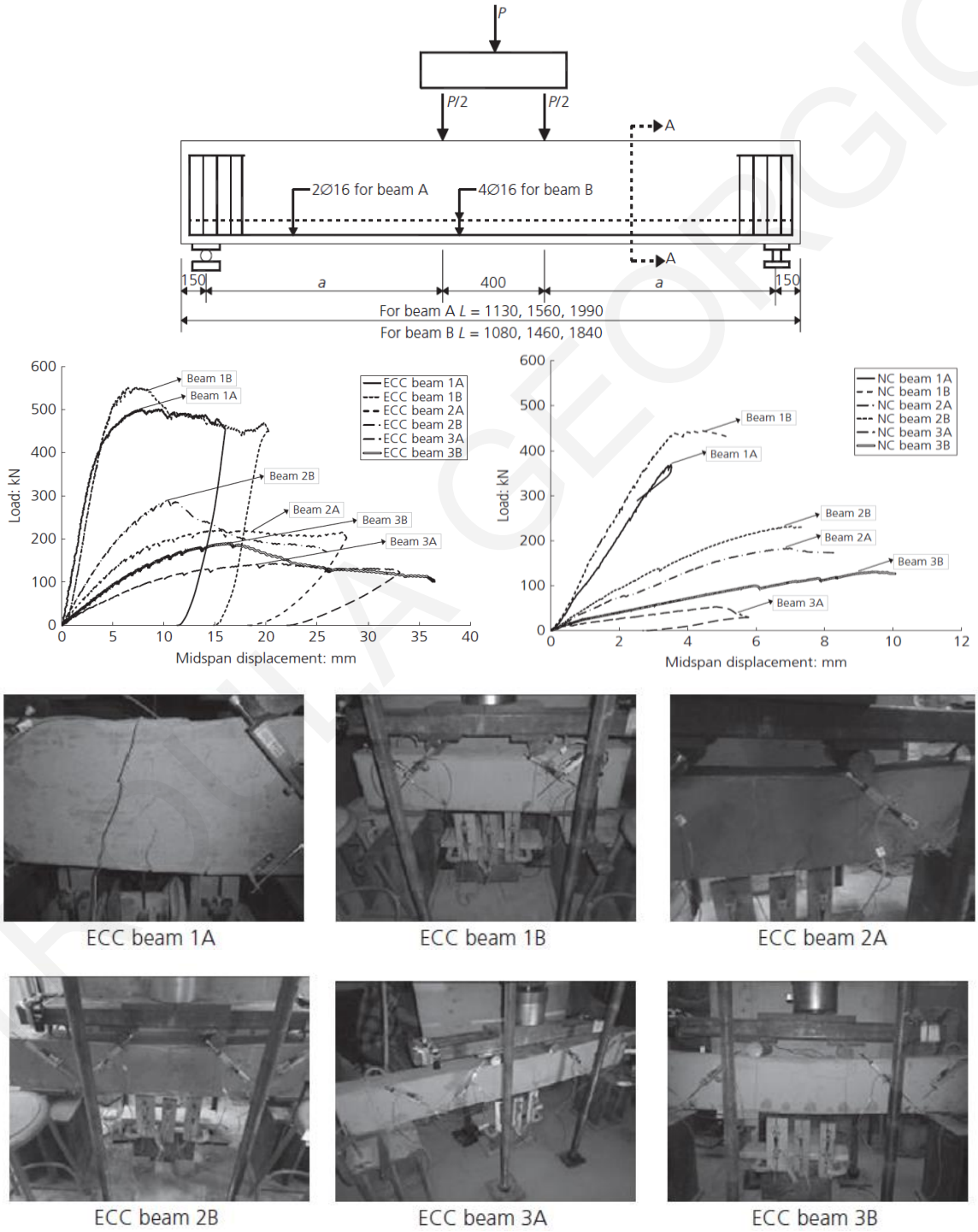

Figure 7.2: Beam details of Alyousif et al. [139] and Load-deflection curves

7.3 Description of the test data

The scaled reinforced prismatic members studied in the thesis were tested under four point bending in order to investigate the flexural behavior of steel-reinforced SHFRCC components (R-SHFRCC). Control samples were also tested with the same mix proportioning as the SHFRCC but without the use of fibers. The four point bending test was chosen as it enables the study of pure flexural response in the constant moment region. With this specimen form, and provided that the shear strength exceeds the shear forces developed in the shear span, flexural failure occurs within the constant moment region. Parameters of study in the experimental program were: (a) The effect of using tension-resilient materials on the flexural capacity of a beam, (b) the interaction of the SHFRCC and reinforcement in excess of the balanced section reinforcement ratio, and (c) the use of compression reinforcement and (d) confinement through the additional use of stirrups. All the beams had a 100mm square cross section, while the shear span ratio (= the distance between the load application point and the support, normalized by the beam sectional height (h)) took on values of 2 and 3.5 by increasing the length of the shear span. The beams were designed so as to avoid shear failure by opting for shear span ratios a/h≥2 and by the simultaneous use of stirrups. The central constant moment region between the points of load application was 100mm for all specimens. Figure 7.3 shows the beam reinforcement configuration and the loading setup as well as the deflection recording system. Five LVDTs were used to record the vertical deflections at the support points, under the load points and at the beam midspan.

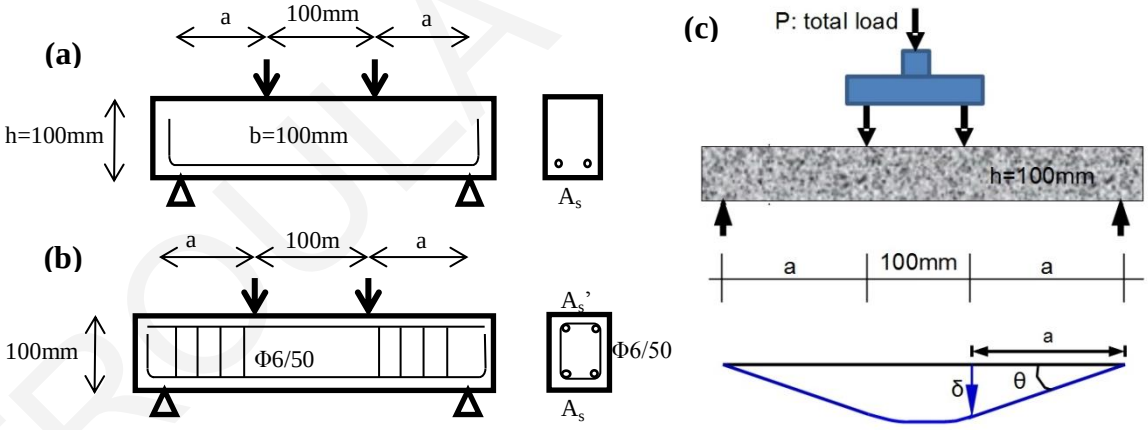

Figure 7.3: Test configuration for four point bending and reinforcement details for a) beams with flexural reinforcement and b) beams reinforced with longitudinal bars in the compressive and tensile region and stirrups to eliminate shear failure, c) definition of specimen rotation θ in the shear span (reference to rotation capacity)

Table 7.1 lists the type of matrix used, the a/h ratio, and the steel reinforcement ratios for tension (ρ_s), compression (ρ_s'), and the transverse reinforcement ratio comprising rectangular stirrups, (ρ_w). Three identical specimens were tested for each parameter combination. Reinforcement ratios are defined as follows:

$$\rho_s = \frac{A_s}{b \cdot d} \quad , \quad \rho_s' = \frac{A_s'}{b \cdot d} \quad , \quad \rho_w = A_{st} \cdot \frac{b_c + d_c}{b_c \cdot d_c \cdot s} \tag{7.1}$$

Parameters A_s, A_s' represent the areas of tension and compression reinforcement, whereas A_{st} is the area of the stirrup bar; b and h are the width and height of the member cross section, b_c and d_c are the width and depth of the confined core (measured to the centroid of the stirrup), s is the spacing of stirrups (on centers – o.c.) and d is the effective depth of the cross-section.

Table 7.1: Beam denomination, cementitious composite, shear span ratio and reinforcement

Denom.	**Mix. Design.**	**a/h**	**Bottom Reinf.**	**Top Reinf.**	**Stirrups**	ρ_s	ρ_s'	ρ_w
F10-BS1/BS2/BS3	F10	2	2Φ8	2Φ6	Φ6/50	0.0132	0.0074	0.021
F7-S14/S15/S16	F7	2	2Φ8	-	-	0.0132	-	-
F7-SS17/SS18/SS19	F7	2	2Φ8	2Φ8	Φ6/50	0.0132	0.0132	0.021
F7-S8/S9/S10	F7	3.5	2Φ8	-	-	0.0132	-	-
F7-SS1	F7	3.5	2Φ8	2Φ8	Φ6/50	0.0132	0.0132	0.021
F9-S1/S2/S2	F9	2	2Φ14	2Φ6	Φ6/50	0.0405	0.0074	0.021

In support of the flexural tests, specimens were prepared and tested for characterization of the cementitious material (uniaxial tensile and compressive strength) and steel reinforcement used in the beams. The materials' complete stress-strain expressions were used later in evaluating the flexural strength of the members. Again, three specimens were tested for each material and for each type of test done. Material properties are shown in Table 7.2 for the steel bars, Table 7.3 for the tensile properties and Fig. 7.4 for the uniaxial compressive behavior of the cementitious matrices.

Table 7.2: Steel reinforcement characteristic points from tensile tests

Steel Reinf.	ε_{sy}	ε_{sh}	ε_{su}	f_{sy}	f_{sh}	f_{su}
φ6	0.0026	0.026	0.02	312	320	376
φ8	0.0026	0.038	0.02	537	539	606
φ14	0.0036	0.023	0.02	559	573	663

Table 7.3: Tensile stress-strain curve characteristic points for tested mixes

SHFRCC tension	ε_{ty}	ε_{tmax}	ε_{tu}	f_{ty}	f_{tmax}
F7	0.000125	0.0080	0.013	2.5	2.8
F9	0.000500	0.0065	0.020	3.0	3.7

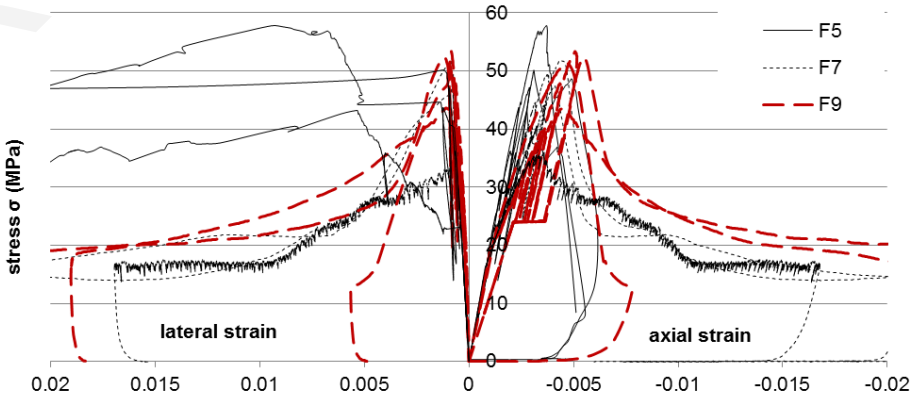

Figure 7.4: Stress-axial strain (right) and Stress-lateral strain (left) for uniaxial compression

7.4 Experimental behavior of beams under flexure

The resistance curves of the specimens from the four-point bending tests are depicted in Fig. 7.5. Photo inserts for one of the three tested specimens in each group are shown to illustrate the cracking pattern developed and the type of failure. The vertical axis in the plots represents the total machine load (P). Moment capacity is calculated from the product M=a·$(P/2)$, where a is the shear span (=aspect ratio times the cross sectional height). The control specimens which were fabricated with the Plain Cementitious Mix (specimens F10-BS1/BS2/BS3, no fibers) showed the typical reference reinforced concrete beam behavior, i.e.: (a) The load increased linearly with increasing deflection up to yielding of the longitudinal tension reinforcement; (b) Strain hardening occurred after yielding and up to the failure load, which in this case was marked by crushing of the cementitious composite cover at the extreme fiber of the beam in compression; (c) Yielding load was in the order of 32 kN (from statics, M_y=0.2 m·32 kN/2=3.2 kNm, for a=0.2 m) and the corresponding chord rotation at specimen yielding was in the order of 1% (this is calculated as the relative deflection at the load points divided by the length of the shear span, Fig. 7.3 (c)); (d) The failure load increased to 40 kN (M_u=0.2 m·40 kN/2=4 kNm).

In terms of deformation response, yielding occurred at a deflection of the load point by 2 mm, whereas the maximum deflection reached 6mm, which corresponds to a chord rotation of θ=6mm/200mm=0.03=3% and a chord rotation ductility of μ_θ=3, since θ_y=2 mm/200 mm=1%).

The results from the beams with the fiber reinforced composites with a low ratio of tensile reinforcement (beams with ρ_s=0.0132) demonstrated a different type of behavior: For the beams with a shear span ratio of 2 yielding of longitudinal reinforcement (at a load P=45 kN) was preceded by an instantaneous increase in load capacity up to a maximum load (P=50 kN) and was followed by a small loss of strength to the level of a residual load that remained almost constant thereon (P=40 kN), up to large deflection values in the order of 20 mm ($\mu_\delta=\delta_u/\delta_y$=20/2.5=8). This reduction appeared concurrently with localization of strain at the location of a single crack that initiated within the constant moment region. Even though crack localization was evident, load capacity was maintained at an almost constant value. During crack localization, cracking of the extreme layer under compression was observed, but fibers bridging the cracks and transferring load prevented the occurrence of spalling of cover material. The main difference between the beams with the low shear span ratio of a/h=2 and the higher shear span ratio a/h=3.5 is that in the latter case no shear cracks were reported in the shear span lengths. SHFRCC specimens with the smallest shear span ratio that contained no shear reinforcement (F7-S14/S15/S16) exhibited a lower postpeak flexural moment capacity as compared with specimens that contained both compression reinforcement and steel stirrups (F7-SS17/SS18/SS19). This is attributed to the shear strength and confining action imparted by the stirrups and the commensurate increase of the axial strength of the compression zone.

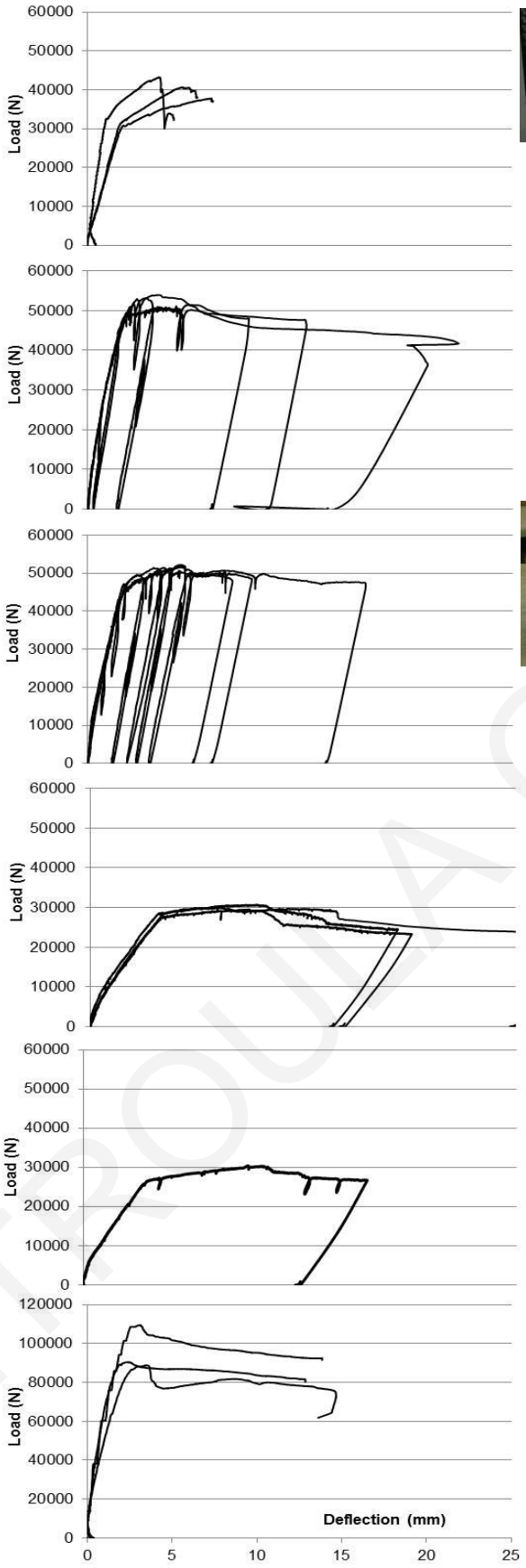

F10BS2, ρ_s=0.0132, ρ_s'=0.0074, ρ_w=0.021

F7S16, ρ_s=0.0132, ρ_s'=0, ρ_w=0

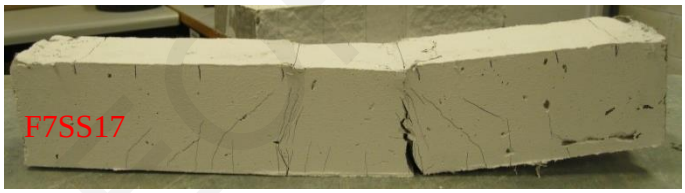

F7SS17, ρ_s=0.0132, ρ_s'=0.0132, ρ_w=0.021

F7S10, ρ_s=0.0132, ρ_s'=0, ρ_w=0

F7SS11, ρ_s=0.0132, ρ_s'=0.0132, ρ_w=0.021

F2TC, ρ_s=0.0405, ρ_s'=0.0074, ρ_w=0.021

Figure 7.5: Load-deflection diagrams of four point bending tests on small scale beams with reinforcement and corresponding failure cracks

In the case where the greatest amount of tensile reinforcement ratio had been used (beams F9-S1/S2/S2), the behavior remained ductile but it was obvious that the neutral axis appeared to shift toward the middle of the depth of the beam, subjecting a large area of the cross section under compression. In this case, the load experienced a postpeak reduction after attaining its peak value. The peak value was associated with yielding of the flexural reinforcement and reached values of 90 kN. Increasing the deflection beyond the limit associated with the peak moment magnitude led to a reduction of member resistance to a residual strength lower than the yield capacity. The residual strength, in the order of 80 kN, was maintained to large levels of deformation. Note here that residual strength is in the order of 85% of the maximum load, a value used for R/C structures to calculate ductility. Ultimate deflections reached values of 15 mm, giving deflection ductility of $\mu_\delta=\delta_u/\delta_y$=15/2.5=6.

7.5 Analysis of the results

7.5.1 Cross sectional analysis

In order to better understand the mechanics underlying the experimentally observed behavior of the R-SHFRCC specimens the moment-curvature relationship was calculated for the cross-sections examined in order to relate selected milestone points of the behavior to the materials' state of stress and strain at each point. To this end, a minimum of three points are required to define the full moment-curvature behavior of the R-SHFRCC beams. These are, (a) yielding of the flexural steel reinforcement, (b) flexural strength, and (c) residual moment at failure. Using the plane sections remaining plane and normal to the member axis assumption, layered analysis is conducted to evaluate through iteration the neutral axis depth, x, that will satisfy force equilibrium ($\Sigma N_i=0$) for a given curvature value (ϕ); flexural moment about the centroid of the cross section is calculated for the converged value of x. Materials' stress-strain laws in tension and compression used in this analysis were obtained by curve fitting of the experimental envelopes obtained from the respective material tests, as follows.

(a) Stress-strain relationship for steel reinforcement in tension and compression:

$$\begin{aligned} &\text{for } \left|\varepsilon_{s,i}\right| \le \varepsilon_{sy}:\ \sigma_{s,i}=E_s\cdot\varepsilon_{s,i};\quad \text{for}\,\varepsilon_{sy}<\left|\varepsilon_{s,i}\right|\le\varepsilon_{sh}:\sigma_{s,i}=\text{sgn}(\varepsilon_{s,i})\cdot f_{sy};\\ &\text{for}\left|\varepsilon_{s,i}\right|>\varepsilon_{sh}:\ \sigma_{s,i}=\text{sgn}(\varepsilon_{s,i})\cdot(f_{sy}+(\left|\varepsilon_{s,i}\right|-\varepsilon_{sy})\cdot e\cdot E_s) \end{aligned} \tag{7.2}$$

where ε_{sy} is the yield strain, ε_{sh} is the strain at the onset of strain hardening, and e the strain-hardening ratio (Fig. 7.6 (a)); (sgn is the sign function).

(b) Cementitious composite in tension:

Based on the test results the matrix response in uniaxial tension is linear up an apparent yielding strain, ε_{ty}, followed by strain hardening up to a strain of ε_{tmax}; upon crack localization, strain softening ensues till failure at an ultimate strain, ε_{tu} (Fig. 7.6 (b)):

$$\text{For } \varepsilon_{ct,i} < \varepsilon_{ty}: \quad \sigma_{ct,i} = \varepsilon_{ct,i} \cdot \frac{f_{ty}}{\varepsilon_{ty}} \tag{7.3a}$$

$$\text{For } \varepsilon_{ty} < \varepsilon_{ct,i} < \varepsilon_{t\,max}: \quad \sigma_{ct,i} = f_{ty} + \left(\varepsilon_{ct,i} - \varepsilon_{ty}\right) \cdot \frac{f_{t\,max} - f_{ty}}{\varepsilon_{t\,max} - \varepsilon_{ty}} \tag{7.3b}$$

$$\text{For } \varepsilon_{t\,max} < \varepsilon_{ct,i} < \varepsilon_{tu}: \quad \sigma_{ct,i} = f_{t\,max} - \left(\varepsilon_{ct,i} - \varepsilon_{t\,max}\right) \cdot \frac{f_{t\,max}}{\varepsilon_{tu} - \varepsilon_{t\,max}} \tag{7.3c}$$

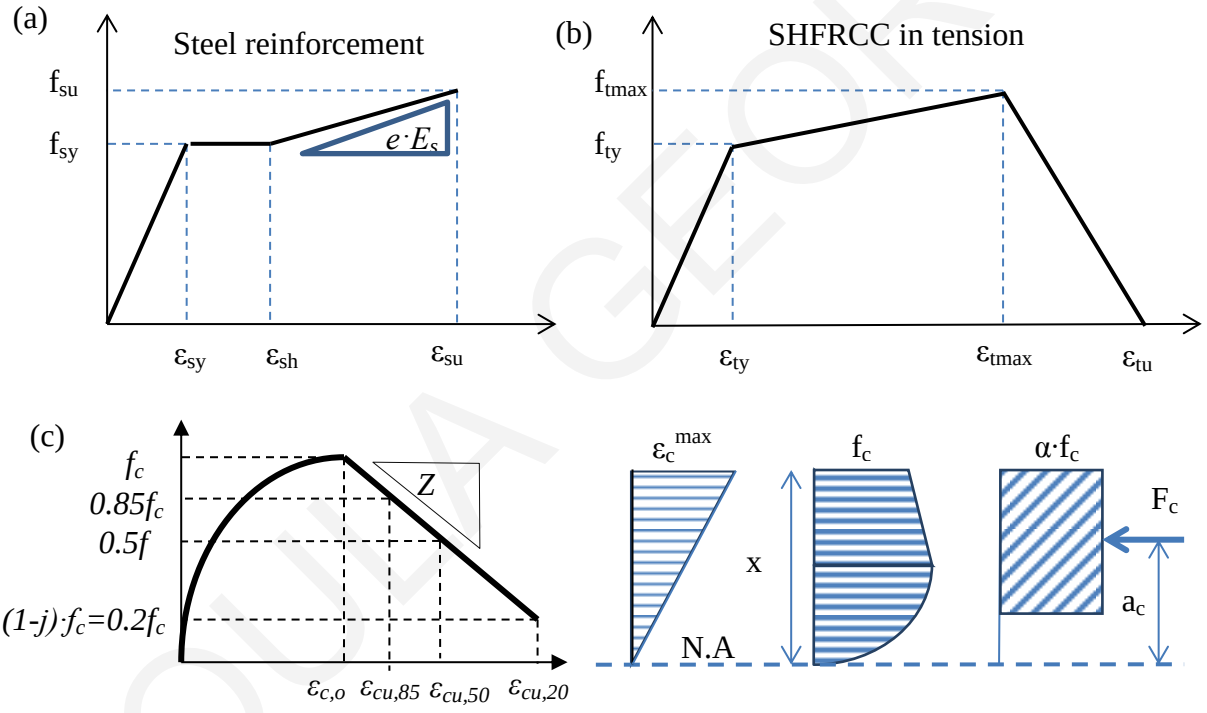

Figure 7.6: (a) Steel reinforcement material law, (b) Fiber reinforced cementitious composite material law under tension and (c) Stress-strain law under compression and equivalent stress block

(c) Cementitious composite in compression

The stress-strain relationship assumed for concrete under uniaxial compression is shown in Figure 7.6 (c). The ascending branch is approximated using a Hognestad type parabola (Eq. 7.6 (c)) extending from zero stress to the compressive strength (f_c), with ε_{co} the strain corresponding to the peak compressive stress. Beyond that strain value the strength degrades with increasing compressive strain. This behavior is modelled using the confinement model by Park et al. 1982 [131], whereby the slope of the descending branch, Z is calculated from the postpeak strain ($\varepsilon_{cu,50}$) associated with a 50% reduction of strength ($Z=0.5 f_c/(\varepsilon_{cu,50} - \varepsilon_{co})$), (Eq. 7.4b, Fig. 7.6 (c)). Values of maximum stress, strain at

maximum stress and slope of the descending branch are obtained after calibration of this model with the results of the experimental uniaxial compression tests conducted on composite samples and are listed in Table 5. Parameter (*j*) in Equation (4b) marks the fraction of compression resistance lost at the ultimate strain of the composite, i.e., $j=1-(f_u/f_c)$. Therefore,

For $\varepsilon_c<\varepsilon_{co}$ $\quad \sigma_c = f_c\left[2\frac{\varepsilon_c}{\varepsilon_{co}}-\left(\frac{\varepsilon_c}{\varepsilon_{co}}\right)^2\right]$ (7.4a)

For $\varepsilon_{co}<\varepsilon_c<\varepsilon_{cu}$ $\quad \sigma_c = f_c-(\varepsilon_c-\varepsilon_{co})\cdot Z \geq (1-j)\cdot f_c$ (7.4b)

Ultimate strain ε_{cu} is defined at a residual stress equal to 20% of the material compressive strength (Table 7.4). When longitudinal and transverse reinforcements confine the compression zone the values of ε_{co}, maximum compressive stress f_c, and ε_{cu} increase, whereas |Z| decreases (the postpeak branch descends more mildly). The confinement model of Park, Priestley and Gill [131] is used to represent the behavior of the confined material in compression; parameter ρ_w represents the volumetric ratio of steel stirrup reinforcement (calculated as per Eq. 7.1).

$$f_{cc} = f_c + \rho_w \cdot f_{yw}\ , \qquad \varepsilon_{cc} = \varepsilon_{co}\cdot\left(\frac{f_{cc}}{f_c}\right)^2; \qquad \varepsilon_{cc,50} = \varepsilon_{c,50} + \lambda\cdot\rho_w\cdot\left(\frac{b_c}{s}\right)^{1/2} \tag{7.5}$$

Parameter (λ) quantifies the effectiveness of confinement. In the reference model, λ = 0.75 for normal-weight concrete. In the case of the fiber cementitious matrix this constant (λ) may take on values greater than 0.75 on account of the confining effect exerted by the fibers. A sensitivity analysis is conducted here in order to study the effect of λ on the calculated *M-ϕ* relationship of an R-SHFRCC cross section. Table 7.4 lists the values considered for λ for all mixes.

Table 7.4: Material parameters and characteristic points of stress-strain diagrams under compression

Unconf.	**E (MPa)**		**$\sigma_{c,o}$**	**$\varepsilon_{c,o}$**	**$\varepsilon_{c,50}$ (50% f_c)**	**Z (MPa)**	**$\varepsilon_{cu,20}$**
F5	19653		50.37	0.00319	0.00497	14148.876	0.006038
F7	19901		49.30	0.003395	0.00702	9278.277	0.009195
F9	20149		48.22	0.00360	0.00907	4407.678	0.012352
Confin.		**λ**	**$\sigma_{cc,o}$**	**$\varepsilon_{cc,o}$**	**$\varepsilon_{cc,50}$ (50% f_c)**	**Z (MPa)**	**$\varepsilon_{ccu,20}$**
F5	19653	0.75	60.0640	0.00453	0.039244	865.286	0.060068
F7	19901	1	59.58	0.00496	0.046395	718.890	0.071257
F9	20149	0.75	58.50	0.00529	0.038602	878.331	0.058583
F9	20149	0.85	58.50	0.00529	0.042539	785.462	0.064883
F9	20149	1	58.50	0.00529	0.048445	677.940	0.074333

7.5.2 Observations for Moment-Curvature Response from Test and Analysis

To enable interpretation of the experimental results the experimental response is corroborated through flexural analysis with particular emphasis on the state of stress that occurs in the critical sections in the constant moment region (where failure occurred). Calculated *M-ϕ* diagrams are plotted in Figure 7.7 for all specimens of the experimental program, as well as the corresponding stresses for a

sample of the specimens. Specific benchmarks marked in the figures correspond to (i) first cracking of the composite, (ii) attainment of maximum tensile strength in the extreme tensile fiber, (iii) maximum tensile strain of the extreme layer under tension, (iv) yielding of the flexural steel reinforcement, (v) attainment of compressive strength in the extreme compressive fiber, and (vi) attainment of ultimate compressive strain capacity in the extreme compressive fiber.

A bilinear *M-ϕ* was obtained in the case of the reference beams containing no fibers (F10-BS1/BS2/BS3) resembling the response of ordinary under-reinforced concrete beams (here the term under-reinforced refers to the content of tension reinforcement being kept below the balanced failure limit, i.e. $\rho<\rho_{bal}=0.4f_c/f_y$, as per Park and Pauley [140]). Eventual failure occurs either by crushing of the compression zone or rupture of the steel reinforcement in tension. However, the characteristics of the M-ϕ diagram of R-SHFRCC members depend mostly on the amount of the flexural reinforcement ratio (Fig. 7.7). In specimens with lower amounts of flexural reinforcement (F7-S14/S15/S16, F7-SS17/SS18/SS19, ρ_s= 0.0132) the familiar bilinear behavior of common under-reinforced concrete beams persists, but the displacement ductility is significantly enhanced, to $\mu_\Delta=\delta_u/\delta_y$=15/2=7.5 (mm/mm). Both analysis and tests of F7-SS17/SS18/SS19 (ρ_s= 0.0132) concur to a flexural moment strength increase over F10-BS1/BS2/BS3 by almost 25% owing to the contribution of the fibers in the tensile zone. Beyond yielding of the flexural reinforcement the flexural strength increased with the magnitude of imposed deformation up to the point where the extreme layer under tension attained the ultimate tensile strain of the composite (ε_{tu}). Upon further increase of imposed displacement beyond the peak point, strain localization occurred, manifested in the load displacement envelope with a rather mild softening branch. As illustrated by sectional analysis, failure was initiated after the extreme compressive layer attained the failure strain, $\varepsilon_{cu,20}$.

In the case of the beams F9-S1/S2/S2 the ratio of tension reinforcement was three times as high as the reinforcement ratio used in the previous cases. Despite the multiple cracking demonstrated by these specimens it was obvious from the cracking patterns that the compressive zone extended down to half the height of the beam and an extensive crushing zone was established almost from the beginning of the test. As evidenced in the *M-ϕ* curve, concrete strains in the extreme compression fiber exceeded the strain at peak stress (ε_{co}), even prior to yielding of the flexural reinforcement. Upon reinforcement yielding the *M-ϕ* curve starts to decay from peak, owing to the large strains in the compressive zone that correspond to the post-peak softening branch of the *σ-ε* curve for SHFRCC in compression; to maintain equilibrium of axial forces a larger part of the cross section is engaged in tension, thereby lowering the position of the stress resultant in the compression zone and the corresponding lever arm thereby leading to a reduced flexural strength.

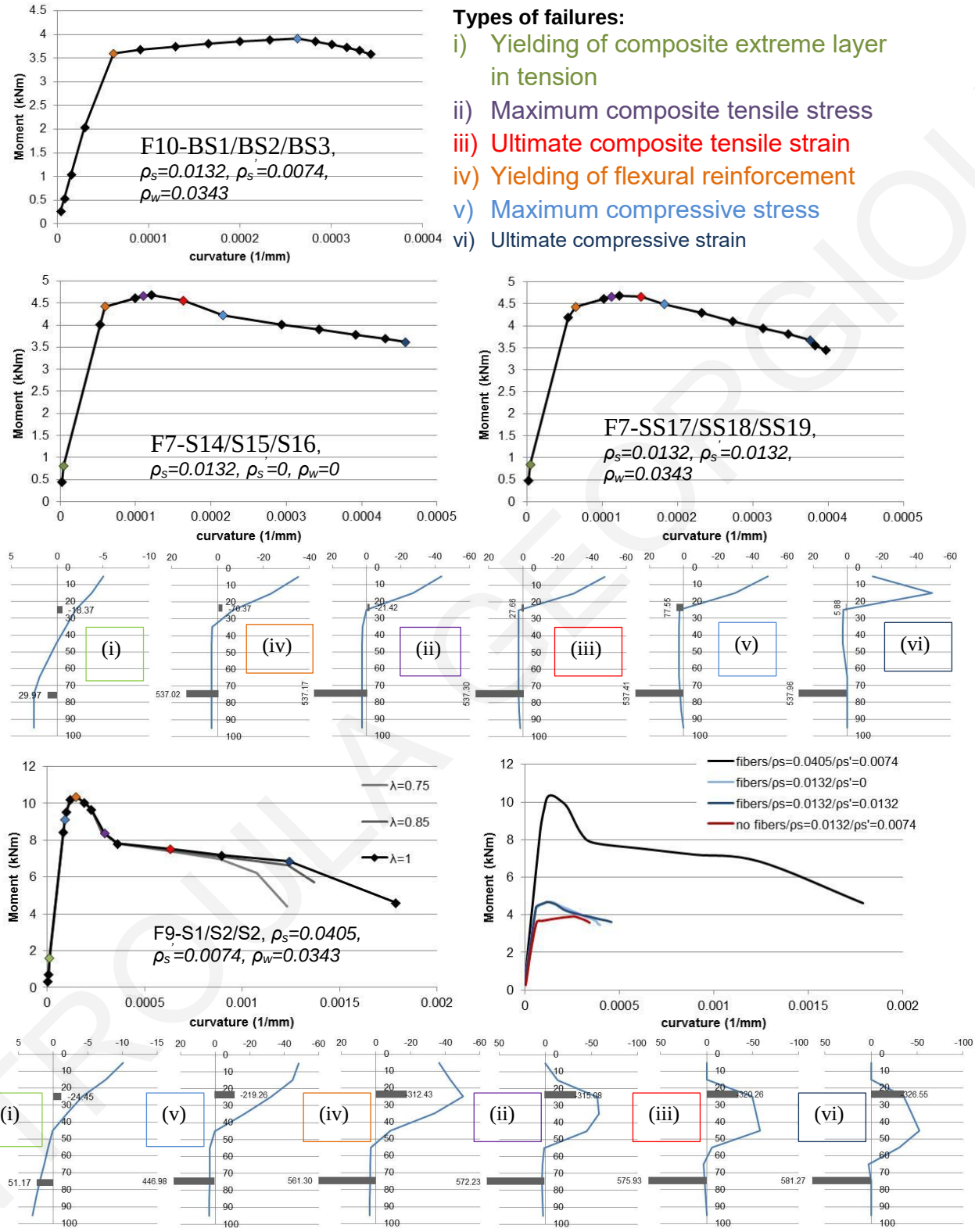

Figure 7.7: Moment-curvature relationship for all tested cross-sections.

The latter type of behavior that is attributed to the high percentage of the tensile steel reinforcement is normally not a desired type of behavior for structural design due to the sharp decrease in moment capacity just past the yielding point of flexural reinforcement. In ordinary reinforced concrete members

code provisions use upper bound limits for the flexural reinforcement ratios (ρ_s-ρ'_s) to prevent brittle behavior due to over-reinforcement. Extending the same concept to SHFRCC members a limit for the tension steel reinforcement ratio $\rho_{s,bal}$ is derived, considering the simultaneous contribution of fiber reinforcement.

7.6 Design Expressions

7.6.1 Balanced reinforcement ratio in SHFRCC matrix

In order to preclude the occurrence of concrete compression crushing prior to yielding of tension reinforcement it is an established practice in design to limit the difference in the ratios of compression and tension reinforcement to levels below a critical value referred to as $\rho_{bal} = 0.4 f_c'/f_y$, as per Park and Pauley [140] (for ductile flexural failure). Based on the M-ϕ analysis of the two example cases considered, namely F7-SS17/SS18/SS19 with a low reinforcement ratio (ρ_s=0.0132), and F9-S1/S2/S2 with a high reinforcement ratio (ρ_s=0.0405) it was observed that in the first case steel reinforcement yielding preceded attainment of the compressive strain of concrete at maximum compressive stress (ε_{co}), whereas in the latter case, concrete in the extreme layer under compression attained its maximum stress prior to yielding of the flexural reinforcement. The value ρ_s=0.0405 of specimen F2TC already exceeds the conventional limit for the nominal material strengths used herein, i.e., ρ_{bal} = 0.4·49/500=0.392. However brittle failure is mitigated on account of the ductility of the SHFRCC matrix in the compression zone. Thus, the case of the R-SHFRCC, specimens demonstrated extensive postpeak ductility (curvature ductility in the order of μ_φ=0.00124/0.000147=8.46) – although a significant moment strength loss occurred just after yielding of the reinforcement. Note however that the limit value of ρ_{bal} used in this discussion was defined considering ordinary concrete; evidently this variable cannot identify the transition between failure by yielding of the reinforcement and concrete crushing when considering R-SHFRCC members. In order to redefine the ρ_{bal} limit for R-SHFRCC the contribution of fibers to ductility and strain resilience of the cementitious composite in tension and effective confinement in compression would need to be considered.

Following the same concepts as with flexural analysis of ordinary concrete, the complexity caused by the nonlinearity of the compressive stress-strain law over a varying strain profile is simplified using an equivalent rectangular stress block of uniform stress intensity ($\alpha \cdot f_c$) in order to calculate the resultant force and its point of application in the compression zone (Fig. 7.6(c)) [70]. Expressions are listed below for the intensity and lever arm of the equivalent compressive stress block derived with reference to Eq. 7.4 (a) and (b). Parameter $\varepsilon_c^{\max}$ is the maximum compressive strain at the extreme compressed fiber of the cross-section. All strain parameters are normalized with respect to ε_{co} (normalized variables are marked by a bar: $\bar{\varepsilon} = \varepsilon / \varepsilon_{co}$).

for $\varepsilon_c^{\max} < \varepsilon_{co}$, $\alpha = \bar{\varepsilon}_c^{\max}\left(1-(\bar{\varepsilon}_c^{\max}/3)\right)$, $\mathrm{a_c} = x\cdot\left(2-0.75\bar{\varepsilon}_c^{\max}\right)/\left(3-\bar{\varepsilon}_c^{\max}\right)$ (7.6)

for $\varepsilon_{co} < \varepsilon_c^{\max} < \varepsilon_{cu}$

$$\alpha = 1-\frac{1}{3}\left(\bar{\varepsilon}_c^{max}\right)^{-1} + j\cdot\left(1-0.5\left(\bar{\varepsilon}_c^{max}\right)^{-1} - 0.5\bar{\varepsilon}_c^{max}\right)\cdot\left(\bar{\varepsilon}_{cu}-1\right)^{-1} \quad (7.7a)$$

$$\mathrm{a_c} = x\cdot\frac{1-\frac{1}{6}\left(\bar{\varepsilon}_c^{\max}\right)^{-2} + j\cdot\left(1-\frac{1}{3}\left(\bar{\varepsilon}_c^{\max}\right)^{-2} - \frac{2}{3}\bar{\varepsilon}_c^{\max}\right)\left(\bar{\varepsilon}_{cu}-1\right)^{-1}}{2-\frac{2}{3}\left(\bar{\varepsilon}_c^{\max}\right)^{-1} + j\cdot\left(2-\left(\bar{\varepsilon}_c^{\max}\right)^{-1} - \bar{\varepsilon}_c^{\max}\right)\left(\bar{\varepsilon}_{cu}-1\right)^{-1}} \quad (7.7b)$$

Where *j* has been defined earlier as the strength loss fraction endured by concrete when it reaches its residual capacity. With reference to the case of pure flexure, the height of the compression zone (x) is obtained from equilibrium of forces on the cross section of the flexural member:

$$\Sigma \mathrm{N} = 0 \Rightarrow a\cdot x\cdot f_c\cdot b = f_{ct}^{ave}\cdot(h-x)\cdot b + A_s\cdot f_y \Leftrightarrow x = d\,\frac{f_{ct}^{ave}+\rho_s\cdot f_y}{a\cdot f_c + f_{ct}^{ave}} \quad (7.8)$$

Upon substitution of Eq. (7.6-7) and setting the strain in the extreme layer under compression equal to the strain at peak compressive stress, $\varepsilon_c^{\max} = \varepsilon_{co}$ (therefore $\bar{\varepsilon}_c^{max} = 1$), it follows that $\alpha = \bar{\varepsilon}_c^{\max}\left(1-(\bar{\varepsilon}_c^{\max}/3)\right) = 0.666$ and $\mathrm{a_c} = x\cdot\left(2-0.75\bar{\varepsilon}_c^{\max}\right)/\left(3-\bar{\varepsilon}_c^{\max}\right) = 0.625\cdot x$. Parameter ϕ_{bal} is defined as the curvature for which steel reinforcement will reach yielding ($\varepsilon_{s,i}=\varepsilon_{sy}$) and the extreme concrete strain in the compression zone will be at the point of peak stress, ε_{co}. Thus, ϕ_{bal} may be used to differentiate the mode of failure. By replacing ($\mathrm{a_c}$) and (α) in Eq. 7.8 and by using the geometric relations of the neutral axis depth based on the linear distribution of strains the balanced reinforcement ratio is resolved.

$$\Rightarrow x = \frac{f_{ct}^{ave}+\rho_s\cdot f_y}{0.666\cdot f_c + f_{ct}^{ave}}d = \frac{\varepsilon_{co}}{\varepsilon_y+\varepsilon_{co}}\cdot d \Rightarrow \rho_{sbal} = \left[\left(\frac{\varepsilon_y}{\varepsilon_{co}}+1\right)^{-1}\cdot\left(\frac{2}{3}+\frac{f_{ct}^{ave}}{f_c}\right) - \frac{f_{ct}^{ave}}{f_c}\right]\cdot\frac{f_c}{f_y} \quad (7.9)$$

It is noted here that the balanced reinforcement ratio is mostly related to the compressive strength of the composite in question; the tensile strength of the composite is also a parameter, however, it affects the result to a lesser extent. The limit of Eq. 7.9 for the case of F7-S14/S15/S16 is ρ_{sbal}= 3.2% lower than that established for normal concrete (where the contribution of concrete in tension is neglected). The balanced ratio according to the experimental results marks the state of strain in the extreme layer under compression that can be used to determine Moment Capacity of a cross-section. If $\rho_s < \rho_{bal}$ then the state of stress in the extreme layer under compression lies on the ascending branch of the stress-strain law (use of Eq. 7.4a and 7.6) whereas if $\rho_s > \rho_{bal}$ the state of stress is in the descending branch (use of Eq. 7.4b and 7.7).

7.6.2 Design Expressions for the Flexural Strength of R-SHFRCC elements

To simplify the problem of practical design of R-SHFRCC the following simplifying assumption has been made: Average uniform tensile stress is taken for the tensile zone of the cementitious composite $f_{ct}^{ave} = 0.5(f_{cty} + f_{ctmax})$ for calculations leading to and at yielding of the flexural reinforcement (M_y); the material tensile strength, $f_{ct,max}$ is used for the estimation of the moment capacity (M_{max}). Based on the above assumption and the cross-sectional analysis of the beams with tensile reinforcement lower than ρ_{sbal} equilibrium of moments and forces is used to derive closed form expressions for the determination of the moment capacity of reinforced SHFRCC beam sections, with reinforcement only in the tensile zone (singly-reinforced) and reinforcement in both the tensile and compressive region (doubly reinforced).

7.6.2.1 Singly-reinforced SHFRCC sections

Three benchmark points are used to define the resistance curve of the R-SHFRCC beams in the case when the reinforcement ratio in the tensile zone is lower than the balanced reinforcement ratio. These are, (a) the point where the flexural reinforcement first reaches yielding ($\varepsilon_s = \varepsilon_{sy}$), (b) the point at peak flexural strength - that point is characterized by strain at the extreme tension fiber reaching the strain value at peak stress as determined by the uniaxial tension test ($\varepsilon_{ct} = \varepsilon_{ct,max}$) (as is shown by the cross sectional analysis Fig. 7.7) and (c) the point in the softening branch where the extreme compression layer reaches the limit of 80% strength loss ($\varepsilon_c = \varepsilon_{cu,20}$) and is the residual moment that remains constant for a great range of curvature after a substantial loss of resistance. The flexural moment at each of these benchmark points is determined based on the equations that correspond to the strain profiles at the respective points depicted in Fig. 7.8.

Force equilibrium is used in all cases to determine the neutral axis depth. The depth of compression zone x, normalized by height of the cross section is denoted by ξ. The equations of the resultant forces are the same for cases (a) and (b), whereas they change in case (c) owing to the reduced acting depth of the composite in tension, marked by $z=\zeta \cdot h$. Note that as tension cracks penetrate deeper into the tension zone, the active depth of this zone $z<h-x$ (i.e., $\zeta<1-\xi$) where tensile stresses may develop in the composite is gradually reduced.

For cases (a) and (b)

$$\Sigma N = 0 \Rightarrow a \cdot x \cdot f_c \cdot b - f_{ct}^{ave} \cdot (h-x) \cdot b - A_s \cdot f_y = 0 \Rightarrow \xi = \left(\rho_s \frac{f_{sy}}{f_c} + \frac{f_{ct}^{ave}}{f_c} \right) / \left(\alpha + \frac{f_{ct}^{ave}}{f_c} \right) \quad (7.10a)$$

For case (c)

$$\Sigma N = 0 \Rightarrow a \cdot x \cdot f_c \cdot b - f_{ct}^{ave} \cdot z \cdot b - A_s \cdot f_y = 0 \quad (7.10b)$$

The flexural moment of a beam with flexural reinforcement and strain resilience of the cementitious composite may be determined from the profile of Fig. 7.8 (a), as the combined moment produced by the flexural reinforcement and the composite in tension:

$$M = F_t \cdot \left(a_c + \frac{h-x}{2} \right) + F_s \cdot (d - x + a_c) = f_{ct}^{ave} \cdot (h-x) \cdot b \cdot \left(a_c + \frac{h-x}{2} \right) + A_s \cdot f_y \cdot (d - x + a_c) \quad (7.11a)$$

In the case of the ultimate strength prior to failure by crushing of the extreme layer under compression, fibers only act within a tension zone close to the neutral axis with a height determined as z, therefore the equation for computing the normalized flexural Moment at that critical point becomes:

$$M_u = f_{ct}^{ave} \cdot z \cdot b \cdot \left(a + \frac{z}{2} \right) + A_s \cdot f_y \cdot (d - x + a) \quad (7.11)$$

An example of application of the above analysis is given in Table 7.5 where the results are corroborated with the experimental values.

a) Case 1. $\rho_s < \rho_{sbal}$ (singly-reinforced beam)

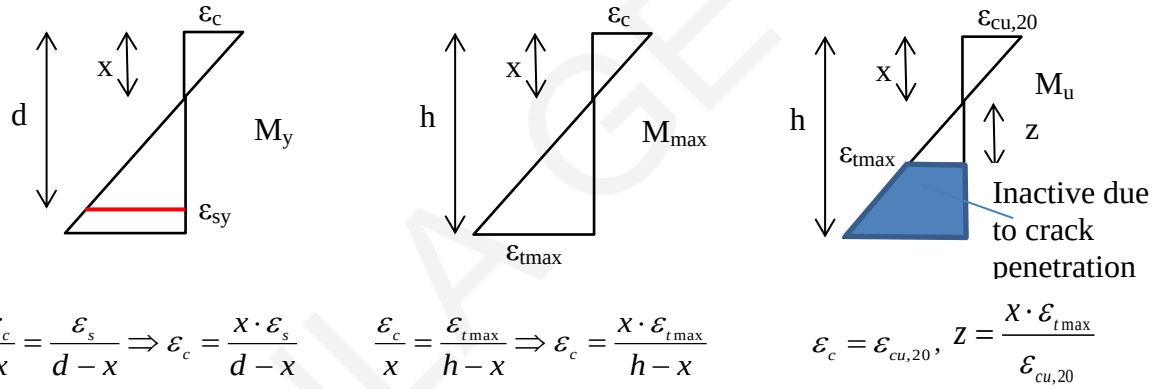

$$\frac{\varepsilon_c}{x} = \frac{\varepsilon_s}{d-x} \Rightarrow \varepsilon_c = \frac{x \cdot \varepsilon_s}{d-x} \qquad \frac{\varepsilon_c}{x} = \frac{\varepsilon_{t\max}}{h-x} \Rightarrow \varepsilon_c = \frac{x \cdot \varepsilon_{t\max}}{h-x} \qquad \varepsilon_c = \varepsilon_{cu,20},\ z = \frac{x \cdot \varepsilon_{t\max}}{\varepsilon_{cu,20}}$$

b) Case 2. $\rho_s < \rho_{sbal}$ (doubly-reinforced beam)

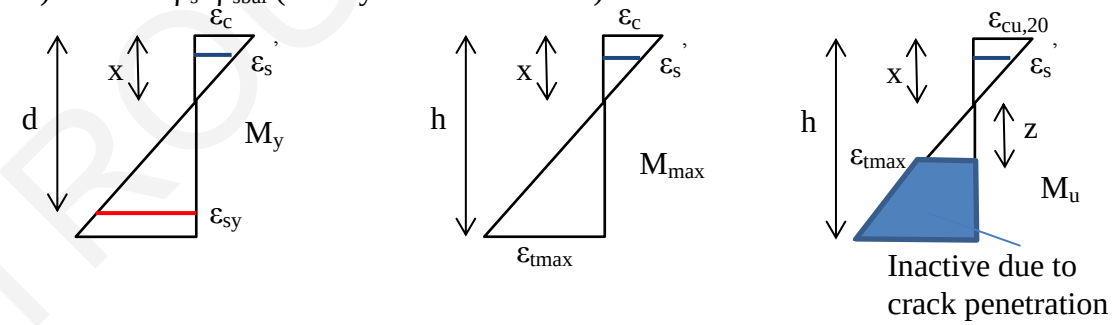

$$\varepsilon_c = \frac{x \cdot \varepsilon_{sy}}{d-x}, \quad \varepsilon_s' = \frac{(x-d') \cdot \varepsilon_{sy}}{d-x} \qquad \varepsilon_c = \frac{x \cdot \varepsilon_{t\max}}{h-x}, \quad \varepsilon_s' = \frac{(x-d') \cdot \varepsilon_{t\max}}{h-x} \qquad \varepsilon_c = \varepsilon_{cu,20}, z = \frac{x \cdot \varepsilon_{t\max}}{\varepsilon_{cu,20}}, \quad \varepsilon_s' = \frac{(x-d') \cdot \varepsilon_{cu,20}}{x}$$

Figure 7.8: Strain profiles for the formulation of equations for calculation moment capacities

7.6.2.2 Doubly reinforced cross sections

Compression reinforcement enhances flexural ductility as it provides an additional source of resistance in the compressive zone, assisting concrete to equilibrate the forces of tension reinforcement and axial load. Analysis is conducted here considering the point when the tension steel has yielded. The compression reinforcement with an area of A_s' is located at a distance d' from the extreme compression fiber. The three benchmark points that may be used to define the envelope of the R-SHFRCC beams are again (a) the point where the flexural reinforcement first attains yielding ($\varepsilon_s = \varepsilon_{sy}$), (b) the point of peak flexural strength: here the strain in the extreme tension fiber is, $\varepsilon_{ct} = \varepsilon_{ct,max}$, and (c) the point at which failure initiates, where the extreme compression strain in the cover will reach the limit associated with the residual strength ($\varepsilon_c = \varepsilon_{cu,20}$). The Moment capacity at each of these benchmark points will be determined based on the equations provided by the strain profiles at each point.

Force equilibrium is used in all cases to determine the neutral axis depth. The equations of the resultant forces are the same for cases (a) and (b), while they change due to the height of the acting depth of the composite under tension, marked by z.

For cases (a) and (b) $$\Sigma N = 0 \Rightarrow a \cdot x \cdot f_c \cdot b + A_s' \cdot f_s'(\varepsilon_s') - f_{ct}^{ave} \cdot (h - x) \cdot b - A_s \cdot f_y = 0 \qquad (7.12a)$$

For case (c) $$\Sigma N = 0 \Rightarrow a \cdot x \cdot f_c \cdot b + A_s' \cdot f_s'(\varepsilon_s') - f_{ct}^{ave} \cdot z \cdot b - A_s \cdot f_y = 0 \qquad (7.12b)$$

The moment capacity of a beam with flexural reinforcement and strain hardening cementitious composite may be determined from the profile of Fig. 6 (b); moments are taken about the point of application of the compressive force as:

$$M = F_t \cdot \left(a + \frac{h - x}{2} \right) + \left(F_s - F_s' \right) \cdot (d - x + a) = f_{ct}^{ave} \cdot (h - x) \cdot b \cdot \left(a + \frac{h - x}{2} \right) + \left(A_s \cdot f_y - A_s' \cdot f_s'(\varepsilon_s') \right) \cdot (d - x + a) \qquad (7.13a)$$

Equation 7.13a applies both to the cases of yielding of flexural reinforcement (a) and flexural capacity of the beam (b). In the case of the ultimate capacity prior to failure by crushing of the extreme layer under compression, fibers only act at a zone close to the neutral axis with a height determined as *z*, therefore the equation for computing Moment at that critical point becomes:

$$M_u = f_{ct}^{ave} \cdot z \cdot b \cdot \left(a + \frac{z}{2} \right) + \left(A_s \cdot f_y - A_s' \cdot f_s'(\varepsilon_s') \right) \cdot (d - x + a) \qquad (7.13b)$$

An example of application of the above analysis is given in Table 7.5 and the results show good agreement to the experimental results.

Table 7.5. Examples of application for determining ρ_{bal}, M_y, M_{max}, M_u

	F7-S14/S15/S16			**F7-SS17/SS18/SS19**		
	M_y	M_{max}	M_u	M_y	M_{max}	M_u
b	103.56	103.56	103.56	102.44	102.44	102.44
h	102.14	102.14	102.14	104.16	104.16	104.16
d	78.14	78.14	78.14	80.16	80.16	80.16
c	20	20	20	20	20	20
A_s	100.53	100.53	100.53	100.53	100.53	100.53
A_s'	0.00	0.00	0.00	100.53	100.53	100.53
ρ_s	0.0124	0.0124	0.0124	0.0122	0.0122	0.0122
ρ_s'	0.0000	0.0000	0.0000	0.0122	0.0122	0.0122
x_{bal}	43.96	43.96	43.96	45.09	45.09	45.09
f_{tave}	2.65	2.8	2.8	2.65	2.8	2.8
ρ_{sbal}	0.032	0.032	0.032	0.032	0.032	0.032
	CASE 1	**CASE 1**	**CASE 1**	**CASE 2**	**CASE 2**	**CASE 2**
x	32.18	25.64	18.38	31.31	25.51	19.86
z			16.00			17.28
ε_c	0.00	0.00	0.01	0.00	0.00	0.01
ε_{cmax}	0.54	0.79	2.71	0.50	0.76	2.71
α	0.45	0.58	0.62	0.42	0.57	0.62
a	20.86	16.33	8.52	20.35	16.28	9.20
ε_s'				0.00039	0.00015	-0.00018
N_t	19200.71	22182.23	4638.22	19777.46	22558.22	4956.56
N_s	53985.13	53985.13	53985.13	53985.13	53985.13	53985.13
N_s'				8073.00	3149.07	-3705.11
N_c	73185.83	76167.36	58623.35	65689.59	73394.28	62646.80
M (analysis)	**4.68**	**4.93**	**3.76**	**4.30**	**4.86**	**4.10**
M (exper.)	**4.75**	**5.31**	**3.71**	**4.68**	**5.14**	**4.76**

7.7 Conclusions

In this Chapter the investigation of the behavior of R/SHFRCC illustrated the improved ductility of beams consisting of an SHFRCC matrix. Various reinforcement ratios were considered in the tests so as to cover the entire range of under-reinforced and over-reinforced beam-sections in flexure containing either singly reinforced in tension or also containing compression reinforcement. The contribution of fibers both in tension and compression due to bridging of cracks, enhanced the tensile capacity and resisted spalling of the beam zone under compression. These effects were reflected in the ductility of the resistance curves of the specimens considered and were quantified in the cross-sectional analysis, which showed that the Moment-curvature behavior of such composite beams can be modeled by at least three benchmark points, associated with yielding of the tensile flexural reinforcement, the attainment of the sections' flexural strength, and the residual moment capacity that remains constant up

to very high levels of curvature. The experimental procedure as well as the cross sectional analysis showed that members with reinforcement ratios even larger than the balanced reinforcement ratio may exhibit large amounts of ductility owing to the beneficial action of the fibers in the zone under compression thereby resisting spalling and crushing of the cementitious composite. Equations for the determination of the full Moment capacity of R/SHFRCC in cases of flexural elements containing reinforcement ratios below the balanced ratio are extracted; these expressions are corroborated with the experimental results.

Results of this research indicate some rules that should be used for the design of R/SHFRCC:

- The balanced reinforcement ratio for R/SHFRCC beams is lower than that for normal concrete and can be calculated based on the beam geometry and materials' characteristics (Eq. 7.9)
- It is recommended that flexural moments resulting from ultimate limit load combinations (1.35G+1.5Q) should be lower than the residual moment of the member (M_u) (Eq. 7.11b for singly reinforced or Eq. 7.13b for doubly reinforced members)
- Shear strength design of a member should be performed based on the flexural capacity of the member after yielding using a uniform tensile stress block in the tension zone equal to the maximum post-cracking strength of the SHFRCC matrix $f_t^{ave}=f_{tmax}$ (Eq. 7.11a for singly reinforced or Eq. 7.13a for doubly reinforced members)

Chapter 8: Shear

8.1 Introduction

The new generation of fiber reinforced cementitious composites made with Polyvinyl Alcohol (PVA) fibers and high amounts of fly ash show advantageous mechanical properties in terms of very large tensile strain capacity and ductility and are considered the future of cement based construction. The challenge that remains is to establish pertinent new design rules and analysis procedures and to adapt existing ones specifically tailored to structures made of these materials. Of great importance for structural design – and a prerequisite to the introduction of these materials in construction - is the shear capacity of beams with and without any shear reinforcement. Some of the most important parameters contributing to shear resistance of normal concrete are a) dowel action intersecting the cracks, b) the friction between crack faces and aggregate interlock and c) the residual diagonal strength of cracked concrete.

Two types of tests may be performed in order to determine shear behavior: a) direct shear tests and (b) tests on beams. Direct shear tests may explain the basic shear transfer behavior while beams may be used to estimate the structural behavior of these composites in shear. The direct shear behavior may be investigated with push-off tests. From previous tests on the use of fibers in concrete, it is reported that fibers generally improve the shear strength and ductility of concrete and that they may partially replace the use of stirrups. The use of push-off tests was intended as a means to experimentally investigate the direct shear behavior of SHFRCC and relate shear to the tensile properties.

Simultaneously four-point bending tests were conducted on scaled beam specimens considering several values of shear span aspect ratio in order to determine the behavior of this novel ductile concrete in shear. Tests were conducted on mixes with and without longitudinal and shear reinforcement; specimens comprising the plain mix (i.e. no fibers) were also tested for benchmarking. Experimental values of strength were compared with estimates obtained from Eurocode 2 [141] for normal-weight concrete.

8.2 Shear in Push-off specimens

8.2.1 Mixes and specimen detailing

The direct shear behavior of the mixes was investigated with the use of uncracked push-off specimens. The specimens had dimensions of 250x500x100 mm as shown in Figure 8.1, with a shear plane area of 100x200=20000 mm^2 as proposed from previous research [99], [100]. The exact dimentions a, b, c, d, e, f, g, h, i and d are given in Appendix 4A.7. Two were the parameters of the investigation: a) the mix design – the use or not of fibers and b) the presence of steel stirrups crossing the shear plane. Three identical specimens were tested for each type of test and mix design.

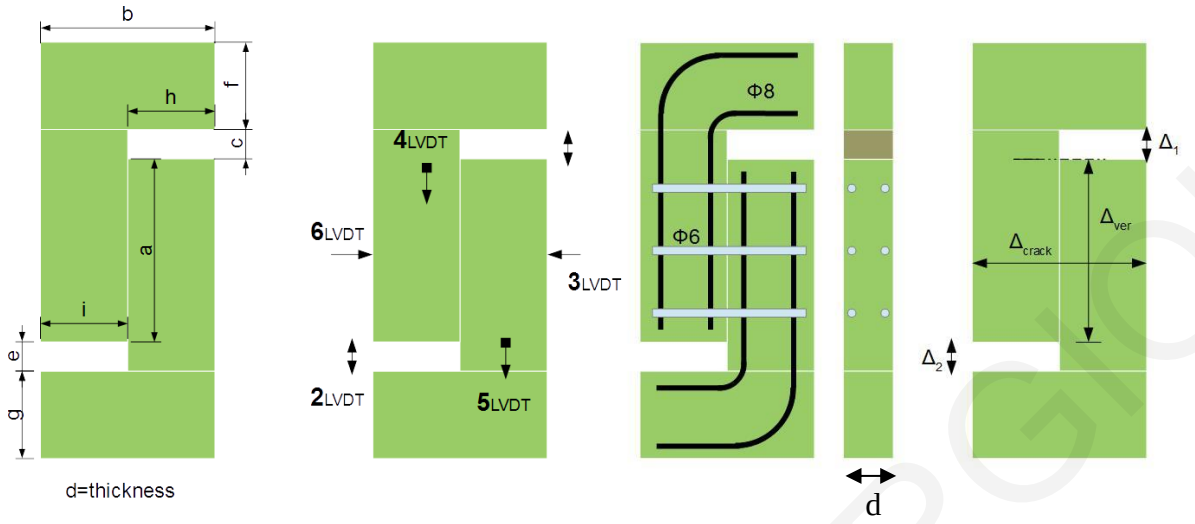

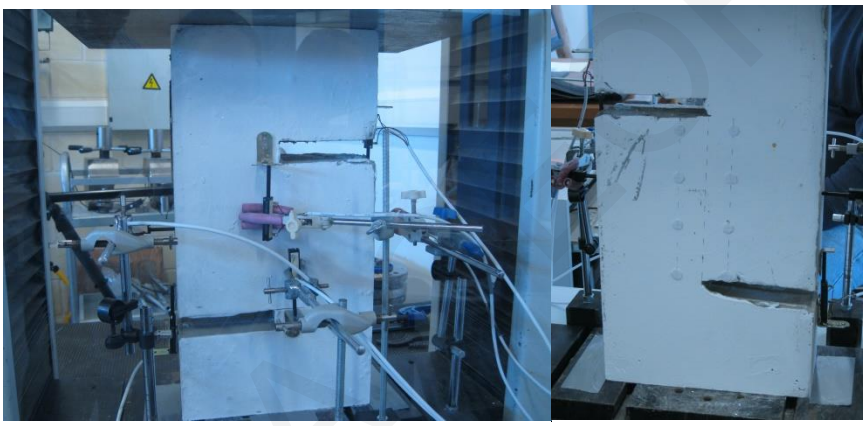

Figure 8.1: (a) Push-off specimen and dimensions, (b) LVDTs positions and measuring lengths, c) steel reinforcement, d) definition of deformation for graphic presentation

The characteristics of all tested specimens are recorded in Table 8.1, as well as the displacement controlled loading rate. Geometric details of the reinforcement for the beams under four point bending are given in Figure 8.1 (c). Other than the 6 LVDTs used to record deformation of the specimens targets were placed on both sides of the diametric plane and tracked through video recording for the deduction of shear deformations. For ease of understanding of the figures a new identification code is given in the last column of Table 8.1. PM is when the cementitious matrix has no fibers, while SHFRCC is the mix with fibers. When the identification –S is used it means that steel reinforcement is crossing the shear plane.

Table 8.1: Specimen designation – dimensions – rate of loading for push off tests

Specimen designation	Test	Material	Displacement rate	Reinforcement	
F10-S1/S2/S3	Push off	F10	7.5μm/s	-	PM
F5-S1/S2/S3	Push off	F5	15μm/s	6Φ6	PM-S
ShF7-1/2/3	Push off	F7	15μm/s	-	SHFRCC
F7-S1/S2/S3	Push off	F7	15μm/s	6Φ6	SHFRCC-S

8.2.2 Results from the Push-off tests

Failure crack patterns of all tested specimens are depicted in Figure 8.2. The first series of specimens created for the push off test without fibers or steel crossing the shear plane had no reinforcement on the top, bottom and vertical cross sections. This led the specimens to fail in flexure, an undesirable type of failure. New specimens had to be made after that, having reinforcement crossing all other possible failure planes other than the main shear plane. For the cases of the SHFRCC specimens without any reinforcement FRP sheets where used to prevent the wrong types of failures. The new specimens with the mix without the fibers and without any steel reinforcement crossing the shear plane (PM) had an abrupt failure after the creation of the first crack.

Figure 8.2: Push-off crack patterns for all specimens

Figure 8.3 shows the sequence of crack formation of one of the specimens without fibers but with steel reinforcement (PM-S). In the beginning a shear crack is created along the shear plane. After cracking of the shear plane and due to the absence of aggregates the friction on the shear plane was minimum and the full shear load was transferred through dowel action of the steel bars. Lateral deformation was initially concentrated at the main shear crack but as the vertical deformation increased the steel bars deformed as well, pushing off and delaminating the cover. The specimen showed compressive cracks at the top and bottom ends of the main shear crack. Both at the regions under compression and in the cover on both sides of the main shear crack the composite started to delaminate rapidly with the composite cover spalling. Spalling reached half of the width of the specimen (125 mm) and deformation of the steel reinforcement was visible over the 125 mm delaminated distance.

Figure 8.3: Crack sequence on both sides of a specimen without fiber but with steel reinforcement crossing the shear plane (Specimen F5-S1 or PM-S)

In the case of the fiber reinforced mix without stirrups multiple cracking was witnessed prior to crack localization and failure of the sample. The cracks formed in an inclined to the shear plane angle

(as shown in Fig. 8.4), with evidence of compression zones at the top and bottom edges of the shear plane. Failure of the fibers was mixed between rupture and pull-out. The width of the zone where cracks were formed was approximately 4cm but in no case was the composite laterally delaminating.

Figure 8.4: Crack sequence on both sides of a specimen without fiber but with steel reinforcement crossing the shear plane (Specimen shF7-1 or SHFRCC)

The same type of crack development was evident in the fiber reinforced matrix with stirrups crossing the shear plane as shown in Fig. 8.5. In these specimens though, the inclination of the cracks was greater than the inclination developed in the specimens without the steel reinforcement. Small

dislocation of the cracks was developed at the places where the steel stirrups were crossing the cracks. The width of the zone where cracks were formed was in the order of 6cm, without spalling of the fiber cementitious matrix. The tests in this case were terminated at the point where shear deformation was no longer possible due to the geometry of the sample (closing of the horizontal gaps due to excessive dislocation with no failure).

Figure 8.5: Crack sequence on both sides of a specimen without fiber but with steel reinforcement crossing the shear plane (Specimen F7-S1 or SHFRCC-S)

The machine load versus the LVDTs measured deformations of one of the push-off specimens (PM-S), are depicted in the diagrams of Figure 8.6 (a). The diagram of the crack opening ($\Delta_{crack}=\Delta_{6lvdt}+\Delta_{3lvdt}$) for the specimen with stirrups and no fibers (PM-S) shows a near to zero lateral expansion up to the maximum load. At maximum load the crack is created and after that, deformation accounts for the crack opening width. The small lateral expansion that develops prior to the maximum load is attributed

to elastic deformations. In the beginning of the descending branch the load capacity diminishes from maximum linearly with progressive crack widening, manifesting the loss of concrete contribution to the shear resistance. The remaining strength that continues to be constant, for greater deformations, is the contribution of the steel reinforcement to the shear capacity. The vertical deformation (Δ_{vert}) of the shear plane (between the crack faces) is in good agreement with the upper (Δ_1) and lower (Δ_2) recess deformations. Here the slope of the ascending branch shows that shear deformation increases shear resistance prior to crack localization, with deformations of the shear plane up to 2 mm (length of shear plane is 200 mm). After crack is formed, shear capacity diminishes down to a residual value that corresponds to the contribution of the steel reinforcement crossing the shear plane.

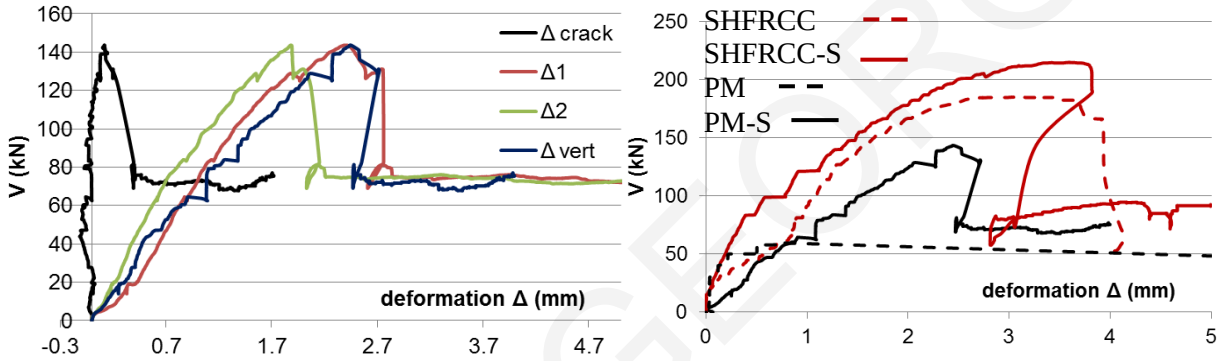

Figure 8.6: (a) Machine Load-LVDTs deformation for specimen PM-S and (b) Machine Load-crack opening from all tested specimens

In Figure 8.6 (b) the diagrams of Total Load versus crack opening (Δ_{crack}) of all push off tests are displayed. The beam with the PM mix and without steel reinforcement showed abrupt failure at a load of 60kN. After the peak load that was accompanied by a strong noise the specimen was split in two pieces. Average shear stress attained by these specimens was in the order of 2.5 MPa (=50000 N/20000 mm^2) determined as the fraction of the total applied load by the cross section area under shear. The addition of steel reinforcement (6 bars of 6mm diameter) to the plain mix increases the shear capacity to 5.8 MPa while the addition of fibers only of 2% by volume increases the shear capacity to 7.5 MPa, almost triple the strength of the plain mix. Also the addition of fibers increases the shear deformation on the vertical axis of anti-symmetry of the specimen, and while the plain mix breaks at a shear deformation of γ=0.5/200=0.25%, the mix with the fibers reaches a deformation of 3.5/200=1.75%. Shear strength reached higher levels in the specimens with the fiber reinforced mixes, even though compressive strength of the SHFRCC mix was lower than that of the plain mix. This implies that shear strength is related mainly to the tensile stress-strain relationship of the mixes and not to the compressive strength. Stiffness of the specimens was greater in the case of the samples with stirrups, manifesting that steel reinforcement played an important role in resisting shear even prior to crack initiation. In the case of the SHFRCC mix without the steel stirrups, cracking initiated at shear stresses of 2.7 MPa close to 1/3 of the maximum shear stress of the samples (7.5 MPa). Past that point stresses

were transferred across the crack through the fibers, thereby developing a type of tension stiffening. At a load value corresponding to the ultimate capacity of the plain SHFRCC, fibers started to rupture and the specimen collapsed. All samples containing steel reinforcement after the ultimate load, exhibited a load drop down to an average shear stress of 4 MPa, where only stirrups continued to resist shear, and while this value remained constant in the case of the mix without the fibers, there was an increase in resistance in the case of the fiber reinforced matrix, relating bending resistance of the stirrups to the tensile characteristics of the surrounding matrix.

Table 8.2: Characteristic load/shear stress/shear deformation values for push off tests

Specimens	P_{max} **(kN)**	τ_{max} **(MPa)**	γ
PM	60	2.5	0.5/200=0.25%
PM-S	140	5.8	
SHFRCC	180	7.5	3.5/200=1.75%
SHFRCC-S	200	8.3	

8.3 Shear in small scale beam members

New types of fiber reinforced cementitious composites comprise a mix design that differs from normal concrete mixes in that no coarse aggregates are included. With the addition of synthetic fibers that act as mass reinforcement large deformation capacities were attained; the fibers have been shown to be mobilized after the occurrence of first cracking, bridging the cracks and transferring stresses through cracked regions, thereby imparting a very resilient behavior for the material in tension. In this Section of Chapter 8 the experimental behavior of a series of four point bending tests with various a/d ratios for steel reinforced beams are presented.

8.3.1 Code provisions for the shear design of beams

Models for the shear resistance of reinforced concrete members have been implemented in Code provisions in order to eliminate brittle shear failure. The mechanics of shear resistance were investigated by various researchers and were attributed to the opening of the cracks, the reduction of aggregate interlock, the capacity of the compressive zone to transfer shear due to excessive strains-cracking-spalling and due to the reduction of dowel action related to the interfacial bond between the flexural reinforcement and the surrounding concrete due to splitting cracks. The capacity based design that is implemented both by the Eurocode 2 [141], as well as in the ACI Building Code [48] requires that the shear strength provided to a structural member should exceed by a margin the shear demand required from equilibrium in order to sustain flexural yielding. The Codes ensure this by requiring the use of transverse reinforcement able to resist a significant part of the design shear force if it is shown that the concrete contribution term to shear strength is lower than the shear demand.

Little documented test evidence is available regarding the performance of SHFRCC materials when this is used as the matrix in reinforced concrete structural members. As it is a recent advent in concrete materials technology, its use in structural design is not fully supported with the critical mass of data and observation regarding the structural performance of the resulting members. Previous investigations underscore the need for improved design expressions so as to quantify dependably the strength of SHFRCC members in shear and flexure, as this is the most prevalent state of stress in practical RC member detailing (Kabele and Kanakubo [93]). To address this interesting open issue, a series of scaled beam tests are undertaken for the present Chapter, investigating the structural performance of members under combined shear and flexure.

The first parameter of the experimental study is the shear span to depth ratio, known as aspect ratio, and its effect on the contribution of the SHFRCC material in the mechanics of shear of structural elements. The experimental program investigates the interaction of steel reinforcement (longitudinal and transverse) with the use of fibers in the composite. Reference beams with the same mix design without any fibers but with the same patterns of steel reinforcement are used to quantify the contribution of reinforcement to shear strength. The shear span ratio as well as the percentage of the flexural reinforcement are used to alter the mode of failure between shear and flexure. Finally mechanistic models are established, obtained from first principles, in order to interpret the structural response of the specimens (strength and mode of failure), and are used to derive simple design expressions by which to estimate the contribution to shear resistance of flexural components comprising Reinforced SHFRCC (R/SHFRCC).

8.3.1.1 ACI Building Code

Hoops for confinement and buckling control are required over a length of 2h from the face of the supports. The spacing of the hoops is specified in ACI Code Section 18.6.4.4 [48], while in the rest of the beam hoops are required at a maximum distance of $d/2$. The probable moment strength M_{pr} of the beam member is based on the dimensions and reinforcement assuming a tensile strength of $1.25f_y$, and ACI 18.6.4.1 [48] requires that the beam is designed for a shear V_d:

$$V_d = \frac{M_{pr}}{L_s}, \text{ where } M_{pr} = 1.25 \cdot f_y \cdot A_s \cdot \left(d - \frac{a}{2} \right) \text{ and } a = \frac{1.25 \cdot f_y \cdot A_s}{0.85 \cdot f'_c \cdot b} \qquad (8.1)$$

The concrete contribution to shear V_c is taken as zero as per ACI 18.6.5.2 [48] when the V_d due to plastic hinging exceeds half of the maximum shear V_u within the span.

$$V_c = 2\lambda \cdot \sqrt{f_c} \cdot b_w \cdot d \text{ , and } V_s = V_u / \phi - V_c \qquad (8.2)$$

where φ is the strength reduction factor, which for shear sensitive members seismically designed this factor takes the value 0.6. The maximum shear reinforcement is set by the ACI 22.5.1.2 [48] as:

$$V_{s,\max} = 8 \cdot \sqrt{f_c} \cdot b_w \cdot d \quad (8.3)$$

And the stirrups required are calculated as:

$$\frac{A_v}{s} = \frac{V_s}{f_{ty} \cdot d} \quad (8.4)$$

8.3.1.2 Eurocode

Section 6.2.1 of Eurocode EN1992-1-1 [141] states that when the shear resulting from loads is greater than the one provided only by concrete $V_{Ed}>V_{Rd,c}$ then sufficient shear reinforcement should be provided in order that $V_{Ed}\leq V_{Rd}$ (where V_{Rd} is described by Eq. 6.8 Section 6.2.3). Eq. 6.8 in Section 6.2.3 [141] gives the shear resistance of members with vertical shear reinforcement as:

$$V_{Rd,s} = \frac{A_{sw}}{s} z \cdot f_{ywd} \cdot \cot\theta \quad (8.5a)$$

$$V_{Rd,max} = a_{cw} \cdot b_w \cdot z \cdot \nu_1 \cdot f_{cd} / (\cot\theta + \tan\theta) \quad (8.5b)$$

$$\nu_1 = \nu = 0.6\left[1 - \frac{f_{yk}}{250}\right] \quad (8.5c)$$

Shear strength of non-prestressed concrete beams without shear reinforcement is estimated according with CEN EN 1992 [141]:

$$V_{Rd,c} = C_{Rk,c} \cdot k \cdot (100 \cdot \rho_l \cdot f_c)^{1/3} \cdot b \cdot d \quad (8.6)$$

with $C_{rk,c}$ =0.18 MPa (used without material safety factor).

8.3.1.3 New Model Code

The New Model Code [49] has included the design of FRC, in Section 7.7. For the beams without shear reinforcement Section 7.7.3.2.2 gives the shear resistance by:

$$V_{Rd,F} = \left\{ \frac{0.18}{\gamma_c} \cdot k \left[100 \cdot \rho_l \left(1 + 7.5 \cdot \frac{f_{Ftuk}}{f_{ctk}} \right) \cdot f_{ck} \right]^{1/3} + 0.15\sigma_{cp} \right\} \cdot b_w \cdot d \quad (8.7)$$

Where f_{Ftuk} as stated by the Code should be determined by a direct axial-tensile test, while and Eq. 8.7 is calibrated based on steel fiber concrete research and should be re-calibrated for other types of materials. In beams with shear and longitudinal reinforcement Section 7.7.3.2.3 [49] states that the total shear resistance is the sum of the concrete contribution, the shear reinforcement and the fibers intersecting the design shear crack.

$$V_{Rd} = V_{Rd,c} + V_{Rd,s} + V_{Rd,F} \quad (8.8)$$

In Section 7.7.3.2.4 [49] it is stated that the minimum shear reinforcement may be omitted if the following condition is fulfilled:

$$f_{Ftuk} \geq \frac{\sqrt{f_{ck}}}{20} \quad (8.9)$$

Again Eq. 8.9 is based on steel fiber concrete research and should be checked for other types of materials. Also when a large amount of longitudinal reinforcement in the compressive zone is present, enough stirrups should be applied in order to avoid compression buckling of the reinforcing bars.

8.3.1.4 JSCE Recommendations

The Japan Society of Civil Engineers issued the first Recommendations for the design and construction of High Performance Fiber Reinforced Cement Composites (HPFRCC) with multiple fine cracks in 2008 [50]. Section 6.3.3 of the JSCE Recommendations [50] deals with the issue of shear design of linear members. The shear capacity of a member of SHFRCC and steel may be obtained by Eq. 8.10. In this Equation the shear capacity of a HPFRCC member is the sum of the capacities of the matrix V_{cd}, the fibers V_{fd} and the shear steel reinforcement. The shear strength of the matrix is derived from the specification for normal concrete. The Equation giving the beneficial actions of the fibers is exerted by the Recommendations for Design and Construction of Ultra High-Strength Fiber Reinforced Concrete Structures [52] – referred to hereafter as "Recommendations". The nominal strength of the beam V_{yd} as stated by the code is assumed to be reduced by a factor of 0.7 due to the multiple cracking that appears under service loads for these types of composites.

$$V_{yd} = V_{cd} + V_{sd} + V_{fd} + V_{ped} \quad (8.10)$$

V_{ped} refers to the case where prestressed steel is used in the member. V_{cd} is the shear strength of a member without shear reinforcement and without the contribution of the fibers.

$$V_{cd} = \beta_d \cdot \beta_p \cdot \beta_n \cdot f_{vcd} \cdot b_w \cdot d / \gamma_b \quad (8.11)$$

$$f_{vcd} = 0.7 \cdot 0.20 \cdot \sqrt[3]{f'_{cd}} \ (\mathrm{N/mm^2}), \text{ where } f_{vcd} \leq 0.50 \ (\mathrm{N/mm^2}) \quad (8.12)$$

$$\beta_d = \sqrt[4]{1/d} \quad (d\text{:m}) \qquad \text{when } \beta_d > 1.5, \beta_d \text{ is taken as } 1.5 \quad (8.13)$$

$$\beta_p = \sqrt[3]{100 \cdot p_w} \qquad \text{when } \beta_p > 1.5, \beta_p \text{ is taken as } 1.5 \quad (8.14)$$

$$\beta_n = 1 + M_o / M_d \quad (N'_d \geq 0) \qquad \text{when } \beta_n > 2, \beta_n \text{ is taken as } 2 \quad (8.15)$$

$$\beta_n = 1 + 2M_o / M_d \qquad (N'_d < 0) \text{ when } \beta_n < 0, \beta_n \text{ is taken as } 0 \quad (8.16)$$

In the above, N'_d is the design axial compressive force, M_d is the design bending moment, M_o is the bending moment required to cancel the stress at the extreme tension fiber caused by axial loading, corresponding to the design bending moment, b_w is the width of the member, d is the effective depth,

$p_w=A_s/(b_w \cdot d)$, A_s is the cross-sectional area of the tension reinforcement, f'_{cd} is the design compressive strength of concrete (N/mm^2), $\gamma_b=1.3$ and V_{sd} is the design shear capacity of the shear reinforcement.

$$V_s = \left[A_w \cdot f_{wyd} \cdot \left(\sin a_s + \cos a_s\right) / s_s \right] \cdot z / \gamma_b \qquad (8.17)$$

Where A_w is the total cross-sectional area of the shear reinforcing steel placed at spacing s_s, f_{ywd} is the design yield strength of the shear reinforcement, α_s is the angle of the shear reinforcement to the member axis, s_s is the shear reinforcement spacing, z is the distance from the compressive stress resultant to the centroid of the tensile steel – approximated by d/1.15- and γ_b=1.1. The design shear capacity of the fibers is given by the following Equation:

$$V_{fd} = \left(f_{vd} / \tan \beta_u\right) \cdot b_w \cdot z / \gamma_b \qquad (8.18)$$

with f_{vd} being the design tensile yield strength of HPFRCC, f_{vd}=0 when f_{vd}<1.5N/mm^2, β_u is the angle of the diagonal crack surface to the member axis (β_u=45^o), γ_b=1.3. In the case where the member is partly reinforced by HPFRCC, then shear capacity should be determined by appropriate methods, such as tests, as stated by the Recommendations [50].

The diagonal compressive capacity V_{web} (upper limit in allowable shear force) that is depended on to resist shear force is determined as follows:

$$V_{wcd} = f_{wcd} \cdot b_w \cdot d / \gamma_b \qquad (8.19)$$

where $f_{wcd} = 1.25 \cdot \sqrt{f'_{cd}}$ (N/mm^2) with $f_{wcd} \leq 7.8$ (N/mm^2) and γ_b=1.3. In Figure 8.7 the

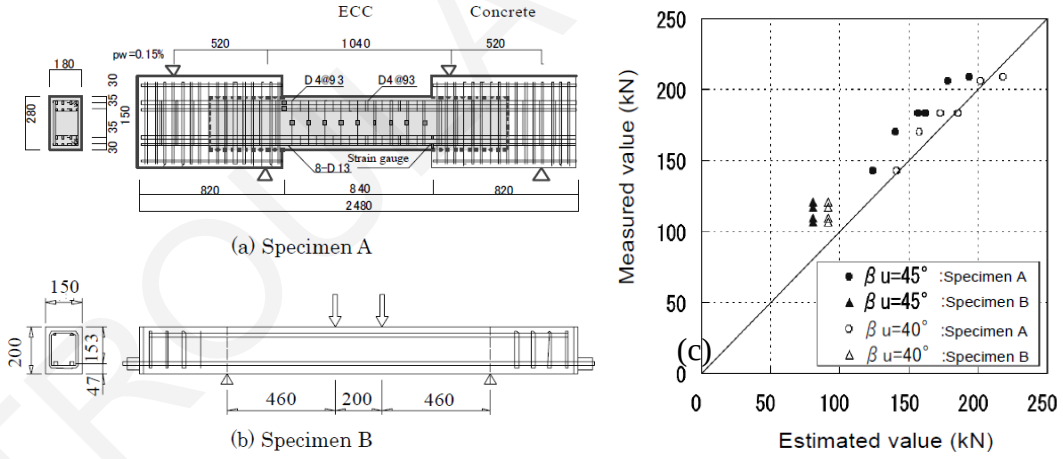

Figure 8.7: (a) and (b) Outline of shear test specimens, (c) Comparison of test and estimated values (safety factor of estimated values is 1.0) [50]

Recommendations [50] gives a series of tests performed to obtain the shear capacity of beam members with and without the use of stirrups and a comparison of the experimental results to the strength estimations obtained from the design shear strength equation. As shown in Fig. 8.7 (c) the results from the equation allow a conservative estimation of the shear capacity of a beam member, but it is also stated that the test data available are too limited and in general appropriate testing should be

used for verification for different beam-section heights or reinforcement ratios. The case of reversed cyclic loading and its impact on the degradation of shear capacities of members is not mentioned at all within these Recommendations.

8.3.2 Experimental Program

8.3.2.1 Specimens, testing setup and procedure

Four-point bending tests were carried out on small scale beams comprising an SHFRCC matrix (mix F7 as described in Chapter 4, Table 4.1). For the sake of comparison a series of reference specimens were also made of the same matrix but without the fibers (mix F5 as described in Chapter 4-Table 4.1, these are identified herein by the acronym HVFA – which refers to the high volume fly ash mix). The combined action between the fiber composite and simultaneous use of flexural and shear reinforcement is investigated for the shear span ratios of a/*h*=1, 2 and 3.5 by the introduction of tension reinforcement at different area ratios and/or stirrups (Table 8.3). Thus, the magnitude of shear force demand is determined by controlling the flexural strength of the beam cross section; this is achieved by varying the area ratio of the flexural reinforcement and the shear span ratio (Table 8.3). Specimen identification code is as follows: The first letter identifies the specimen classification in group A or B which corresponds to HVFA or SHFRCC matrix. The following digit corresponds to the shear span ratio, the next letter ("L") identifies the presence of longitudinal reinforcement (absence of L in the code name means that the specimen contains no longitudinal reinforcement) and the number following identifies the diameter of the longitudinal steel bars used (either 8 or 14 mm) while the third symbol "S" defines the presence of shear reinforcement (similarly, absence of S means no shear reinforcement was used). For example, specimen code B1L8S means a beam specimen comprising SHFRCC matrix, with a shear span ratio of 1 and containing both longitudinal bars of 8 mm diameter and transverse reinforcement. Three identical specimens were tested for each parameter combination. In addition to the beam tests, uniaxial compression and dog-bone direct tensile tests were carried out on cylinder and prism samples of the materials used.

Table 8.3: Beam dimensions and reinforcement (b=100mm, d=100mm).

Name	Composite	a/h	Bottom Reinf.	Top Reinf.	Stirrups	Fig. 8.8
B1L8	SHFRCC	1	2Φ8	-	-	a
B1L8S	SHFRCC	1	2Φ8	2Φ8	Φ6/50	b
A2L8	HVFA	2	2Φ8			a
A2L8S	HVFA	2	2Φ8	2Φ8	Φ6/50	b
B2L8	SHFRCC	2	2Φ8	-	-	a
B2L8S	SHFRCC	2	2Φ8	2Φ8	Φ6/50	b
B2L14	SHFRCC	2	2Φ14	-		a
B2L14S	SHFRCC	2	2Φ14	2Φ6	Φ6/50	b
B3.5L8	SHFRCC	3.5	2Φ8	-	-	a

The beam specimens had a 100mm square cross section and geometric and reinforcing details as shown in Fig. 8.8. The 4-point load tests were conducted under displacement control, at a displacement rate of 1.5μm/sec and 3μm/sec for the plain and reinforced beams respectively. The load frame had 100mm distance between the intermediate rollers. The beams were supported on end rollers at a variable distance "a" from the intermediate loads (the shear span "a" was a parameter of study) as shown in Figure 8.8. Five LVDTs were used to record the vertical deflection at the supports, at the load points and in the middle of the beams. When tested, the specimen extended 50 mm beyond the supports in order to ensure proper anchorage of the longitudinal reinforcement (Fig. 8.8).

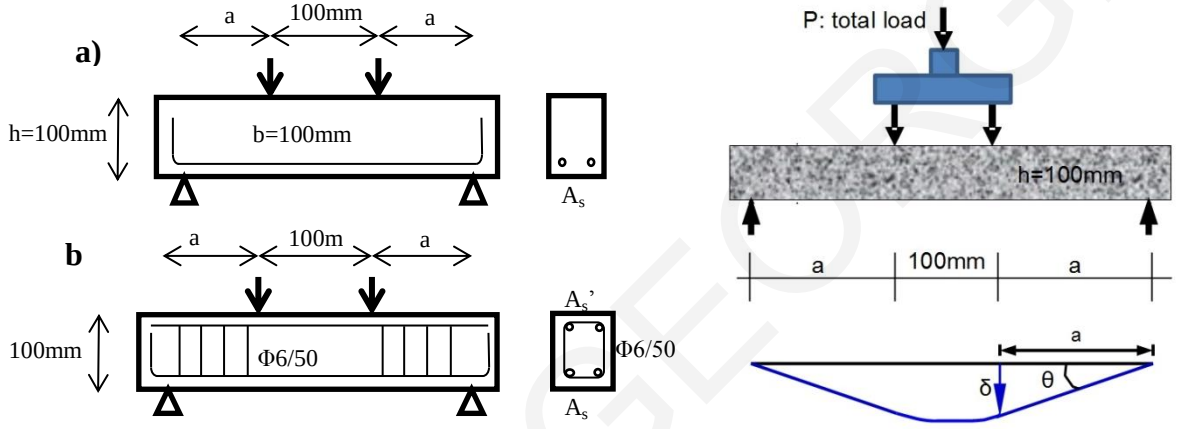

Figure 8.8: Test configuration for four point bending and reinforcement details for (a) beams with flexural reinforcement placed so as to increase the magnitude of shear demand in the beam shear spans, (b) beams reinforced with longitudinal bars and stirrups for shear strength and (c) Definition of specimen rotation θ in the shear span (reference to rotation capacity)

8.3.2.2 Test Results and Discussion

The results from the steel reinforced beams are compared with beams of the same size and shear span ratio but without any reinforcement (described in detail in Chapter 7). When longitudinal steel reinforcement was added, the flexural moment capacity of the beams increased and hence the shear demand in the shear spans increased by a commensurate amount. The failure mechanism depended on two parameters: the shear span ratio and the percentage of flexural reinforcement used. The moment-shear interaction diagram is plotted in Fig. 8.9 (black dots represent the SHFRCC specimens with no steel reinforcement, red represent the HVFA specimens A1, A2L8 and A2L8S, blue dots and dashed line refer to specimens with longitudinal and transverse reinforcement, and orange dots and solid line correspond to specimens with longitudinal bars only). The slope of the many radial lines refer to the different a/*h* ratios of the specimens.

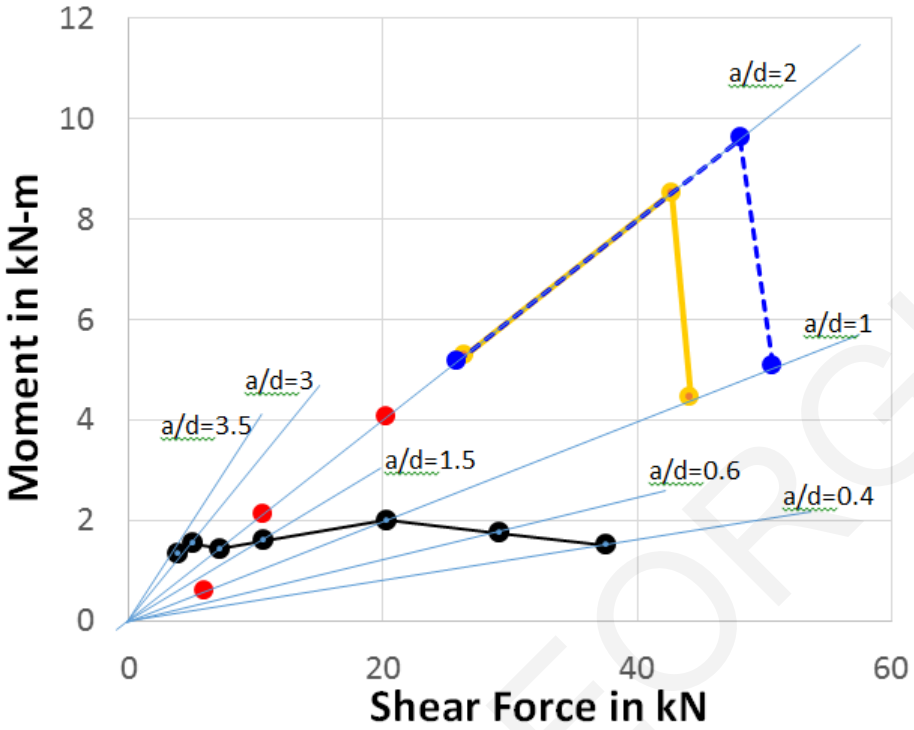

Figure 8.9: Moment-shear interaction diagram (black dots represent the SHFRCC specimens with no steel reinforcement, red represent the HVFA specimens A1, A2L8 and A2L8S, blue dots and dashed line refer to specimens with longitudinal and transverse reinforcement, and orange dots and solid line correspond to specimens with longitudinal bars)

Figure 8.10 shows the crack formation and the Load-Load point deflection diagrams in all cases with steel reinforcement. The beams with the HVFA composite matrix without stirrups (A2L8) failed in a brittle manner due to a large bond-shear crack which developed in one of the shear spans. The crack started as an inclined shear crack extending from the flexural reinforcement up to the compressive zone at an angle, and near failure it extended towards the longitudinal reinforcement anchorage. After the compressive zone cracked there was no mechanism in the cross-section to transfer the compressive stresses and the beam collapsed. When shear reinforcement was added as well as longitudinal compression reinforcement, the mode of failure became ductile and showed the typical characteristics of ductile behavior where after yielding of the reinforcement, the members' moment capacity increased beyond a deflection ductility of 3.5, followed by compression zone cover crushing. The use of stirrups in this case eliminated brittle shear failure.

Moment capacity of the reinforced cross section (2Φ8, h=100mm, d=76mm) was estimated as per Eq. 8.20 to be 3.38kNm, where z is the internal lever arm and d the effective depth. The shear force necessary to be provided for the shear span ratio of 2 in order for the yield moment to be developed was estimated as $V_{flex}=M/a=16.9$kN (total machine Load P=33.9kN).

$$M_R = z \cdot A_s \cdot f_y = 0.85 \cdot d \cdot 2 \cdot \pi \cdot \frac{d_b^2}{4} \cdot f_y \quad (8.20)$$

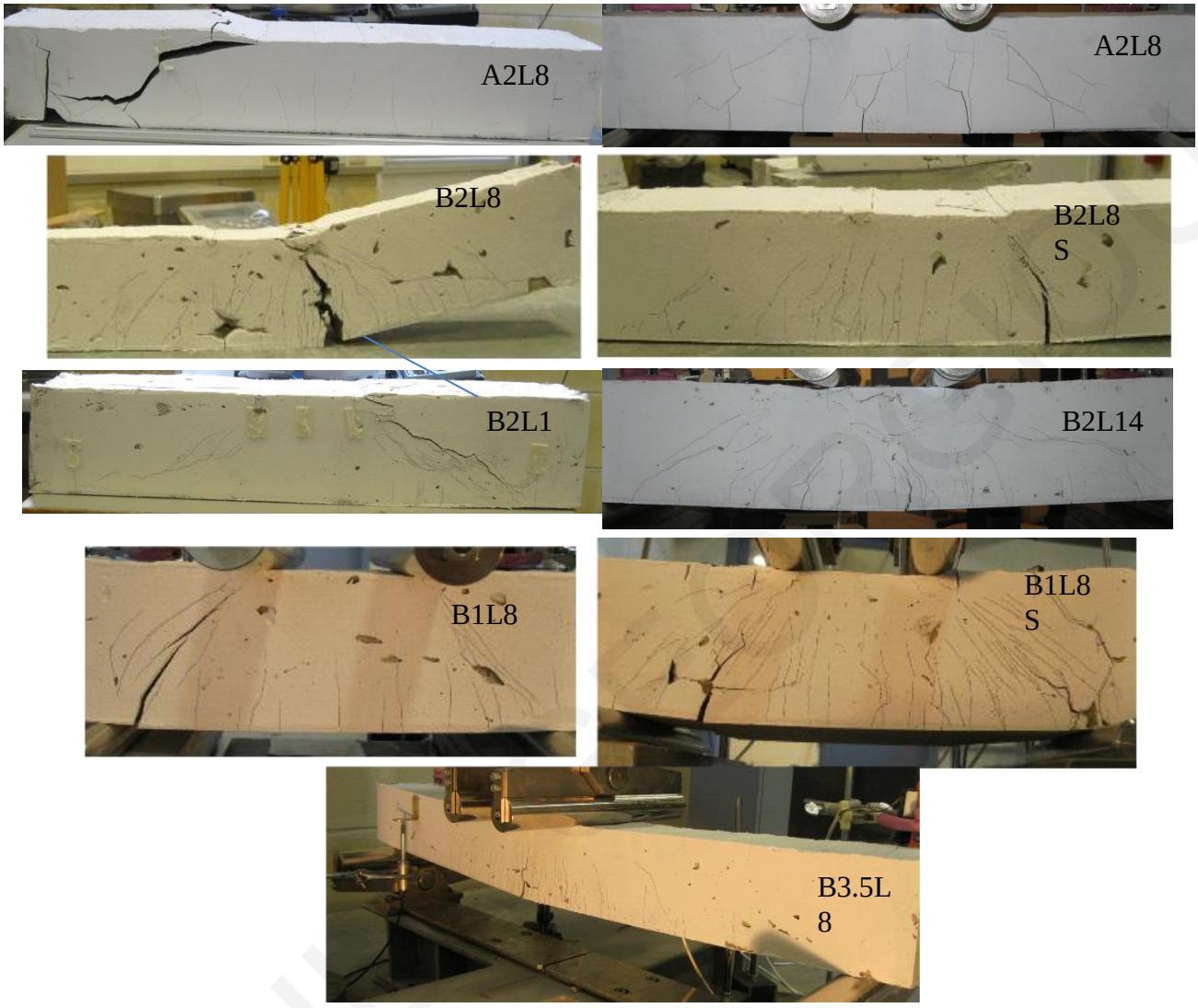

Figure 8.10: Crack pattern on beams with longitudinal and transverse reinforcement under four-point loading and Load-Deflection diagrams for all a/d ratios with steel reinforcement.

In the case without any stirrups (specimen A2L8) the theoretical yield force in the shear span (V = 16.9 kN) was not reached and the cross section failed in a brittle manner, at a shear force of 10.6 kN. Shear strength of non-prestressed concrete beams without shear reinforcement was estimated according

with CEN EN 1992 [141], and according with Tureyen and Frosch [142] (included in the ACI445 report, see Eq. 8.22). The former is based on empirical calibration with results from normal weight concrete tests, with $C_{rk,c}$ =0.18 MPa (used without material safety factor); the aggregate interlock term was neglected here in light of the absence of coarse aggregates. The latter model is based on the mechanistic result that only the compression zone, *c*, of a beam carries shear. In this case the shear strength of concrete is set equal to its tensile strength taken ≈$0.4\sqrt{f_c}$.

$$V_{c,EN} = C_{Rk,c} \cdot k \cdot (100 \cdot \rho_l \cdot f_c)^{\frac{1}{3}} \cdot b \cdot d = 0.18 \cdot 2 \cdot (100 \cdot 0.0132 \cdot 50)^{\frac{1}{3}} \cdot 100 \cdot 76 = 11.06\ kN \quad (8.21a)$$

$V_{c,ACI445} = 0.4 \cdot \sqrt{f_c} \cdot b \cdot c$ ➔ $V_{c,ACI445}=0.4\cdot\sqrt{50}\cdot100\cdot35=9.9$ *kN (compr. zone c*= 1/3*h* = 35 mm) (8.21b)

Thus, contribution of the concrete and the flexural reinforcement to the shear capacity of the beam according with the prevalent design codes would be 9.9÷11 kN, which bounds the range of the experimentally measured shear strength of specimen A2L8 (=10.6 kN). Strength was increased by the addition of stirrups in the case of specimens A2L8S to 20.3 kN. When shear reinforcement was used in the case of reinforced HVFA beams, the cross section attained its theoretical yield load (40.548 kN). After yielding, hardening of the steel reinforcement increased the moment capacity of the element cross section and caused an increase in the normal strain of the extreme compressed layer, leading to crushing failure of the concrete compression zone cover.

In the cases with SHFRCC very few signs of shear failure were seen in the damaged state of the unreinforced specimens, whereas some form of shear-related failure was observed in the reinforced SHFRCC (R/SHFRCC) specimens for all shear span ratios and contents of flexural reinforcement, even though only in the shorter specimens it was shear-flexure cracks that prevailed with cracks clearly attributable to shear distress. From among the R/SHFRCC specimens, those that exhibited a ductile flexural behavior were the beams with the lower amounts of longitudinal reinforcement and a larger shear span to depth ratio, B2L8, B3.5L8, and beams containing transverse reinforcement, B1L8S, B2L8S, B2L14S. Beams that failed in brittle fashion had a short shear span (B1L8, shear strength of 44.2 kN) or large amounts of longitudinal reinforcement (B2L14, shear strength of 42.66 kN). Because each specimen differs from its predecessor by a quantum leap in strength affected by a single parameter change, it is possible to quantify this parametric effect through comparative evaluation of the examined cases. In performing this comparative evaluation, the model proposed by JSCE for establishing the strength of R/SHFRCC members is selected as the underlying concept [50]: Shear strength, V_R, is obtained as the sum of (a) the cementitious matrix contribution over the web, V_c, (b) the shear reinforcement, V_w, and (c) the fiber contribution, V_f, as shown by Eq. (8.22a).

(a) Contribution of fibers to shear strength: Comparison between specimen groups A1 and B1, where the only difference is in the matrix (HVFA vs SHFRCC) indicates a significant strength leap

from the plain to the SHFRCC case. The B1 series of specimens failed in a mixed flexure-shear mode. Actually, shorter specimens in the B-series category such as B0.4 and B0.6 illustrate that even higher contribution to shear strength could be attained by the addition of fibers, to the amount of 37.6 kN (case B0.4); considering that the estimated V_c terms for the plain concrete are in the order of 9.9 to 11.0 kN (see Eq. 8.21), it is clear that the available shear strength that may be provided by the fibers is a substantial component. Considering specimens B1L8 and B2L14 both of which failed by shear, it follows that the fiber contribution is 44.2-11 kN=33.2 kN (for B1L8) and 42.66-11 = 31.66 kN (for B2L14). These two estimations obtained from the two groups of specimens are considered rather close in light of the fact that higher push-off pressures are exerted on the cover concrete by the 14mm bars in dowel action in B2L14 as compared to B1L8, thereby leading to earlier splitting and strength loss.

(b) Contribution of stirrups to shear strength: Comparison between specimen groups A2L8 and A2L8S provide a lower bound for the stirrup contribution, V_w=20.27kN-10.6kN = 9.67 kN. This result divided by the yield force of a stirrup layer which is estimated as, $A_{st} \cdot f_{yw}$ = *2x29 mm^{2}x300 MPa = 17.4kN*, illustrates that stirrups were not stressed nearly at their yielding point, so that the apparent flexural failure of A2L8S occurred by concrete crushing in the compression zone. Note that the nominal stirrup contribution is 29.6 kN at stirrup yielding, so stirrups were engaged to 30% of their capacity effectively altering the failure mode from shear to flexure. Similarly, specimens B2L14 and B2L14S provide a lower bound for the stirrup contribution term, V_w = 48.1kN-42.66kN = 5.44 kN, indicating that a much lower percent of stirrup engagement is sufficient to alter the mode of failure from shear to flexure even at high shear stress demand effected by a longitudinal reinforcement ratio of 4%. Clearly, the remainder of the required shear strength is supplemented by the fibers of the SHFRCC mix. This is also confirmed through comparison of specimens B2L8 and B2L8S both of which developed flexural failure at the same shear force in the span of 26.35 kN and 25.9 kN respectively, indicating that here the addition of stirrups was overwhelmed by the already available contribution of the fibers, rendering them unnecessary. This is confirmed through comparison with the companion group of A2L8 specimens; actually the difference between A2L8S which is stirrup confined and failed in flexure, and B2L8 which had the same amount of longitudinal reinforcement but contained no stirrups underscores the confining action imparted by the fibers in the compression zone eventually making a substantial difference in the flexural mode of failure (crushing and delamination of the concrete cover in the compression zone of A2L8S as compared to intact compression zone of B2L8 at the same level of deflection).

8.3.3 Estimation of the Shear Strength of R/SHFRCC beams

8.3.3.1 Background

The key ingredient of the so-called engineering beam theory (BT) is the kinematic assumption of plane sections remaining plane and normal to the neutral axis after bending, which is considered relevant for regions where flexural action is the predominant mode of response (B-regions) as shown in Fig. 8.11. The beam theory is not valid in the proximity of geometric or load discontinuities or disturbances which according to Saint Venant's Principle extend within a member's depth from the discontinuity (D-regions MacGregor [97]). (Thus, B-regions are thought to exist in the middle part of a shear span only if the a/h ratio exceeds 2).

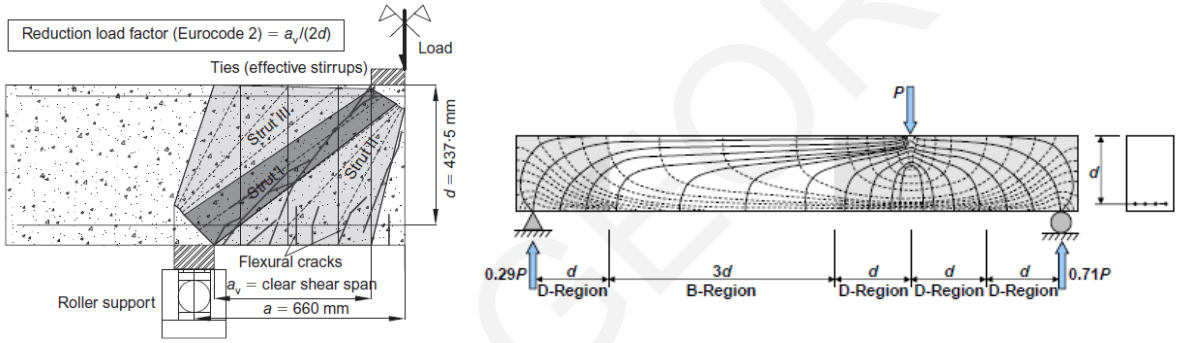

Figure 8.11: Typical crack pattern and load paths in a short span beam 1<a/d<2 with stirrups [143], (b) stress trajectories within B- and D-regions of a flexural member (adapted from Birrcher [144])

The behavior of the D-regions suggests that after cracking the elastic stress field in the member is disrupted owing to loss of tensile strength, causing major reorganization of the internal forces along the principal compressive stress path in the form of compression struts, while reinforcement is represented as a tension tie needed to maintain equilibrium with the struts; regions where struts and ties converge are referred to as joints (MacGregor [97]). Failure may be caused in the struts due to transverse tension if no reinforcement exists to restrain cracking. Other types of failure are as follows: **(a)** if transverse reinforcement exists, the additional load carried by the strut may lead to concrete crushing; **(b)** yielding of the tension ties, **(c)** failure of tie anchorage beyond the joint region, or **(d)** failure of the nodal zones. Both the ACI [48] (ACI Code Chapter 23: Strut and Tie Models) and the Eurocode [141] (Eurocode 2 Chapter 6.5: Design with Strut and Tie model) have provisions for designing separately members or parts that act as D-regions.

According to the experimental results that were summarized in the previous sections, SHFRCC beams without any steel reinforcement present strain hardening behavior, since fibers that bridge the cracks in the tensile zone of the beams, transfer loads and act as reinforcement. Also it was shown that when shear demand was increased by the addition of reinforcement in the cross section of the SHFRCC beams, then the shear strength that was mobilized exceeded substantially the contribution of the

compression zone, attesting to the contribution of the SHFRCC material over the entire beam web (i.e., in both compression and tension zones). According with the test results from beams without steel reinforcement (see Fig. 8.9 that records the capacity of the beams in terms of flexural moment), it is clear that all beams with shear spans over a/*h*>1 have the same moment capacity and based on their longer spans those beams develop flexural failures and act as B-regions where beam theory applies, whereas the beams with shear spans a/*h*≤1 developed higher capacities in terms of moment while having the same cross-sectional dimensions leading to the assumption that those beams act as D-regions, requiring different modeling. This behavior is also seen in the beams having the same a/h ratios when steel reinforcement is added in the cross sections.

8.3.3.2 Proposed model for the determination of shear strength of R/SHFRCC beams

According to the experimental results presented in this study the differences in the observed behavior of the specimens are related to their respective shear span ratios. An important point of interest is the interpretation of the mechanics of shear resistance in the presence of sustained tensile strength of the material in the tension zone, which will enable the derivation of design expressions for calculating shear strength in plain and steel-reinforced beams comprising an SHFRCC matrix. This problem here is addressed by reference to the fundamental principles underlying shear behavior modeling used in conventional concrete, through pertinent modification of the concrete contribution component. In this context two alternative approximations to the mechanics of shear force transfer of flexural members are considered: (a) the Engineering beam theory, which is expected to be relevant only in the case of longer specimens and (b) Strut and tie models are used to also obtain alternative strength estimations, considered to be particularly applicable to specimens with shorter shear spans (a/*h*<2).

(a) Engineering Beam Theory (BT):

The shear flow associated with flexure is estimated by considering the difference in normal stresses between two adjacent beam cross sections in the shear span based on the beam theory.

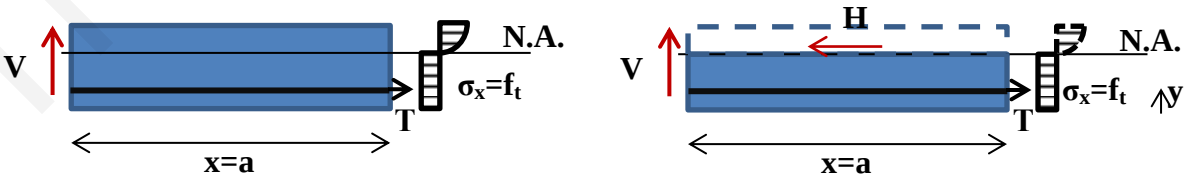

Figure 8.12: (a) Beam segment of length x=a with the normal stresses and (b) horizontal cross section of the lower part (tension zone) based on beam theory for calculation of the shear flow $q=\Delta H/\Delta x$

The shear span depicted in Fig. 8.12 is analyzed in order to estimate the shear capacity of the member of a beam. The moment at the end of the shear span may be calculated as:

$$M = V \cdot x = V \cdot \mathrm{a} \qquad (8.23)$$

The distribution of stresses at the end of the shear span within the region under tension is assumed to be constant and equal to the tensile strength of the composite material. A simplistic assumption is that over the shear span the tensile stress mobilized in the tensile zone follows the moment according with the Engineering beam theory. This assumption indicates that the normal tensile stresses in the region under tension varies linearly in *x*, attenuating linearly along the beam span following the moment. Setting the peak tensile stress equal to the material tensile strength at the location of peak moment it follows that:

$$\sigma_x = \frac{f_t \cdot x}{\mathrm{a}} \tag{8.24}$$

Considering the free body diagram of an elementary segment Δx of a horizontal cross section of the lower part (tension zone), and by using $\Sigma F_x=0$ the horizontal shear force (*H*) acting over the cut is estimated.

$$\Sigma \mathrm{F_x} = 0 \Rightarrow H - T - \Sigma \mathrm{F_t} = 0 \Rightarrow H = T + \int \sigma_x dA = \pi d_b \cdot n_b \cdot f_b \cdot \mathrm{x} + b \cdot \frac{f_t \cdot x}{\mathrm{a}} \int_0^y dy = \pi d_b \cdot n_b \cdot f_b \cdot \mathrm{x} + b \cdot \frac{f_t \cdot x}{\mathrm{a}} \cdot y \tag{8.25}$$

The shear flow (*q*) associated with flexure is estimated by considering the difference in normal stresses between two adjacent beam cross sections in the shear span ($q=H/\Delta x$). Considering the free body diagram of an elementary segment Δx, as depicted in Fig. 8.12, the shear flow at a distance *x* from the tension face is calculated and from there the corresponding shear stress, $\tau(x,y)$, as follows:

$$\tau_{xy} = \frac{\Delta \mathrm{H}}{\Delta \mathrm{A}} = \frac{\pi d_b \cdot n_b \cdot f_b}{b} + \frac{b \cdot \frac{f_t \cdot x}{\mathrm{a}} \cdot y}{b \cdot x} = \frac{\pi d_b \cdot n_b \cdot f_b}{b} + \frac{f_t \cdot y}{\mathrm{a}} \tag{8.26}$$

To evaluate the shear strength of the SHFRCC cross section, the maximum shear stress that develops in the critical section at the neutral axis location where the state of stress is pure shear, denoted her as τ_{max}, is used.

$$\begin{aligned} V &= b\int_0^y \left(\frac{\pi d_b \cdot n_b \cdot f_b}{b} + \frac{f_t \cdot y}{\mathrm{a}} \right) dy + b \cdot \frac{2}{3} \cdot \left(\frac{\pi d_b \cdot n_b \cdot f_b}{b} + \frac{f_t \cdot y}{\mathrm{a}} \right) \cdot (h - y) = \\ &= b \frac{\pi d_b \cdot n_b \cdot f_b}{b} (y - c_1) + b \frac{f_t \cdot y^2}{2 \cdot \mathrm{a}} + b \cdot \frac{2}{3} \cdot \frac{\pi d_b \cdot n_b \cdot f_b}{b} \cdot (h - y) + b \cdot \frac{2}{3} \cdot \frac{f_t \cdot y}{\mathrm{a}} \cdot h - b \cdot \frac{2}{3} \cdot \frac{f_t \cdot y^2}{\mathrm{a}} = \\ &= \pi d_b \cdot n_b \cdot f_b \cdot (y - c_1 + \frac{2}{3}(h - y)) + b \cdot \frac{f_t \cdot y}{\mathrm{a}} \left(\frac{4\mathrm{h} - \mathrm{y}}{6} \right) \\ &= \pi d_b \cdot n_b \cdot f_b \cdot (\frac{1}{3} y - c_1 + \frac{2}{3} h) + b \cdot \frac{f_t \cdot y}{\mathrm{a}} \left(\frac{4\mathrm{h} - \mathrm{y}}{6} \right) \end{aligned} \tag{8.27}$$

where c_1 is the clear cover of the reinforcing bars, the depth of the tensile region of the cross section is taken here as $y=0.6h$, f_b is the bond strength, d_b is the diameter of one reinforcing bar and n_b is the number of reinforcing bars. The factor 2/3 that is used to estimate the integral of shear stresses over the zone under compression is the coefficient "α" that is normally used to deduct the equivalent rectangular stress block used for the flexural analysis of beams as per Georgiou and Pantazopoulou [70] associating

the distribution of stresses to Hognestad's parabola and by setting the strain at the extreme layer under compression ($\varepsilon_{c,max}$) equal to the strain of the composite at maximum compressive stress (ε_{co}).

$$\alpha = \frac{\varepsilon_{c,\max}}{\varepsilon_{co}} \cdot \left(1 - \frac{\varepsilon_{c,\max}}{3\varepsilon_{co}}\right) = \frac{2}{3} \tag{8.28}$$

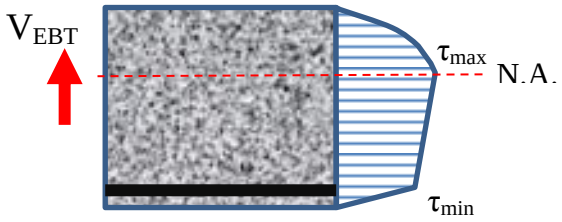

Figure 8.13: Shear stress distribution over the depth of the beam

From Eq. 8.27 three mechanisms contributing to the shear strength of a reinforced beam may be obtained, those being the contribution of the composite region under tension, the contribution of the composite region under compression and the contribution of the bond strength of the reinforcement. Based on the above Eq. 8.29 is revised for the cases of the composites without fibers where the composite in the tensile region does not contribute to shear.

$$V = b\int_0^y \left(\frac{\pi d_b \cdot n_b \cdot f_b}{b}\right) dy + b \cdot \frac{2}{3} \cdot \left(\frac{\pi d_b \cdot n_b \cdot f_b}{b}\right) \cdot (h - y) = \pi d_b \cdot n_b \cdot f_b \cdot (\frac{1}{3} y - c_1 + \frac{2}{3} h) \tag{8.29}$$

The tensile strength of the cementitious materials used was obtained indirectly by the four point bending tests conducted on unreinforced beams as per the Model Code [49] with the use of the flexural tensile strength:

$$f_{t,fl} = M_y/(bh^2/6) \tag{8.30}$$

Clearly reinforcement bond strength is an important parameter in estimating the shear strength (see Perez and Pantazopoulou [145]). Bond strength may be controlled either by a pull-out failure (for good bond conditions) or by splitting failure (poor bond). Bond strength is increased by the frictional resistance that may be mobilized through stirrups as per Tastani and Pantazopoulou [146]:

$$f_{b,c} = \frac{2\mu}{\pi} \cdot (\sigma_c + \sigma_{st}) = \frac{2\mu \cdot f_t}{\pi \cdot d_b} \cdot \left(c_1 + \frac{A_{st} \cdot e \cdot f_{y,st}}{n_b \cdot f_t \cdot s}\right) \Rightarrow f_{b,c} = 0.57 \frac{c_1}{d_b} f_t + 0.19 \frac{A_{st} \cdot f_{y,st}}{n_b \cdot d_b \cdot s} \tag{8.31}$$

In Eq. 8.31 the coefficient of friction for deformed steel is taken μ=0.9, while the coefficient e=0.33 averages stirrup-induced confining pressures over the spacing s [146, 147]. Also, A_{st} is the area of the stirrup legs crossing the potential splitting plane, s is the spacing of stirrups (=50mm here), n_b is the number of bars restrained by a stirrup (here, n_b=2) and d_b is the typical diameter of the main bar while c_1 is the concrete cover. Values of bond strength for each beam are given in Table 8.4. Results for all specimens obtained from application of Eq. 8.29 are depicted in the diagram of Figure 8.15.

(b) Strut and Tie Approach

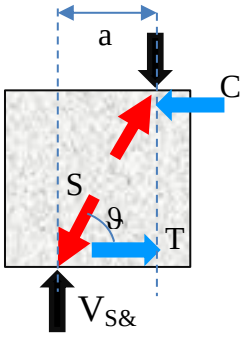

$$T = S\cos\vartheta;$$
$$V_{S\&T} = S\sin\vartheta;$$
$$\Rightarrow V_{S\&T} = T\tan\vartheta$$

Figure 8.14: Strut and Tie model

In the cases of the short beams (a/h≤1) without steel reinforcement the beam theory underestimates the sustained shear force measured in the tests. Note that beam theory is more appropriately applied to the B-region of beams. As short shear span beams do not transfer shear through beam action but rather, through a truss-mechanism (MacGregor [97]), the corresponding strength of a pertinent Strut and Tie model as depicted in Fig. 8.14 is also calculated, with due consideration of the limiting mechanisms described in the previous section. For a given set of loads the model embodies a system of forces in equilibrium with the external loads and support reactions. For the unreinforced members equations governing the behavior are as follows:

$$T = S\cos\vartheta; V = S\sin\vartheta; \Rightarrow V = T\tan\vartheta \quad (8.32)$$

The ultimate strength of the tension tie (i.e. the resultant force of the SHFRCC matrix normal stresses in the tension zone) is equal to $T=a{\cdot}f_t{\cdot}b{\cdot}(h\text{-}c)$ where c is the depth of compression zone and α a coefficient to account for the shape of the normal tensile stress block in the tension zone ($1/2\leq\alpha\leq1$). For failure of slender elements the lower bound value is considered for α on account of the wide crack penetration from the tension face into the web. After parametric investigation of SHFRCC sections in flexure it was concluded that the height of tension zone, $(h\text{-}c)$ may be approximated as $0.6h$ near the ultimate limit state of concrete compression crushing, therefore, $T\approx0.6\alpha{\cdot}f_t{\cdot}b{\cdot}h$ (this is consistent with the suggested geometry of the truss for deep beams, by Schaich et al [148]). For the case where steel reinforcement is used in the tensile region then the tie should also consider the contribution of the SHFRCC in the tensile zone) - as well as the tensile strength of the steel bars which is always limited by the anchorage capacity beyond the node of the strut and tie system over the support. The anchorage capacity usually controls – according with MC 2010 [49] a bar with a hook immediately past the support can anchor a tensile force equal to $50A_bf_b$, which is generally less than the yield force of the reinforcement, f_yA_b. Another plausible mechanism of failure could be compression softening of the diagonal strut due to parallel cracking - 60% of the strut strength is assumed in the EC2 [141], when referring to plain concrete, but in order to account for the effective confinement imparted by the fibers that cross the cracks, higher amounts could be defended. The black curve on the right hand side marks

the delayed failure of SHFRCC as compared to the dashed line for plain concrete; to estimate the effective width of the strut (b_{ef}) Schlaich and Weischede [149] recommended that b_{ef} be taken equal to $l/3$, where l is the length of the strut. Therefore ultimate compressive strut strength is $S=(0.6\sim0.8)\cdot f_c\cdot b\cdot b_{ef}$. Values of shear strength based on the proposed strut and tie model for all beams are listed in Table 8.4.

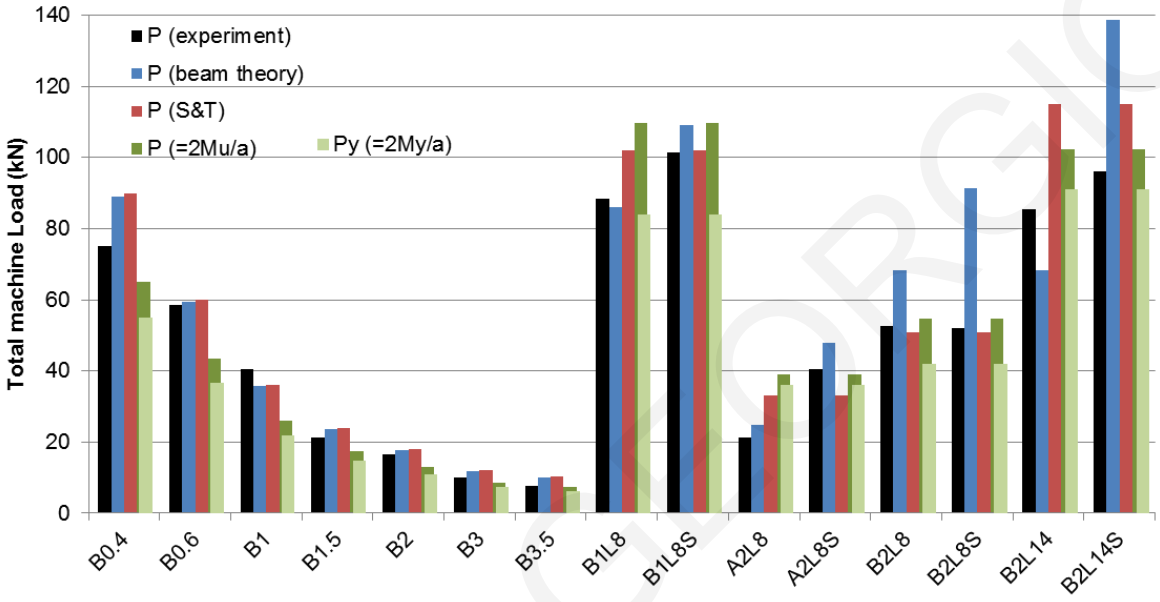

Figure 8.15: Comparison of strength estimates for all specimens: Shear capacity of members based on beam theory P (beam theory), Failure load based on strut and tie model P (S&T), Flexural Shear demand at maximum flexural load and at yield P (=2M_u/a and 2M_y/a) and Experimental failure load P (experiment) for all beams

In Fig. 8.15 the experimental results are compared with the values calculated from the alternative models examined: these include the values from the strut and tie model analysis (considering the anchorage capacity of the horizontal reinforcement) P (S&T), the shear strength associated with material diagonal tension failure according with the Engineering Beam Theory, P (beam theory =2V_{eb} (Eq. 4)), as well as the flexural shear demand values for yield and maximum moment, P_y (CSA) =2V_y and P_u (CSA) =V_u, (these are the shear forces estimated from cross sectional analysis of each beam, from: $V=M/a$). Cases where the flexural shear demand is the lowest of all estimates are considered to be flexural failures. Note that in most cases the Strut and Tie model produces a good approximation of the failure load, considering both specimens with and without steel reinforcement, regardless of the failure mode that was observed. In light of the complexity of the other approaches it seems that the strut and tie model prevails for its relevance with the experimental results in interpreting the behavior of reinforced SHFRCC elements with a/h ratios ≤2.

Table 8.4: Determination of shear capacity based on proposed model and comparison to failure mode and load

Name	Bot. Reinf.	Top Rein.	Stir.	P (experi.)	M/**V**[1]	P_y (CSA)	P_u (CSA)	f_b	V_{eb} (comp)	V_{eb} (bars)	V_{eb}	P_{eb}	P (S&T)	
A1	-	-	-	12000	0.6/**6**	0	0	0.00	6800	0	6800	13600	N/A	
B0.4	-	-	-	75145	1.5/**37.6**	55000	65000	0.00	46750	0	46750	93500	90000	
B0.6	-	-	-	58433	1.75/**29.2**	36667	43333	0.00	31167	0	31167	62333	60000	
B1	-	-	-	40582	2.02/**20.2**	22000	26000	0.00	18700	0	18700	37400	36000	
B1.5	-	-	-	21262	1.6/**10.6**	14667	17333	0.00	12467	0	12467	24933	24000	
B2	-	-	-	16426	1.44/**7.2**	11000	13000	0.00	9350	0	9350	18700	18000	
B3	-	-	-	10153	1.53/**5.1**	7333	8667	0.00	6233	0	6233	12467	12000	
B3.5	-	-	-	7663	1.34/**3.83**	6286	7429	0.00	5343	0	5343	10686	10286	
B1L8	2Φ8	-	-	88402	4.42/**44.2**	84000	109600	7.84	18700	26264	44964	89927	102000	shear
B1L8S	2Φ8	2Φ8	Φ6/50	101442	5.07/**50.7**	84000	109600	11.42	18700	38265	56965	113930	102000	flexure
A2L8	2Φ8	-	-	21178	2.11/**10.59**	36000	39000	2.85	0	9550	9550	19101	33000	shear
A2L8S	2Φ8	2Φ8	Φ6/50	40548	4.05/**20.27**	36000	39000	6.43	0	21552	21552	43104	33000	flexure
B2L8	2Φ8	-	-	52709	5.27/**26.35**	42000	54800	7.84	9350	26264	35614	71227	51000	flexure
B2L8S	2Φ8	2Φ8	Φ6/50	51931	5.18/**25.9**	42000	54800	11.42	9350	38265	47615	95230	51000	flexure
B2L14	2Φ14	-	-	85329	8.53/**42.66**	91000	102400	4.48	9350	26264	35614	71227	115000	shear
B2L14S	2Φ14	2Φ6	Φ6/50	96200	9.6/**48.1**	91000	102400	10.75	9350	63018	72368	144736	115000	flexure

The tie force of the Strut and Tie model is calculated based on: $T=0.6\cdot h\cdot b\cdot f_{ty}+A_s\cdot f_y$*. Here it is assumed that the height of tension zone effectively participating to the resultant tie force (for SHFRCC) is 60% of *h* (Schleich et al. [24]).

Flexural capacity of the beams was calculated with cross sectional analysis (CSA) by dividing the height of the cross section in ten layers of equal height. Values of yield load (P_y) and ultimate load (P_u) was calculated from yield and ultimate moment values as $P=2\cdot M/a$.

*According with Model Code 2010 the anchorage strength contributed by of a hook to the development capacity of a bar is 50 times the bar area times the bond strength. Thus, considering that the beam specimens extend only 50mm beyond the support so as to accommodate the hook type anchorage, the strength of the bars as tension ties in the nodal region of the strut and tie model adjacent to the support is limited in some cases by the hook capacity.

[1] Bold numbers refer to the experimental shear values.

8.4 Conclusions

Comparing the two mix design cases A (without fibers) and B (SHFRCC), it is concluded that fibers effectively alter the mode of failure of the specimens by providing a substantial increase in load-carrying capacity through (a) the increase in shear resistance of the shear spans and (b) the contribution of the tensile zone of concrete to flexural strength. Comparison of A2L8 group of specimens with the corresponding B2L8 group highlights these effects in a most substantive manner: in the absence of any conventional form of shear reinforcement the shear strength of the B specimens is more than double that of the A specimen group, whereas the failure mode is altered from shear to flexure. To interpret this increase of web shear strength, equally plausible alternative mechanistic models are considered, including a model based on the Engineering Beam Theory and a strut-and-tie alternative that is suitable for shorter beams; in all cases the effective contribution of the SHFRCC tensile zone to the web shear resistance as well as the cover resistance to bar-dowel action up to very large levels of tensile strain is dully considered, as it opens up an innovative prospect of replacing conventional stirrup-confined concrete with an SHFRCC matrix. In particular, for the strut-and-tie alternative, the various possible partial forms of failure that could limit the system strength were identified and explicitly considered, with particular emphasis on the anchorage limitations to the tie development capacity that occur near the strut and tie node.

The models were used to derive design expressions for beam strength depending on the aspect ratio of the shear span. These were used to corroborate successfully the experimentally observed specimen strengths, providing a consistent representation of the involved failure phenomena without burdening the designer with lengthy calculations. Several open issues need to be further addressed by future experiments, however, which would require the extension of the experimental database with larger scale components.

Sustainability is a combination of the structural design by increasing the life time of structures and the material design in order to decrease the exploitation of resources and simultaneously assist in achieving the previous goal. Shorter life time of structures is more costly and resource intensive also if one accounts for the greater maintenance costs required. In this research it was shown that the combined effect of the use of high volume fly ash composites and the use of short discontinuous fibers results in materials that exhibit enormous ductility in tension, compression, shear and flexure if compared to normal concrete. This greener material that uses less resources by the exploitation of the great mass of waste materials such as fly ash can improve the durability of structures and its resistance to extreme events that would place excessively large deformation demands on the structure, well beyond the levels implied by the design intensities of the most extreme accidental loads considered by current codes. The aim of this Chapter was to research the mechanical performance of these cementitious composites that exhibit strain hardening, improved sustainability, high fracture toughness and low resource abuse. Thorough research will enable their adoption by new Codes, enable their spread and development and will give multiple advantages in

the field of construction, widening the area of capabilities for innovative cement-based products. It will also enable the development of effective rehabilitation solutions to durability problems encountered in existing structures due to adverse environmental conditions. From the tests it was seen that in cases where cracking behavior was marked by formation of a large network of fine cracks, a superior overall material toughness was obtained. These findings suggest that a whole new generation of Cement based materials is possible, where tensile strength and strain capacities are so high that they provide a totally different context for formulation of concrete mechanics and consequent reinforcement detailing. Additionally the improved performance can lead to more slender member dimensions, reduced amounts of steel reinforcement particularly for shear and confinement, easing construction effort and energy requirements.

Chapter 9: Bond of steel bars in SHFRCC

9.1 Introduction

Reinforced concrete members rely on steel reinforcement to resist the tensile forces, while stresses are transferred from the concrete to the steel bars through bond. If no bond forces existed then bars would be pulled out of concrete. Bond stresses exist in beam members where the tensile forces in bars changes from point to point and are even related to shear force through [97]:

$$\tau_{avg} = \frac{V}{\pi \cdot \mathrm{d_b} \cdot j \cdot d} \tag{9.1}$$

where $j \cdot d$ is the internal lever arm and d_b is the bar diameter. One the most common tests used to determine the bond strength of bars is the pull out test shown in Fig. 9.1, where a concrete cylinder or prism containing a bar is mounted on steel plates while the steel bar is pulled out. The inconsistencies of this type of test lie in that the concrete near the loaded end of the bar is under compression [150] whereas the steel plate on which the specimen bears as the bar is being pulled out creates friction on the face of the concrete block preventing lateral expansion that would naturally occur due to Poissons' effects. As the concrete block is not allowed to expand freely, unwanted confinement is generated, therefore leading to a spurious increase of bond strength that does not exist in reality. These problems led researchers to seek new types of specimens and testing setups in order to quantify bond strength of bars in concrete.

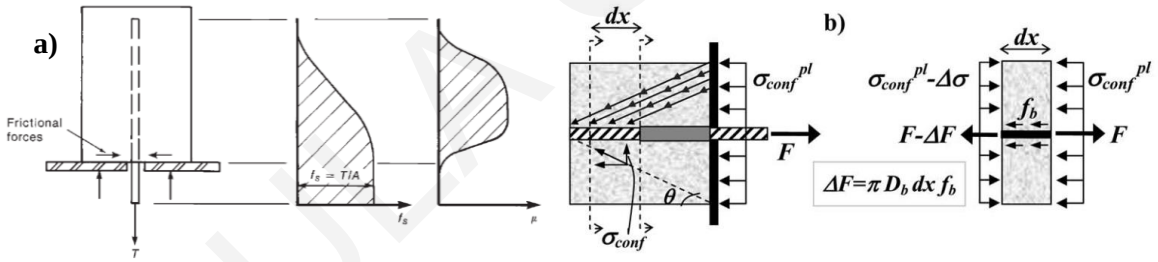

Figure 9.1: (a) Testing method, bar stress and bond stress [97] and (b) stress state in the standard pull-out test [150]

Tastani and Pantazopoulou [150] proposed the direct tension pullout (DTP) test as shown in Fig. 9.2 (i) where a concrete prism contains one bar anchored to one end and a collinear supporting bar on the other, both being pulled in tension. With this geometry the bars transfer tensile stresses to the surrounding concrete, conditions resembling the ones in the tensile zone of members where both the steel bars and the surrounding concrete are in tension. Under these experimental conditions a biaxial tensile stress field exists since both in the longitudinal bar direction but as well as on the transverse to the bar direction the concrete of the cover is mobilized in tension by the bars; the experimental results are expected to give the lowest bound of the bond strength.

Smooth bars resist translation in concrete by adhesion and friction mechanisms, both of them lost quickly due to the decrease of the bar's diameter caused by the Poisson's effect, therefore ribbed bars are most commonly used to secure prolonged engagement of the concrete cover as the bar is being pulled. Fig. 9.2 (ii) shows the mechanisms transferring loads from the bar to the

concrete. These stresses have both a longitudinal and a radial component. The radial component creates splitting cracks parallel to the bar that leads to failure. The load at which splitting cracks occur is related to the cover of the bar, the tensile strength of concrete and the average bond strength. In the cases of large covers the other type of failure is the pull-out failure, where the ribs shear off the concrete cylinder defined by the tips of the ribs between them and the bar is pulled out.

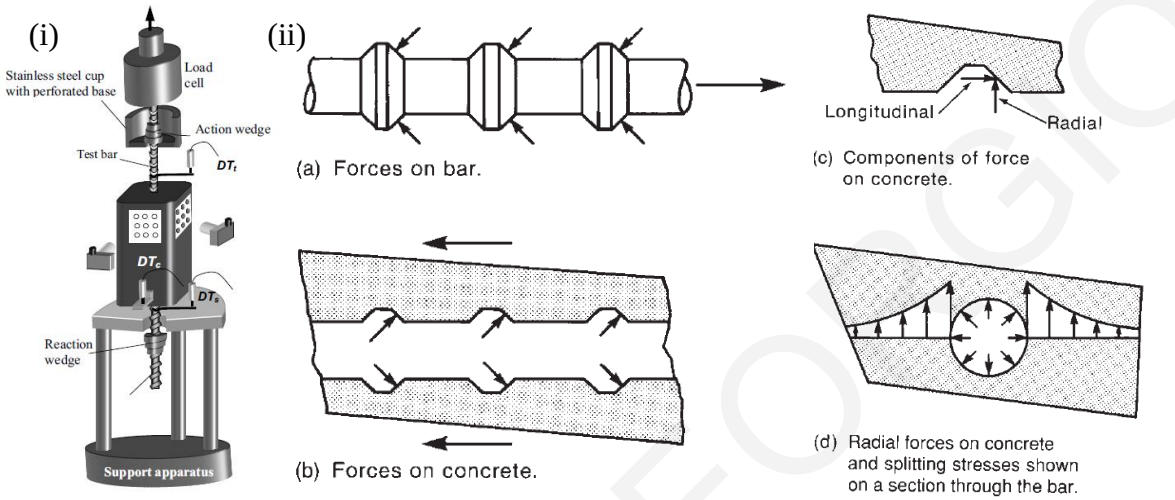

Figure 9.2: (i) Configuration of the DTP bond test [150] and (ii) Bond transfer mechanism [97]

Taking the above mechanics into consideration it is evident that bond mechanism is directly related to the tensile capacity of the surrounding to the bar concrete. The use of a composite that exhibits strain hardening in tension, i.e. multiple cracking, changes the mechanics of the bond resistance mechanisms. The fibers in the composite have the ability to bridge the cracks developed by the bond transfer and provide confinement. In order to investigate these new mechanisms a series of bond tests were performed for the purpose of this thesis. The strength of the cover against splitting as well as the development capacity of bars anchored in SHFRCC are studied through tests conducted on specially designed tension pullout specimens. Parameter of study was the steel bar diameter, the anchorage length of the bars and the bar cover; the matrix comprised PVA-reinforced high fly-Ash content, fine-aggregate concrete with a long term tensile strain capacity in excess of 1% strain. The experimental results obtained from a series of 24 specimens were used to evaluate the bond along the anchorage as proposed by various code provisions.

9.2 Bibliographic Research

9.2.1 Experimental research

Lee et al. [151] investigated the performance of short and long steel bars embedded in SHFRCC. They studied the bond of 13mm bars with an embedment length of 65 mm (l_b=5d_b) and 260 mm (l_b=20 d_b) in normal concrete and SHFRCC, with the apparatus shown in Fig. 9.3. In this test setup steel plates were placed on the left and right surfaces of the concrete blocks and a hole of 80 mm diameter was opened on the top and bottom plates supporting the specimens at the exit

point of the bars in order to reduce the effect of the compression force on the bond behavior and to allow measurement of displacements.

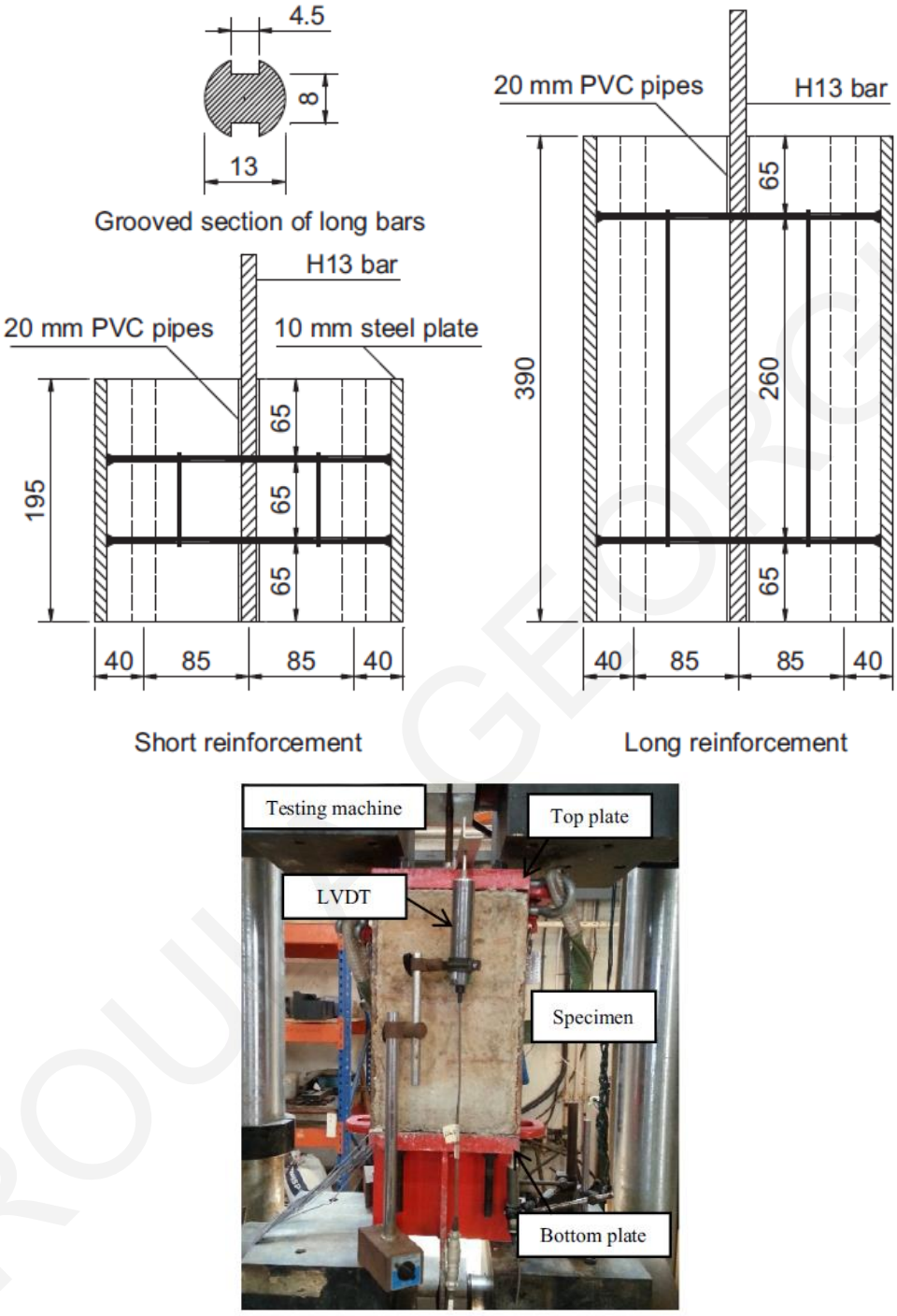

Figure 9.3: Testing setup for pull-out test [151]

Figure 9.4 shows the bond-slip relation of the short embedment length bars from the experimental tests of Lee et al. [151]. Bond strength is calculated assuming constant bond stress distribution along the embedment length. The bars did not reach their yield strength and were pulled out of the surrounding composites for both the SHFRCC and the normal concrete specimens, even though higher bond strengths were obtained for the SHFRCC by 14%. In this test adequate cover prevented splitting cracks and failure.

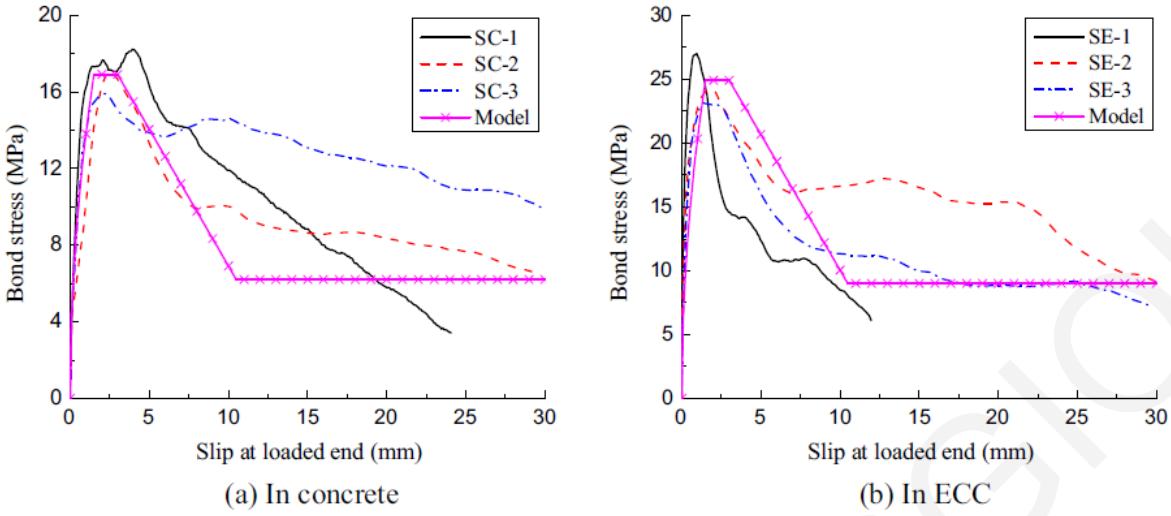

Figure 9.4: Bond-slip relation of short embedment length bars [151]

For the case of the long embedment length bars, they reached their ultimate strength with yielding and hardening of the bars while the surrounding matrix remained intact. The level of bond strength was almost the same for both the normal concrete and SHFRCC matrix but the slip of the bars in the SHFRCC was reduced as shown in Fig. 9.5.

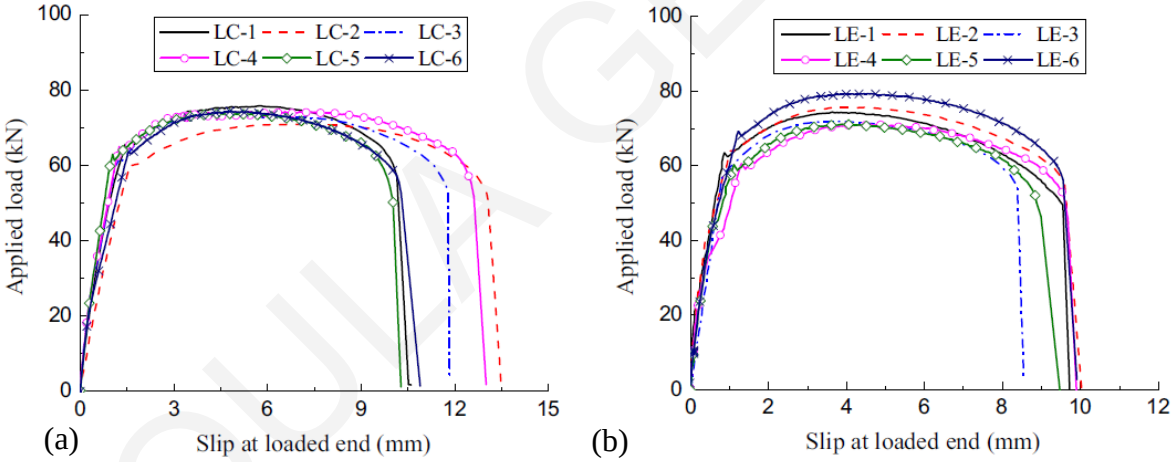

Figure 9.5: Bond-slip relation of long embedment length bars [151] in (a) Concrete and (b) SHFRCC

Chao et al. [152] studied the effect of strain softening and strain hardening fiber reinforced cementitious composites on the bond strength-slip response of deformed bars under monotonic and cyclic loading with the testing configuration shown in Fig. 9.6. The steel bars are embedded in a prism specimen that is loaded through steel plates, with a constant embedment length of 100 mm. The bar diameters were 16 mm and 25 mm with a nominal tensile strength of 420 MPa. Based on ACI Committee 408 (2003), stating that compressive forces on the pull-out test should be located at least at a distance equal to the embedment length away from the steel bar, the researchers did not use bearing plates for loading that would surround the bars but they used four steel plates on the corners of the concrete blocks as shown in Fig. 9.6.

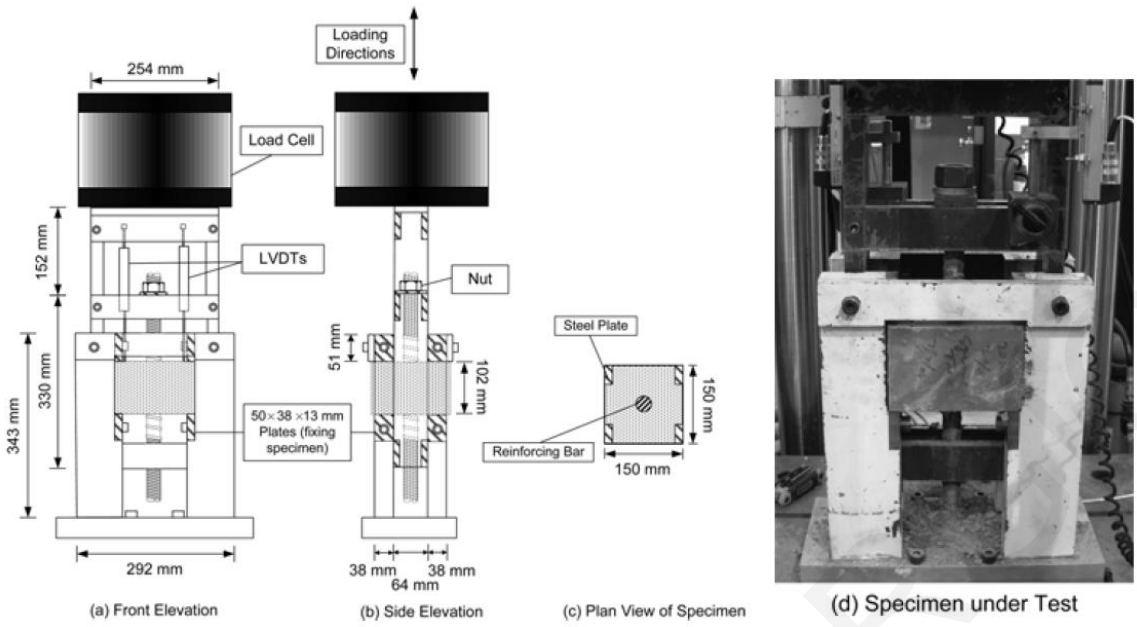

Figure 9.6: Test setup and specimen geometry [152]

Fig. 9.7 shows the tensile stress-strain curves of the fiber reinforced cementitious matrices used in this study for 2% percentage of fibers (fibers used were steel square twisted, rectangular twisted, hooked, UHM-PE fibers and PVA fibers) and the bond-slip law of 25 mm bars embedded in matrices with 1% fiber content. It is evident that the used of fibers in the cementitious matrix improves the pullout behavior of bars when compared to the control specimen, or even the spirally reinforced specimen that showed concrete spalling and a cone-shaped fracture.

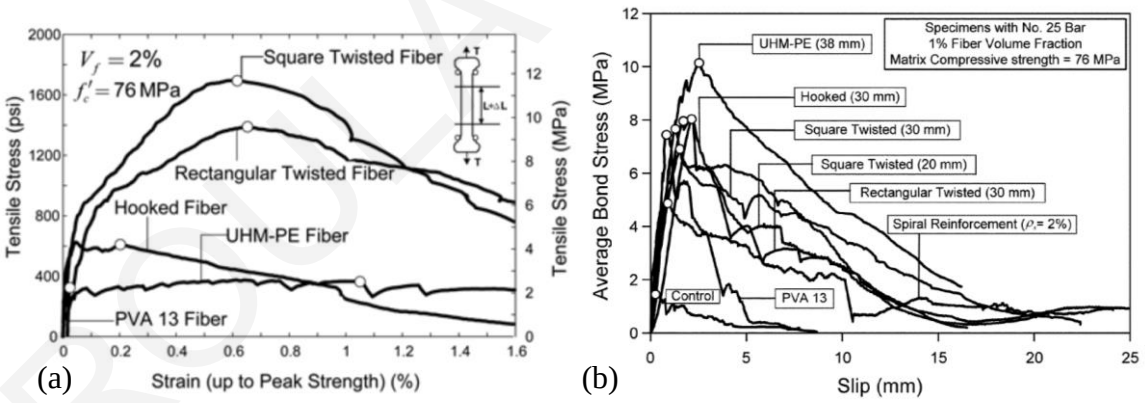

Figure 9.7: (a) Tensile stress-strain curves of the fiber reinforced composites used and (b) Bond-slip curves from all specimens [152]

The crack patterns for selected specimens are shown in Fig. 9.8 (a-f) with the control specimen to exhibit splitting and cracking and the spirally reinforced specimen illustrating a cone shape fracture. In the case of the fiber reinforced matrices, the fibers bridged the cracks and controlled the crack opening, creating multiple cracking and increasing the bond strength. On the same Figure the reversed cyclic loading results from two test specimens are depicted. The specimens with the UHM-PE fibers showed sustainment of their bond strength and stiffness up to 80% of the peak strength loading and a low residual slip in comparison to the plain concrete specimen.

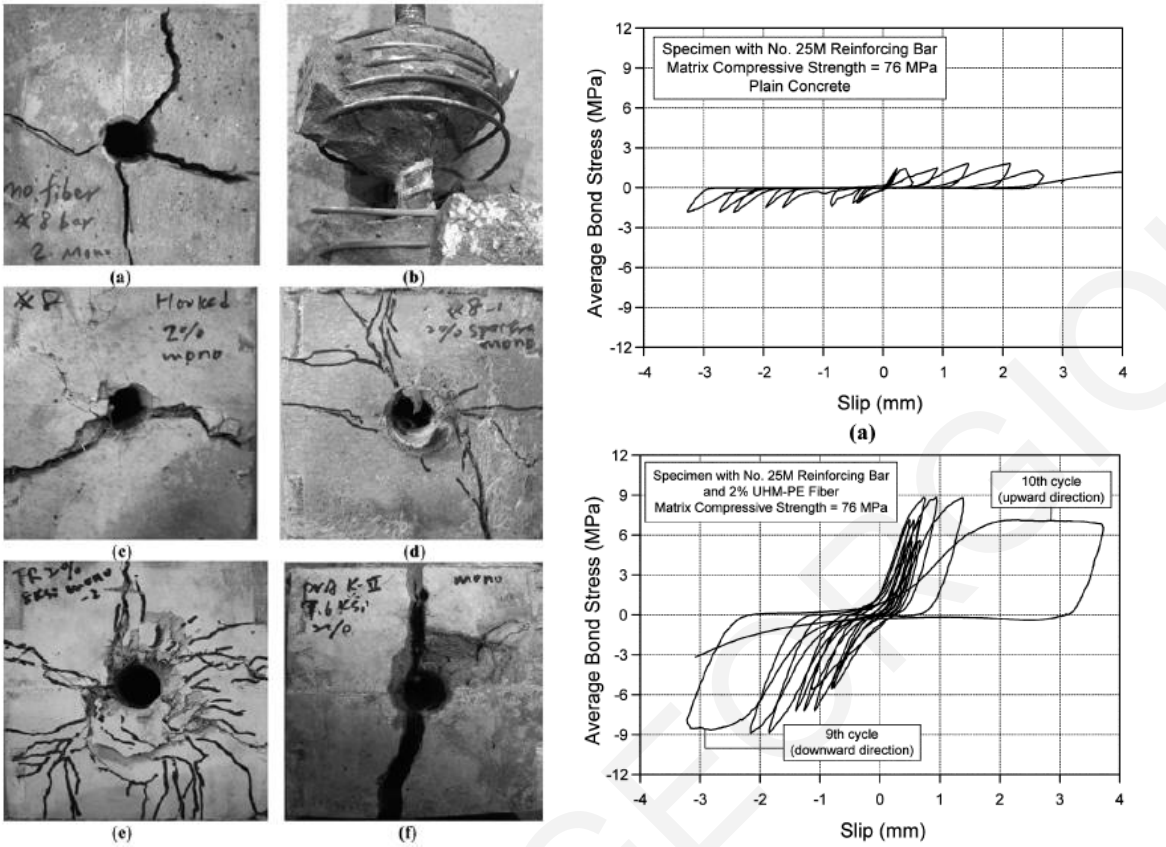

Figure 9.8: Cracking pattern in test specimens with various reinforcements under monotonic loading (No. 25M bar). Specimen with: (a) no fiber; (b) 2% spiral reinforcement; (c) 2% hooked steel fiber; (d) 2% UHM-PE fiber; (e) 2% rectangular steel twisted fiber; and (f) 2% PVA K-II fiber and Comparison of bond stress-slip responses under fully reversed, force-controlled cyclic loading. [152]

Krstulovic-Opara et al. [153] performed pull-out tests on a modified by Ezeldin and Balaguru [154] version of the Danish Standard DS2082 [102] also used by Chapman and Shah [101] shown in Fig. 9.9. Three types of matrices were used in this study; plain concrete, FRC and HPFRC. The crack pattern had the same sequence for all specimens: a crack initiating from A and propagating to B and while the splitting crack was widened a transverse crack initiated at point B. The experiment stopped when the transverse crack extended to the edge of the matrix cylinder.

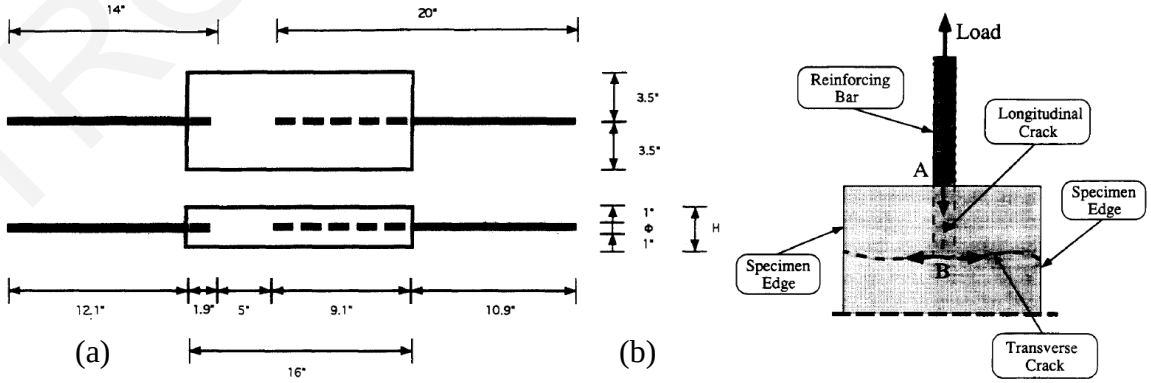

Figure 9.9: (a) Pull-out specimen and (b) crack pattern propagation in [153]

As is seen from the Load-slip curves of Fig. 9.10 the FRC and HPFRC show increased bond strength and ductility in comparison to the plain concrete matrix. This is attributed to the higher

tensile strength and the strain hardening behavior of the HPFRC in tension leading to multiple cracking with smaller crack widths. Additionally the slip at maximum bond strength is increased with increasing tensile strength and toughness of the cementitious matrix. Additionally the research related the final bond-slip resistance to the cover thickness of the bars stating that if the appropriate cover is not used then the strain hardening properties of the matrix do not provide the expected results. Additionally the researchers compare the experimental results to the empirical formulas given by expressions reported in Codes such as the ACI or other researchers and conclude that they cannot be used to predict the bond strength of bars embedded in SHFRCC, developing their own fitted model:

$$u_{ULT} = \left(0.5 + 0.89\frac{c}{d_b}\right)\cdot f_t + \left(1.2 + 0.83\frac{c}{d_b}\right)\cdot T_t^3 \qquad (9.1)$$

where c is the cover (in.), d_b is the bar diameter (in.), f_t is the tensile strength of the matrix (psi) and T_t is the toughness of the matrix (psi). Due to the fact that in their study the embedment length was not a variable, it is not included in the Equation.

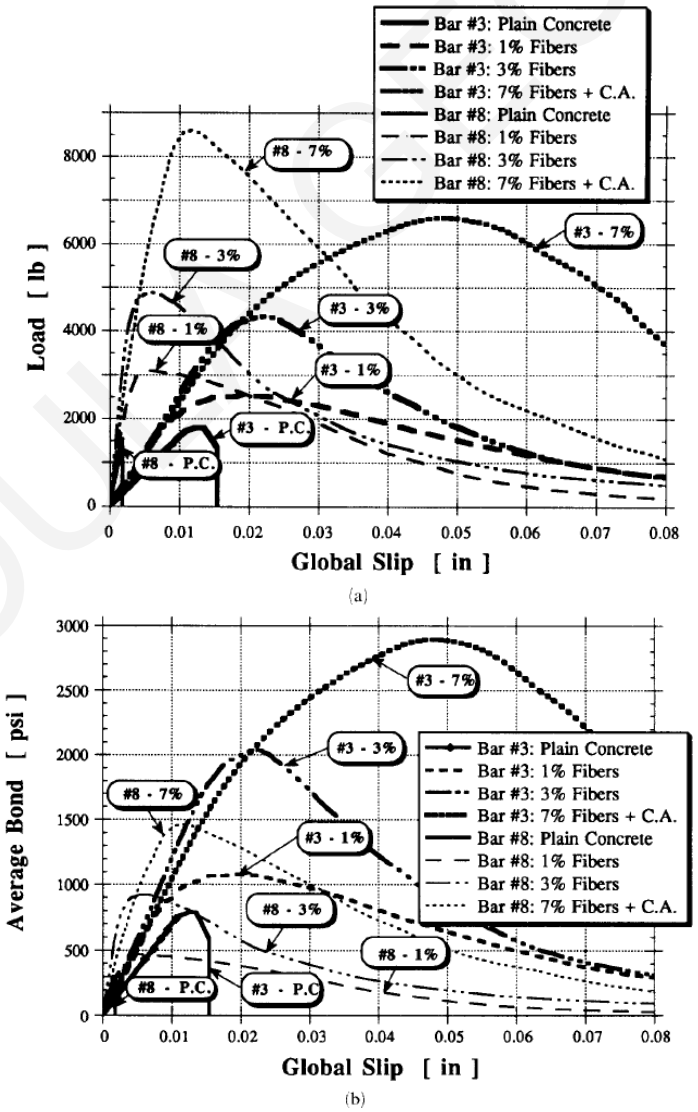

Figure 9.10: (a) Load-slip curves and (b) average bond-global slip curves in [153] (1 lb=4.45 N; 1 psi=0.0069 MPa; 1 in=25.4 mm)

Kanakubo and Hosoya [155] studied the bond-splitting strength of bars in SHFRCC with an aim in reducing the cover thickness and bar spacing. The test setup used in their research is shown in Figure 9.12 (a). A deformed bar of 13 mm was used with rib height and spacing of 1mm and 8.9 mm respectively. The embedment length was 4 times the bar diameter with a cover thickness that was a variable of study: it was set equal to 0.5, 1 and 1.5 times the bar diameter. Failure modes of the various cover thickness specimens are shown in Fig. 9.11 (b). Splitting cracks at the free end appear at the smaller cover thickness, while the side view shows the opening between the concrete and the slit.

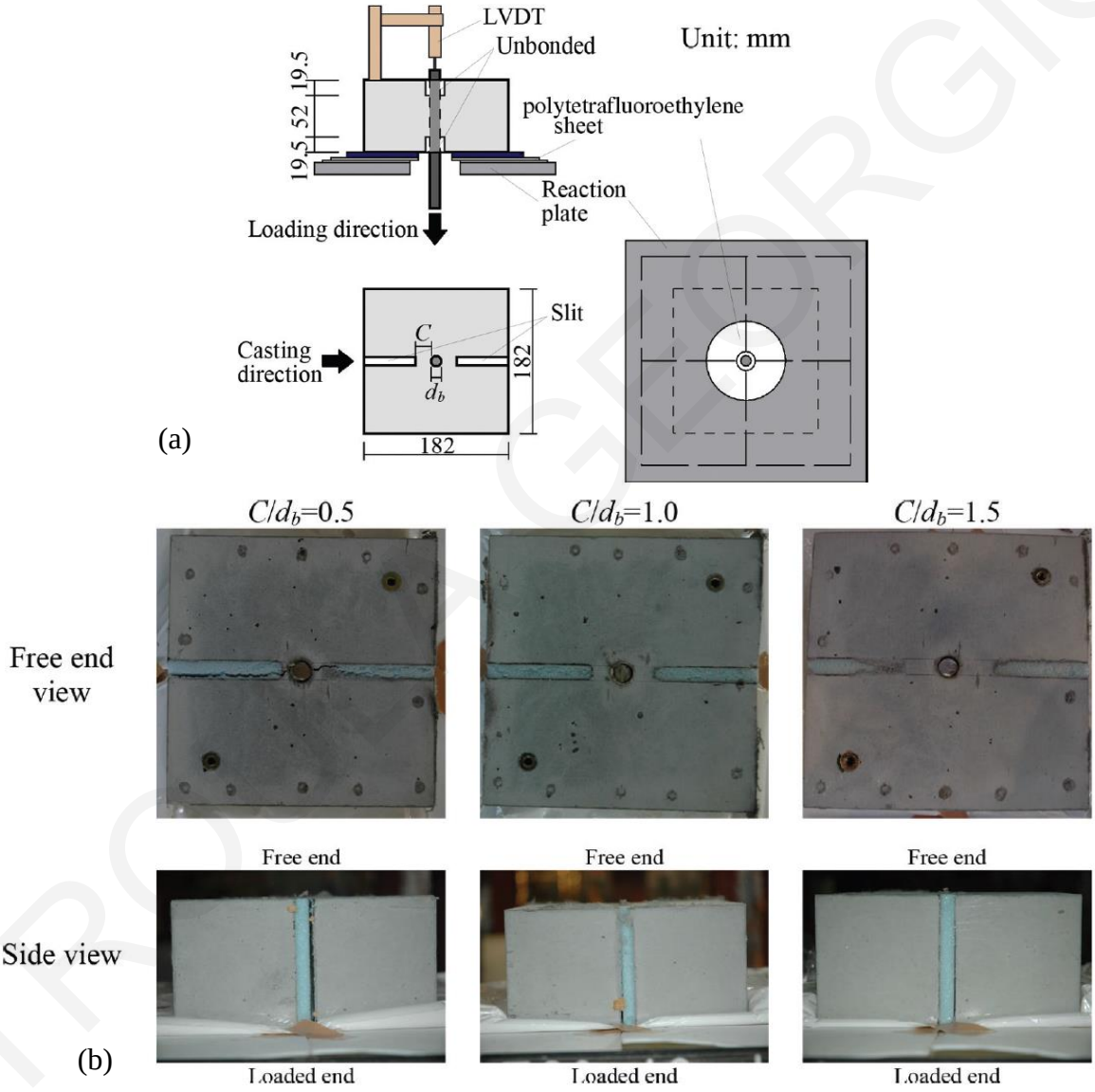

Figure 9.11: (a) Test setup and (b) pull-out specimens after loading [155]

As shown in the diagram of Fig. 9.12 (a) the maximum bond strength increased with increasing cover thickness. The softening branch had a reduced slope if compared to normal concrete and behaved in a ductile manner. The authors propose the following Equations for determining the bond strength:

$$\tau_b = \tau_{bc} + \tau_{bs} \tag{9.2}$$

Equation 9.2 states that bond stress τ_b is given by the sum of the bond provided by the splitting stress τ_{bc} and that engaged by the confinement provided by transverse reinforcement, τ_{bs}. The bond resistance to splitting provided by the SHFRCC is given in Eq. 9.3 assuming uniform tensile strength over the embedment length and using equilibrium of stresses:

$$\tau_{bc} = \sigma_t \cdot \frac{2c}{d_b} \cdot \frac{l_s}{l_b} \cdot \cot a \tag{9.3}$$

In Eq. 9.3 d_b is the diameter of the bar, l_b is the embedded length, σ_t is the tensile strength of SHFRCC, c is the cover thickness, l_s is the splitting length, α is the angle between principal bearing stress and axial direction. The confinement effect of the stirrups is calculated based on the proposal of Yasojima and Kanakubo [156] as per Eq. 9.4.

$$\tau_{bs} = \sqrt{0.018 \cdot \frac{b \cdot p_w}{N_t \cdot d_b} \cdot \frac{h_r}{9 d_w} \cdot E_s \cdot \sigma_B} \cdot \cot a \tag{9.4}$$

Where b is the width of the beam, p_w is the stirrup ratio, N_t is the number of main bars, d_b is the diameter of the main bar, h_r is the rib height, d_w is the diameter of the stirrup, E_{st} is the elastic modulus of the stirrup, σ_B is the compressive strength of the SHFRCC and α is the angle between principal bearing stress and axial direction (taken as 56°). Comparison of results between the proposed formula and the experiments are shown in Fig. 9.12 (b).

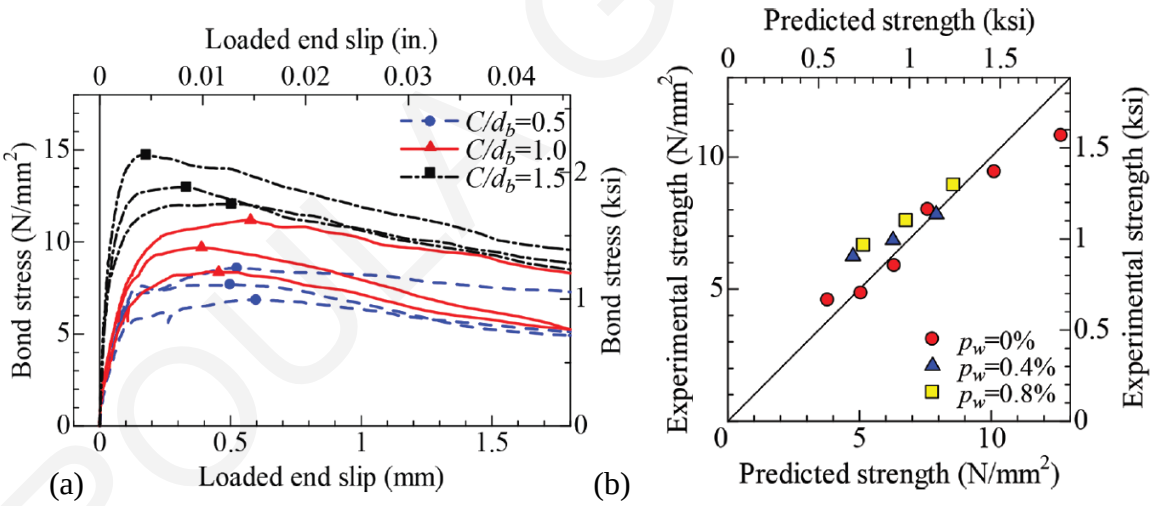

Figure 9.12: (a) Bond stress-slip curves from pull-out test and (b) comparison of experimental results with predicted strength [155]

Asano and Kanakubo [157] studied the effect of the size of cover with regards to the length of the fibers and its effect on bond strength with the testing setup shown in Fig. 9.13. The variables are the bar diameter (10, 13, 16 and 22mm) and the cover of the reinforcement (c/d_b=0.5, 1.0, 1.5 and 2), while the bond length remains constant for all specimens as 4 times the bar diameter.

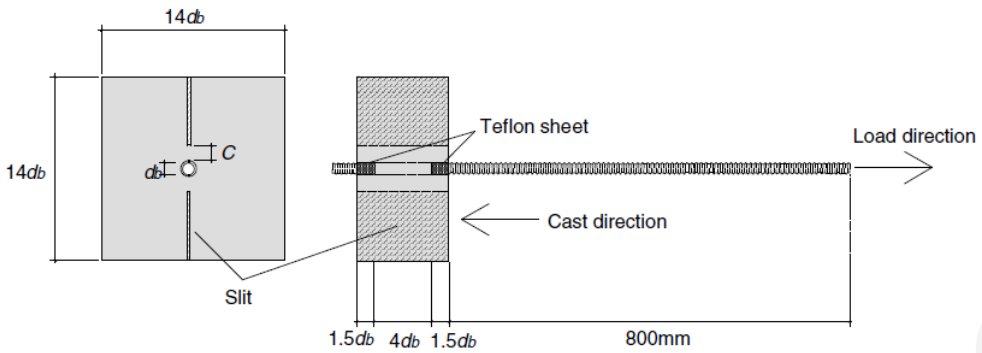

Figure 9.13: Shape of specimen and loading setup [157]

The bond stress-load end slip for all specimens are depicted in the diagrams of Fig. 9.14. The bond stress shows to decrease gradually after the maximum and its postpeak slope becomes steeper as the maximum bond stress increases. In all cases there is an increase of bond strength with increasing cover thickness and decreasing bar diameter.

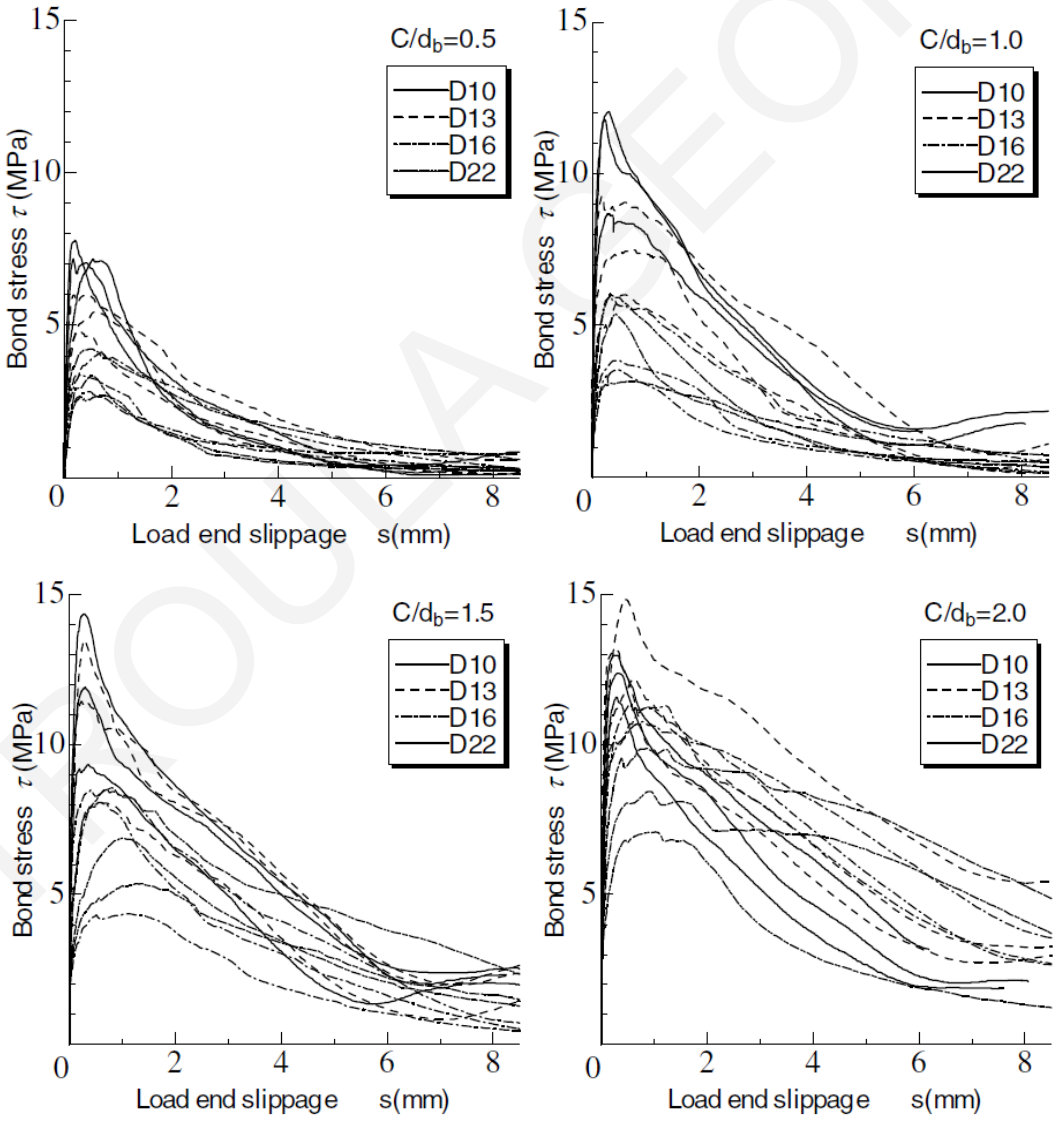

Figure 9.14: Bond stress-load end slip [157]

Saleem et al. [158] studied the bond strength of high strength steel (HSS) in Ultrahigh performance concrete (UHPC). Parameters of study were the bar diameter (10 and 22 mm) and the embedment length (10, 12, 14 and 48 times the diameter for Φ10 and 14, 16, 18 and 21 times the bar diameter for Φ22). They concluded that load capacity increased with increasing embedment length but they witnessed a variation in slip that they concluded it was due to local failure of concrete, leading to change in stiffness. They also witnessed that the Φ10 bars crossed the yield strain of 0.004 with the embedment length of $12d_b$ whereas the $18d_b$ embedment length calculated to be the one leading Φ22 bars to yielding showed premature local failure of the load-bearing area. All the Φ22 bars showed localization of cracking in the load region of the bar that leaded to crushing of concrete.

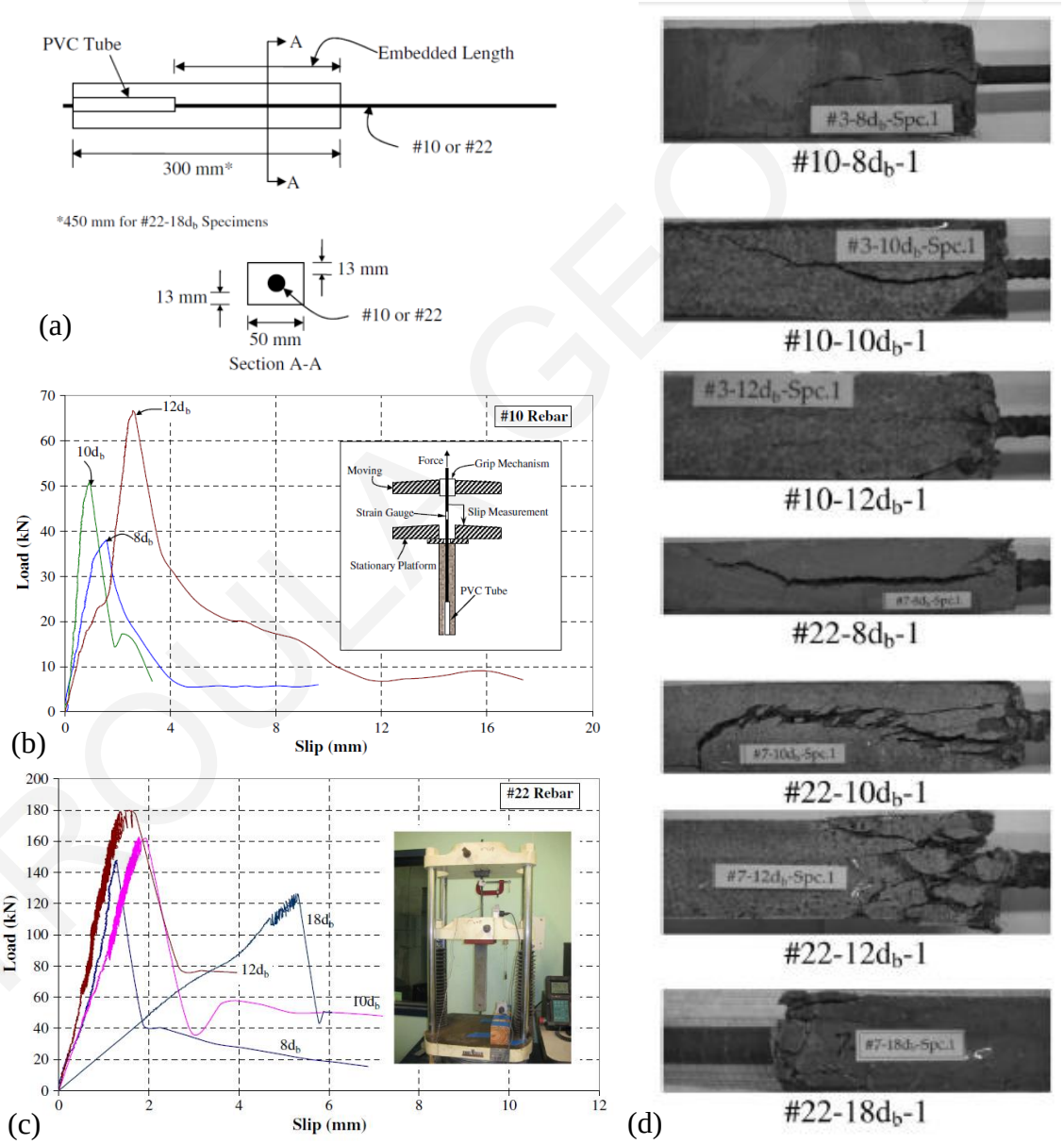

Figure 9.15: (a) Pull-out test specimen schematics, (b) Load-slip responses for Φ10, (c) Load-slip responses for Φ22 and (d) Modes of failure [158]

The above reported experimental data are the only ones available for bond strength of deformed steel bars in SHFRCC. Most of the tests are conducted in a manner that introduces compressive

stresses close to the loaded end of the bars, while in none of the above tests did the bars reach their yield value nor was any steel strain hardening possible for the bars. The variables studied were limited to either one or two of the following: bar diameter, cover thickness, embedment length. Taking the above into consideration no conclusive results for the bond-slip relation of steel bars in SHFRCC can be made.

9.2.2 Code Provisions

9.2.2.1 Analysis of bond stresses

Figure 9.16 shows a concrete cylinder of $2c_b$ diameter containing a bar subjected to pull-out. The radial component of the bond mechanism causes tensile stresses on the surrounding concrete having the distribution shown in Fig. 9.16 (b), but it is assumed to be in triangular distribution as shown in Fig. 9.16 (c) [97]. Splitting occurs when the maximum tensile strength f_{ct} in concrete is reached. Assuming that the ratio of the average tensile stress to the maximum tensile stress is 0.5 and the forces act at 45°, then the average bond strength at failure is calculated as:

$$\mu_{ave,u} = f_{ct} \cdot \left(\frac{c_b}{d_b} - \frac{1}{2} \right) \tag{9.5}$$

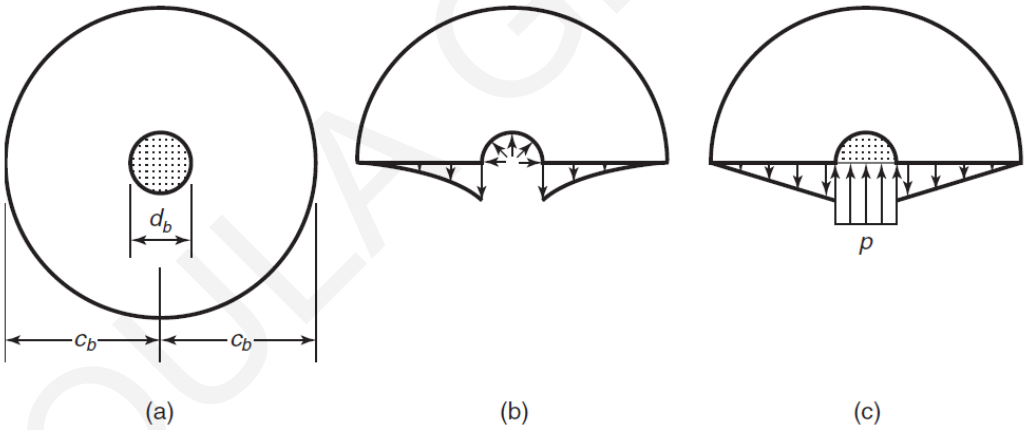

Figure 9.16: Concrete stresses in a circular concrete prism [97]

Due to the variation of bond strength along the length of a bar, MacGregor and White [97] use the concept of the development length l_d, which is the minimum required length of a bar necessary for it to reach its yield stress. Using an average bond stress of Δf_s the development length is estimated as:

$$l_d = \frac{f_y \cdot d_b}{4\mu_{ave,u}} \tag{9.6}$$

Combining Eq. 9.5 and 9.6 the development length may be estimated as function of the tensile strength of concrete:

$$l_d = \frac{f_y \cdot d_b}{4 f_{ct} \cdot \left(\frac{c_b}{d_b} - \frac{1}{2} \right)} = \frac{f_y \cdot d_b^2}{2 f_{ct} \cdot (2c_b - d_b)} \tag{9.7}$$

9.2.2.2 ACI Code

ACI Code Section 25.4.2.3 [48] gives a basic expression for determining the development length:

$$l_d = \frac{3}{40\lambda} \frac{f_y}{\sqrt{f'_c}} \frac{\psi_t \cdot \psi_e \cdot \psi_s}{\left(\frac{c_b + K_{tr}}{d_b} \right)} \cdot d_b \tag{9.8}$$

Where the confinement term $(c_b+K_{tr})/d_b$ is limited to 2.5 or smaller in order to avoid pull-out bond failures and the development length is not to be taken less than 12 in (304.8 mm). ψ_t is the bar location factor, ψ_e is an epoxy-coating factor, ψ_s is the bar size factor, λ is the lightweight concrete factor, c_b is the smaller distance measured from the edge of concrete to the center of a bar or half of the center-to-center spacing of the bars and K_{tr} is a transverse reinforcement factor.

Using the above equation to estimate the development lengths required for two bars of 8mm and 10mm diameter, that were used in the experimental tests and taking factors ψ_t, ψ_e,ψ_s and λ equal to 1, f_y=500 MPa, f_c=50 MPa, K_{tr}=1 and c_b=30 and 32 mm (for the 8 and 10 mm bars respectively) then the development length for the 8mm bar is l_d=204 mm and for the 10 mm bar is l_d=255 mm.

9.2.2.3 Model Code

The anchorage length is given is Section 6.1.3.3 of the New Model Code (2010) [49] as:

$$l_b = a_4 \frac{d_b \cdot \sigma_{sd}}{4 f_{bd}} \geq l_{b,\min} \tag{9.9}$$

Where α_4 is a function of the percentage of reinforcement anchored or lapped within $0.65l_b$ from the center of the anchorage or lap length considered. The minimum lap or anchorage length is defined as:

$$l_{b,\min} > \max\left\{ 0.3 \cdot \frac{l_b \cdot f_{yd}}{\sigma_{sd}}; 15 \cdot d_b; 200mm \right\} \tag{9.10}$$

Where σ_{sd} is the stress at yielding of the reinforcement and f_{bd} is the design ultimate bond strength (Section 6.1.3.2):

$$f_{bd} = (a_2 + a_3) \cdot f_{b,0} + 2 p_{tr} < 2 \cdot f_{b,0} + 0.4 p_{tr} < 2.5\sqrt{f_{ck}} \tag{9.11}$$

And $f_{b,o}$ is the basic bond strength, an average stress on the nominal surface of the bar over the bond length l_b (Section 6.1.3.1):

$$f_{b,0} = n_1 \cdot n_2 \cdot n_3 \cdot n_4 \cdot \sqrt{f_{ck}/20} / \gamma_c \tag{9.12}$$

Where n_1 is a coefficient for ribbed or plain bars, n_2 represents the casting position, n_3 represents the bar diameter, n_4 represents the characteristic strength of steel reinforcement.

9.2.2.4 Eurocode

Eurocode 2 [21] in Section 8.4.2 gives the design value for the ultimate bond strength as:

$$f_{bd} = 2.25 n_1 \cdot n_2 \cdot f_{ctd} \tag{9.13}$$

Where n_1 is the coefficient related to the bond conditions, n_2 is a coefficient related to the bar diameter and f_{ctd} is the design value of concrete tensile stress according to 3.1.6 (2) P.

The basic required anchorage length $l_{b,rqd}$ assuming constant bond stress is given in Section 8.4.3:

$$l_{b,rqd} = \frac{d_b \cdot \sigma_{sd}}{4 f_{bd}} \tag{9.14}$$

And the design anchorage length l_{bd} is given in Section 8.4.4:

$$l_{bd} = a_1 \cdot a_2 \cdot a_3 \cdot a_4 \cdot a_5 \cdot l_{b,rqd} \geq l_{b,\min} \tag{9.15}$$

Where α_1 is the effect of the form of the bars assuming adequate cover, α_2 is for the effect of concrete minimum cover, α_3 is the effect of confinement, α_4 is the effect of welded transverse bars, α_1 is the effect of pressure transverse to the plane of splitting and $l_{b,min}$ is the minimum anchorage length, where for anchorages in tension $l_{b,min} > \max\{0.3 l_{b,rqd}; 10 d_b; 100\text{mm}\}$.

9.2.2.5 JSCE Recommendations for SHFRCC

The basic development length l_d is given in Section 8.4.5 of the Japan Society of Civil Engineers Recommendations for SHFRCC [50] as:

$$l_d = a \frac{f_{yd}}{4 f_{bod}} d_b \geq 20 d_b \tag{9.16}$$

Where f_{bod} is the design bond strength of SHFRCC estimated as:

$$l_{bod} = 0.28 f'^{2/3}_{ck} / \gamma_c \leq 3.2 (N/mm^2) \tag{9.17}$$

And α is related to the concrete cover and the transverse reinforcement by k_c:

$$k_c = \frac{c}{d_b} + \frac{15 A_t}{s \cdot d_b} \tag{9.18}$$

The Recommendations [50] state that the calculation of the development length is based on the Standard Specification for concrete structures. They use experimental results with beams made with 2% fiber content shown in Fig. 9.17, with 25 mm bars with a minimum concrete cover of 10 mm. The Recommendations [50] also state that the fibers in SHFRCC matrix confine the surrounding matrix, however due to the lack of sufficient data they use the equations for normal concrete structures in order to calculate the basic development length.

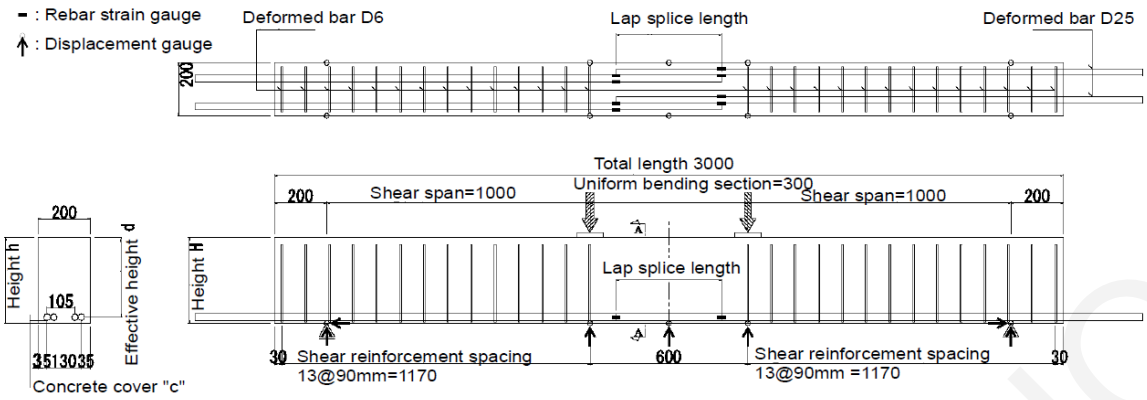

Figure 9.17: Experimental setup of pullout tests on bars in SHFRCC [50]

Table 9.1 gives the required anchorage length for two bar diameters (8 and 10mm) and different concrete covers as required from the equations provided from the four Codes and Standards described in the previous sections, taking the safety factors equal to 1. The bar diameters selected for the calculation are those that were used in the experimental program of this Thesis for the pull-out tests.

Table 9.1: Required anchorage length by different Codes

Bar diameter	**Cover (clear)**	l_{bd} *(ACI)*	l_{bd} *(MC)*	l_{bd} *(EC)*	l_{bd} *(JSCE)*
8	9.5	302.78	274.07	104.26	281.25
8	22.8	204.38	200.00	100.00	187.50
8	25.8	204.38	200.00	100.00	187.50
10	12	204.38	340.80	130.08	351.56

9.3 Description of experimental procedure

9.3.1 Testing Setup

A series of pullout tests were performed in the present thesis in order to investigate the parameters affecting bond of steel bars in SHFRCC. Study variables were the bar diameter, (i.e., 8 and 10 mm deformed steel bars S500 were used), the cover thickness c/d_b=1.2, 2.8, 3.2, where c is the clear cover of the bars, and the embedment length taking on values of 50, 80 and 120 mm. A number of 24 tests were performed, with 3 specimens for each combination. Combinations of bar diameter, cover and embedment length are shown in Table 9.2.

Table 9.2: Specimen Combinations for pullout tests

Specimen	d_b *(mm)*	c/d_b	l_b *(mm)*
F8A5C1/1-3	8	1.2	50
F8A8C1/1-3	8	1.2	80
F8A12C1/1-3	8	1.2	120
F8A8C2/1-3	8	2.8	80
F8A8C3/1-3	8	3.2	120
F8B5C1/1-3	10	1.2	50
F8B8C1/1-3	10	1.2	80
F8B12C1/1-3	10	1.2	120

The testing setup used for this study was a modification of the direct-tension pullout bond test developed by Tastani (2006) as shown in Figure 9.18. The test specimen comprised of a cementitious composite prism with a rectangular cross section. Two collinear bars of the same diameter were embedded on the two opposite sides of the specimen with embedment lengths of l_b and l_b+50 mm. Between the two bars a distance of 50 mm was left without any steel reinforcement. These parameters determined the height of the cementitious composite prism as $2l_b$+100 mm in order to avoid direct tension failure in the central 50 mm region between the bars. Thus, the tensile strength of SHFRCC (predicted tensile strength=3 MPa) was used to determine the width of the cross-section: for the cementitious composite cross section to support the ultimate tensile strength of the bar (=500 MPa), the required width of the cross section was estimated equal to 260 mm. The depth of the cross-section was determined by the variables of the experimental procedure as $2c+d_b$.

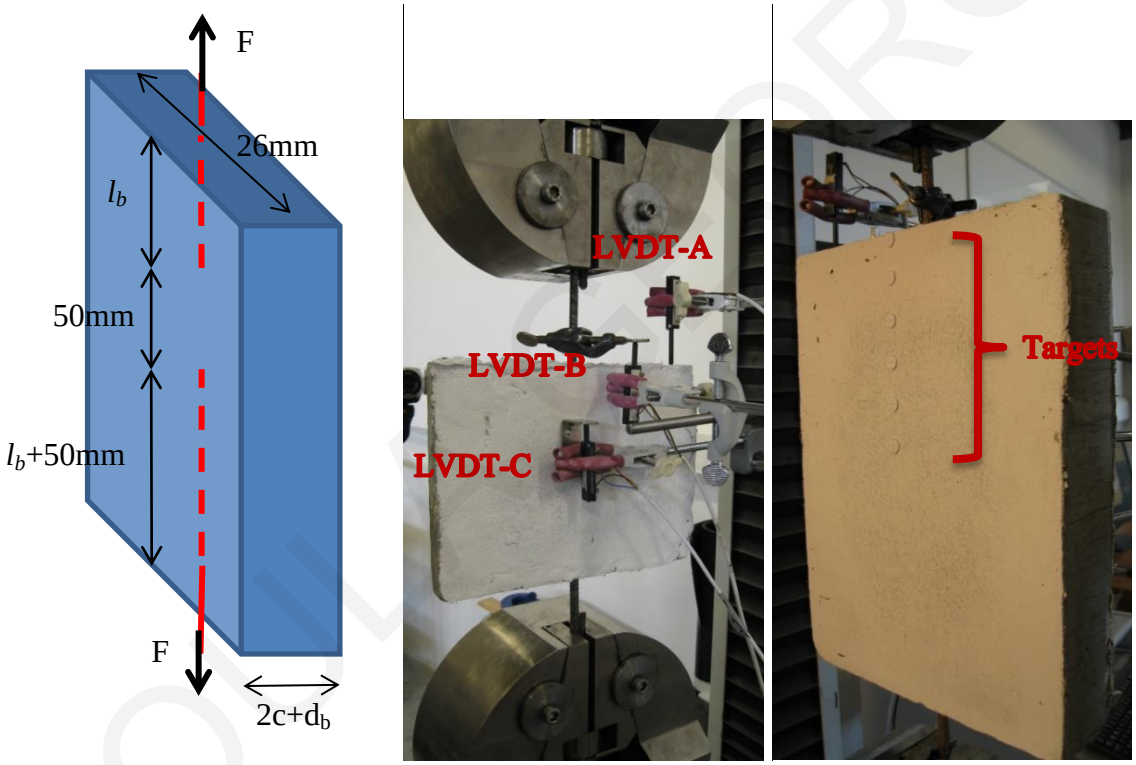

Figure 9.18 Specimen setup for pullout tests

The two bars were mounted on the clamps of the testing machine; the bottom clamp where the bar with the longer embedment length was fixed, whereas the top clamp imposed tensile loads on the bar with the shorter embedment length. Three LVDTs were used to measure displacement; one was mounted on the top bar, one on the top horizontal surface of the cementitious prism and one on the front surface of the prism at the end of the embedment length. Additionally targets of 10 mm diameter were placed on the back side of the concrete prism along the embedment length of the shorter bar. An electronic measurement acquisition system was used to record simultaneously load and deformations, while a camera was used to record the translation of the targets. The specimens were tested under displacement control with a velocity of 2.5 μm/sec.

9.3.2 Mixing and Casting of the Specimens

The 24 specimens were cast on the same day and accompanying tensile coupons, cylinders and small prisms were made in order to test the same cast SHFRCC properties in tension and compression. The molds were made of wood and were placed horizontally with a casting height of $2c+d_b$. Two holes were made on the top and bottom sides of the molds and the reinforcement passed through them, while outside the molds it was secured at the proper height in order to assure that no dislocation would take place during casting and that the bars would be axially placed extending collinearly in the same direction. The casting did not include any vibration of the FRC and after casting plastic sheets were placed over the free surface of the specimens and were left for 24 hours. After that period the specimens were removed from the molds and were wrapped in wet burlap sheets as shown in Fig. 9.19 where they were moist cured for a period of 100 days, at which age they were tested.

Figure 9.19: Specimen casting for pullout tests

9.3.3 Material Properties

Direct tensile tests and uniaxial compressive tests were performed to obtain the stress-strain curves of the SHFRCC material in which the bars for the pullout tests were embedded. The testing procedures for the tensile and compressive tests are described in Chapter 4 of this thesis. The stress-strain curves from the tests are depicted in Fig. 9.20. Characteristic points of the stress-strain curve for the three specimens of the SHFRCC in tension and their average values are given in Table 9.3. Additionally to the cementitious composite, coupons of the two different diameter bars were tested under uniaxial tension. The procedure of testing for the steel reinforcement is also described in Chapter 4. The yield stress of the deformed bars is 540 MPa and ultimate tensile stress in the order of 700 MPa.

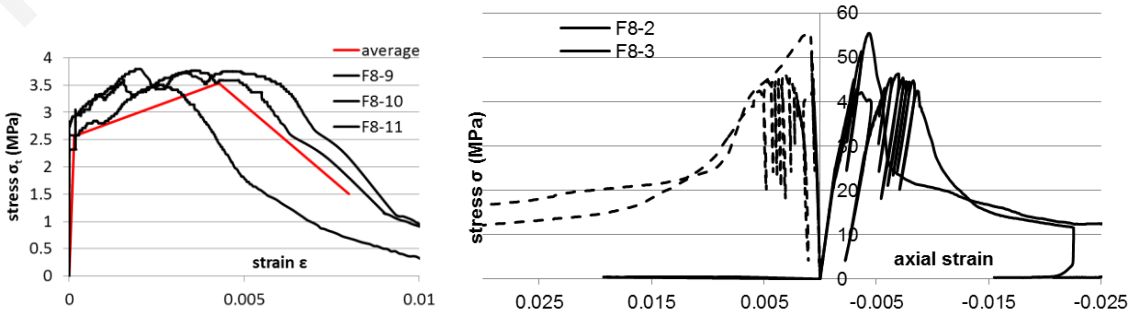

Figure 9.20: Stress-strain curves in tension and compression of SHFRCC mix for pullout specimens

Table 9.3: Characteristic points of the stress-strain curve for the three specimens of the SHFRCC in tension

E=	18301.95	MPa		
	f_{ty}	ε_{ty}	F_{tmax}	ε_{tmax}
F8-9	2.32	0.0002	3.599	0.005
F8-10	2.58	0.0002	3.58	0.00484
F8-11	2.79	0.00002	3.416	0.003
average	2.56	0.00014	3.532	0.00428

9.4 Experimental results from the pullout tests

9.4.1 Modes of failure

The full load-displacement curves from all specimens of the pull-out test are reported in Appendix B as well as the cracks that were formed on each specimen. A usual type of bond failure for deformed bars embedded in normal concrete is the splitting type failure. This failure occurs when the cracks emanating from the bars reach the nearest boundaries of the concrete surface, and in the absence of adequate crack confinement (such as by fibers or spirals) split the prism in several parts. The splitting failure is initiated by the wedging action of the ribs as the bar moves with respect to the concrete. The ribs create sufficient radial force components that split the concrete. Splitting is characterized by planar like cracks in planes radial to the axis of the bar. For the 24 specimens of deformed bars embedded in SHFRCC, even though planar cracks appeared on the sides where the cover was minimum, a clear splitting failure did not occur to any specimen. The fibers within the cementitious matrix provided a type of confinement that resisted splitting of the surrounding cementitious composite. Various covers provided a different confinement level as seen from samples of the same embedment length but with different cover thickness.

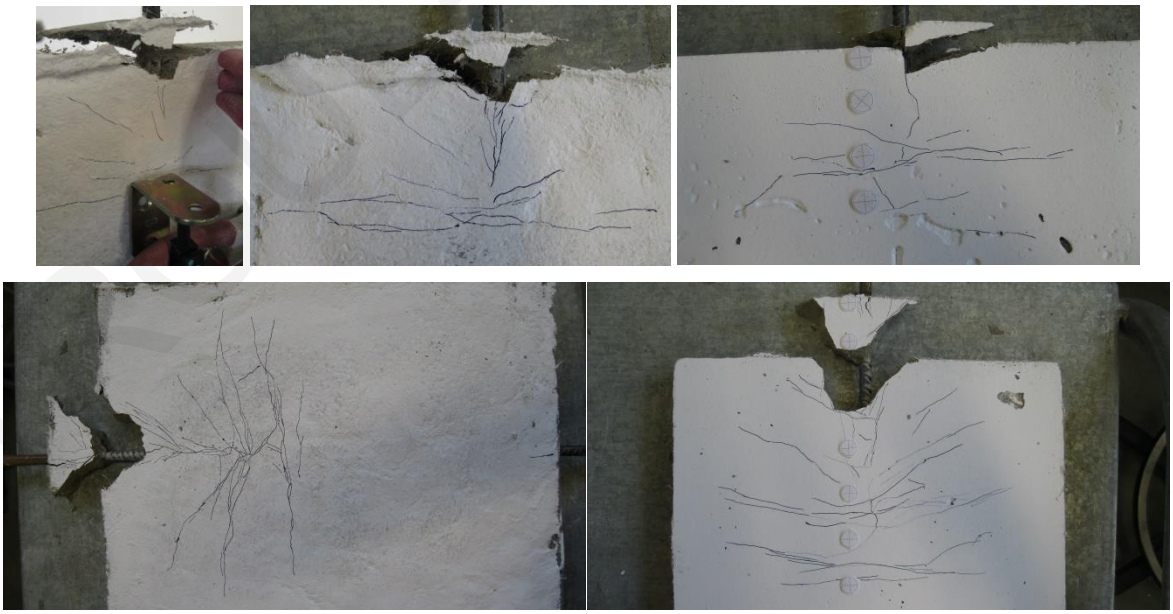

Figure 9.21: Cone shape failures of specimens F8A5C11 (top) and F8A12C11 (bottom)

Another type of failure that was observed was the “cone” type failure of only two specimens, as depicted in Fig. 9.21, that were not in the same series type therefore it cannot be taken as characteristic type of failure for the specific embedment lengths or cover thickness. Additionally

the cone failure was observed close to the loaded end of the bar and the separation appeared well on the descending branch of the load-deformation curves and was not marked by any characteristic load drop.

In most of the other cases, all specimens with smaller cover thickness and embedment lengths, frictional failure occurred. In that type of failure the bar pulled out from the concrete prism while the prism, although cracked, remained together. As ultimate bond stress was reached, shear cracks in concrete between ribs formed and propagated until the concrete was sheared and slip occurred. The crack evolution for the pull-out failure is depicted in Fig. 9.22 and 9.23.

Figure 9.22 shows the crack evolution of one of the two bars that exhibited the cone failure. Initially a crack was formed along the length of the bar at the points of smaller cover thickness. Simultaneously a horizontal crack was formed indicating the transfer of stresses from the bar to the concrete. This horizontal crack was located close to the unloaded end of the bar. While the crack parallel to the bar propagated towards the unloaded bar end, multiple cracks formed perpendicular to the direction of loading due to tensile stresses. Past the peak load, any new cracks ceased to form, since the bar's ribs had sheared off the concrete between the ribs and the bar experienced pull-out failure. The cone failure usually is considered a symptom of pull-out failure under high confinement, therefore the fibers were very effective in confining the test bar leading to mixed pullout – cone failure as shown in Fig. 9.22.

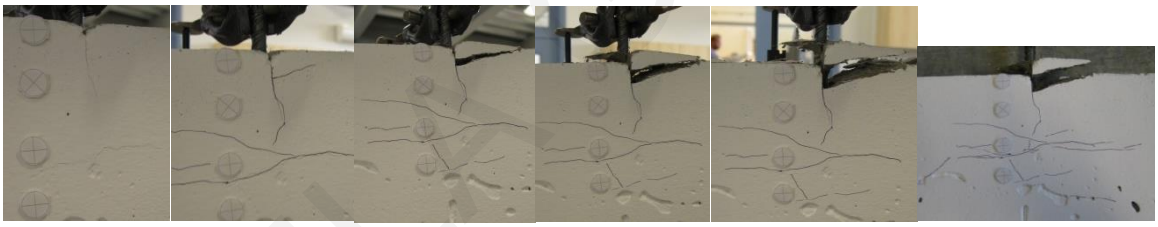

Figure 9.22: Evolution of crack formation for specimen F8-A5-C1-1

Figure 9.23 shows the crack formation evolution for one of the specimens that exhibited pull-out failure without any cone being shaped. Primarily cracks form parallel to the embedded bar in the smaller cover sides of the specimen. The concrete due to the fibers bridging the cracks can sustain tensile stresses and does not present splitting failure. Multiple cracking is observed around the bar as the bar being pulled out creates radial tensile stresses on the surrounding concrete. After the first crack is formed, the composite that has strain hardening properties in tension, increases the resistance at the crack location due to the fibers bridging the crack, leading the next crack to be formed at another location. Additionally multiple diagonal cracks are formed with a direction initiating from the bar's axis and propagating diagonally to the upper part of the concrete, with an angle "θ_{cr}". This diagonal crack indicates the angle between the principal tensile stresses and the principal compressive stresses that are formed in the cementitious matrix due to the radial and longitudinal forces that are developed in the composite from the bar's ribs. In the specific example of specimen F8-A8-C1-2 this angle is 57^{o}. After the maximum bond capacity is reached, that is

related to shear delamination of the cementitious matrix between the ribs, the bond pulls out of the matrix, without any additional cracks opening.

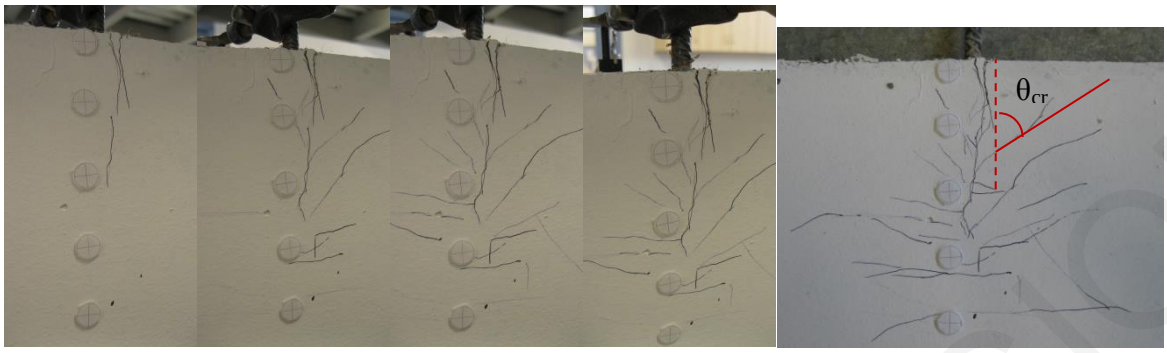

Figure 9.23: Evolution of crack formation for specimen F8-A8-C1-2

Finally the specimens with the longer embedment lengths (120 mm) and the wider cover thickness did not fail in bond. The bars reached their yield value and presented their hardening up to some measured deformation of the bar. After the steel bar yielded hardening of the bar was initiated giving rise to further increase of load. For all specimens of the same series, pullout failure of the bar started to occur while the bar was hardening. At the final stage the bar pulled out from the prism. This is due to the decrease of bond strength with increasing slip.

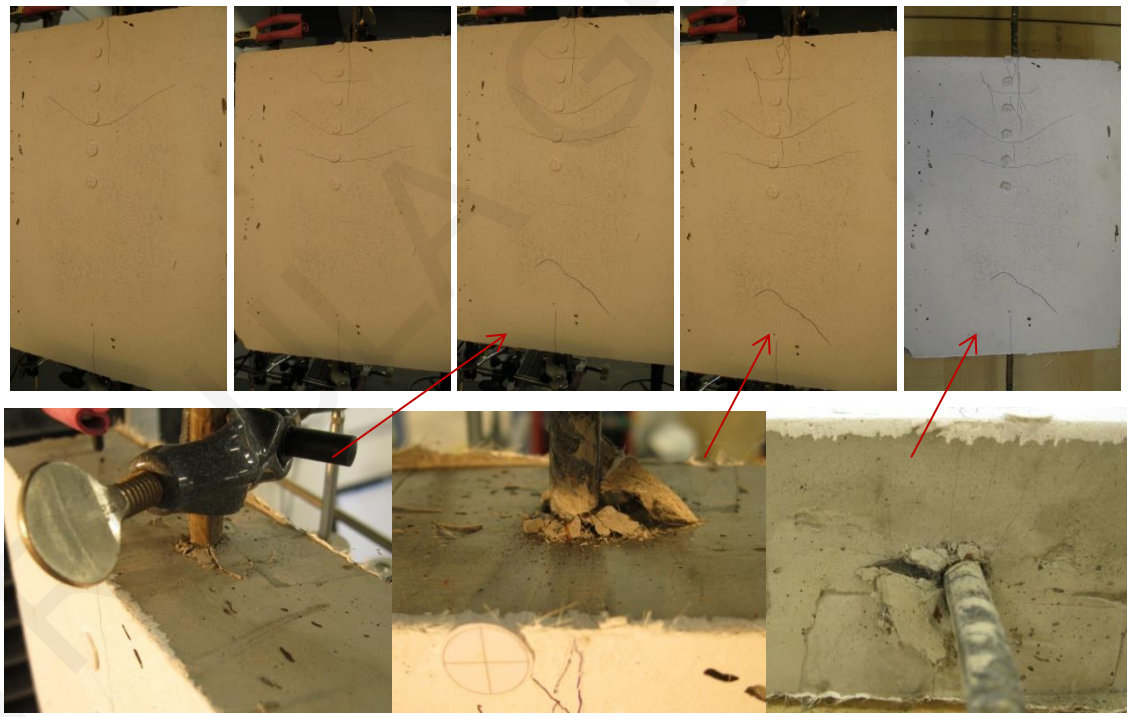

Figure 9.24: Evolution of crack formation for specimen F8-A12-C3-2

Figure 9.24 shows the progressive crack formation for one of the specimen in this series. Initially cracks initiate from the bar's loaded edge towards the embedment length of the bars, at both bar locations. This is due to the large embedment lengths of the two bars that are more than adequate to support yielding. Additionally horizontal cracks, transverse to the main splitting cracks appeared. The horizontal crack spacing was much greater with regards to the smaller cover thickness prisms. After some slip magnitude, the bar deformations concentrated towards the end of

the test specimen (i.e., with the shorter embedment length). The crack inclination angle varied, with the cracks being steeper closer to the loaded bar end. With slipping of the bar some delamination of the composite around the bar appeared, but this was limited due to the confining action of the fibers. Multiple cracks were formed radially around the bar, but in no case splitting of the composite was seen.

9.4.2 Bond-slip curves

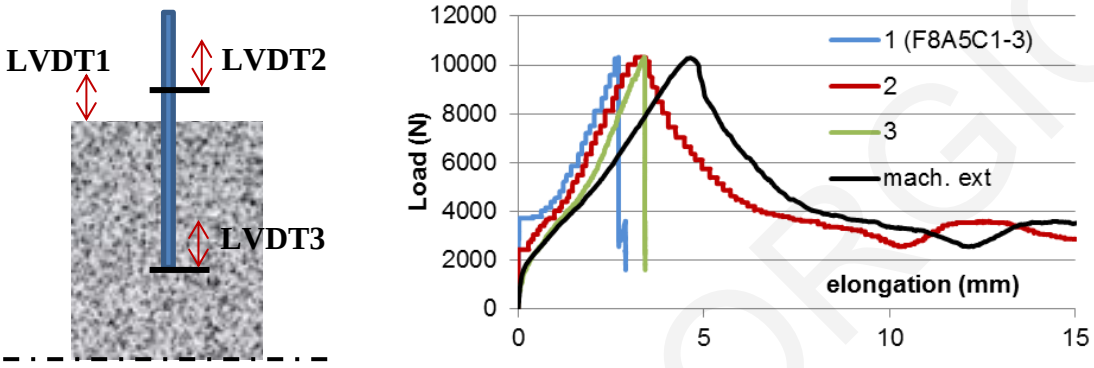

Figure 9.25: Measuring equipment for pull-out test and load-deflection curves for F8-A5-C1-3

Displacement, i.e., slip, is defined herein as the differential movement between the reinforcing bar and the surface of the concrete. The net slip is equal to the average displacement recorded by the LVDTs minus the elastic elongation of the free portion of the bar. From the data, the average equivalent bond stress, τ, was calculated in terms of the load *P* applied to the reinforcing bar for each specimen: $\tau = P/\pi dL$; thus, bond stress was calculated assuming a uniform bond stress distribution along the embedded length of the bar. However, in reality bond stress distribution is non-uniform.

Figure 9.26 shows the average bond strength versus slip curves for all tested specimens. For all cases that the bar did not surpass its yield strength, values of slip are determined by the LVDTs as $s=\Delta_2-\Delta_1-\Delta_{bar}$, where Δ_{bar} is the elongation of the length of the bar between the composites top surface and the point where the LVDT2 is mounted on the bar. This elongation is calculated based on the stress that is developed on the bar divided by the Modulus of Elasticity of the bar and multiplied by the length. In the cases that the bar exceeded yielding, calculation of the bar elongation was more complicated. Thus, the elongation of the bar followed an elastic branch up to the yielding of the bar, at a strain of ε_{sy}=0.0026, with a slope equal to the modulus of elasticity. Then the strain was calculated based on the characteristic points at yield (0.0026, 518 MPa) and initiation of hardening (0.038, 539 MPa). On the hardening part the strain was calculated based on the characteristic points of initiation of hardening (0.038, 539 MPa) and failure (0.15, 606 MPa). If pullout failure occures prior to tensile failure of the bar the bar's elongation follows a descending branch that initiaties from the maximum plastic bar elongation with a negative slope equal to the initial Modulus of elasticity.

The residual bond strength as shown from the experiments is related mostly on the cover depth and not the bar diameter or bond length. It takes on values of 1-2 MPa for the smallest cover (C1) and in the order of 4 MPa for the thicker covers.

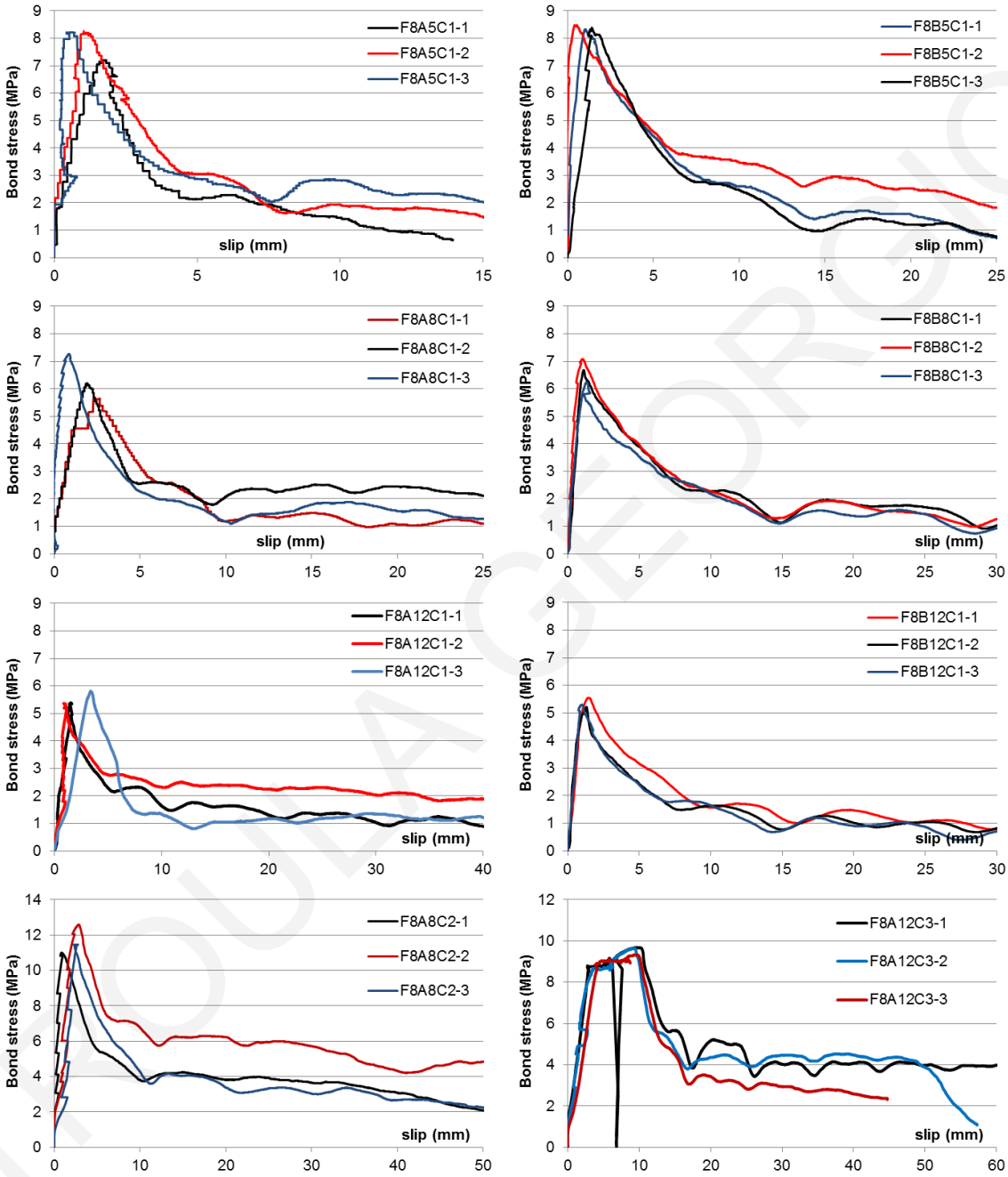

Figure 9.26: Average bond stress-slip curves for all tested specimens

9.4.3 Comparison of average bond strength with Model Code [49]

The average maximum bond stresses as developed from the experiments are given in Table 9.4, with an average value for each test series as well as the failure mechanism for each specimen.

Table 9.4: Average bond stress from experimental program

specimen	d_b	l_b	c/d_b	τ_{max}	Failure mode
F8A5C1-1	8	50	1.21	7.20	pullout/cone
F8A5C1-2	8	50	1.17	8.26	splitting
F8A5C1-3	8	50	1.18	8.22	splitting
F8A5C1	8	50	1.19	7.89	
F8A8C1-1	8	80	1.13	5.69	pullout
F8A8C1-2	8	80	1.16	6.20	pullout
F8A8C1-3	8	80	1.29	7.27	pullout
F8A8C1	8	80	1.19	6.39	
F8A8C2-1	8	80	2.82	11.00	pullout
F8A8C2-2	8	80	2.87	12.59	pullout
F8A8C2-3	8	80	2.86	11.46	pullout
F8A8C2	8	80	2.85	11.69	
F8A12C1-1	8	120	1.22	5.39	pullout/cone
F8A12C1-2	8	120	1.09	5.37	pullout
F8A12C1-3	8	120	1.16	5.81	pullout
F8A12C1	8	120	1.15	5.53	
F8B5C1-1	10	50	1.22	8.33	splitting
F8B5C1-2	10	50	1.21	8.48	splitting
F8B5C1-3	10	50	1.18	8.39	splitting
F8B5C1	10	50	1.20	8.40	
F8B8C1-1	10	80	1.11	6.68	pullout
F8B8C1-2	10	80	1.18	7.08	pullout
F8B8C1-3	10	80	1.18	6.24	pullout
F8B8C1	10	80	1.16	6.67	
F8B12C1-1	10	120	1.15	5.55	pullout
F8B12C1-2	10	120	1.09	5.22	pullout
F8B12C1-3	10	120	1.10	5.30	pullout
F8B12C1	10	120	1.11	5.36	
F8A12C3-1	8	120	3.27	8.71/9.68	yield/pullout
F8A12C3-2	8	120	3.25	8.7/9.65	yield/pullout
F8A12C3-3	8	120	3.13	9.03/9.32	yield/pullout
F8B12C1	8	120	3.22	8.81/9.55	

The average bond stress that was developed is compared with the values obtained for the design of bond as per the New Model Code in Fig. 9.27. The design ultimate bond strength f_{bd} according with MC-2010 was discussed in detail in earlier sections (see Eqn. 9.11).

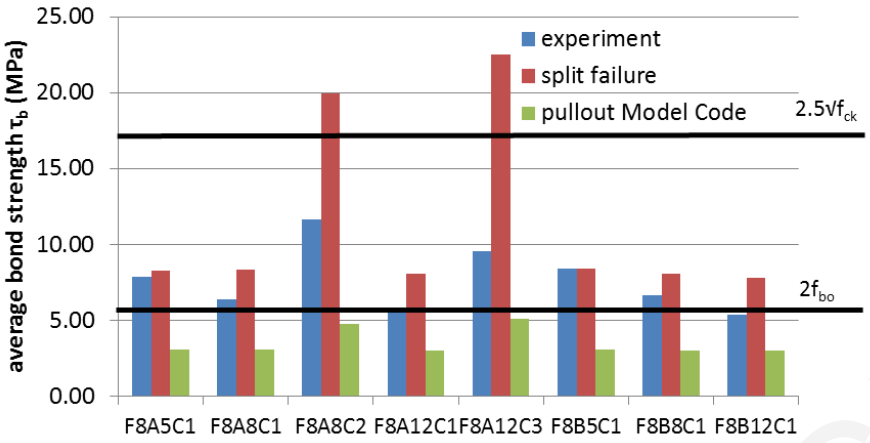

Figure 9.27: Average bond strength from experiments, splitting failure and MC provision for pullout

Even though no safety factor was used for the estimation of the bond strength as per the Model Code, the Code estimation seems to consistently underestimate the bond strength in the occasion where steel bars are embedded in SHFRCC. The under estimation is in the order of 50% or more as shown in Fig. 9.27.

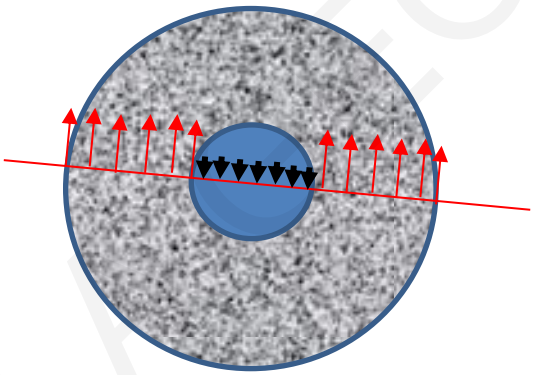

Figure 9.28: Stress distribution for estimation of splitting failure

For the estimation of the splitting capacity of the cover, the maximum radial stress that may be developed is related to the tensile stress capacity and cover thickness as shown in Fig. 9.28. In the case of SHFRCC the tensile stresses that may be developed from the cementitious cover have a maximum value:

$$d_b \cdot p_{rad} = 2 \cdot c \cdot f_{t\max} \tag{9.19}$$

Considering that the radial pressure is associated to the bond stresses along the bar axis with an angle of 45° (equal to the slope of the ribs) then the maximum bond stress for a slip failure may be estimated as:

$$f_{bsplt} = p_{rad} = \frac{2 \cdot c \cdot f_{t\max}}{d_b} \tag{9.20}$$

The values of bond split failure extracted from Eq. 9.20 are also depicted in the bar chart of Fig. 9.27. Using a capacity based approach the failure and associated anchorage strength that was observed during the tests is the minimum of two values: the pullout bond strength and the splitting

failure bond strength. For the cases F8A5C1 and F8B5C1 where splitting failure occurred, Eq. 9.20 give a precise estimation of the splitting failure bond strength.

9.5 Conclusions

The experimental study presented in this chapter documents the bond behavior of deformed bars embedded in SHFRCC matrix and anchored in a tensile stress field. The direct tension test setup considers bond to occur in the most adverse conditions, where development of the bar force occurs in a cover that is also subjected to longitudinal tension, as would happen in the tension zone of a beam. Parameters of study were the diameter and the anchorage length of the bars, as well as the cover thickness; the matrix comprised PVA-reinforced high fly-Ash content, fine-aggregate concrete with a tensile strain capacity in the order of 1%. Ribs of the deformed bar engage the SHFRCC matrix exerting inclined compression stresses. The radial component creates splitting cracks parallel to the bar that leads to failure. The load at which splitting crack occurs is related to bar diameter, cover width and tensile strength of SHFRCC. Performance of anchorages in SHFRCC surpassed all possible expectation – the cover contribution to development capacity of the bar was sustained even in cases of small covers ($c=d_b$) and up to excessive amounts of slip. Clearly, the performance resembled that of confined anchorages, effected by the sustained tensile strength of the SHFRCC owing to the action of the dispersed fibers. Splitting cracks if they occurred (in the cases of small cover thickness) were hardly visible and did not open to enable unrestrained passage of the bar as would occur in normal concrete. Instead, pullout failure occurred in most cases – marked by the formation of a sheared cylinder that was defined by the tips of the ribs – a characteristic performance of confined anchorages. The experimental results obtained for different covers and embedment lengths were used to evaluate the average bond for split failure.

Chapter 10: Reversed Cyclic loading of SHFRCC large scale members

In order to examine the resistance of SHFRCC members under seismic loads two large scale beams were tested under cyclic loading. One of the two beams was constructed with the high volume matrix without the fibers and detailing was designed based on the Eurocode provisions. The other beam was constructed with the SHFRCC mix with fibers but with the minimum amount of shear reinforcement. No axial load was applied on the specimens during loading. Note that whereas a few research programs have been conducted in order to study the behavior of SHFRCC-beams under monotonic loading, strength and ductility of structural members comprising these materials have not yet been fully determined for the case of seismic loading.

10.1 Literature Review

10.1.1 Cyclic behavior of SHFRCCs

Earthquake ground motion imposes reversed cyclic loading on structures. The analysis and design of structures in seismically active areas need to take these effects under consideration. The design philosophy of Codes for concrete members reduces seismic loads by a response coefficient (behavior factor) q in order to create more slender members and reduce the cost of structures. This decrease in the load carrying capacity of the structures affects the requirements for ductility μ and energy dissipation of members. Especially in Frame Structures, where Capacity Design is used, the "strong column-weak beam" requirement forces the creation of plastic regions in the beam-ends and at the base of ground columns. Therefore beam and column hinging regions must be detailed specifically in order to maintain their shear capacity as seismic loading imposes yielding in the longitudinal reinforcement [97] both in the tensile and the compressive region.

Ductility of beam members is influenced by the geometry details, the percentage of the reinforcement, the composite material's stress-strain properties and the shear span ratio. The concrete's tensile strength was neglected in calculating moment capacity of members due to the brittle nature of concrete, while in the region of the beams under compression spalling of the concrete cover reduces the capacity of the zone under compression and usually leads to brittle failures. Additionally for the shear design of the beams that undergo reversed cyclic loading, causing diagonal shear cracking (X-shape cracks), the concrete's contribution to shear is neglected and stirrups are required to transfer all shear loading. This leads to excessive amounts of detailing, denser placement of shear reinforcement that complicates construction and casting.

In light of these practical limitations the use of a new type of composite material reinforced with short discontinuous fibers that exhibits strain hardening properties (SHFRCC) under tension and improved performance in compression could be an answer to the many issues that appear. The improved performance in tension mitigates also to the composite's behavior in shear as seen in the short span beams subjected to cyclic loading in previous studies [159]. Fisher and Li [160] who studied the combined behavior of steel reinforcement in SHFRCC matrix have shown that strain

hardening behavior of both components past yielding prevents localization of deformations leading to uniformly distributed yielding of the reinforcement over the length of the specimens they tested, increasing energy dissipation. The flexural behavior of beams with SHFRCC and FRP bars were experimentally investigated by Yuan and Pan [161], that concluded that wide cracks opening in normal concrete, diffuse to wider areas with many micro cracks in SHFRCC, leading to higher deformability and compatibility of deformations of the FRP reinforcement with the surrounding matrix, reducing bond splitting. Additionally the shear rupture of the bars that appears usually at the crack locations due to stress concentrations was avoided and the SHFRCC showed no delamination.

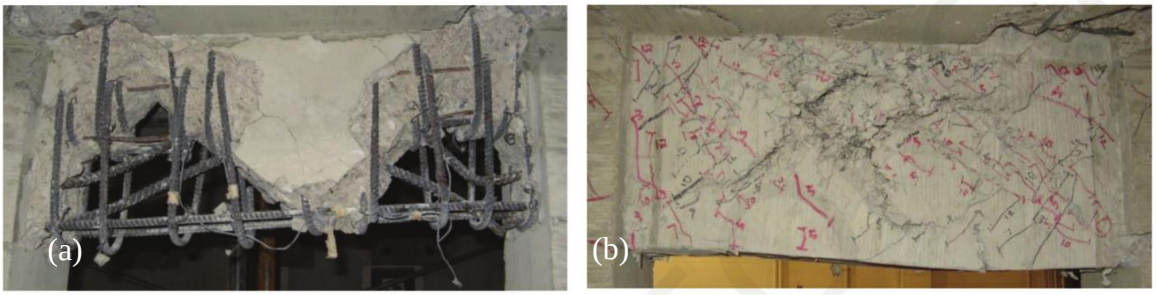

Figure 10.1: Coupling beams (a) reinforced concrete beam and (b) Strain Hardening Composite [162]

The cyclic response of steel R/SHFRCC members were investigated by some limited research. HPFRC precast coupling beams with short span-depth ratios were tested by Lequesne et al. [162]. Comparative results between normal concrete and SHFRCC coupling beams are shown in Fig. 10.1, where SHFRCC had multiple small cracks and no delamination, while the normal concrete beam showed excessive damage.

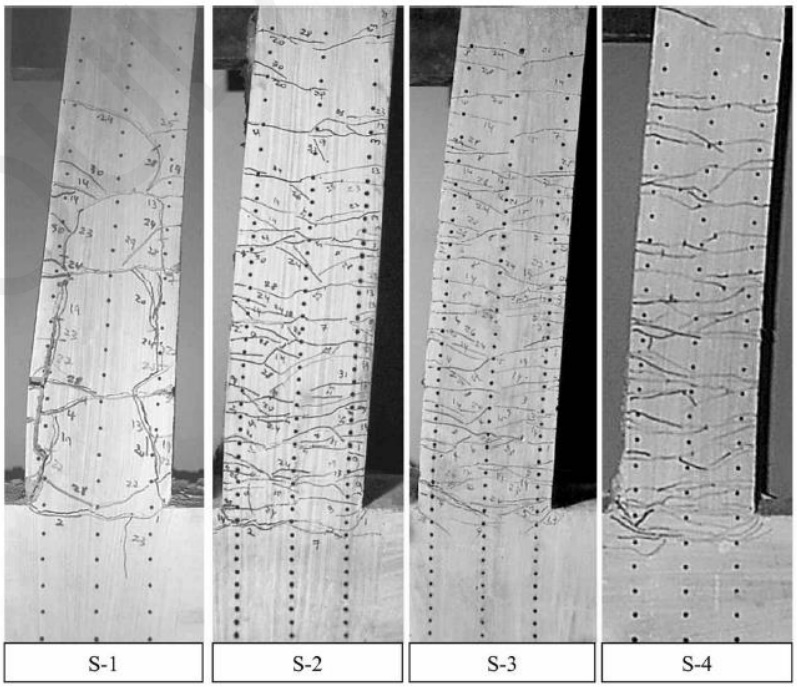

Figure 10.2 Deflected shape and damage pattern of specimens at 7% drift [163]

In Figure 10.2 the results of the experimental investigation of Fisher and Li [163] are depicted. In this research the combination of FRP and SHFRCC is explored. Contrary to normal concrete reinforced with FRP reinforcement (limited ductility due to the stiffer and brittle nature of FRP and brittle concrete matrix) the combination of FRP reinforcement and strain hardening composites was investigated expected to create more ductile members. In Figure 10.2 S1 comprises normal concrete, while the other three members are made of SHFRCC. The FRP reinforcement was from aramid for all 4 specimens, while shear reinforcement was added in specimens S1 and S2 only. The S4 specimen had sand coated bars intended to improve the interfacial bond-slip relation. Through the experimental results the SHFRCC created multiple cracking increasing interfacial bond and increased deflection capacity. The increased strength of the SHFRCC reduces the tensile and compressive stresses on the FRP reinforcement although conclusively FRP-reinforced ECC members do not have significant energy absorption capacity compared with conventional steel reinforced members.

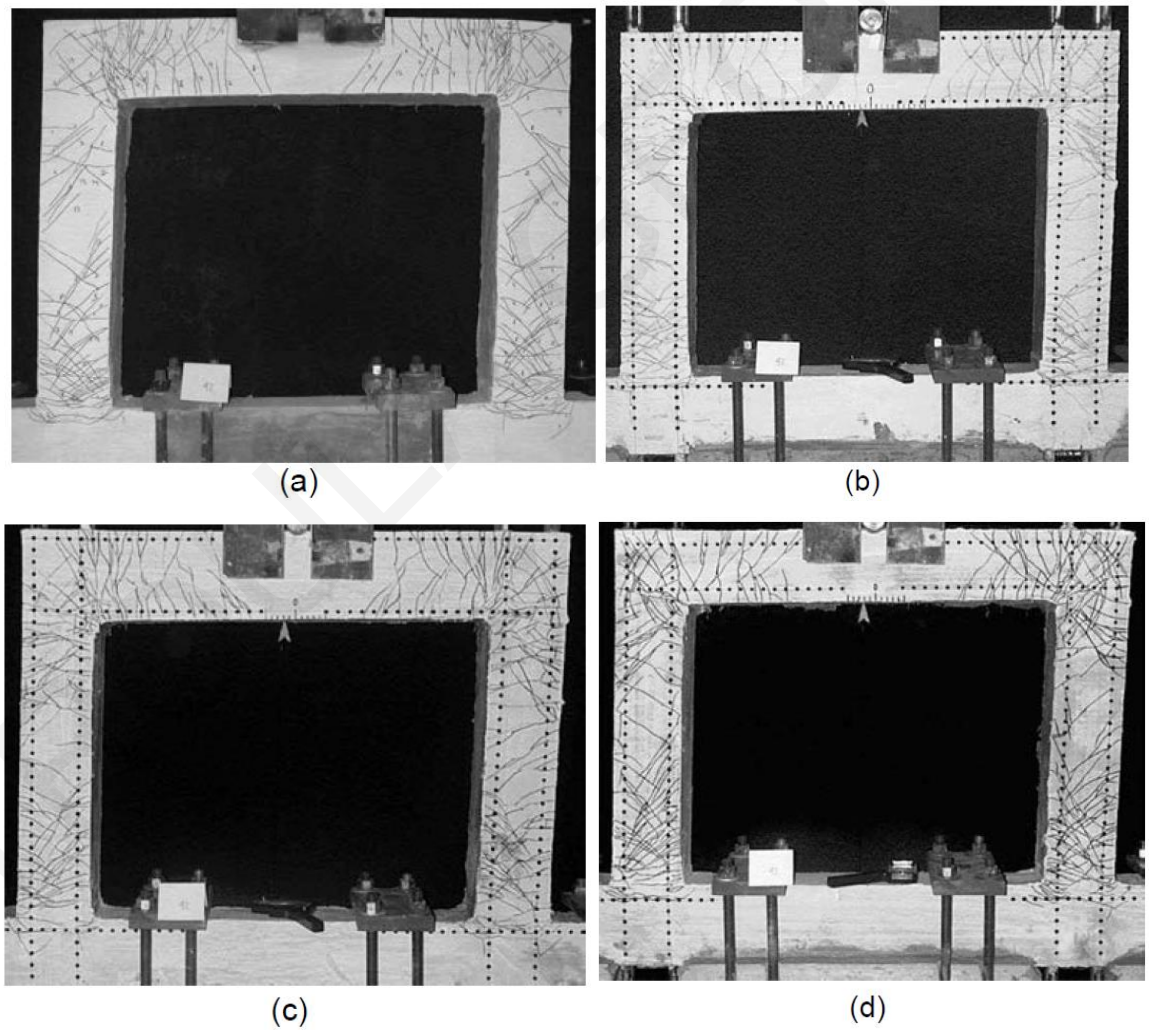

Figure 10.3: Deformed shape at 4% drift of: (a) Specimen S-1; (b) Specimen S-2; (c) Specimen S-3; and (d) Specimen S-4. [90]

Figure 10.3 shows the damage of four frames subjected to reversed cyclic loading performed by Fisher and Li [90] with beams in the four frames being reinforced with steel bars while columns'

reinforcement varied between frames: (a) S1 steel reinforced columns, (b) S2 aramid FRP reinforced columns, (c) S3 CFRP 6mm bars reinforced columns and (d) S4 CFRP 8 mm bars reinforced columns. The S1 frame showed multiple cracking until a drift of 4% (yield drift 0.5%, i.e., ductility of 8), at which point cracking localized at the beam-column interface with widening of the crack width with increasing displacement. In S-2 frame the beam remained almost uncracked, while cracking at the columns was stabilized at 2% drift at the columns' base and top. In S3, yielding was the same with S2 (at 1% drift) but cracking in the beams was extensive as well as in the columns and extended throughout the full members length. In this specimen after 3% drift shear cracks were formed at the column bases, while at 4% drift it was obvious that the hinge regions extended approximately to member's depth from the joints. Specimen S4 showed an evenly distributed shear crack formation after a 2% drift throughout their entire length and the frame showed constant applied load and greater ductility.

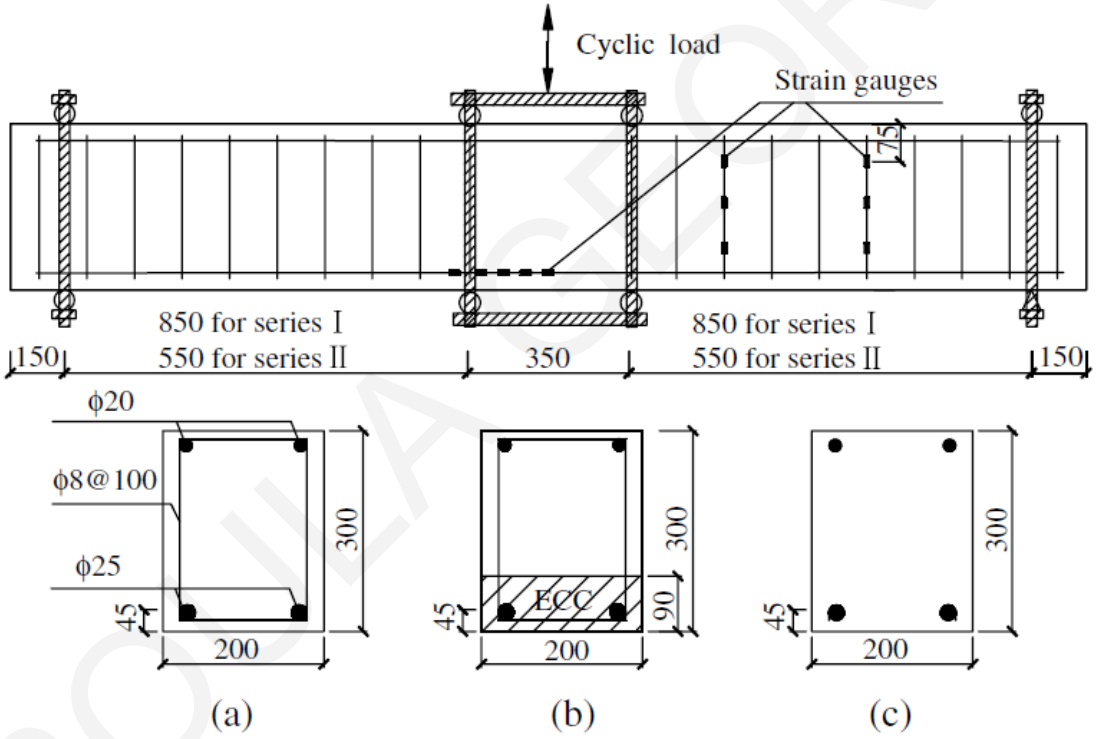

Figure 10.4: Schematic illustration of test setup and specimen details [164]

Yuan et al. [164] performed tests on steel reinforced ECC and combined ECC/concrete beams (Fig. 10.4) to study their seismic behavior by performing reversed cyclic loading four point bending. In this paper, steel reinforced concrete or SHFRCC beams and variable aspect (=shear span to depth) ratios were tested. The SHFRCC beam exhibited higher flexural strength, deformation and energy dissipation in relation to the concrete beam. A significant increase of strength (by a factor of 4) was observed in flexure and shear - but as also shown by the SHFRCC beams without stirrups, their strength was greater than those of concrete beams containing stirrup reinforcement. As seen in Figure 10.5 no delamination between the concrete and the SHFRCC layer was observed.

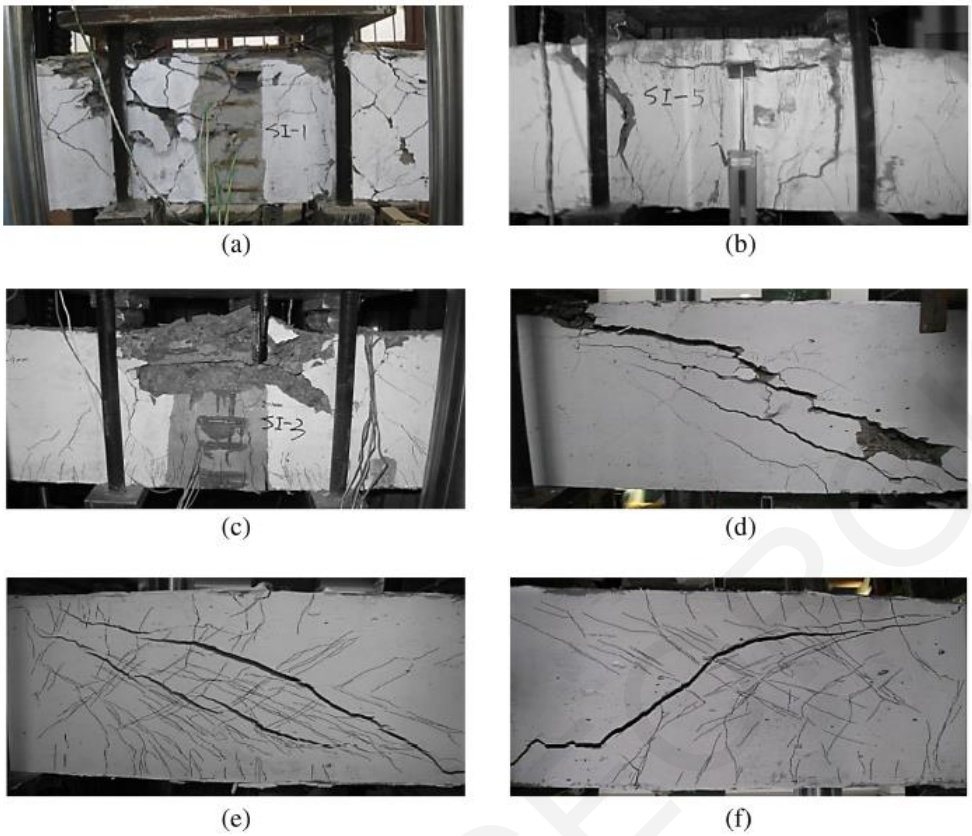

Figure 10.5: Final crack patterns of specimens: (a) S-1; (b) S-2; (c) S-3; (d) S-4; (e) S-5; (f) S-6 [164]

Parra-Montesinos and Chompreda [165] (Fig. 10.6) studied the deformation capacity and shear strength of flexural members from SHFRCC under reversed cyclic loading. In the tests both fibers and steel reinforcement was added in the specimens in order to resist shear stresses. The shear contribution of the stirrups was evaluated by their strain during the experiments. Based on their limited results the authors propose an equation for the determination of the shear strength of SHFRCC members with shear reinforcement, proposing a 60 degree crack angle in regards to the longitudinal axis.

$$V_n = 0.3 \cdot \sqrt{f'_c} \cdot b_w \cdot d + A_v \cdot f_{yv} \cdot n_v \qquad (10.1)$$

Where n_v is the number of layers of hoops and crossties (whole number) crossed by a 60 degree angle diagonal crack. For all specimens tested within this study, with or without stirrups, the fibers assisted the members to reach drift capacities higher than 4% and when compared to the control R/C members, the SHFRCC members displayed multiple cracking and greater ductilities. The strain hardening beams gave a lower bound of shear resistance of $0.3\sqrt{f'_c}$, a limit after which members started to exhibit shear failure. For the specimens without web reinforcement buckling of the longitudinal reinforcement appeared but it was only evident over plastic hinge rotations of 4%, while this phenomenon did not appear in the cases with stirrups. The beneficial action of the SHFRCC acting also on the region under compression creates enough confinement to the longitudinal reinforcement in order to preclude buckling.

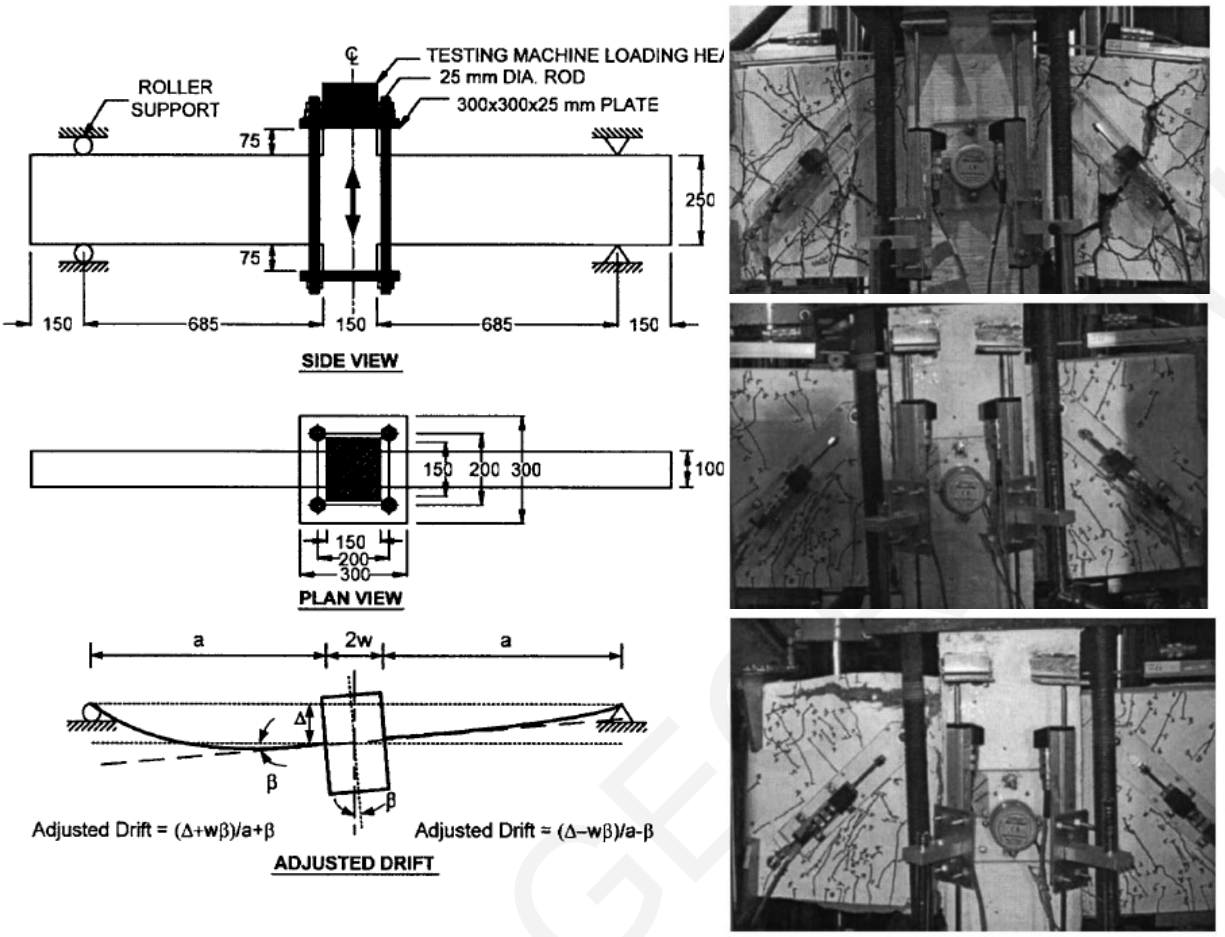

Figure 10.6: (a) Test configuration and calculation of member drift, (b) Damage in plastic hinge regions of specimen at 4% drift, (c) Cracking pattern at 4% drift and (d) buckling of top longitudinal reinforcement at 7.0 drift [165]

As seen from the above review on the experimental research concerning the reversed cyclic loading of steel reinforced SHFRCC members, until now very limited experimental results are available in order to support generalized conclusions. It is evident though from research that SHFRCC due to its unique properties, can work effectively together with steel reinforcement and improve ductility.

10.1.2 Code provisions of seismic design of columns

The reversed and repeated loading imposed on concrete members during an earthquake has been found to diminish their resistance to shear. This was investigated by various researchers and its attributed to the opening of the cracks, the reduction of aggregate interlock, the capacity of the compressive zone to transfer shear due to excessive strains-cracking-spalling and due to the reduction of dowel action related to the interfacial bond between the flexural reinforcement and the surrounding concrete due to splitting cracks. The capacity based design that is implemented both by the Eurocode 8 Part 1, as well as by the ACI Building Code requires that under no circumstances the reduced shear resistance at hinge locations of beam members may be surpassed. The codes ensure this by imposing the use of transverse reinforcement able to resist the full shear

load, considering no contribution of the concrete core to shear resistance, and able to create adequate confinement for the concrete and prevent buckling of the longitudinal reinforcement.

10.1.2.1 ACI Building Code

Dense stirrups for confinement and buckling control are required over a length of 2h from the face of the supports. The spacing of the stirrups is specified in ACI Code Section 18.6.4.4, whereas over the remaining beam length the required stirrups need be spaced at least at a maximum distance of *d*/2. The first stirrup is placed at *s*/2 from the face of the support. The probable moment strength M_{pr} of the beam member is based on the dimensions and reinforcement assuming a tensile strength of 1.25f_y, and ACI 18.6.4.1 requires that the beam is designed for a shear force adequate to support the probable moment strength over the shear span:

$$V_d = \frac{M_{pr}}{L_s}, \text{ where } M_{pr} = 1.25 \cdot f_y \cdot A_s \cdot \left(d - \frac{a}{2}\right) \text{ and } a = \frac{1.25 \cdot f_y \cdot A_s}{0.85 \cdot f'_c \cdot b} \quad (10.2)$$

The concrete contribution to shear V_c is taken as zero as per ACI 18.6.5.2 when the V_d due to plastic hinging exceeds half of the maximum shear V_u within the span.

$$V_c = 2\lambda \cdot \sqrt{f_c} \cdot b_w \cdot d \,,\; V_s = V_u / \phi - V_c \quad (10.3)$$

Where φ is the strength reduction factor, which for shear sensitive members seismically designed this factor takes the value 0.6. The maximum shear reinforcement is set by the ACI 22.5.1.2 as:

$$V_{s,\max} = 8 \cdot \sqrt{f_c} \cdot b_w \cdot d \quad (10.4)$$

10.1.2.2 Eurocode

In Eurocode 8 Section 5.4.2.2 it is stated that the design of shear forces for beams should be determined based on the capacity design rule with equilibrium of the beams under the seismic load and the end moments of the beam corresponding to positive and negative directions of the seismic load (Fig. 10.7). Plastic hinges are taken to form in the ends of the beams. Shear resistance should be based on the end moments of the beams in order to fulfill the capacity design method and to prevent shear failure.

End moments are calculated as: $$M_{i,d} = \gamma_{\mathrm{Rd}} \cdot M_{Rb,i} \cdot \min\left(1, \frac{\sum M_{Rc}}{\sum M_{Rb}}\right) \quad (10.5)$$

The regions within two beams depth measured from the ends of the beam are considered to be critical regions. The ductility requirement of these critical regions should be at least equal to the μ_φ value given in Section 5.2.3.4 (3). The reinforcement in the compression zone of the critical regions should be at least half of that provided in the tensile zone, additionally to the compression reinforcement that is needed for the seismic action.

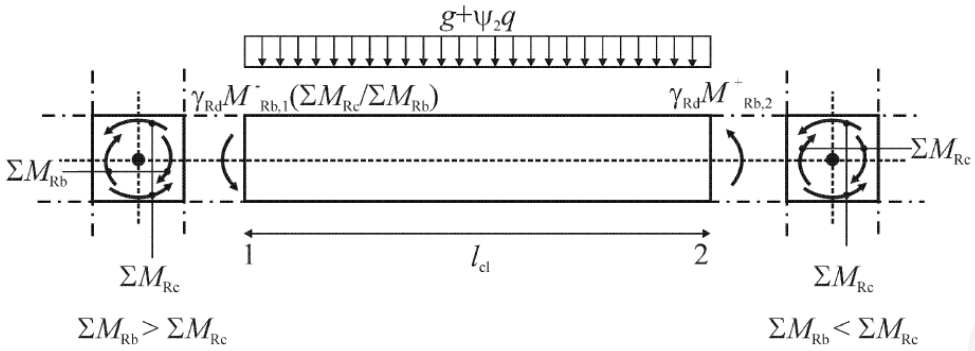

Figure 10.7: Capacity design values of shear forces on beams (EC8)

The hoops in the critical regions should follow some specific conditions:

a) The diameter of the hoops shall not be less than 6 mm

b) The spacing of the hoops shall not exceed: $s = \min(h_w/4, 24d_{bw}, 225, 8d_{bL})$

c) The first hoop shall be placed at least 50 mm from the beam end section

Section 6.2.1 of Eurocode EN1992-1-1 states that when the shear resulting from loads is greater than the one provided only by concrete $V_{Ed} > V_{Rd,c}$ then sufficient shear reinforcement should be provided in order that $V_{Ed} \leq V_{Rd}$ (where V_{Rd} is described by Eq. 6.8 Section 6.2.3). Equation 6.8 of Section 6.2.3 gives the shear resistance of members with vertical shear reinforcement as:

$$V_{Rd,s} = \frac{A_{sw}}{s} z \cdot f_{ywd} \cdot \cot\theta \text{ and } V_{Rd,\max} = a_{cw} \cdot b_w \cdot z \cdot \nu_1 \cdot f_{cd} / (\cot\theta + \tan\theta) \quad (10.6)$$

For Ductility Class High (DCH) section 5.5.3.1 of EN 1998-1 states that in the critical regions of primary seismic beams the strut inclination θ shall be 45°. Based on the ratio ζ between the minimum and maximum shear forces acting on the beam design of the shear reinforcement varies as follows:

a) $\zeta \geq -0,5$ then shear reinforcement is computed in accordance with EN 1992-1-1.

b) $\zeta < -0,5$ then almost full reversal of shear forces is expected then if:

   i. if $|V_E|_{\max} \leq (2+\zeta) \cdot f_{cd} \cdot b_w \cdot d$ then (a) shall apply

   ii. if $|V_E|_{\max} > (2+\zeta) \cdot f_{cd} \cdot b_w \cdot d$ inclined reinforcement should be provided in two directions

10.1.2.3 New Model Code

The New Model Code has included the shear design of FRC, in Section 7.7. Equations from the Model Code are described in detail in Chapter 8.3.1 of this Thesis. The Model Code has no special provisions for the calculation of shear strength of SHFRCC for cyclic loading conditions.

10.1.2.4 JSCE Recommendations

The Japan Society of Civil Engineers "Recommendations for the design and construction of High Performance Fiber Reinforced Cement Composites (HPFRCC) with multiple fine cracks"

deal with the issue of shear design of linear members [50] (as listed in Chapter 8.3.1 of this thesis) but the case of reversed cyclic loading and its impact on the degradation of shear capacities of members is not mention at all within these Recommendations.

10.2 Experimental Procedure

10.2.1 Specimen Design and Detailing

The research included the reversed cyclic loading of two large scale specimens with the geometry shown in Fig. 10.8. Each specimen consisted of two cantilever flexural members with a shear span ratio of 3.5 connected with a stiff node used for loading by the actuator in both directions. The beams are supported on rollers both on their bottom and top faces. Each beam behaves as a cantilever with a constant shear load equal to half of the machine load and moments are linearly increasing from zero at the supports to $M=(P/2)\cdot L_s$ at the connection with the rigid node, where L_s is the shear span length. One of the two connecting flexural members of each specimen is designed as per the research target, while the other connecting beam is heavily reinforced (both in the longitudinal and transverse direction) in order to preclude any failure.

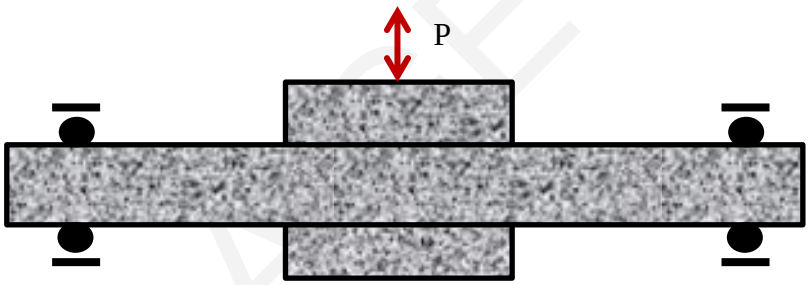

Figure 10.8: Test setup for reversed cyclic loading

Two large scale specimens were tested. One was constructed with SHFRCC mix with PVA fibers of 2% by volume, while in the other the cementitious matrix was the same as that of the SHFRCC but without the fibers. The cementitious matrix was reinforced as per the Eurocode [5] provisions for a DCM. In the case of the SHFRCC beam, the longitudinal reinforcement remained the same while the transverse reinforcement used was the minimum required to prevent buckling of the longitudinal bars. Detailed description of the members is given in the following sections. The purpose of these tests was to investigate the beneficial action of the fibers on the shear capacities of members under reversed cyclic loading.

10.2.2 Design of members

The reference column, upon which the scale factor for the specimens was used to calculate member geometry was considered to be constructed with high fly ash content cementitious composite without fibers. The column detailing follows the design for Ductility Class Medium according to Eurocode 8 (EN 1998-1 [5]). Given the dimensions and strength of the available testing frame it was decided to make the specimens at a scale of 1:2. Thus, all dimensions and

reinforcement detailing of the test specimens was calculated for the full scale and then reduced to half.

Column Parameters for design: f_c=50 MPa, Axial Load=0 kN, cross section 400x400 mm, H=2.8 m, c=40 mm

Detailing for primary columns as per EC8 [5] for DCM:

The critical region length should be the greater value from: h_c, b_c, *0.45 m*, $l_c/6$. The minimum percentage of flexural reinforcement should be 1% and the maximum 4%. The minimum diameter of the longitudinal reinforcement d_{bL} is 8 mm, while the minimum number of bars on each side of the member is 3. The maximum spacing between restrained bars on each side is 200 mm and the distance of unrestrained bars from the nearest restrained bar should be less than 150 mm. For the transverse bars outside the critical region, the diameter of the stirrups should be at least the greater between 6mm and $d_{bL}/4$. The spacing between the stirrups should be at least the minimum of 20 d_{bL}, h_c, b_c, 400mm. Within the critical region the maximum spacing between bars is the minimum between $8d_{bL}$, $b_o/2$ and 175 mm. Eight bars of 20 mm diameter were chosen to be placed on the full scale specimen based on the detailing provision of the EC8. Therefore the 1:2 scaled specimens has the following characteristics considering that the material parameters such as the compressive strength of the cementitious material and the yielding strength of the reinforcement remain constant:

1:2 Scaled Column Parameters: f_c=50 MPa, Axial Load=0 kN, cross section 200x200 mm, H=1.4 m, c=20 mm, the number of bars on each side remains the same (three bars on each side) but their diameter is reduced to 10 mm. Given the geometry of the member an iterative layer analysis was used to determine the M-φ curve of the cross sections. An excel worksheet was prepared as described in Chapter 8. The kinematic assumption of plane sections remaining plane and normal to the member axis is used; the cross section is divided in layers of equal height. For a given curvature value (φ), the neutral axis depth, x, is calculated iteratively so as to satisfy equilibrium of forces normal to the cross section ($\Sigma N_i=0$). The flexural moment is calculated with respect to the centroid of the cross section after convergence in the value of x. The materials' stress-strain laws in tension and compression were obtained by curve fitting of the experimental envelopes obtained from the respective material tests. As seen in the diagram of Fig. 10.9 the yield moment of the Control Member is 22.27 kNm and its maximum moment is 26.47 kNm.

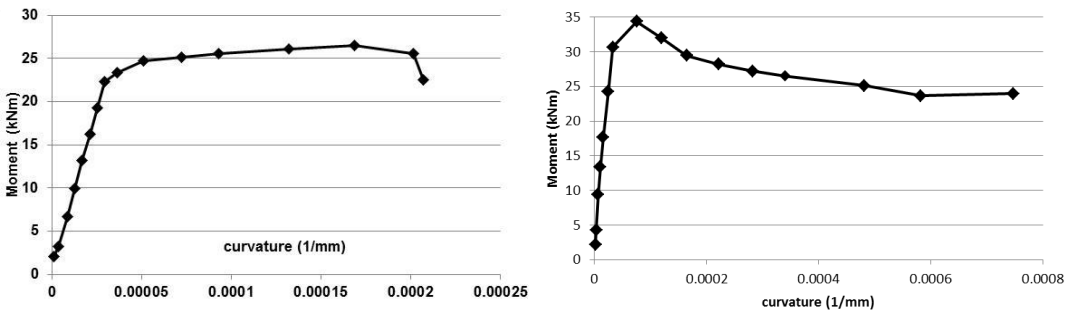

Figure 10.9: M-φ diagram of the 1:2 scaled members (a) Member A: Control and (b) Member B: SHFRCC

The maximum Moment of the member determined from the cross-sectional analysis was used to determine the shear force demand as per Eq. 10.7:

$$V_{Ed} = 1.1 \cdot \frac{\sum M_{Rc}^{ends}}{l_{cl}} = 1.1 \cdot \frac{26.47}{0.7} = 41.6kN \quad (10.7)$$

The required amount of stirrups, with stirrup diameter of 6 mm and a yield stress of 300 MPa is:

$$s = \frac{A_{sw}}{V_{Rd,s}} z \cdot f_{ywd} \cdot \cot\theta = \frac{3 \cdot \pi 6^2 / 4}{41600} \cdot 0.9 \cdot 169 \cdot 300 \cdot \cot 45 = \frac{5158015}{166400} = 90 \Rightarrow s \le 90mm \quad (10.8)$$

The maximum distance between stirrups in the critical region is also subjected to the detailing specification which is 80 mm (min{8d_{bL}=80 mm, b_o/2=80 mm, 175 mm}). Therefore the stirrups placed were Φ6/80 with 3 legs in each direction.

For the case of the member with the SHFRCC matrix with 2% per volume of fibers the same geometry of the cross-section was applied as well as the same longitudinal bars (8Φ10). In order to obtain the beneficial results of the use of fibers on the shear strength and ductility of the member the stirrups placed were not based on the shear demand. Only the provision for the DCL class of column members was followed in order to assure that no buckling of the reinforcement would be observed. Spacing of the stirrups in this occasion is the minimum from among the following values: 120d_{bL}=1200, 0.6h_c=120, 0.6b_c, 240 mm. Therefore stirrups that were placed were Φ6/120 with two legs in each direction. Detailing of the stirrups for the two cross sections is depicted in Fig. 10.10.

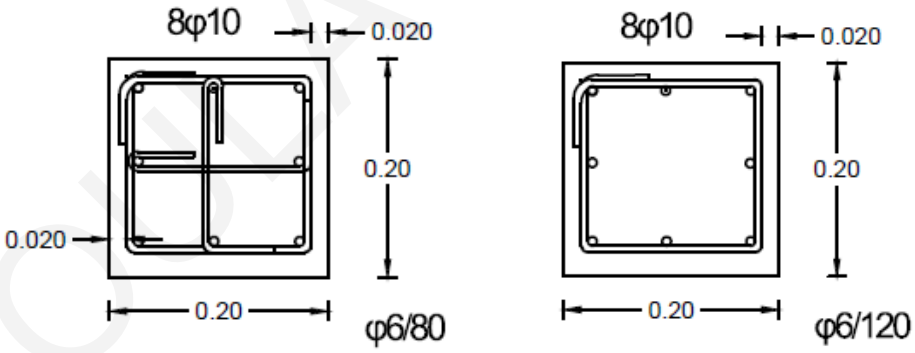

Figure 10.10: Stirrup detailing for (a) Member A: Control and (b) Member B: SHFRCC

10.2.2.1 Member A: Control

The Control Member A, had a cross section of 200x200 mm. The cementitious matrix was composed of the reference cementitious mix studied in the present thesis, but without fibers (F11/12 mixes are described in Chapter 4), and was reinforced with 8 steel bars of 10 mm diameter. The longitudinal bars' tensile yield strength was 500 MPa. The stirrups were of mild steel (f_y=300 MPa) of a 6 mm diameter without ribs and were place at distances of 80 mm, except in the last 300 mm of the members that were placed every 50 mm. Stirrups were placed on each corner of a longitudinal bar by using one square stirrup and two L-shape stirrups as shown in Fig. 10.11.

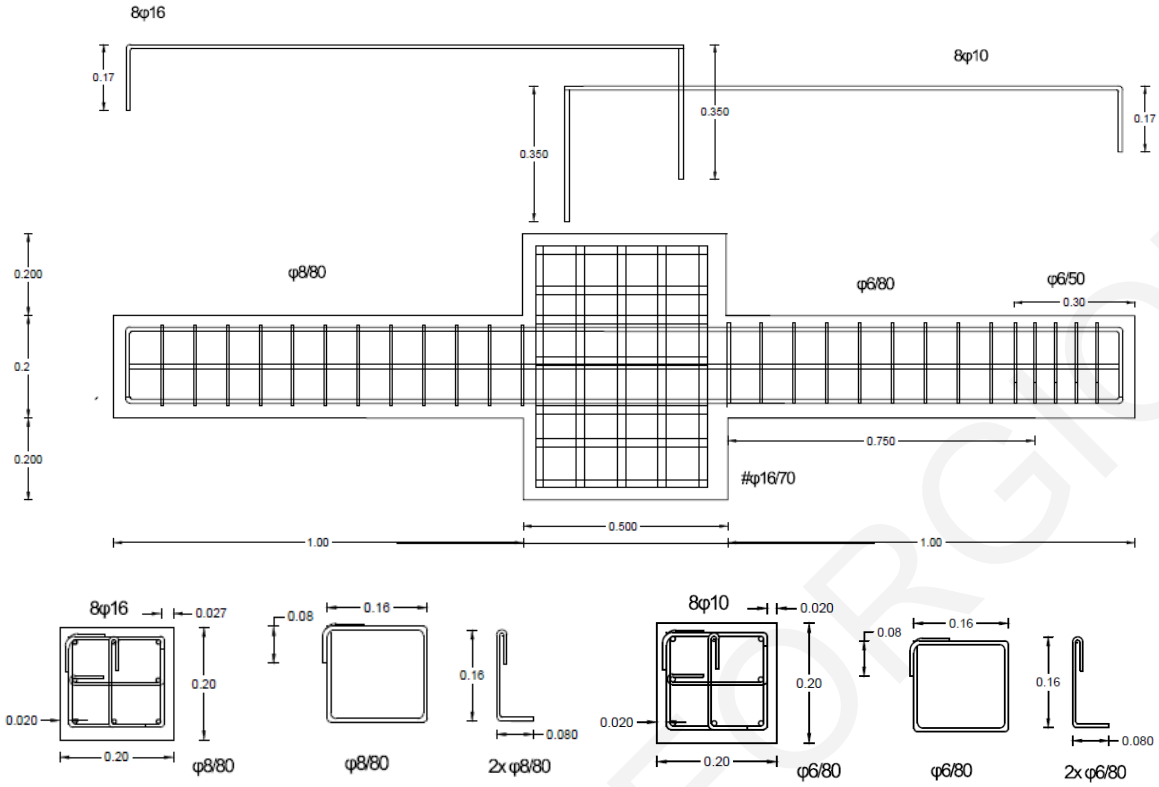

Figure 10.11: Detailing for Member A: Control, cementitious composite without fibers

10.2.2.2 Member B: SHFRCC

The SHFRCC Member B, also had a cross section of 200x200 mm. The cementitious matrix was composed of the mix with 2% PVA fibers (F9 mix as described in Chapter 4), and was reinforced with 8 steel bars of 10 mm diameter. The longitudinal bars tensile yield strength was 500 MPa. The stirrups were of mild steel (f_y=300 MPa) of a 6mm diameter without ribs and were placed at distances of 120 mm, except in the last 300 mm of the members that were placed every 50 mm. One square stirrup setup was placed and by this only the four bars on the corners of the member were at the corner of a stirrup as shown in Fig. 10.12.

10.2.2.3 Supporting Member

The Moment-curvature diagram of the SHFRCC member shows that the Maximum moment, due to the beneficial action of the fibers both in the tensile and the compressive zone of the cross-section reaches the value of 35 kNm. Therefore the supporting member's reinforcement was chosen to be 8 bars of 16mm diameter for the longitudinal reinforcement and 8mm bars for stirrups with a distance of 80 mm and three legs in each direction, as depicted in Fig. 10.12. All the longitudinal bars were very well anchored within the rigid zone.

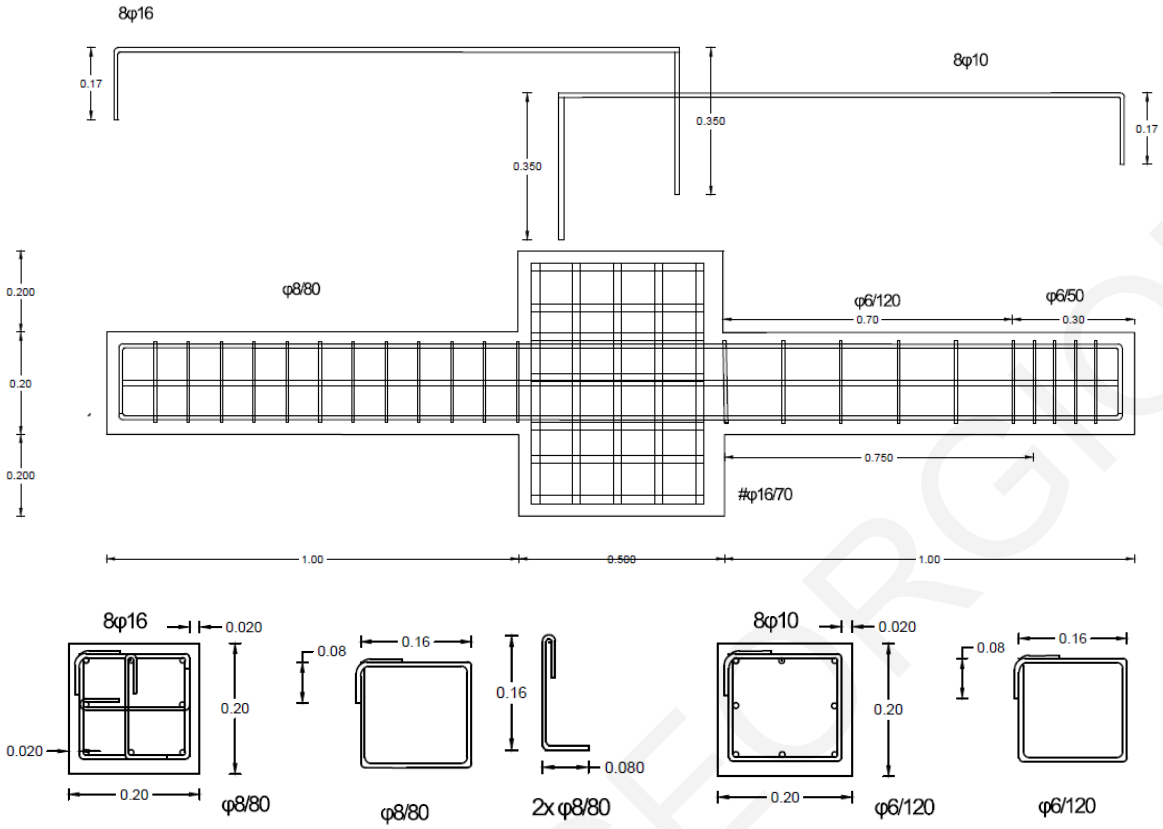

Figure 10.12: Beam Detailing for cementitious composite with fibers

10.2.2.4 Rigid Node

The central rigid node connecting the two beams in each specimen had to be very well designed in order to receive the reversed cyclic loading and transfer it to the beams and ensure that the longitudinal bars would be well anchored. A "cage" type reinforcement was chosen as shown in Fig. 10.13 with closed stirrups encasing the node. The reinforcement that was parallel to the longitudinal axis of the beams had 16 mm bars with a spacing of 70 mm, while the vertical reinforcement that was parallel to the loading direction was 16mm diameter bar with a spacing of 70mm with the geometry shown in Fig. 10.13.

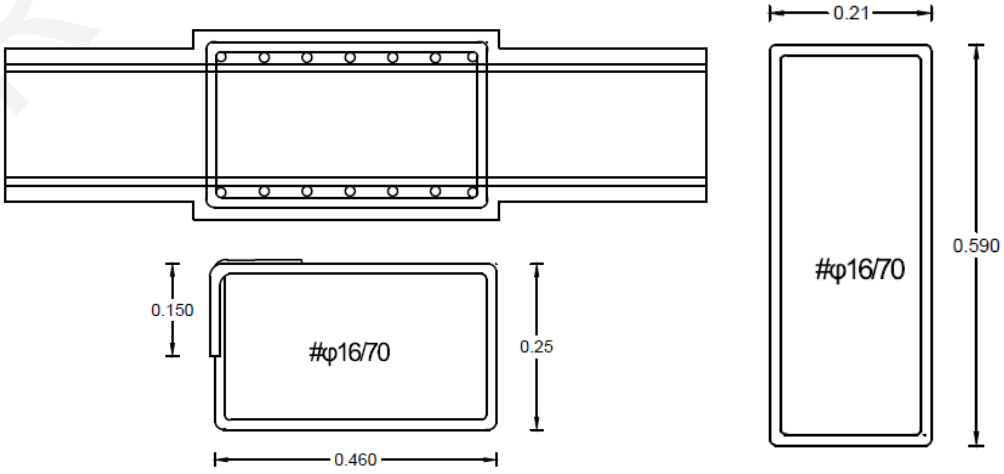

Figure 10.13: Central rigid node detailing

10.2.3 Test Setup

The two large scale double beams were tested at the Concrete Technology and Structures Laboratory of the University of Cyprus. The test was conducted on a 250 kN MTS hydraulic actuator, digitally controlled and attached on a self–reacting steel frame (Fig. 10.14). Large and small–scale structural components and structural systems can be tested under static and dynamic loading conditions using this apparatus.

Figure 10.14: MTS hydraulic actuator attached on a self–reacting steel frame

The double beam was supported on rollers at the edges in order to allow rotation at the supports while the central rigid node was connected to the load actuator with two plates connected to each other; this setup does not allow horizontal translation of the rigid node, while it allows the beams to expand away from the node without creating any axial loads. The supports were specifically designed for this purpose and are shown in Fig. 10.15 (a). The rollers had to be placed both on the top and bottom sides of the beams and supported on the loading frame in order to prevent upward movement during the reversed loading. The height of the supports was elaborated in order for the specimen to be supported and the loading actuator would be at the center height of its full travelling distance, in order to exploit its full length for the reversed cyclic loading (distances for the placement of all equipment and the specimen are shown in Fig 10.15 (c)). For the central rigid node, the concrete specimen was placed on the bottom plate and then the MTS pushed the top plate on the concrete node up to a Load of 5 kN. Then the bars connecting the two plates were placed and tightened and the specimen was lifted from the central node setup and placed on the supports. Fig. 10.15 (b) shows the design of the setup and a photo of the actual placement. The test specimen

had a total length of 2.50 m, while the cross section of the beams was 200x200 mm. The shear span had a length of 700 mm, giving a shear span ratio a/h=3.5.

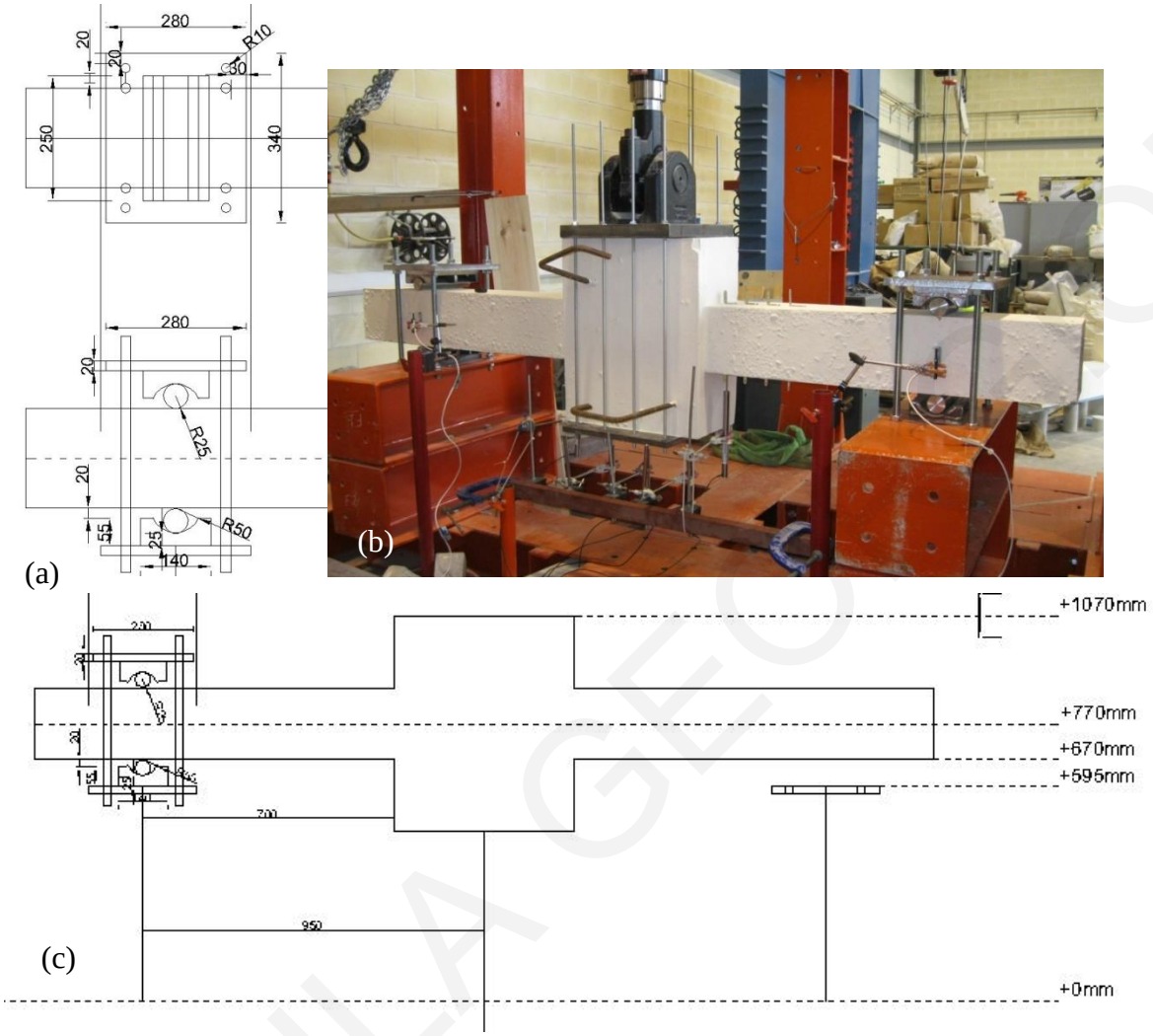

Figure 10.15: (a) Roller support design, (b) Beam setup photo and (c) Setup distances

10.2.4 Measuring equipment

In order to measure deflections and deformations of the beam during the test 13 LVDTs with different travel-lengths were used. LVDTs 1 to 5 had a travel distance of 100 mm and were placed as follows: LVDTs 1 to 3 were placed under the bottom steel plate that was holding the middle rigid node and transferring loads from the actuator to the specimen, LVDTs 4 and 5 were placed on the bottom side of the two beams at a distance of 30 mm from the rigid node. DTs 1 to 8 had a travel distance of 40mm and were placed as follows: DTs 5 and 6 were placed so as to measure the vertical deflection of the neutral axis at the ends of the shear spans of the two beams (middle of height) and DTs 1 to 4 and DTs 7 and 8 were placed on the top and bottom sides (three on each side) of the Control and SHFRCC members close to the rigid node, at the zone where the plastic hinges were expected to form. The measuring system setup and photos from the actual placement are depicted in Fig. 10.16. All the measuring equipment was mounted on a system of metallic

beams that were not in contact to the steel frame in order to avoid measuring deformations caused by the movement of the frame during loading.

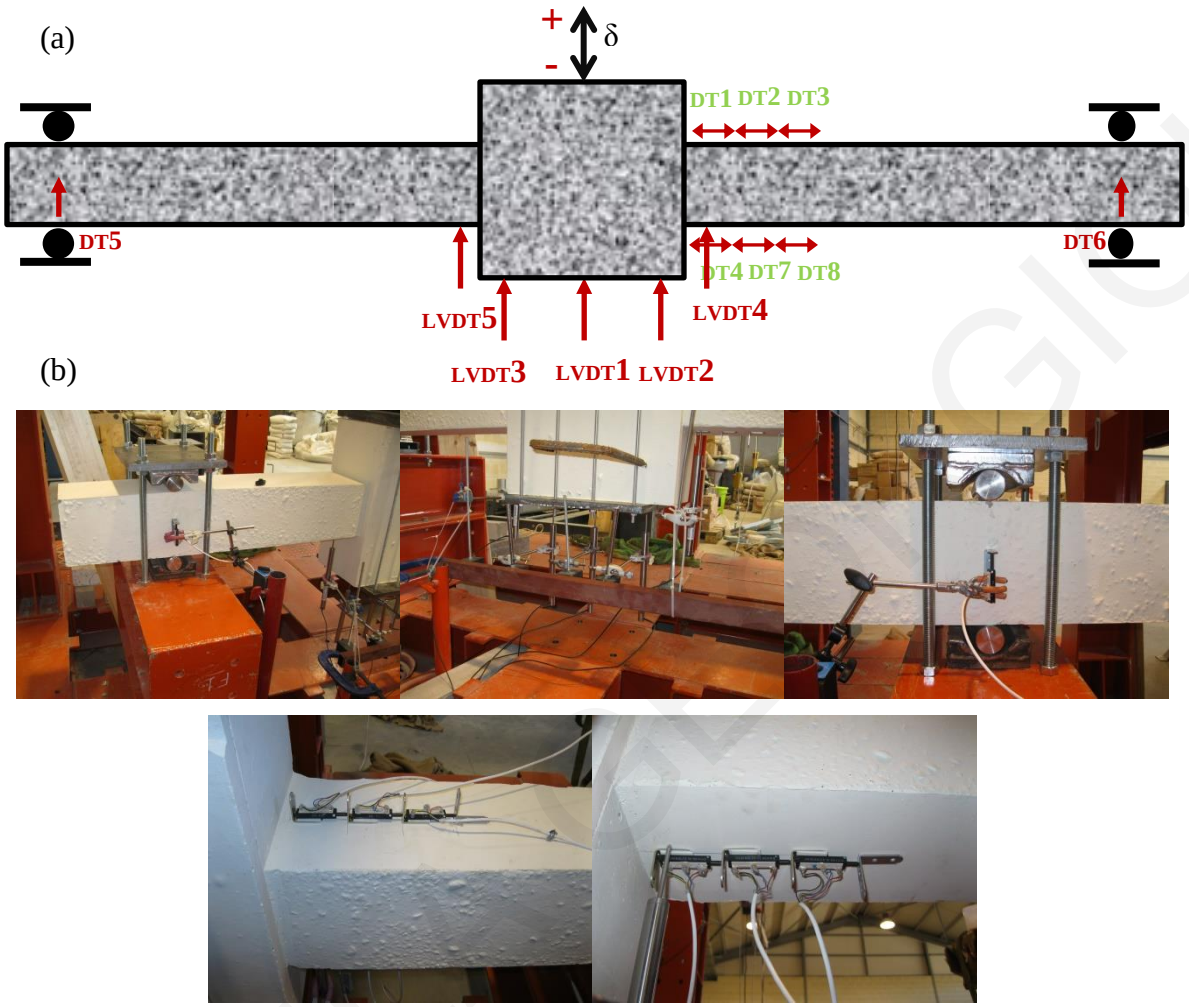

Figure 10.16: (a) Measuring system setup, (b) photos of all LVDTs placed on specimen

10.2.5 Material properties from preliminary tests

Compressive tests on cylinders of 100x200mm were performed on all mixes used for the construction of the members used for the reversed cyclic loading, while uniaxial tensile tests were performed on samples of the SHFRCC mix. Additionally the steel bars used as reinforcement were tested under uniaxial tension. The experimental setup and procedures for these tests are described in detail in Chapter 4. The mix for the SHFRCC was F9 and for the rigid node and supporting beam of the same specimen the mix used was F10. For the control specimen mixes used was F11 and F12. The stress-strain diagrams of the mixes and photographic material are listed in Appendix 4B.

10.2.6 Reversed cyclic loading

A cyclic displacement history with full reversal of deflection was applied on the beam. Three cycles were imposed for each displacement level up to a displacement of 18 mm, two for the displacement of 22.5 mm and one for the rest of the displacement levels. The amplitudes of

displacement and number of cycles are listed in Table 10.1. Twenty cycles were employed for the reversed loading as shown in Fig 10.17, while loading was stopped at each peak in order to record the new cracks that were formed. The test was performed under displacement control with a rate of 3mm/min and was controlled by the actuator's movement. The chosen displacement level, that was used to determine the amplitude, was the deflection of the beams at yielding of the flexural reinforcement Δ_y.

Table 10.1: Number of cycles and amplitude

No. of cycles	3	3	3	3	3	2	1	1	1
Amplitude Δ (mm)	2.25	6.00	9	13.5	18	22.5	27	31.5	36

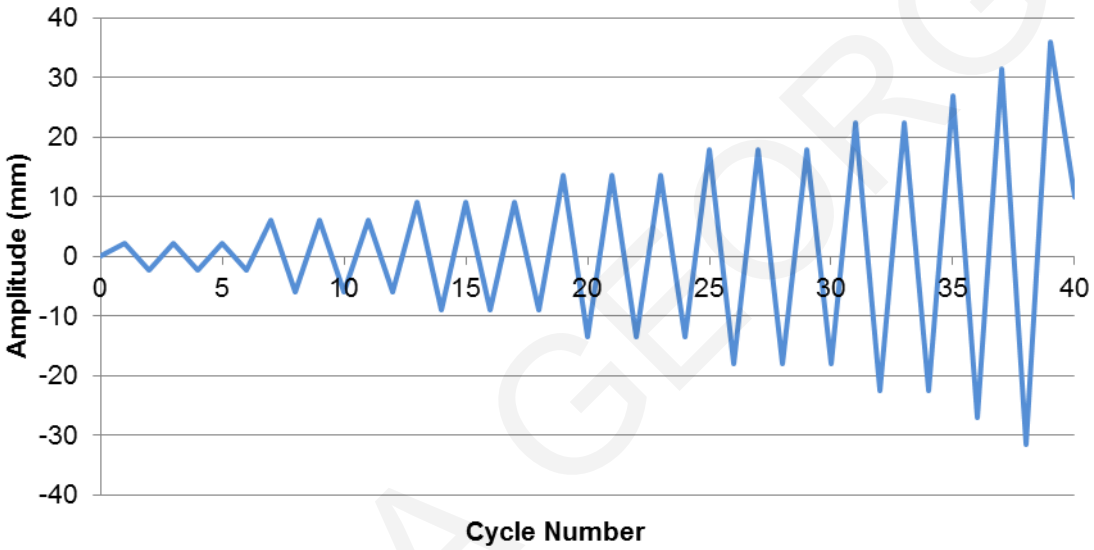

Figure 10.17: Cyclic load pattern used in testing

The strain rate imposed on the beam's compressive and tensile zone was calculated for deciding the displacement rate. The objective was that it be slow enough so that the test is quasistatic and therefore no rate effects may be traced in the material performance. To assess the magnitude of the rate with respect to the standard material tests, the compression strain rate occurring in the compression zone of the beam was calculated as shown in Table 10.2. The drift rate was calculated based on the displacement rate as $\theta=\delta/L$, where θ is the drift rate, δ is the displacement rate and L is the shear span length. From the drift rate curvature was computed as $\varphi=3\theta/L$. From the curvature values and assuming a neutral axis depth of x=160/3=55 mm, the normal strains in the extreme layer under compression and extreme layer under tension were obtained as $\varepsilon_c=\varphi \cdot x$ and $\varepsilon_t=\varphi \cdot (h-x)$ respectively. The strain rates of the cyclic loading are as shown in Table 10.2. Based on the research of Pajak [96] the strain rates determined are low enough not to influence the strength obtained from the materials.

The expected yield curvature for the Control member was estimated based on the same procedure and was used in order to determine the target displacement levels shown in Table 10.1. Based on the Moment-curvature diagram of Fig. 10.9 that was an estimation of the behavior of the

control member the yield curvature was 0.000037 and therefore $\theta=\varphi \cdot L/3=0.000037 \cdot 700/3=0.00863$ and yield deflection $\delta_y=0.00863 \cdot 700=6.04$ mm.

Table 10.2: Strain rate of the material based on the displacement rate

δ	3	mm/min
θ	0.00429	1/min
φ	1.837E-05	1/rad/min
ε_c	0.00147	1/min
ε_t	0.0022	1/min

10.3 Experimental Results

The Shear Load-Deflection diagrams from the two members are depicted in Fig. 10.18. The deflection recorded is based on the central LVDT1 that measures the deflection at the middle of the lower steel plate. Deflection is considered positive when the beam moves up and negative when moving down. During moving in the positive deflection the top fibers of the beams are expanding being under tensile strains and bottom fibers of the beam's cross sections are under compression. The Load is positive when the top cross section is under tension. Shear in the spans is half the total Load $V=P/2$. In order to calculate the total deflection of the beams the average deflection at the supports (DT5+DT6)/2 is deducted from the total deflection of the central measuring LVDTs.

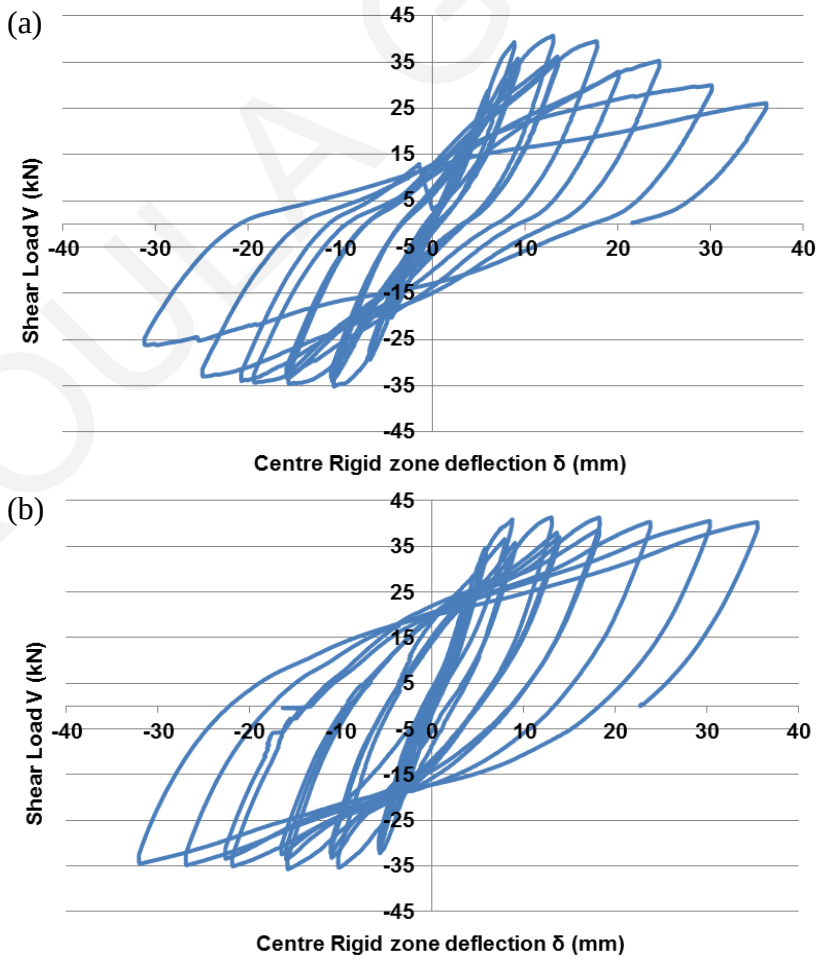

Figure 10.18: Shear Load-Vertical deflection of central rigid node for the (a) CONTROL and (b) SHFRCC

The diagrams of Fig. 10.18 show the behavior of the two tested members under reversed cyclic loading. The Control member shows yielding of the reinforcement at a deflection of 6.8 mm and a shear load of 34.7 kN. Past the yield point the specimen showed some mild hardening with a peak shear load of 40.7 kN at a central rigid node deflection of 12.8 mm. After the peak load softening of the curve initiated with a remaining shear load of 25 kN in the last cycle of 36 mm deflection. During the second and third cycle of each target deflection the shear load capacity decreased, while the loading path of the following higher target displacement coincided with the lower target of the last excursion. As deflection increased the residual deformations of the specimen also increased, while the energy absorption of the consequent cycles decreased. The shear load-deflection curve of the SHFRCC member shows yielding at a deflection of 7.6 mm and 39 kN shear load. Past the yielding the load carrying capacity remained constant throughout the remaining cycles at a shear load of 41 kN even at a deflection level of 36 mm. The energy absorption capacity appeared to increase with each cycle and the members showed great ductility levels. The same type of behavior was observed if the right beams' force-deflection diagram is considered as shown in Fig. 10.19. As shown on the diagrams of Fig. 10.19 the deflection values measured at the hinge zone of the beams had higher values than those of the steel plate at the central rigid node. This was due to the accumulation of damage at the rigid node and the partial rotation of the node with the supporting beam.

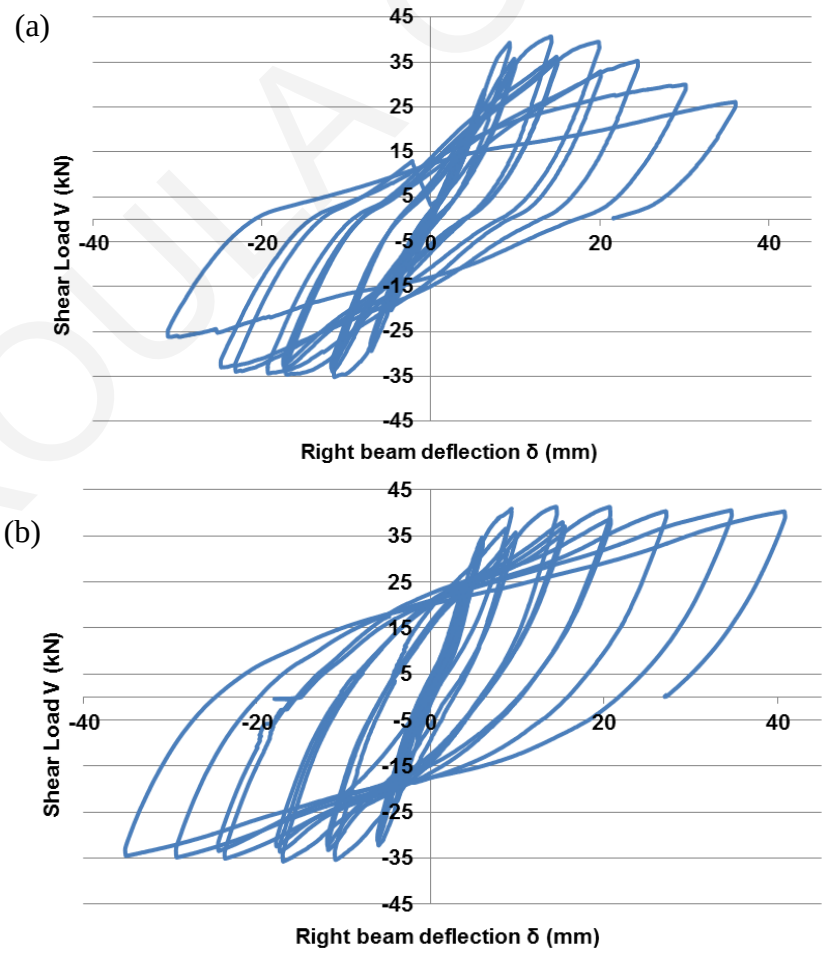

Figure 10.19: Shear Load-Right Beam deflection for the (a) CONTROL and (b) SHFRCC

The Shear Load-Drift diagrams of the tested beams are depicted in Figure 10.20 (a). The drift θ is calculated as the deflection of the beam divided by the shear span length. This deflection though does not take into consideration the rotation of the rigid node with the control beam. To account for this the load-drift ratio diagrams were corrected: the adjusted drift is calculated as shown in Fig. 10.20 (b) by the rotation of the rigid zone β, where in our case is obtained from the differential deformations of LVDT2 and LVDT3 divided by their horizontal distance. The diagrams with the adjusted drift ratio values are depicted in Fig 10.20 (c) and show a tendency for increase in the drift values if compared to those without the adjustment. When the load-drift ratio diagrams of the CONTROL and SHFRCC beams are closely observed it is found that there is a reduction of "pinching" of the hysteresis loops when compared with the load-drift ratio diagrams when drift is adjusted taking into consideration the rigid node's rotation. The decrease of load capacity in the diagrams is associated with the material degradation in the extreme layers. At the last level of loading large portions of the composite within the plastic region had spalled off the specimen and the reinforcement experienced excessive buckling.

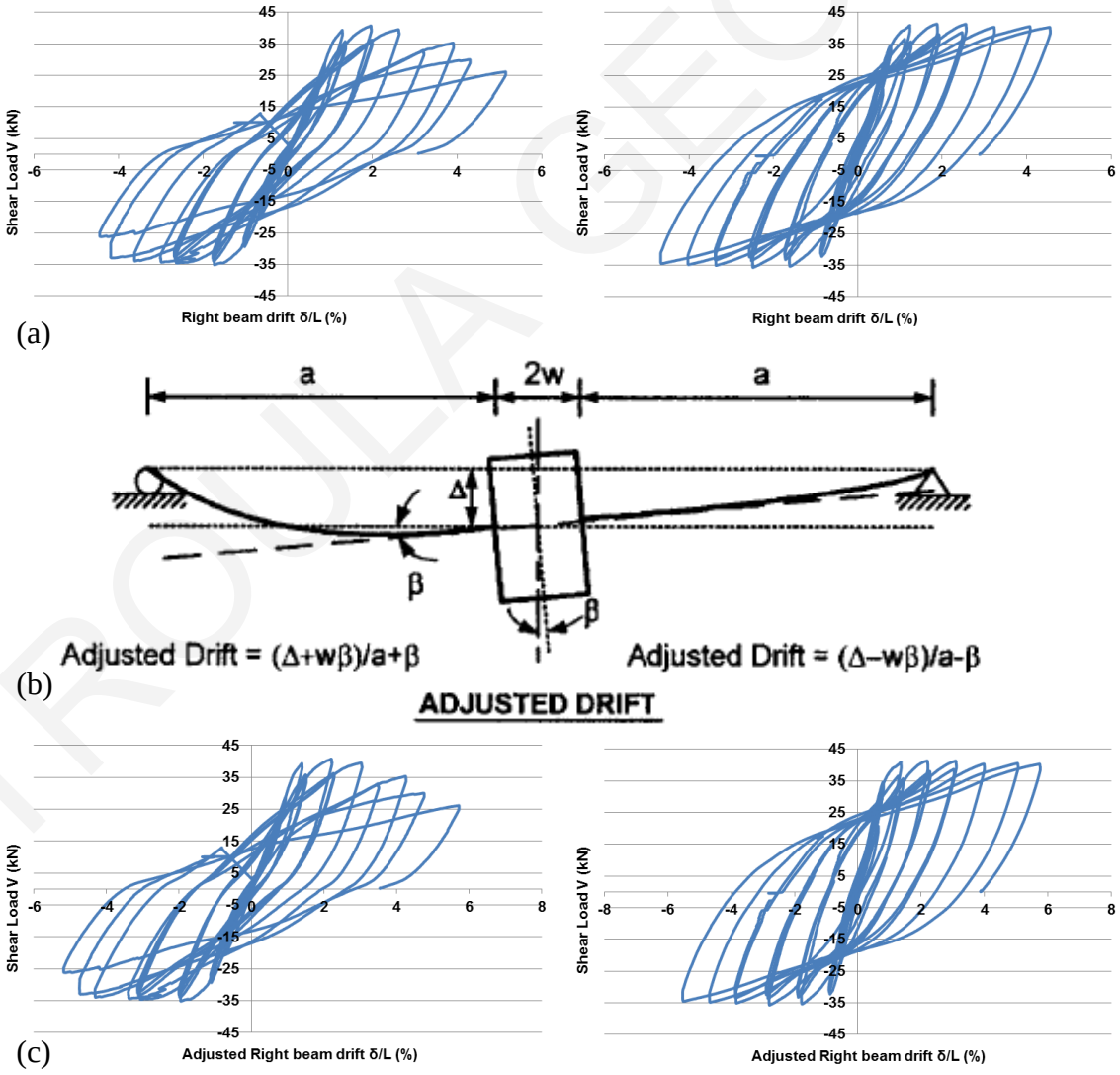

Figure 10.20: a) Shear Load-Drift for the CONTROL (left) and SHFRCC (right) b) calculation of member drift [165], and c) Shear Load-Adjusted Drift for the CONTROL (left) and SHFRCC (right)

Photos of the progressive failure of the Control and SHFRCC members are given in Appendix 10.A. The results indicate that the SHFRCC member -even though it only had Φ6/120 perimeter stirrups as compared to the Control member who had Φ6/80 stirrups (3 legs parallel to the loading) - showed an improved behavior under reversed cyclic loading due to the presence of the fibers that contributed to the transfer of loads, the confinement of the regions under tension and compression, the increase of shear capacity of the member and the sustained load capacity up to large levels of deflections. Up to the point that the experiment with the SHFRCC was stopped the load-drift curve did not show any load drop leading to drift ductility in the order of μ_θ=6/1=6 (at the end of the test at which no load drop was observed) as compared with the Control beam that was designed as per the Eurocode, that attained a drift ductility of μ_θ=4/1=4 at a load drop of 20% of the maximum load.

Chapter 11: Finite element modeling of the tests on HVFA and SHFRCC

Finite element analysis has witnessed a remarkable advancement since the first publication of the method in the 1960s; today, some sophisticated tools suitable for simulating concrete have been developed and are gaining acceptance. However there is still a lack of robustness where concrete modeling is concerned, which is mostly associated with strain softening in the absence of the stabilizing influence of reinforcement. Instability may be caused if stiffness in any element degrades to zero or is negative, an event that is simultaneous with progressive cracking due to tensile stresses and strains, loss of bond between concrete and steel, or failure of aggregate interlock and dowel action [166]. The material properties that are used as input parameters define the relevance of the analysis results; mesh sensitivity and path dependence are common features of the analysis performance in these circumstances. In extending the existing modeling frameworks to the class of SHFRCC materials, apart from elimination of mechanisms of aggregate interlock owing to the absence of coarse aggregate, there is still a lack of knowledge in many parameters that are essential input, such as fracture energy, tensile stress-strain in the softening range and the anticipated crack spacing. Empirical equations used to calibrate these variables for normal concrete cannot be directly transplanted in the SHFRCC materials on account of the fundamental differences in the constitutive behavior of the two material types. The high volume of fly ash within the mix design, the lack of coarse aggregates and the addition of fibers also change dramatically the ratio of compressive to tensile strength of the composite and the fracture energy, whereas it facilitates the strain hardening effect in tension; it was also shown that fibers exert a passive confining effect which increases the strain ductility in compression in the same manner as conventional lateral pressure – however, although behavior is elastoplastic in uniaxial tension, the behavior in uniaxial compression remains below the transition point (i.e. it is softening, albeit with a much milder pace as compared to common concrete).

11.1 Concrete Damage Plasticity Model in ABAQUS

Based on previous F.E. studies of brittle-like materials of the available options to model the inelastic-softening behavior of concrete, the non-associated plasticity theory framework offers a powerful simulation environment that would be appropriate for the problem of SHFRCC. A calibrated model in the general purpose finite element code ABAQUS that implements the essentials of non-associated plasticity simulation is the so-called Concrete Damage Plasticity (CDP) model. The model background was developed by Lubliner [167] including some modifications proposed later by Lee and Fenves [168]. As implemented, CDP is suitable for both static and dynamic analyses. The model comprises yield and loading functions in order to reflect the pressure sensitivity of the failure envelope to confining pressure, and plastic potential function to determine the direction and magnitude of plastic deformation; an attractive aspect of the CDP model is the ability to model strain hardening of the behavior of a composite even in direct tension.

Damage is explicitly considered in reducing the elastic component of the response. Therefore, a starting point in the development of the CDP is the decomposition of strain rate effects to the elastic and plastic components as follows:

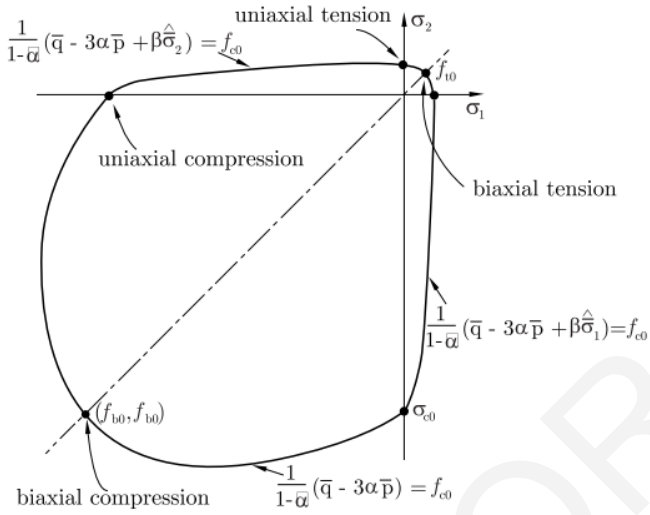

Figure 11.1: Biaxial yield surface in the constitutive model CDP from ABAQUS Manual [6].

In the CDP model strain rate decomposition is assumed as:

$$\dot{\varepsilon} = \dot{\varepsilon}^{el} + \dot{\varepsilon}^{pl} \tag{11.1}$$

Where $\dot{\varepsilon}$ is the total strain rate, $\dot{\varepsilon}^{el}$ is the elastic part of the strain rate and $\dot{\varepsilon}^{pl}$ is the plastic part of the strain rate. The stress-strain relations are governed by scalar damaged elasticity:

$$\sigma = (1-d)\cdot D_o^{el} : \left(\varepsilon - \varepsilon^{pl}\right) = D^{el} : \left(\varepsilon - \varepsilon^{pl}\right) \tag{11.2}$$

where D_o^{el} is the initial (undamaged) elastic stiffness of the material, $D^{el} = (1-d)\cdot D_o^{el}$ is the degraded elastic stiffness and d is the scalar stiffness degradation variable which can take values from zero (undamaged material) to one (fully degraded material). The single degradation variable means that the stiffness degradation is isotropic. Damage states in tension and compression are characterized independently by two hardening variables, $\tilde{\varepsilon}_t^{pl}$ and $\tilde{\varepsilon}_c^{pl}$, which are the equivalent plastic strains in tension and compression respectively. The evolution of the hardening variables is given by the following expression:

$$\tilde{\varepsilon}^{pl} = \begin{bmatrix} \tilde{\varepsilon}_c^{pl} \\ \tilde{\varepsilon}_t^{pl} \end{bmatrix} \text{ and } \dot{\tilde{\varepsilon}}^{pl} = h\left(\bar{\sigma}, \tilde{\varepsilon}^{pl}\right)\cdot \dot{\varepsilon}^{pl} \tag{11.3}$$

Cracking (tension) and crushing (compression) in concrete are represented by increasing values of the hardening (softening) variables. These variables control the evolution of the yield surface and the degradation of the elastic stiffness. Plastic flow is governed by a flow potential function $G(\bar{\sigma})$ according to non-associative flow rule:

$$\dot{\varepsilon}^{pl} = \lambda \frac{\partial G(\bar{\sigma})}{\partial \sigma} \tag{11.4}$$

The plastic potential function *G* is also defined in the effective stress space. The material properties that are required as input parameter for the analysis are as follows:

a) Density of the composite
b) Elastic material characteristics that are defined by the modulus of elasticity and the Poisson's ratio.
c) Concrete Damage Plasticity option is used to describe the compressive stress-strain relationship outside the elastic range. The plastic strain values are used here and not the total strain values.

The first pair of parameters marks the onset of plasticity. The essential parameters that are required to define the full response of the material in ABAQUS are *β, m, f* and *γ*. The parameters *β* and *m* describe the shape of the flow potential function and *f* and *γ* determine the shape of the yield function. In this model for the flow potential *G*, the Drucker-Prager hyperbolic function is determined by this form:

$$G(\bar{\sigma}) = \sqrt{(f_c - m \cdot f_t \cdot \tan\beta)^2 + \bar{q}^2} - \bar{p} \cdot \tan\beta - \sigma \tag{11.5}$$

Where f_t and f_c are the uniaxial tensile and compressive strengths of the material, β is the dilation angle measured in the p-q plane at high confining pressure and *m* is the eccentricity of the plastic potential surface. The eccentricity defines the rate at which the plastic potential function approaches the asymptote and increasing values of m provides more curvature to the flow potential. The non-associative flow rule that is used here requires a loading surface definition. The plastic damage concrete model uses a yield condition based on the loading function proposed by Lubliner [167] in the form:

$$F = \frac{1}{1-\alpha}\left(\bar{q} - 3 \cdot \alpha \cdot \bar{p} + \theta\left(\tilde{\varepsilon}^{pl}\right)\langle \bar{\sigma}_{\max} \rangle - \gamma\langle -\bar{\sigma}_{\max} \rangle\right) - \sigma\left(\tilde{\varepsilon}^{pl}\right) \tag{11.6}$$

The shape of the loading surface in the deviatoric plane is determined by parameter γ, while parameter α is calculated based on Kupfer's curve (Fig. 11.3). The Macauley bracket is defined as $\langle x \rangle = 0.5 \cdot (|x| + x)$. The function $\theta\left(\tilde{\varepsilon}^{pl}\right)$ is given as:

$$\theta\left(\tilde{\varepsilon}^{pl}\right) = \frac{\bar{\sigma}_c\left(\tilde{\varepsilon}_c^{pl}\right)}{\bar{\sigma}_t\left(\tilde{\varepsilon}_t^{pl}\right)}(1-a) - (1+a) \tag{11.7}$$

Where $\bar{\sigma}_t$ and $\bar{\sigma}_c$ are the effective tensile and compressive cohesion stresses. The parameter α depends on the ratio of the biaxial compressive strength to the uniaxial compressive strength and is defined as:

$$a = \frac{(f_{bo}/f_c) - 1}{2(f_{bo}/f_c) - 1} \tag{11.8}$$

Where f_{bo} is the compressive strength under biaxial loading (see Fig. 11.1). The parameter γ is identified from the full triaxial tests and is prescribed in the form:

$$\gamma = \frac{3(1-\rho)}{2\rho+3} \tag{11.9}$$

where $\rho = \frac{\left(\sqrt{J_2}\right)_{TM}}{\left(\sqrt{J_2}\right)_{CM}}$ is defined at a given state $\overline{p}$. Typical values of ρ for normal concrete are in the range of 0.64 to 0.8 [167]. Identification of these parameters may be established via direct tensile and compressive tests of the material. Additionally multiaxial tests are needed. The characteristic cracking and crushing points for normal concrete are defined from the stress-strain curve under tension and compression as shown in Figure 11.2. For normal concrete it is usually assumed that the range of concrete elasticity is $0.3f_c$ in compression and $0.7f_t$ in tension [169]. The elastic modulus is based on the concrete elasticity values in compression and is the same for tension and compression based on the material input parameters.

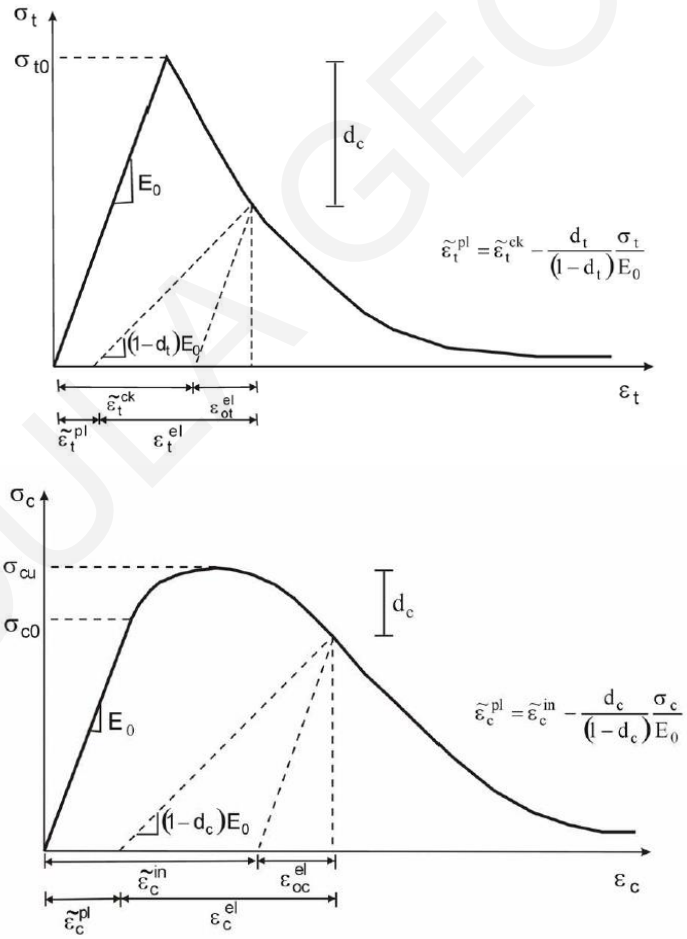

Figure 11.2: Tensile and compressive stress-strain curves of CDP model for normal concrete from ABAQUS Manual [6]

Material models exhibiting softening behavior and stiffness degradation may lead to severe convergence difficulties that can be avoided by using viscoplasticity and permitting stresses to be outside the yield surface. The viscoplasticity strain rate tensor $d\varepsilon_v^p$ is defined as:

$$d\varepsilon_v^p = \frac{1}{\mu}\left(\varepsilon^p - \varepsilon_v^p\right) \tag{11.10}$$

The parameter μ is the viscosity parameter representing the relaxation time of the viscoplastic system and ε^p is the plastic strain evaluated in the inviscid backbone model. The solution of the viscoplastic system relaxes to that of the inviscid case as $\Delta t/\mu \to \infty$, where Δt is the time increment. When a small value of the viscosity parameter - as compared to the time increment- is used, this helps improve the rate of convergence of the model in the softening regime without compromising the results [6]. Cylinders and tensile coupons with the dimensions used in the experimental program are modeled in ABAQUS in order to calibrate the material laws of all the mix designs in tension and compression. Due to lack of any multiaxial tests, the biaxial failure envelope by Kupfer & Gerstle (failure curve in plane stress [170]) for a concrete of 50 MPa compressive stress is used here. The parameter γ is identified as 0.666, adopted from previous research for normal concrete [170].

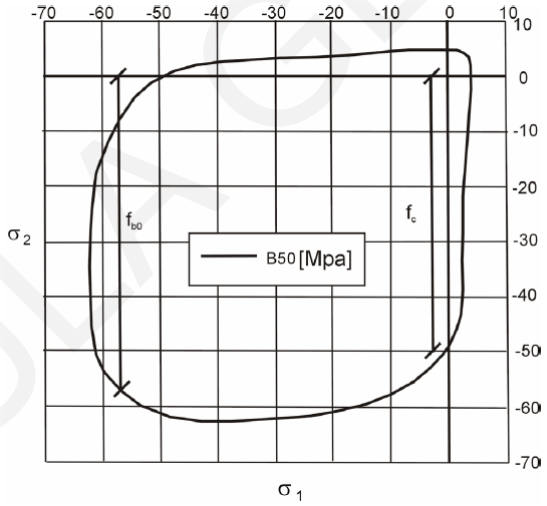

Figure 11.3: The Kupfer & Gerstle Biaxial failure envelope for concrete class B50 [170]

11.2 Material laws in tension and compression

The determination of the tensile strength of the HVFA composite without fibers cannot be derived from uniaxial tensile tests since the specimens made for that purpose disintegrated at the time of demolding. Model Code [49] in Chapter 5.1 provides calibrated equations for the determination of the mean value of the tensile strength of concrete, that may be estimated indirectly from the characteristic compressive strength f_{ck}, the mean splitting strength $f_{ct,sp}$ or the mean flexural strength $f_{ct,fl}$.

Based on the compressive strength of concrete and for concrete class ≤50 MPa then the tensile strength is determined by Eq. 11.11a, while the lower and upper bound values of the characteristic tensile strength f_{ctm}, may be estimated from Eq. 11.11b-c.

$$f_{ctm} = 0.3 \cdot \left(f_{ck}\right)^{2/3} \tag{11.11a}$$

$$f_{ctk,\min} = 0.7 \cdot f_{ctm} \tag{11.11b}$$

$$f_{ctk,\max} = 1.3 \cdot f_{ctm} \tag{11.11c}$$

If the tensile strength is measured via the splitting strength or the flexural strength then a conversion factor A is proposed by the code (Eq. 11.12). The conversion factor as stated by the code may be determined either from uniaxial tensile tests or by the factors given by the Code. The conversion factor given for the splitting test takes the value of A_{sp}=1, even though it is stated that values of this factor in existing national and international codes may vary from 0.67 to 0.95. The splitting strength $f_{ct,sp}$ is the mean value of the splitting test as determined from the ISO4108 as per Eq. 11.13.

$$f_{ctm} = A_{sp} \cdot f_{ct,sp} \tag{11.12}$$

$$f_{ct,sp} = \frac{2 \cdot P}{\pi \cdot d \cdot l} \tag{11.13}$$

In order to estimate the mean tensile strength from the mean flexural strength $f_{ct,fl}$ a different conversion factor A_{fl} is proposed by the New Model Code [49] that may be estimated by Eq. 11.15, where h_b is the beam depth, α_{fl}=0.06 and flexural strength $f_{ct,fl}$ is determined from the four point bending beam test from Eq. 11.16.

$$f_{ctm} = A_{fl} \cdot f_{ct,fl} \tag{11.14}$$

$$A_{fl} = \frac{a_{fl} \cdot h_b^{0.7}}{1 + a_{fl} \cdot h_b^{0.7}} \tag{11.15}$$

$$f_{ct,fl} = \frac{P \cdot L}{b \cdot d^2} \tag{11.16}$$

The fracture energy of concrete G_f [N/m], defined as the energy required to propagate a tensile crack of unit area, is used for the application of fracture mechanics for the analysis for concrete members. Therefore, it is used as the material's characteristic to resist tensile stress and should be determined from uniaxial tensile tests, but also indirectly from three point bending tests on notched beams. The fracture energy is related to the water/cement ratio, the maximum aggregate size and the age of the concrete. If tests are not available then a calibrated expression in the New Model Code [49] is recommended:

$$G_F = 73 \cdot f_{cm}^{0.18} \tag{11.17}$$

A bilinear stress strain relation is given for the uncracked normal-weight concrete and a stress-crack opening relation for the cracked section and these two curves as shown in Fig. 11.4 may be used to define the full tensile failure of concrete. The equations used to describe the bilinear relation are as follows:

$$\sigma_{ct} = E_{ct} \cdot \varepsilon_{ct} \text{ for } \sigma_{ct} \le 0.9 \cdot f_{ctm} \quad (11.18a)$$

$$\sigma_{ct} = f_{ctm} \cdot \left(1 - 0.1 \frac{0.00015 - \varepsilon_{ct}}{0.00015 - 0.9 \cdot f_{ctm} / E_{ct}} \right) \text{ for } 0.9 \cdot f_{ctm} \le \sigma_{ct} \le f_{ctm} \quad (11.18b)$$

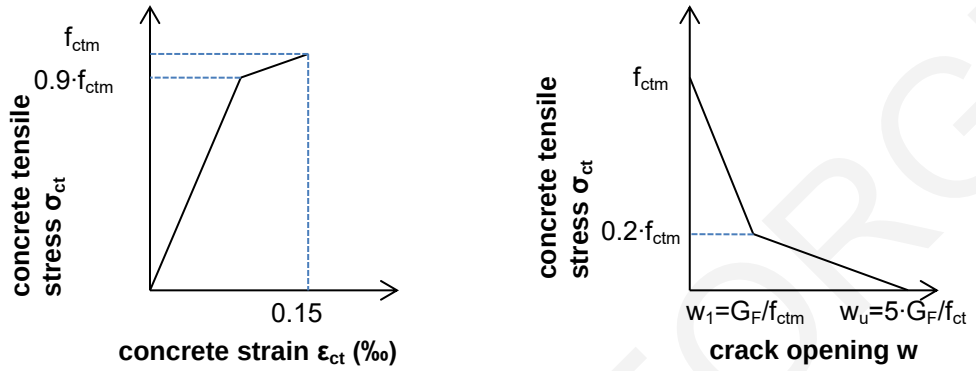

Figure 11.4: Schematic representation of the stress-strain and stress-crack opening relation for uniaxial tension (according to fib Bulletin 42 [171])

For the cracked section the behavior is treated as bilinear. At a value of 90% of the tensile strength the microcracks cause loss of stiffness in a localized failure zone, growing and forming a discrete crack. The stresses and deformations in the fracture zone are related to a fictitious crack opening w (according to fib Bulletin 42 [171]). As per Fig. 11.4 the two discrete crack opening points at 80% load drop and the ultimate crack opening are determined from the fracture energy and the mean tensile strength of concrete.

Table 11.1: Tensile strength from compressive, splitting and flexural strength of mix F5

From compression	**F5**	**From split**	**F5**	**From flexure**	**F5**
f_{cm}	50.37			$f_{ct,fl}$	3.33
$f_{cm} = f_{ck} + 8$	42.37	P_{max}		A_{fl}	0.601138
$f_{ctm} = 0.3 \cdot (f_{ck})^{2/3}$	3.646086	f_{ctm}	1.347	f_{ctm}	2.001789
$G_F = 73 (f_{cm})^{0.18}$ (N/m)	143.2826		143.2826		66.60981
$w_1 = G_F / f_{ctm}$	0.039298		0.106372		0.033275
$w_c = 5\ G_F / f_{ctm}$	0.196488		0.531858		0.166376
$\varepsilon_1 = \varepsilon_{cr} + w_1 / l_c$	0.00801		0.021424		0.006805
$\varepsilon_u = \varepsilon_{cr} + w_u / l_c$	0.039448		0.106522		0.033425
εcr	0.000182		6.73E-05		0.0001

The procedure described above was used to determine the tensile stress-strain curves for the composites without fibers by using the various equations that relate tensile strength to the compressive, splitting and flexural strength of concrete. The results for one mix without fibers (F5) based on the actual compressive, splitting and flexural strength of the composite are shown in

Table 11.1 and the resulting stress-strain diagrams are shown in Fig. 11.5. Modulus of Elasticity was 20000 MPa and the mesh size was 5 mm. The results show a great discrepancy between the diagrams proposed to be used for the analysis of the composite. This may be attributed to the special mix design used for the mix F5 that has a high volume content of fly ash, a small amount of water/cement ratio and has no coarse aggregates.

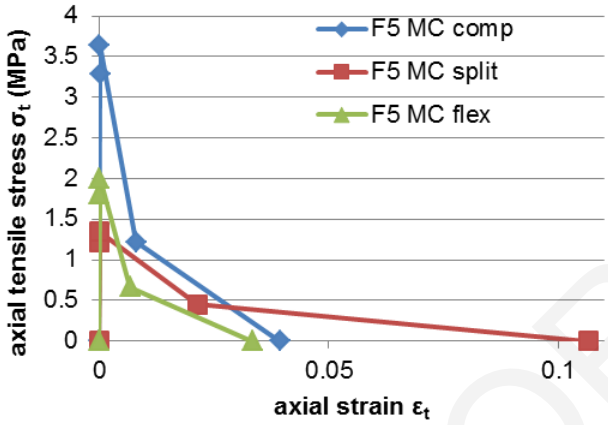

Figure 11.5: Tensile stress-strain curves estimated from MC based on the compressive, splitting and flexural strength of a composite with HVFA and no fibers.

The formation of microcracks in finite element analyses of normal concrete is defined by introducing a crack opening law that can be defined in one of three ways: a) fracture energy, b) stress-strain or c) stress displacement relationship. The fracture energy G_f is a material parameter that gives the amount of energy required to open a unit area of a crack and for ordinary concrete takes values between 50 to 200 N/m. One of the test methods that can be used to determine this parameter is the three point bending test on a notched prism, according to RILEM TC-50 FMC [172]. When the model has no reinforcement the approach based on the stress-strain law introduces mesh sensitivity to the results [6] and therefore it is better to use the fracture energy or the stress-crack opening approach. The ratio of the biaxial to the uniaxial compressive strengths has been taken equal to 1.16 based again on the results by Kupfer & Gerstle [170].

Modeling of the uniaxial compressive test was performed based on the actual experimental tests setup. A cylinder of 100 mm of diameter and 200 mm of height was simulated. Only one quarter of the cross section was used in the model due to the axisymmetry of the specimen. The two planes that were also axes of symmetry of the specimen were constrained only to the symmetry level. The bottom nodes of the model were restricted only in the direction of load in order to avoid any spurious lateral confinement by restraining the lateral translation of the nodes. The load was applied as a static displacement-controlled translation of the top surface nodes as shown in Fig. 11.6. The mesh size was 5mm for refined output, by using a sensitivity analysis in regards to the fracture energy of the composite under uniaxial tension as recommended in ABAQUS.

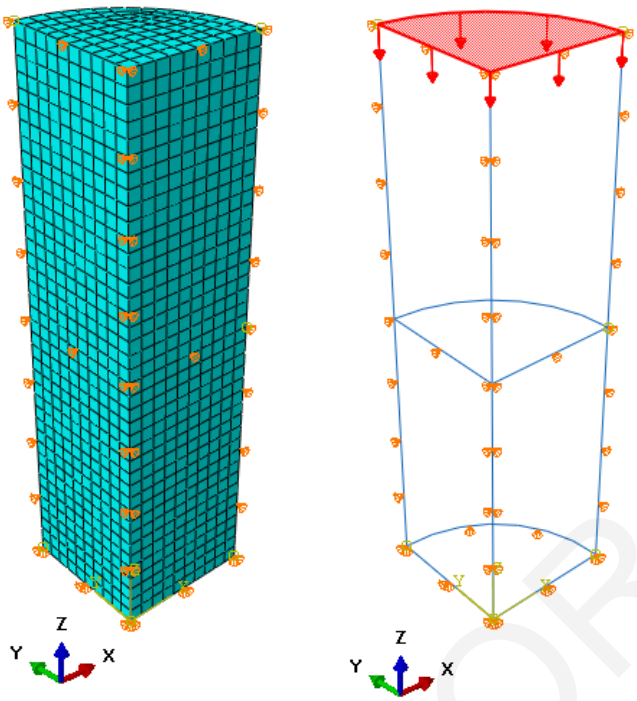

Figure 11.6: Modelling of the uniaxial compression test in Abaqus

FEM requires the stress-strain data provided to be entered as objective values and the modulus of elasticity to correspond to the slope defined by the tangent to the uniaxial stress strain curve near zero strain. Nominal values of stress and strain may be converted to objective values using the following equations: $\sigma_{tru}=\sigma_{nom}\cdot(1+\varepsilon_{nom})$ and $\varepsilon_{tru}=ln(1+\varepsilon_{nom})$. The modulus of elasticity is calculated from the first non-zero objective stress divided by the first non-zero objective strain. Objective strain may be converted to plastic strain by: $\varepsilon_{pl}=\varepsilon_{tru}-\sigma_{tru}/E$. The same procedure is followed both for the tensile and compressive behavior. Since the modulus of elasticity adopted in FEM is the same both for tension and compression the tensile stress-strain curve is adapted to the value provided for compression. The original nominal stress-strain curves are the values attained from uniaxial compression and direct tensile tests. In the case of the mixes without fibers the four point bending test results were used to extract the tensile strength of the composite to be used in the analysis. Additionally the evolution of the scalar damage variable for compression and tension are provided in the material laws in ABAQUS. An example of the material properties used to model one of the mixes without fibers and one with fibers are provided in Tables 11.2 and 11.3.

Table 11.2: The material parameters of CDP model for a composite without fibers

Material's parameters	**F5**	**The parameters of CDP model**	
		β	56
Concrete Elasticity		**m**	0.1
E (MPa)	20015	**$f=f_{bo}/f_c$**	1.16
v	0.312	**γ**	0.666
Concrete Compression Hardening		**Concrete Compression Damage**	
Stress (MPa)	**Crushing strain**	**DamageC**	**Crushing strain**
10.005	0	0	0
20.019	0.00004067	0	0.00004067
30.047	0.00005757	0	0.00005757
40.085	0.00011502	0	0.00011502
50.139	0.00027107	0	0.00027107
57.985	0.00081732	0	0.00081732
40.164	0.00208492	0.307340024	0.00208492
30.135	0.00298428	0.480298068	0.00298428
20.096	0.00378447	0.653428571	0.00378447
10.051	0.00458487	0.826662548	0.00458487
Composite Tension Stiffening		**Composite Tension Damage**	
Stress (MPa)	**Cracking strain**	**DamageT**	**Cracking strain**
2	0	0.0000	0
1.5	0.000138889	0.2500	0.000138889
1	0.000277778	0.5000	0.000277778
0.5	0.000416667	0.7500	0.000416667
0.2	0.0005	0.9000	0.0005
0.0001	0.0025		

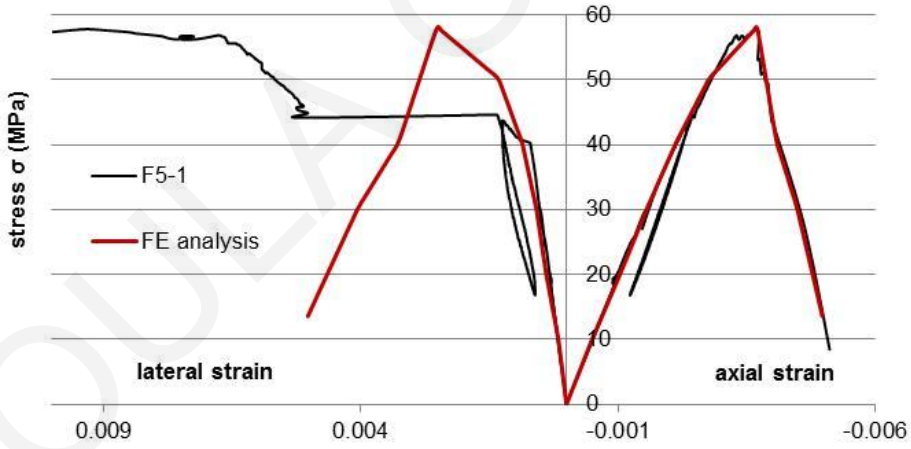

Figure 11.7: Uniaxial compression test results and Finite Element Analysis results for mix F5

Table 11.3: The material parameters of CDP model for a composite with fibers

Material's parameters	F7	The parameters of CDP model	
		β	
Concrete Elasticity		m	0.1
E (GPa)	16979.16	f=fbo/fc	1.16
v	0.305	γ	0.666
Concrete Compression Hardening		Concrete Compression Damage	
Stress (MPa)	Crushing strain	DamageC	Crushing strain
20.0236	0	0	0
25.03975	0.000114	0	0.000114
30.0621	0.000297	0	0.000297
35.09065	0.00052	0	0.00052
40.1276	0.000822	0	0.000822
45.171	0.001132	0	0.001132
47.60472	0.001307	0	0.001307
45.1935	0.001629	0.046741	0.001629
40.18	0.002123	0.152489	0.002123
35.168	0.002717	0.258207	0.002717
30.1515	0.003261	0.364019	0.003261
25.13625	0.003955	0.469805	0.003955
20.2	0.008761	0.573925	0.008761
15.3	0.018902	0.677279	0.018902
Composite Tension Stiffening		Composite Tension Damage	
Stress (MPa)	Cracking strain	DamageT	Cracking strain
2.5	0	0.0000	0
2.8	0.00786	0.0000	0.00786
2.5	0.010662	0.1071	0.010662
2	0.018132	0.2857	0.018132
1.5	0.02	0.4643	0.02
1	0.04	0.6429	0.04
0.5	0.06	0.8214	0.06
0	0.08		

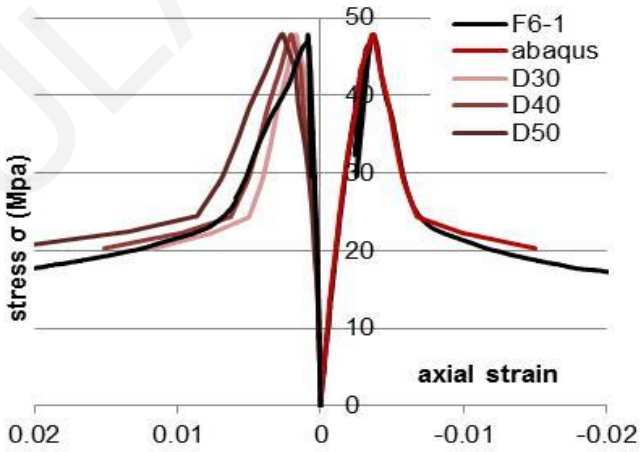

Figure 11.8: Stress-strain curves from experiment and FEM with various dilation angles

A number of trials were performed in FEM in order to determine a pertinent value for the dilation angle of the SHFRCC that was subsequently used in all analyses. Three different dilation angles were considered (30, 40, 50) and the results from FE analysis are compared against the experimental records as shown in Figure 11.8. A discrepancy is observed on the stress values obtained by FEM analysis for axial strains greater than 0.006. This concerns the experimental and

the FE simulation curves with respect to the axial deformation values due to the use of the option given in FEM for consideration of non-linear geometry.

The stress-strain curve that is imported in FEM must relate the mesh size of the FE model with reference to the crack size formed in the strain-softening part of the behavior where strain is localized at a single crack. The mesh size was chosen as l_c=5 mm and the strain at a stress residual equal to $f'_t/3$, according to Model Code (MC) [49]; these variables are related to the energy G_f that will be consumed when crack localization occurs. If calculated according with the New Model Code [49] expressions which had been calibrated for normal concrete, the energy G_f of fiber reinforced composites is seriously underestimated leading to erroneous estimations.

Table 11.4: Characteristic values of mix F5 and average

	v	**D (mm)**	**H (mm)**	**σ_{max} (MPa)**	**45% σ_{max} (MPa)**	**E (MPa)**	**ε (max stress)**
F5-1	0.327	99.94	198.94	57.77	26.00	19656.00	-0.00372
F5-2	0.327	100.11	197.54	43.21	19.45	19613.73	-0.00277
F5-3	0.327	99.92	195.58	50.13	22.56	19688.40	-0.00310
AVE	0.327	99.99	197.35	50.37	22.667	19652.71	-0.00320

In the case where the MC equations were used for the composite under research then for a compressive stress f_{cm}=47.83 MPa and f_{ck}=47.83-8=39.83 MPa, the tensile stress adopted for simulation would be $f_{ctm}=0.3\cdot(39.83)^{2/3}$=3.5 MPa, which is greater than the result from the uniaxial tensile test (f_{tmax}=3.1MPa). The fracture energy assumed by the Model Code would be, $G_F=73\cdot(47.83)^{0.18}$=146.44 (N/m). This energy when used to estimate the crack widths at $f'_t/3$ and at ultimate, leads to w_1= 0.1464 / 3.10=0.0469 (mm) and $w_c= 5\cdot G_F / f_{ctm}$= 0.2343 (mm). The cracking strain at which localization will occur is the strain at maximum load from the uniaxial tests ε_{tmax}=0.008. Then stains are estimated from, $\varepsilon_1=\varepsilon_{cr}+ w_1/l_c$=0.008+0.0469/5=0.01737 and $\varepsilon_u=\varepsilon_{cr}+ w_u/l_c$=0.05486.

Table 11.5: Tensile Stress-stain curve input values for FE modeling

	With MC G_f	Best fit trial		
σ	ε	ε	*Δf=8MPa* *$f_{cm}= f_{ck}+8$* *C<50 then $f_{ctm}=0.3\cdot(f_{ck})^{2/3}$* *$G_F=73\cdot(f_{cm})^{0.18}$ in (N/m)* *$w_1= G_F / f_{ctm}$* *$w_c= 5\ G_F / f_{ctm}$* *$\varepsilon_1=\varepsilon_{cr}+ w_1/l_c$* *$\varepsilon_u=\varepsilon_{cr}+ w_u/l_c$*	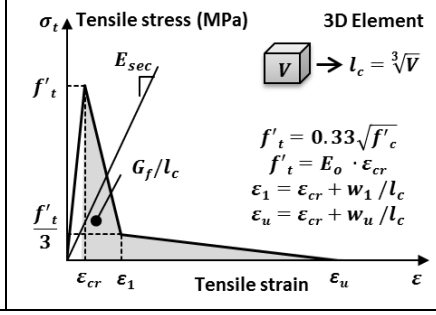
2.8003	0	0		
3.1248	0.0078	0.0079		
1.5165	0.0108	0.02		
1.033	0.017	0.04		
0.000	0.055	0.08		

When the above parameters from Table 11.5 are imported in FEM the stress-strain curve in uniaxial tension in the region of the strain softening behavior does not concur with the experimental results (see Fig. 11.9a). This implies that the New Model Code [49] equation used to determine the fracture energy and thereafter to define strains in the post peak region consistently underestimates the actual strain capacity of the materials, leading to erroneous estimation of the

post-peak slope of the curve. In the uniaxial tensile tests performed (See Par. 4.1) the strain used for the stress-strain diagram in tension is the elongation of the critical section in the middle of the specimen divided by the gauge length which was set equal to 100 mm. This elongation in the strain hardening part of the behavior may be translated into strain since multiple cracking appears in the full length of the specimen. However, after the peak stress is reached and strain localization begins to develop at a single crack, the elongation measured is the crack width at which all deformation is accumulated. Stress diminishes in a less brittle way as compared to normal concrete, since through that crack the fibers rupture or pull out as the width of the crack increases. Various attempts were made by importing different tensile stress-strain diagrams in the CDP model, until the actual stress strain curve from the experimental results was attained. The imported data resulting in best fit with the dog-bone tensile tests are given in Table 4 and the fitted curve is shown in Figure 11.9 (b).

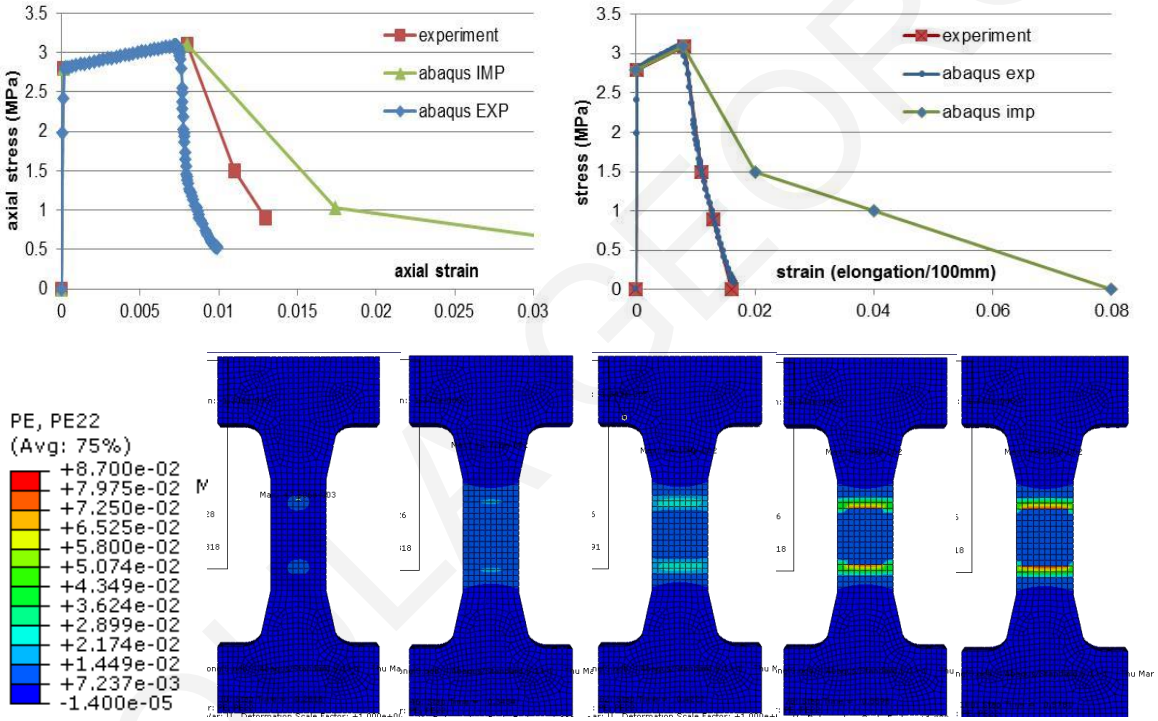

Figure 11.9: (a) and (b) Comparison of experimental tensile stress strain curve with FE modeling input and output data based on different fracture energies and (c) plastic strain evolution during uniaxial tension

The green line in the plot of Fig. 11.9 (b) represents the input properties of the SHFRCC in tension that should be imported in the FE model for the specific dimension of the mesh size (l_c=5 mm) in order for the output of the analysis to be consistent with the experimental results. Due to the geometry and axial similarity of the problem FE modeling presents two identical cracks as shown in Fig. 11.9 (c). The strain that was exported by FE and is expressed with the blue line of Fig 11.9 (b) is calculated as the one extracted by the experiment (red curve), as the elongation of the middle length that had constant cross section (25x50 mm) divided by its length of 100mm. In the case of FEM the elongation includes two similar cracks, while in the actual experiment it is most likely that strain will be concentrated at a single location. The actual crack elongation after the occurrence of strain softening was as measured in the experiment ε=0.016-0.008=0.008

(mm/mm) or w_{usoft}=0.008x100=0.8 mm. Ultimate strain of a single fiber at rupture was calculated as 1600/40000=0.04 (mm/mm). If the full length of the fiber was deformed with stress being constant to all the length of the fiber then deformation of the fiber would have been 0.04*12=0.48 mm. If compared to the actual crack elongation (0.8 mm) this estimated value could not explain the full crack width therefore leading to the conclusion that crack width comprises partial pull-out of the fibers and partial elongation of the fibers due to strain. The fracture energy G_f is the area under the stress-crack opening curve in the strain softening branch past the ultimate stress. For the SHFRCC it is calculated as G_f=1065 N/m a value much greater than the expected one for ordinary strength mortars and concretes which was found to be in the order of 50 N/m and 130 N/m respectively[49].

11.3 Split cylinder modeling

The split cylinder test is used as an indirect method to determine the tensile strength of concrete since direct tensile tests are difficult to be conducted on brittle materials. The split cylinder test will be used in this case to calibrate the material law in tension for the basic matrix of the composite (i.e., the cementitious material without fibers), so as to be used in FE analysis of more complex structures. The cylinder with a diameter of 100 mm and a height of 100 mm was simulated in full 3D using ABAQUS with a mesh size of 5 mm with 8-node structured elements, by seeding the parts every 5mm and then creating an automated mesh. The middle x-y and y-z planes were constrained as symmetry planes. The bottom edge was constrained in the y direction and displacement was imposed with a static loading case on the top edge nodes as seen in Fig. 11.10.

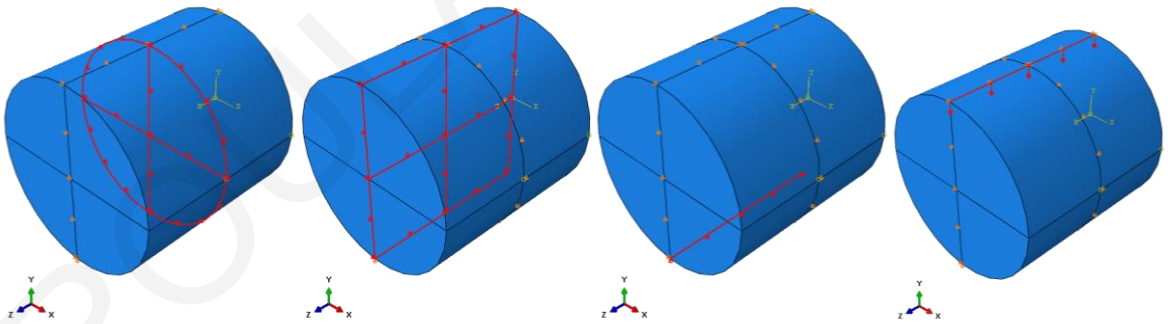

Figure 11.10: Modeling of the split cylinder test in ABAQUS constrains and load application by displacement

Figure 11.11 presents the results of a FE analysis of the split cylinder test of the fiberless cementitious material. The deformation that is depicted with a scale factor of 10 shows localization of cracking in the central y-z plane. The load-vertical deflection diagram shows three characteristic points: a) the initiation of yielding, b) maximum load and c) crack localization and postpeak loss of resistance.

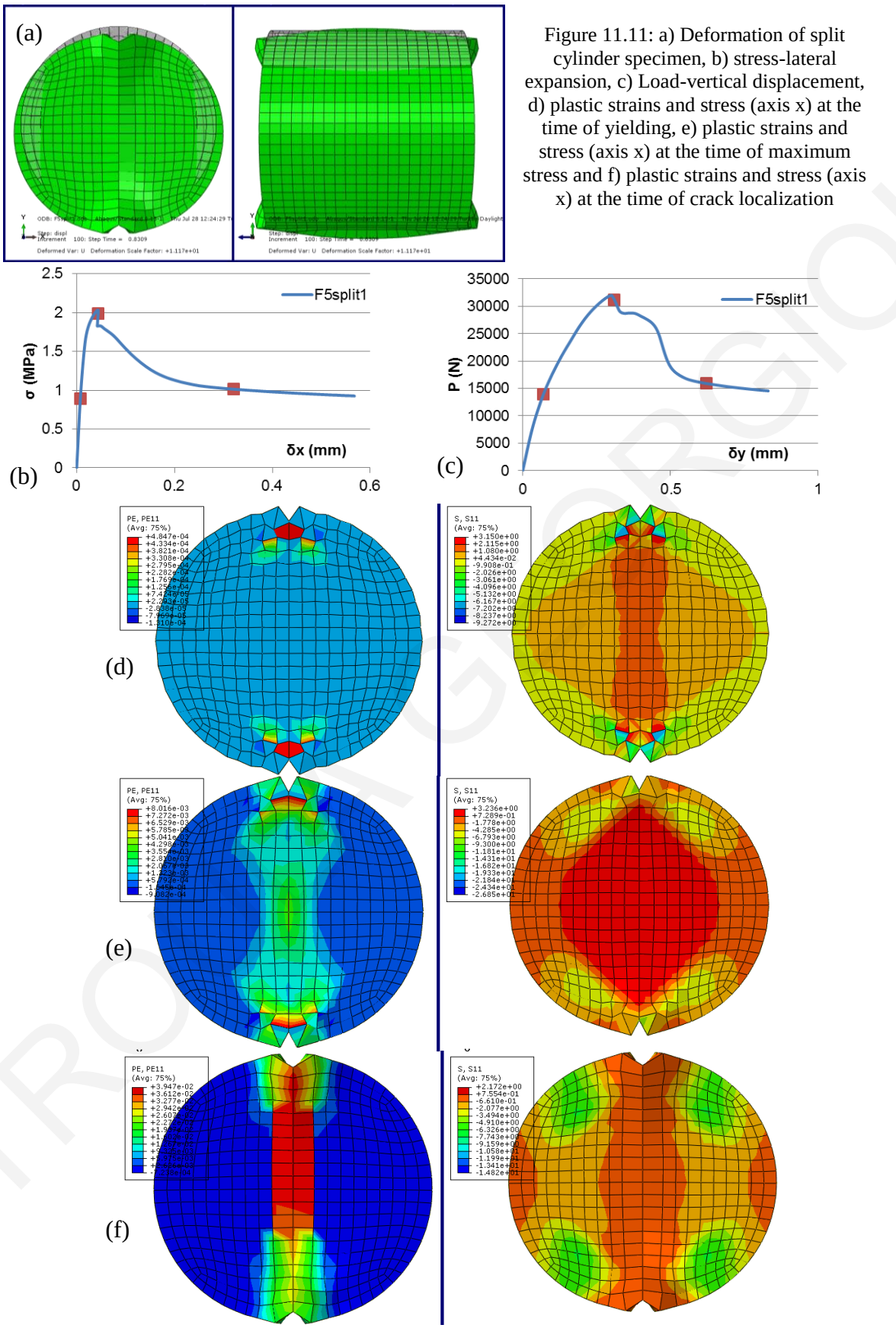

Figure 11.11: a) Deformation of split cylinder specimen, b) stress-lateral expansion, c) Load-vertical displacement, d) plastic strains and stress (axis x) at the time of yielding, e) plastic strains and stress (axis x) at the time of maximum stress and f) plastic strains and stress (axis x) at the time of crack localization

The same characteristic points are depicted in the stress-lateral expansion diagram. Stress in that case is calculated as $\sigma=2P/(\pi ld)$ which assumes a constant stress state over the entire critical plane that is under tension. The plastic strains and stresses in the x-direction are plotted in the same

figure for the three characteristic points in order to better analyze the stress distribution over the height of the crass section. At the time of yielding plastic strains initiate on the top and bottom edges of the cross-section while the rest of the specimen has not yet reached maximum stress. At peak load the full cross section has passed beyond the elastic range of the behavior of the material and plastic strains are evident over the full height, but with variable distribution over it. Maximum strains occur at the center of the critical cross section and near the edges. At this point tensile stresses are localized in the center of the specimen while part of the load is transferred with compressive stresses over a depth of 20 mm on each side of the specimen measured from the external perimeter. At the time of crack localization plastic strain continuous to grow only in the center of the specimen and load drops with extensive lateral expansion.

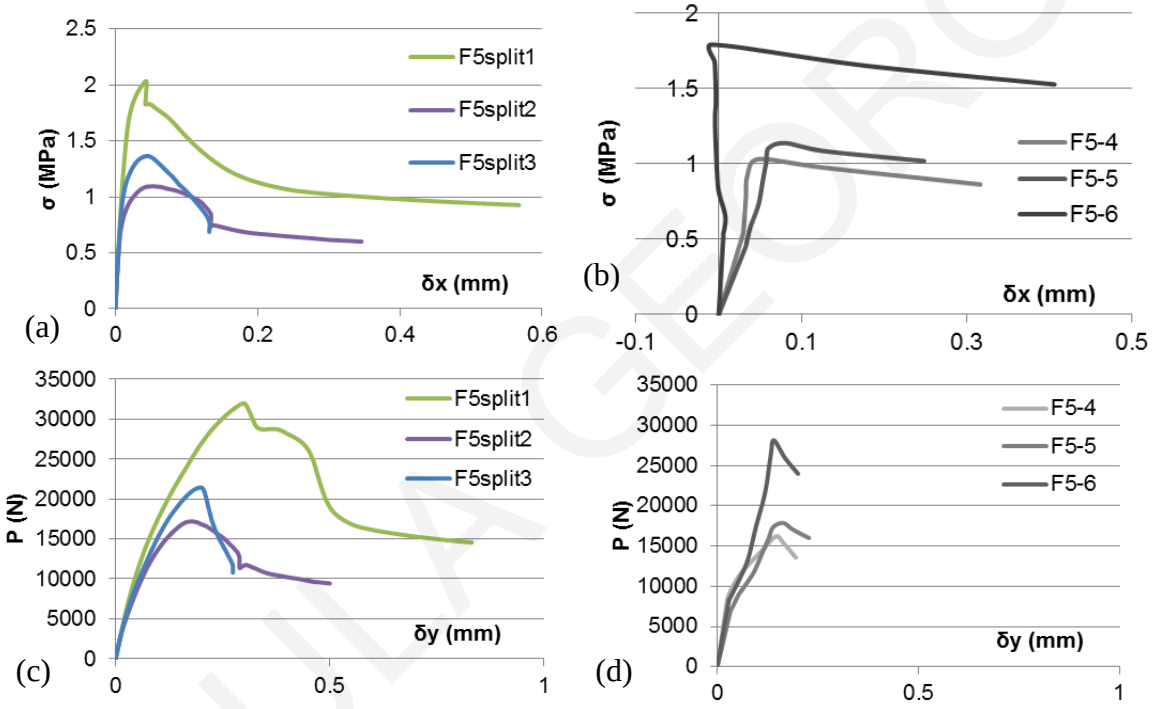

Figure 11.12: (a) Stress-strain curves from FEM with various tensile curves, (b) experimental results of the split test and (c) and (d) corresponding Load-deformation curves

The three possible tensile stress-strain curves shown in Fig. 11.11 are used to perform the FE analysis and the results are compared with the experimental results in Fig. 11.12. The curves on the left represent the FE analysis and the diagrams on the right the experimental results for three specimens from the same matrix without fibers (F5). The variation between the FE models is the tensile stress-strain law used to represent the fiberless cementitious matrix. The three possible laws that were used were extracted from the compressive strength, the splitting load and the flexural load – they correspond to the cases F5split1, F5split2 and F5split3 respectively. The tensile stress capacity resulting from the F5split1 material law (deducting tensile strength from the compressive strength) gives much higher values of load capacity whereas the other two models are closer to the experimental results. In all cases though the softening branch from the FEA is much less steep than the one recorded from the experiment where brittle rupture was witnessed. This suggests that the

fracture energy is used to determine the softening behavior, as per the Model Code provisions, is much less for the type of matrix used in this study – most likely due to the absence of any aggregates.

Table 11.6: Characteristic values obtained from FE modelling of the split test

	$A_{sp}=\sigma_{max}/f_t$	f_t	σ_{max} *(from FE analysis)*
F5split1	0.558	3.646	2.033
F5split2	0.812	1.347	1.094
F5split3	0.682	2.002	1.364

Finally the influence of the use of damage properties in tension is shown in Fig. 11.13. The use of damage in the CDP model for the FEA increases the maximum load attained and the slope of the descending branch of the stress-lateral deformation, leading to a quicker failure of the specimen.

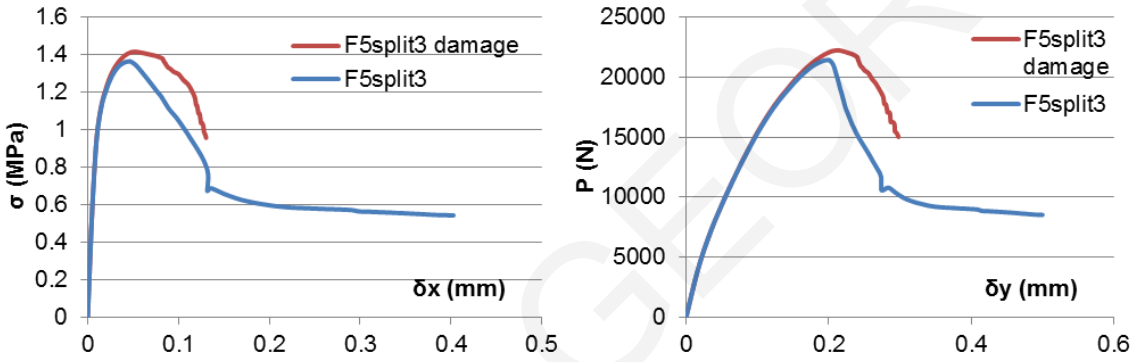

Figure 11.13: Stress-strain and load deformation curves from FEM with damage used in the material model

11.4 Modeling of flexural tests without reinforcement

11.4.1 Three point bending test

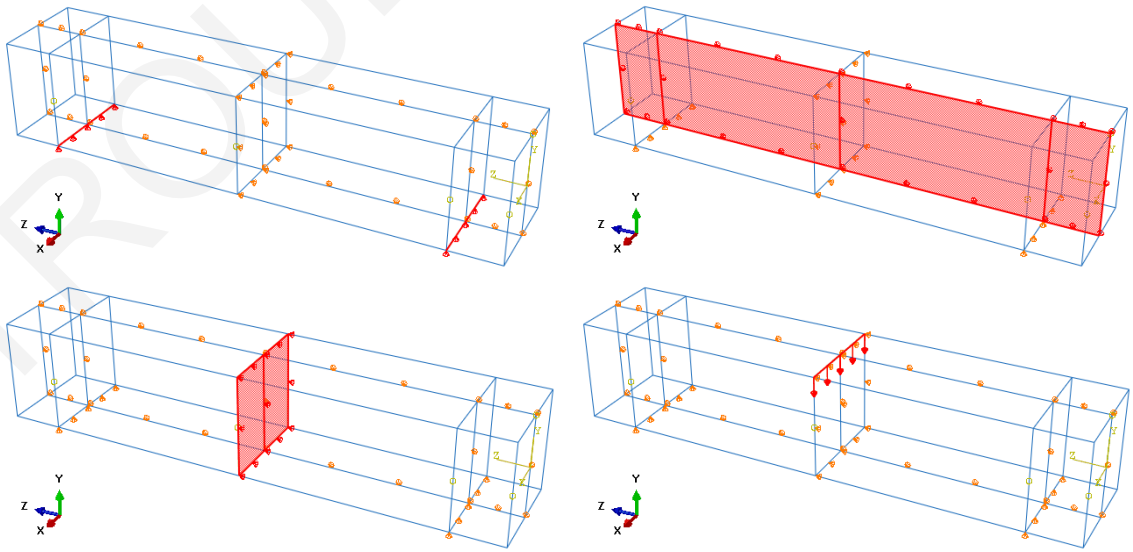

Figure 11.14: Modeling and constraints of the three point bending test

The three point bending test was performed in ABAQUS simulating the full beam with dimensions 100x100x500 mm. The supports that had a distance of 400 mm between them were

modeled by restricting vertical translation of the corresponding beam nodes. Two planes of symmetry were used, one in the middle x-y plane and on in the middle y-z plane at which planes displacement of all nodes in the z and x direction respectively were constrained as shown in Fig. 11.14. Load was applied as displacement with a general static procedure.

The material properties used for the three point bending simulation in ABAQUS for one of the composites without fibers (F5) are those resulting from the four point bending according to the Model Code [49] provisions. The Load-Deflection curve that results from this analysis gives the diagram depicted in Fig. 11.15. Peak Load value resulting from the analysis is 6 kN. The same diagrams from the experimental tests are also shown in the same Figure 11.15. The experimental values vary between 7 and 8.5 kN. There is a difference of 25% with the result from the analysis being lower than the experimental value. This difference is familiar when modeling forces that are experimentally determined from the three and four point bending setups. The experimental setup of the three point bending localizes peak stress in a single cross section that is under the load application point. This means that if there are cross-sections of the member that have lower resistance those will not appear in the analysis. On the contrary, the testing setup of the four point bending has steady moments and therefore stresses in a wider range of the tested specimen, promoting failure in the cross section with the least resistance.

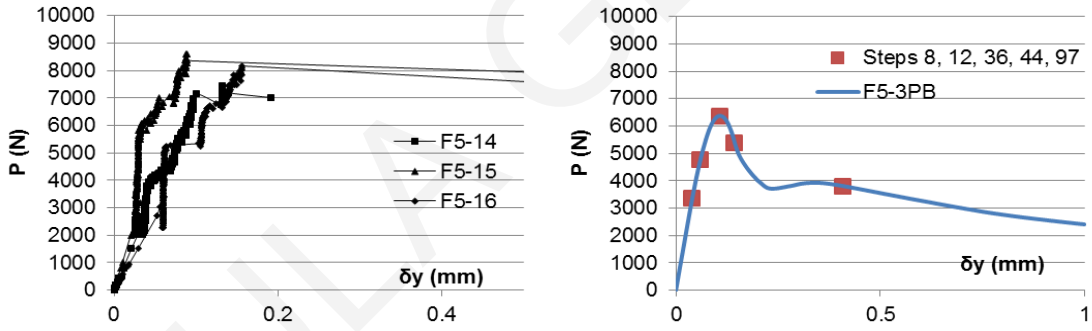

Figure 11.15: Load-deflection diagrams from 3-point bending tests on mix F5 from experiments (left) and ABAQUS FEM (right)

Therefore the tensile stress capacity computed from a four point bending test is always lower from the one determined by the three point bending test. Therefore, when the tensile strength determined by a four point bending test is used in the FEA for a three point bending test the results will be lower than those obtained from the actual test. The descending branch of the experimental test as shown in the diagram of Fig. 11.15 was not captured by the measuring device used in the experiment due to the sudden failure while the softening part of the stress-strain curve in tension that was imported in the FEA gave a full load-deflection curve that does not actually correspond to the experimental results and cannot be verified by them.

On the Load-displacement diagram of Fig. 11.15 five characteristic points are marked with the step of the analysis to which they correspond. The plastic strains (PE33) and stresses (S33) of the whole model for each of the steps are shown in Fig. 11.16. The first point marks the yielding of the extreme layer under tension (step 8). The second point (step 12) with a load between yielding and

ultimate corresponds to the attainment of the maximum tensile stress in the extreme layer under tension. After this point, load capacity continues to grow as plastic strain (crack length) penetrates up to one third of the height of the beam where peak load is attained (step 36). After that, load capacity decreases rapidly and strain is fully localized at the crack location.

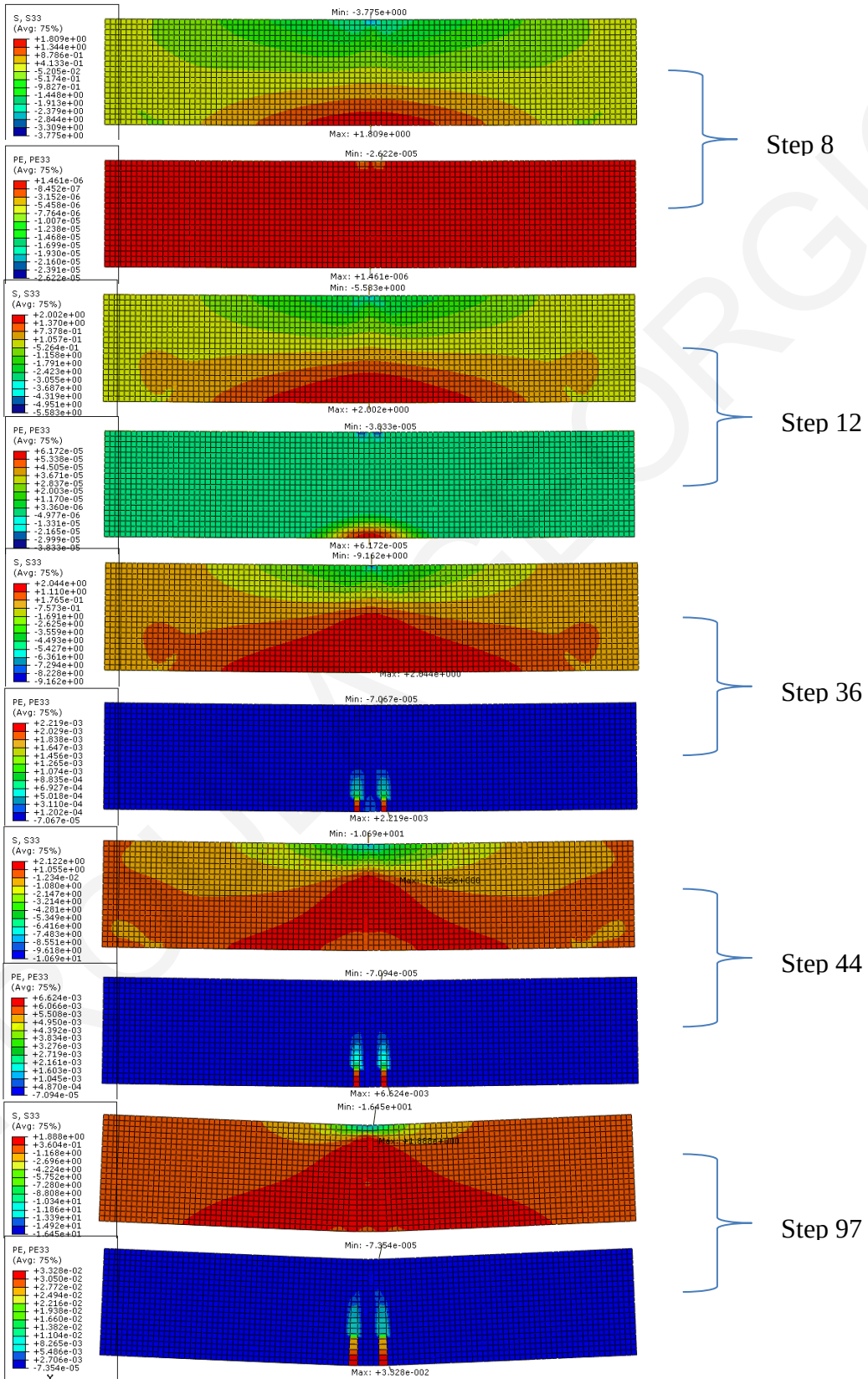

Figure 11.16: Plastic strains (PE33) and stresses (S33) of the 3-point model of mix F5 for various steps

11.4.2 Four point bending test

Modeling of the four point bending test for the composite without fibers was performed in ABAQUS. The full specimen was simulated. At the supports only the vertical translation of the nodes was restricted, while the middle planes of the specimen were used as symmetry axes, restricting z-translation of all the nodes in the middle x-y plane and x-translation of all the nodes of the y-z plane. Imposed translation in the y direction was performed as the static load case on the nodes under the load application points as per the experimental setup (Fig. 11.17).

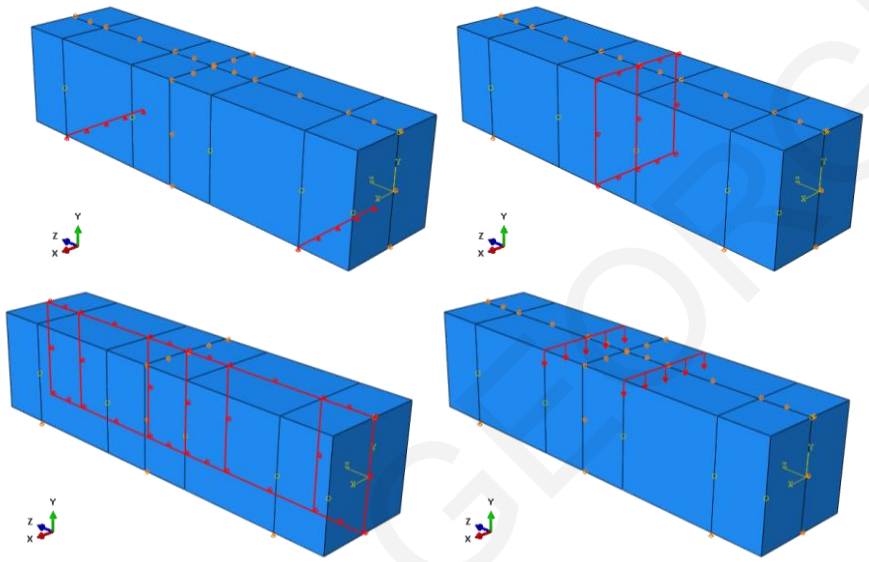

Figure 11.17: Constrains and vertical imposed displacement for the 4-point bending test simulation in ABAQUS

11.4.2.1 Four point bending of the fiberless composite

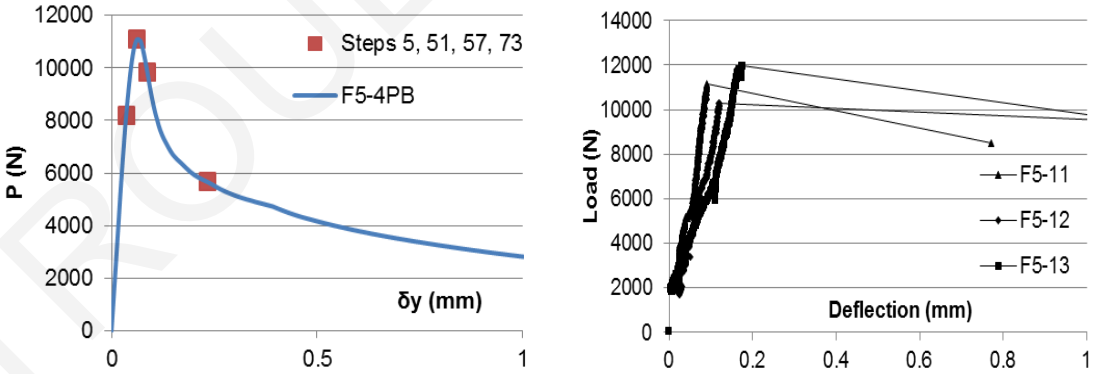

Figure 11.18: Load-LPD of 4-point bending of mix F5 from FEM (left) and experiment (right)

The analysis performed in ABAQUS with the composite stress-strain law (same with case F5split3) gave the Load-LPD (Load point deflection) shown in Fig. 11.18. The maximum load and vertical displacement at maximum load are in good agreement with the experimental results shown in the second diagram of the same figure. The descending branch of the Load-LPD curve cannot be compared with the experimental results, since during the experiment, after load reached its ultimate

value, failure of the specimens was very brittle and the equipment used did not have the ability to record at the speed needed the actual load degradation with time.

Some characteristic points are marked on the Load-LPD as step points. The plastic strains (PE) and stresses (S) in the direction parallel to the z-axis of the beam for these characteristic points are reported in Fig. 11.19. At Step 5 which is the first point depicted the extreme layer under tension has just passed the yield point of the material under tension. The second characteristic point is Step 51 where the extreme layer under tension has reached the maximum tensile stress values and strain localization has initiated. This corresponds to the maximum attained load in the Load-LPD curve. After the strain is localized in the two sections in the beam area inside the load application points the third set of figures depict Step 51 at which the stress in the extreme layer under tension has reached the point of inflection of the descending branch of the tensile stress-strain curve. Finally Step 73 marks the initiation of zero tensile capacity of the extreme layer under tension.

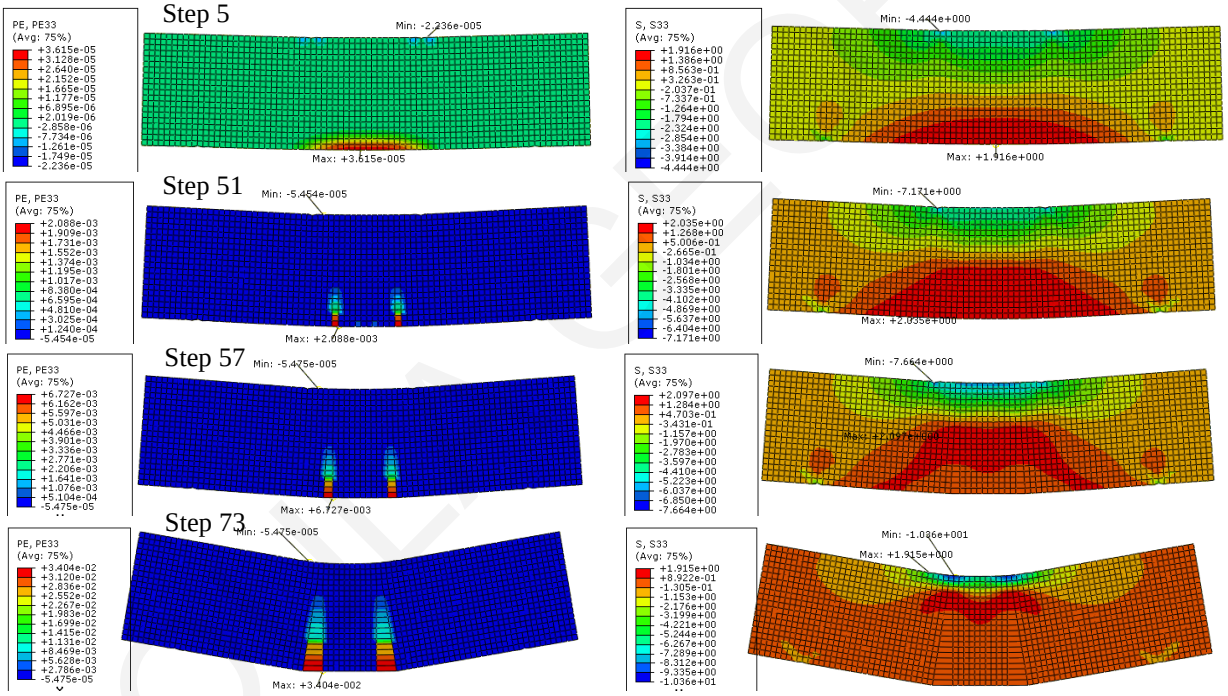

Figure 11.19: Plastic strains (PE) and stresses (S) in the direction parallel to the z-axis of the beam for various steps from FEM

11.4.2.2 Four point bending of the SHFRCC

Additionally FEM was performed for the beams with the SHFRCC that were tested under 4-point loading. In order to verify whether the uniaxial material tests truly represent the material behavior in a structural member, the different *a/d* ratio beams were simulated with FE and analyzed. The stress-strain curves extracted from the uniaxial tension and compression tests were imported as the material parameters in the FE program. Exploring the underlying relation between the uniaxial test results and the performance of structural elements is necessary for further development of standards for practical use. Previous research (experimental and numerical investigation) comparing the experimental results by Ohno (test beams with *a/d*=1.5) with the

results of FE analysis using a constitutive model proposed by Kabele[173] showed that the input tensile stress-strain relation gave unrealistic results, with greater stiffness, strength and ductility. Only when the input curve was the lower bound fit of the experimental results and the strain capacity was reduced there could a better match be achieved with the experimental results.

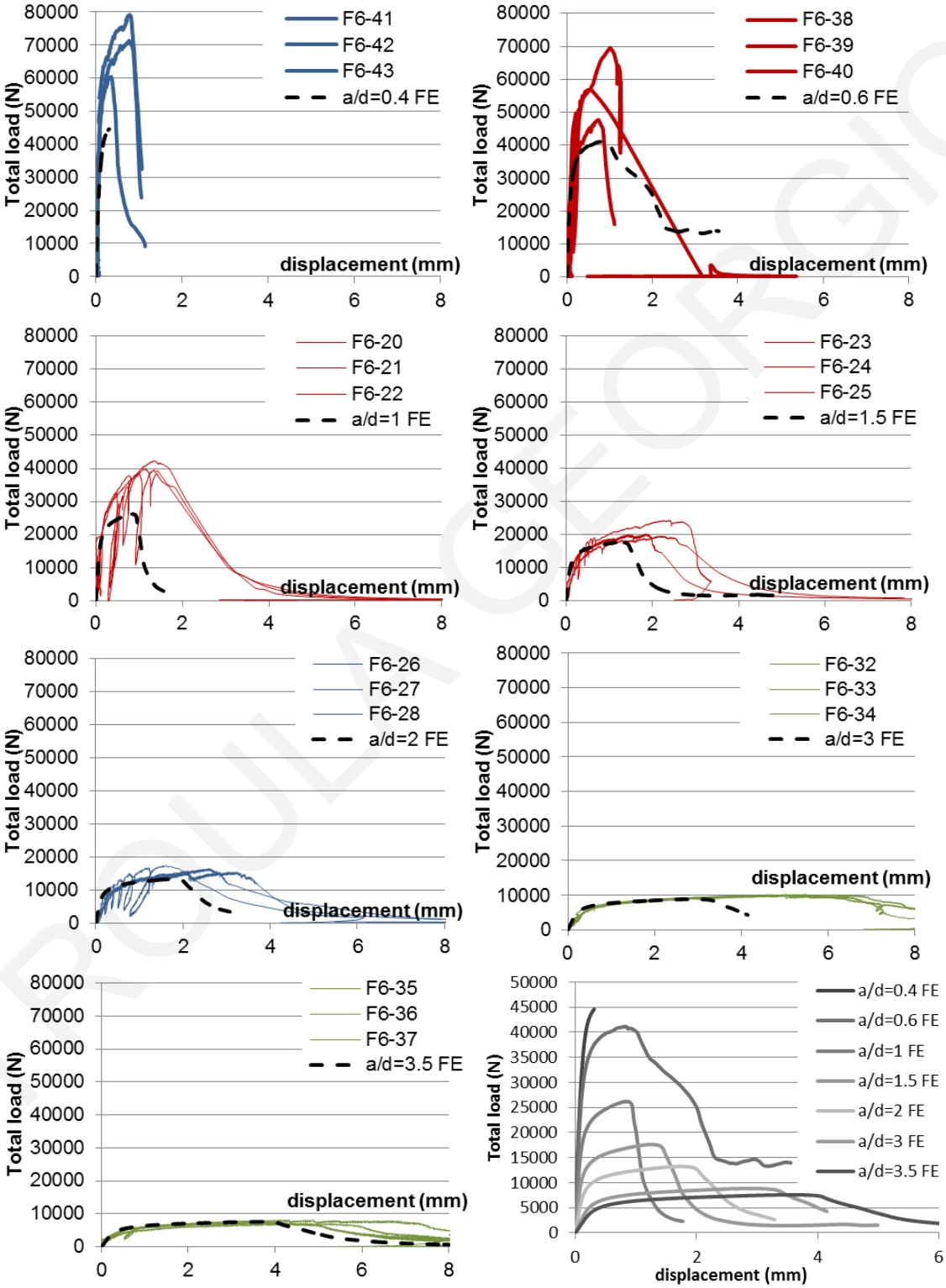

Figure 11.20: Experimental results vs FE analysis for a/d=0.4,0.6,1,1.5,2,3,3.5

The use of the Concrete Damage Plasticity model (ABAQUS [167]) gives the Load-LPD diagrams depicted in Fig. 11.20 for the various shear span ratio beams. Additionally for each shear

span ratio the results are compared to those obtained from the experiments. The results of FE modeling consistently underestimate the members' properties measured in the tests. More specifically the strength and stiffness in the hardening part of the behavior of the smaller span members that have shear ratios a/d<1, is found to be almost half in the analysis as compared to the corresponding experimental value. The deformation capacity was also underestimated, but this increases as the shear span ratio increases, and this could be attributed to the pined end condition which, according with Kanakubo [80], may reduce the obtained tensile strength and strain due to cracking producing secondary moments.

The tests demonstrated a high influence of the shear span ratio on the performance of the beams. The small shear span ratio beams with a/d<1 developed both flexural and shear cracks with the final failure mechanism to be combined shear/flexure mode. The capacity of the beams in terms of Moment suggest that the failure mechanism of the short beams with a/d<1 is enhanced due to the arching effect of the strut and tie mechanisms developed in the shear span ratio and implies that the load-deflection resistance curve of the beam does not characterize the flexural behavior of the composite, but rather the combined shear/flexure failure of the shear span. Further experimental investigation of the shear span ratio should be performed prior to the introduction of guidelines in the standards, which up to now recommend using beams with a/d=1, i.e. JCI [53], for determination of the tensile properties of the SHFRCC material through inverse analysis.

11.5 Modeling of beams with longitudinal reinforcement

Some of the beam specimens with steel reinforcement where chosen to be modelled in ABAQUS in order to verify that the parameters of the SHFRCC used in the CDP model for FEM can produce results that correspond to the actual experimental values. Three different types of beams were chosen from the various types of beams tested, which were made from the same mix design (F7) but with different shear span ratios. This was done since it was seen from the analysis of the beams without reinforcement that the results from FEM do not match the experimental curve in the lower shear span ratios. The details of the beams that were simulated in ABAQUS are listed in Table 11.7. All beams had the same cross-sectional area of 100x100 mm, the same longitudinal reinforcement but three different shear span ratios. The mix and steel reinforcement characteristics that were imported for the material parameters in ABAQUS are given in Table 11.3 and Table 4.5 respectively.

Table 11.7: Beam denomination, cementitious composite, shear span ratio and reinforcement

Denom.	**Mix. Design.**	**a/h**	**Bottom Reinf.**	**Top Reinf.**	**Stirrups**	**ρ_s**	**ρ_s'**	**ρ_w**
F7-S8/S9/S10	F7	3.5	2Φ8	-	-	0.0132	-	-
F7-S14/S15/S16	F7	2	2Φ8	-	-	0.0132	-	-
F7-S20/S21/S22	F7	1	2Φ8	-	-	0.0132	-	-

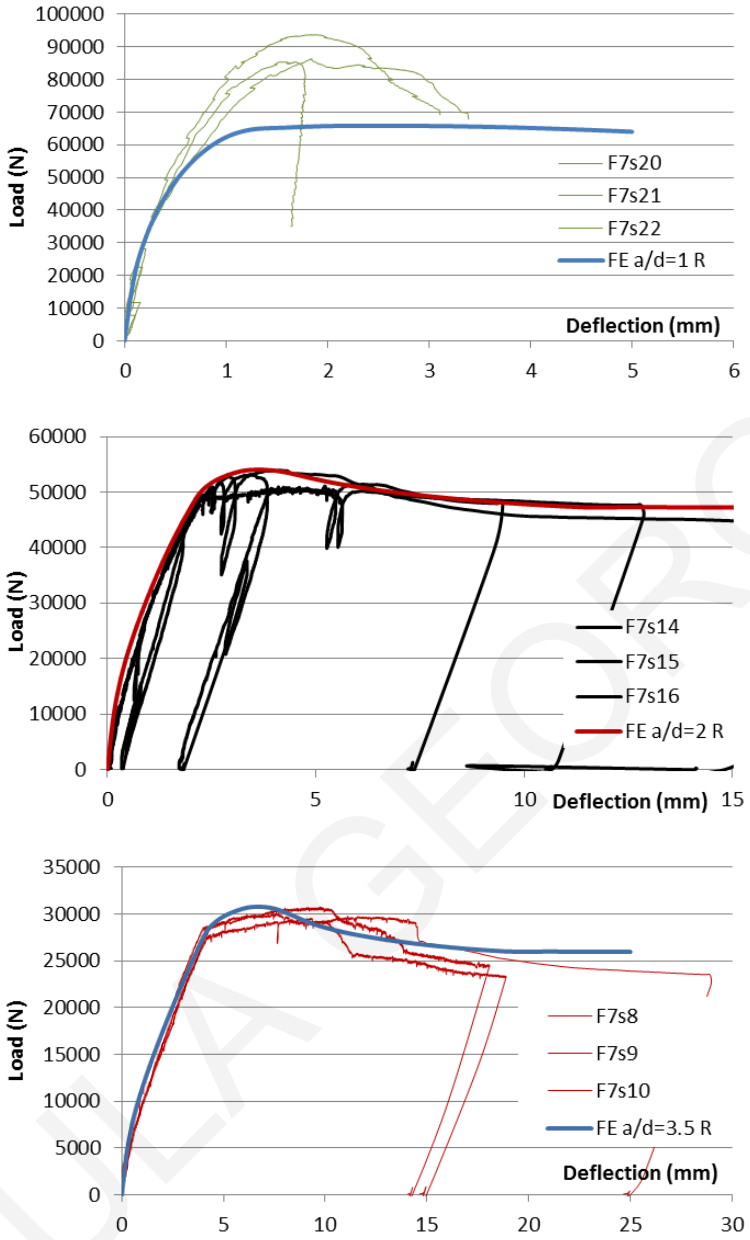

Figure 11.21: Experimental results vs FE analysis for beams with a/d=1, 2, 3.5 and steel reinforcement

The Load-LPD curves obtained by the FEM analysis are compared with the experimental results in Figure 11.21. It is evident that the initial stiffness of the model captures with great accuracy the actual stiffness of the R/SHFRCC beams for all the cases of the shear span ratios up to the yielding of the reinforcement. For the longer shear span ratios of 2 and 3.5, the post-yielding branch (hardening) and the softening branches are also in good agreement with the experimental results both in terms of flexural capacity and in terms of deflection. For the shortest shear span ratio a significant discrepancy between the failure modes is depicted. The experiments showed a brittle shear type of failure of the beams at a Load in the order of 85-90 kN, while the FEM showed a flexural behavior with yielding in the order of 65 kN and a great plastic branch after yielding. Further experimental and analytical investigations are needed in the small range of shear ratios to explore the source of the brittleness.

11.6 Modeling of the Push-off tests

The lack of a mechanical model to estimate the push-off behavior of cementitious composites and the interaction with steel reinforcement at sliding failure planes may be resolved with the use of finite element modeling and analysis. The attempt here is to use the concrete damage plasticity model provided in ABAQUS in order to approach the experimental results. Without using specific shear crack models with multiple varying parameters, a plasticity model that takes into consideration the compressive and tensile behavior of a composite member was used in order to model in a first attempt the HVFA mixes members. The advantage of this model is the ability to import the law in tension which is an intrinsic property of any fiber-reinforced composite.

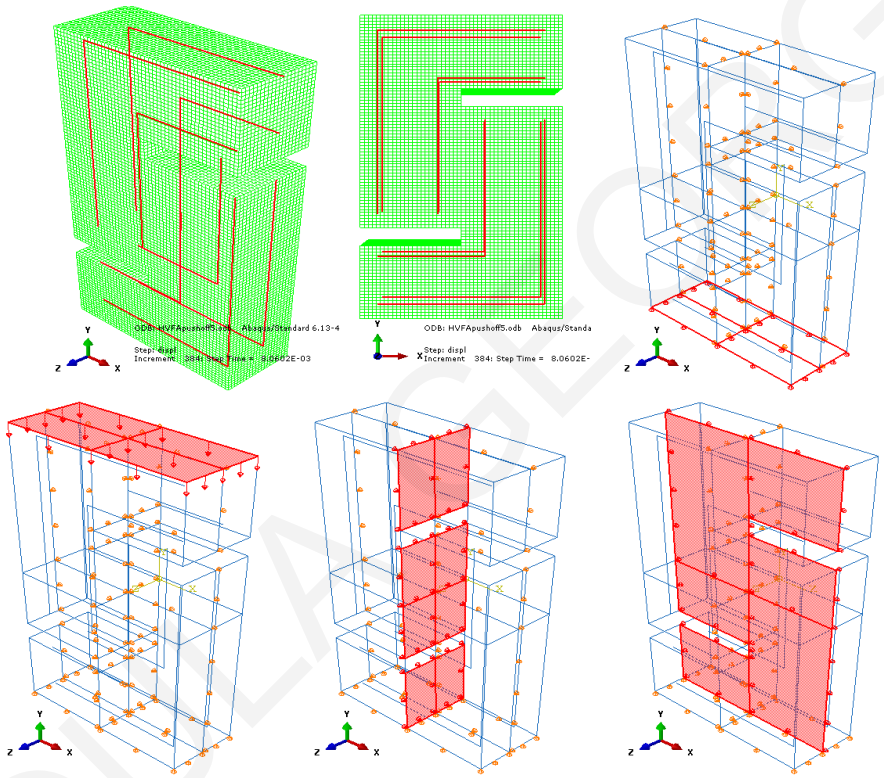

Figure 11.22: Modeling of the Push-off specimens without stirrups in ABAQUS

The push-off specimens without stirrups crossing the critical cross section were modeled in ABAQUS as shown in Fig. 11.22. Constrains were applied in the y-displacement at the bottom of the specimen, in the x-displacement at the middle y-z plane and in the z-displacement at the middle y-x plane, the intersection of which defined the symmetry axis of the specimen. Displacement was applied at the top of the specimen with a static incremental procedure. The steel reinforcement that was used to control cracking on the specimen outside the critical shear cross-section was embedded inside the composite specimen and was simulated as a truss element having as cross-section that of the bars that were used in the experimental program.

The analysis of a composite without fibers and no stirrups crossing the critical shear plane was performed first with the composite being simulated with the Concrete Damage Plasticity model. The material's compressive behavior was according to the uniaxial compressive tests. For the law of the material under tension any of the three approaches presented in Par. 11.2 if adopted give

unrealistic results for the push-off specimen as compared to the actual test results. The results with these laws give Total Load values in the order of 120 kN which is more than double the actual Load that was applied in the experiments. This great variability is attributed to the fracture energy that is used in Par. 11.2 to calculate the stress and strain values after localization of cracking of the composites. The equation that is given by the MC2010 is calibrated with normal concrete that contains higher water/cement ratios, aggregates and contains no fly ash. Therefore in order to approach the experimental results with the FE analysis various stress-strain values of the descending branch were adopted and the results are compared in Fig. 11.23. As shown in Fig. 11.23 the fracture energy affects greatly the maximum Load obtained from the analysis. After the attainment of the peak tensile stress at the critical shear cross section, crack localization occurs and the Load-crack opening curve displays a notional yield point. Beyond that the load increases further to ultimate failure. If the fracture energy used in the analysis is very large (as compared to the actual), then load values twice as high as the yield load may be attained. The final fracture energy that approached more accurately the experimental results was the T5 stress-strain law, with a fracture energy 20 times smaller than that of T1 (Fig. 11.23(b)).

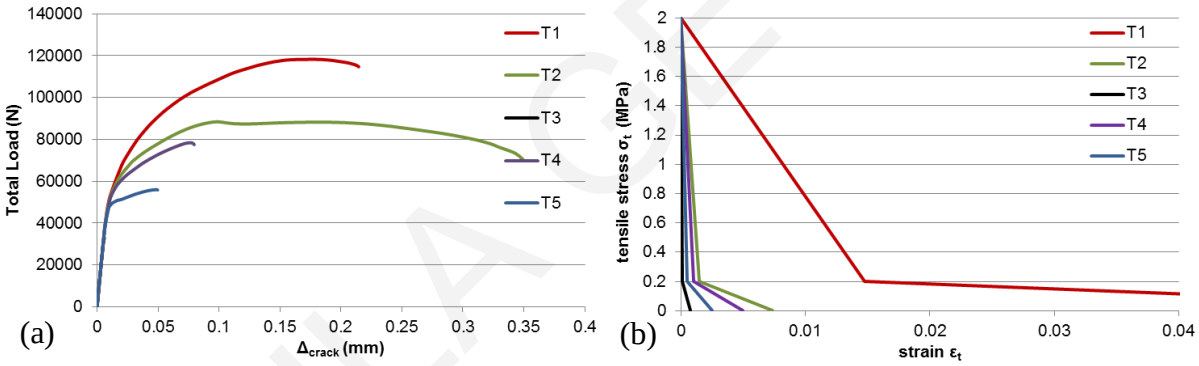

Figure 11.23: Push-off Load-crack opening diagrams for various stress-strain curves used for the tensile law of the composite without fibers and the respective tensile stress-strain curves.

For the cases were stirrups (6Φ6) were used in the specimens those were simulated with truss elements with elastic-plastic behavior and were embedded in the cementitious composite. The analysis was suddenly aborted when the composite was entering the softening branch of its behavior with the algorithms unable to reach convergence therefore the viscosity parameter was chosen to be altered so that the analysis could be completed. The viscosity parameter as stated previously must have values lower than the time increment which in this case was 0.01. Trials between models with various viscosity parameters were performed in order to see the variation in the resulting load of the analysis. As shown in Fig. 11.24 if a viscosity parameter of 0.001 is used, maximum load resulting from the analysis is in the order of 350 kN, while in the case where the viscosity is 10^{-5} load is only 125 kN. The slope of the ascending branch of the Load-crack opening diagram of the model with the smallest viscosity is the same with that of the zero viscosity parameter diagram, leading to the conclusion that the selected range of value of viscosity does not

influence the results from the analysis. The FE model S3 with a viscosity of 10^{-4} approaches best the experimental results, with a peak Load in the order of 150 kN as shown in Fig. 11.24.

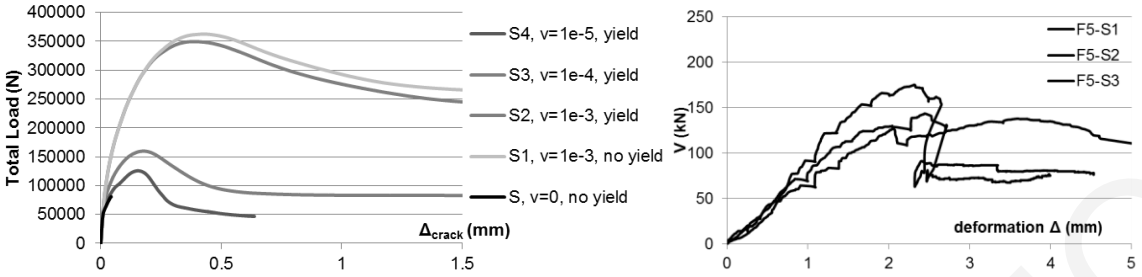

Figure 11.24: FE analysis of Push-off specimens of a composite without fibers (F5) with 6Φ6 crossing the critical shear plane (left) and experimental results (right).

11.7 Conclusions

In this Chapter, the experimentally determined properties in uniaxial tension and compression of two mix designs with high volume cement replacement with fly ash, with and without the use of coated fibers, were used to calibrate analytical models of the behavior of those composites in tension, compression, split, flexure and shear. Results obtained from FE modeling analysis were compared with the experimental load-deflection curves. Tensile, flexural and compressive strength of a material as proposed by Model Code [49] are connected with equations calibrated with normal concrete. It was shown that these calibrated empirical expressions do not apply in the case of mixes with high amounts of FA, no coarse aggregates and low water content with or without fibers. As tensile strength is a very important analysis parameter, procedures for its proper determination must be incorporated into Modern Codes for these types of materials. Results obtained from direct tensile tests may underestimate the resistance and strain capacity of the composite when this is placed in a 3-D state of stress. Flaws and size effects (in terms of possible voids during compaction for the estimation of stress from the specimens' area, and the gauge length used in estimation of average strain from crack widths) may result in lower values than what may be supported in the presence of a more complex stress state.

In order to verify whether the uniaxial material tests truly represent the material behavior in a structural member, the different a/d-ratio beams were simulated with FE and analyzed. Indeed, understanding the underlying relation between the uniaxial test results and the performance of structural elements is necessary for further development of standards for practical use. In this case, by using the Concrete Damage Plasticity model, the results of FE modeling consistently underestimate the members' properties measured in the tests. More specifically the strength and stiffness in the hardening part of the behavior of the smaller span members that have shear ratios of a/d<1, is found almost half in the analysis as compared to the corresponding experimental value. The deformation capacity was also underestimated, but this increases as the shear span ratio increases, and this could be attributed to the pined end condition which may reduce the obtained tensile strength and strain due to cracking, thereby producing secondary moments. The flexural strength of the beams suggest that the failure mechanism of the short beams with a/d<1 is enhanced

due to the arching effect of the strut and tie mechanisms developed in the shear span ratio and implies that the load-deflection resistance curve of the beam does not characterize the flexural behavior of the composite, but rather the combined shear/flexure failure of the shear span. Further experimental investigation of the shear span ratio should be performed prior to the introduction of guidelines in the standards, which up to now recommend using beams with a/d=1, i.e. JCI [53], for determination of the tensile properties of the SHFRCC material through inverse analysis.

Conclusions

Sustainability in construction translates into a design framework that combines criteria and methods in structural design, intended to increase the life time of structures, and in material design, intended to reduce the exploitation of resources and to simultaneously assist in achieving the previous goal. Shorter life time of structures is more costly and resource intensive also if one accounts for the greater maintenance costs required. In this Thesis it was shown that the combined effect of the use of high volume fly ash composites and short discontinuous fibers results in a class of materials that exhibit enormous ductility in tension, compression, shear and flexure as compared to normal concrete. This greener material that uses less resources by the exploitation of the great mass of waste materials such as fly ash has better packing than normal concrete at the material microstructure, and therefore can improve the durability of structures. It is also very ductile and resilient to tension; this enhances its resistance to extreme events that would place excessively large deformation demands on the structure, well beyond the levels implied by the design intensities of the most extreme accidental loads considered by current codes.

The aim of the Thesis was to research and characterize the mechanical performance of these cementitious composites when used as structural materials, with special emphasis on their strain hardening properties, the improved sustainability attributes, the high fracture toughness and the commensurately reduced abuse of resources. An objective of the research was to contribute, through better understanding and qualification of structural design rules using these materials in lieu of concrete, their adoption by new Codes, and to enable their spread and development and recognition of the benefits they bring in the field of construction, widening the area of capabilities for innovative cement-based products. It is also expected that an advanced understanding of the material behavior will also enable the development of effective rehabilitation solutions to durability problems encountered in existing structures due to adverse environmental conditions.

In the Preliminary study that was performed for this Thesis a number of different coating agents and material variations were examined in order to experimentally achieve a fiber reinforced cementitious composite with strain hardening properties in tension. Additionally an innovative dog-bone shaped specimen and testing arrangement was designed and constructed for the purposes of direct uniaxial tensile tests required to be performed for material characterization. The mix that exhibited the best performance had coated 12 mm PVA fibers. It was used in an extensive experimental research in order to characterize the material under a variety of stress states. The mechanical performance of SHFRCC in combination with steel reinforcement was studied in order to evaluate its structural performance. For this extensive experimental program more than 2.5 tn of materials were used, that were mixed in fourteen different batches.

A large number of tests (approximately 300) were conducted in the main phase of the research involving multiple identical specimens in most cases so as to establish repeatability and experimental scatter; these included uniaxial tension, uniaxial compression, three point bending,

four point bending on small scale beams with and without steel reinforcement with various shear span ratios, push-off tests, pull-out tests and two larger scale members under reversed cyclic loading. The test results were then used in combination in order to investigate the performance of the SHFRCC under various loading states and understand the underlying mechanics of its performance. From the tests it was seen that in cases where cracking behavior was marked by formation of a large network of fine cracks, a superior overall material toughness was obtained with the SHFRCC material.

Some of the most important findings and novel contributions of this Thesis are as follows:

-A customised dog-bone specimen was developed for the needs of the experimental program, designed to minimize end effects by the introduction of pertinent spherical hinge gripping devices which were fabricated for this purpose.

-Several analytical tools were developed for the purpose of material property characterization through inverse analysis, in response to the familiar use of three-point and four-point bending prisms for testing cementitious materials in tension by the majority of practitioners.

-Contrary to common concrete the dilative behavior of the SHFRCC material is rather controlled resembling the behavior of confined concrete; data were obtained and calibrated in order to facilitate nonlinear modeling of the structural response of SHFRCC components in advanced simulation platforms.

-The effective confining action of the PVA coated fibers was quantified through comparison of compression tests conducted on SHFRCC specimens and on confined HVFA specimens. This pressure was estimated in the range of 7.2 MPa and was directly related to the splitting strength of the composite.

-A strong flexural moment-shear force interaction diagram was observed through the experiments on beam models. It was shown that the relevance and accuracy of tensile stress – strain relationships obtained through inverse analysis from short span specimens as recommended by JCI leads to erroneous estimates exactly because for the recommended aspect ratio of the shear span of the JCI specimen the interaction is most significant.

-Investigation of the behavior of R/SHFRCC illustrated the improved ductility of beams due to the contribution of fibers and these effects were quantified in cross-sectional analysis at the ultimate limit state considering a depth of crack penetration in the tensile zone of the member propagating inwards from the extreme tension face. Equations for the determination of the balance reinforcement ratio and the full Moment capacity of R/SHCC in cases of flexural elements containing reinforcement ratios below the balanced ratio were extracted and some rules that should be used for the design of R/SHFRCC were indicated such as:

- The balanced reinforcement ratio for R/SHFRCC beams is lower than that for normal concrete and can be calculated based on the beam geometry and materials' characteristics
- It is recommended that flexural moments resulting from ultimate limit load combinations (1.35G+1.5Q) should be lower than the residual moment of the member (M_u)

- Shear strength design of a member should be performed based on the flexural capacity of the member after yielding using a uniform tensile stress block in the tension zone equal to the maximum post-cracking strength of the SHCC matrix $f_t^{ave}=f_{tmax}$

-For the shear capacity the experimental results were compared with the values calculated from the alternative models that were proposed in this Thesis which were: (a) the strut and tie model analysis (considering the anchorage capacity of the horizontal reinforcement) and (b) the shear strength associated with material diagonal tension failure according with the Engineering Beam Theory and related to the bond properties of the longitudinal bars. The Strut and Tie model produced a good approximation of the failure load of reinforced SHFRCC elements with a/h ratios ≤2, considering both specimens with and without steel reinforcement, regardless of the failure mode that was observed and prevailed for its relevance with the experimental results in interpreting the behavior.

-Based on the pull-out tests it was concluded that the confinement effect exerted by the fibers suppresses the low strength mode of cover splitting even for covers as low as 10 mm. The experiments showed that for the smaller cover thickness ($c=1.2d_b$) with values ranging from 5-8 MPa, irrespective of the bond length, the peak value of bond stress occurred at a slip s_y of 1.2 mm, while for the greater covers $c=2.8d_b$ and $c=3.2d_b$ the associated slip values were 2.8 mm and 3.2 mm respectively, and bond strength reached values as high as 10 MPa. The splitting strength was described with a simple equation that gave good estimations of the experimental specimens and a basis for the calibration of bond-slip relations for further use of reinforced SHFRCC members in the construction industry was laid; the large scale beams under reversed cyclic loading hold promise for the possible reduction of shear reinforcement without compromise in strength and for improved ductility, both of which are greatly required for structures in areas with increased seismic activity.

-Advanced nonlinear Finite Element modeling was performed on a number of specimens from the experimental program. The Concrete Damage Plasticity model was calibrated based on uniaxial tension and compression tests and it was then used for the simulation of plain SHFRCC beams under flexure and steel reinforced SHFRCC beams. The model was shown to successfully capture modes of failure related to flexure but it could not reproduce the compression/shear failures of the shorter beams.

These findings suggest that a whole new generation of Cement based materials is possible, where tensile strength and strain capacities are so high that they provide a totally different context for formulation of concrete mechanics and consequent reinforcement detailing. Additionally the improved performance can lead to more slender member dimensions, reduced amounts of steel reinforcement particularly for shear and confinement, easing construction effort and energy requirements, all of which will be the subject of future research.

Future Research Plans

A next step in the direction of promoting and advancing the research of the present study is to prequalify through further testing and corroboration studies of the procedures developed for characterization of the SHFRCC materials in tension and the design rules derived for shear, anchorage, flexure and deformation capacity. In this regard the nonlinear Finite element code will prove invaluable as it is intended to serve as a vehicle for assessing the sensitivities of the design methods and performance criteria developed. The longer ranging research plans include the following:

1) The present study has opened up the prospects into the field of innovative cementitious composites which can revolutionize the construction industry, particularly in the areas of precast construction, retrofitting, as well as in the areas of high quality blocks for advanced masonry construction.

2) Further understanding of scale effects is needed for structural engineering applications: Although ample evidence exists that with the elimination of coarse aggregate and the introduction of dispersed fiber reinforcement scale effects are suppressed, yet this need be persistently pursued through pertinent experimental campaigns. The panel tester developed for shear tests of large shell and plate elements in shear will be used in this endeavor in order to produce the necessary experimental database for modelling shear in SHFRCC.

3) Strengthening of elements with the novel cementitious material studied in this thesis is a plausible application in the form of layers, patch repairs or jackets. Strategies by which to use the SHFRCC in various retrofit applications and case studies would need to be carried out.

4) The self consolidating properties and the pumpability of the material need to be further promoted by further improvement of surfactants and the possible use of hybrid fiber mixes.

5) A thorough investigation of the behavior of various types of structural components under reversed cyclic loading will further enhance confidence in the use in seismic applications.

6) Last, but not least, an extensive campaign of accelerated tests of exposure of elements to aggressive environments (fire, chloride – induced corrosion and freeze thaw) would be needed in order to characterize thoroughly the various aspects of durability of the material.

References

1. Naaman, A.E., Reinhardt, H.: Proposed classification of HPFRC composites based on their tensile response. Mater. Struct. 39, 547–555 (2006).
2. Fischer, G., Wang, S., Li, V.C.: Design of Engineered Cementitious Composites (ECC) for processing and workability requirements. In: Proceedings of the International Symposium on Brittle Matrix Composites 7 (2003).
3. Li, V.C.: From micromechanics to structural engineering - The design of cementitious composites for civil engineering applications. J. Struct. Mech. Earthq. Eng. 10, 37s–48s (1993).
4. Naaman, A.: High performance fiber reinforced cement composites: classification and applications. In: CBM-CI international workshop. pp. 389–401. , Karachi, Pakistan (2007).
5. EN1998-1-2004: Eurocode 8. Design of structures for earthquake resistance—Part 1: general rules, seismic actions and rules for buildings. , Brussels (2004).
6. Hibbitt, Karlsson and Sorensen, Pawtucket, R.: ABAQUS/Standard Analysis User's Manual, (2010).
7. Yokota, H., Rokugo, K., Sakata, N.: JSCE Recommendations for Design and Construction of High Performance Fiber Reinforced Cement Composite with Multiple Fine Cracks. In: High Performance Fiber Reinforced Cement Composites 2: Proceedings of the International Workshop (1996).
8. Lawler, J.S., Zampini, D., Shah, S.P.: Microfiber and Macrofiber Hybrid Fiber-Reinforced Concrete. 595–604 (2005).
9. Marshall, D.B., COX, B.N.: A J-integral method for calculating steady-state matrix cracking stresses in composites. Mech. Mater. 7, 127–133 (1988).
10. Li, V.C., Wu, C., Wang, S., Ogawa, A., Saito, T.: Interface Tailoring for Strain-Hardening Polyvinyl Alcohol- Engineered Cementitious Composite (PVA-ECC). ACI Mater. J. 463–472 (2003).
11. Yang, E.-H., Li, V.C.: Strain-hardening fiber cement optimization and component tailoring by means of a micromechanical model. Constr. Build. Mater. 24, 130–139 (2010).
12. Kanda, T., Li, V.C.: Interface propertie and apparent strength of high-strength hydrophilic fiber in cement matrix. J. Mater. Civ. Eng. 10, 5–13 (1998).
13. Redon, C., Li, V., Wu, C., Hoshiro, H., Saito, T., Ogawa, A.: Measuring and modifying interface properties of PVA fibers in ECC matrix. J. Mater. Civ. Eng. 13, 399–406 (2001).
14. Li, V.C.: Advances in ECC research. ACI Spec. Publ. 1–28 (2002).
15. Li, V.C., Mishra, D., Wu, H.: Matrix design for pseudo-strain-hardening fibre reinforced cementitious composites. Mater. Struct. 586–595 (1995).
16. Li, V.C., Wu, H., Chan, Y.: Effect of Plasma Treatment of Polyethylene Fibers on Interface and Cementitious Composite Properties. J. Am. Ceram. Soc. 79, 700–704 (1996).
17. Lepech, M.D., Li, V.C.: Water permeability of engineered cementitious composites. Cem. Concr. Compos. 31, 744–753 (2009).
18. Sahmaran, M., Li, V.: Transport properties of engineered cementitious composites under chloride exposure. ACI Mater. J. 104, 604–611 (2007).
19. Miyazato, S., Hiraishi, Y.: Transport properties and steel corrosion in ductile fiber reinforced cement composites. In: ICF XI - 11th International Conference on Fracture (2005).
20. Li, V.C., Stang, H.: Elevating FRC Material Ductility to Infrastructure Durability. In: 6th RILEM Symposium on Fiber-Reinforced Concretes (FRC) - BEFIB 2004. pp. 171–186 (2004).
21. EN1992-1-1: Eurocode 2. Design of Concrete Structures. Eurocode 2 (EC2) (2004).
22. Stahel, W.: The performance economy. Palgrave MacMillan, UK (2010).
23. Cradle to Cradle, Product-life.org.
24. Dynamic city projects, http://dynamiccities.org/urban-agricultevertical-farming/.
25. Schnaiberg, A.: The Environment: From Surplus to Scarcity. Oxford University Press, New York (1980).
26. Rubenstein, M.: Mitigating Emissions from Cement. (2009).
27. ACI Committee 232: Use of fly ash in concrete. , Farmington Hills, MI (2003).
28. Van Zijl, G.P.A.G., Wittmann, F.H., Oh, B.H., Kabele, P., Toledo Filho, R.D., Fairbairn, E.M.R., Slowik, V., Ogawa, A., Hoshiro, H., Mechtcherine, V., Altmann, F., Lepech, M.D.:

Durability of strain-hardening cement-based composites (SHCC). Mater. Struct. 45, 1447–1463 (2012).
29. Thomas, M.: Optimizing the Use of Fly Ash in Concrete. , United States (2007).
30. Anon: An investigation of the pozzolanic nature of coal ashes. Eng. News. 71, 1334–1335 (1914).
31. National Research Council of the National Academies: Managing Coal Combustion Residues in Mines, Committee on Mine Placement of Coal Combustion Wastes. (2006).
32. Research Triangle Park: Human and Ecological Risk Assessment of Coal Combustion Wastes. (2007).
33. Goguen, C.: Fly Ash – A Hazardous Material? Precast Solut. Mag. (2010).
34. Mehta, P.K.: Natural pozzolans: Supplementary cementing materials in concrete. CANMET Spec. Publ. 86, 1–33 (1987).
35. Davis, R.E., Carlson, R.W., Kelly, J.W., Davis, H.E.: Properties of cements and concretes containing fly ash. J. Am. Concr. Institude. 33, 577–611 (1937).
36. ASTM C618: Standard Specification for Coal Fly Ash and Raw or Calcined Natural Pozzolan for Use. (2015).
37. CAN/CSA A3001-03: Cementitious materials for use in concrete. , Toronto (2003).
38. ACI Committee 211: Guide for Selecting Proportions for High-Strength Concrete with Portland Cement and Fly Ash. 93, (1998).
39. Bilodeau, A., and Malhotra, V.M.: High-volume fly ash system: Concrete solution for sustainable development. ACI Mater. J. 97(1), 41–48 (2000).
40. Bouzoubaa, N., Tamtsia, B., Zhang, M.H., Chevrier, R.L., Bilodeau, A., Malhotra, V.M.: Carbonation of Concrete Incorporating High Volumes of Fly Ash. In: SP-234, A. (ed.) Proceedings of the Seventh CANMET/ACI International Conference on the Durability of Concrete. pp. 283–304. American Concrete Institute,Farmington Hills, MI, (2006).
41. Song, G., Zijl, G. V.: Tailoring ECC for Commercial Application. Proc. 6th RILEM Symp. fiber. 1391–1400 (2004).
42. Wang, S., Li, V.C.: Polyvinil alcohol fiber reinforced engineered cementitious composites: material design and performances. In: Proceedings of International workshop on HPFRCC in Structural Applications. pp. 23–26. , Honolulu, Hawaii, USA (2006).
43. Peled, A., Shah, S.P.: Processing Effects in Cementitious Composites: Extrusion and Casting. J. Mater. Civ. Eng. 15, 192–199 (2003).
44. Wittmann, F.H., Zijl, G.P.A.G. Van: RILEM TC HFC , SUBCOMMITTEE 2 : Durability of strain hardening fiber-reinforced cement-based composites, SHCC. In: HPFRCC Workshop. , Honolulu, Hawaii, USA (2005).
45. van Zijl, G.P.A.G., Wittmann, F.H., Oh, B.H., Kabele, P., Toledo Filho, R.D., Fairbairn, E.M.R., Slowik, V., Ogawa, A., Hoshiro, H., Mechtcherine, V., Altmann, F., Lepech, M.D.: Durability of strain-hardening cement-based composites (SHCC). Mater. Struct. 45, 1447–1463 (2012).
46. Kunieda, M., Denarié, E., Brühwiler, E., Nakamura, H.: Challenges for strain hardening cementitious composites - deformability versus matrix density. In: Reinhardt, H.W. and Naaman, A.E. (eds.) 5th International RILEM Workshop on High Performance Fiber Reinforced Cement Composites (HPFRCC5). pp. 31–38. , Mainz, Germany (2007).
47. Li, V.C., Kong, H., Chan, Y.: Development of self-compacting engineered cementitious composites. In: Proceedings International Workshop on Self-Compacting Concrete. pp. 46–59. , Kochi, Japan (1998).
48. ACI Committee 318: Building Code Requirements for Reinforced Concrete and Commentary (ACI 318- 08/ACI 318R-08), (2008).
49. FIB Model Code: Model Code 2010. Federation Internationale du Beton (fib) (2010).
50. Concrete Committee JSCE: Recommendations for Design and Construction of High Performance Fiber Reinforced Cement Composites with Multiple Fine Cracks (HPFRCC). (2008).
51. Japan Society of Civil Engineers: Standard specifications for concrete structures: Materials and Construction. (2005).
52. Uchida, Y., Niwa, J., Tanaka, Y., Katagiri, M.: Outlines of JSCE "Recommendations for Design and Construction of Ultra High Strength Fiber Reinforced Concrete Structures." Concr. J. 43, (2005).

53. JCI Standard: Method of test for bending moment – curvature curve of fiber-reinforced cementitious composites. (2007).
54. Rokugo, K., Kanda, T., Yokota, H., Sakata, N.: Applications and recommendations of high performance fiber reinforced cement composites with multiple fine cracking (HPFRCC) in Japan. Mater. Struct. 42, 1197–1208 (2009).
55. Rokugo, K.: Tension tests and structural applications of strain-hardening fiber- reinforced cementitious composites area Mjornell. (2010).
56. Lepech, M., Li, V.: Large-scale processing of engineered cementitious composites. ACI Mater. J. 105(4), 358–366 (2008).
57. Li, V.C.., Fischer, G.., Kim, Y.., Lepech, M.., Qian, S.., Weimann, M.., Wang, S..: Final Report on Durable Link Slabs for Jointless Bridge Decks Based on Strain-Hardening Cementitious Composites. , Michigan (2003).
58. Lepech, M., Li, V.: Design of green engineered cementitious composites for improved sustainability. ACI Mater. J. (2008).
59. Kim, Y., Fischer, G., Li, V.C.: Performance of Bridge Deck Link Slabs Designed with Ductile Engineered Cementitious Composite. ACI Struct. J. 101, 792–801 (2004).
60. Kesner, K.E., Billington, S.L.: Experimental Response of Precast Infill Panel Connections and Panels Made with DFRCC. J. Adv. Concr. Technol. 1, 327–333 (2003).
61. Qian, S., Li, V.C.: Simplified Inverse Method for Determining the Tensile Strain Capacity of Strain Hardening Cementitious Composites. J. Adv. Concr. Technol. 5, 235–246 (2007).
62. Qian, S., Lepech, M.D., Kim, Y.Y., Li, V.C.: Introduction of Transition Zone Design for Bridge Deck Link Slabs Using Ductile Concrete. ACI Struct. J. 106, 96–105 (2009).
63. Yang, E.: Designing added functions in engineered cementitious composites, (2008).
64. Balaguru, P.: High-performance fiber-reinforced concrete mixture proportions with high fiber volume fractions. ACI Mater. J. 4–9 (2004).
65. Parra-Montesinos, G.J.: High-performance fiber-reinforced cement composites: An alternative for seismic design of structures. ACI Struct. J. 102, 668–675 (2005).
66. Parra-Montesinos, G.: High Performance Fiber Reinforced Concrete in Earthquake-Resistant Construction. Struct. Mag. 20–22 (2007).
67. Lim, Y.M., Li, V.C.: Durable Repair of Aged Infrastructures Using Trapping Mechanism of Engineered Cementitious Composites. Cem. Concr. Compos. 19, 373–385 (1997).
68. Fuller, W.B., Thompson, S.E.: The Laws of Proportioning Concrete. Trans. ASCE. 33, 223–298 (1907).
69. Shin, S.K., Kim, J.J.H., Lim, Y.M.: Investigation of the strengthening effect of DFRCC applied to plain concrete beams. Cem. Concr. Compos. 29, 465–473 (2007).
70. Georgiou, A., Pantazopoulou, S.: Effect of fiber length and surface characteristics on the mechanical properties of cementitious composites. Constr. Build. Mater. 1216–1228 (2016).
71. ASTM C496: Standard Test Method for Splitting Tensile Strength of Cylindrical Concrete Specimens. ASTM Int. 1–5 (2006).
72. ASTM C293: Standard Test Method for Flexural Strength of Concrete (Using Simple Beam With Center-Point Loading). (2010).
73. Georgiou, A. V, Pantazopoulou, S.J., Petrou, M.F.: Experimental Analysis of Fiber Reinforced Cementitious Composites with Increased Toughness. In: 10th HSTAM International Congress on Mechanics. pp. 25–27 (2013).
74. ASTM C1609: Standard Test Method for Flexural Performance of Fiber-Reinforced Concrete (Using Beam With Third-Point Loading) 1. 1–9 (2010).
75. Kasai, Y., Ikeda, N.: Testing Method of Concrete. , Tokyo: Gijutsu Shoin. (1993).
76. Kanakubo, T., Shimizu, K.: Tensile characteristics evaluation of DFRCC—round Robin test results by JCI-TC. In: International RILEM Workshop on High Performance Fiber Reinforced Cementitious Composites in Structural Applications. pp. 27–36 (2005).
77. Chandrangsu, K., Naaman, A.: Innovative Bridge Deck with Reduced Reinforcement and Strain-Hardening Fiber Reinforced Cementitious Composites. ACI Struct. J. 101, 57–64 (2004).
78. Toutanji, H.A., El-Korchi, T., Katz, R.N., Leatherman, G.L.: Behavior of Carbon Fiber Reinforced Cement Composites in Direct Tension. Cem. Concr. Res. 23, 618–626 (1993).
79. Mier, J.G.M. Van, Vliet, M.R.A. Van: Uniaxial tension test for the determination of fracture parameters of concrete : state of the art. Eng. Fract. Mech. 69, 235–247 (2002).

80. Kanakubo, T.: Tensile Characteristics Evaluation Method for Ductile Fiber-Reinforced Cementitious Composites. J. Adv. Concr. Technol. 4, 3–17 (2006).
81. Kanda, Tetsushi, V.C.L.: Effect of fiber strength and fiber-matrix interface on crack bridging in cement composites. J. Eng. Mech. 125, 290–299 (1999).
82. Shimizu, K., Kanakubo, T., Kanda, T., Nagai, S.: Shear behavior of steel reinforced PVA-ECC beams. In: 13th World Conference on Earthquake Engineering (2004).
83. Furuta, M., Kanakubo, T., Kanda, T., Nagai, S.: Evaluation of uni-axial tensile model for high performance fiber reinforced cementitious composites. J. Struct. Constr. Eng. (Transactions AIJ). 568, 115–121 (2003).
84. Sato, Y., Fukuyama, H., Suwada, H.: A proposal of tension-compression cyclic loading test method for ductile cementitious composite materials. J. Struct. Constr. Eng. Archit. Inst. Japan. 539, 7–12 (2001).
85. Veerasak, L.: Moment -rotation response and punching shear resistance of high performance fiber reinforced cementitious composite structural members, (2006).
86. Sirijaroonchai, K.: A Macro-scale Plasticity Model for High Performance Fiber Reinforced Cement Composites. (2009).
87. Song, G.: Matrix Manipulation to Study ECC Behaviour. (2005).
88. Molapo, K.T.: The behaviour of Strain-hardening cement composites under biaxial compression. (2010).
89. Chao, S.: Bond Characterization of Reinforcing Bars and Prestressing Strands in High Performance Fiber Reinforced Cementitious Composites under Monotonic and Cyclic Loading, (2005).
90. Fischer, G., Li, V.C.: Intrinsic response control of moment-resisting frames utilizing advanced composite materials and structural elements. ACI Struct. J. (2003).
91. Carpinteri, A., Brighenti, R., Spagnoli, A., Vantadori, S.: Tensile Cracking Behaviour of Strain-Hardening Cement-Based Composites using a Micromechanical Lattice Model. CP2009. 0, (2013).
92. Bentur, P.A., Alexander, M.G.: CEMENTITIOUS COMPOSITES A review of the work of the RILEM TC 159-ETC : Engineering of the interfacial transition zone in cementitious composites. Mater. 33, 82–87 (2000).
93. Kabele, P., Kanakubo, M.: Experimental and Numerical investigation of shear behavior of PVA-ECC in structural elements. In: Reinhardt, H.W. and Naaman, A.E. (eds.) Proceedings of the Fifth International Workshop on HPFRCC (HPFRCC5). , Mainz, Germany (2007).
94. Georgiou, A., Pantazopoulou, S., Petrou, M.: Increasing ductility of FRCC with proprietary coating agents. In: 10th fib International PhD Symposium in Civil Engineering. , Quebec City (2014).
95. Pantazopoulou, S.J., Tastani, S., Thermou, G., Triantafyllou, T., Monti, G., Bournas, D., Guadagnini, M.: Background to the European seismic design provisions for retrofitting RC elements using FRP materials. Struct. Concr. 17, 194–219 (2016).
96. Pajak, M.: The Influence of the Strain Rate on the Strength of Concrete Taking into Account the Experimental Techniques. Archit. Civ. Eng. Environ. 3, 77–86 (2011).
97. MacGregor, J., Wight, J.: Reinforced concrete: Mechanics and design 6th edition. PEARSON.
98. ASTM C78: C78M-10 - Standard Test Method for Flexural Strength of Concrete (Using Simple Beam with Third-Point Loading). (2010).
99. Valle, M., Buyukozturk, O.: Behavior of fiber reinforced high-strength concrete under direct shear. ACI Mater. J. 122–133 (1993).
100. Buyukozturk, O., Bakhoum, M., Beattie, S.: Shear behavior of joints in precast concrete segmental bridges. J. Struct. Eng. 116, 3380–3401 (1990).
101. Chapman, R., Shah, S.: Early-age bond strength in reinforced concrete. ACI Mater. J. 501–510 (1987).
102. Danish Standards Organization: Pull Out Test (DS 2082). , Copenhagen, Denmark (1980).
103. EFNARC: Specification and Guidelines for Self-Compacting Concrete. Rep. from EFNARC. 44, 32 (2002).
104. EN 206:2013: Concrete - Specification, performance, production and conformity, (2013).
105. EN 12350-8:2010: Testing fresh concrete Part 8: Self -compacting concrete - Slump- flow test. (2010).

106. EN 12350-9:2010: Testing fresh concrete, Part 9: Self compacting concrete- V-funnel test. Br. Stand. (2010).
107. EN 12350-10: 2010: Testing fresh concrete, Part 10: Self compacting concrete- L box test. Br. Stand. (2010).
108. Li, V.C., Wang, S., Wu, C.: Tensile strain-hardening behavior or polyvinyl alcohol engineered cementitious composite (PVA-ECC). ACI Mater. J. 98, 483–492 (2001).
109. Stang, H., Li, V.C.: Classification of fiber reinforced cementitious materials for structural applications. 6th RILEM Symp. Fiber-Reinforced Concr. - BEFIB 2004. 197–218 (2004).
110. Ostergaard, L., Walter, R., Olesen, J.: Method for determination of tensile properties of engineered cementitious composites (ECC). In: Proceedings of ConMat'05 (2005).
111. Bažant, Z.: Concrete fracture models: testing and practice. Eng. Fract. Mech. 69, 165–205 (2002).
112. van Zijl, G.P.A.G., Slowik, V., Toledo Filho, R.D., Wittmann, F.H., Mihashi, H.: Comparative testing of crack formation in strain-hardening cement-based composites (SHCC). Mater. Struct. 49, 1175–1189 (2016).
113. Naaman, A.E.: A Statistical Theory of Strength for Fiber Reinforced Concrete, PhD Thesis, (1972).
114. Archontas, N., Pantazopoulou, S.J.: Microstructural Aspects of the Mechanical Behavior of Nanomodified Cementitious Materials. In: NICOM 4 (2012).
115. BS 1881: testing concrete. Part 116: 1983: BSI (1983) BS 1881: testing concrete. Part 116: 1983 method for determination of compressive strength of con- crete cubes. British Standard Institute, London, (1983).
116. Rocco, C., Planas, J., Elices, M.: Review of the splitting-test standards from a fracture mechanics point of view. Cem. Concr. Res. 31, 73–82 (2001).
117. Rocco, C., Guinea, G. V, Elices, M.: Size effect and boundary conditions in the Brazilian test : Experimental verification. Mater. Struct. 32, 210–217 (1999).
118. Olesen, J.F., Østergaard, L., Stang, H.: Nonlinear fracture mechanics and plasticity of the split cylinder test. Mater. Struct. 39, 421–432 (2006).
119. Rocco, C., Guinea, G.V., Planas, J., Elises, M.: Experimental analysis of rupture mechanisms in the brazilian test. In: Fracture Mechanics of Concrete Structures FRAMCOS-3. pp. 121–130. AEDIFICATIO Publishers, D-79104 Freiburg, Germany, Gifu, Japan (1998).
120. Timoshenko, S., Woinowshy-Krieger, S.: Theory of plates and shells. McGrawl - Hill, New York (1959).
121. Timoshenko, S., Goodier, J.N.: Theory of Elasticity. McGraw-Hill Book Company, New York, NY (1951).
122. Chen, W.F.: Plasticity in Reinforced Concrete. McGrawl - Hill, New York (1982).
123. Georgiou, A., Pantazopoulou, S.: Determination of direct tensile stress-strain curve from simple three point bending tests. In: FRC 2014 Joint ACI-fib International Workshop (2014).
124. Imran, I., Pantazopoulou, S.J.: Experimental Study of Plain Concrete under Triaxial Stress. ACI Mater. J. 93, 589–601 (1997).
125. Shah, S., Rangan, B.: Fiber reinforced concrete properties. ACI J. Proc. 126–137 (1971).
126. Shah, S.P., Rangan, B. V.: Effects of Reinforcements on Ductility of Concrete. J. Struct. Div. 96, 1167–1184 (1970).
127. Zanganeh, M., Pantazopoulou, S.J.: Triaxial tests of Fiber-reinforced concrete. J. Mater. Civ. Eng. 15, 340–348 (2001).
128. Popovics, S.: A numerical approach to the complete stress-strain curve of concrete. Cem. Concr. Res. 3, 583–599 (1973).
129. Tastani, S.P., Pantazopoulou, S.J., Zdoumba, D., Plakantaras, V., Akritidis, E.: Limitations of FRP jacketing in confining old-type reinforced concrete members in axial compression. J. Compos. Constr. 10, 13–25 (2006).
130. Kent, D.C., Park, R.: Flexural Members with Confined Concrete. J. Struct. Div., ASCE. 1969–1990 (1971).
131. Park, R., Priestley, M.J.N., Gill, W.D.: Ductility of square-confined concrete columns. J. Struct. Div., ASCE. 108, 929–950 (1982).
132. Pantazopoulou, S., Mills, R.: Microstructural aspects of the mechanical response of plain concrete. ACI Mater. J. M26, 605–616 (1995).

133. Imran, I.: Applications of non-associated plasticity in modelling the mechanical response of concrete, (1994).
134. Pantazopoulou, S.J.: Role of expansion on mechanical behavior of concrete. J. Struct. Eng. 121, 1795–1805 (1995).
135. Archontas, N.D., Pantazopoulou, S.J.: Microstructural behavior and mechanics of nano-modified cementitious materials. Adv. Concr. Constr. 3, 15–37 (2015).
136. Daniel, J.I., Ahmad, S.H., Arockiasamy, M., Ball, H.P., Batson, G.B., Criswell, M.E., Dorfmueller, D.P., Fernandez, A. V, Gale, D.M., Antonio, J., Hackman, L.E., Hoff, G.C., Johnston, C.D., Leppert, M.A., Macdonald, C.N., Mangat, P.S., Marsh, H.N., Mitchell, N.C., Molloy, H.J., Nanni, A., Porter, M.L., Ramakrishnan, V., Schrader, E.K., Galinat, M.A., Smith, G.D., Smith, P.A., Speakman, J.D., Stevens, D.J., Swamy, R.N., Venta, G.J., Wu, S.T., Zellers, R.C., Zollo, R.F.: State-of-the-Art Report on Fiber Reinforced Concrete Reported by ACI Committee 544. 96, (2002).
137. Georgiou, A. V, Pantazopoulou, S.J.: Shear Span Length Relation to Tensile Properties of Strain Hardening Cementitious Composites. In: 11th HSTAM International Congress on Mechanics. , Athens (2016).
138. Han, S., Jang, S., Kang, S., Yun, H.: Flexural Performance and Cracking Behavior of Expansive SHCC Beams. In: 15WCEE. , Lisboa (2012).
139. Alyousif, A., Anil, O., Sahmaran, M., Lachemi, M., Yildirim, G., Ashour, A.F.: Comparison of shear behaviour of engineered cementitious composite and normal concrete beams with different shear span lengths. Mag. Concr. Res. 68, 217–228 (2016).
140. Park, R., Pauley, T.: Reinforced concrete structures. Wiley, New York (1975).
141. CEN: Eurocode 2: Design of Concrete Structures – Part 1: General rules and rules for buildings. CEN (1992).
142. Tureyen, A.K., Frosch, R.J.: Concrete Shear Strength : Another Perspective. (2004).
143. Vollum, R.L., Sagaseta, J.: Shear design of short-span beams. Mag. Concr. Res. 62, 267–282 (2010).
144. Birrcher, D., Tuchscherer, R., Huizinga, M., Bayrak, O., Wood, S., Jirsa, J.: Strength and Serviceability Design of Reinforced Concrete Deep Beams. Rep. no. 0- 5253-1. (2009).
145. Martin-Perez, B., Pantazopoulou, S.J.: Effect of bond, aggregate interlock and dowel action on the shear strength degradation of reinforced concrete. Eng. Struct. 23, 214–227 (2001).
146. Tastani, S.P., Pantazopoulou, S.J.: Behavior of Corroded Bar Anchorages. ACI Struct. J. 756–766 (2007).
147. Priestley, M., Seible, F., Calvi, G.: Seismic Design and Retrofit of Bridges. John Wiley, New York (1996).
148. Schlaich, J., Schafer, K., Jennewein, M.: Toward a Consistent Design of Structural Concrete. PCI J. 32, 74–150 (1987).
149. Schlaich, J., Weischede, D.: Detailing of concrete structures. Comite Euro-International du Beton, Paris (1982).
150. Tastani, S.P., Pantazopoulou, S.J.: Direct Tension Pullout Bond Test: Experimental Results. J. Struct. Eng. 136, 731–743 (2010).
151. Lee, S., Kang, S., Hai, K., Yang, E.: Experimental and analytical investigation on bond-slip behaviour of deformed bars embedded in engineered cementitious composites. Constr. Build. Mater. 127, 494–503 (2016).
152. Chao, S., Naaman, A.E., Parra-Montesinos, G.: Bond Behavior of Reinforcing Bars in Tensile Strain-Hardening Fiber-Reinforced Cement Composites. ACI Struct. J. 106, 897–906 (2009).
153. Krstulovic-Opara, N., Watson, K. a., LaFave, J.M.: Effect of increased tensile strength and toughness on reinforcing-bar bond behavior. Cem. Concr. Compos. 16, 129–141 (1994).
154. Ezeldin, A.S., Balaguru, P.N.: Bond Behavior of Normal and High Strength Fiber Reinforced Concrete. ACI Mater. J. 86, 515–524 (1990).
155. Kanakubo, T., Hosoya, H.: Bond-Splitting Strength of Reinforced Strain-Hardening Cement Composite Elements with Small Bar Spacing. ACI Struct. J. 189–198 (2014).
156. Yasojima, A., Kanakubo, T.: Local bond splitting behavior of RC members with lateral reinforcement. In: 14th World Conference on Earthquake Engineering. , Beijing, China (2008).

157. Asano, K., Kanakubo, T.: Study on Size Effect in Bond Splitting Behavior of ECC. In: Parra-Montesinos, G.J., Reinhardt, H.W., and Naaman, A.E. (eds.) HPFRCC 6. pp. 137–144. RILEM (2010).
158. Saleem, M.A., Mirmiran, A., Asce, F., Xia, J., Mackie, K.: Development Length of High-Strength Steel Rebar in Ultrahigh Performance Concrete. J. Mater. Civ. Eng. 25, 991–998 (2013).
159. Kanta, T., Watanabe, S., Li, V.C.: Application of pseudo strain hardening cementitious composites to shear resistant structural elements. In: FRAMCOS-3. pp. 1477–1490. , Freiburg, Germany (1998).
160. Fischer, G., Li, V.C.: Effect of fiber reinforcement on the response of structural members. Eng. Fract. Mech. 74, 258–272 (2007).
161. Yuan, F., Pan, J.L.: Experimental study on flexural behaviors of engineered cementitious composite beams reinforced with FRP bars. In: FRAMCOS-8. (2013).
162. Lequesne, R., Parra-Montesinos, G., Wight, J.: Seismic Response of Fiber-Reinforced Concrete Coupled Walls. ACI Struct. J. 113, 435–445 (2016).
163. Fischer, G., Li, V.C.: Deformation Behavior of Fiber-Reinforced Polymer Reinforced Engineered Cementitious Composite (ECC) Flexural Members under Reversed Cyclic Loading Conditions. ACI Struct. J. 100, 25–35 (2003).
164. Yuan, F., Pan, J., Dong, L., Leung, C.K.Y.: Mechanical Behaviors of Steel Reinforced ECC or ECC / Concrete Composite Beams under Reversed Cyclic Loading. J. Mater. Civ. Eng. 26, 1–8 (2014).
165. Parra-Montesinos, G., Chompreda, P.: Deformation capacity and shear strength of fiber reinforced cement composite flexural members subjected to displacement reversals. J. Struct. Eng. 133, 421–431 (2006).
166. V.Chaudhari, S., A. Chakrabarti, M.: Modeling of Concrete for Nonlinear Analysis using Finite Element Code ABAQUS. Int. J. Comput. Appl. 44, 14–18 (2012).
167. Lubliner, J.J., Oliver, S., Onate, E.: A plastic-damage model for concrete. Int. J. Solids Struct. 25, 229–326 (1989).
168. Lee, J., & Fenves, G.L.: Plastic-damage model for cyclic loading of concrete structures. J. Eng. Mech. 124(8), 892–900 (1998).
169. Jankowiak, T., Lodygowski, T.: Identification of parameters of concrete damage plasticity constitutive model. Found. Civ. Environ. Eng. 53–69 (2013).
170. Kupfer, H., Hilsdorf, H., Rusch, H.: Behavior of Concrete Under Biaxial Stresses. J. Proc. 66, 656–666 (1969).
171. fib Bulletin No. 42: Constitutive modelling for high strength. (2008).
172. RILEM TC-50 FMC: Determination of the fracture energy of mortar and concrete by means of three-point bend tests on notched beams. Mater. Struct. 18, 285–290 (1985).
173. Kabele, P.: Equivalent continuum model of multiple cracking. Eng. Mech. (Association Eng. Mech. 9, 75–90 (2002).

Appendices

Appendix 4A: Specimen dimensions and type of testing for each mix design

Table 4A.1: Uniaxial tensile tests

Name	Weight (kg/m^3)	b (mm)	d (mm)	Age (days)	Test speed (mm/sec)
F1-8	1641.4	50.58	26.3	103	0.0025
F1-9	1566.9	49.8	25.99	103	0.0025
F1-10	1588.2	50.94	25.61	104	0.0025
F2-8	1561.2	50.64	25.84	105	0.0025
F2-9	1541.9	50.16	26	105	0.0025
F2-10	1537.8	51.16	25.53	105	0.0025
F3-8	1534.7	51.19	25.61	106	0.0025
F3-9	1531.1	50.04	26.43	106	0.0025
F3-10	1465.5	50.02	24.26	106	0.0025
F4-8	1589.3	51.14	26	105	0.0025
F4-9	1542.7	50.18	25.22	105	0.0025
F4-10	1505.6	49.91	25.3	105	0.0025
F6-8	1490.9	51.68	25.63	103	0.0025
F6-9	1494.9	50.61	25.42	103	0.0025
F6-10	1473.1	50.51	25.7	103	0.0025
F7-8	1509.6	50.52	25.67	96	0.0025
F7-9	1530.6	50.13	25.23	96	0.0025
F7-10	1500.9	51.11	25.78	96	0.0025
F8-9	1606.45	50.2	26.73	149	0.0025
F8-10	1578.99	52.18	26.74	149	0.0025
F8-11	1631.96	49.83	26.8	149	0.0025
F9-1	0	50.67	26.8	123	0.0025
F9-2	0	51.44	26.71	123	0.0025
F9-3	0	50.54	26.44	123	0.0025
number of tests performed				24	

Table 4A.2: Uniaxial compression tests

Name	d (mm)	L (mm)	Density (kg/m^3)	Age (days)	Test speed		
F1-1	99.77	198.16	1973.026	103	4μm/sec		
F1-2	100.03	197.56	1920.179	103	1.5μm/sec		
F1-3	99.75	197.05	1914.087	103	1.5μm/sec		
F2-1	100.1	197	1915.463	106	1.5μm/sec		
F2-2	100.13	198.59	1893.744	106	1.5μm/sec		
F2-3	100.4	196.76	1888.766	106	1.5μm/sec		
F3-1	100	198.33	1908.8	107	1.5μm/sec		
F3-2	99.98	197.81	1907.822	107	1.5μm/sec		
F3-3	99.87	196.85	1912.662	107	1.5μm/sec		
F4-1	99.97	196.99	1939.042	105	1.5μm/sec		
F4-2	99.77	198.55	1948.664	105	1.5μm/sec		
F4-3	100.04	196.13	1942.29	105	1.5μm/sec		
1F5F2	100.13	197.29	2049.367	105	1.5μm/sec	F5	2 layers CFRP
2F5F2	99.38	195.12	2077.025	105	3μm/sec	F5	2 layers CFRP
3F5BF2	100.26	196.43	2055.732	105	3μm/sec	F5B	2 layers CFRP
1F5BF3	100.09	192.27	2049.155	105	3μm/sec	F5B	3 layers CFRP
2F5CF3	99.88	195.57	2037.768	110	3μm/sec	F5C	3 layers CFRP
3F5CF3	100.06	196.28	2049.973	110	3μm/sec	F5C	3 layers CFRP
F5-1	99.94	198.94	2070.682	103	1.5μm/sec	F5	
F5-2	100.11	197.54	2067.219	103	1.5μm/sec	F5	
F5-3	99.92	195.58	2082.843	103	1.5μm/sec	F5	
F5B-1	99.77	198.17	2050.705	103	1.5μm/sec	F5B	
F5B-2	99.69	195.39	2048.011	103	1.5μm/sec	F5B	
F5B-3	99.97	198.94	2060.602	103	1.5μm/sec	F5B	
F5C-1	99.87	198.53	2059.028	104	1.5μm/sec	F5C	
F5C-2	99.81	196.32	2065.181	104	1.5μm/sec	F5C	
F5C-3	99.99	195.66	2058.249	104	1.5μm/sec	F5C	
F5S3-1	99.9	199.67	2354.4	104	1.5μm/sec	F5C	φ8/3
F5S3-2	99.97	197.67	2362.066	104	1.5μm/sec	F5C	φ8/3
F5S3-3	99.91	196.58	2368.609	104	1.5μm/sec	F5C	φ8/3
F5S5-1	99.73	197.12	2263.629	104	1.5μm/sec	F5	φ8/5
F5S5-2	100.02	197.15	2268.062	104	1.5μm/sec	F5	φ8/5
F5S5-3	99.94	199.26	2262.801	104	1.5μm/sec	F5	φ8/5
F5S8-1	99.74	199.17	2219.189	104	1.5μm/sec	F5B	φ8/8
F5S8-2	99.9	196.72	2202.865	104	1.5μm/sec	F5B	φ8/8
F5S8-3	99.52	195.84	2210.066	104	1.5μm/sec	F5B	φ8/8
F6-1	100.04	197.63	1861.436	104	1.5μm/sec		
F6-2	99.96	196.33	1912.524	104	1.5μm/sec		
F6-3	99.85	198.37	1872.629	104	1.5μm/sec		
F7-1	99.97	196.62	1917.032	96	1.5μm/sec		
F7-2	100.19	197.66	1914.238	96	1.5μm/sec		

F7-3	100.09	196.53	1888.157	96	1.5μm/sec		
F8-1	100.04	196.04	1894.639	153	1.5μm/sec		
F8-2	99.96	195.82	1886.27	153	1.5μm/sec		
F8-3	99.96	195.89	1889.694	153	1.5μm/sec		
F9-7	101.17	194.19	0	125	1.5μm/sec		
F9-8	100.29	195.55	0	125	1.5μm/sec		
F9-9	100.18	195.91	0	125	1.5μm/sec		
F10-4	100.14	196.39	0	119	1.5μm/sec		
F10-5	100.47	194.96	0	119	1.5μm/sec		
F10-6	100.25	193.88	0	119	1.5μm/sec		
F14-1	99.71	193.67	0	81	1.5μm/sec		
F14-2	100.11	195.57	0	81	1.5μm/sec		
F14-3	99.93	192.65	0	81	1.5μm/sec		
F14-G1	101.17	190.99	0	81	3μm/sec		1 layer GFRP
F14-G2	100.83	192.03	0	81	3μm/sec		1 layer GFRP
F14-G3	101.03	190.74	0	81	3μm/sec		1 layer GFRP
F14-2G1	101.44	190.95	0	82	3μm/sec		2 layer GFRP
F14-2G2	101.72	189.14	0	82	3μm/sec		2 layer GFRP
F14-2G3	100.34	191.58	0	82	3μm/sec		2 layer GFRP
F14-C1	100.57	192.91	0	82	3μm/sec		1 layer CFRP
F14-C2	100.95	193.97	0	82	3μm/sec		1 layer CFRP
F14-C3	101.25	190.46	0	82	3μm/sec		1 layer CFRP
number of tests performed				63			

Table 4A.3: Split Cylinder tests

A/A	WEIGHT	D	L	ρ (kg/m^3)	age at test	TEST SPEED
F1-4	1495.2	99.98	99.81	1908.135	105	3μm/sec at 300μm 8μm/sec
F1-6	1446.6	99.88	96.23	1918.629	105	3μm/sec at 300μm 8μm/sec
F1-7	1501	100.09	100.54	1897.451	105	3μm/sec at 300μm 8μm/sec
F2-4	1472.2	100.09	98.86	1892.67	105	3μm/sec
F2-5	1452.9	100.02	98.11	1884.772	105	3μm/sec
F2-7	1477.9	100.2	99.21	1889.141	105	3μm/sec
F3-4	1470	100.14	97.77	1909.003	107	3μm/sec
F3-5	1479	99.96	99.45	1895.051	107	3μm/sec
F3-7	1449	100.16	96.05	1914.664	107	3μm/sec
F4-4	1504.2	100.17	98.47	1938.369	105	3μm/sec
F4-6	1490.7	100.13	97.15	1948.629	105	3μm/sec
F4-7	1512.8	100.2	98.07	1956.23	105	3μm/sec
F5-5	1640.6	100.07	101.27	2059.796	125	1.5μm/sec
F5-6	1607.7	100.12	98.81	2066.677	125	1.5μm/sec
F5-7	1573.7	99.97	97.15	2063.716	125	1.5μm/sec
F6-4	0	99.69	94.42	0	491	3μm/sec
F6-5	0	100.03	102.96	0	491	3μm/sec
F6-6	0	99.58	93.2	0	491	3μm/sec
F9-4	0	100.11	99	0	124	3μm/sec
F9-5	0	100.28	98.04	0	124	3μm/sec
F9-6	0	100.07	98.09	0	124	3μm/sec
F10-1	0	100.14	96.89	0	118	3μm/sec
F10-2	0	100.17	97.4	0	118	3μm/sec
F10-3	0	99.85	97.5	0	118	3μm/sec
number of tests performed					24	

Table 4A.4: Three point bending tests

A/A	WEIGHT	B (mm)	D (mm)	L (mm)	ρ (kg/m3)	age at test	TEST SPEED
F1-14	9721.6	102.51	100.67	500	1884.089	104	0.4μm/sec at 150μm 1.5μm/sec
F1-15	9679.9	100.62	100.36	500	1917.149	104	0.4μm/sec at 100μm 1.5μm/sec
F1-16	9689.8	100.62	100.36	500	1919.11	102	0.4μm/sec at 100μm 1.5μm/sec
F2-14	9988.4	101.24	100.67	500	1960.08	105	1.5μm/sec
F2-15	9945	100.08	101.09	500	1965.981	105	1.5μm/sec
F2-16	9891.8	100.54	100.31	500	1961.653	105	1.5μm/sec
F3-14	9388.2	100.75	100.08	500	1862.173	109	1.5μm/sec
F3-15	9562	101.08	100.45	500	1883.491	109	1.5μm/sec
F3-16	9417.1	100.65	100.69	500	1858.434	109	1.5μm/sec
F4-14	9653.2	99.37	100.11	500	1940.745	104	1.5μm/sec
F4-15	9778.4	100.96	100.07	500	1935.729	104	1.5μm/sec
F4-16	9867.1	99.44	101.13	500	1962.359	104	1.5μm/sec
F5-14	10067.2	98.09	99.83	500	2056.141	103	1.5μm/sec
F5-15	10156.9	100.68	100.26	500	2012.428	103	1.5μm/sec
F5-16	10106	98.39	99.97	500	2054.89	103	1.5μm/sec
number of tests performed						15	

Table 4A.5: Four point bending tests without steel reinforcement

A/A	B	D	L	L (sup.)	ρ (kg/m3)	age at test	TEST SPEED	a/h
F1-11	104	100.28	350	300	1911.982	105	0.8μm/sec at 300μm 3μm/sec	1
F1-12	102.68	100.38	355	300	1879.425	105	0.8μm/sec at 300μm 3μm/sec	1
F1-13	101.06	100.4	350	300	1879.283	105	0.8μm/sec at 300μm 3μm/sec	1
F2-11	100.63	100.36	356	300	1905.586	105	0.8μm/sec at 300μm 3μm/sec	1
F2-12	101.4	99.97	350	300	1961.253	105	3μm/sec	1
F2-13	101.11	100.15	350	300	1935.156	105	3μm/sec	1
F3-11	100.83	99.97	350	300	1871.632	109	3μm/sec	1
F3-12	98.97	100.92	353	300	1885.028	109	3μm/sec	1
F3-13	100.65	99.98	353	300	1881.013	109	3μm/sec	1
F4-11	101.41	100	353	300	1933.279	104	3μm/sec	1
F4-12	99.35	101.02	347	300	1962.552	104	3μm/sec	1
F4-13	99.51	100.18	352	300	1946.677	104	3μm/sec	1
F5-11	98.5	100.36	348	300	2067.852	103	3μm/sec	1
F5-12	101.45	100.01	350	300	2026.271	103	3μm/sec	1
F5-13	99.89	100.55	350	300	2044.076	103	3μm/sec	1
F6-20	103.21	103.46	400	300	0	104	3μm/sec	1
F6-21	102.23	101.92	400	300	0	105	3μm/sec	1
F6-22	103.1	103.31	400	300	0	105	3μm/sec	1
F6-23	99.95	100.18	500	400	0	105	3μm/sec	1.5
F6-24	99.92	100.81	500	400	0	105	3μm/sec	1.5
F6-25	99.05	100.04	500	400	0	105	3μm/sec	1.5
F6-26	100.96	103.45	600	500	0	106	1.5μm/sec at a/2	2
F6-27	101.37	102.98	600	500	0	106	1.5μm/sec at a/2	2
F6-28	104.86	102.05	600	500	0	106	1.5μm/sec at a/2	2
F6-32	102.53	101.55	800	700	0	106	1.5μm/sec at a/2	3
F6-33	102.1	103.35	800	700	0	106	1.5μm/sec at a/2	3
F6-34	101.76	103.36	800	700	0	106	1.5μm/sec at a/2	3
F6-35	103.46	102.86	900	800	0	107	3μm/sec at a/2	3.5
F6-36	102.44	102.46	900	800	0	107	3μm/sec at a/2	3.5
F6-37	103.8	101.96	900	800	0	107	3μm/sec at a/2	3.5
F6-38	101.64	100.56	270	220	1849.076	107	3μm/sec	0.6
F6-39	99.89	100.11	270	220	1893.706	107	3μm/sec	0.6
F6-40	100.77	100.52	270	220	1839.749	114	3μm/sec	0.6
F6-41	100.97	100.51	230	180	1826.658	114	3μm/sec	0.4
F6-42	100.48	100.38	230	180	1839.969	114	3μm/sec	0.4
F6-43	101.32	100.97	230	180	1822.977	114	3μm/sec	0.4
F7-29	105.33	102.77	700	600	0	106	1.5μm/sec at a/2	2.5
F7-30	107.57	102.6	700	600	0	106	1.5μm/sec at a/2	2.5
F7-31	110.3	102.76	700	600	0	106	1.5μm/sec at a/2	2.5
F7B1	101.64	100.02	350	300	0	488	3μm/sec	1
F8-B1	102.22	99.81	500	400	0	482	3μm/sec	1.5

F8-B2	102.74	100.72	500	400	0	482	3μm/sec	1.5
F8-B3	101.38	101.17	500	400	0	482	3μm/sec	1.5
F13-B1	100.59	100.2	500	400		83	3μm/sec	1.5
F13-B2	102.63	100.67	500	400		83	3μm/sec	1.5
number of tests performed						45		

Table 4A.6: Four point bending tests with steel reinforcement

A/A	B (mm)	D (mm)	L (mm)	L (sup) (mm)	TEST DATE	age at test	a/h	Reinf.
F7-S8	104.34	103.23	900	700	104	3μm/sec at a/4	3	2φ8
F7-S9	103.76	102.68	900	700	104	3μm/sec at a/4	3	2φ8
F7-S10	101.65	103.26	900	700	104	3μm/sec at a/4	3	2φ8
F7-SS11	104.96	102.44	900	700	104	3μm/sec at a/4	3	2φ8+2φ8+φ6/50
F7-S14	101.08	102.68	600	500	104	3μm/sec at a/2	2	2φ8
F7-S15	102.82	101.4	600	500	104	3μm/sec at a/2	2	2φ8
F7-S16	103.56	102.14	600	500	104	3μm/sec at a/2	2	2φ8
F7-SS17	102.44	104.16	600	500	105	3μm/sec at a/2	2	2φ8+2φ8+φ6/50
F7-SS18	102.42	103.18	600	500	105	3μm/sec at a/2	2	2φ8+2φ8+φ6/50
F7-SS19	102.06	103.29	600	500	105	3μm/sec at a/2	2	2φ8+2φ8+φ6/50
F7-S20	101.77	104.16	380	300	106	6μm/sec	1	2φ8
F7-S21	103.5	100.22	380	300	106	6μm/sec	1	2φ8
F7-S22	104.4	101.91	380	300	106	6μm/sec	1	2φ8
F7-SS23	102.94	101.97	380	300	106	6μm/sec	1	2φ8+2φ8+φ6/50
F7-SS24	102.67	100.58	380	300	106	6μm/sec	1	2φ8+2φ8+φ6/50
F7-SS25	102.67	100.58	380	300	106	6μm/sec	1	2φ8+2φ8+φ6/50
F9-B1	102.41	104.17	600	500	129	3μm/sec at a/2	2	2φ14
F9-B2	102.31	102.86	600	500	129	3μm/sec at a/2	2	2φ14
F9-B3	101.61	103.22	600	500	129	3μm/sec at a/2	2	2φ14
F9-S1	102.42	102.71	600	500	129	12μm/sec	2	2φ14+2φ6+φ6/50
F9-S2	104.68	103.93	600	500	129	12μm/sec	2	2φ14+2φ6+φ6/50
F9-S3	104.68	103.93	600	500	129	12μm/sec	2	2φ14+2φ6+φ6/50
F10-B1	101.95	106.44	600	500	122	3μm/sec at a/2	2	2φ8
F10-B2	102.11	102.42	600	500	122	3μm/sec at a/2	2	2φ8
F10-B3	102.93	103.99	600	500	123	3μm/sec at a/2	2	2φ8
F10-BS1	103.11	104.74	600	500	124	6μm/sec	2	2φ8+2φ8+φ6/50
F10-BS2	102.06	106.95	600	500	124	6μm/sec	2	2φ8+2φ8+φ6/50
F10-BS3	102.14	105	600	500	124	6μm/sec	2	2φ8+2φ8+φ6/50
number of tests performed					28			

Table 4A.7: Push-off tests

A/A	a	b	c	d	e	f	g	h	i	date at test	TEST SPEED	
F5S-1	188.34	255.8	28	102.82	27.89	116.51	137.1	126.25	126.4	99	15μm/sec	6φ6
F5S-2	201.77	254.21	28.53	102.39	28.63	128.08	130.53	127.81	132.82	99	15μm/sec	6φ6
F5S-3	224.11	255.39	28.27	100.66	28.39	115.06	107.99	124.18	126.17	99	15μm/sec	6φ6
SHF7-1	206.06	257.34	28.44	101.97	28.73	120.07	115.57	127.81	129.89	110	7.5μm/sec	
SHF7-2	205.56	255.78	29.68	103.46	29.64	123.39	115.94	125.25	125.26	110	7.5μm/sec	
SHF7-3	182.8	256.01	29.64	104.16	29.74	123.87	127.45	127.44	128.83	110	7.5μm/sec	
F7-S1	194.81	254.29	28.08	101.5	28.16	118.82	136.48	126.32	133.49	85	15μm/sec	6φ6
F7-S2	215.32	255.64	28.35	104.29	28.52	112.77	121.84	131.03	125.22	86	15μm/sec	6φ6
F7-S3	194.76	255.66	28.39	102.53	27.72	125.98	122.64	125.73	123.06	86	15μm/sec	6φ6
F10-S1	202.045	254.76	29	103.33	27.68	120.5	112.33	129.11	129.32	117	7.5μm/sec	
F10-S2	213.65	256.34	29.33	104.97	28.13	113.77	128.33	128	123.68	117	7.5μm/sec	
F10-S3	212.995	257.68	29.98	105.72	27.55	107.71	126.96	129.63	125.73	107	7.5μm/sec	
number of tests performed										12		

*all dimensions in mm

Table 4A.8: Pull-out tests

A/A	date at test	TEST SPEED	Bar	L_b	h (2c+φ)	c		l'	
F8-A5-C1-1	126	0.025mm/sec	8	50	27.36	9.68	1.21	22.18	
F8-A5-C1-2	126	0.025mm/sec	8	50	26.79	9.395	1.17	22.11	
F8-A5-C1-3	126	0.025mm/sec	8	50	26.9	9.45	1.18	22.07	
F8-A8-C1-1	126	0.025mm/sec	8	80	26.05	9.025	1.13	22.06	
F8-A8-C1-2	126	0.025mm/sec	8	80	26.52	9.26	1.16	22.1	
F8-A8-C1-3	128	0.025mm/sec	8	80	28.56	10.28	1.29	22.16	
F8-A12-C1-1	128	0.025mm/sec	8	120	27.46	9.73	1.22	22.15	
F8-A12-C1-2	128	0.025mm/sec	8	120	25.43	8.715	1.09	22.17	
F8-A12-C1-3	128	0.025mm/sec	8	120	26.52	9.26	1.16	22.02	
F8-A8-C2-1	141	0.025mm/sec	8	80	53.18	22.59	2.82	22.2	22.48
F8-A8-C2-2	141	0.025mm/sec	8	80	53.93	22.965	2.87	22.17	
F8-A8-C2-3	141	0.025mm/sec	8	80	53.78	22.89	2.86	22.31	
F8-A12-C3-1	134	0.025mm/sec	8	120	60.39	26.195	3.27	22.14	
F8-A12-C3-2	141	0.025mm/sec	8	120	59.99	25.995	3.25	22.01	22.11
F8-A12-C3-3	141	0.025mm/sec	8	120	58.14	25.07	3.13	22.38	22.38
F8-B5-C1-1	128	0.025mm/sec	10	50	34.31	12.155	1.22	22.06	
F8-B5-C1-2	128	0.025mm/sec	10	50	34.28	12.14	1.21	22.1	
F8-B5-C1-3	128	0.025mm/sec	10	50	33.64	11.82	1.18	22.23	
F8-B8-C1-1	134	0.025mm/sec	10	80	32.29	11.145	1.11	22.02	
F8-B8-C1-2	134	0.025mm/sec	10	80	33.6	11.8	1.18	22.04	
F8-B8-C1-3	134	0.025mm/sec	10	80	33.51	11.755	1.18	22.32	
F8-B12-C1-1	134	0.025mm/sec	10	120	32.99	11.495	1.15	22.43	
F8-B12-C1-2	134	0.025mm/sec	10	120	31.84	10.92	1.09	22.4	
F8-B12-C1-3	134	0.025mm/sec	10	120	31.99	10.995	1.10	22.21	
number of tests performed			24						

*all dimensions in mm

Table 4A.9: Steel bars tensile tests

Bar Ref	Date of test	Diameter (mm)	Test speed
FS-6-1	17-05-16	5.74	0.1mm/sec at 15mm 1mm/sec
FS-6-2	17-05-16	5.38	0.1mm/sec at 15mm 1mm/sec
FS-6-3	17-05-16	6.24	0.1mm/sec at 15mm 1mm/sec
FS-8-1	17-05-16	7.98	0.1mm/sec at 15mm 1mm/sec
FS-8-2	17-05-16	8.15	0.1mm/sec at 15mm 1mm/sec
FS-8-3	17-05-16	7.9	0.1mm/sec at 15mm 1mm/sec
FS-10-1	17-05-16	9.48	0.1mm/sec at 15mm 1mm/sec
FS-10-2	17-05-16	9.87	0.1mm/sec at 15mm 1mm/sec
FS-10-3	17-05-16	9.71	0.1mm/sec at 15mm 1mm/sec
S10-1	21-05-15	10	0.1mm/sec at 15mm 1mm/sec
S10-2	21-05-15	10	0.1mm/sec at 15mm 1mm/sec
S10-3	21-05-15	10	0.1mm/sec at 15mm 1mm/sec
S8-1	21-05-15	8	0.1mm/sec at 15mm 1mm/sec
S8-2	21-05-15	8	0.1mm/sec at 15mm 1mm/sec
S8-3	21-05-15	8	0.1mm/sec at 15mm 1mm/sec
S6-1	21-05-15	5.3	0.1mm/sec at 15mm 1mm/sec
S6-2	21-05-15	5.3	0.1mm/sec at 15mm 1mm/sec
S6-3	21-05-15	5.3	0.1mm/sec at 15mm 1mm/sec
number of tests performed		18	

Appendix 4B: Diagrams from all experiments

4B1: Uniaxial tensile test results

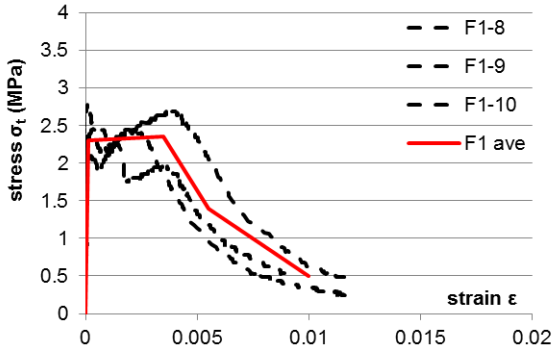

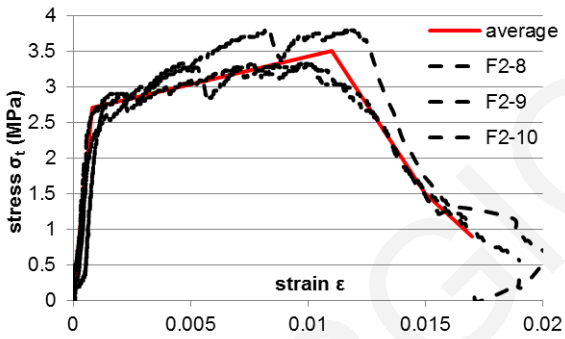

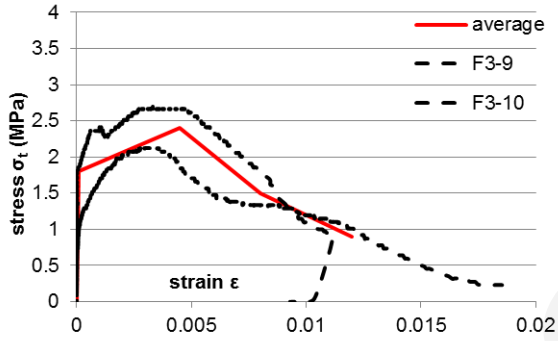

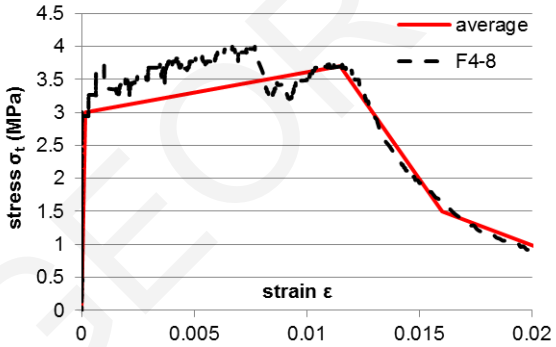

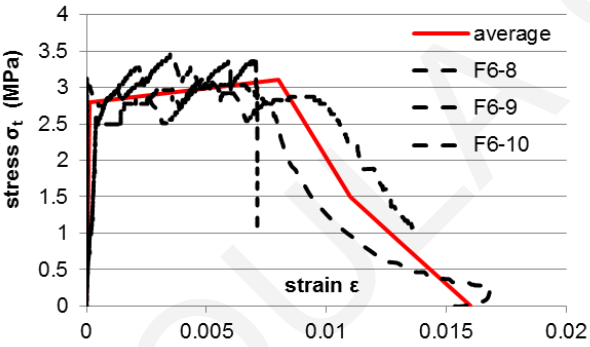

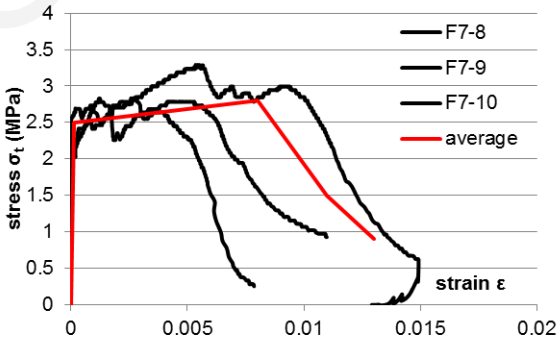

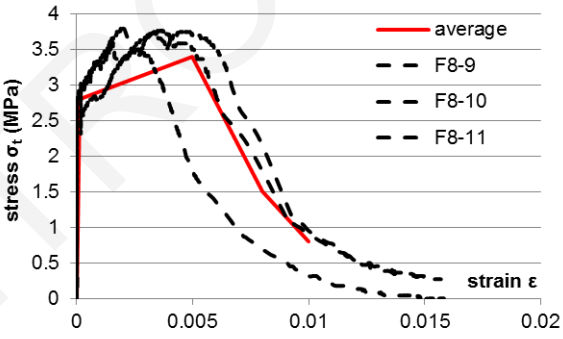

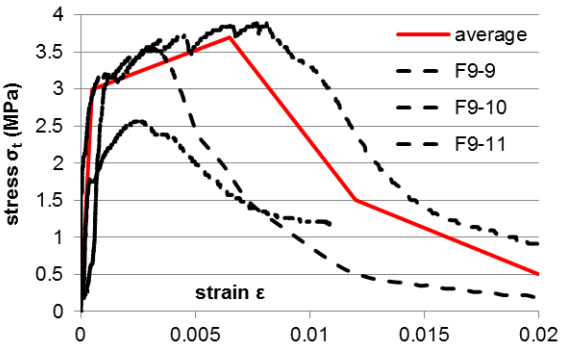


F1-9


F1-10

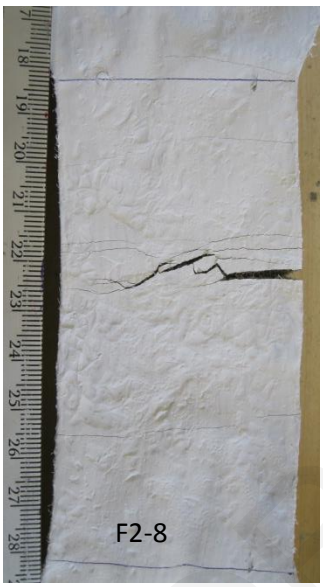
F2-8


F2-9

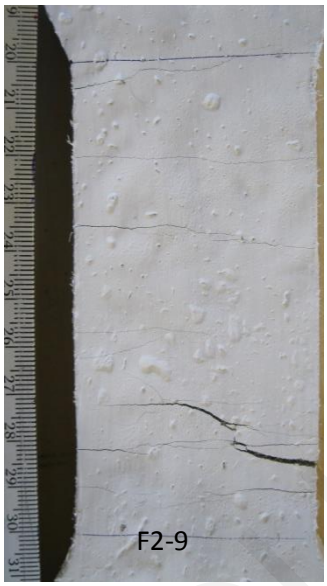
F2-9

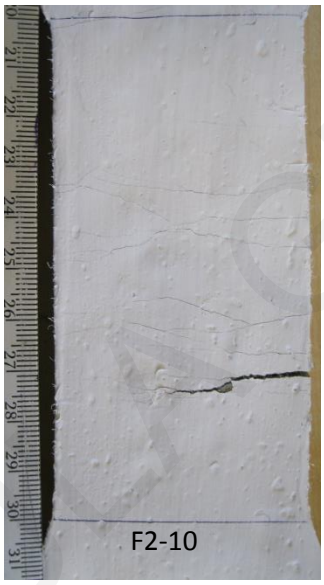
F2-10

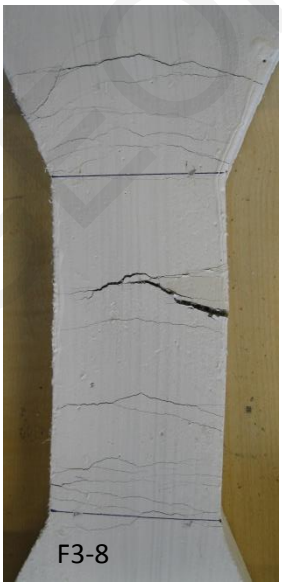
F3-8


F3-10


F4-9

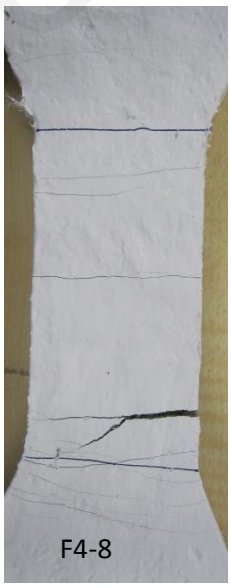
F4-8


F6-8

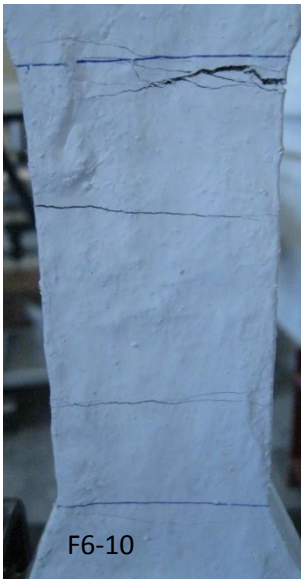
F6-10


F7-8

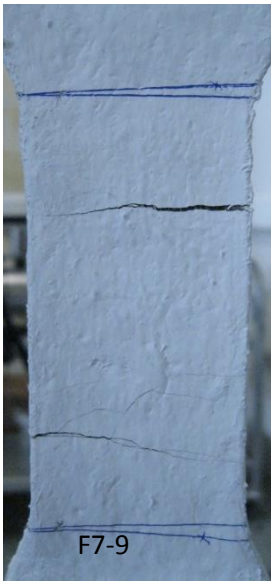
F7-9

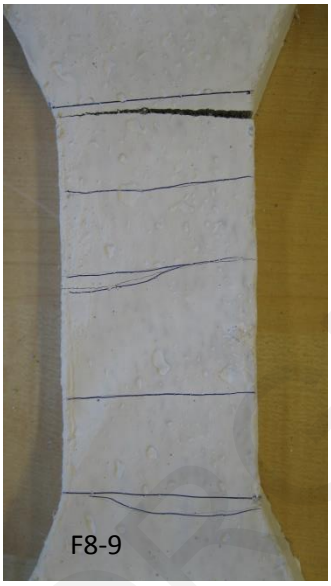
F8-9


F8-11


F9-10

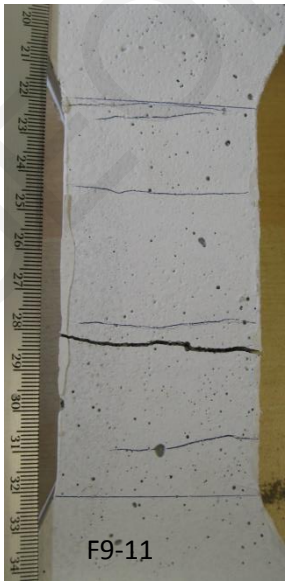
F9-11

4B2: Uniaxial compression test results

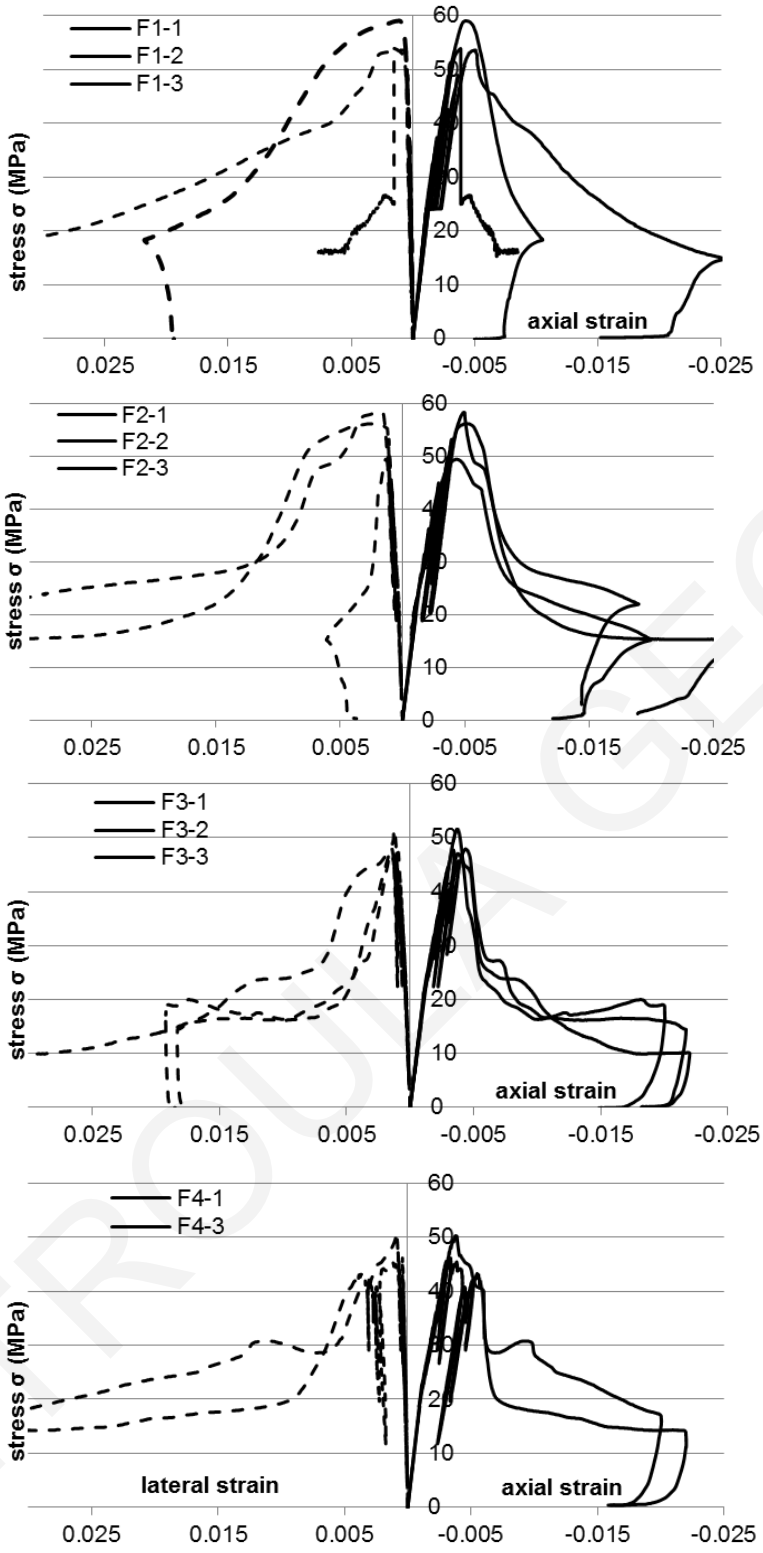

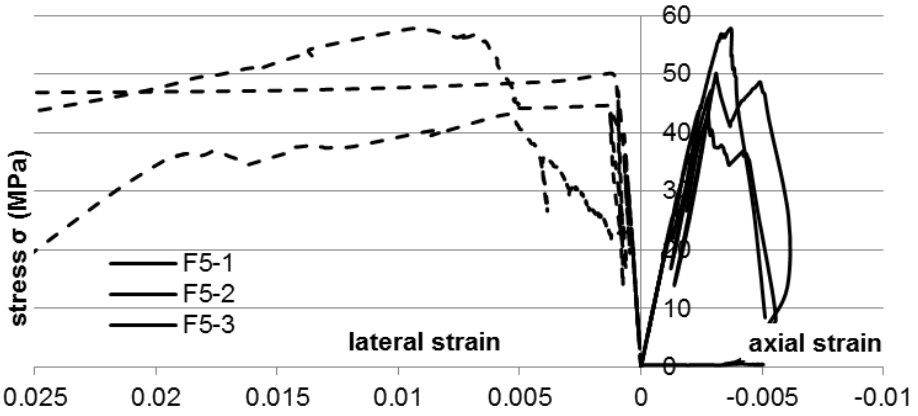

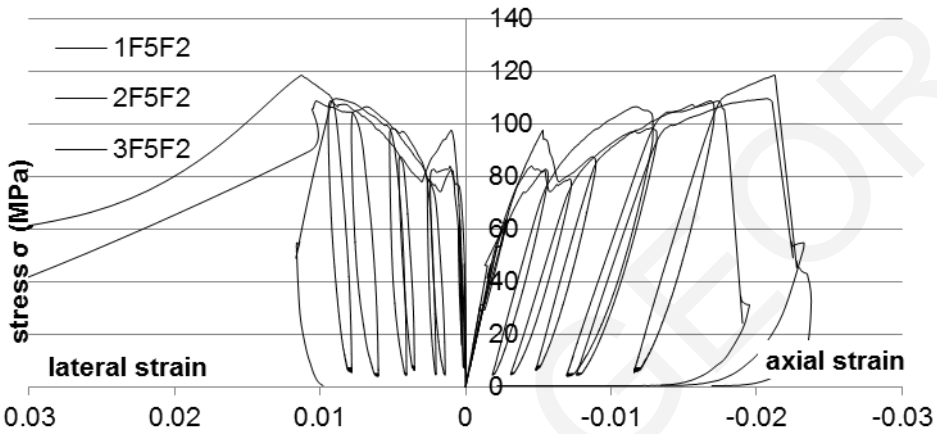

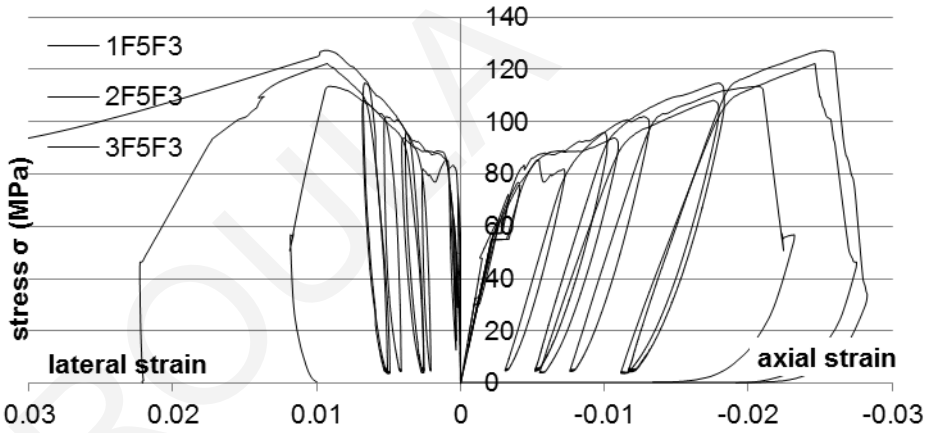

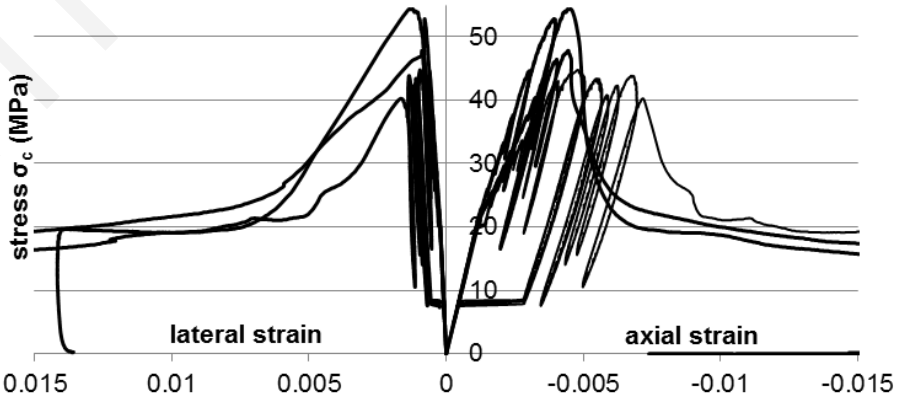

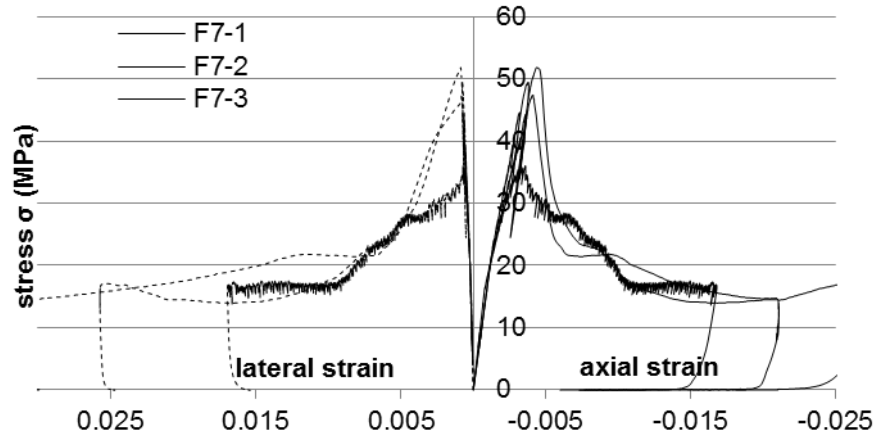

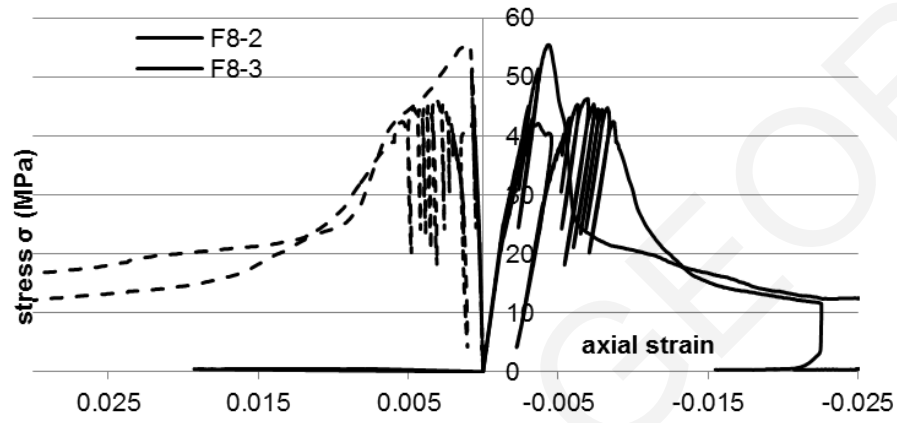

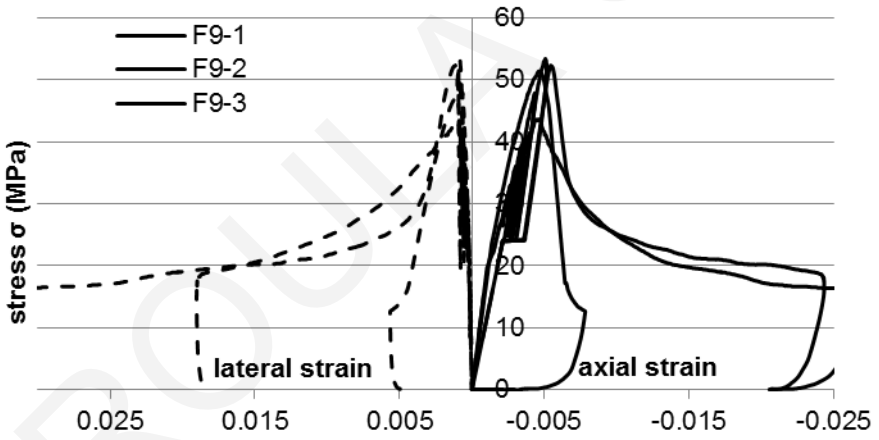

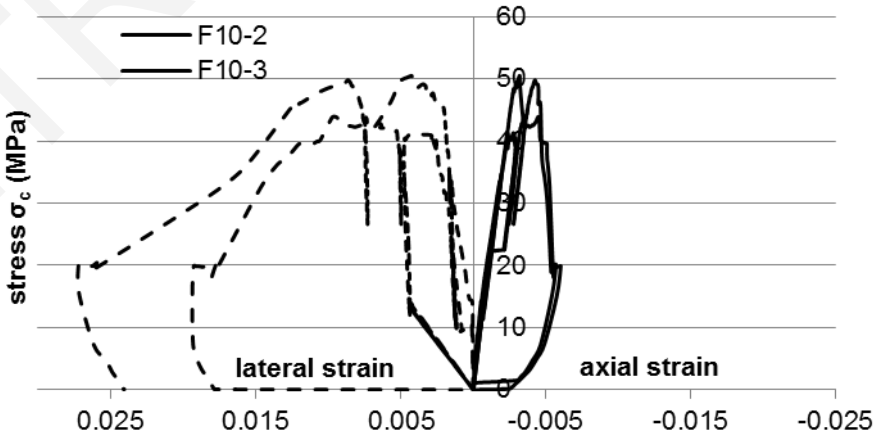

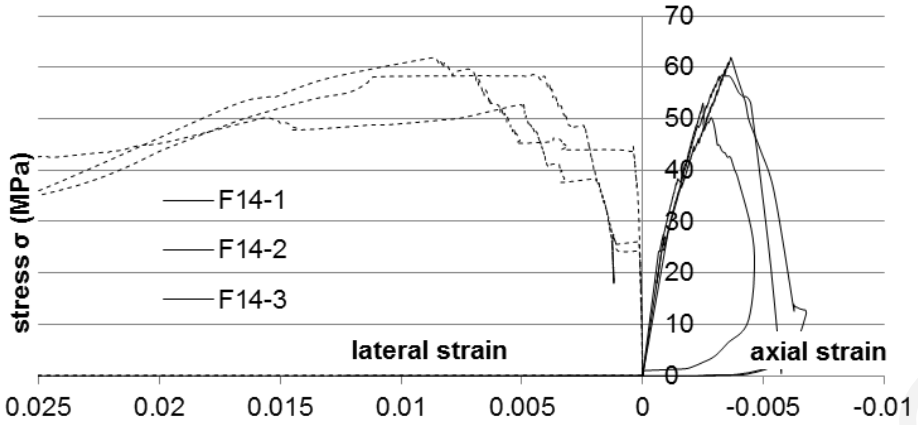

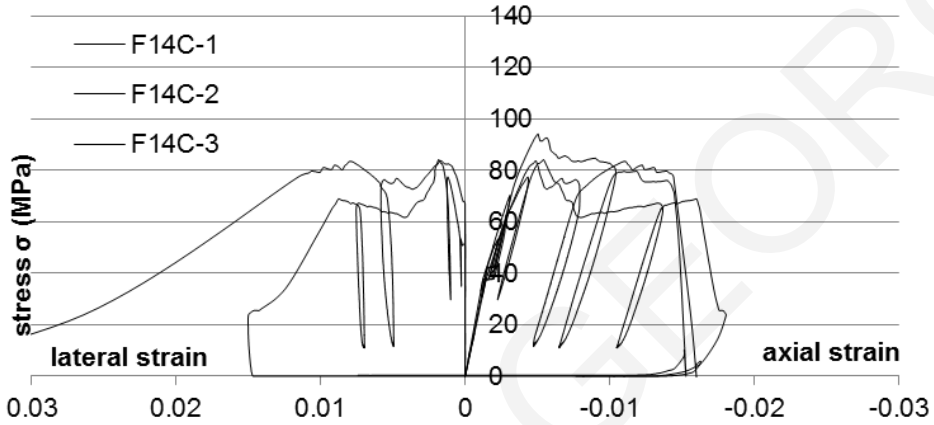

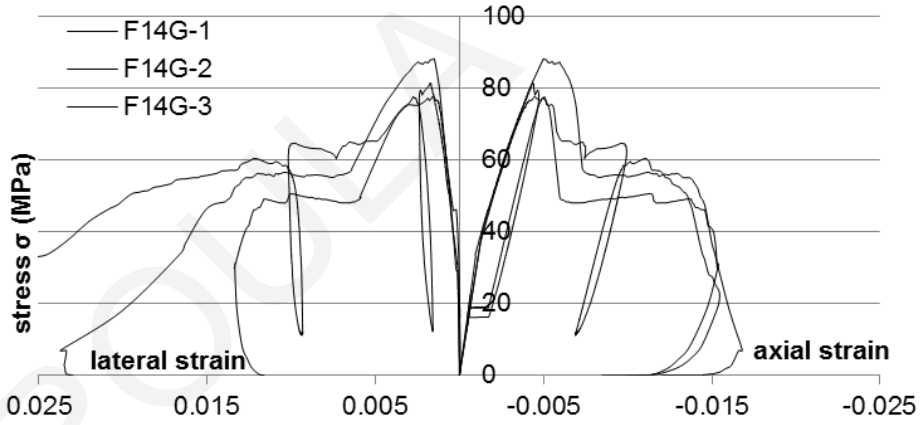

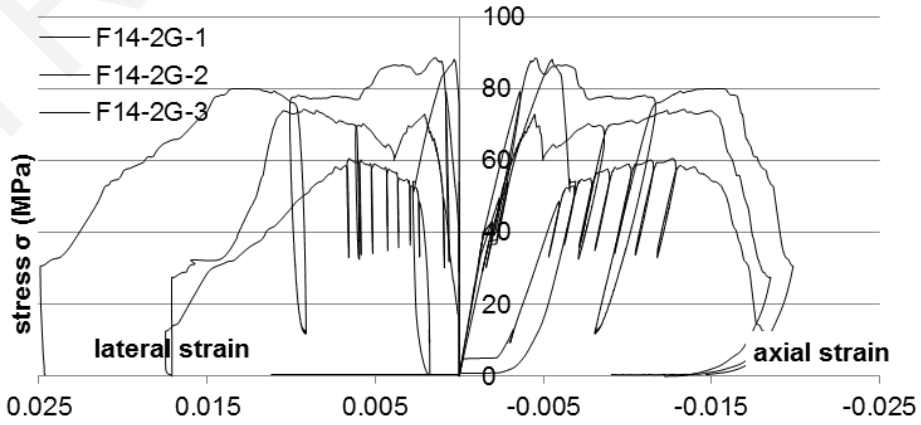

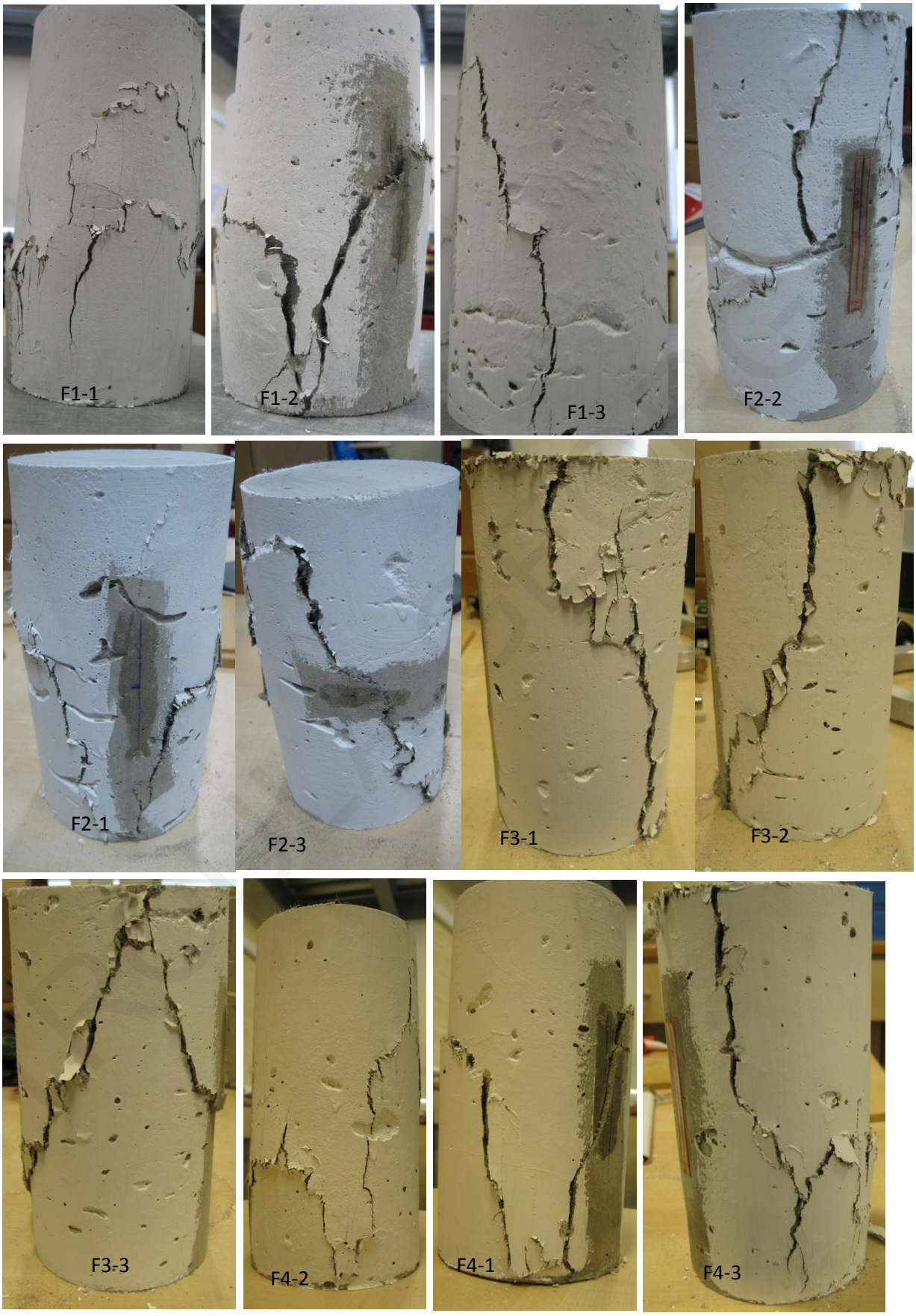
F1-1
F1-2
F1-3
F2-2
F2-1
F2-3
F3-1
F3-2
F3-3
F4-2
F4-1
F4-3

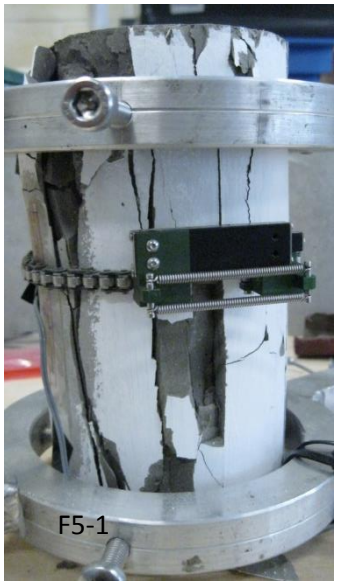
F5-1


F5-2


F5-3


F5S8-1


F5S8-2


F5S8-3


F5S5-1


F5S5-2


F5S5-3


F5S3-1


F5S3-2


F5S3-3


1F5F2


2F5F2


3F5F2


1F5F3


3F5F3


F6-1


F6-2


F6-3


F7-1


F7-2


F7-3

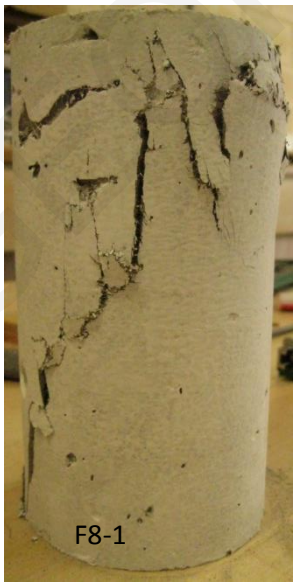
F8-1


F8-2


F8-3


F9-7


F9-8


F9-9


F10-5


F14G-1


F14G-2


F14G-3


F14G2-1


F14G2-2


F14G2-3


F14C1-1


F14C1-2


F14C1-3

4B3: Split cylinder test results

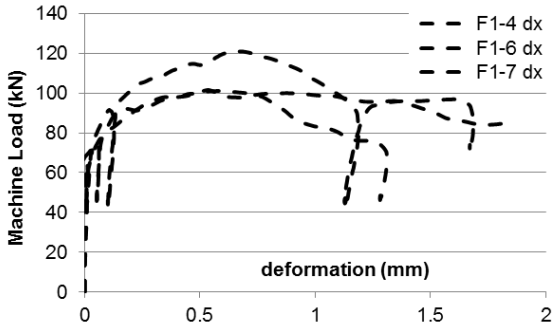

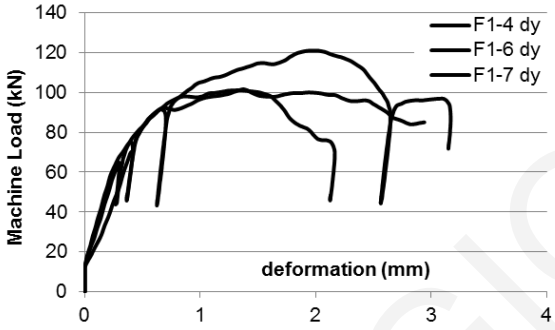

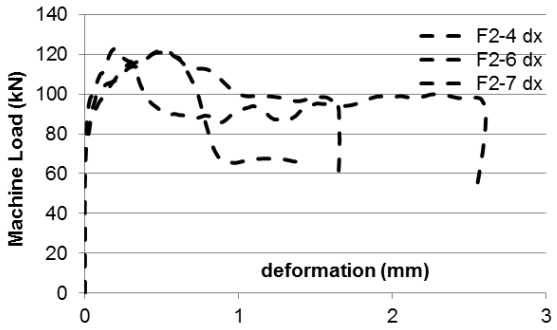

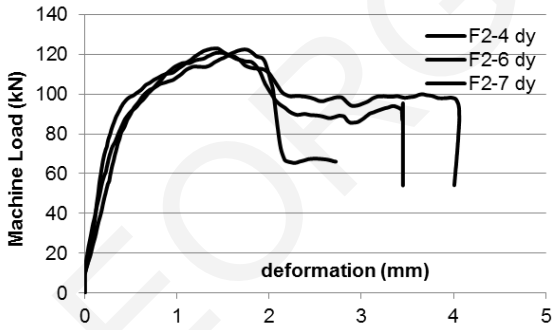

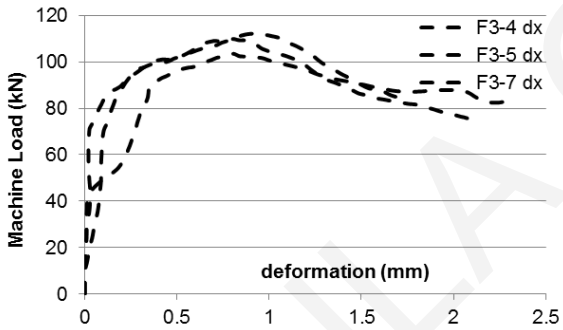

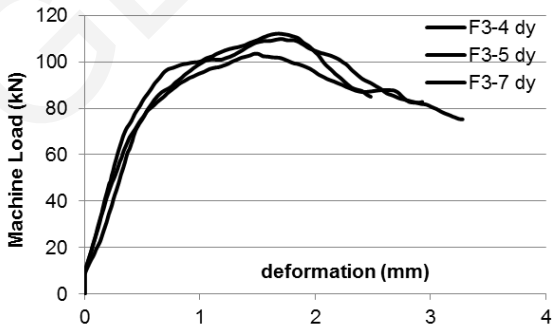

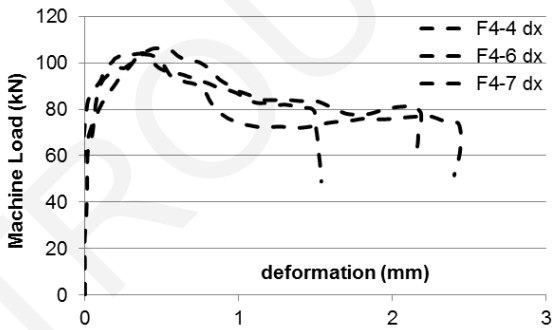

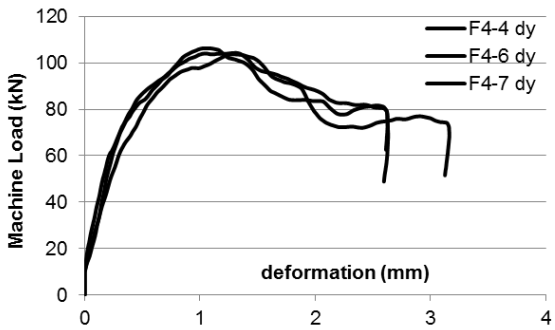

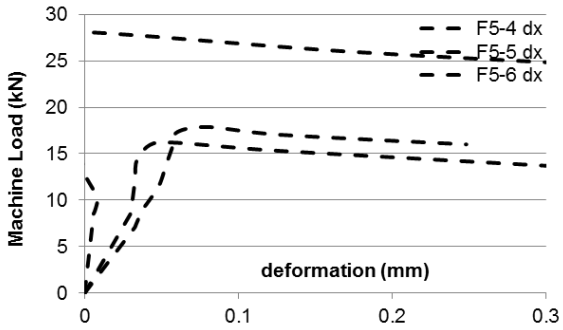

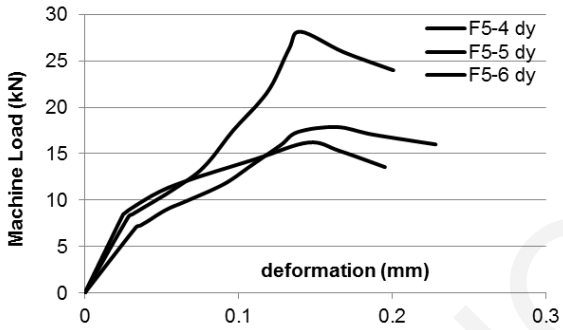

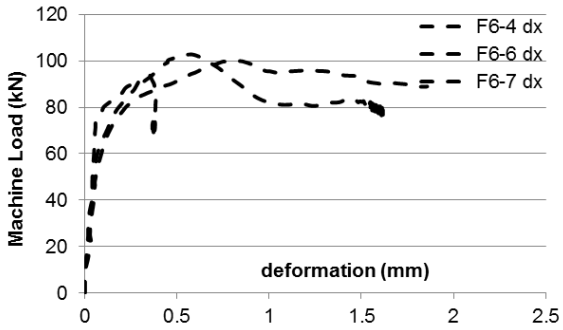

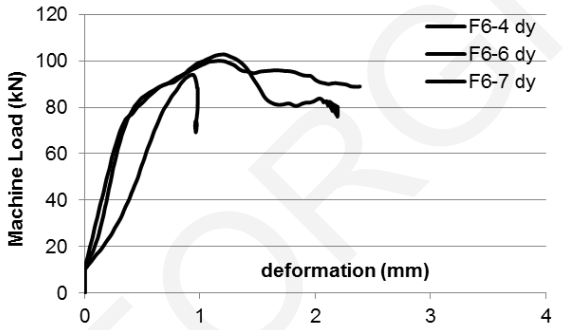

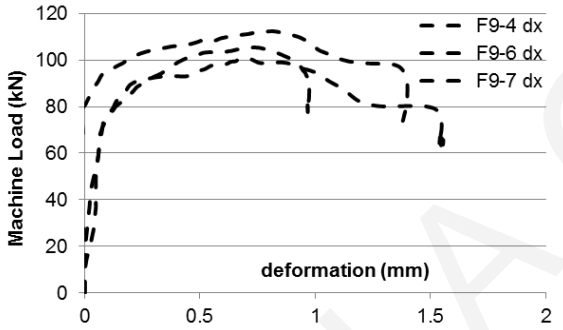

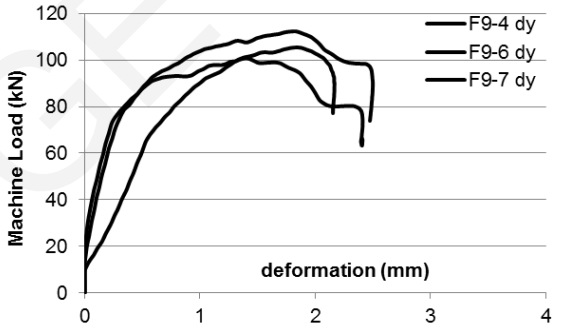

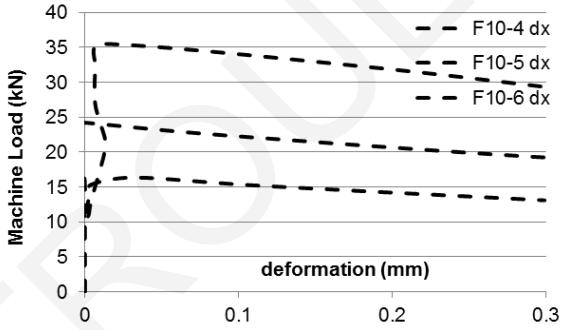

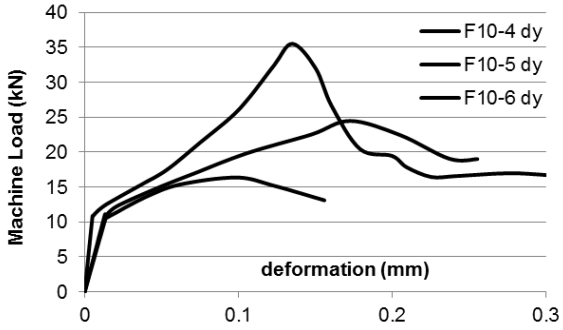

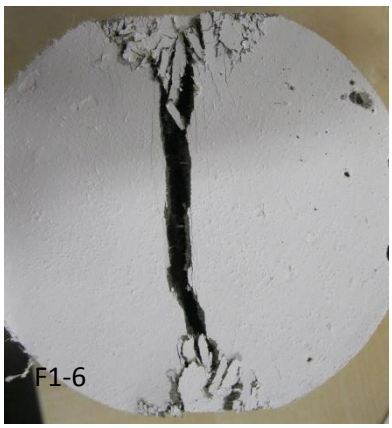
F1-6

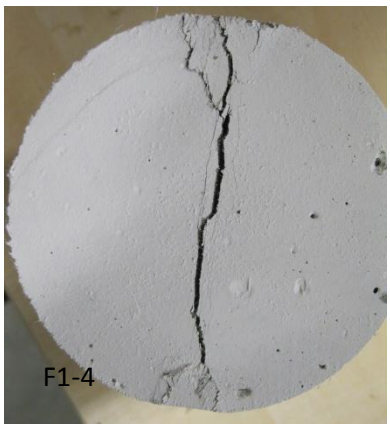
F1-4

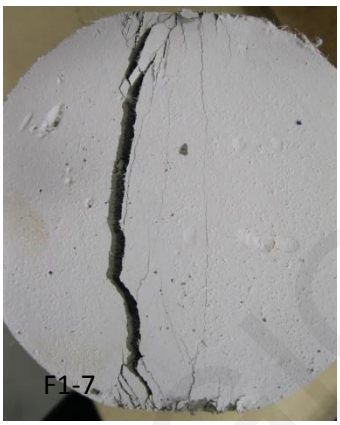
F1-7

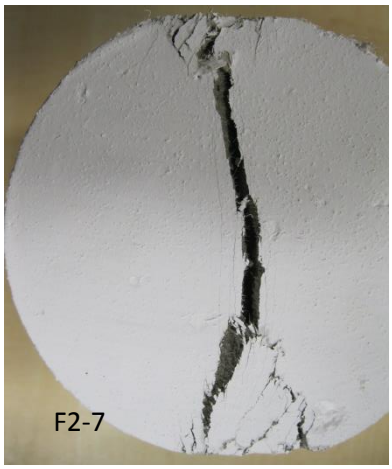
F2-7

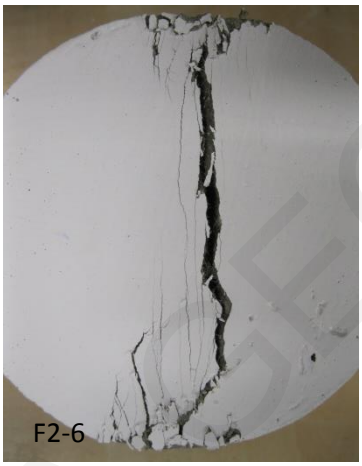
F2-6


F2-5

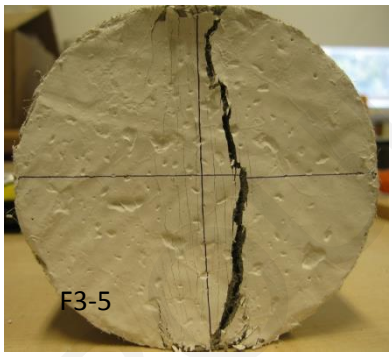
F3-5

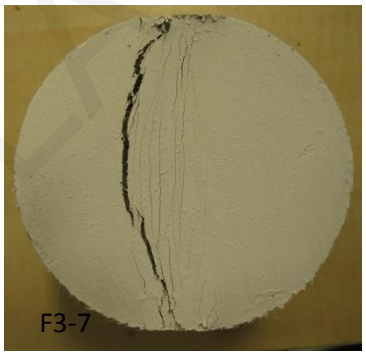
F3-7

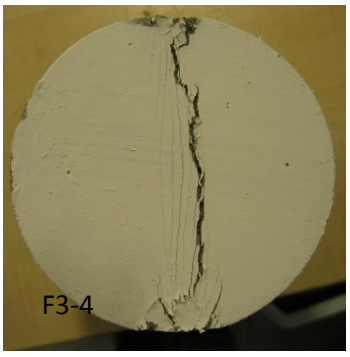
F3-4

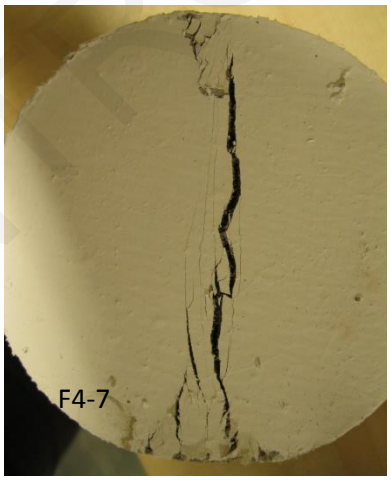
F4-7

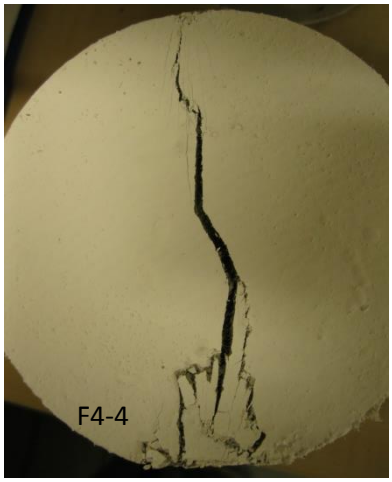
F4-4

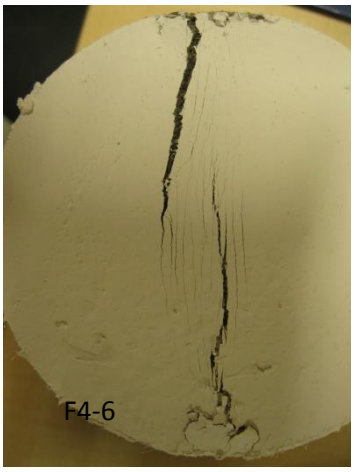
F4-6

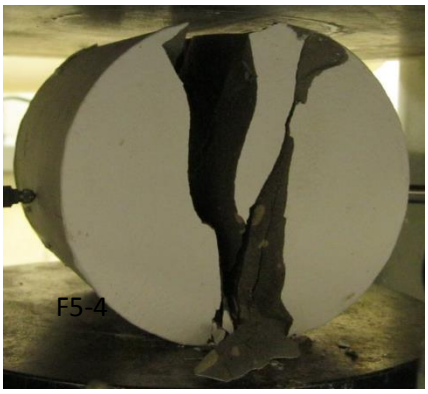
F5-4

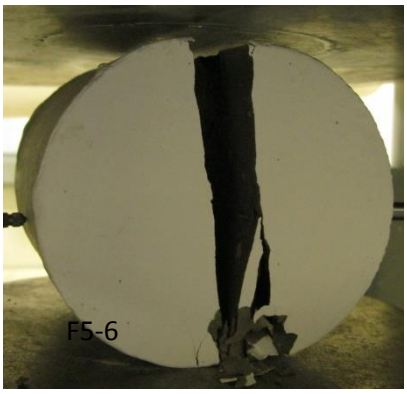
F5-6

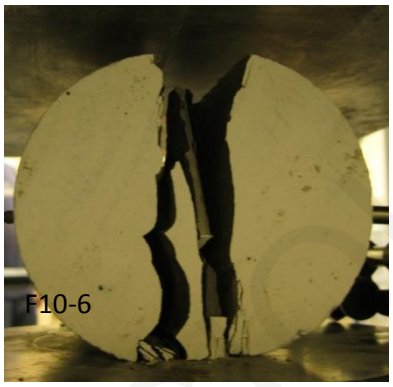
F10-6

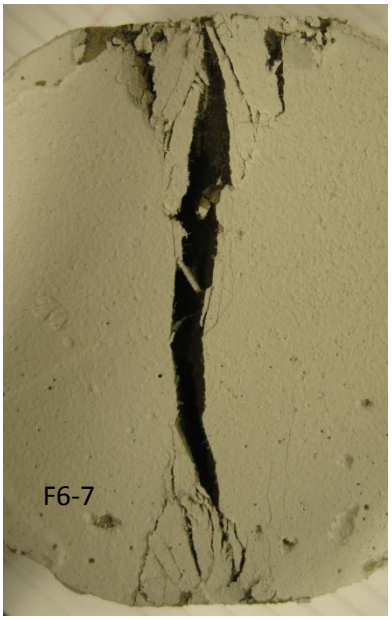
F6-7

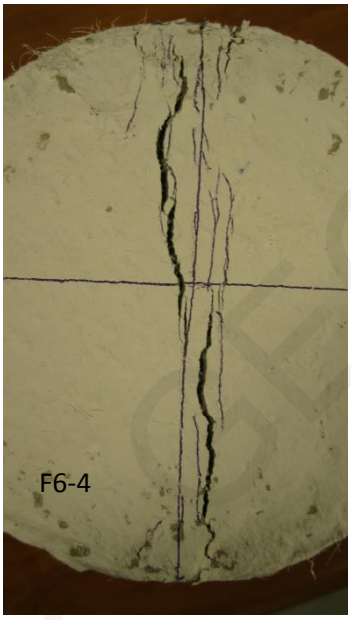
F6-4

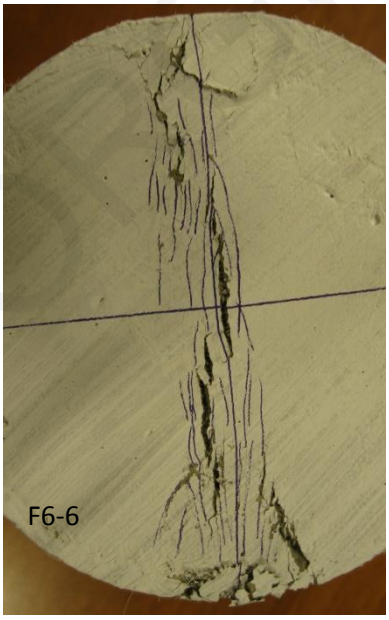
F6-6


F9-4

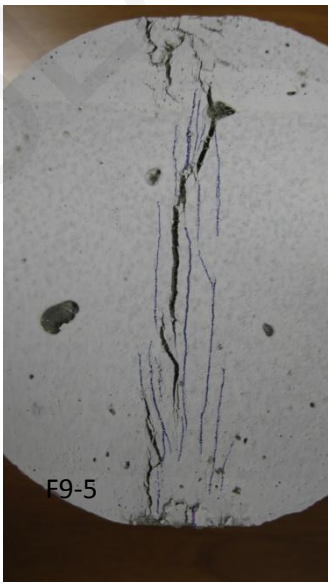
F9-5

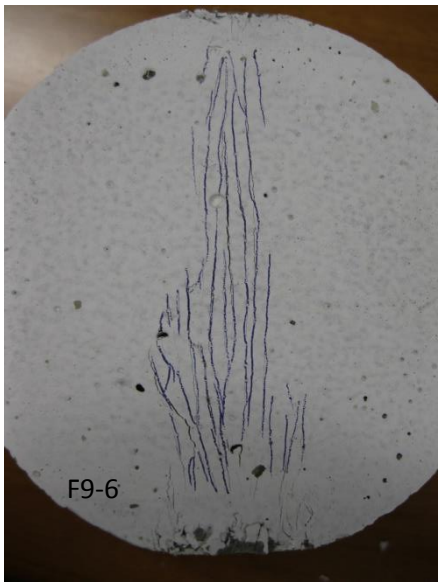
F9-6

4B4: Three point bending test results

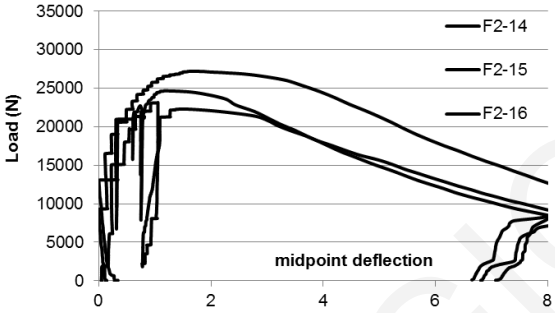

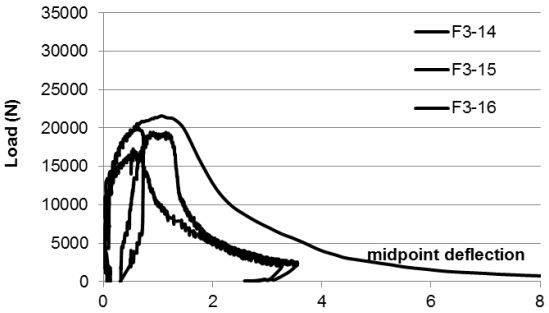

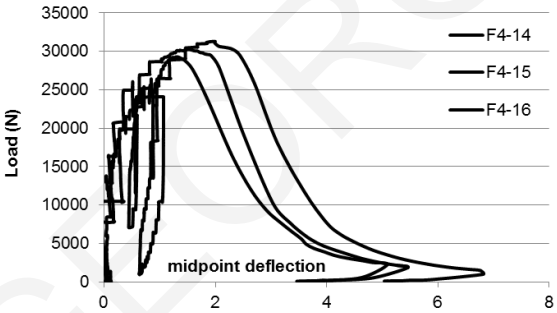

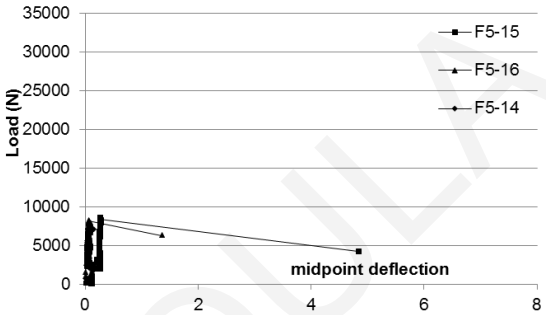

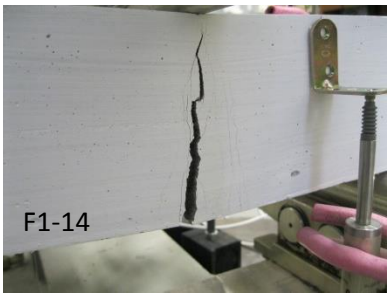
F1-14

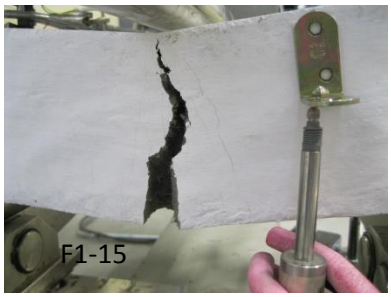
F1-15

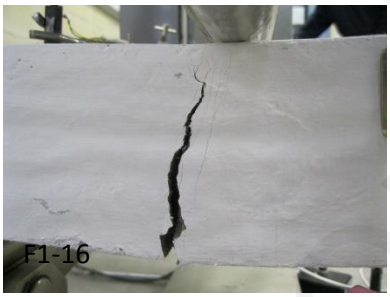
F1-16

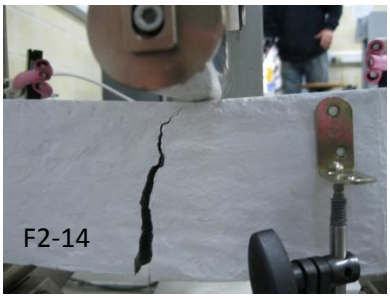
F2-14

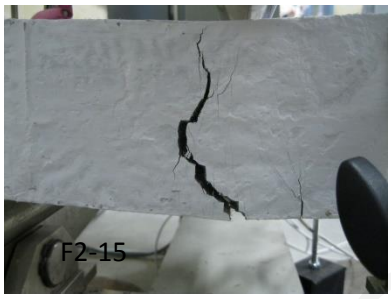
F2-15

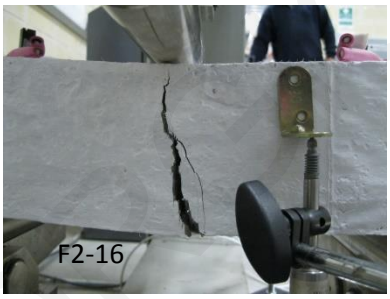
F2-16

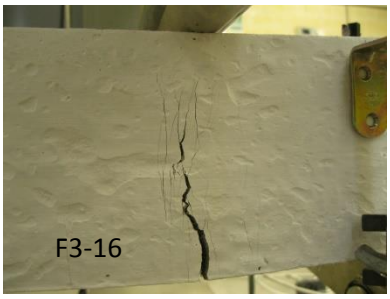
F3-16

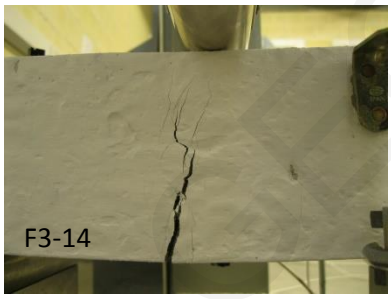
F3-14

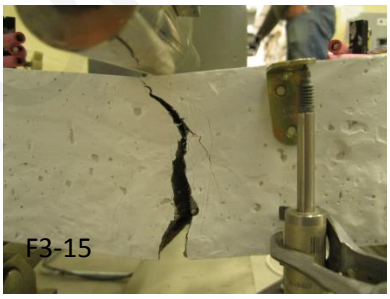
F3-15

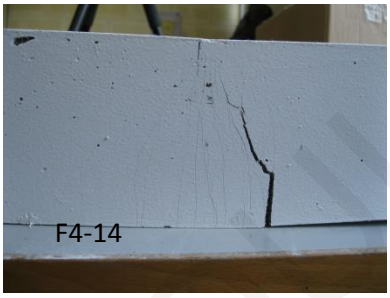
F4-14

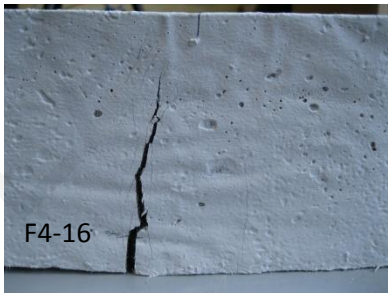
F4-16


F4-15

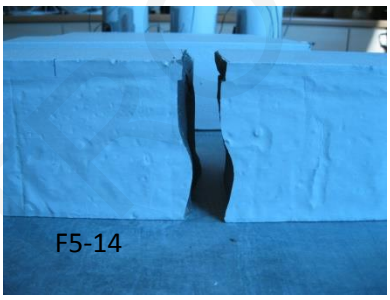
F5-14

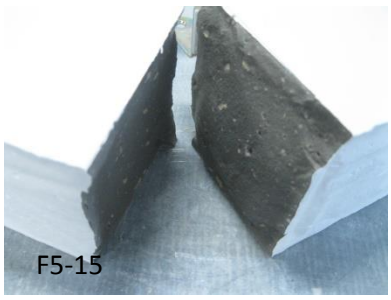
F5-15

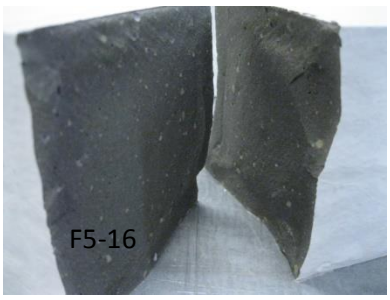
F5-16

4B5: Four point bending test results (beams without steel reinforcement)

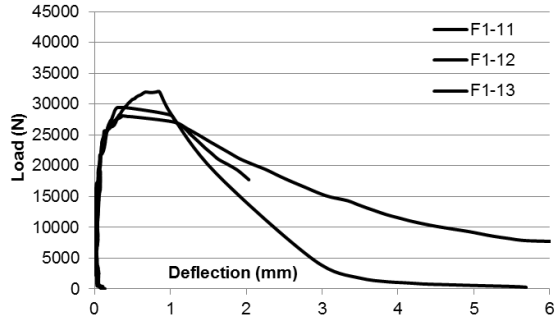

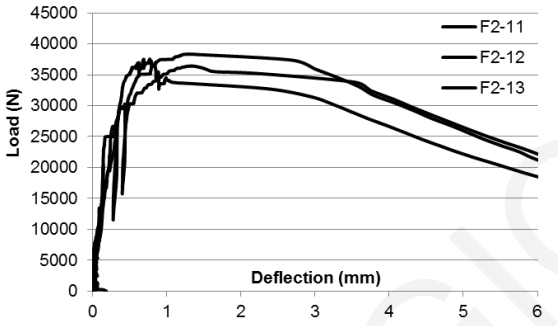

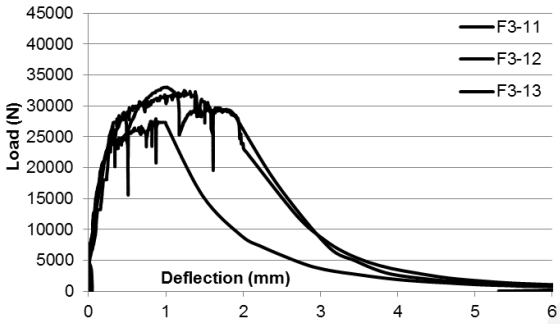

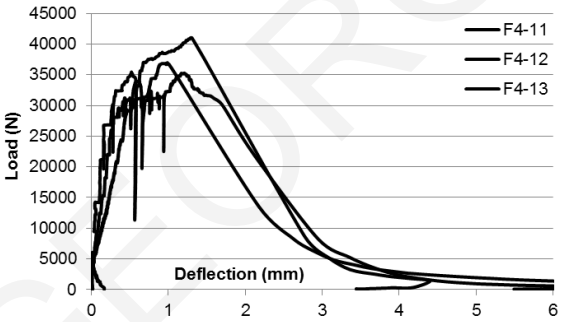

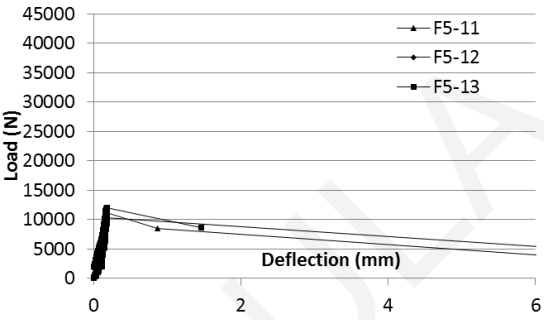

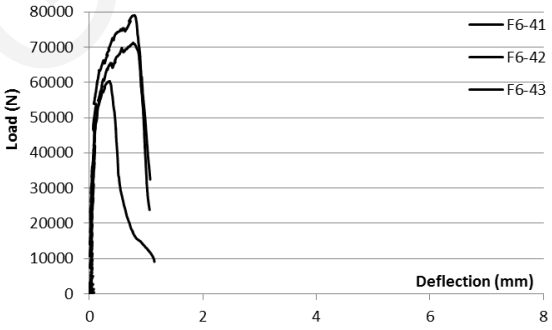

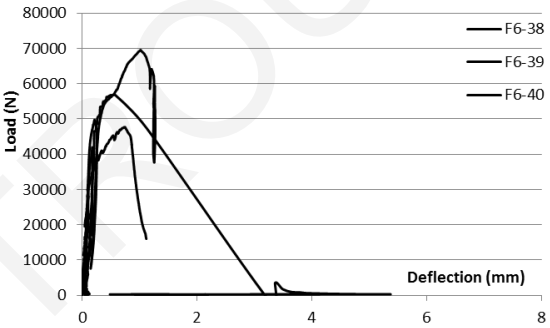

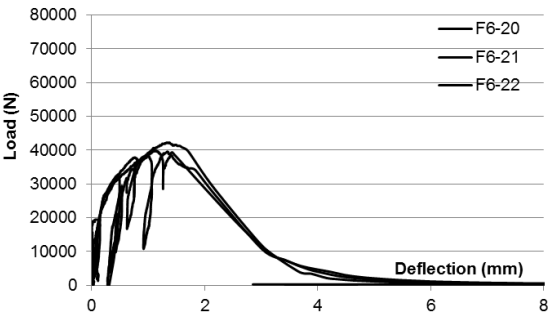

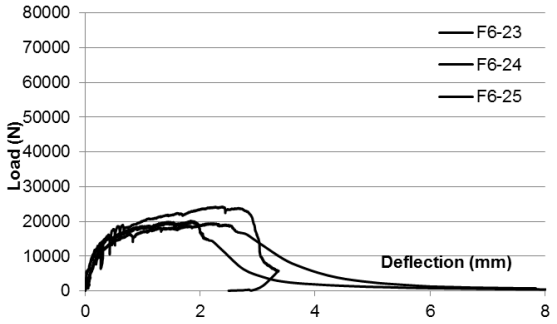

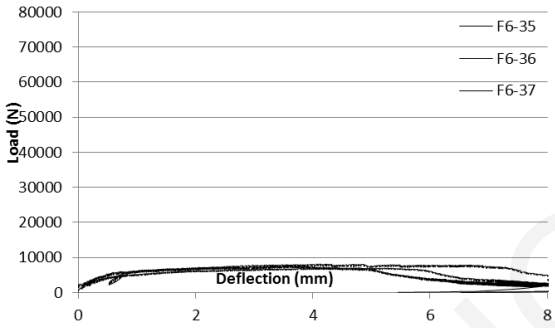

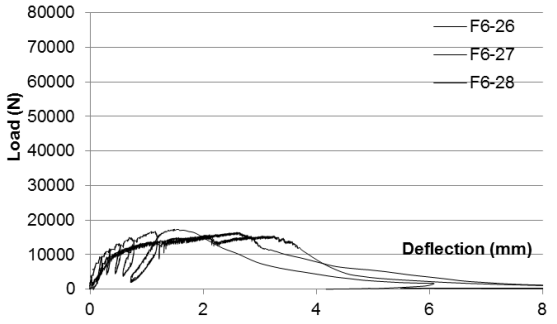

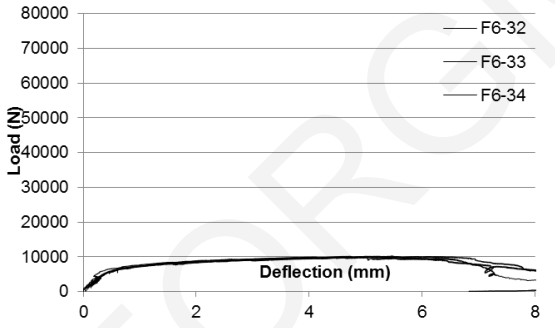

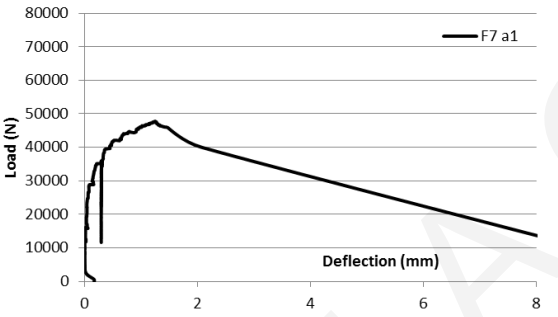

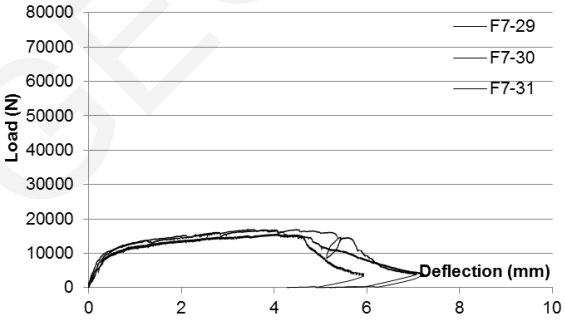

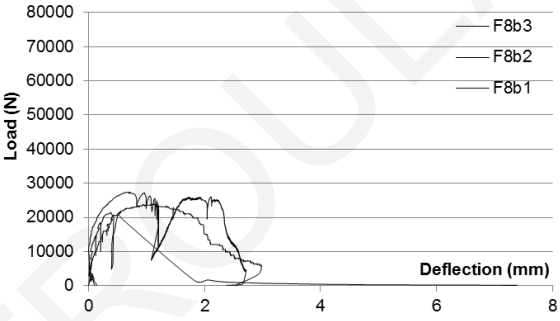

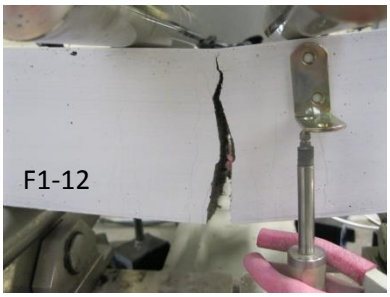
F1-12

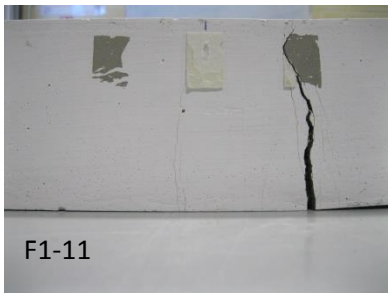
F1-11

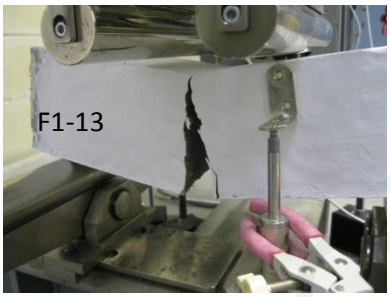
F1-13

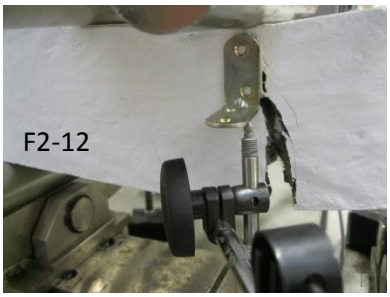
F2-12

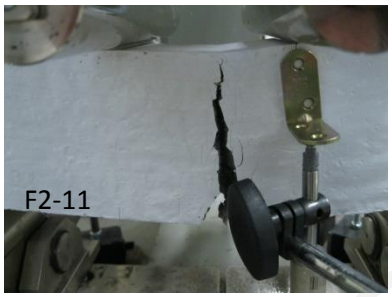
F2-11

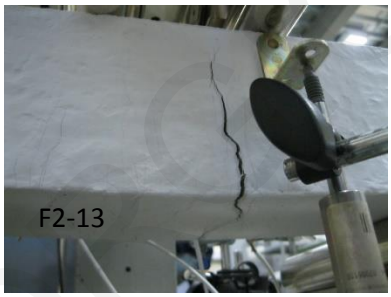
F2-13

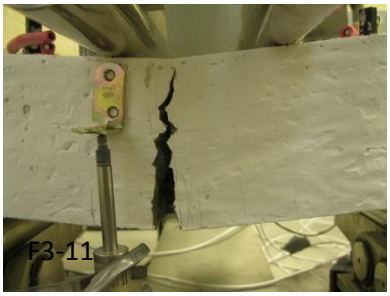
F3-11

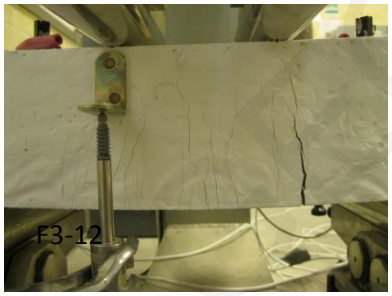
F3-12

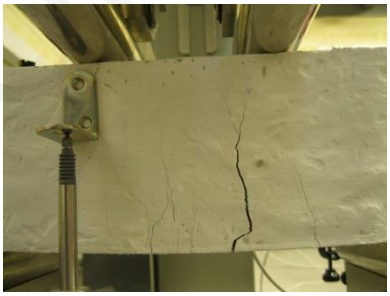

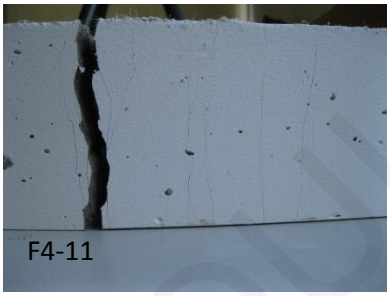
F4-11

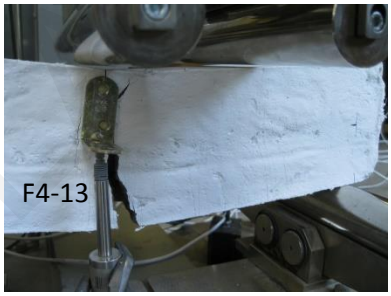
F4-13

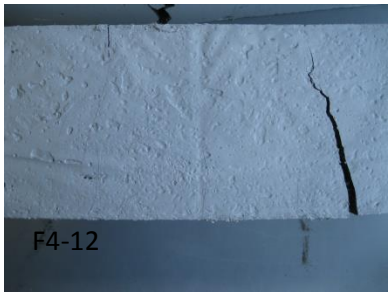
F4-12

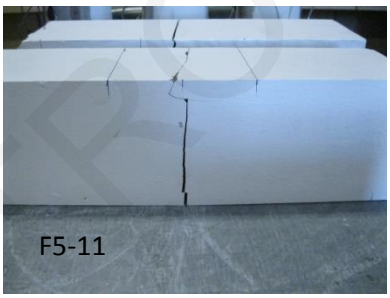
F5-11


F5-12

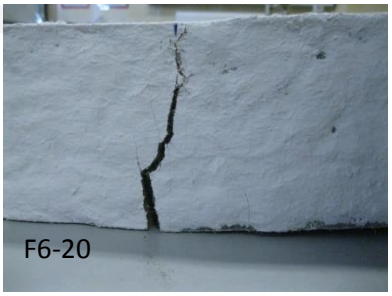
F6-20

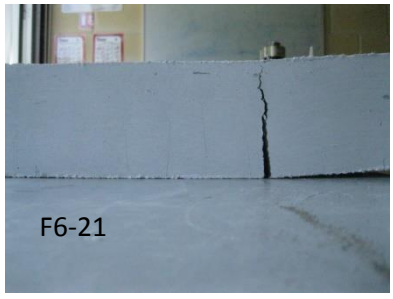
F6-21

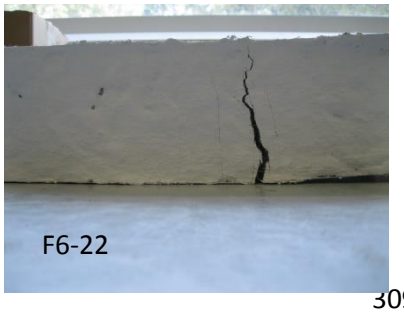
F6-22


F6-23


F6-24

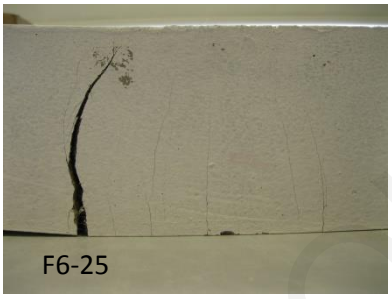
F6-25


F6-26

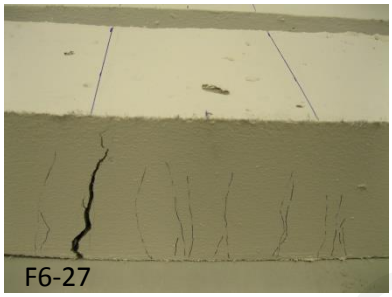
F6-27

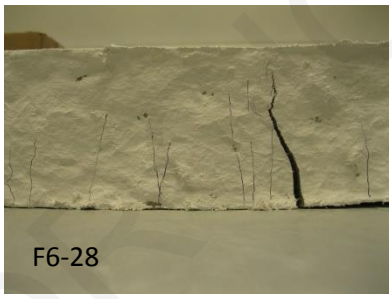
F6-28


F7-29


F7-30

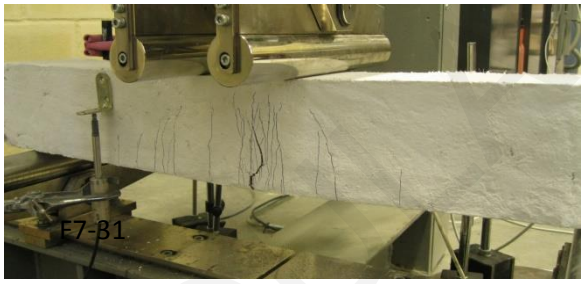
F7-31


F6-32

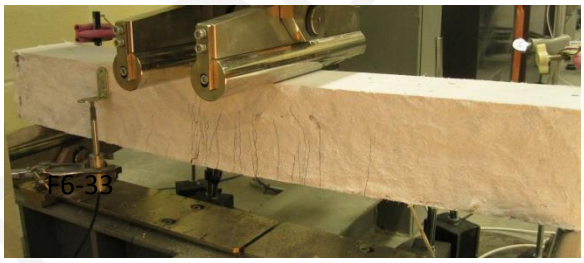
F6-33


F6-34

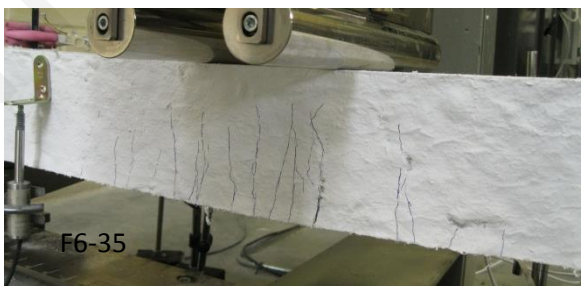
F6-35

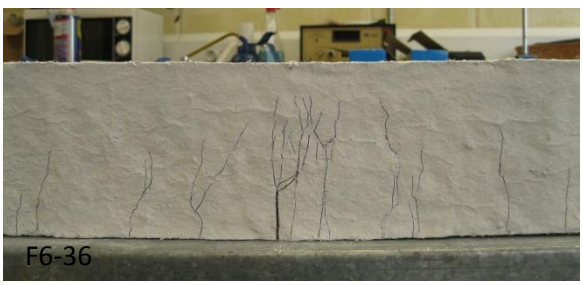
F6-36

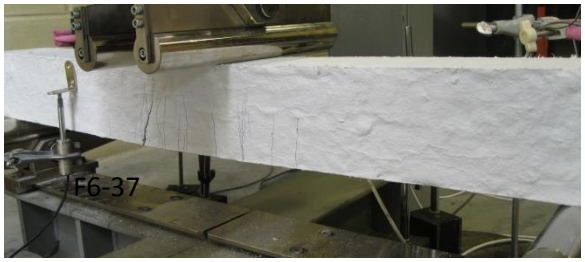
F6-37

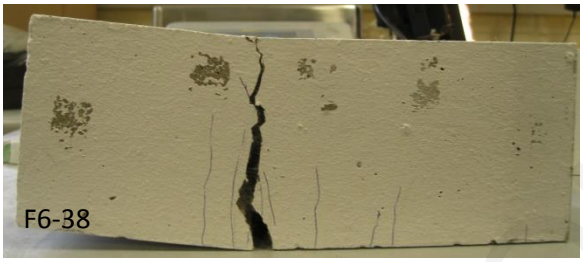
F6-38


F6-39


F6-42

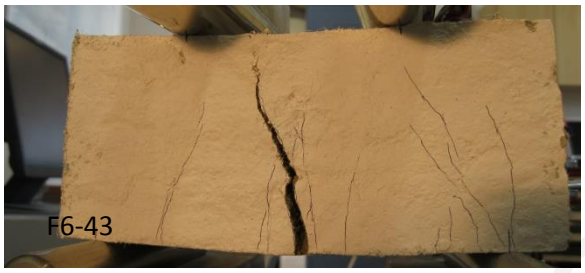
F6-43

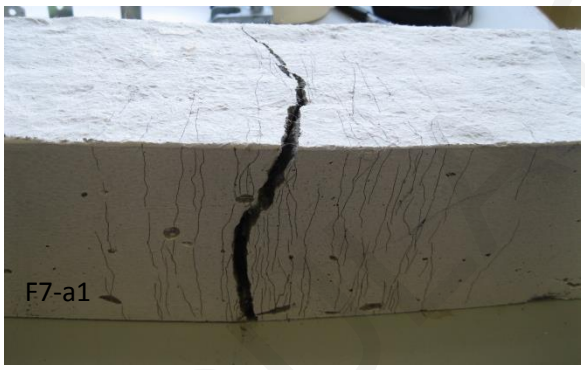
F7-a1

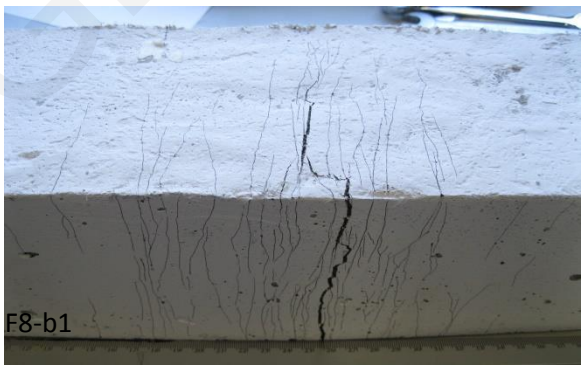
F8-b1


F8-b2


F8-b3

4B6: Four point bending test results (beams with steel reinforcement)

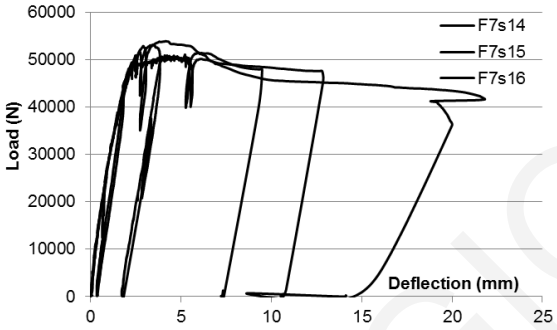

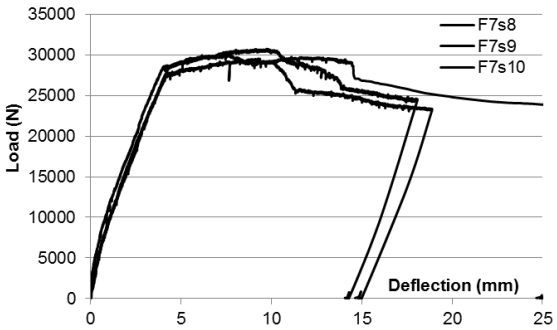

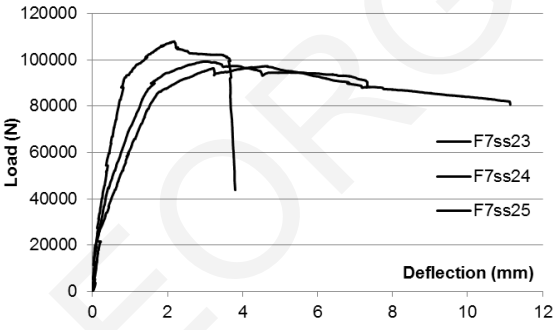

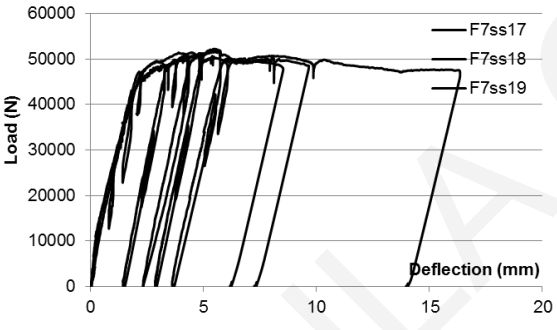

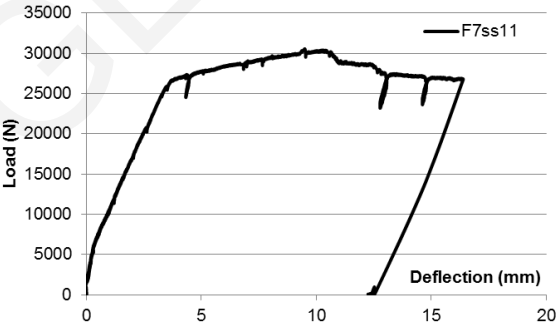

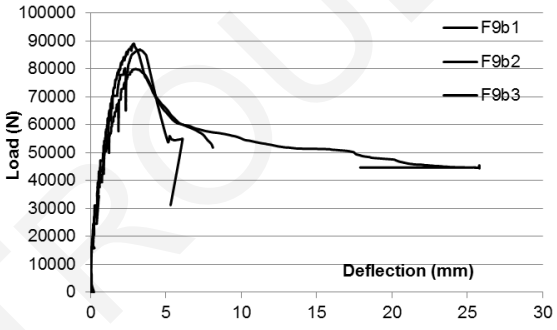

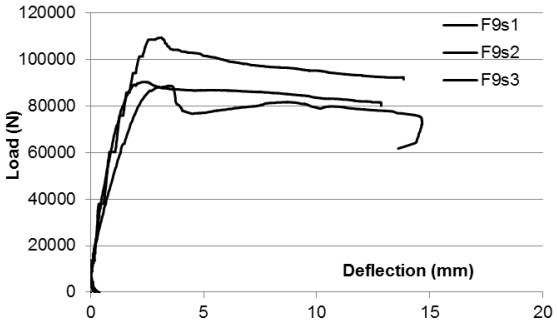

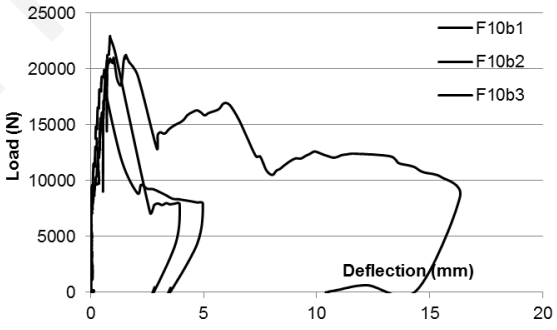

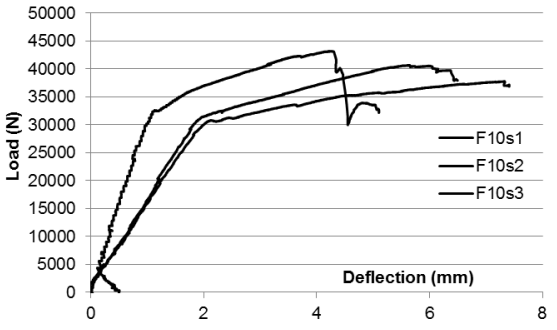

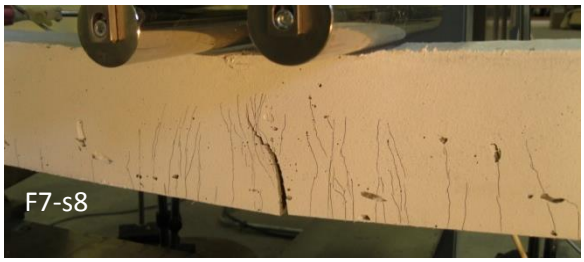
F7-s8

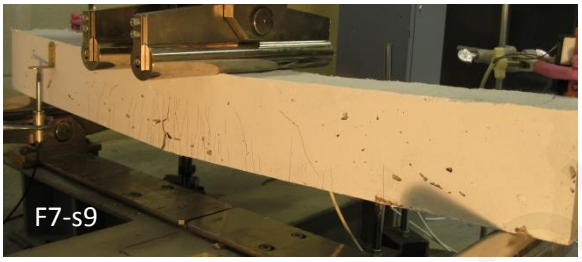
F7-s9

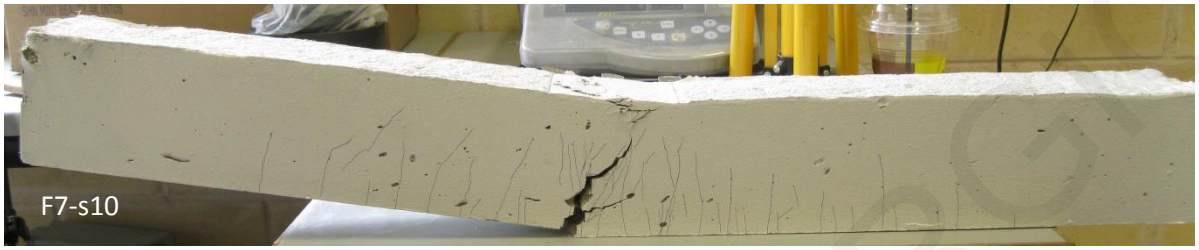
F7-s10

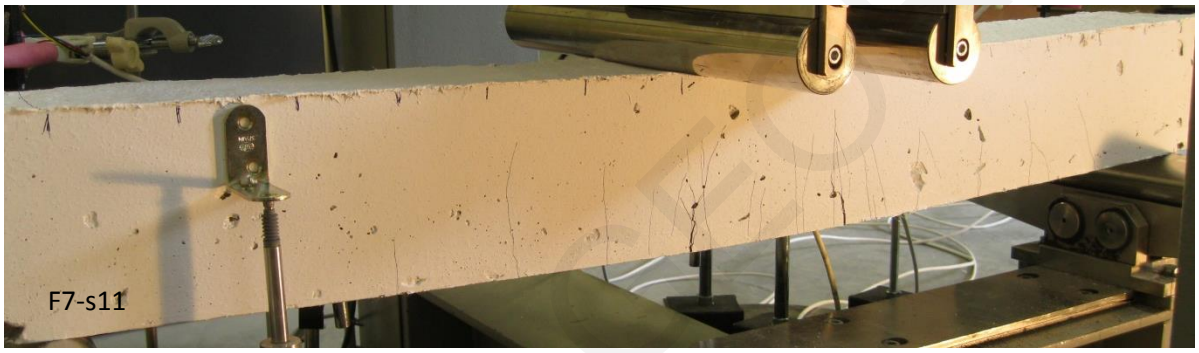
F7-s11


F7-s14


F7-ss19


F7-ss18

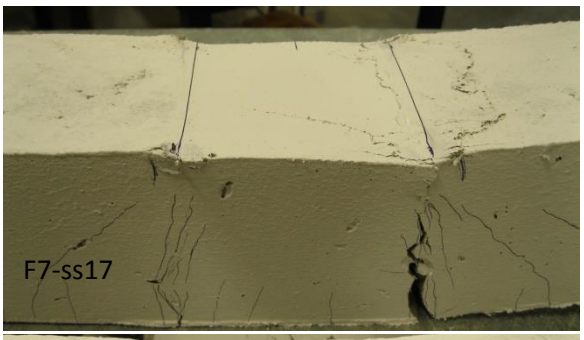
F7-ss17

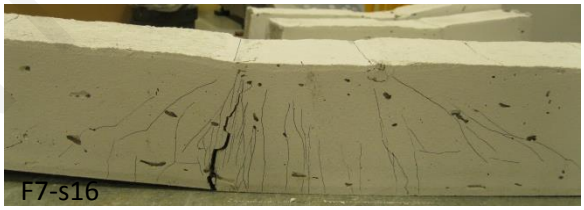
F7-s16

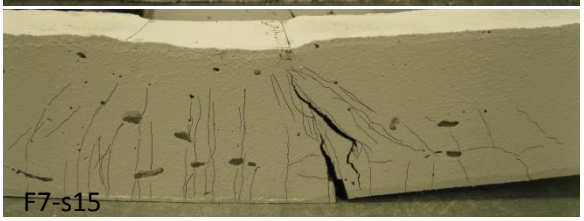
F7-s15

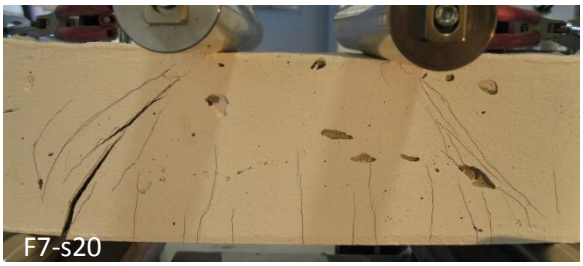
F7-s20

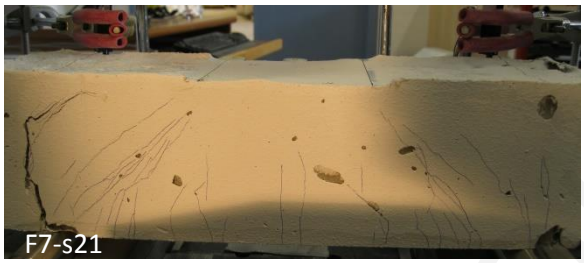
F7-s21

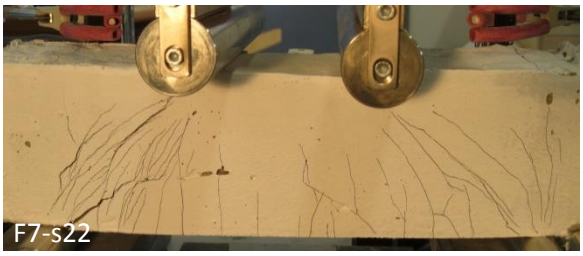
F7-s22

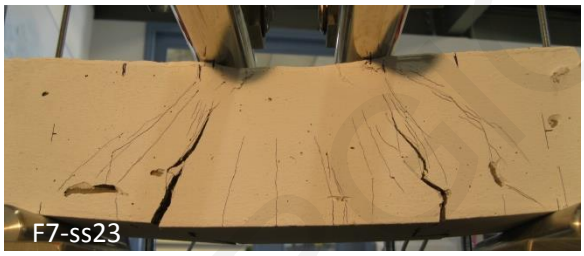
F7-ss23

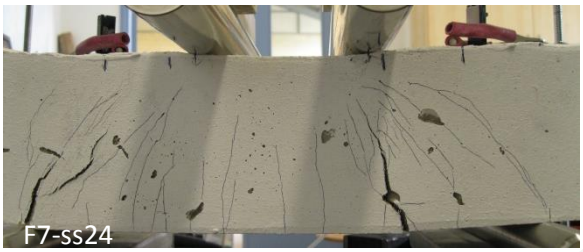
F7-ss24


F7-ss25


F9-b1


F9-b2


F9-b3

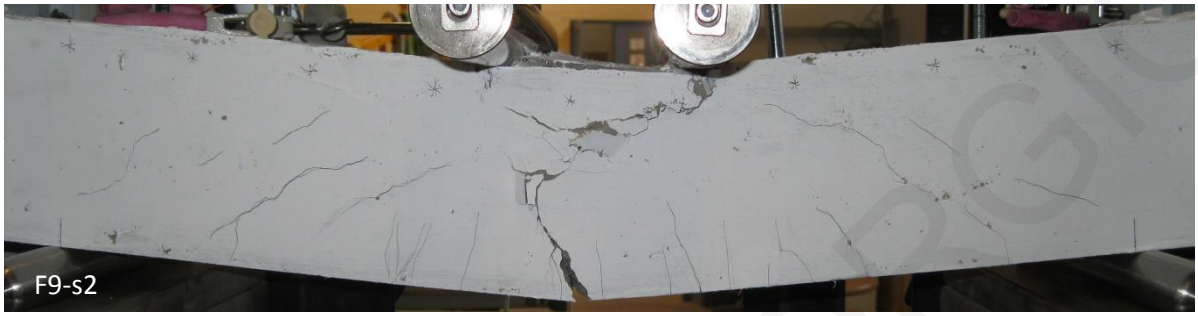

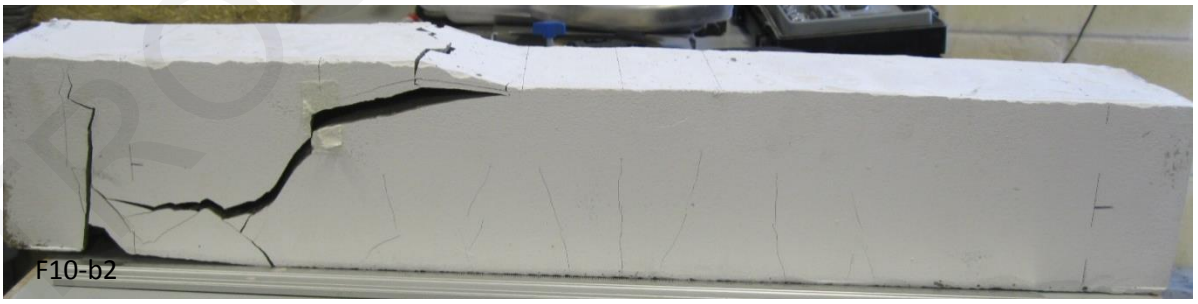

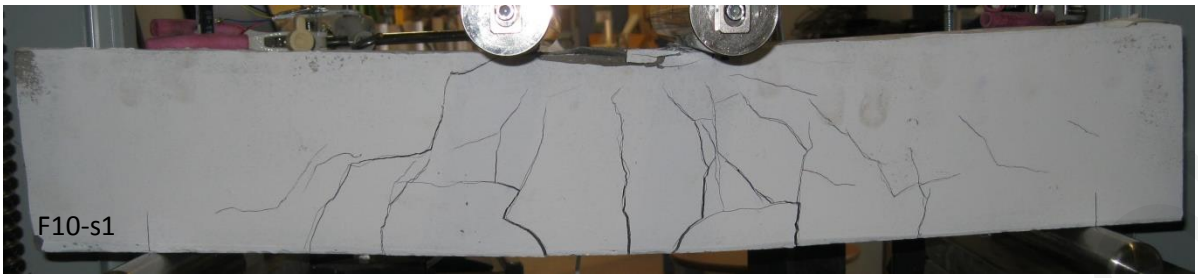

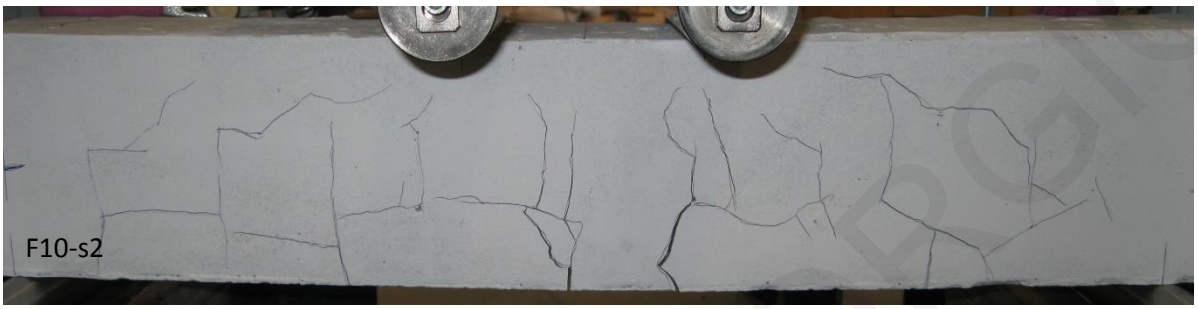

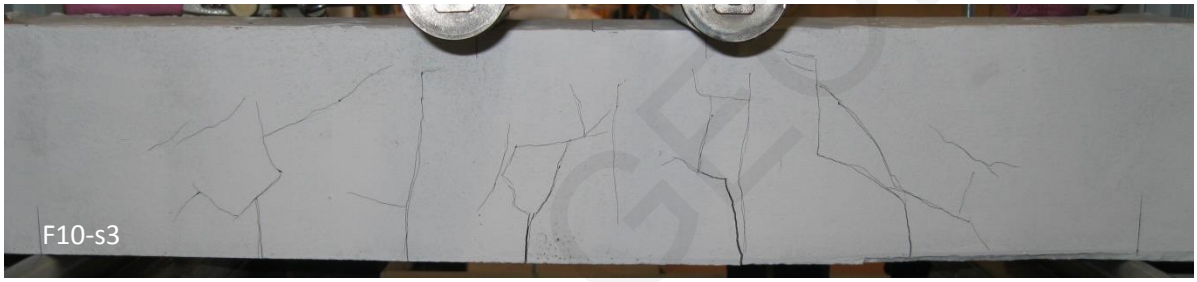

4B7: Push-off test results

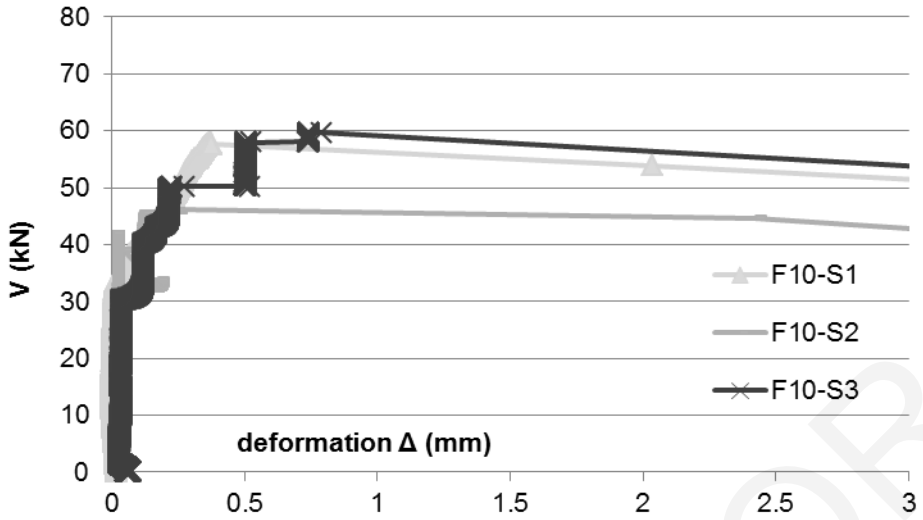

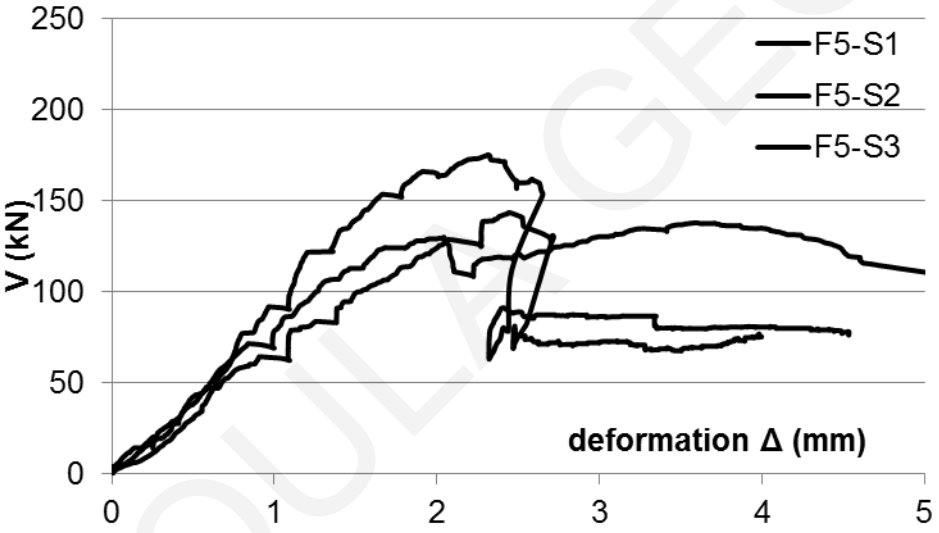

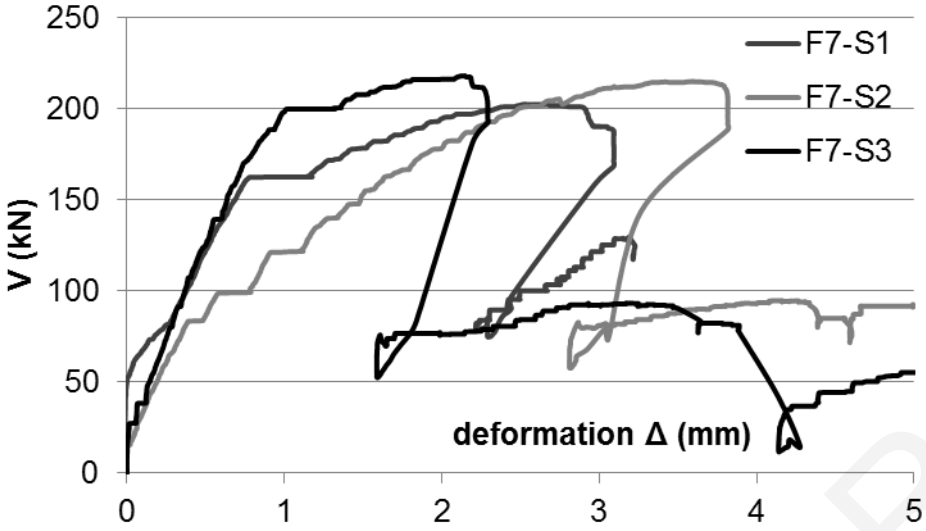

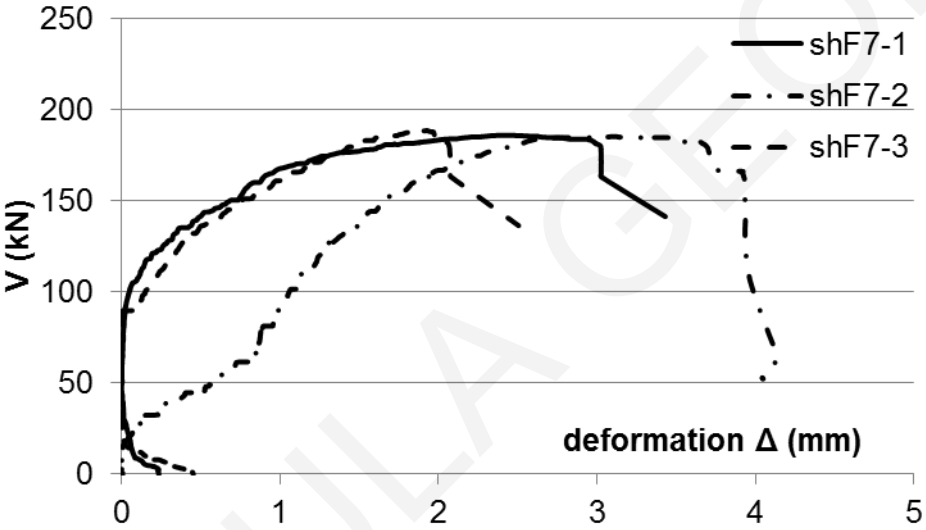


F7-s1


F7-s2


F7-s3


shF7-1

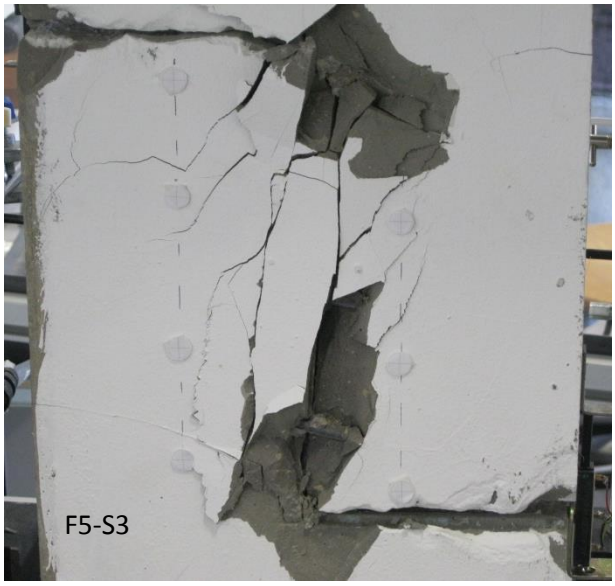
F5-S3


F10-S2


F10-S1

4B8: Pull-out test results

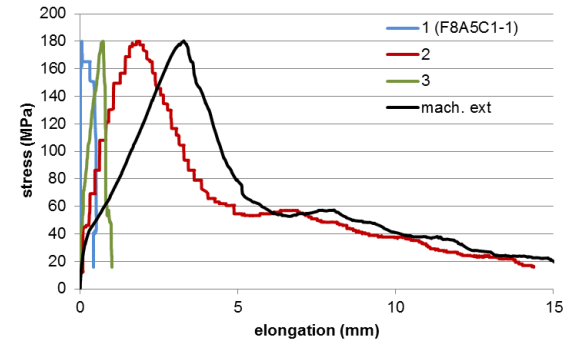

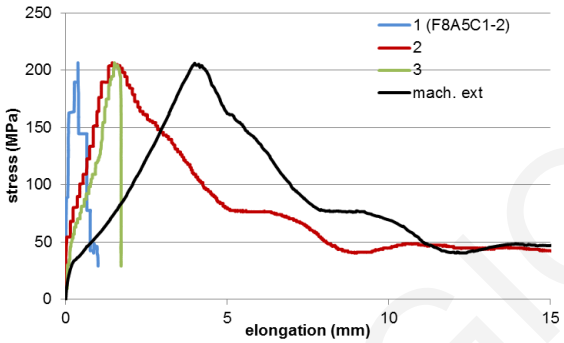

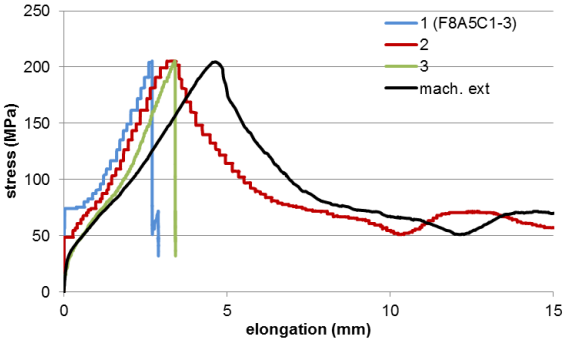

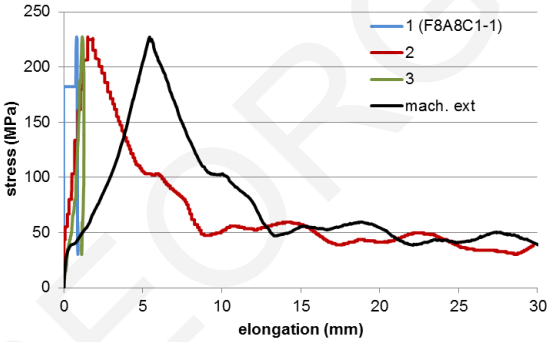

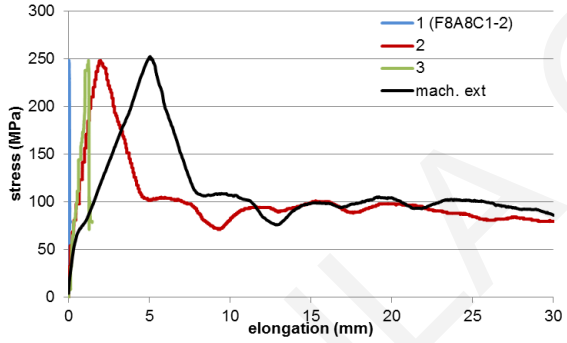

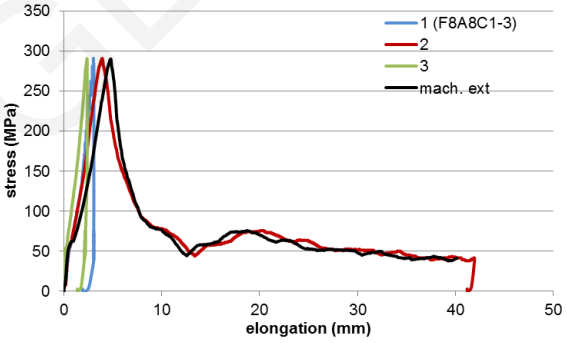

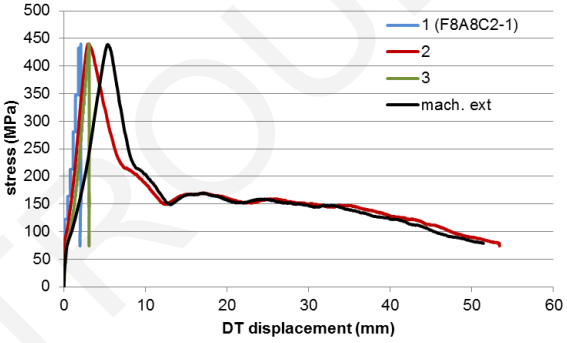

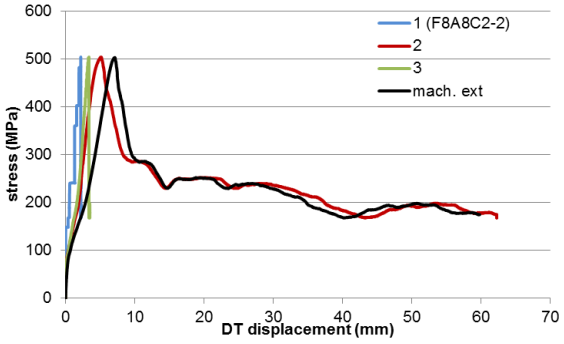

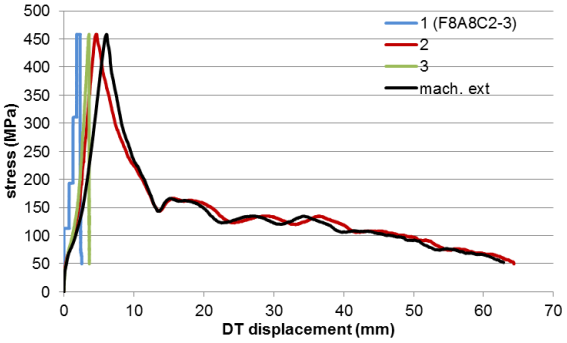

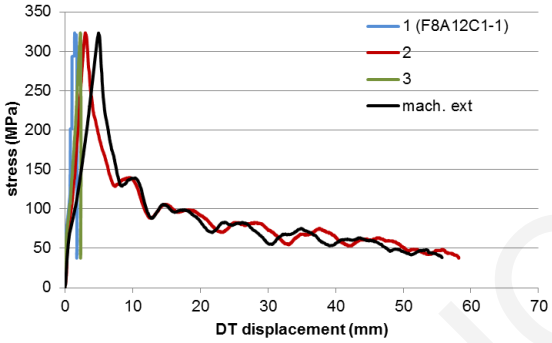

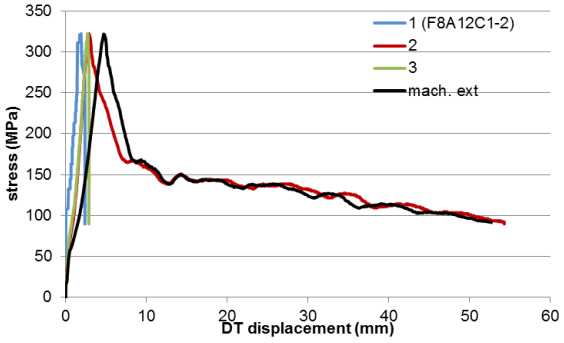

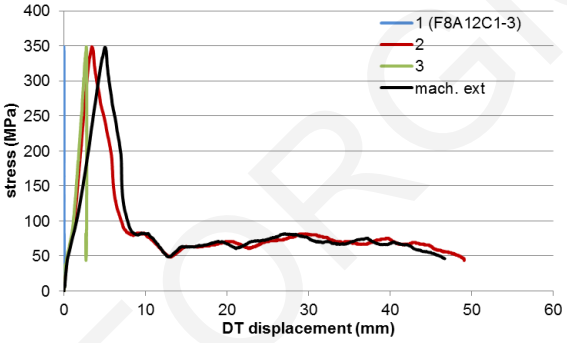

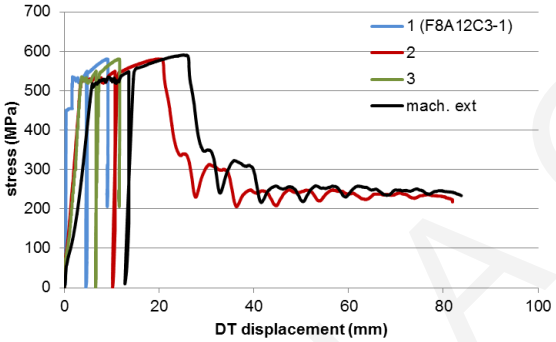

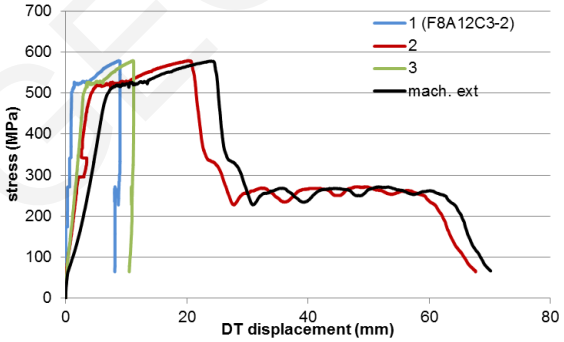

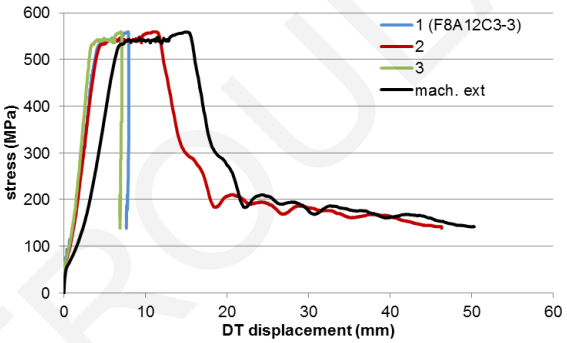

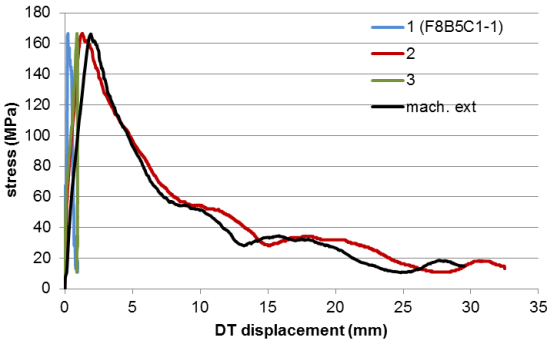

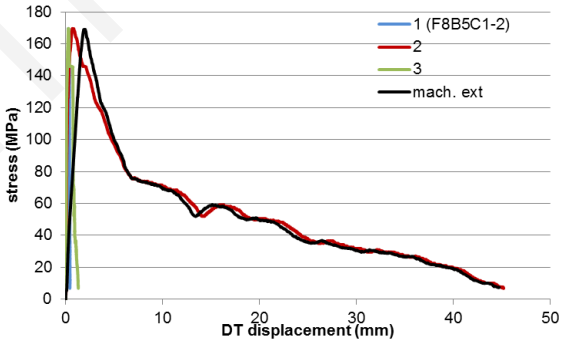

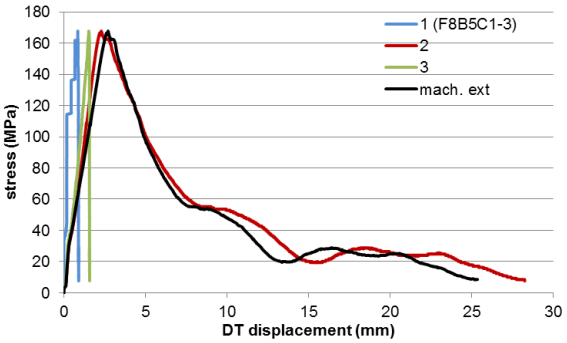

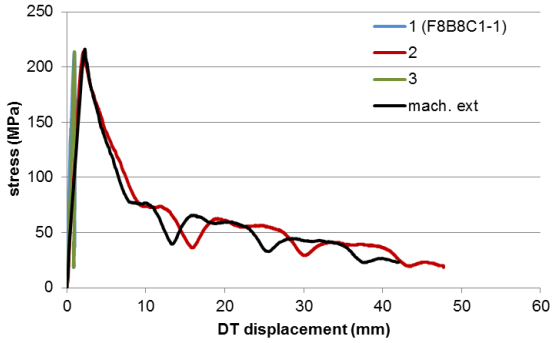

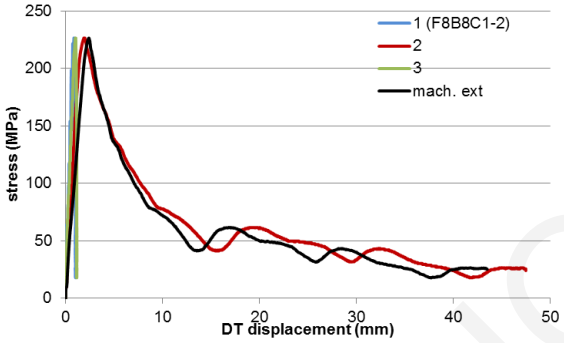

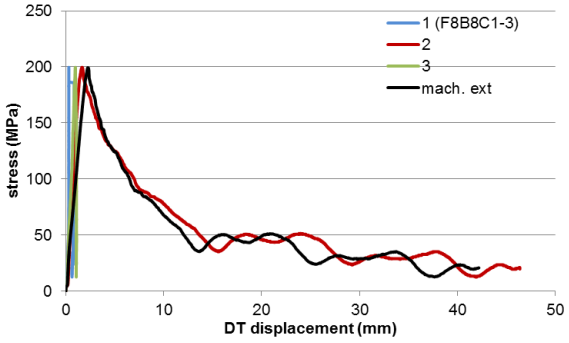

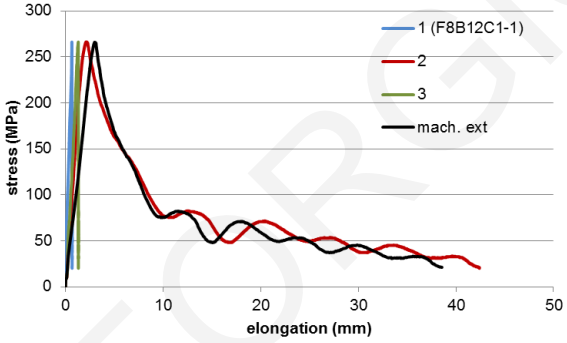

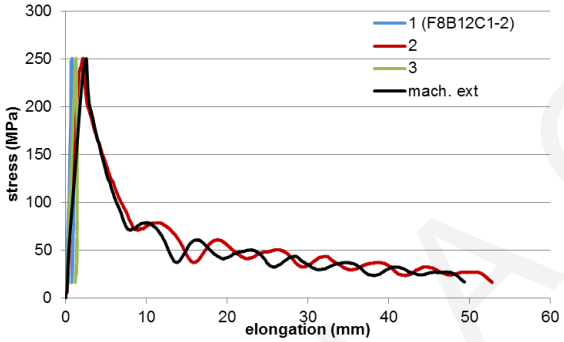

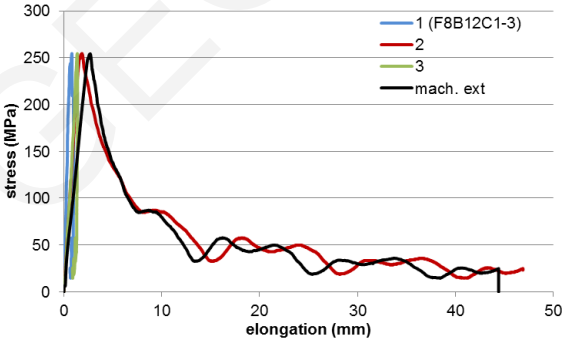

i) F8A5C11

ii) F8A5C12

iii) F8A5C13

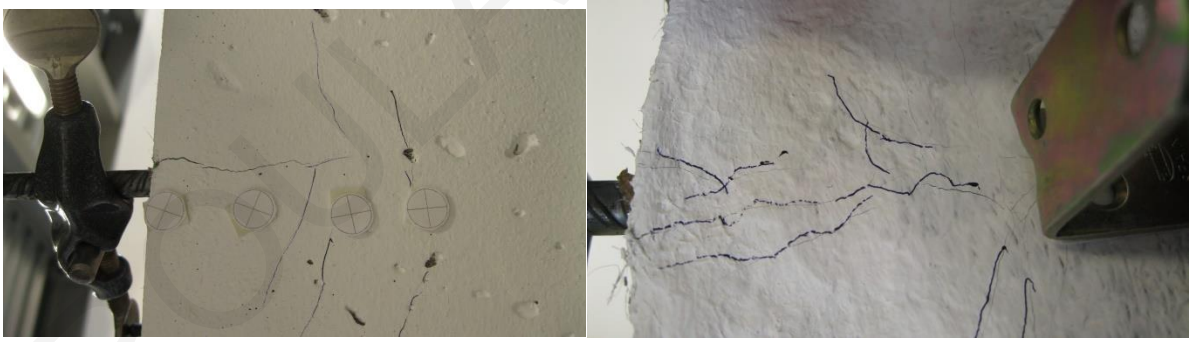

i) F8A8C11

ii) F8A8C12

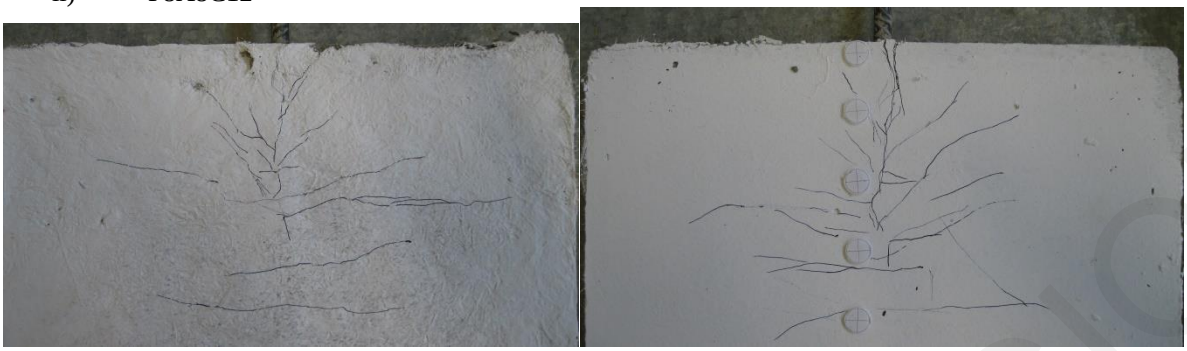

iii) F8A8C13

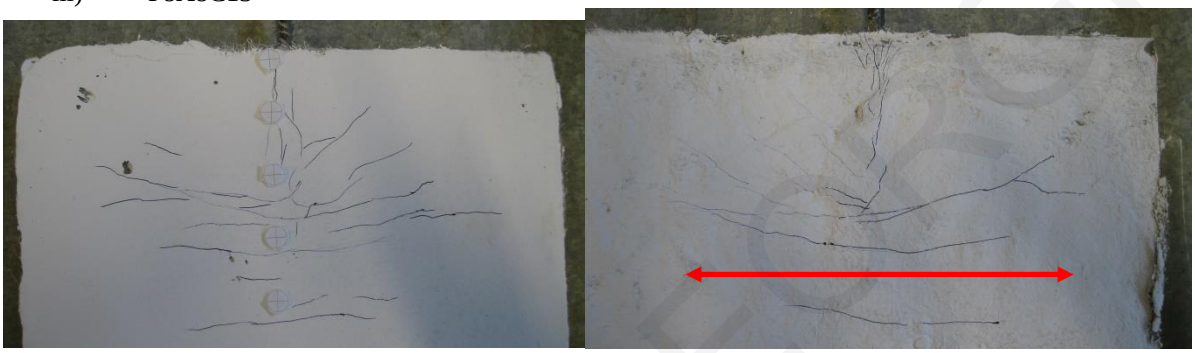

i) F8A8C21

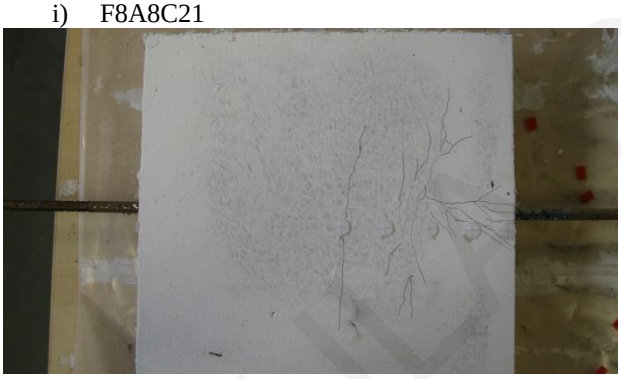

ii) F8A8C22

iii) F8A8C23

i) F8A12C11

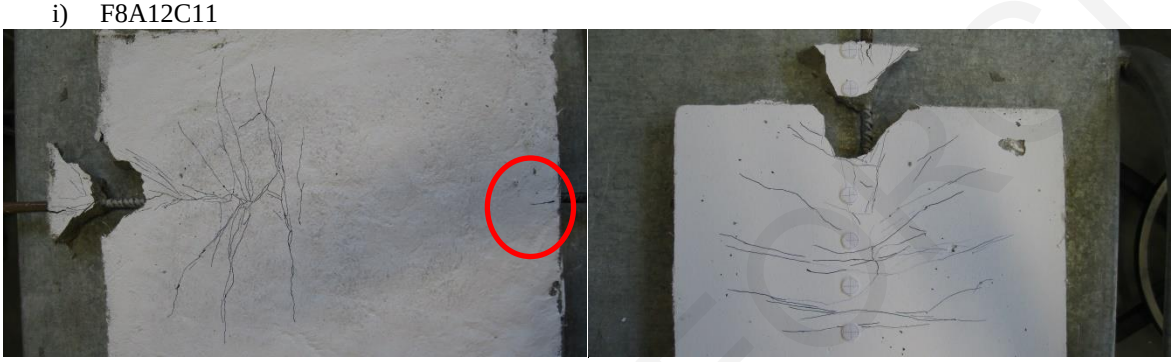

ii) F8A12C12

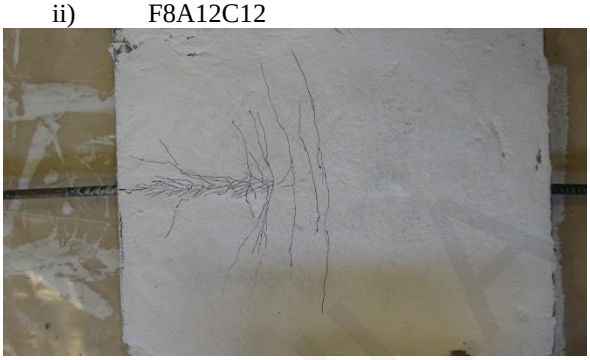

iii) F8A12C13

j) F8A12C31

iv) F8A12C32

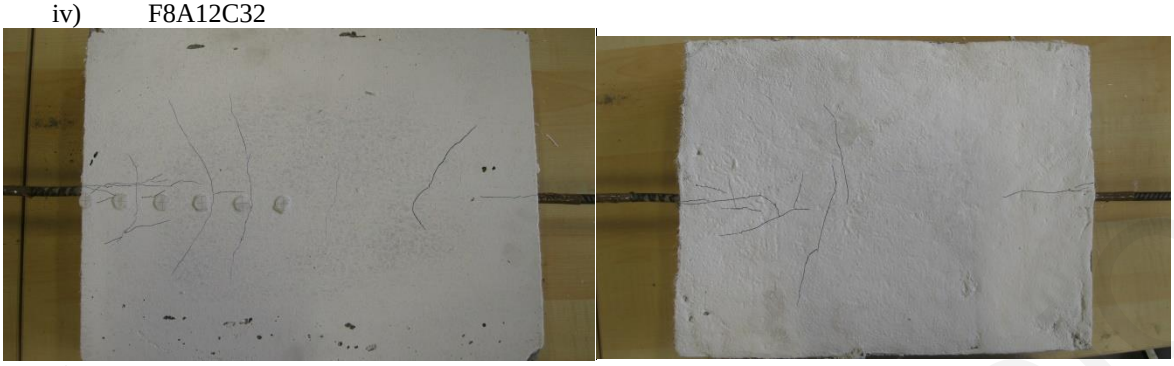

v) F8A12C33

i) F8B5C11

ii) F8B5C12

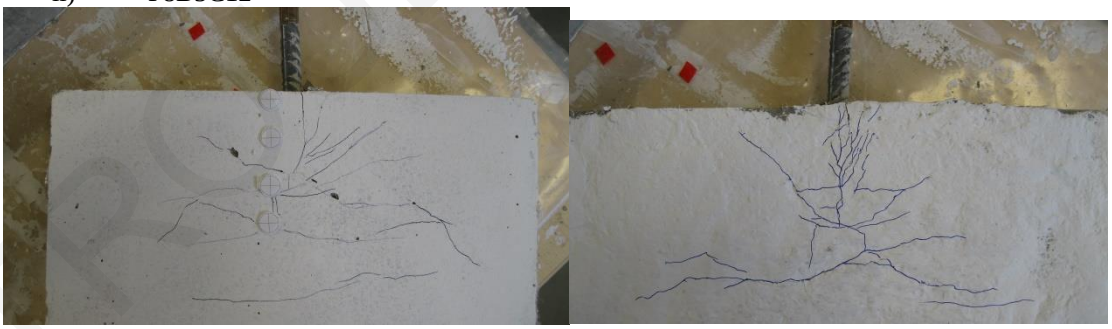

iii) F8B5C13

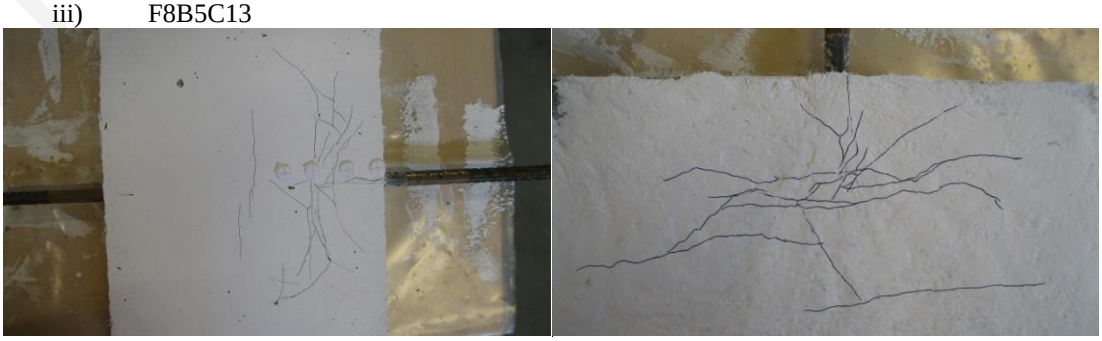

i) F8B8C11

ii) F8B8C12

iii) F8B8C13

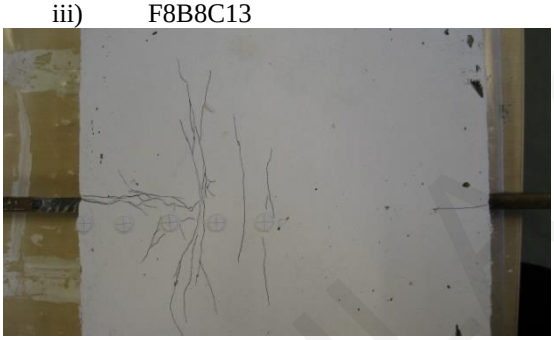

k) F8B12C11

vi) F8B12C12

vii) F8B12C13

APPENDIX 10.A-Control Specimen

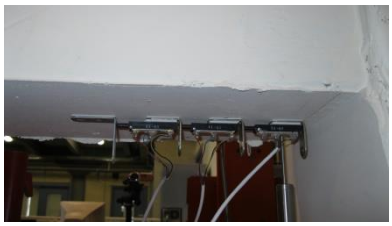

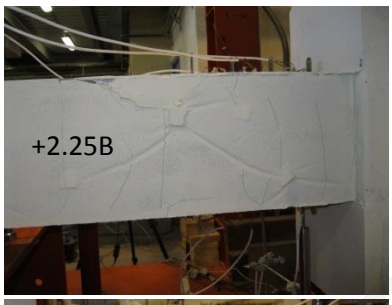

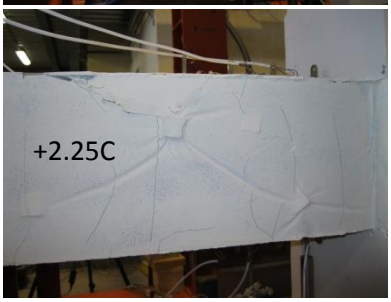

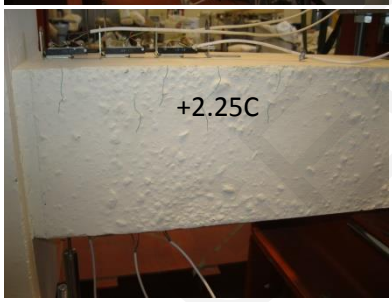

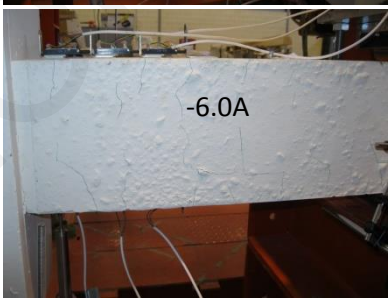

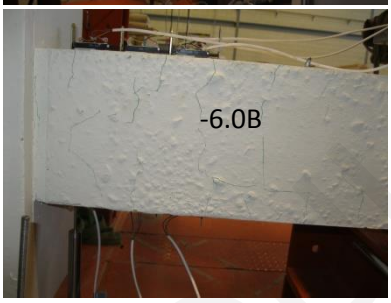

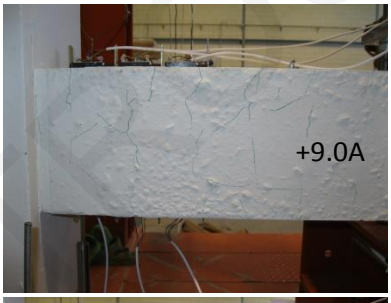

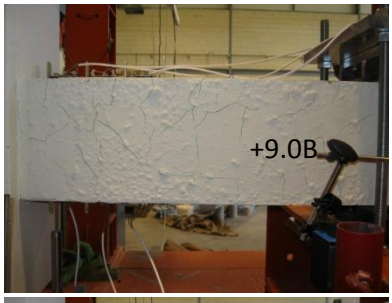

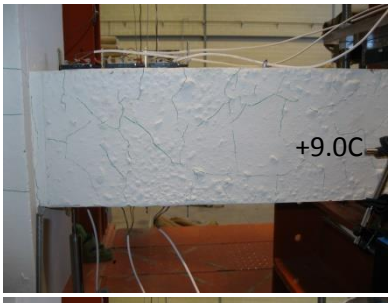

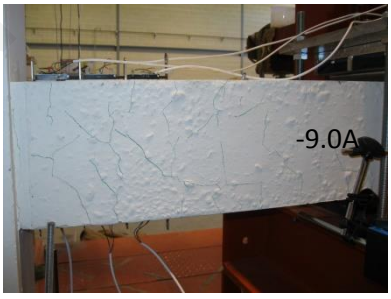

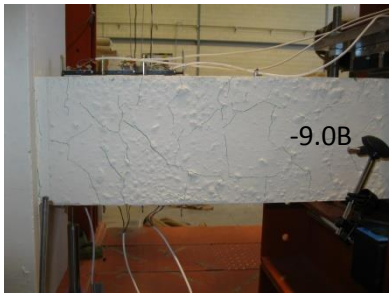

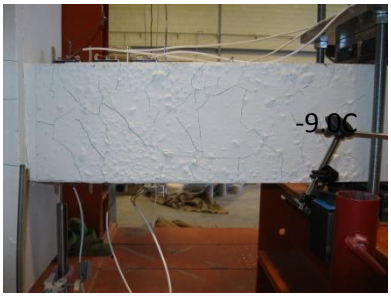

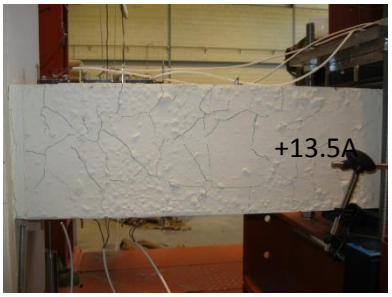
+13.5A

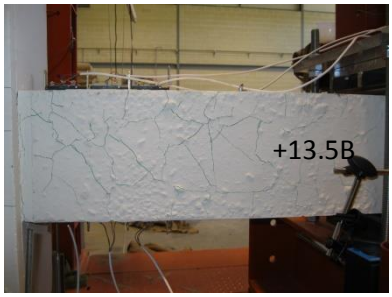
+13.5B

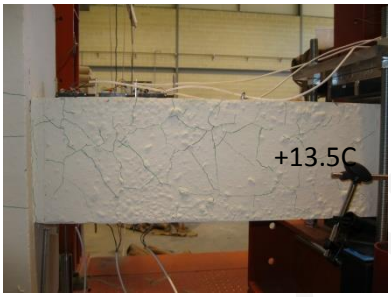
+13.5C

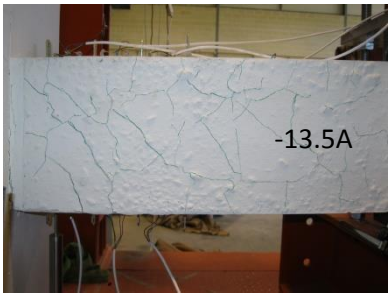
-13.5A

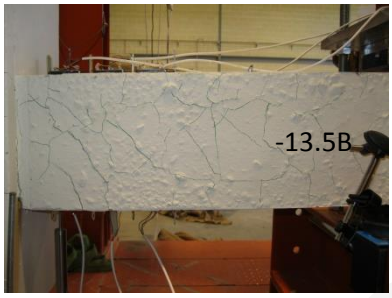
-13.5B

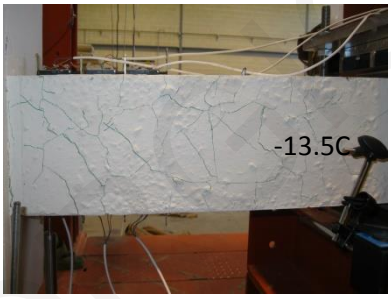
-13.5C

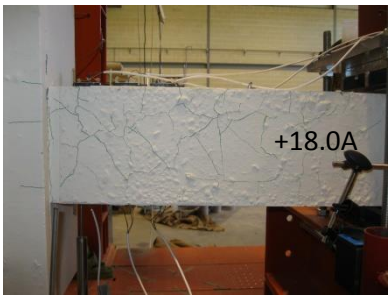
+18.0A

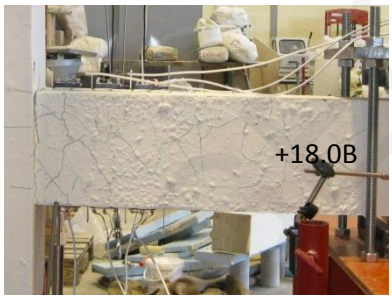
+18.0B

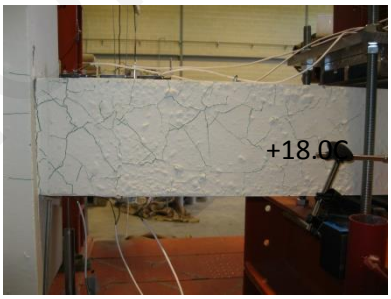
+18.0C

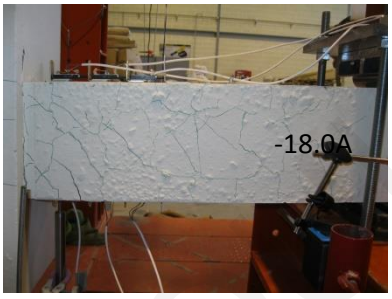
-18.0A

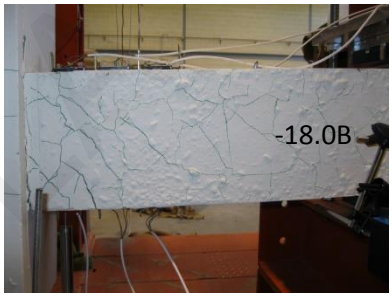
-18.0B

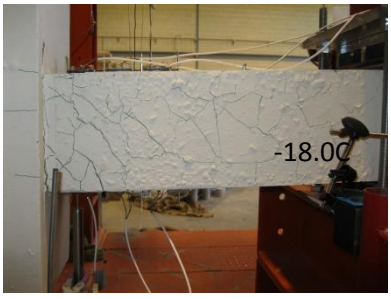
-18.0C

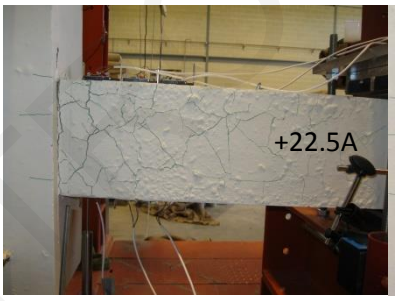
+22.5A


-22.5A

APPENDIX 10.B-SHFRCC Specimen

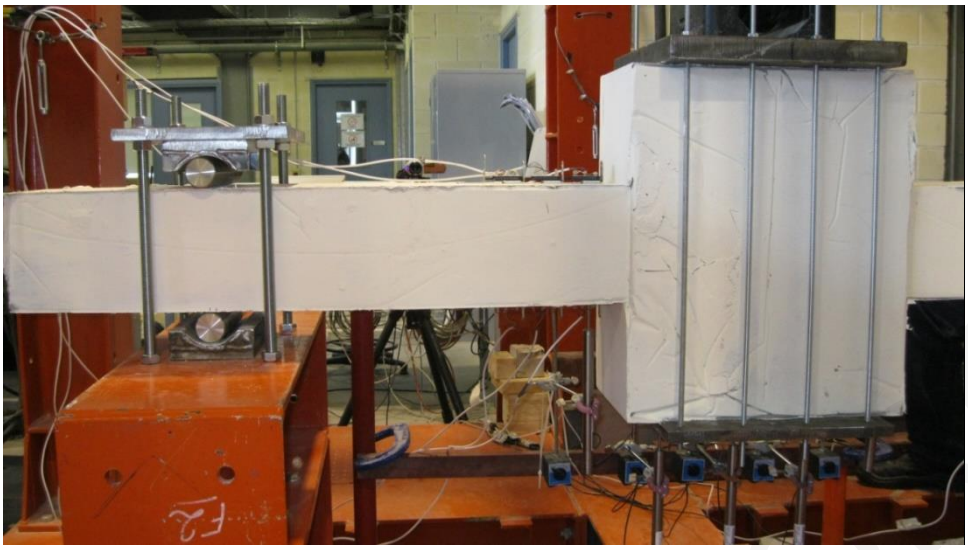

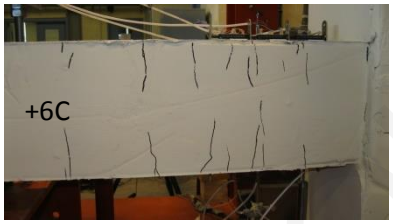

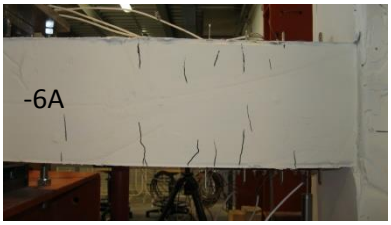

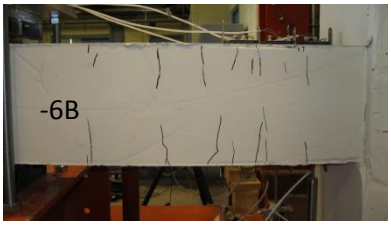

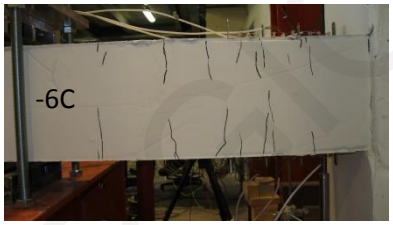

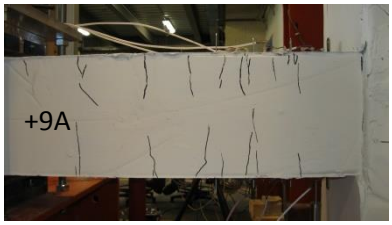

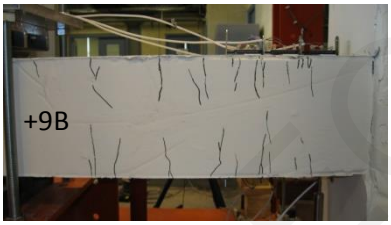

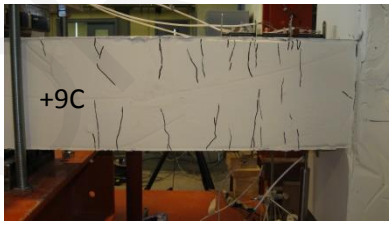

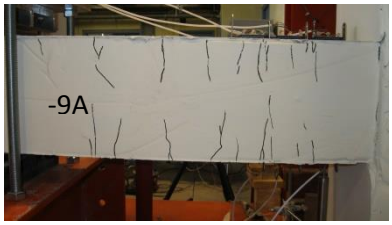

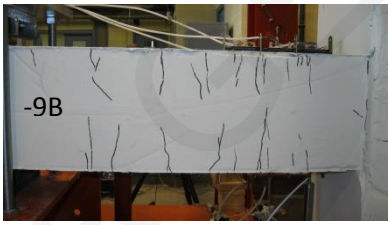

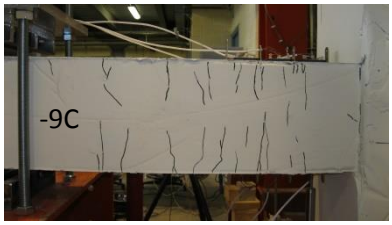

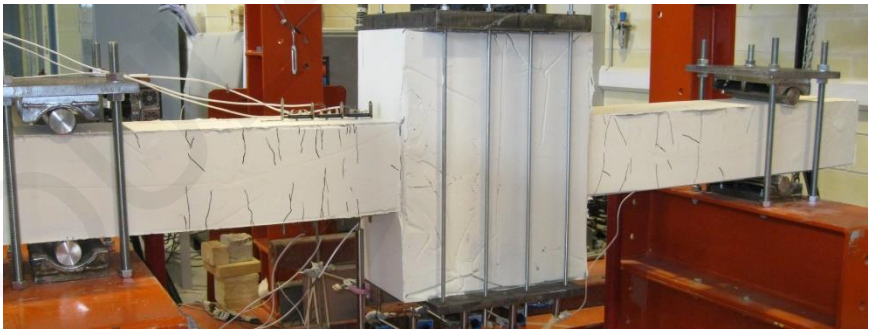

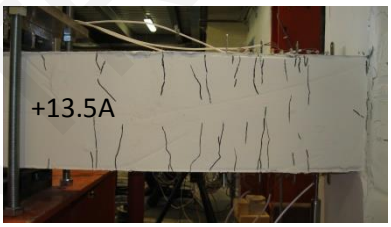

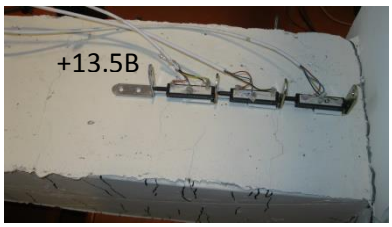

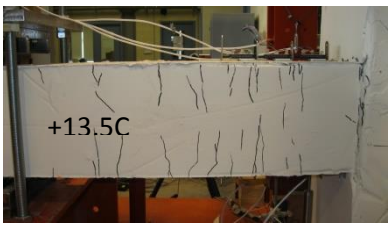

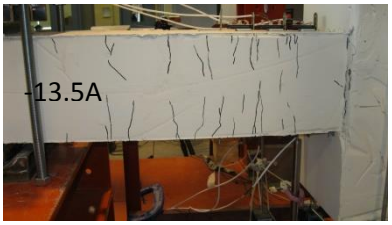
-13.5A

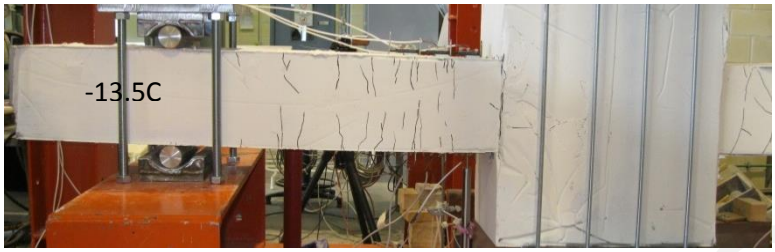
-13.5C

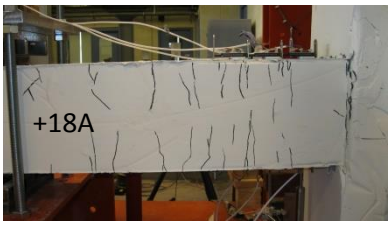
+18A

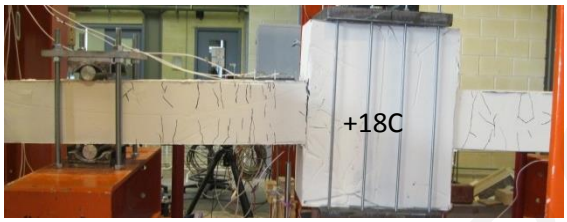
+18C

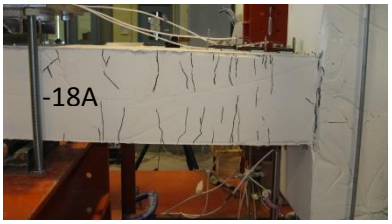
-18A


-18C

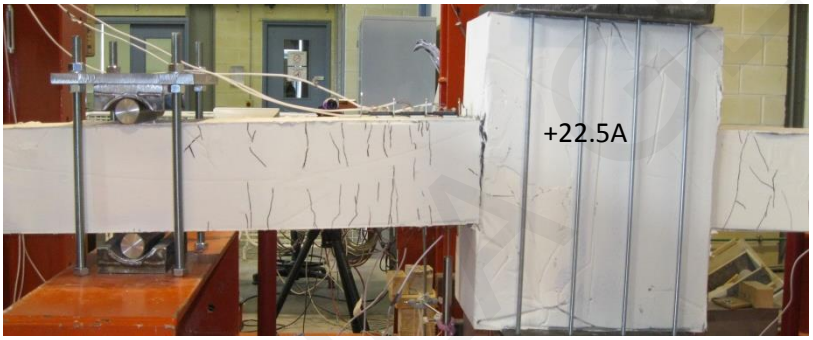
+22.5A


+22.5A


+22.5B


-22.5A


-22.5A


-22.5C